AUG 1 9 19[illegible]
MF-08304-N
387

NAS 1.55:3040

NASA Conference Publication 3040

Earth Science Geostationary Platform Technology

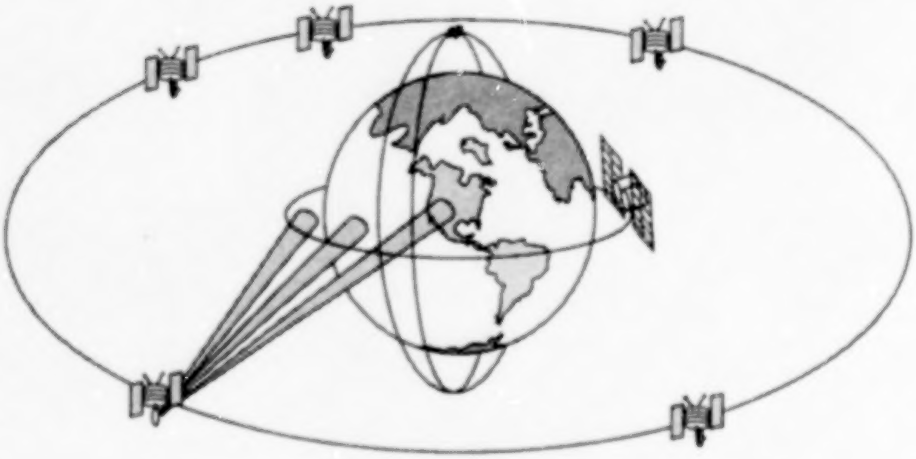

Proceedings of a workshop held at
NASA Langley Research Center
Hampton, Virginia
September 21-22, 1988

NASA

NASA Conference Publication 3040

Earth Science Geostationary Platform Technology

Edited by
Robert L. Wright
and Thomas G. Campbell
Langley Research Center
Hampton, Virginia

Proceedings of a workshop sponsored by the
National Aeronautics and Space Administration,
Washington, D.C., and held at
NASA Langley Research Center
Hampton, Virginia
September 21-22, 1988

NASA
National Aeronautics and
Space Administration
Office of Management
Scientific and Technical
Information Division
1989

I

PREFACE

The National Aeronautics and Space Administration (NASA) is actively involved in a Mission to Planet Earth initiative, as described in the Ride report (Leadership and America's Future in Space), to better understand our home planet. One phase of that initiative is the establishment and maintenance of a global observation system in space to perform integrated, long-term measurements of Earth sciences processes. The Earth Sciences Geostationary Platform (ESGP) is one of the candidate systems of the Mission to Planet Earth initiative.

A technology workshop for Earth Science Geostationary Platforms was held at the NASA Langley Research Center on September 21-22, 1988 to address problems in science and four technology areas related to the ESGP mission. The technology areas include: large space antenna, microwave sensors, electromagnetics-phased array adaptive systems, and optical metrology. The objective of the workshop was to review the applicability and readiness of the science and technologies for the Earth Science Geostationary Platform and to identify areas requiring additional technology development to meet the scientific requirements proposed for the mission. In addition, a technology development plan was formulated to address the technology needs identified.

Robert L. Wright
Thomas G. Campbell
NASA Langley Research Center

CONTENTS

PREFACE iii

ATTENDEES ix

WORKSHOP COMMITTEE xiii

KEYNOTE PRESENTATIONS

INTRODUCTORY REMARKS 3
Martin Sokoloski

INTRODUCTORY REMARKS 11
James Dodge

OPERATIONAL REQUIREMENTS AND THE GEOSTATIONARY PLATFORM 29
James K. Sparkman, Jr.

SCIENCE

SCIENCE REQUIREMENTS FOR PASSIVE MICROWAVE SENSORS ON EARTH SCIENCE GEOSTATIONARY PLATFORMS 37
A. J. Gasiewski and D. H. Staelin

GEOSTATIONARY EARTH SCIENCE PLATFORM CONCEPTS 55
M. M. Herardian

LARGE SPACE ANTENNA TECHNOLOGY
Session Chairman: Allan W. Love
Rockwell International

LARGE SPACE ANTENNA CONCEPTS FOR ESGP 65
Allan W. Love

LARGE-DIAMETER GEOSTATIONARY MILLIMETER WAVELENGTH ANTENNA CONCEPT 69
W. S. Gregorwich, H. A. Malliot, and A. K. Sinha

DESIGN OF A LOW-FREQUENCY (5-20 GHz), 15-METER-DIAMETER PASSIVE RADIOMETER FOR GEOSTATIONARY EARTH SCIENCE PLATFORMS 83
A. K. Sinha

STRUCTURES FOR REMOTELY DEPLOYABLE PRECISION ANTENNAS 109
J. M. Hedgepeth

UNFURLABLE, CONTINUOUS-SURFACE REFLECTOR CONCEPT 129
J. E. Stumm and S. Kulick

ADVANCES IN LARGE INFLATABLE REFLECTORS 137
M. Thomas and G. Williams

MICROWAVE SENSOR TECHNOLOGY
Session Chairman: Calvin T. Swift
University of Massachusetts

COHERENT RADAR MEASUREMENT OF OCEAN CURRENTS FROM GEOSTATIONARY ORBIT 155
R. E. McIntosh

MILLIMETER RADIOMETER SYSTEM TECHNOLOGY 167
W. J. Wilson and P. N. Swanson

SYNTHETIC APERTURE INTERFEROMETRIC RADIOMETER (SAIR) 179
C. S. Ruf

RAIN RADARS FOR EARTH SCIENCE GEOSTATIONARY PLATFORMS: SOME POSSIBILITIES 191
S. P. Gogineni and R. K. Moore

ELECTROMAGNETICS - PHASED ARRAY ADAPTIVE SYSTEMS TECHNOLOGY
Session Chairman: Y. Rahmat-Samii
Jet Propulsion Laboratory

LARGE ANTENNA MEASUREMENT AND COMPENSATION TECHNIQUES 203
Y. Rahmat-Samii

A COMPARISON OF REFLECTOR ANTENNA DESIGNS FOR WIDE-ANGLE SCANNING 217
M. Zimmerman, S. W. Lee, B. Houshmand, Y. Rahmat-Samii, and R. J. Acosta

ARRAYS FOR SPACE APPLICATIONS 241
Harvey K. Schuman, Paul Antonik, and Carmen Malagisi

CONJUGATE FIELD APPROACHES FOR ACTIVE ARRAY COMPENSATION 265
R. J. Acosta

REFLECTOR SURFACE DISTORTION ANALYSIS TECHNIQUES (THERMAL DISTORTION ANALYSIS OF ANTENNAS IN SPACE) 273
R. Sharp, M. Liao, J. Giriunas, J. Heighway, A. Lagin, and R. Steinbach

MESH SURFACES FOR REFLECTOR APPLICATIONS 295
Frank Kauffman

ANTENNAS FOR 20/30 GHz AND BEYOND 313
C. Harry Chen, William C. Wong, and S. Jim Hamada

OPTICAL METROLOGY TECHNOLOGY
Session Chairwoman: Sharon LaFleur
NASA Langley Research Center

APPLICATIONS OF FM-CW LASER RADAR TO ANTENNA CONTOUR MAPPING 331
A. R. Slotwinski

REMOTE ATTITUDE MEASUREMENT SENSOR (RAMS) 339
H. W. Davis

PRECISION SEGMENTED REFLECTOR, FIGURE VERIFICATION SENSOR 369
Paul K. Manhart and Steve A. Macenka

TECHNOLOGY PANEL REPORTS

REPORT OF THE SCIENCE PANEL 377
A. J. Gasiewski

REPORT OF THE LARGE SPACE ANTENNA TECHNOLOGY AND ELECTROMAGNETICS - PHASED ARRAY ADAPTIVE SYSTEMS TECHNOLOGY PANELS 379
Allan W. Love and Y. Rahmat-Samii

REPORT OF THE MICROWAVE SENSOR TECHNOLOGY PANEL 381
Calvin T. Swift

REPORT OF THE OPTICAL METROLOGY TECHNOLOGY PANEL 385
Sharon LaFleur

SUMMARY OF QUESTIONNAIRE RESPONSES 387

CONCLUDING REMARKS

CONCLUDING REMARKS
Martin Sokoloski 395

James Dodge 397

ATTENDEES

M. C. Bailey
NASA Langley
Hampton, VA

Richard A. Birch
GE - Astro
Philadelphia, PA

J. Ernest Blair
Harris Government Aerospace Systems Div.
Melbourne, FL

Hans-Juergen C. Blume
NASA Langley
Hampton, VA

Arthur F. Boland
Industrial Activities Office, OASD
Alexandria, VA

Jim A. Boyd
Harris Corporation
Government Aerospace Systems
Melbourne, FL

Jim Breckinridge
Jet Propulsion Laboratory
Pasadena, CA

John Butler
NASA MSFC
Huntsville, AL

Thomas G. Campbell
NASA Langley
Hampton, VA

Robert Chandler
Digital Optics
Lancaster, PA

Stanley Chang
Space and Communications Group
Hughes Aircraft Co.
Los Angeles, CA

C. Harry Chen
TRW
Antenna Systems Lab
Redondo Beach, CA

Hsi Chen
Ford Aerospace
Reston, VA

J. L. Christian, Jr.
NASA LeRC
Cleveland, OH

John C. Cleary
USAF RADC/OCDS
Griffiss AFB, NY

Denis Connolly
NASA LeRC
Cleveland, OH

Hugh W. Davis
Ball Aerospace Systems Group
Boulder, CO

Cris Deros
TRW
Redondo Beach, CA

Carmine E. DeSanctis
NASA MSFC
Huntsville, AL

John E. Dixson
Ford Aerospace Corporation
Palo Alto, CA

James Dodge
NASA Headquarters
Washington, DC

Bill Duff
Atlantic Research Service Corporation
Alexandria, VA

Vincent Falcone
Air Force Geophysics Lab/LYS
Hanscom Air Force Base, MA

Jeff T. Farmer
NASA Langley
Hampton, VA

John Fedors
NASA Langley
Hampton, VA

L. Bernard Garrett
NASA Langley
Hampton, VA

A. J. Gasiewski
Massachusetts Institute of Technology
Cambridge, MA

S. P. Gogineni
University of Kansas
Lawrence, KS

William L. Grantham
NASA Langley
Hampton, VA

W. S. Gregorwich
Lockheed Missiles & Space Company, Inc.
Palo Alto, CA

Hussain A. Haddad
Ball Communication Systems Division
Broomfield, CO

Dr. John M. Hedgepeth
Astro Aerospace Corporation
Carpinteria, CA

M. M. Herardian
Lockheed Missiles & Space Company, Inc.
Sunnyvale, CA

Travis Hill
TRW
Redondo Beach, CA

Edward Hinson
NASA Langley
Hampton, VA

Larry Holak
Harris Corp. GASD
Melbourne, FL

Gary Jedlovec
NASA MSFC
Huntsville, AL

Gordon Johnston
NASA Headquarters
Washington, DC

Frank Kauffman
N. C. State University
Raleigh, NC

Vernon Keller
NASA MSFC
Huntsville, AL

Bruce M. Kendall
NASA Langley
Hampton, VA

Bob Kenimer
NASA Langley (Ret.)
Hampton, VA

Wilbur A. Kuipers
Astro Aerospace Corporation
Carpinteria, CA

Shel Kulick
Composite Optics
San Diego, CA

Sharon LaFleur
NASA LaRC
Hampton, VA

Shung-Wu (Andy) Lee
University of Illinois C-U
Electromagnetics Lab
Urbana, IL

Allan W. Love
Rockwell International
Satellite & Space Electronics Division
Seal Beach, CA

Steve Macenka
Jet Propulsion Laboratory
Pasadena, CA

Susan A. MacKeen
Ford Aerospace Corporation
Reston, VA

Carmen S. Malagisi
Atlantic Research Services Corporation
Rome, NY

Robert McIntosh
University of Massachusetts
Amherst, MA

Karl J. Moeller
NASA Langley
Hampton, VA

Gary S. Parks
Jet Propulsion Laboratory
Pasadena, CA

Garry D. Qualls
NASA Langley
Hampton, VA

Yahya Rahmat-Samii
Jet Propulsion Laboratory
Pasadena, CA

Charles A. Raquet
NASA Lewis
Cleveland, OH

Gabriel M. Rebeiz
University of Michigan
Ann Arbor, MI

Samuel Reynolds
Hughes Aircraft Co.
Los Angeles, CA

Larry Rowell
NASA Langley
Hampton, VA

Dr. Christopher S. Ruf
Jet Propulsion Laboratory
Pasadena, CA

Lyle C. Schroeder
NASA Langley
Hampton, VA

W. C. Scott
Aerojet ElectroSystems Co.
Washington, DC

G. Richard Sharp
NASA Lewis
Cleveland, OH

John W. Sherman, III
NOAA/NESDIS/ORA
Washington, DC

James Shiue
NASA Goddard
Greenbelt, MD

Dr. A. K. Sinha
Lockheed Missiles & Space Company, Inc.
Sunnyvale, CA

Anthony Slotwinski
Digital Signal
Springfield, VA

William T. Smith
Virginia Tech
Blacksburg, VA

Martin Sokoloski
NASA Headquarters
Washington, DC

James Sparkman
NOAA, NESDIS, E/OSD-1
Washington, DC

Roy Spencer
NASA MSFC
Huntsville, AL

Warren Stutzman
Virginia Tech
Blacksburg, VA

Dr. Paul N. Swanson
Jet Propulsion Laboratory
Pasadena, CA

Calvin T. Swift
Department of Electrical & Computer Eng.
Amherst, MA

Charles B. Sykes
Atlantic Research Services Corporation
Rome, NY

Israel Taback
The Bionetics Corp.
Hampton, VA

Tadashi Takano
Jet Propulsion Laboratory
Pasadena, CA

Dr. Bill C. Tankersley
Harris Government Aerospace Systems Div.
Melbourne, FL

R. J. Trew
North Carolina State University
Raleigh, NC

Stephen S. Tompkins
NASA Langley
Hampton, VA

Geoffrey T. Williams
L'Garde, Inc.
Tustin, CA

Greg Wilson
NASA MSFC
Huntsville, AL

Dr. William J. Wilson
Jet Propulsion Laboratory
Pasadena, CA

Robert Wright
NASA Langley
Hampton, VA

J. Allen Zak
NASA Langley
Hampton, VA

Martin L. Zimmerman
University of Illinois C-U
Electromagnetics Lab
Urbana, IL

WORKSHOP COMMITTEE

General Chairmen

Chairman

Dr. Martin Sokoloski
Information Sciences and Human Factors Division
NASA - Office of Aeronautics and Space Technology

Co-Chairman

Dr. James Dodge
Mesoscale Atmospheric Research
NASA - Office of Space Sciences and Applications

Technical Program Chairman

Thomas G. Campbell
Head, Antenna and Microwave Research Branch
Guidance and Control Division
NASA - Langley Research Center

Administrative Chairman

Robert L. Wright
NASA - Langley Research Center

Workshop Administrative Assistant

Deborah L. Sullivan
NASA - Langley Research Center

ESGP - Technical Panel Chairpersons

Dave Staelin, MIT, Science
Roy Spencer, MSFC, Science
A.J. Gasiewski, MIT, Science
Calvin T. Swift, Univ. of Mass., Microwave Sensor Technology
Allan Love, North American Rockwell, Large Space Antenna Technology
Yahya Rahmat-Samii, Jet Propulsion Laboratory, Electromagnetics - Adaptive Array Technology
Sharon LaFleur, NASA - Langley Research Center, Optical Metrology Technology

Keynote Presentations

E
S
G
P

INTRODUCTORY REMARKS

Martin Sokoloski
Information Sciences and Human Factors Division
NASA Office of Aeronautics and Space Technology

FAR-TERM GOALS OF EARTH SYSTEM SCIENCE

The far-term goals of Earth System Science are given in figure 1. NASA's Office of Space Science and Application (OSSA) is responsible for Earth observation, astrophysics, solar physics and other science missions, while the Office of Aeronautics and Space Technology (OAST) is responsible for most of the research, development and technology in the space arena. To assist in accomplishing these goals, OAST has pushed forward a new initiative, called the "Civil Space Technology Initiative (CSTI)," which supports a host of science missions including the Earth Observation System (EOS) mission and the Earth Science Geostationary Platform (ESGP) "Mission to Planet Earth."

FAR TERM: 1995 AND BEYOND

- INTEGRATED GLOBAL OBSERVATIONS OF EARTH
- INFORMATION SYSTEM FOR EARTH SYSTEM SCIENCE
- SUSTAINED SUPPORT BY FEDERAL AGENCIES

Figure 1

THE CHALLENGE

Establishment of the goal of obtaining a scientific understanding of the entire Earth system on a global scale presents the challenge shown in figure 2. One of the major objectives of this workshop is to define the enabling technologies that must be developed to meet that challenge relative to the ESGP "Mission to Planet Earth" and specifically involving radiometric instruments.

THE GOAL

TO OBTAIN A SCIENTIFIC UNDERSTANDING
OF THE ENTIRE EARTH SYSTEM
ON A GLOBAL SCALE

THE CHALLENGE

TO DEVELOP THE CAPABILITY TO PREDICT
THOSE CHANGES THAT WILL OCCUR IN THE
NEXT DECADE TO CENTURY

Figure 2

GLOBAL CHANGE TECHNOLOGY DEVELOPMENT

The development scheme for global change technology for the geostationary platform is shown in figure 3. The objectives and characteristics of the platform are presented on the left and the required enabling technologies are shown on the right. The ESGP mission will concentrate on the optics and sensors and the geo-structures for these large postulated radiometric structures. The technology readiness dates for these technologies are in the late 1990's.

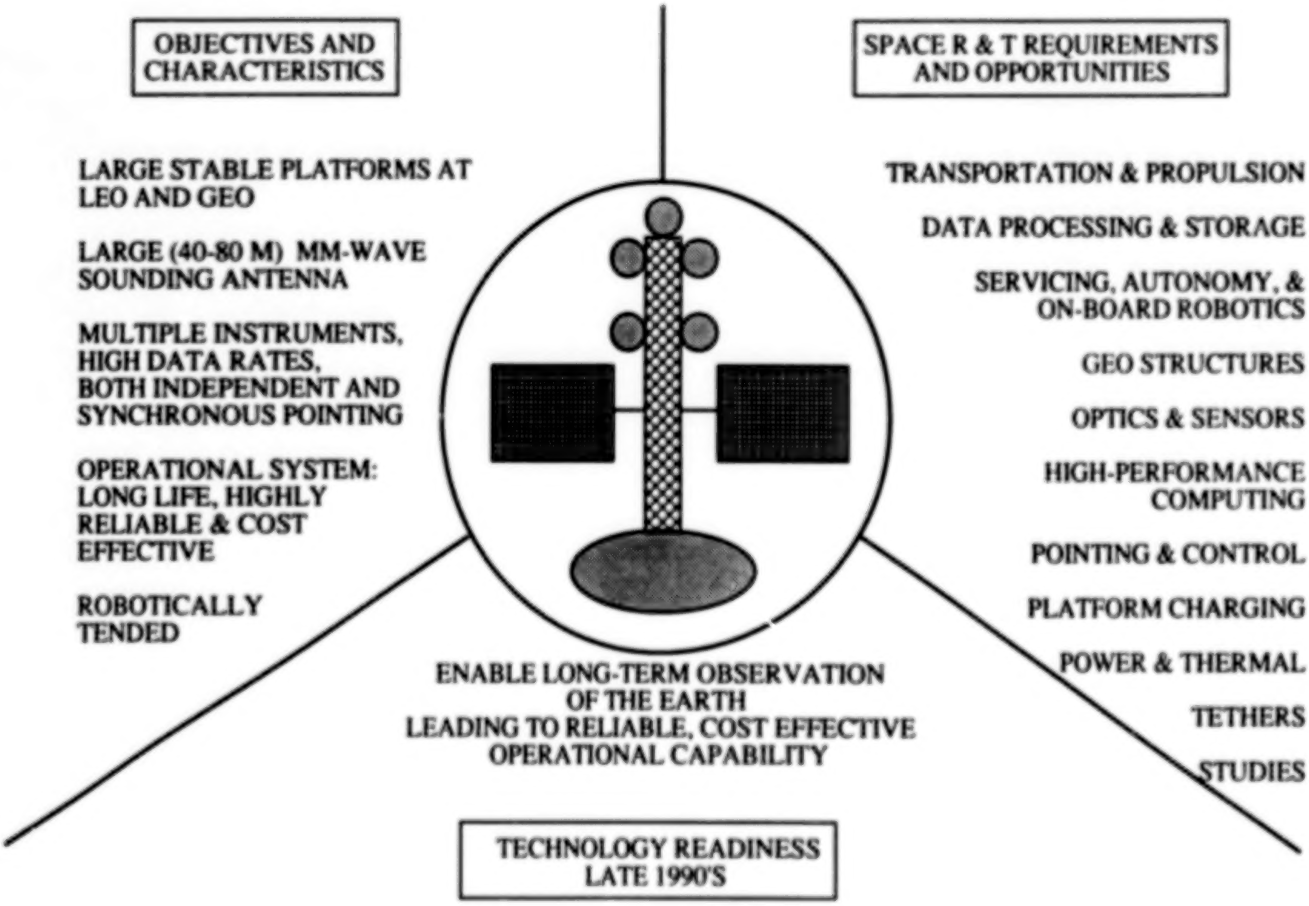
OBJECTIVES AND CHARACTERISTICS
LARGE STABLE PLATFORMS AT LEO AND GEO
LARGE (40-80 M) MM-WAVE SOUNDING ANTENNA
MULTIPLE INSTRUMENTS, HIGH DATA RATES, BOTH INDEPENDENT AND SYNCHRONOUS POINTING
OPERATIONAL SYSTEM: LONG LIFE, HIGHLY RELIABLE & COST EFFECTIVE
ROBOTICALLY TENDED
SPACE R & T REQUIREMENTS AND OPPORTUNITIES
TRANSPORTATION & PROPULSION
DATA PROCESSING & STORAGE
SERVICING, AUTONOMY, & ON-BOARD ROBOTICS
GEO STRUCTURES
OPTICS & SENSORS
HIGH-PERFORMANCE COMPUTING
POINTING & CONTROL
PLATFORM CHARGING
POWER & THERMAL
TETHERS
STUDIES
ENABLE LONG-TERM OBSERVATION OF THE EARTH LEADING TO RELIABLE, COST EFFECTIVE OPERATIONAL CAPABILITY
TECHNOLOGY READINESS LATE 1990'S

Figure 3

NEAR-TERM TIME LINE

To meet the technology readiness dates of the late 1990's, it is necessary to conduct studies now (1988-89 time frame) to determine what technology will impact the global change technology (fig. 4). Then, the strategy is to go forward with a new initiative in the 1990 time frame. If the initiative can be successfully included in the President's budget, then, hopefully, a focused technology program can be started in the 1991 time frame. This workshop is therefore exceedingly important in providing the necessary information to develop this initiative.

- CONDUCT STUDIES IN FY 1988-89
- SPACE R & T BASE REINVESTMENT IN FY 1990
- FOCUSED TECHNOLOGY PROGRAM IN FY 1991

Figure 4

GLOBAL CHANGE TECHNOLOGY INITIATIVES

Some of the global change technology initiatives are shown in figure 5. There will be some synergy between some of these efforts, such as the large space structures work in the Materials and Structures Division and the sensors, optics, material and modeling work in the Information Sciences Division. A more detailed look at some of the requirements in the On-board Robotics/Servicing and Propulsion areas is shown in figure 6.

CONDUCT STUDIES IN FY 1988-89

- SSTAC AD HOC STUDY
- SYSTEMS ANALYSIS STUDIES
- REFINE AND DEVELOP FOCUSED PROGRAM PLANNING

SPACE R & T BASE REINVESTMENT IN FY 1990

- BASIC/GENERIC RESEARCH IN TECHNOLOGIES THAT SUPPORT EARTH OBSERVATION MISSIONS
- FUNDAMENTAL KNOWLEDGE NECESSARY TO PURSUE FOCUSED GLOBAL CHANGE TECHNOLOGY INITIATIVE
- CONTINUED ENHANCED STUDIES EFFORT
  ROLL-IN FUNDING FROM IN-SPACE EXPERIMENTS

FOCUSED TECHNOLOGY PROGRAM IN FY 1991

SPACE R & T BASE REINVESTMENT EXAMPLES

- ● SPACE ENERGY CONVERSION
    - -POWER AUTOMATION
    - -THERMAL CONTROL APPROACHES (HEAT PIPE MATERIALS, COOLER OPTIONS, ETC.)
- ● PROPULSION
    - -PROPULSION REQUIREMENTS/CONTAMINATION
- ● MATERIALS AND STRUCTURES
    - -TETHER MATERIALS AND REQUIREMENTS
- ● SPACE DATA AND COMMUNICATIONS
    - -NEURAL NETWORK RESEARCH
- ● INFORMATION SCIENCES
    - -SENSORS/OPTICS MATERIALS AND MODELING
- ● CONTROLS AND GUIDANCE
    - -POINTING AND VIBRATION ISOLATION OPTIONS
- ● SYSTEMS ANALYSIS
    - -ENVIRONMENTAL INTERACTIONS MODELING (CONTAMINATION, CHARGING, MICROMETEOR)
    - -SERVICING OPTIONS AND APPROACHES

Figure 5

ON-BOARD ROBOTICS/SERVICING

R & T PROGRAM SCOPE:

DEVELOP TECHNOLOGY CAPABILITY FOR ON-BOARD ROBOTIC MAINTENANCE, AND COORDINATED OPERATION WITH FREE FLYING TELEROBOTIC SERVICER

ENABLE:

LONG-TERM OPERATION OF GEOSYNCHRONOUS AND OTHER PLATFORMS

SIGNIFICANCE:

LONG-TERM PLATFORM OPERATION, SELF MAINTENANCE, AND COOPERATIVE WORK WITH TELEROBOTIC SERVICER

TECHNICAL ISSUES:

- SUBSYSTEM AUTOMATION AND SYSTEM LEVEL INTEGRATION
- PLATFORM ROBOTIC MOBILITY AND INTERFACE WITH SUBSYSTEM MODULES
- DEFINITION OF INTERFACE WITH TELEROBOTIC SERVICER
- SERVICING OF ACTIVELY AND CRYOGENICALLY COOLED SYSTEMS

BUDGET:

	FY90	FY91	FY92	FY93	FY94	FY95
$M		6	12	18	18	18

PROPULSION

R & T PROGRAM SCOPE:

DEVELOP LONG-LIFE, HIGH SPECIFIC IMPULSE, LOW CONTAMINATION PROPULSION SYSTEMS

ENABLE:

LONG-TERM RELIABLE PROPULSION SYSTEM FOR ORBIT TRANSFER, ORBIT MANEUVERING AND STATIONKEEPING, WITH MINIMUM CONTAMINATION AND RESUPPLY REQUIREMENT

SIGNIFICANCE:

PROPELLANT RESUPPLY AND LIFE OF THE PROPULSION SYSTEM ARE MAJOR DRIVERS IN THE LIFE AND OPERATING COST OF PLATFORMS

SENSITIVE LONG-TERM MEASUREMENTS OF GLOBAL CLIMATE CHANGE COULD BE COMPROMISED BY THE BUILDUP OF CONTAMINANTS ON SENSORS AND OPTICS

TECHNICAL ISSUES:

DEFINITION OF PROPULSION SYSTEM REQUIREMENTS AND TRADEOFFS FOR ORBIT TRANSFER, ORBIT MAINTENANCE AND ORBIT MANEUVERING

HIGH-PERFORMANCE, HIGH SPECIFIC IMPULSE, LOW CONTAMINATION, AND RELIABLE PROPULSION SYSTEM OPTIONS

BUDGET:

	FY90	FY91	FY92	FY93	FY94	FY95
$M		4	9	13	13	13

Figure 6

CONCLUDING REMARKS

One major objective of this workshop is to define the enabling technologies that are out in the fringes and must be developed to maximize the science return and satisfy the harsh science requirements projected by the OSSA for the geostationary platform (ESGP) mission.

INTRODUCTORY REMARKS

James Dodge
Mesoscale Atmospheric Research
NASA Office of Space Sciences and Applications

INTRODUCTION

There is insufficient time to present all of the logic of the Geostationary Platform Science Working Group, so I'll give a kaleidoscope of the plans for the Earth Science Geostationary Platform mission (fig. 1). This presentation will include why we need geostationary platforms, the guidelines that were derived from the science requirements, near- and far-term platform configurations, technology and programs studies that are required, and programmatics. Although most of the instruments have not as yet been designed, a straw man set of instruments developed by scientists from a number of disciplines will be presented.

- The role of GEO platforms in Earth system science
- Guidelines for platform development
- Straw man instrument set
- Sample data images
- Realistic platform configurations
- Expendable launch vehicles (ELV)
- Technology and program studies required
- Programmatics

Figure 1

THE ROLE OF GEOSTATIONARY PLATFORMS

The four Earth Orbiting System (EOS) polar platforms (two US, one from Japan and one from ESSA) with 40 to 45 sensors on them will produce 100 megabits per second per platform for 20 years. With this vast wealth of data, what is the role of the geostationary platform (fig. 2)? Polar orbiters cannot study processes that occur on a short time scale. The polar orbiters pass over a particular point only several times per day per platform. Although they provide a snapshot at that particular time, they do not see rapidly varying phenomena, things that vary continuously throughout the day. Because the polar orbiter passes over at the same time each day, the effects of varying solar angles cannot be determined.

The continuous view from the geostationary platform can provide a perspective of the diurnal processes and short-term (random) variations that are needed for accurate physical modeling and/or parameterization in global models.

- Geostationary observations provide physical understanding of diurnal processes and short-term variations
    - Observe complete diurnal cycle without aliasing
    - Observe rapidly varying phenomena
    - Observe simultaneous observations over large areas

- New short-term processes must be understood to enable accurate physical modeling and / or parameterization in global models

Figure 2

PHYSICAL EFFECTS REQUIRING GEO

A number of physical effects require continuous (ie, GEO platform) viewing (fig. 3). Sun angle variations, temperature, and moisture cycling during the day (from dew in the morning to the hot afternoon) make a great deal of difference on the observation of vegetation stress. A single snapshot even at high resolution doesn't help unless there are frequent observations to study the diurnal effects. Then, these effects can be interjected into the numerical models with the polar orbiting data to project longer term variations, such as decades to centuries.

Other parameters that can be detected from geostationary orbit include ozone and sulfur dioxide levels, lightning occurrences, minor atmospheric constituents, and ecosystem evolution. Many of these parameters will be difficult to detect, but they are of great scientific interest.

- Sun - angle variations
- Diurnal temperature and moisture cycle effects
- Soil moisture estimation from surface temperature change
- Rapid phytoplankton blooms and sediment loading
- Ozone and sulfur dioxide transport
- Lightning occurrences
- Minor atmospheric constituent source detection
- Diurnal ecosystem evolution
- Atmospheric water vapor effect correction

Figure 3

WHAT CAN'T BE OBSERVED FROM POLAR EOS?

Although the polar EOS will make snapshot measurements of many important parameters, it will not be able to measure the diurnal variations of parameters such as those shown in figure 4. Also, polar observations cannot obtain adequate statistical samplings of events such as lightning and volcanic activity that occur infrequently, stochastically.

Data in the visible and infrared ranges from the NOAA GEOS spacecraft of hurricane Gilbert just before it hit Jamaica on September 12, 1988 provided estimates of cloud height, cloud coverage and winds. (These estimates would have been impossible from the polar EOS). Advanced sounders will permit temperature and moisture variations with height over the entire optical disk approximately every 15 minutes. An imager in geostationary orbit will monitor other spectral bands. With the appropriate resolution in the appropriate band, time evolution studies of water vapor, ozone gradients, vegetation color, smog and dust storms are possible.

Diurnal Variations of

- Precipitation
- Atmospheric water vapor
- Vegetation color
- Terrestrial ecosystems
- Air / land energy fluxes
- Tropospheric pollutant generation and motion
- Smog dynamics
- Dust storms
- Surface emissivity
- Ocean color - productivity
- Total ozone gradients and cut-off maxima

Occurrences of

- Lightning discharges
- Volcano initiation

Figure 4

RESOLUTION

Resolution from the polar EOS is in the 2-km to 8-km range. But the scientists want resolution in the 10's of meters range. There are observations of surface temperature taken from NASA's high-altitude aircraft (U2 and ER2) using the MANS sensor (a device like the thematic mapper with various bands that have been augmented in chains so that both water vapor and fine scale water vapor can be detected) that meet these resolution criteria. The instrument provides high-resolution surface temperatures showing mountains and rivers as well as sea surface temperatures. These data are important because measurements from current meteorological satellites are too coarse to study vegetation changes. With a new spectrometer with higher resolution in geostationary orbit, observations like those from the high-altitude aircraft are possible. The difficult thing to accomplish to get these high resolutions is spacecraft stability. The pointing stability required for this resolution (10's of meters) is approximately 1/10,000 degrees from geostationary orbit.

Considering both near-term and far-term geostationary platforms, the high-resolution measurements may have to wait for the more advanced, second generation platform to achieve this level of pointing accuracy.

LIGHTNING MAPPER

Such a transient phenomenon as lightning only lasts from 20 - 30 milliseconds. To capture this event, the sensor must be stationary and look continuously at the Earth. A momentary blink of the eye will miss the event. The current sensor design has a refresh rate of about 1 millisecond. The sensor maps for a millisecond, then refreshes for a millisecond and maps for another millisecond. This ensures measuring all the lightning events that occur.

NEEDS LIST

The Science Steering Committee has met 5 times and plans to meet again in October of 1988 in Durham, New Hampshire. From its previous meetings, the Science Steering Committee has developed a needs list of instruments that can provide significant data from geostationary orbit. The needs list is presented in figure 5, in order of descending priority.

- Moderate resolution imaging spectrometer (GEOMODIS)
- Infared vertical sounder - spectrometer
- High-frequency passive microwave image sounder
- Ozone mapper (GEOOMS)
- Lightning mapper
- Earth radiation budget (climate radiation radiometer)
- Solar package (solar spectrometer, active cavity radiometer, x-ray images)
- High-resolution imaging spectrometer (GEOHIRIS)
- Low-frequency passive microwave image
- Laser ranges
- Data collection system
- Space environment monitor

Figure 5

NASA HEADQUARTERS GUIDELINES FOR ESGP

The full needs list in figure 5 is obviously unrealistic. In addition to being unbelievable at the higher levels of management, it is also too expensive. It became necessary to constrain it to something that could be done. Therefore, NASA Headquarters developed a series of guidelines, as shown in figure 6. First, the observations should complement and overlap those from the EOS polar platform program. Without an overlap with the polar data (simultaneous observations), it will be difficult to interpret the polar data. Plans call for a near-term and a future design, instead of a single geostationary platform. The simplicity guideline will ensure reduced costs and improved schedule adherence. Some of the original designs were very sophisticated and complicated, and were not achievable.

- Observations should complement EOS platform program
  - Diurnal variability
  - Cloud-free opportunities
  - Key short-term variable
  - Targets of opportunity
  - Relay of EOS polar data product to researchers

- An overlap with the first NASA polar platform is required

- Plans should include both a near-term and a future design

- Simplicity will pay off in reduced cost and improved schedule adherence

Figure 6

PLATFORM ASSUMPTIONS

Based upon what could be observed from geostationary orbit and the needs for including data in numerical models, it makes sense to study the Earth as an integrated, interacting system. The assumptions for a near-term geostationary platform are given in figure 7. Facility instruments would be selected in much the same fashion as they were selected for the polar platform. Lessons from the GOES program dictated a return to basics and stressed some obvious problems:

1. Big systems with moving parts cause momentum fluctuations (use electrical solutions to minimize need for momentum compensation)
2. Thin structures can have thermal distortions
3. A very solid stable structure is needed (due to small angular tolerances)

Other countries and agencies must be provided an opportunity to install their sensors on the platform (on a non-interference basis). A real-time data system is a requirement. An Earth-observing satellite data information system (EOSDIS) is currently being planned, but it may not have the capacity required for the ESGP data, data delivery or data analysis.

- A key purpose of the near-term platform is research concerning physical processes related to the Earth interacting as a system
- Facility instruments will be chosen
- Where feasible designs will stress electronic rather than mechanical solutions to minimize need for momentum compensation
- Assume that formal opportunities will be provided for operational instrument prototype testing for other agencies and other countries
- Assume that opportunities will be provided for other NASA offices and / or commercial interests to use portions of the platform on a non-interference basis
- A real-time data delivery, interpretation and display system will be provided

Figure 7

GUIDELINES FOR NEAR-TERM ESGP

The guidelines that have been developed for the near-term Earth Sciences Geostationary Platform are listed in figure 8. The GEO Platform new start is targeted for FY 93 with the launch scheduled for FY 98. The future or far-term mission could be scheduled for a launch date as early as 2005, depending on how rapidly the technology can be developed. This will allow more time for the development of more sophisticated, longer term items such as the very large antenna and the high pointing accuracy and stability that will be required.

The guidelines also assume a substantial launch vehicle capability (Titan III) with a 2000 lb to 3000 lb payload capability, and a compact thermally compensated bus structure. Launch will be directly to geostationary orbit, and limited servicing options will be available.

- Target FY 93 geoplatform new start
- Assume FY 98 launch of near-term platform
- Assume directly to geostationary orbit
    - No stopping or assembly at LEO
- Assume substantial launch vehicle capability (Titan III equivalent)
- Assume compact thermally - compensated bus structure
    - 2000 to 3000 lb payload capability
- Assume limited servicing options
    - Unmanned
    - No de-orbit to LEO
    - No complicated on-board robots

Figure 8

NOAA SYSTEMS ON A GEOPLATFORM

The National Oceanographic and Atmospheric Administration (NOAA) has provided inputs of what they would like on a geoplatform. Recommended systems are listed in figure 9.

2 ea.	G-imagers	(GOES-I,-M*)
2 ea.	G-sounders	(GOES-I,-M*)
1 ea.	SEM package	
1 ea.	Solar X-ray imager (SXI)	
1 ea.	Data collection system (transponder)	
1 ea.	Search & rescue system (transponder)	
1 ea.	Imager broadcast system	
1 ea.	Sounder broadcast system	
1 ea.	WEFAX broadcast system	

Recommendations

Microwave sounder **	
Lightning mapper	
Solar constant inst.	(ACRIM type)
Earth rad. inst.	(ACRIM type)
Ocean color scanner	

* Probably modified to AMRIR-type dual-purpose instrument.

** Probably rated operational status.

Figure 9

STRAW MAN "FLATBED" INSTRUMENT LIST

Combining the original needs list from the Science Steering Committee (fig. 5) with the assumptions (fig. 7) and guidelines (fig. 8), a somewhat smaller straw man list of instruments is presented in figure 10. This list provides a more realistic approach to a "Flatbed" platform, assuming only one copy of each instrument.

1. Moderate resolution imaging spectrometer (GEOMODIS)
2. Michelson interferometer spectrometer
3. Lightning mapper
4. High-frequency passive microwave image / sounder
5. Ozone mapper (GEOOMS)
6. Climate radiation radiometer
7. Active gravity radiometer
8. Solar spectrometer
9. X-ray imager
10. High-resolution imaging spectrometer (GEOHIRIS)
11. Data collection system
12. Space environment monitor

Figure 10

TYPICAL ESGP DESIGN

A number of different design and packaging concepts have been explored, both in-house and by industry. A typical ESGP design is shown in figure 11. This concept uses a single copy of the instruments in the strawman list of figure 10, a 4.4-m microwave antenna, and solar panels mounted on moderately sized arms.

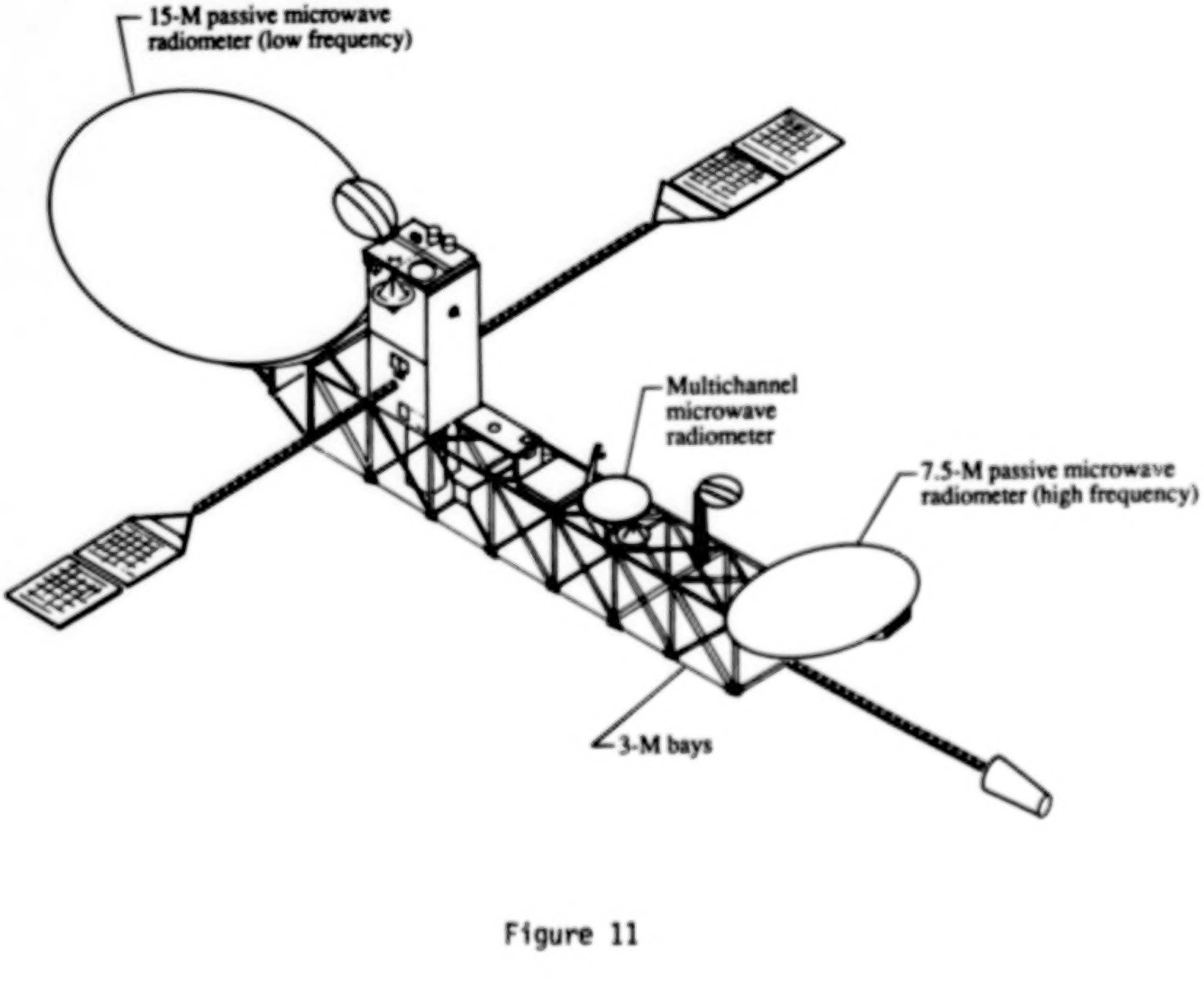
15-M passive microwave radiometer (low frequency)
Multichannel microwave radiometer
7.5-M passive microwave radiometer (high frequency)
3-M bays

Figure 11

FEASIBILITY STUDIES

Although this concept is relatively simple, a number of feasibility studies must be completed to support a launch in FY 99. These studies (fig. 12) include the use of facility instruments, commitments from other organizations, system designs, and launch vehicle and full system integrations. Funding has been requested for an FY 89 start on these studies and the viability of this concept will be known in the near future.

1. Facility instrument studies
2. Other agency, country, and commercial / instrument studies
3. Bus design, power system, and limited on-orbit augmentation
4. Launch vehicle integration
5. Data system (on-board, downlink and distribution) & EOS DIS compatibility
6. Platform command / control operations
7. Full system interactions

Figure 12

NEAR-TERM ESGP SCHEDULE

The schedule for the near-term ESGP mission is shown in figure 13. Currently under way are Science Steering Committee and Phase A feasibility studies. Once feasibility has been confirmed, Phase B activity would begin in mid-FY 91 and Phase C/D would commence in mid-FY 93 for a FY 99 launch.

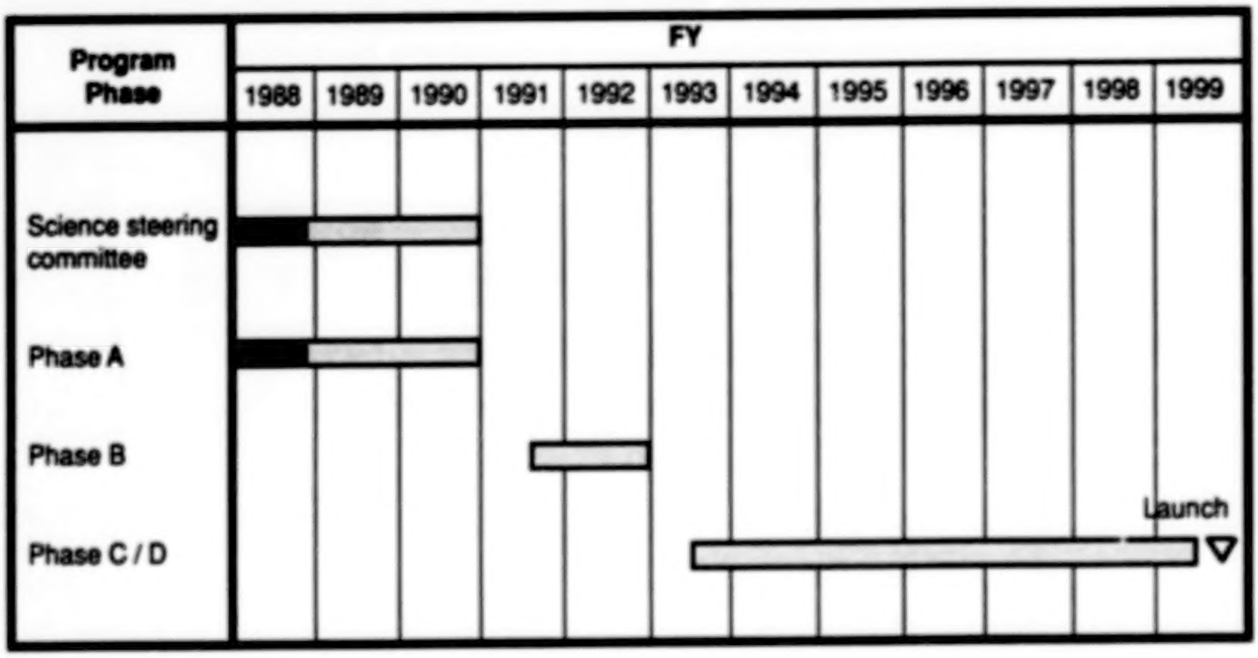

Figure 13

SPECIFIC TECHNOLOGY STUDIES

In addition to the feasibility studies, studies of specific technologies (fig. 14) must be undertaken. The question of electrical versus mechanical scanning must be addressed (electrical scanning may be better if vibration must be controlled). If precise ground locating is required, then pointing stability is essential. High-frequency microwave antennas (greater than 200 GHz) with radiometric accuracy (antenna figure tolerance) of $\lambda/50$ eliminate the use of wire mesh and unfurlable antennas. Hence, accurately milling large solid antennas may become a requirement (on-orbit thermal stresses now become a problem). Eventually, frequencies as low as 5 GHz may be required, resulting in extremely large antennas (too large for the first series of geostationary platforms). And servicing the platform on orbit will prove to be an extremely difficult problem that must be considered.

- Electrical vs. mechanical scanning
- Platform stability
- Pointing and control
- High-frequency microwave antenna high-precision reflectors
- Large low-frequency antennas
- Servicing

Figure 14

CONCLUDING REMARKS

One of the current designs (with the needs list constrained to just a few instruments) is shown in figure 11. This is a compact, solid truss-structure design, with both a 7 1/2 and a 15 m antenna. Much work must be done to make this radiometrically alive.

There are many problems that need to be considered before the Earth Science Geostationary Platform becomes a reality, including:

1. Multiple platforms for phasing approaches with communication between the platforms
2. Adaptive structures and electronic feeds instead of mechanican scans
3. Improved detectors at 220 GHz, especially if arrays of microwave detectors at that frequency are required
4. Higher resolutions and more sensitive arrays (even at infrared bands)

The objective of this workshop is to address problems in Science and four technology areas (Large Space Antenna Technology, Microwave Sensor Technology, Electromagnetics-Phased Array Adaptive Systems Technology, and Optical Metrology Technology) and provide a technology readiness report to the Science Steering Committee.

OPERATIONAL REQUIREMENTS AND THE GEOSTATIONARY PLATFORM

James K. Sparkman, Jr.
Office of Systems Development, NESDIS
National Oceanic and Atmospheric Administration
Washington, D.C.

For 22 years -- from ATS-1 to GOES-H -- a single technology has dominated imaging from geosynchronous altitudes. In 1990, with the scheduled launch of GOES-I, a major change will occur which will in turn open the way for the Geostationary Platform. The Platform may then accelerate development of the Earth Sciences and also provide research data useful for severe storm forecasts and hazard warnings. Most important of all, the Platform may solve problems that will impact the new GOES spacecraft.

ATS-1, like all but one of the ATS-series and all U.S. operational geostationary spacecraft to date, was spin-stabilized. Hundreds of pounds of gyro-rotating mass twirling at 100 RPM provided a dynamic stability that kept such moving parts as imager scan-mirrors from wiggling the spacecraft in reaction. From aboard a spinning spacecraft, a Spin-Scan Cloud Camera, and its descendants to today's combination imager-sounder*, permitted Earth observations to be made.

But the spin-scan principle has its limitations. Scan lines must be full-Earth wide, from western horizon to eastern. Changes in North-South observations must await the stepwise movement of the scan mirror. Even worse, the radiometer detectors gather photons from an Earth scene only during the short period of each rotation when the instrument views the Earth. (However, a compensating factor just as important as platform stability is that a rapidly spinning spacecraft receives almost a constant solar heating load, all day and all year.) Although a de-spun platform was later added atop a spinning satellite for the use of pointing high-gain antennas, it was not stable enough for an imager.

The need for improved observations of severe storms has led NOAA to a decision to replace spinning geostationary spacecraft with a three-axis-stabilized type (non-spinning) vehicle already common among communications spacecraft and demonstrated by INSAT. The change will begin with GOES-I. Also, the current spin-scan imager with sounder channels (VAS)* will be replaced by separate instruments capable of independent aiming. A design for each with double-gimballed mirrors frees imaging and sounding from horizon to horizon scanning. North-South mirror movement will occur without stepping between locations. The same freedom applies as well to the new sounder, but sounding is inherently a slower process, because of the low radiant energy levels involved. The slower sounder (7.5 hours for a full-disc sounding, vs. one-half hour for a full-disc image) will plod along examining storm air-mass stability, while the agile imager leaps from threatening squall line to flash-flood to nascent tornado, sampling area-rectangles perhaps 100 miles on a side. Images show the direction and speed of storm movement. Air-mass stability --the temperature and moisture structure of the near-by source-air of a potential storm -- discloses the probable severity and duration of winds and floods.

---

* The GOES imager-sounder now in use is called VAS, for VISSR (Visible & Infrared Spin-Scan Radiometer) Atmospheric Sounder.

The gains achieved by staring sensors (versus intermittent looks while spinning) reduce the time for soundings almost by half (13.5 hours to 7.5 hours for a full disc). Imaging is comparably speeded. But the price paid is found in spacecraft stability. Scan-mirror movements are expected to cause apparent movement of the viewed Earth image. While NOAA's polar orbiters are comparable in size and weight to the GOES-I/M series, their stability requirements are far less severe. Spacecraft vibrations affect images in proportion to the spacecraft altitude. Low Earth orbiters look down 850 km to nadir sub-point; GOES imagers are 35,800 km above the Earth's surface; platform vibrations are thus magnified 40 times. And, for polar orbiters which move from sunlight to night during a 102 min orbit, solar heating is neither long enough in duration, nor protracted enough from any given angle, to seriously distort the structure carrying stability controls and instrument arrays. In geostationary orbits, where a spacecraft is sunlit for six months, and insolated for 12 hours without hiatus on a given face, variable thermal expansions of the structure can be significant. The impacts on control systems and on the ground-location of fields of view are serious.

I am sure we all view a Geostationary Platform as an exciting opportunity for experiments in larger spacecraft design, innovative instrument development and a renaissance in data collection for all the Earth Sciences. But there are other aspects to such a Platform. The challenges it faces are those that must be met before the capabilities of any non-spinning geostationary satellite for remote sensing can be enlarged. Even communications spacecraft are involved. For example, high-stability spacecraft will become necessary, if laser-links are to be used between spacecraft, or from space to spot-targets on the Earth, Moon or Mars.

A special problem is that of large diameter -- or large array -- antennas for microwave passive remote sensing in bands between 20 and 200 GHz. While use of the infrared "atmospheric window" for soundings is now in its third decade as an operational tool, it has limitations. Clouds, even wispy cirrus bands, block outgoing infrared radiation. Ultimately, the result is to degrade calculations of surface and cloud-top temperatures and to largely eliminate computation of soundings below cloud levels. Either of these problems is serious. Errors in sensed cloud-top temperatures result in errors in estimates of the cloud-top heights and so to the heights of "cloud drift" winds assumed from sequential images of cloud position. Loss of soundings from cloudy regions means, for the severe storm forecaster, that he is unable to see into the storm he wishes to probe. (He can have soundings from clear air nearby, but the results are less than what is needed.) By contrast, some microwave channels are able to penetrate all but the heaviest rains. By careful channel selection, we can obtain temperature stability, and rainfall as well.

Diameters for microwave antennas grow large because (a) microwave wave-lengths demand a relatively larger antenna for the same field of view than visible and thermal-IR channels, and (b) we need finer probes to examine storms. It is a cruel jest that, in general, we need only large fields of view (for global forecasting) from low-flying polar orbiters, but want 1 km resolutions or less from geostationary spacecraft. The result is a stone-wall challenge for space hardware designers. Couple to this a requirement for a microwave antenna to scan (at least over the continental U.S.), without slewing the remainder of the spacecraft (if other sensors are carried), and the magnitude of the task soars.

Our emphasis on microwave sounders does not mean that interest in IR soundings has vanished. For several years, NOAA has funded studies of the feasibility of replacing GOES sounder filter-wheel channel selectors with an interferometer. Soundings based on more and, especially, narrower spectral channels, it is hoped, will result in increased vertical resolution of both temperature and moisture profiles. (NASA is following the same road in its interest in AIRS (Atmospheric Infrared Sounder) for flight on a Polar Platform. Whether AIRS uses an interferometer or a grating spectrometer is a question to be answered more by cost or mechanical complexity, than by operational principles.)

The role of the Geostationary Platform in high-altitude spacecraft technology is unique. Since its goal is for ultra-high resolution imagers and large diameter antennas for microwave sensing, it must find solutions for the problems of spacecraft stability while faced with movement reactions and thermal loading on structures. These challenges alone, and the potential solutions required, without regard to payloads, warrant our support for the project. The proposed payload is whipped-cream, on top.

We see, in this outline of events from the first ATS geostationary spacecraft to the next generation of GOES, a symbiosis of parallel programs: NOAA's decision to seek a staring imaging system with high resolution (1 km at nadir) and precise navigation of pixels (to permit calculation of winds from clouds seen in time-sequence views) has led to space industry efforts to solve stability problems with today's technology. This available industrial know-how permits planning for a Geostationary Platform, a vehicle which requires a three-axis spacecraft for its scientific goals. Its data collection will assist NOAA serve its data users. And, most important of all in the present time-frame, the Geostationary Platform's need to surpass GOES-I in stability and navigation will allow NOAA to purchase of a better spacecraft when the need arises.

Whether or not the NASA Geostationary Platform becomes a carrier for NOAA's operational instruments, we see that the Platform will greatly enhance the information flow to the same data users that NOAA serves, and advance future space technology for operations and research.

Science

Science Requirements
for
Passive Microwave Sensors
on
Earth Science Geostationary Platforms

A.J. Gasiewski and D.H. Staelin
Research Laboratory of Electronics
Massachusetts Institute of Technology
Cambridge, Massachusetts

1 Meteorological Considerations

The science requirements for a passive geosynchronous microwave sounder are dictated by 1) the spectrum of oxygen, water vapor, and liquid and frozen hydrometeors, 2) the spatial and temporal scales for variation of atmospheric temperature, water vapor, and precipitation, 3) the area of the region to be mapped, 4) receiver sensitivity, 5) the geosynchronous observation geometry. Specifications for a spaced-based antenna and receiver are determined from these requirements.

Vertical sounding of atmospheric temperature can be performed using channels within the 5-mm O_2 absorption band (near 60-GHz) and the 118.75-GHz O_2 absorption line (Fig. 1 and Table 1) [1,2], although the 118-GHz line offers higher spatial resolution for diffraction-limited apertures of fixed size. Water vapor sounding can be performed using channels near the 183-GHz H_2O absorption line, although the weaker 22-GHz H_2O line is also useful for integrated water vapor retrieval [3,4]. Window channels at frequencies adjacent to the O_2 and H_2O lines facilitate the estimation of surface emissivity, which impacts both passive temperature and water vapor retrievals. Since precipitation exhibits only broad spectral features, sounding requires channels

Table 1: List of channels for passive sounding of tropospheric temperature, clouds and water vapor, and precipitation. The primary (P) channels are required for retrieval of the particular meteorological parameter, while the secondary (S) channels provide useful information to support retrievals.

Frequency (GHz) and # of channels	Meteorological Parameter			Comments
	Temperature	Water Vapor	Precipitation	
6 (1)			P	Window
10 (1)			P	Window
18 (1)			P	Window
22 (1)		S		H_2O line
31-37 (1)	S		P	Window
50-60 (5)	P		P	O_2 Complex
90-110 (1)	S	S	P	Window
118 (8-11)	P		P	O_2 line
166 (1)	S	P	P	Window
183 (3-4)		P		H_2O line
220-230 (1)		S	P	Window

distributed over a decade in frequency [5,6]. These include window channels near 6, 10, 18, 31-37, and 90-110 GHz, which are particularly useful over ocean; 6 and 10 GHz are the most accurate over heavy precipitation (> 15 mm/hr) and 31-110 GHz are sensitive to weaker precipitation ($\leq$ 15 mm/hr) and ice scattering by glaciated cell tops. Oxygen channels at 50-60 and 118 GHz are particularly useful over land because of the altitude-probing property of the weighting functions; these can be used to retrieve cell top altitude. Additional channels near 160 and 220 GHz provide higher precipitation sensitivity over land and diffraction-limited spatial resolution than any lower frequency precipitation channels.

The primary advantage of geosynchronous observations is the ability to monitor rapidly evolving meteorological processes, such as hurricanes, strong convection, water vapor transport, and temperature anomalies. Precipitation should ideally be observed at intervals as short as 10 minutes, although complete disk coverage at this rate would not be necessary. Slightly less stringent temporal requirements must be met for observation of water vapor. In the case of atmospheric temperature, which does not evolve as quickly as water vapor or precipitation, observation intervals as short as 30 minutes are desirable, but observations separated by up to 2 hours are useful. When used in conjunction with full-disk infrared (IR) sounders, a passive microwave sounder covering 20% of the Earth's disk with a scan time of 1 hour would be adequate for observing regions obscured by IR-blocking clouds, with the proviso that the scanned region can be arbitrarily selected. Passive microwave coverage of the full disk every 10 minutes would be ideal.

The sizes of convective precipitation cells have been observed to vary from ~2 km to over 200 km. Over deep convection, brightness perturbations have been observed to be as large as -200 K near 90 GHz, 183 GHz, and the transparent channels near 118 GHz [7,8,9]. Such microwave brightness temperature structure is comparable with atmospheric temperature structure associated with severe storms. Indeed, horizontal atmospheric temperature gradients as high as 1 °C/km have been measured in the eyes of hurricanes [10]. Morphological information from brightness imagery is useful for distinguishing thermal and precipitating events, however, without sufficient spatial resolution, cold, spatially unresolved precipitation cells and atmospheric temperature or water vapor anomolies can be indistinguishable by their brightness temperature signatures. Hence, 3-dB footprints smaller than 2 km at 220 GHz are ultimately desirable for both unambiguous retrievals of atmospheric temperature and water vapor, and detection of precipitation, although 3-dB footprints up to 20 km in diameter at this frequency would still be useful. Similar spatial resolution is ultimately desirable at frequencies as low as 6 GHz, but will be much more difficult to obtain.

Although polarization information has been shown to be useful in the retrieval of precipitation at slant angles over water [11], the inclusion of vertical and horizontal polarization sensitivity is not deemed to be of primary importance. This is especially true for microwave frequencies above 100 GHz, where passive observations of precipitation are essentially unpolarized.

In summary, the requirements for the geosynchronous remote sensing of atmospheric temperature, water vapor, clouds, and precipitation are shown in Tables 2, 3, and 4. These requirements are categorized as "adequate" and "ideal"; the adequate microwave requirements are necessary for any significant improvement in hydrologic cycle observability, and assume IR coverage of clear-air and broken-cloud regions. The ideal requirements indicate a transition to a region of diminishing scientific returns on the hardware investment.

Table 2: Requirements for passive microwave temperature sounding from geosynchronous orbit.

	Adequate	Ideal
Frequency (GHz)	110-120	50-120
Coverage	20% of disk/hr	full disk
Spatial Resolution		
at 120 GHz	50 km	20 km
Temporal Resolution	30-120 min	30 min
Radiometric Accuracy	≤ 1.5 K	≤ 0.5 K
Radiometric Sensitivity	≤ 0.5 K	≤ 0.2 K

Table 3: Requirements for passive microwave cloud and water vapor sounding from geosynchronous orbit.

	Adequate	Ideal
Frequency (GHz)	110-183	22-183
Coverage	20% of disk/hr	full disk
Spatial Resolution		
at 183 GHz	30-50 km	10 km
Temporal Resolution	30-120 min	10-30 min
Radiometric Accuracy	≤ 1.5 K	≤ 0.5 K
Radiometric Sensitivity	≤ 0.6 K	≤ 0.3 K

Table 4: Requirements for passive microwave precipitation sounding from geosynchronous orbit.

	Adequate	Ideal
Frequency (GHz)	110-220	6-220
Coverage	10% of disk/hr	full disk
Spatial Resolution	20 km @ 220 GHz	6 km @ 6 GHz
Temporal Resolution	30-60 min	10-30 min
Radiometric Accuracy	≤ 3 K	≤ 1.5 K
Radiometric Sensitivity	≤ 0.5 K	≤ 0.3 K

2 General Antenna and Receiver Considerations

The radiometric sensitivity is most critical for the retrieval of atmospheric temperature and water vapor, and should be no worse than 0.5 K for the O_2 channels, and comparable for the H_2O channels. Small biases in the sensor calibration can be accounted for by in-flight comparison against forward transfer calculations based on radiosonde measurements. However, the absolute accuracy of the instrument should be kept to within 2 to 3 times the radiometric sensitivity. The sensitivity and accuracy requirements are slightly less rigid for the precipitation channels. Precise in-flight sensor calibration using two known brightness temperatures is necessary to achieve this accuracy. Careful attention must be given to calibration errors due to internal reflections and receiver nonlinearities.

In order to meet the sensor sensitivity requirements for all spots, constraints on the antenna efficiency and sidelobe levels are necessary. The constraints can be discussed by defining five angular regions, as in Fig. 2 :

1) **Main lobe.** The main lobe region includes all angles within the first antenna pattern null, and subtends approximately $3.26\lambda/D$ radians for a filled aperture with a linear field illumination taper, where D is the aperture diameter and λ is the wavelength. In this case, the peak main lobe gain G_M is approximately $0.75\,(\pi D/\lambda)^2$, or $G_M = 102.1 - 20 \log R$ dBI (decibels relative to isotropic), where R is the desired 3-dB equatorial footprint size (in km). An aperture efficiency of 75% has been assumed [12]. Thus, for spatial resolutions R of 2 to 20 km, the required main lobe gains are 96 to 76 dBI, respectively.

The main lobe efficiency is the fraction of the total captured power from within the main lobe region. This should exceed 95%, (and more ideally 97%). The corresponding average sidelobe level over all angles outside the main lobe becomes -13 dBI (ideally -15 dBI), although more stringent constraints on the peak sidelobe levels must be met for specific angular regions.

2) **Near-sidelobes.** The near-sidelobe region is defined to be the angular region within approximately 10 to 15 beamwidths of the the main lobe, but not including the main lobe. In this region, sidelobe levels will necessarily be the largest, comprising approximately 3% (ideally 2%) of the total stray radiation. Some enhancement of the raw image can be achieved via deconvolution of the near-sidelobe antenna pattern.

3) **Limb sidelobes.** The limb sidelobe region is the angular region (outside of the near sidelobe region) containing all angles which cross the Earth's limb during a full disk scan. The sidelobes in the limb region will alternately view cold space (2.7 K) and the Earth's disk (~ 250 K), depending upon the particular spot being

observed. Thus, the limb-sidelobe region subtends an angle of 17.4°. By requiring the maximum antenna temperature fluctuation due to the sweep of limb sidelobes to be less than 0.05 K, a constraint is placed on the average limb sidelobe level, which can be met by requiring that the peak limb sidelobe level G_L remain below -13.6 dBI, or, relative to the main lobe gain, $G_L \leq -115.7 + 20 \log R$ dB. Thus, for 2 to 20 km spatial resolution, all limb sidelobes should remain at least 110 to 90 dB below the main lobe gain, respectively. Within these constraints, the maximum stray radiation from the limb region will remain less than 0.03%. Relaxing the maximum limb-sweep antenna temperature fluctuation to 0.2 K reduces the limb sidelobe constraint by only 6 dB.

4) **Ecliptic sidelobes.** The ecliptic region is defined to contain all angles which directly view the sun or moon. Thus, the ecliptic region is an angular strip bounded at the elevation angles $\epsilon = \pm 37.9°$, and subtending the ecliptic plane. The sun can be modelled as a blackbody of temperature between 6,000 K (at 220 GHz) and 10,000 K (at 6 GHz), and subtends an angle of 0.53° . (The moon subtends nearly the same angle, but exhibits a brightness temperature less than 400 K, and hence can be negelected.) Within the ecliptic region, all radiometric fluctuations due to the passage of the sun through the antenna sidelobes should remain less than 0.05 K. This is satisfied by requiring that all ecliptic sidelobes levels remain below 0 dBI, or at least $102.1 - 20 \log R$ dB below the main lobe gain. This is a less stringent requirement than for the limb sidelobe levels, but is particularly important for antennas exhibiting grating lobes, for example, thinned arrays.

5) **Ortho-ecliptic sidelobes.** The ortho-ecliptic region is the complement of the ecliptic region, and contains all angles which never directly view the sun, moon, or Earth. In this region, the peak sidelobe level can rise to values above isotropic (0 dBI), provided that the main lobe efficiency requirement is met. Thus, the maximum stray radiation from the ecliptic and ortho-ecliptic regions should remain below 2% (ideally 1%), requiring the average sidelobe level over these two regions to remain below -17 dBI (ideally -20dBI).

3 Implementation using a Filled-Aperture Sensor

For filled-aperture sensors with linear field illumination taper, the 3-dB beamwidth $\theta_{3dB} = 1.3\lambda/D$, and the required diameter for a given equatorial resolution R is $D(\mathrm{m}) \approx 13900/\left(f(\mathrm{GHz})\ R(\mathrm{km})\right)$ (see Table 5). The 3-dB footprint at 60° latitude will cover approximately 3.2 times the area as at the equator.

The spatial and temporal observation requirements place constraints on the available integration time per spot τ, as suggested in Table 6 for a single-spot, filled-aperture sensor. In this arrangement, a single feed assembly is used by all channels, although the feed assembly might consist of more than one feed horn to accomodate channels over a wide frequency range. The brightness sensitivity of a radiometer operated in the total power mode is given by:

$$\Delta T_{RMS} = \frac{T_R + T_A}{\sqrt{B\tau}} \qquad (1)$$

where T_R is the receiver noise temperature, T_A is the antenna temperature, which typically ranges from 100 to 300 K, and B is the channel bandwidth, which typically ranges from 100 MHz for an O_2 channel to 1000 MHz for a window channel. Double-sideband noise temperatures T_R for room-temperature receivers range from approximately 500 K to 1500 K for frequencies ranging from 50 to 200 GHz, respectively. By cooling the receivers to 80 K, the receiver temperatures might vary from 400 K to 1000 K, respectively. Table 7 shows how the sensitivity of a typical 100-MHz O_2 channel with B =100 MHz and T_R =1000 K would depend on the scan parameters for a mapping time of 30 minutes. From Eq. 1, reductions in T_R below 100 to 200 K will not improve the sensitivity significantly.

The sensitivity of a filled-aperture sensor can be improved by employing several feed assemblies, each with a separate receiver, in a multiple-spot arrangement. By orienting a row of adjacent spots transverse to the scan direction, the desired area to be imaged is covered by wide swaths. In this case, the available integration time per spot is multiplied by the number of feed-plus-receiver assemblies N_f, hence the sensitivity is improved by $1/\sqrt{N_f}$. Due to the decreasing marginal cost of adding additional feed and receiver assemblies, the total cost of the feeds and receivers for the multiple-spot sensor should increase as $(N_f)^\alpha$, where $\alpha < 1$.

Perhaps a more significant advantage of a multiple-feed system for a mechanically scanned sensor is the reduction in the slew rate necessary for the physical scan of the primary beam-forming element. Consider a filled-aperture sensor using a parabolic reflector. For this case, satisfactory momentum compensation can be difficult to achieve for the maximum slew rates required by a single-spot sensor (Table 8). These rates are reduced by $1/N_f$ for the multiple-spot sensor. A reduction in slew rate of the parabolic reflector can also be achieved with a Cassegrain configuration employing a nutating subreflector. The light-weight subreflector scans the main beam at a high rate in a direction transverse to the slow raster motion of the main reflector. The required number of lateral spots for a 10°/min slew rate and 30-min mapping time are tabulated in Table 9 for various scan parameters. For either the multiple-feed or nutating-subreflector sensors, a main reflector with a large f/D ratio is desirable in order to minimize off-axis aberations at the extreme transverse spots.

Table 5: Required antenna beamwidth θ_{3dB} and diameter D for various spatial resolutions and channel frequencies.

Parameter		Equatorial Resolution R (km) 5	10	20	40	60
Beamwidth θ_{3dB} (arc min)		0.48	0.96	1.92	3.83	5.76
Aperture diameter D (m)	at 6 GHz	463	232	116	58	39
	at 18 GHz	154	77	39	19	13
	at 60 GHz	46	23	12	5.8	3.9
	at 118 GHz	23	12	5.9	2.9	2.0
	at 183 GHz	15	7.6	3.8	1.9	1.3
	at 220 GHz	13	6.3	3.2	1.6	1.0

Table 6: Available integration time (seconds) per spot for 30-min mapping of various sized regions for a single-spot sensor.

Area Diameter (km)	Equatorial Resolution R (km) 5	10	20	40	60
10,000 (full disk)	0.00045	0.0018	0.0072	0.029	0.065
4,000	0.0028	0.011	0.045	0.18	0.40
2,000	0.011	0.045	0.18	0.72	1.6

Table 7: Receiver sensitivity ΔT_{RMS} for 30-min mapping of various sized regions, assuming $T_R = 1000$ K and $B = 100$ Mhz.

Area Diameter (km)	Equatorial Resolution R (km) 5	10	20	40	60
10,000 (full disk)	4.8	2.4	1.2	0.59	0.39
4,000	1.9	0.95	0.47	0.24	0.16
2,000	0.95	0.47	0.24	0.12	0.08

Table 8: Required antenna scanning rates (°/min) for 30-minute mapping time of various sized regions.

	Equatorial Resolution R (km)				
Area Diameter (km)	5	10	20	40	60
10,000 (full disk)	900	450	225	112	75
4,000	144	72	36	18	12
2,000	36	18	9	4.5	3

Table 9: Required number of transverse spots for 10° /min scanning rate and 30-minute mapping time of various sized regions.

Area Diameter (km)	Equatorial Resolution R (km)				
	5	10	20	40	60
10,000 (full disk)	100	50	25	12	8
4,000	16	8	4	2	2
2,000	8	4	2	1	1

To minimize the angular and linear momentum transferred to the platform by any mechanically scanned elements, coaxial counter-rotating flywheels and collocation of the scanned element's pivot point with element's center of mass should be employed, as illustrated in Fig. 3. Active adjustment of this mechanism can be achieved by correcting the location of small masses attached to the antenna. This can be done using motorized actuators that respond to forces exerted by the antenna on the platform, as measured by strain gauges or other means.

Scattering from reflector surface irregularities reduces the main lobe efficiency by approximately $\exp[-(4\pi\epsilon/\lambda)^2]$, where ϵ is the RMS surface deviation from a true parabola. In order to achieve the desired main lobe efficiency levels, a filled-aperture reflector antenna will be required to have $\epsilon < \lambda/60$ for 95% main lobe efficiency, and $\epsilon < \lambda/75$ for 97% efficiency. At 220 GHz, these RMS deviation limits are 23μ (0.0009 in.) and 18μ (0.0007 in.), respectively. Scattering from struts and feed structures will further reduce the main lobe efficiency.

Diurnal exposure of the main beam-forming element to the sun's direct rays may necessitate some form of thermal stabilization. Aperture phase compensation for thermally induced distortions in a semi-rigid parabolic reflector surface can be achieved by using a series of motorized actuators placed between a supporting ring and the "petals" of the reflector (Fig. 4a-c), as defined by radial slits in the dish. The slits can be made narrow enough so that negligible main-lobe degradation occurs, and can be covered with a flexible foil to minimize edge diffraction. Alternate phase compensation concepts that would achieve equivalent results include Cassegrainian antenna configurations with controlled subreflector surfaces and phase-controlled sub-aperture feed assemblies.

The required amount of compensation can be determined by measuring the distance from the rear of the reflector to a suitable reference plane. Either capacitive or optical metrology could be used for the measurement, although any capacitive sensors should be shielded from the solar wind and light. The reference plane could be constructed from a tensioned membrane, which could be connected to the support ring at three points, or from a lightweight Invar bridgework.

Two-point calibration of a single- or multiple-feed sensor can be achieved by periodically moving a reflecting surface and then an absorbing load in front of the feed assembly. The reflector would be oriented to provide an unobstructed view of cold space, preferably within the ortho-ecliptic region. The absorbing load should be at a stable (±1 K) temperature between 250 K and 350 K, and should be accurately monitored. Inefficiency in the main reflector would not be included in the calibration load measurements, but could be accounted for by measuring the reflector temperature and using *a-priori* knowledge of the reflector loss.

Other concepts for the implementation of large filled-aperture sensors include controlled-surface mesh, membrane, or segmented deployable antennas, Fresnel lenses, and phased-array bootlace lenses. In contrast to filled-aperture reflector antennas, filled-aperture lens antennas are relatively insensitive to small deviations in the lens profile, although lens concepts present other problems in meeting performance specifications over the wide range of frequencies required. In addition, due to minute variations in the insertion losses of the beam-forming elements as the array is scanned, the phased array may require a separate calibration at each spot. This might be performed using beacons positioned at many locations on the Earth.

4 Implementation using Synthetic-Aperture Sensors

Although synthetic aperture interferometers have been used successfully in radio astronomy for imaging point sources, their proposed application to the space-based imaging of extended objects such as the Earth is relatively new [13]. The spatial resolution of the synthesized aperture is related to the maximum element-pair separation distance by nearly the same relation as that of a filled aperture. Brightness sensitivities comparable to filled-aperture single-spot sensors can be obtained if all element-pair correlations are performed simultaneously.

An important issue which deserves attention is the possibility of excessively large near-, limb-, and ecliptic-sidelobes due to undersampling of the visibility function in the $u - v$ plane. This is of particular importance for thinned arrays. One part of the solution is to decrease the individual element field of view to the minimum allowable ($\sim 17.4^\circ$), although this will increase the size of each element. Another part of the solution is to space the elements shoulder-to-shoulder, and then to have additional elements spaced at intermediate positions. Achievement of more than 95% beam efficiency in the synthesized pixels presents a significant challenge.

A practical system for the calibration of synthetic aperture sensors also needs to be developed. As in the case of the phased array, a calibration scheme employing Earth-located beacons might be used.

5 Summary

It is suggested that the science requirements for passive geostationary microwave observations be met by near- and far-term sensors for each of two overlapping bands (Fig. 5), with each band covering no more than a decade in frequency. The low-frequency band includes channels near 6, 10, 18, 22, 31 to 37, and possibly 50 to 60 GHz. The high-frequency band includes channels near 220 to 230, 183, 166, 118, 90 to 110, and possibly 50 to 60 and 31 to 37 GHz. The precise channel specifications will have to comply with international frequency allocations [14].

The near-term goal is a high-frequency sensor based on a filled-aperture solid reflector antenna, which should rely on currently existing technology. The diameter of the reflector should be limited to 4.4 m (the size of the shuttle payload bay), which allows for a sensor partially exceeding the "adequate" spatial resolution requirements. Larger, deployable reflectors are not suggested for the near term unless the technology can be immediately demonstrated. The most critical issues for the near-term sensor are momentum compensation and the design of the feed assembly; these issues are coupled through the desired scan rate. Due to the nascent state of current large space antenna technology, no near-term goals for a low-frequency geostationary sensor are recommended.

The successful demonstration of the near-term (high-frequency) sensor will be essential for the continued development of far-term sensors satisfying the ideal science requirements. The far-term goal includes both a high-frequency sensor which meets the ideal science requirements, and a low-frequency sensor whose design will depend on advances in large antenna technology. The high-frequency sensor should consist of a filled-aperture controlled segmented or controlled semi-rigid antenna with a diameter from 10 to 40 meters.

The low-frequency (far-term) sensor might be based on one of several concepts : 1) a deployable mesh reflector antenna of diameter at least 20 m, which shows promise for use at frequencies up to 30-GHz, 2) a synthetic aperture interferometer of maximum baseline from 100 to 300 m, or 3) a deployable phased-array bootlace lens, of diameter from 100 to 300 m. The first of these, a deployable mesh reflector antenna; will satisfy only the adequate spatial resolution requirements. The last two concepts meet the ideal spatial resolution science requirements, although they present significant structural and meteorological challenges.

References

[1] J.W. Waters, K.F. Kunzi, R.L. Pettyjohn, R.K.L. Poon and D.H. Staelin, "Remote Sensing of Atmospheric Temperature Profiles with the Nimbus-5 Microwave Spectrometer", *J. Atm. Sci.*, Vol. 32, No. 10, 1975.

[2] A.D.S. Ali, P.W. Rosenkranz and D.H. Staelin, "Atmospheric Sounding Near 118 GHz", *J. Appl. Meteorol.*, Vol. 19, No. 10, 1980.

[3] D.H. Staelin, K.F. Kunzi, R.L Pettyjohn, R.K.L. Poon, P.W. Rosenkranz and

J.W. Waters, "Remote Sensing of Atmospheric Water Vapor and Liquid Water with the Nimbus-5 Microwave Spectrometer", *J. Appl. Meteorol.*, Vol. 15, No. 11, 1976.

[4] P.W. Rosenkranz, M.J. Komichak and D.H. Staelin, "A Method for Estimation of Atmospheric Water Vapor Profiles by Microwave Radiometry", *J. Appl. Meteorol.*, Vol. 21, No. 9, 1982.

[5] T.T. Wilheit, A.T.C. Chang, M.S.V. Rao, E.B. Rodgers and J.S. Theon, "A Satellite Technique for Quantitatively Mapping Rainfall Rates over the Oceans", *J. Appl. Meteorol.*, Vol. 16, No. 5, 1977.

[6] R.W. Spencer, "A Satellite Passive 37-GHz Scattering-based Method for Measuring Oceanic Rain Rates", *J. Climate. Appl. Meteor.*, Vol. 25, No. 6, 1986.

[7] ———, J.W. Barrett, P.G. Bonanni and D.H. Staelin, "Aircraft-Based Radiometric Imaging of Tropospheric Temperature Profiles and Precipitation Using the 118.75-GHz Oxygen Resonance", Accepted for publication in *J. Appl. Meteorol.*, 1988.

[8] G.M. Heymsfield and R. Fulton, "Comparison of High-Altitude Remote Aircraft Measurements with the Radar Structure of an Oklahoma Thunderstorm: Implications for Precipitation Estimation from Space", *Mo. Wea. Rev.*, Vol. 116, No. 5, 1988.

[9] I.M. Hakkarinen and R.F. Adler, "Observations of Precipitating Convective Systems at 92 and 183 GHz: Aircraft Results", *Meteorol. Atmos. Phys.*, Vol. 38, 1988.

[10] H.F. Hawkins and S.M. Imbembo, "The Structure of a Small, Intense Hurricane-Inez 1966", *Mo. Wea. Rev.*, Vol. 104, 1966.

[11] R.W. Spencer, H.M. Goodman and R.E. Hood, "Precipitation Retrieval Over Land and Ocean with the SSM/I, Part 1: Identification and Characteristics of the Scattering Signal", Accepted for publication in *J. Atmos. Ocean. Technology*, 1988.

[12] S. Silver, *Microwave Antenna Theory and Design*, McGraw-Hill, New York, 1949.

[13] C.S. Ruf, C.T. Swift, A.B. Tanner and D.M. Le Vine, "Interferometric Synthetic Aperture Microwave Radiometry for the Remote Sensing of the Earth", *IEEE Trans. Geosci. Remote Sensing*, Vol. 26, No. 5, 1988.

[14] Litman, V. and J. Nicholas, *Guidelines for Spaceborne Microwave Sensors*, NASA Reference Publication 1086, National Technical Information Service, Springfield, Virginia, March, 1982.

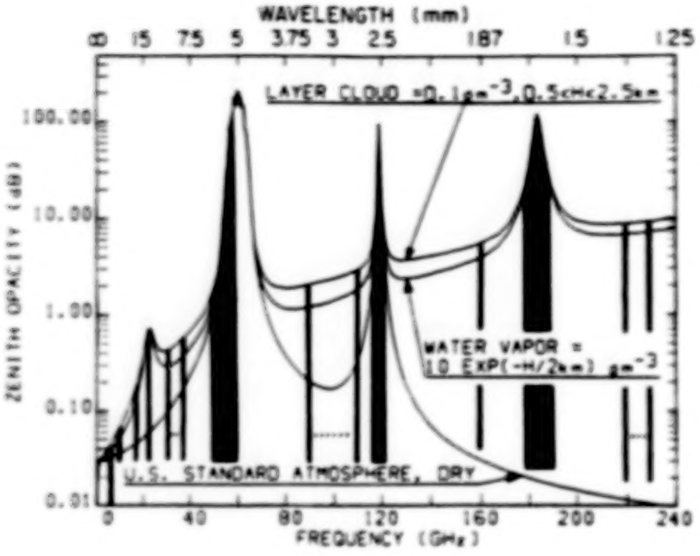

Figure 1: Zenith microwave opacity spectrum of the atmosphere for dry, moist, and cloudy conditions. Channels useful for the sounding of tropospheric temperature, water vapor, clouds, and precipitation are indicated by dark bars; the dots indicate regions over which only a single channel is needed.

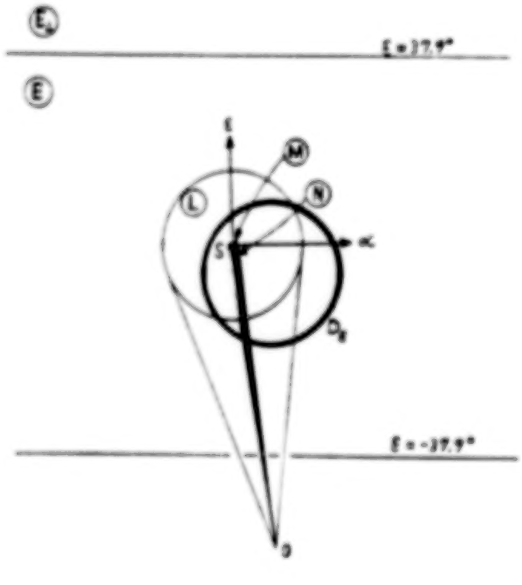

Figure 2: Angular regions for the specification of sidelobe levels and main lobe efficiency for a geosynchronous passive microwave sensor. O is the sensor position, D_E is the outline of the Earth's disk, S is the observed spot, M is the main lobe region, N is the near-sidelobe region, L is the limb-sidelobe region, E is the ecliptic-sidelobe region, $E_\perp$ is the ortho-ecliptic sidelobe region, and ϵ and α define elevation and azimuthal directions relative to the antenna boresight.

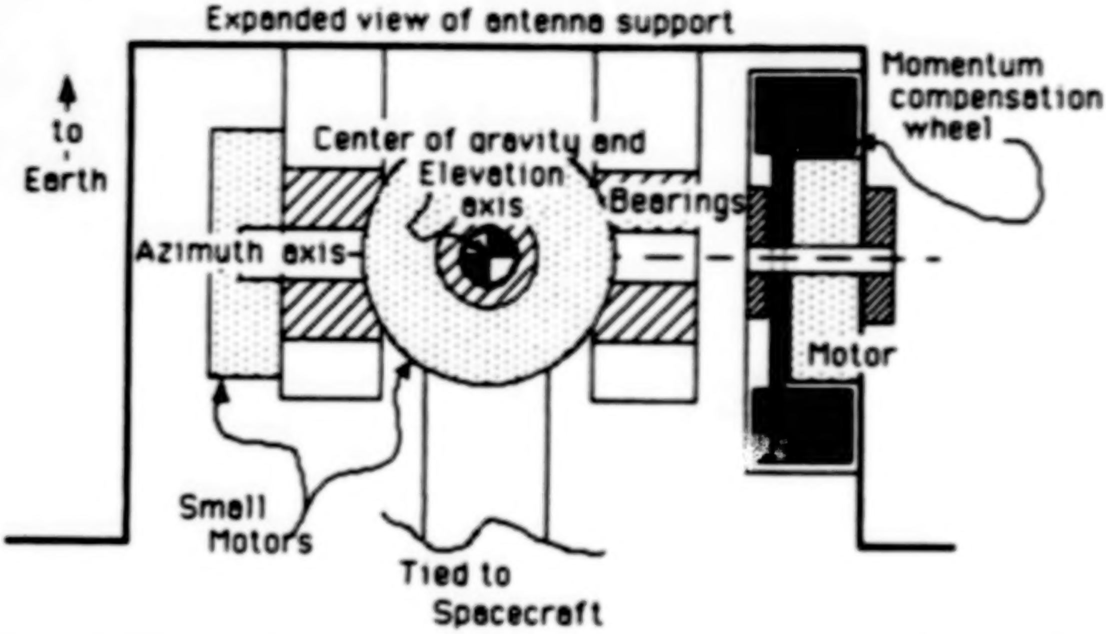
Expanded view of antenna support
to Earth
Momentum compensation wheel
Center of gravity and Elevation axis
Bearings
Azimuth axis
Motor
Small Motors
Tied to Spacecraft

Figure 3: Schematic view of a coaxial angular momentum compensation technique. The antenna pivot is located at the center of mass to minimize the linear momentum transferred to the platform. The momentum wheel axes also pass through the center of mass to minimize excitation of platform vibration modes.

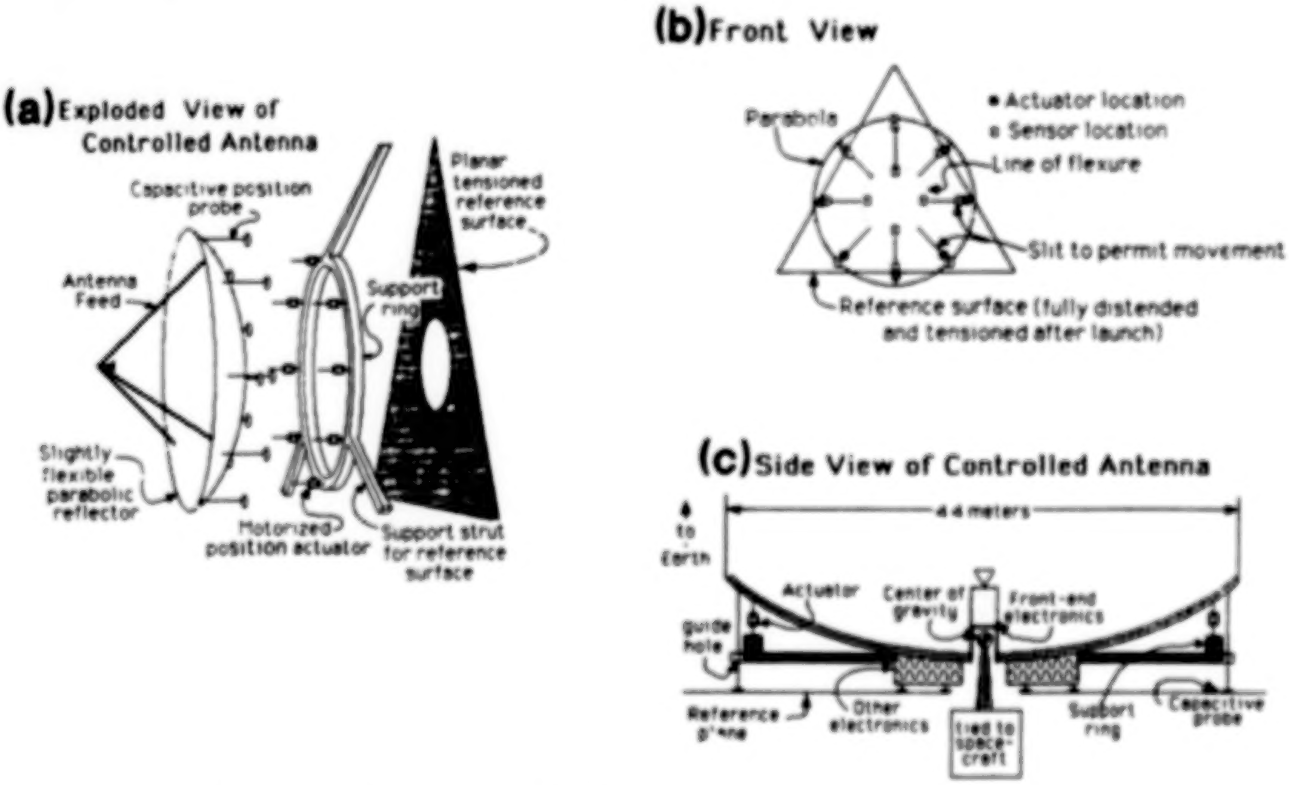
(a) Exploded View of Controlled Antenna
Capacitive position probe
Antenna Feed
Planar tensioned reference surface
Support ring
Slightly flexible parabolic reflector
Motorized position actuator
Support strut for reference surface
(b) Front View
Parabola
• Actuator location
• Sensor location
Line of flexure
Slit to permit movement
Reference surface (fully distended and tensioned after launch)
(c) Side View of Controlled Antenna
to Earth
4.4 meters
Actuator
Center of gravity
Front-end electronics
guide hole
Reference plane
Other electronics
tied to space-craft
Support ring
Capacitive probe

Figure 4: Schematic view of a mechanically scanned sensor employing a controlled, semi-rigid parabolic reflector antenna. (a) Exploded view illustrating reflector, support ring and planar reference surface. (b) Front view illustrating the reflector petals formed by radial slits. (c) Side view illustrating the reflector pivot location and capacitive metrology system.

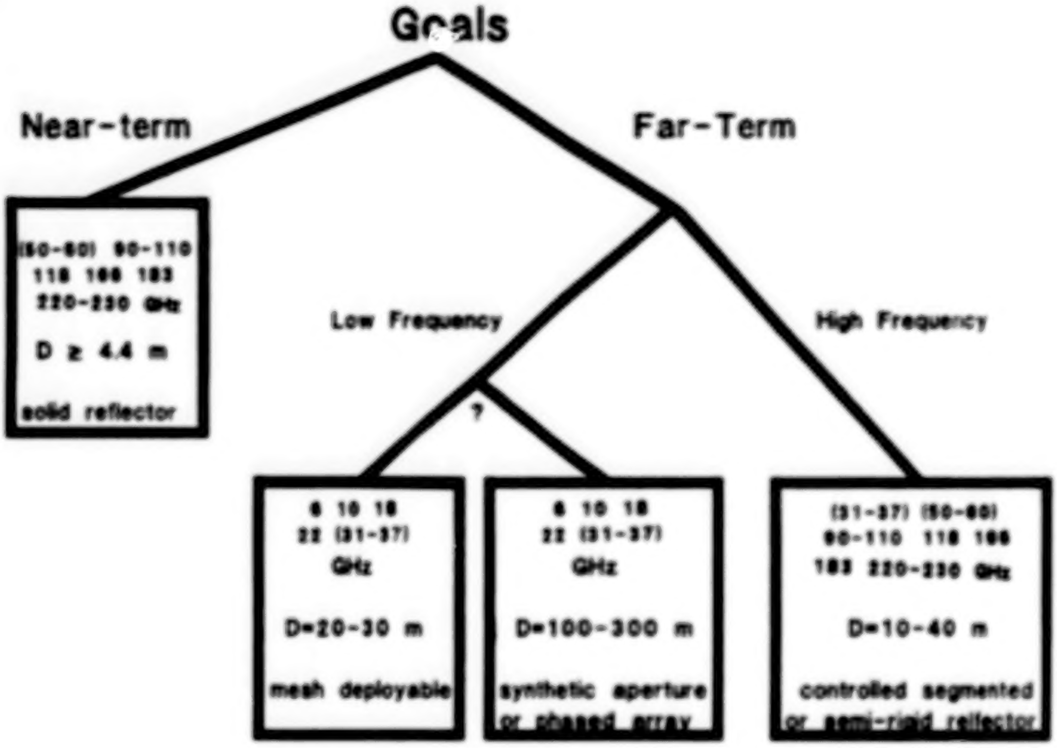
Goals
Near-term
Far-Term
(50-60) 90-110
118 166 183
220-230 GHz
D ≥ 4.4 m
solid reflector
Low Frequency
High Frequency
?
6 10 18
22 (31-37)
GHz
D=20-30 m
mesh deployable
6 10 18
22 (31-37)
GHz
D=100-300 m
synthetic aperture
or phased array
(31-37) (50-60)
90-110 118 166
183 220-230 GHz
D=10-40 m
controlled segmented
or semi-rigid reflector

Figure 5: Suggested near- and far-term sensors for geosynchronous passive microwave observation.

GEOSTATIONARY EARTH SCIENCE PLATFORM CONCEPTS

M. M. Herardian
Lockheed Missiles and Space Company, Inc.
Sunnyvale, CA

Three new concepts are presented for the Geostationary Earth Science Platform. Bus and payload arrangements, with instrument locations on the payload module and basic payload dimensions, are depicted and compared for each concept.

The Titan IV SRMU (with solid rocket motor upgrade) launch vehicle is described and compared to the standard Titan IV. The upgraded Titan IV is capable of launching a 13,500 lb. payload to GEO*. The launch configuration showing each concept packaged within the 16 ft. diameter payload envelope is presented.

*geosynchronous orbit (GEO).

GEOSTATIONARY EARTH SCIENCE PLATFORM CONCEPT 5F-2A

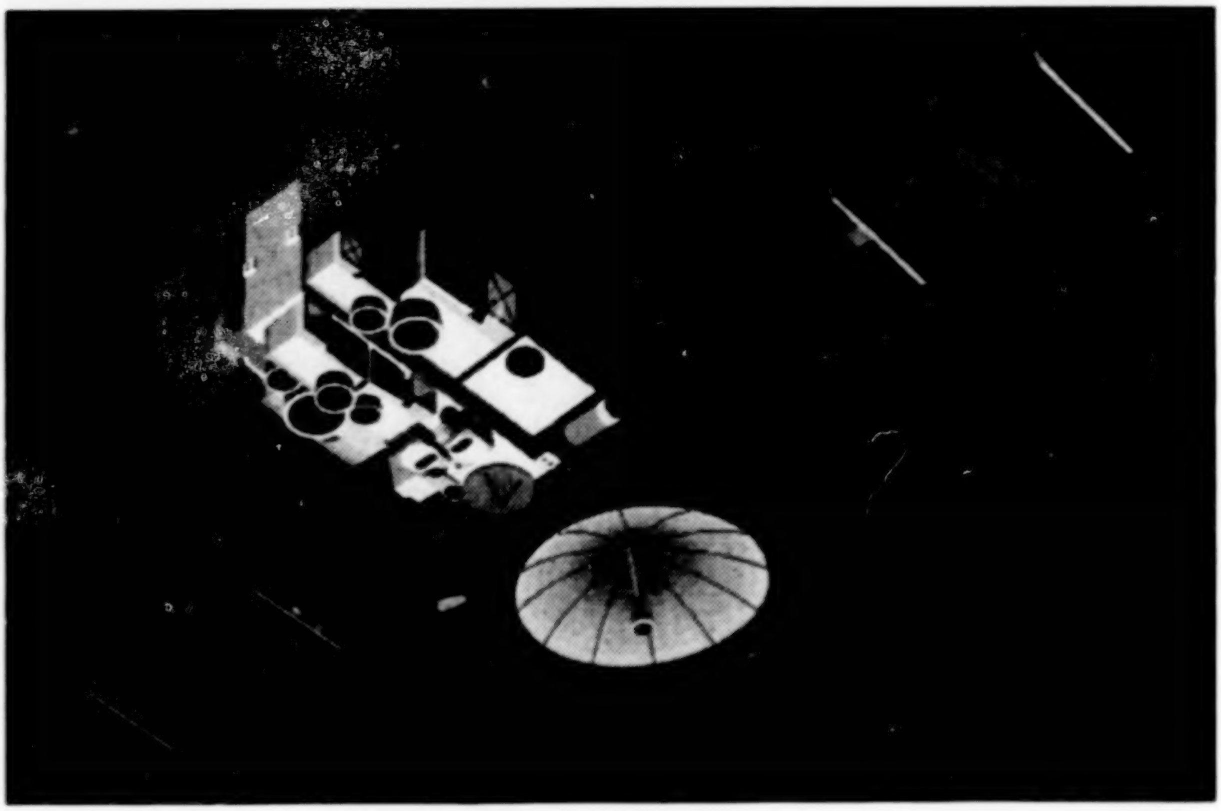

PLATFORM CONCEPT 5F-2A BUS AND PAYLOAD ARRANGEMENT

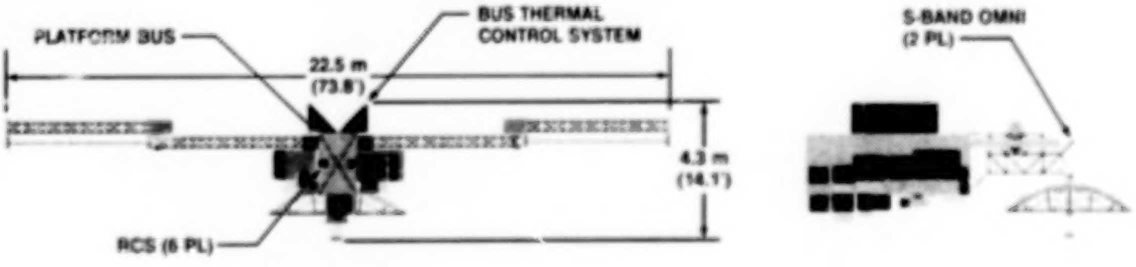
PLATFORM BUS
BUS THERMAL CONTROL SYSTEM
22.5 m
(73.8')
4.3 m
(14.1')
RCS (6 PL)
S-BAND OMNI
(2 PL)

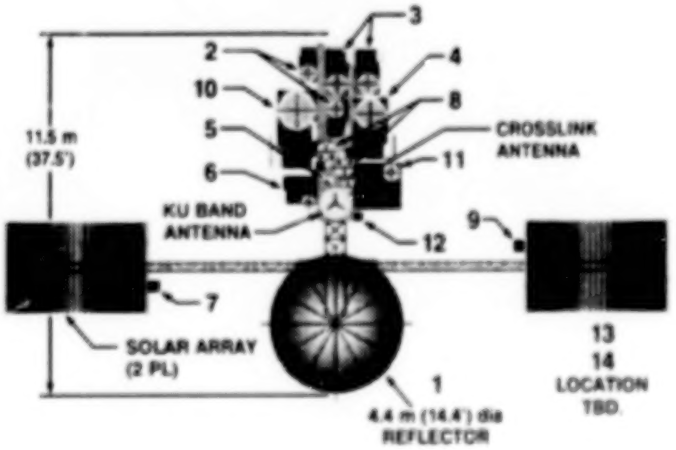
3
2
4
10
8
5
CROSSLINK ANTENNA
11
6
11.5 m
(37.5')
KU BAND ANTENNA
9
12
7
SOLAR ARRAY
(2 PL)
1
13
14
LOCATION TBD.
4.4 m (14.4') dia REFLECTOR

NO.	PAYLOAD INSTRUMENT MODULE	QTY
1	PASSIVE MICROWAVE RADIOMETER (H/F)	1
2	HIGH RESOLUTION IMAGER (NOAA)	2
3	IR SOUNDER (NOAA)	2
4	MICHELSON SOUNDER	1
5	LIGHTNING MAPPER	1
6	OZONE MAPPER	1
7	ACTIVE CAVITY RADIOMETER	1
8	CLIMATE RADIATION RADIOMETER	2
9	X-RAY IMAGER	1
10	MULTISPECTRAL IMAGER	1
11	LASER RANGER	1
12	SOLAR SPECTROMETER	1
13	PASSIVE MICROWAVE RADIOMETER (L/F)	1
14	SPACE ENVIRONMENT MONITOR	1
15	DATA COLLECTION SYSTEM	1

GEOSTATIONARY EARTH SCIENCE PLATFORM CONCEPT 6F-2A

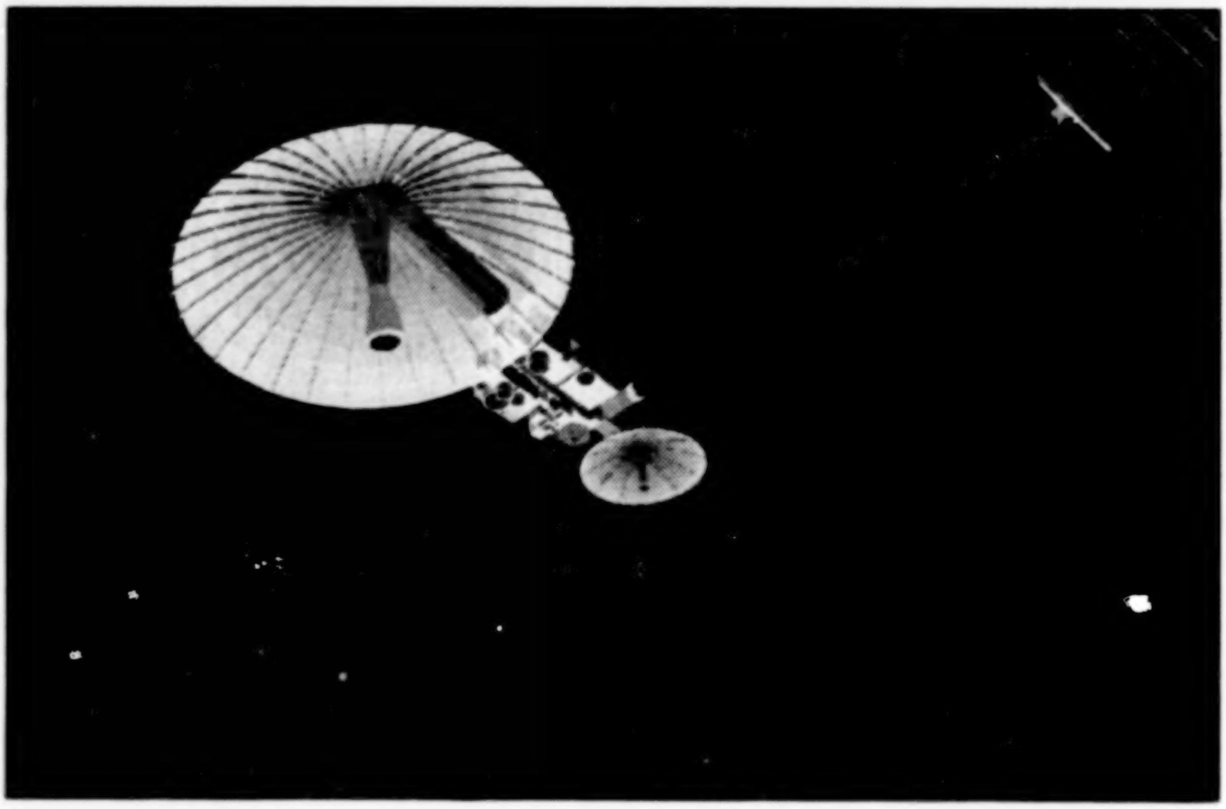

PLATFORM CONCEPT 6F-2A BUS AND PAYLOAD ARRANGEMENT

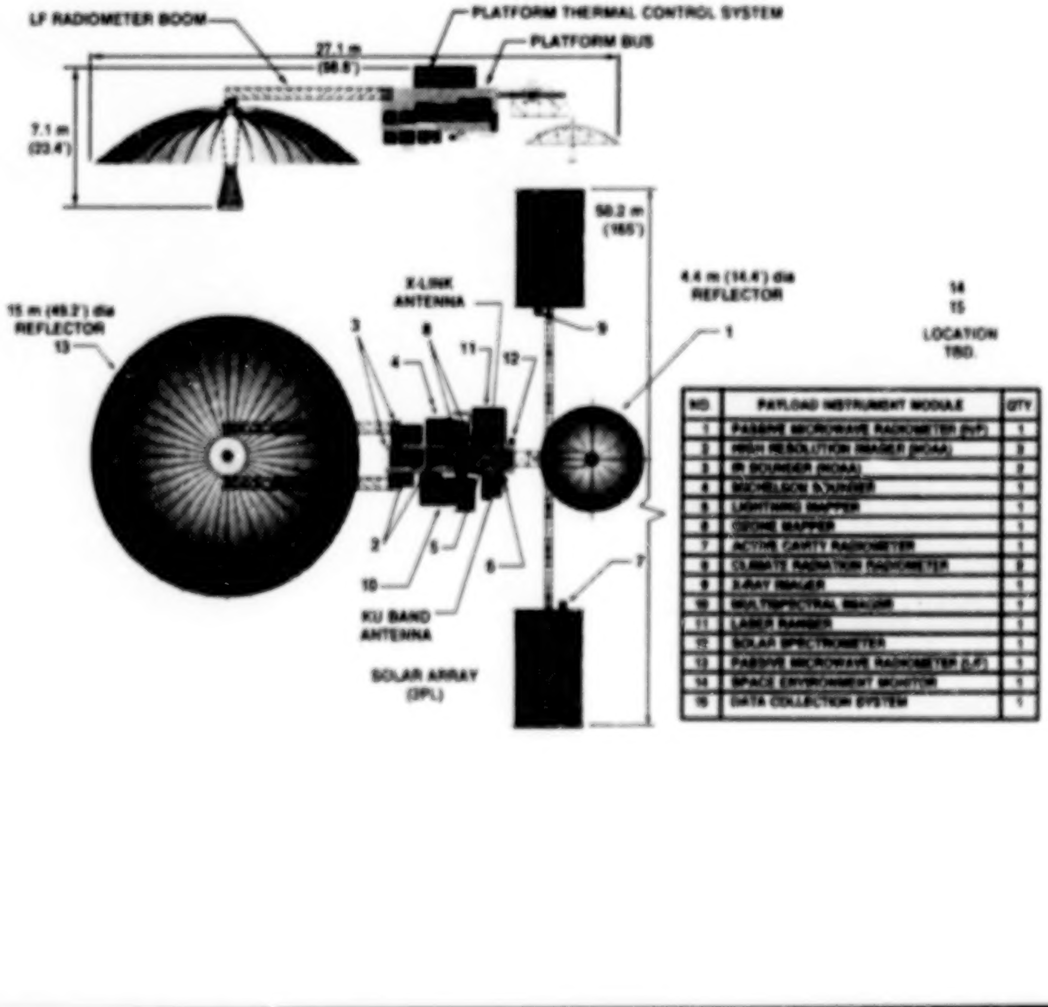
LF RADIOMETER BOOM
PLATFORM THERMAL CONTROL SYSTEM
PLATFORM BUS
27.1 m
(88.8')
7.1 m
(23.4')
50.2 m
(165')
X-LINK
ANTENNA
4.4 m (14.4') dia
REFLECTOR
15 m (49.2') dia
REFLECTOR
13
3
8
4
11
12
9
1
14
15
LOCATION
TBD.
2
5
6
10
7
KU BAND
ANTENNA
SOLAR ARRAY
(2PL)

NO	PAYLOAD INSTRUMENT MODULE	QTY
1	PASSIVE MICROWAVE RADIOMETER (HF)	1
2	HIGH RESOLUTION IMAGER (NOAA)	2
3	IR SOUNDER (NOAA)	2
4	MICHELSON SOUNDER	1
5	LIGHTNING MAPPER	1
6	OZONE MAPPER	1
7	ACTIVE CAVITY RADIOMETER	1
8	CLIMATE RADIATION RADIOMETER	2
9	X-RAY IMAGER	1
10	MULTISPECTRAL IMAGER	1
11	LASER RANGER	1
12	SOLAR SPECTROMETER	1
13	PASSIVE MICROWAVE RADIOMETER (LF)	1
14	SPACE ENVIRONMENT MONITOR	1
15	DATA COLLECTION SYSTEM	1

GEOSTATIONARY EARTH SCIENCE PLATFORM CONCEPT

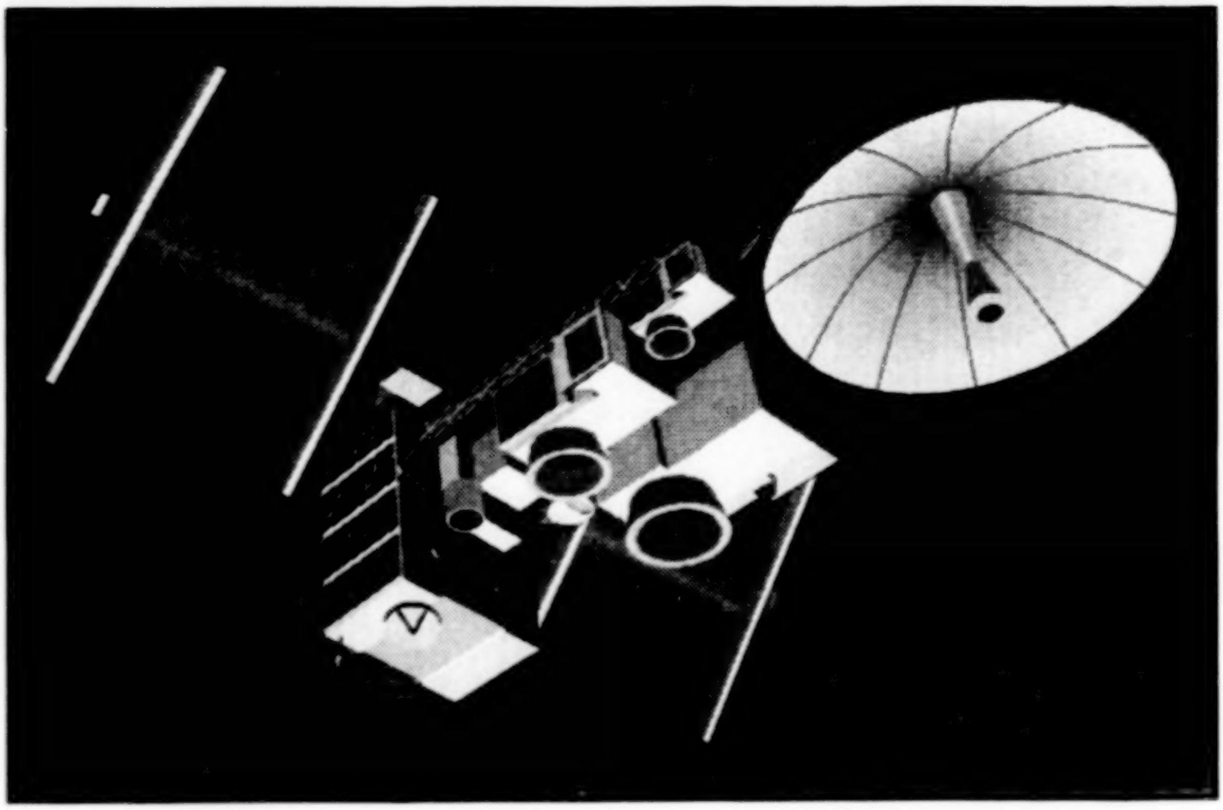

PLATFORM CONCEPT 7F-1B BUS AND PAYLOAD ARRANGEMENT

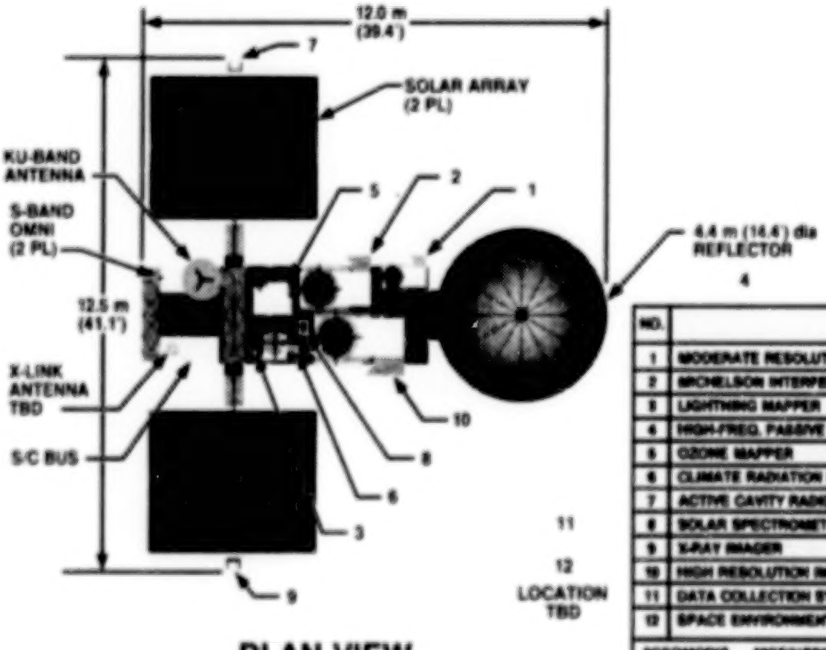
12.0 m
(39.4')
7
SOLAR ARRAY
(2 PL)
KU-BAND
ANTENNA
S-BAND
OMNI
(2 PL)
5
2
1
4.4 m (14.4') dia
REFLECTOR
4
12.5 m
(41.1')
X-LINK
ANTENNA
TBD
S/C BUS
10
8
6
3
11
12
LOCATION
TBD
9

PLAN VIEW

NO.	PAYLOAD
1	MODERATE RESOLUTION IMAGING SPECTROMETER* (NOAA)
2	MICHELSON INTERFEROMETER SPECTROMETER (NOAA)
3	LIGHTNING MAPPER
4	HIGH-FREQ. PASSIVE MICROWAVE IMAGER/SOUNDER
5	OZONE MAPPER
6	CLIMATE RADIATION RADIOMETER
7	ACTIVE CAVITY RADIOMETER
8	SOLAR SPECTROMETER
9	X-RAY IMAGER
10	HIGH RESOLUTION IMAGING SPECTROMETER**
11	DATA COLLECTION SYSTEM
12	SPACE ENVIRONMENT MONITOR

*GEOMODIS **GEOHRIS

GEOSTATIONARY EARTH SCIENCE PLATFORM CONCEPT SUMMARY

CONCEPTS

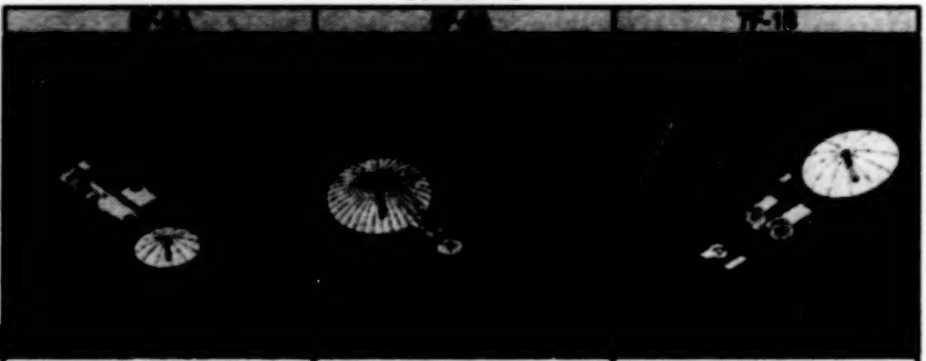

- S/C LIFE 10 YEARS

[illegible]	[illegible]	[illegible]	[illegible]
• SPACECRAFT			
DIMENSIONS	74' x 38' x 14'	165' x 89' x 23'	41' x 39' x 12'
BUS WEIGHT (X30%)	4,211 lb	6,616 lb	4,300 lb
TOTAL WEIGHT BOL	9,914 lb	13,517 lb	8,611 lb
TOTAL POWER	2.3 kW	3.2 kW	2.4 kW
• PAYLOAD			
PAYLOAD WEIGHT	3,620 lb	4,061 lb	2,403 lb
NO. INSTRUMENTS	15	16	10
• LAUNCHER	T-IV SRMU	T-IV SRMU	T-IV SRMU
MAXIMUM PAYLOAD TO GEO	13,500 lb	13,500 lb	13,500 lb

LAUNCH VEHICLE
CONFIGURATION AND CAPABILITY

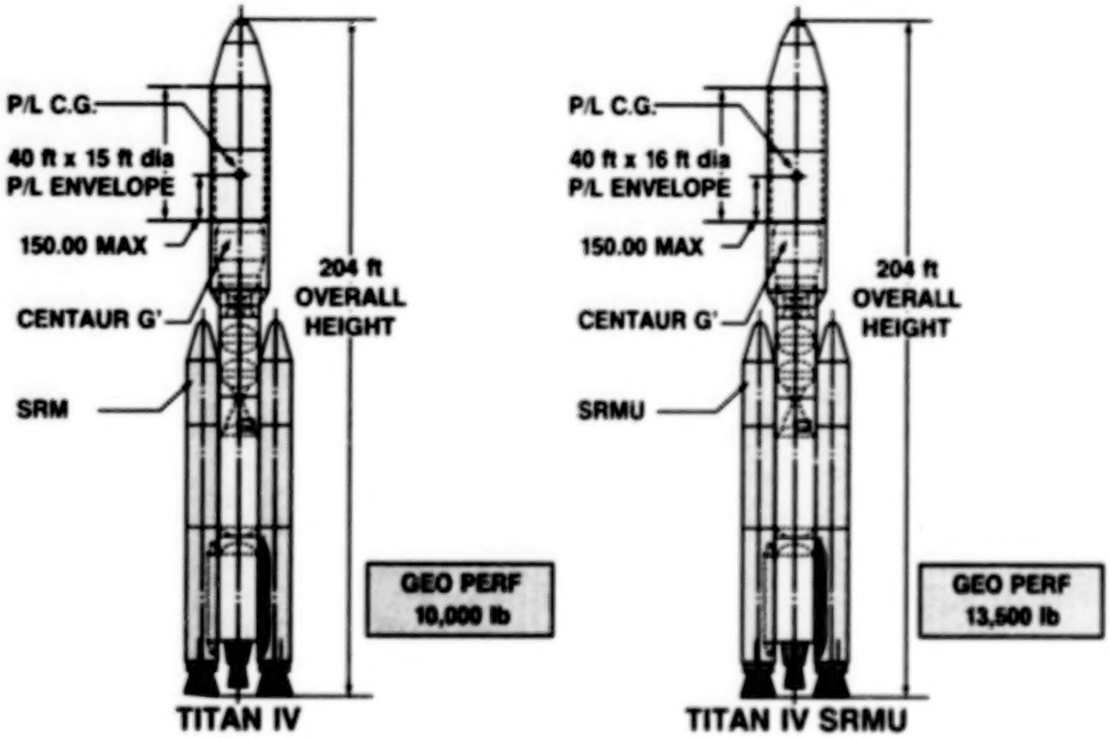
P/L C.G.
40 ft x 15 ft dia
P/L ENVELOPE
150.00 MAX
CENTAUR G'
SRM
204 ft
OVERALL
HEIGHT
GEO PERF
10,000 lb
TITAN IV
P/L C.G.
40 ft x 16 ft dia
P/L ENVELOPE
150.00 MAX
CENTAUR G'
SRMU
204 ft
OVERALL
HEIGHT
GEO PERF
13,500 lb
TITAN IV SRMU

GEOSTATIONARY EARTH SCIENCE
PLATFORM CONCEPT 5F-2A
TITAN IV LAUNCH CONFIGURATION

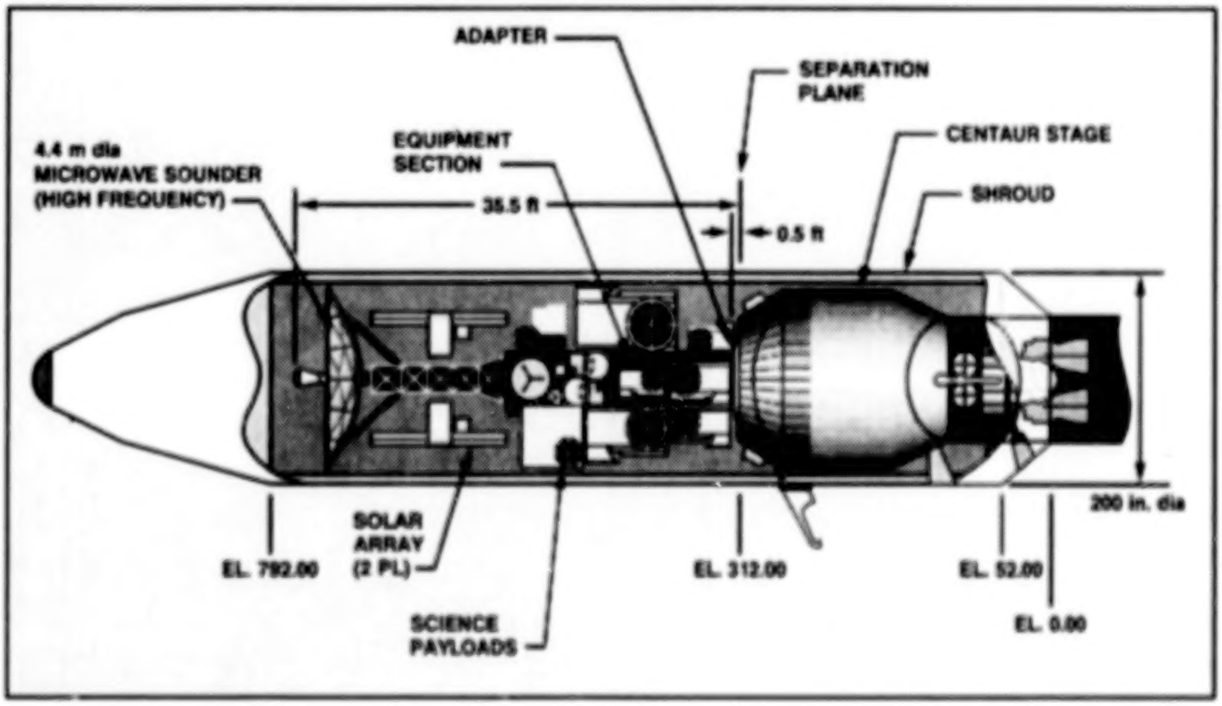
ADAPTER
SEPARATION
PLANE
CENTAUR STAGE
SHROUD
4.4 m dia
MICROWAVE SOUNDER
(HIGH FREQUENCY)
EQUIPMENT
SECTION
35.5 ft
0.5 ft
200 in. dia
EL. 792.00
SOLAR
ARRAY
(2 PL)
EL. 312.00
EL. 52.00
EL. 0.00
SCIENCE
PAYLOADS

GEOSTATIONARY EARTH SCIENCE PLATFORM CONCEPT 6F-2A

TITAN IV LAUNCH CONFIGURATION

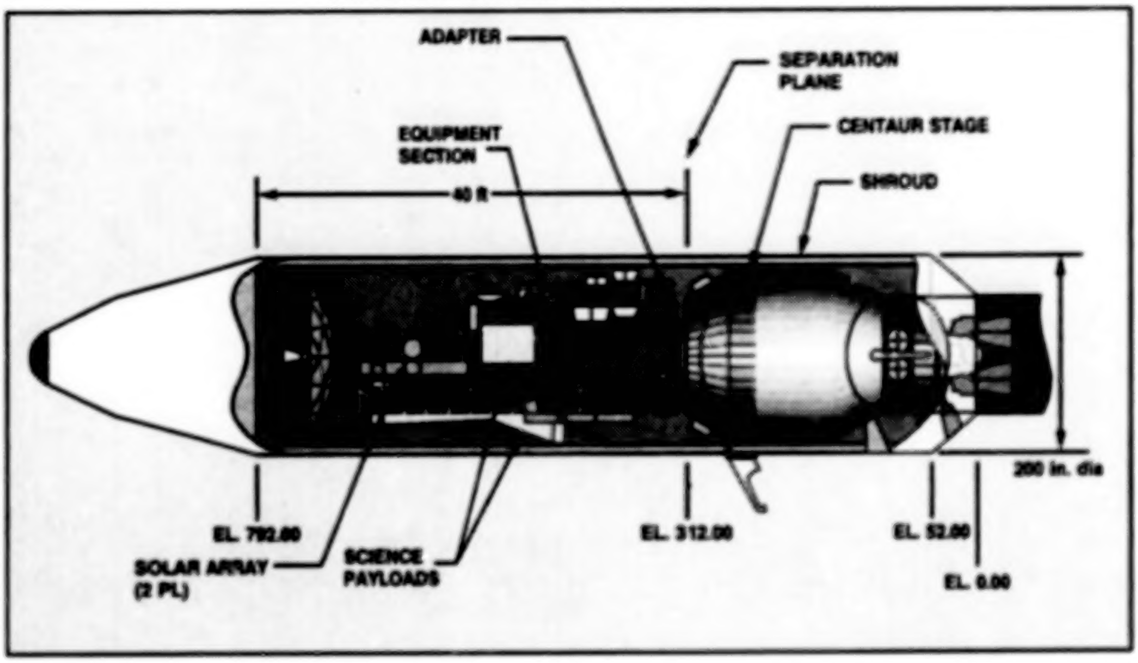
ADAPTER
SEPARATION PLANE
CENTAUR STAGE
EQUIPMENT SECTION
SHROUD
40 ft
200 in. dia
EL. 792.00
EL. 312.00
EL. 52.00
EL. 0.00
SOLAR ARRAY (2 PL)
SCIENCE PAYLOADS

GEOSTATIONARY EARTH SCIENCE PLATFORM CONCEPT 7F-1B

TITAN IV LAUNCH CONFIGURATION

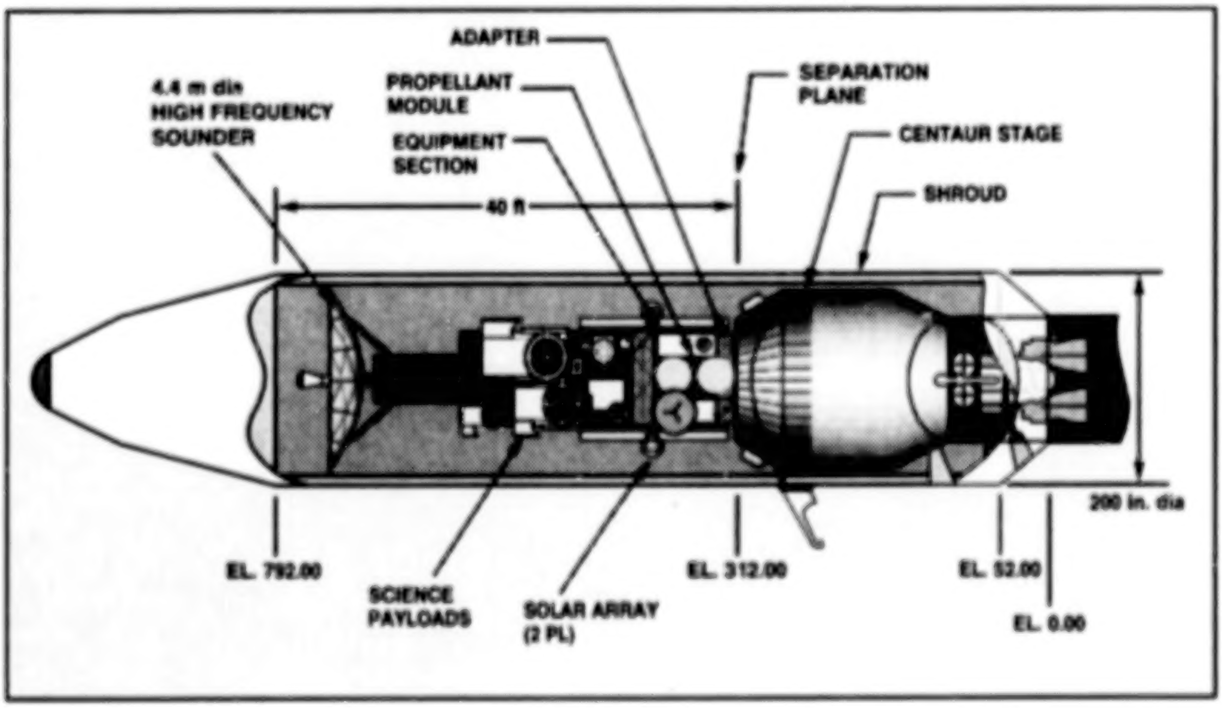
ADAPTER
4.4 m dia HIGH FREQUENCY SOUNDER
PROPELLANT MODULE
SEPARATION PLANE
EQUIPMENT SECTION
CENTAUR STAGE
SHROUD
40 ft
200 in. dia
EL. 792.00
EL. 312.00
EL. 52.00
EL. 0.00
SCIENCE PAYLOADS
SOLAR ARRAY (2 PL)

Large Space Antenna Technology

Session Chairman: Allan W. Love
Rockwell International

LARGE SPACE ANTENNA CONCEPTS FOR ESGP

Allan W. Love, Chairman
Rockwell International
Satellite and Space Electronics Division
Seal Beach, California

INTRODUCTION

As we began this conference, and particularly the session on Large Space Antennas, it was appropriate to note that 1988 marks the 100th anniversary of the birth of the reflector antenna. It was in 1888 that Heinrich Hertz constructed the first one, a parabolic cylinder made of sheet zinc bent to shape and supported by a wooden frame. It stood 2 meters high, had an aperture 1.2 meters wide, a focal distance of 0.12 meters and could be rolled about on casters. What we now call the feed was simply a spark gap-excited dipole placed along the focal line at its mid-point.

A similar reflector, dipole and spark gap detector served as a receiving antenna. With these two antennas and an induction coil to excite the transmitting spark gap, Hertz demonstrated the existence of the electromagnetic waves that had been predicted theoretically by James Clerk Maxwell some 22 years earlier. The frequency was about 450 MHz, corresponding to the 3/2-wavelength resonant dipole length.

In the 100 years since Hertz's pioneering work the field of electromagnetics has grown explosively. I cannot help but wonder what Hertz's astonishment would be if he were permitted a glimpse today of the technology that has grown out of his pioneering work. One of those technologies was the reason for attending this conference. It is the technology of remote sensing of planet Earth by means of electromagnetic waves, using both passive and active sensors located on an Earth Science Geostationary Platform (ESEP). This, of course, is the converse of what radio and radar astronomers have long been doing: remotely observing outer space, both near and far, with electromagnetic sensors on the Earth. For these purposes they have developed some exquisitely sensitive instruments, capable of reaching to the fringes of the known universe, and relying on large reflector antennas to collect the minute signals and direct them to appropriate receiving devices.

These antennas are electrically large, with diameters of 3000 to 10,000 wavelengths and with gains approaching 80 to 90 dB. They must have very smooth surfaces that deviate from the ideal paraboloid by no more than a few hundredths of a wavelength under the combined effects of varying gravitational and wind induced forces as well as changes in ambient temperature.

Some of the reflector antennas proposed for ESGP are also electrically large. For example, at 220 GHz a 4-meter reflector is nearly 3000 wavelengths in diameter, and is electrically quite comparable with a number of the millimeter wave radiotelescopes that are being built around the world. Its surface, too, must meet stringent requirements on rms smoothness, and ability to resist deformation. Here, however, the environmental forces at work are different. There are no varying forces due to wind and gravity, but inertial forces due to mechanical scanning must be reckoned with. With this form of beam scanning, minimizing momentum transfer to the space platform is a problem that demands an answer.

Finally, reflector surface distortion due to thermal gradients caused by the solar flux probably represents the most challenging problem to be solved if these Large Space Antennas are to achieve the gain and resolution required of them.

The session provided a stimulating discussion of these and other problems whose solutions are being investigated by the authors in this publication.

GAINS OF SOME LARGE, GROUND-BASED RADIO TELESCOPE REFLECTOR ANTENNAS

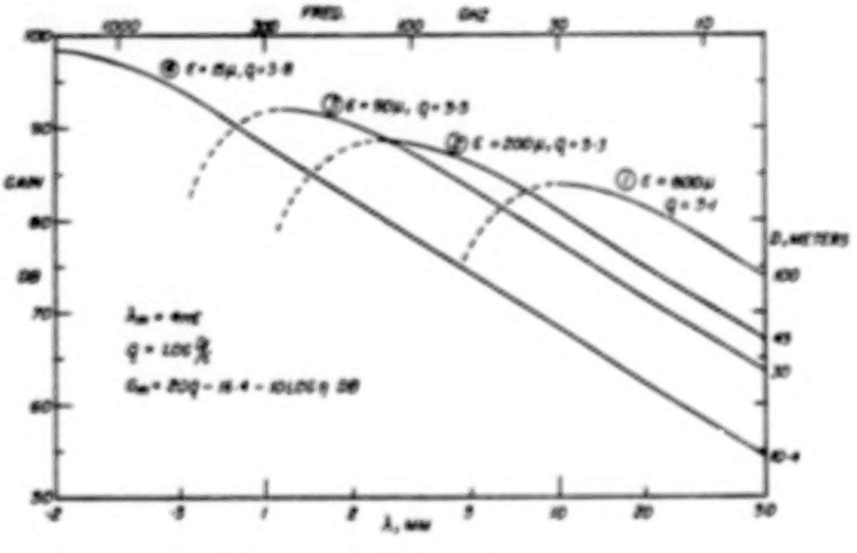

1. MPIFR, BONN FRG (EFFELSBURG, FGR)
2. TOKYO OBSERVATORY (NOBEYAMA, JAPAN)
3. IRAM, FRANCE/GERMANY (PICO VELETA, SPAIN)
4. CALIF. INST. TECHNOLOGY (MAUNA KEA, HAWAII)

THE FIRST REFLECTOR ANTENNA
HERTZ'S PARABOLIC CYLINDER, 1888

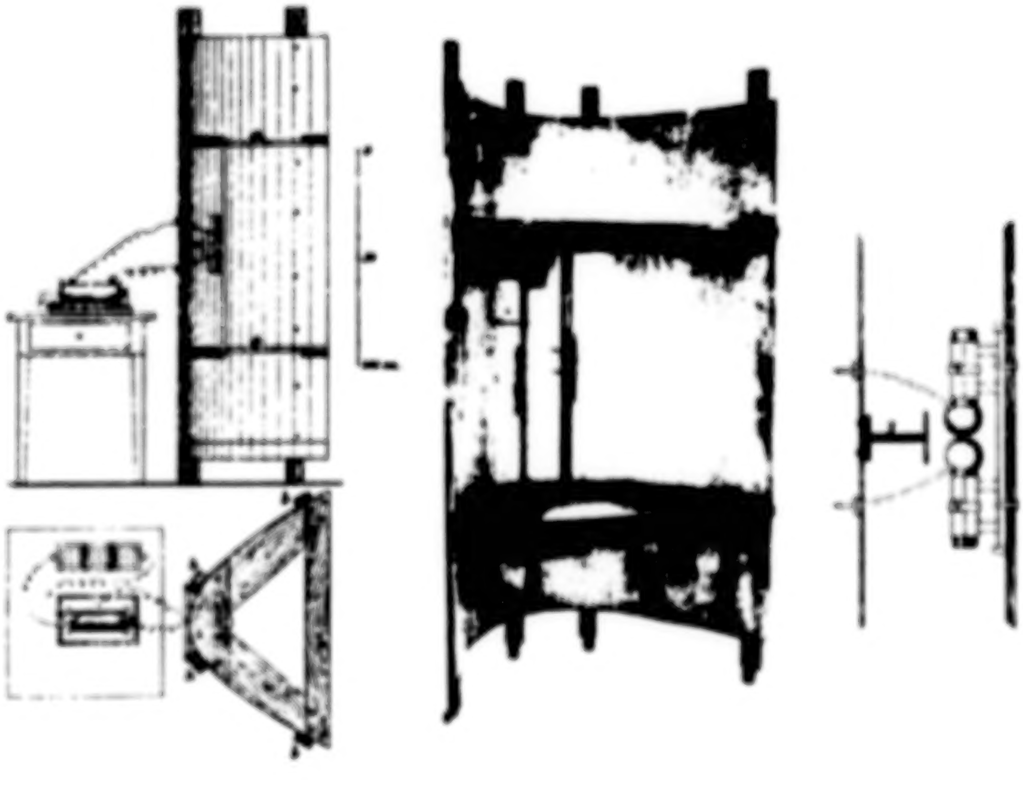

LARGE-DIAMETER GEOSTATIONARY MILLIMETER WAVELENGTH ANTENNA CONCEPT

W. S. Gregorwich,
H. A. Malliot, and
A. K. Sinha
Lockheed Missiles and Space Company, Inc.
Sunnyvale, California

CURVED REFLECTING SURFACE

The concept of a curved reflecting surface by means of an electrostatic membrane appeared as early as 1932 in the British patent (830,473) by Muller. Recent articles (refs. 1,2,3,4) propose the use of the electrostatic membrane in space applications as large-reflector antennas.

A schematic of the concept is shown in Fig. 1. The rigid command surface approximates the desired shape and contains electrodes. The flexible metallized reflector is the electrostatic membrane. By means of bias and control voltages between the membrane and command surface electrodes, the membrane is distended into the desired shape. An optical measurement system provides the feedback data necessary for computer figure control.

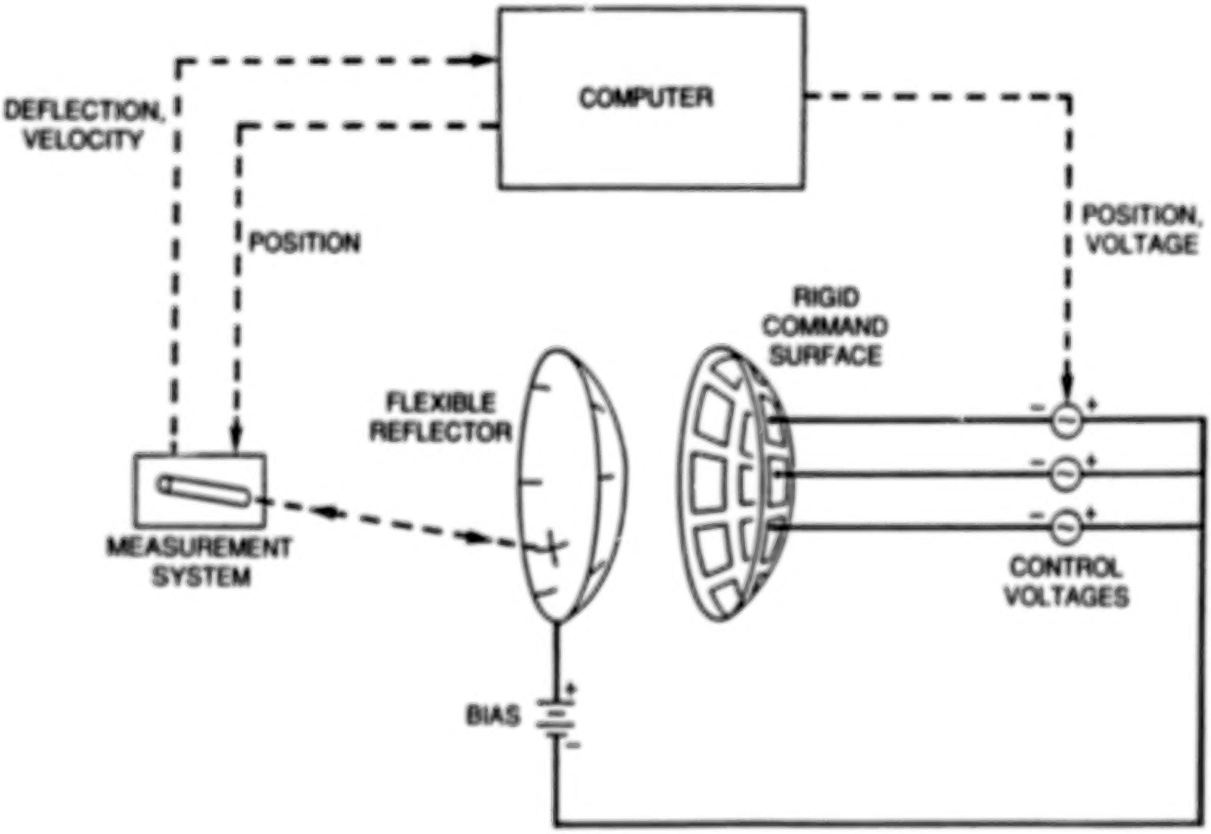
COMPUTER
DEFLECTION,
VELOCITY
POSITION
POSITION,
VOLTAGE
RIGID
COMMAND
SURFACE
FLEXIBLE
REFLECTOR
MEASUREMENT
SYSTEM
CONTROL
VOLTAGES
BIAS
+
−

Figure 1

ELECTROSTATICALLY SHAPED REFLECTOR MODEL

Figure 2 shows a 2-m-diameter electrostatic membrane experiment performed by MIT (ref. 2) and sponsored by Lockheed. Lockheed is presently using electrostatic membrane techniques on high-precision laser mirrors (ref. 5).

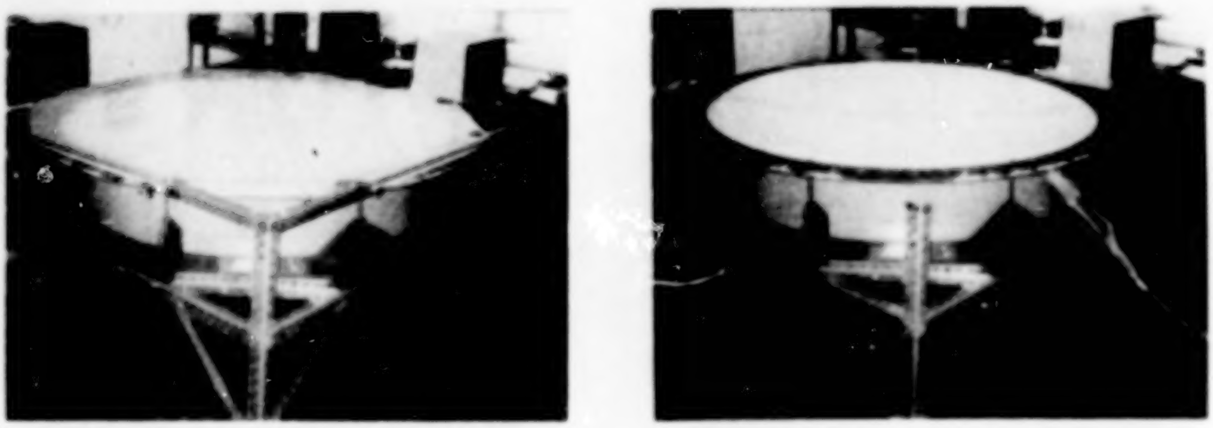

a. Relaxed Membrane

b. Formed Paraboloid

Figure 2

ELECTRODES

The MIT study demonstrated that it does not take many electrodes to form a large precise reflector. It can be seen from Fig. 3 that for a 10-m-diameter antenna (D) with f/D = 1.0 and a root mean square (rms) error ϵ of $\lambda/50$ (where λ = free space wavelength) and $D/\epsilon = 10^6$, one requires only N = 40 electrodes at 220 GHz. Due to the wide influence of a single electrode, few are needed.

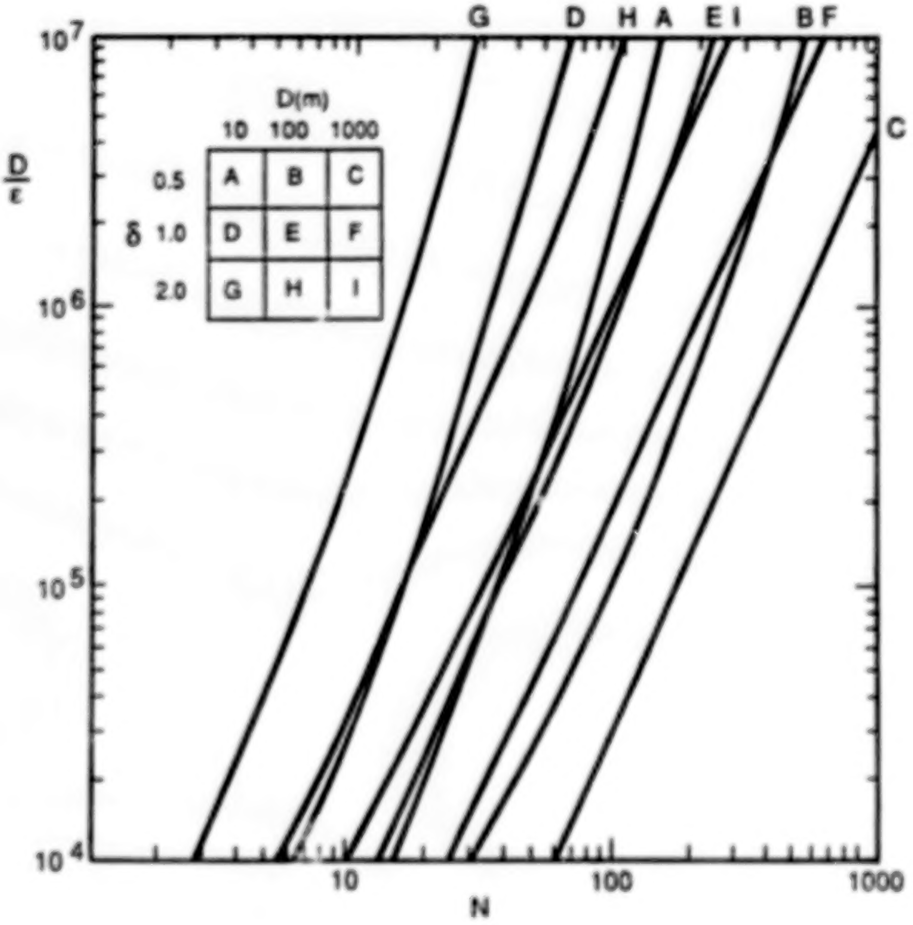

Figure 3

ADVANTAGES OF WRAP-RIB

The NASA Langley Study (ref. 3) demonstrated that for 1-mm rms on a 100-m-diameter antenna only 220 electrodes are required. The report found that the critical design parameters are packaging volume and weight, parts count complexity, and rf performance enhancement. The report found that the wrap-rib design could be used for the command surface and had the salient features of:

- Flight proven hardware
- Lightest weight - only 24 ribs for 100 m diameter at 5 GHz
- Smallest structural packaging volume
- Low total parts count

WRAP-RADIAL-RIP COMMAND SURFACE

The concept of employing the wrap radial rib as the command surface is depicted in Fig. 4. Instead of attaching the metallic mesh on the concave side of the ribs, as normal, the mesh is attached to the convex side and thereby acts as a bottom shield for the electrodes. The membrane acts as the upper shield, thus forming a protective Faraday cage to protect the electrodes from cosmic particles and other space debris. There is a central hub opening to allow the deployment of the feed and optics support structure.

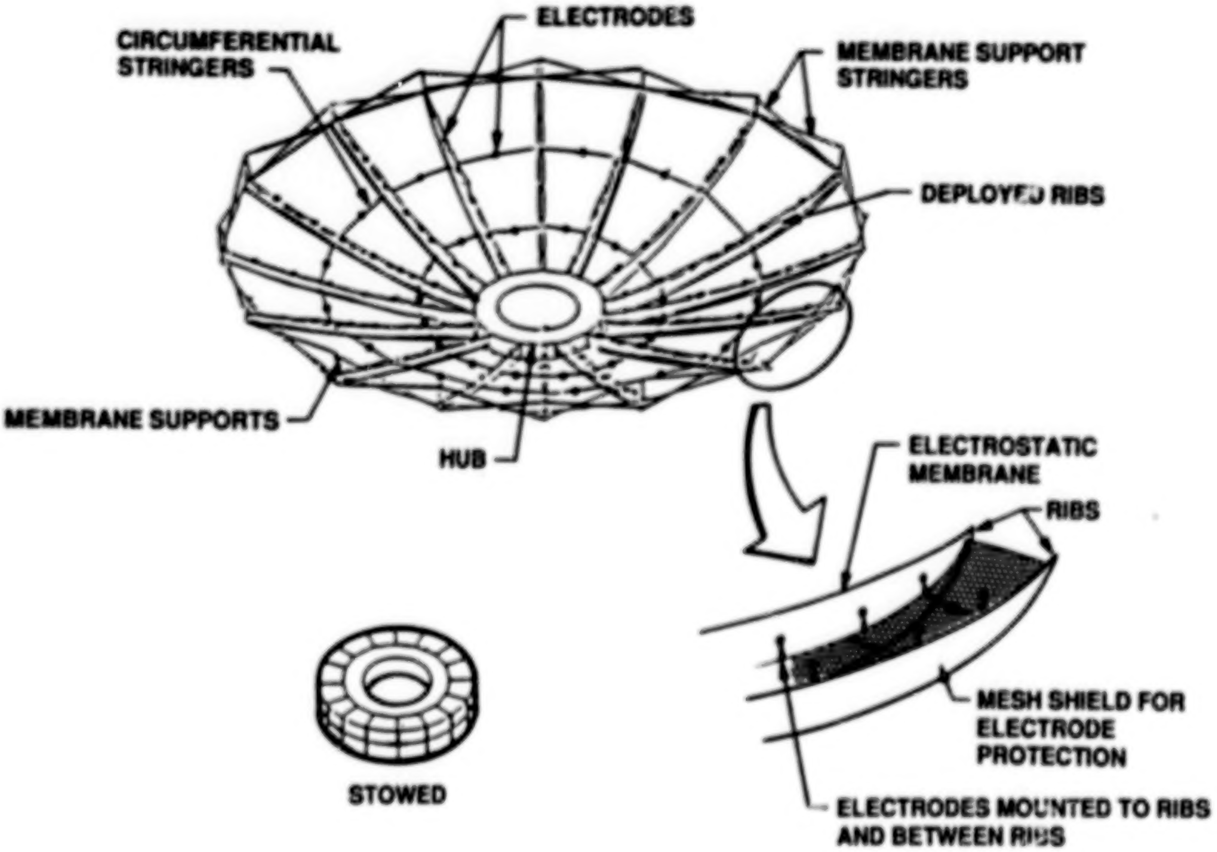
ELECTRODES
CIRCUMFERENTIAL STRINGERS
MEMBRANE SUPPORT STRINGERS
DEPLOYED RIBS
MEMBRANE SUPPORTS
HUB
ELECTROSTATIC MEMBRANE
RIBS
MESH SHIELD FOR ELECTRODE PROTECTION
STOWED
ELECTRODES MOUNTED TO RIBS AND BETWEEN RIBS

Figure 4

The optical system that senses the slope of the membrane is depicted in Fig. 5. It is located above the 0.2-m-diameter array feed. A two-axis scanning mirror scans the slope measurement beam over the membrane surface. A continuous scan in a spiral pattern from the outer edge to the center and continuing in the same direction from the center to the outer edge avoids vibration producing accelerations, minimizes cost, and maximizes reliability. Strong signals are received only when the beam scans over selected sample points where reflective material has been deposited on the membrane. The locations of sample points can be determined from angle resolvers in the scanner or, alternatively, bar codes similar to those used with point-of-sale scanners in supermarkets can be placed adjacent to the sample points.

The membrane slope is measured by using sideband interferometry. A plane-wave laser beam is split to form a reference beam and a membrane illumination beam. A pair of mirrors folds the reference beam onto an imaging sensor at a fixed angle. A partially reflective mirror directs the membrane illumination beam onto a two-axis scanning mirror which directs the beam onto the membrane where it is reflected by diffuse reflective material (e.g., used on projection screens) deposited on the membrane. The membrane illumination beam has a plane wavefront with constant phase over its cross section, but due to the membrane slope the reflected signal beam will have a linear variation of phase over its cross section. Membrane curvature within the area of illumination will also cause variation of the signal beam phase but this can be kept negligible by using a small illumination beam diameter. Part of the incident illumination forms a signal beam incident on the two-axis scanning mirror and is reflected toward the imaging sensor. Interference between the signal beam and the reference beam will produce a fringe pattern with fringe periodicity dependent on the angle between the two-beam wavefronts. Fourier analysis will provide measurement of fringe frequency which is related to the membrane slope by simple geometry.

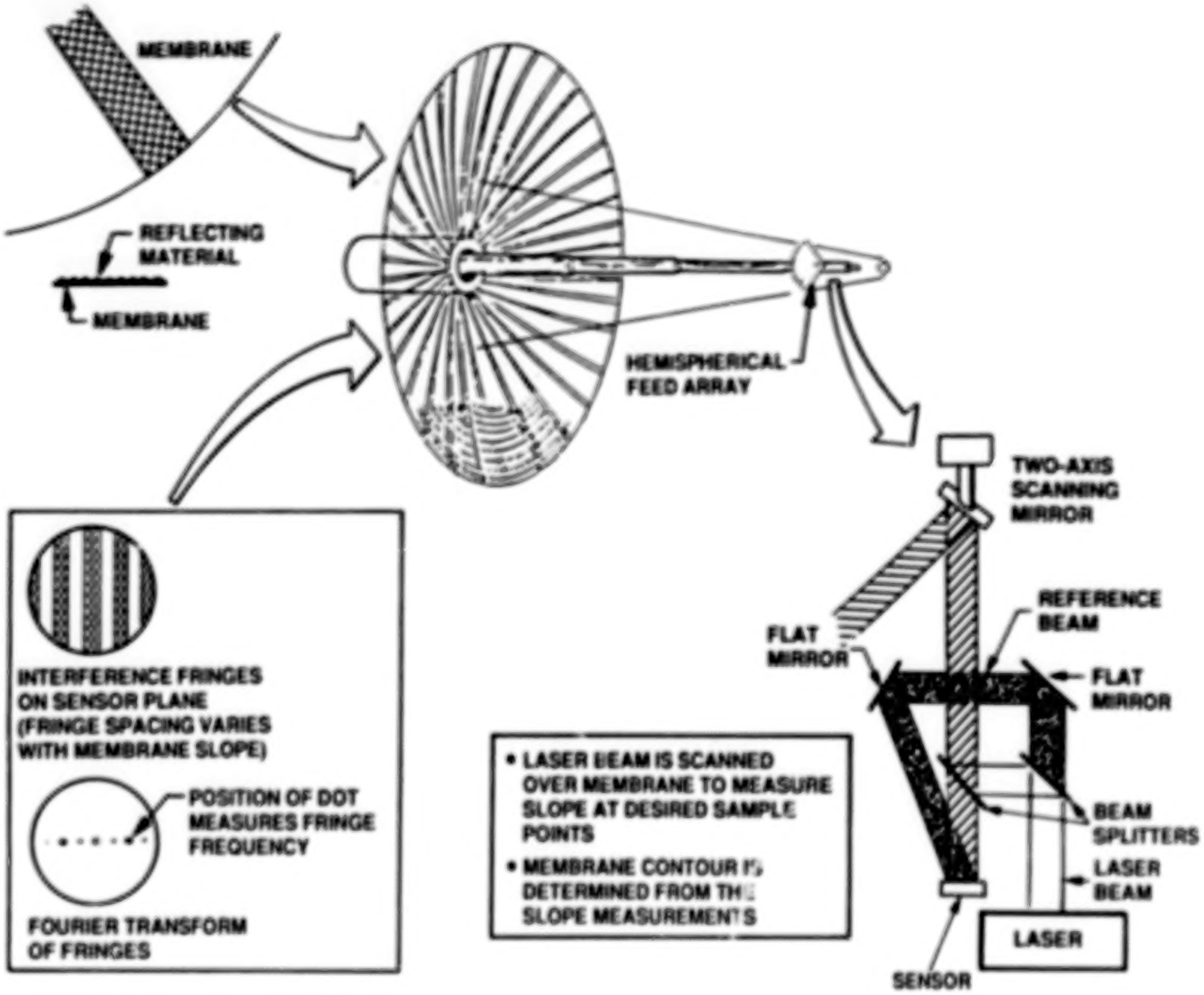
MEMBRANE
REFLECTING MATERIAL
MEMBRANE
HEMISPHERICAL FEED ARRAY
TWO-AXIS SCANNING MIRROR
REFERENCE BEAM
FLAT MIRROR
FLAT MIRROR
BEAM SPLITTERS
LASER BEAM
LASER
SENSOR
INTERFERENCE FRINGES ON SENSOR PLANE (FRINGE SPACING VARIES WITH MEMBRANE SLOPE)
POSITION OF DOT MEASURES FRINGE FREQUENCY
FOURIER TRANSFORM OF FRINGES

- LASER BEAM IS SCANNED OVER MEMBRANE TO MEASURE SLOPE AT DESIRED SAMPLE POINTS
- MEMBRANE CONTOUR IS DETERMINED FROM THE SLOPE MEASUREMENTS

Figure 5

MEMBRANE CONTROL CONCEPT

A feedback control system shown in Fig. 6 is used to minimize the effects of disturbances and to maintain stability. Feedback is based on sensing the membrane slope. Slope data are used to compute the membrane contour. This contour is compared to the desired contour, and voltage adjustments to correct the contour are computed. A voltage controller then adjusts the electrode voltages to the required values. Slope measurements will be corrupted by noise, so smoothing and filtering is used to obtain minimum mean-square-error estimates of slope. The control voltage adjustments are computed to minimize mean square error in control and ensure stability.

The closed-loop dynamic control system will operate in an unstable condition and can incorporate VHSIC technology.

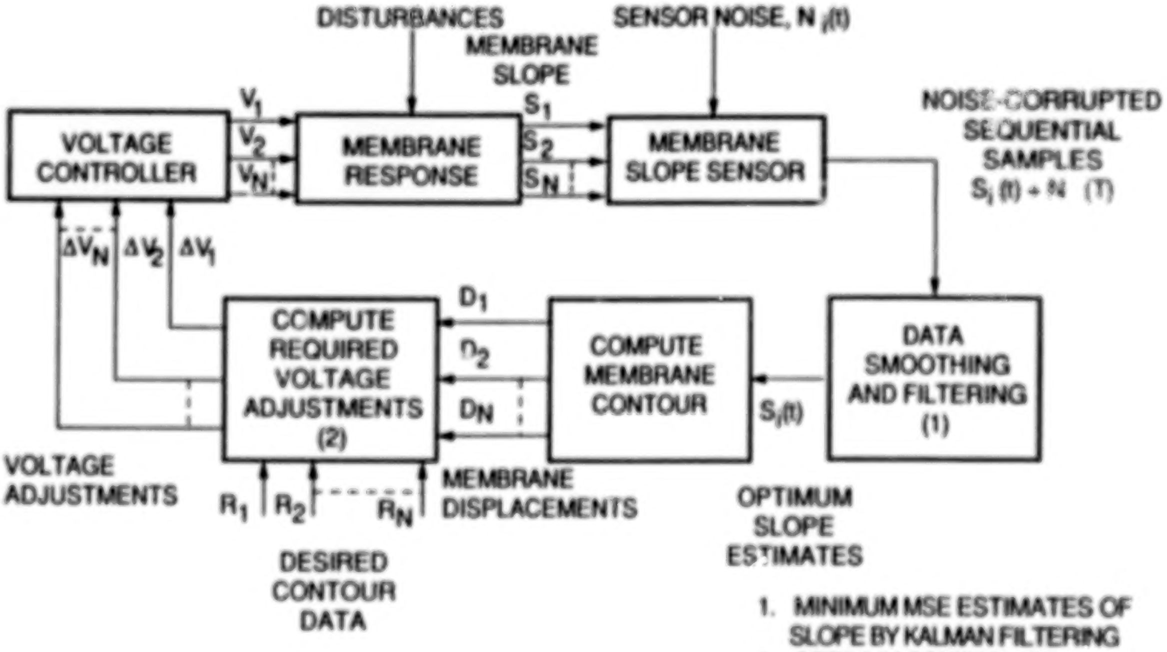

DISTURBANCES
SENSOR NOISE, $N_i(t)$
MEMBRANE SLOPE
V_1
V_2
V_N
S_1
S_2
S_N
NOISE-CORRUPTED SEQUENTIAL SAMPLES
$S_i(t) + N_i(T)$
VOLTAGE CONTROLLER
MEMBRANE RESPONSE
MEMBRANE SLOPE SENSOR
ΔV_N
ΔV_2
ΔV_1
D_1
D_2
D_N
COMPUTE REQUIRED VOLTAGE ADJUSTMENTS (2)
COMPUTE MEMBRANE CONTOUR
$S_i(t)$
DATA SMOOTHING AND FILTERING (1)
VOLTAGE ADJUSTMENTS
R_1
R_2
R_N
MEMBRANE DISPLACEMENTS
OPTIMUM SLOPE ESTIMATES
DESIRED CONTOUR DATA

1. MINIMUM MSE ESTIMATES OF SLOPE BY KALMAN FILTERING
2. OPTIMUM CONTROL OF MEMBRANE CONTOUR SUBJECT TO STABILITY CONSTRAINTS

Figure 6

DUAL-BAND ELEMENTS

To obtain electronic off-axis scan, the dish must be spherical. Parabolic dishes only allow a 10-beamwidth scan for 90% main-lobe efficiency. To scan a spherical dish, the prime focus feed must be either a line source linear array or a hemispherical cluster array as shown in Fig. 5.

The array will consist of dual-band elements depicted in the figure for a Millimeter Wavelength Reflector (ref. 6). The high-band, circular-waveguide elements nested between and within the coax low-band elements will receive energy over the H_2O, and window frequencies of 183 and 220 GHz, respectively. The coax element will receive energy at the O_2, and window frequencies of 60 and 90 GHz, respectively. The mid-band separation ratio of 2.6 (i.e., 200 GHz/75 GHz) is identical to the optimum packing ratio, thus avoiding grating lobes.

The coaxial-array element flown on the Viking deep-space mission will receive all senses of polarization.

It is also possible to include the bands below 60 GHz in the configuration of Fig. 5. By placing an additional cassegrain feed on the central mast with a shuttle tile support mast replacing he graphite-epoxy mast in front of the feed. The tile has a dielectric constant of 1.07 which is essentially transparent to the rf energy and will mechanically support a frequency-selective cassegrain subreflector placed in front of the millimeter wave spherical prime-focus feed of Fig. 7.

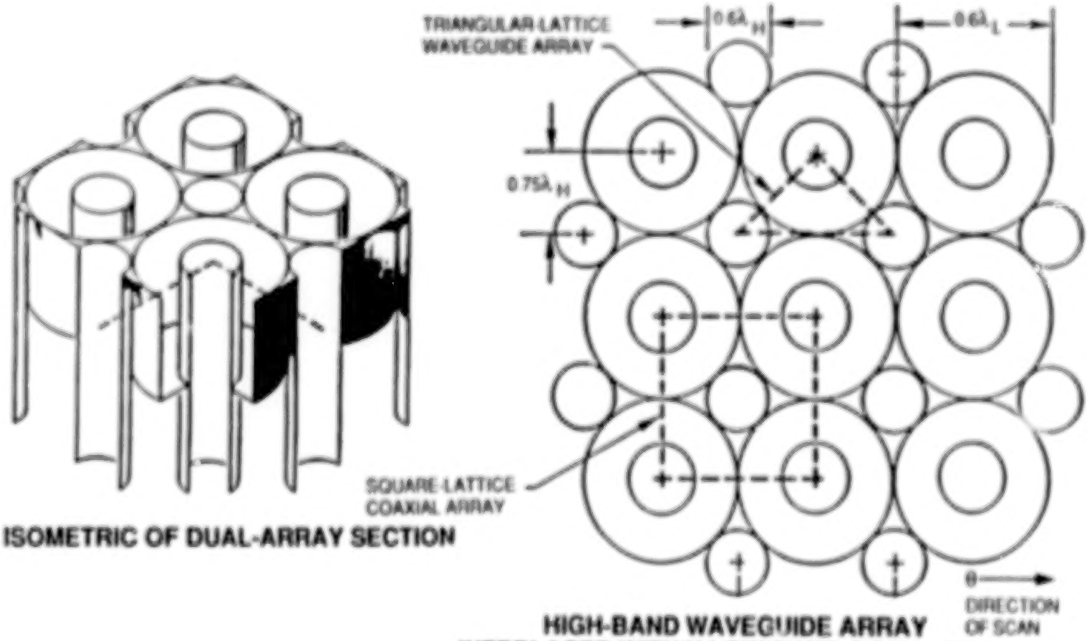
TRIANGULAR-LATTICE WAVEGUIDE ARRAY
$0.6\lambda_H$
$0.6\lambda_L$
$0.75\lambda_H$
SQUARE-LATTICE COAXIAL ARRAY
θ
DIRECTION OF SCAN

ISOMETRIC OF DUAL-ARRAY SECTION

HIGH-BAND WAVEGUIDE ARRAY INTERLACED WITHIN LOW-BAND COAX ARRAY

Figure 7

MILLIMETER WAVELENGTH REFLECTOR

The shuttle tile may also be used to fabricate a rigid, thermally stable 4.4-rm diameter dish. The amorphous S_iO_2 tile material has the lowest coefficient of thermal expansion for a space-qualfied material having a high strength to low mass ratio. A 1 lb, millimeter wavelength reflector that operates from 60 to 90 GHz and fabricated from third-generation shuttle tile is shown in Fig. 8. It has survived a random vibration of 24 g rms.

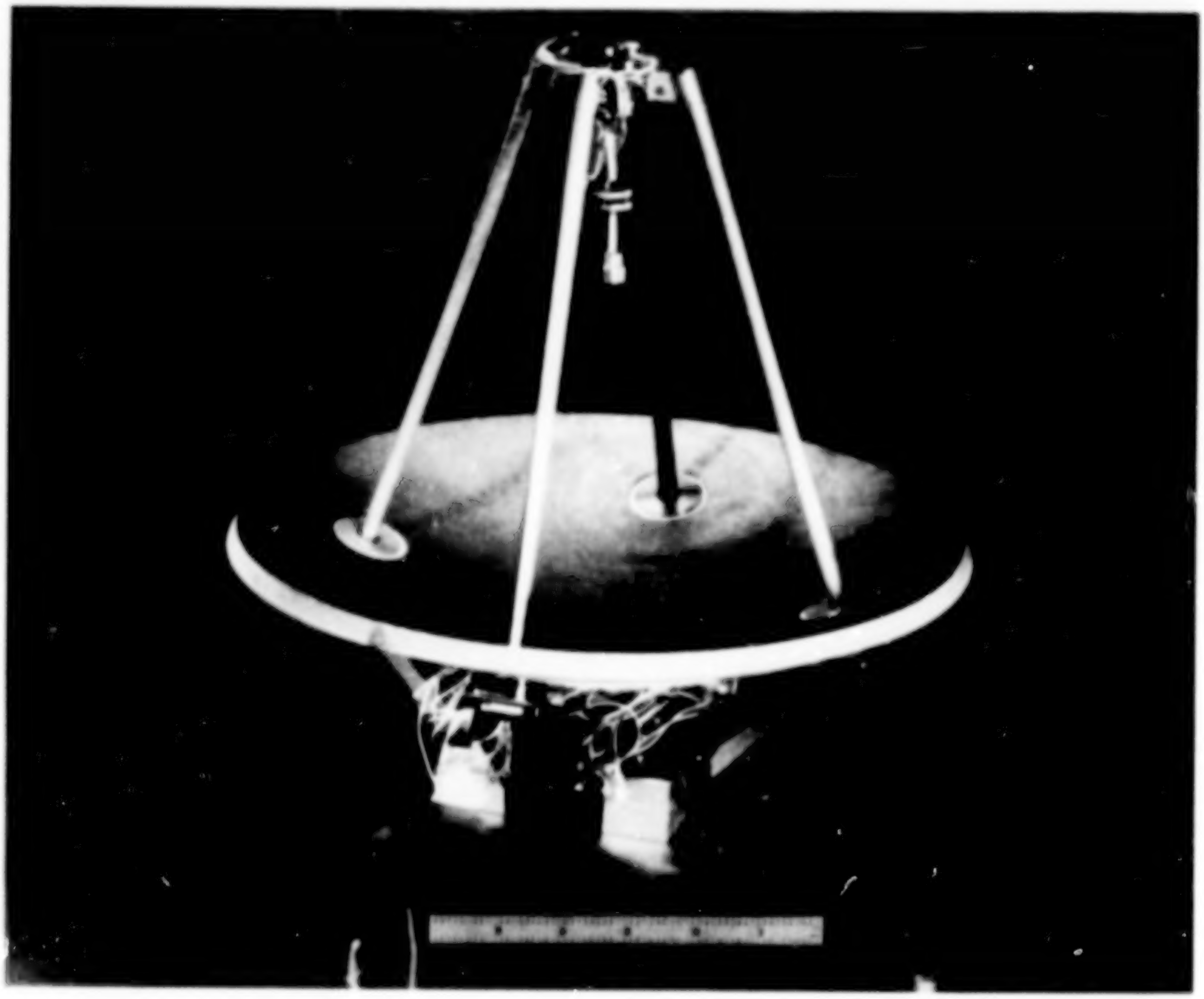

Figure 8

PROOF OF CONCEPT AND DEMONSTRATION MODEL

In conclusion, the wrap-rib, electrostatic-membrane reflector is several orders of magnitude lighter than the nondeployed rigid reflectors and does not have an aperture constrained by the 4.4-m diameter of the launch vehicle envelope.

It is recommended that a scaled demonstration model be fabricated from space-qualified materials and tested for the space environment as follows:

- Use existing 2-m-diameter wrap-rib and space-qualified materials for design and development of electro-static membrane
- Test laser sensor and control system
- Perform control near-field RF test
- Perform thermal vacuum test
- Perform final near-field RF test

REFERENCES

1. Mihora, D.J., Precision Low Mass Membrane Antenna, IEEE Military Microwaves '80, October 1980, pp. 344-349.

2. Lang, Jeffrey H. and Staelin, David H., Electrostatically Figured Reflecting Membrane Antennas for Satellites, IEEE Trans on Automatic Control, Vol. 27, No. 3, June 1982, pp. 666-670.

3. Brook, A.L., et al, Conceptual Design and Analysis of a Large Antenna Utilizing Electrostatic Membrane Management, NASA Contractor Report 3522, May 1982, p. 312.

4. Goslee, J.W., et al, Electrostatic Forming and Testing of Polymer Films on a 16-Foot-Diameter Test Fixture, NASA-TM-86328, Feb 1985, p. 34.

5. Calflin, E. Scott and Bareket, Noah, Configuring an Electrosatic Membrane Mirror by Least-Squares Fitting with Analytically Derived Influence Functions, J. Optical Society of America A, Vol. 3, November 1986, pp. 1833-1839.

6. Gregorwich, W.S., A Multipolarization Dual-Band Array, 1975 IEEE International Antennas and Propagation Symposium, pp. 189-192.

DESIGN OF A LOW-FREQUENCY (5-20 GHz), 15-METER-DIAMETER PASSIVE RADIOMETER FOR GEOSTATIONARY EARTH SCIENCE PLATFORMS*

A. K. Sinha
Lockheed Missiles and Space Company, Inc.
Sunnyvale, California

---

*Some original figures not available at time of publication.

UNITED STATES OF AMERICA
GOVERNMENT PRINTING OFFICE

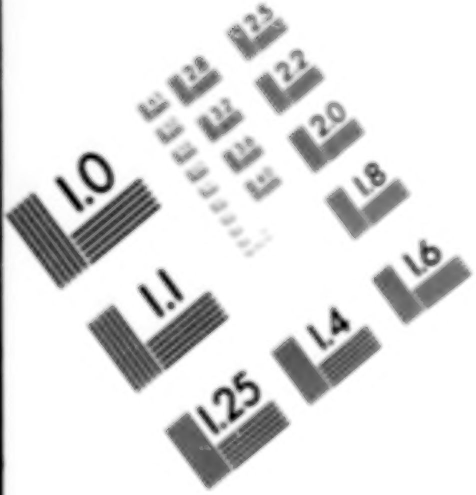
1.0
1.1
1.25
1.4
1.6
1.8
2.0
2.2
2.5
2.8

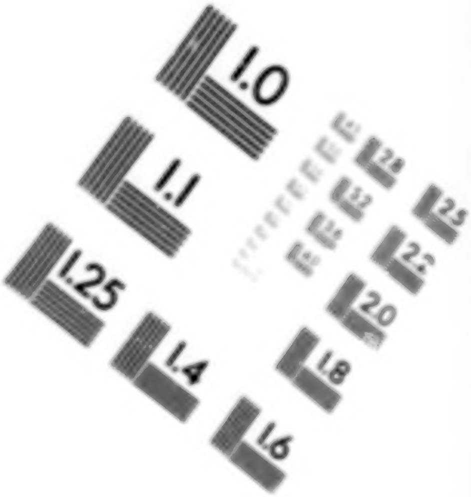
1.0
1.1
1.25
1.4
1.6
1.8
2.0
2.2
2.5
2.8

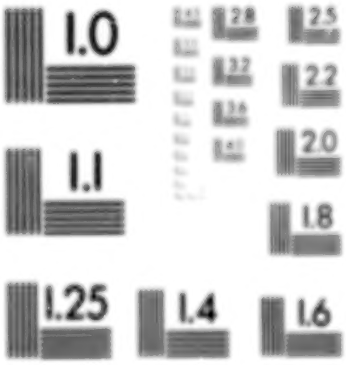
1.0
1.1
1.25
1.4
1.6
1.8
2.0
2.2
2.5
2.8
3.2
3.6
4.0

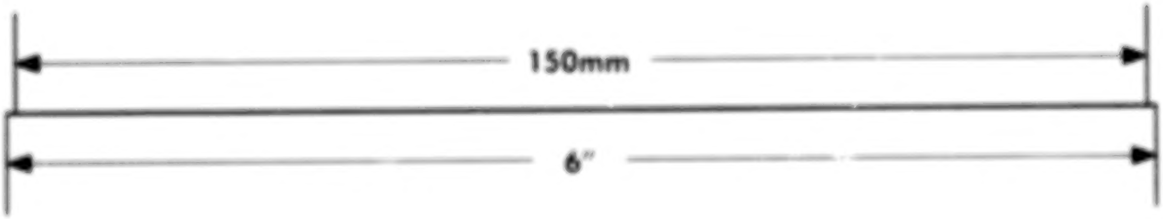

1.0
1.1
1.25
1.4
1.6
1.8
2.0
2.2
2.5
2.8

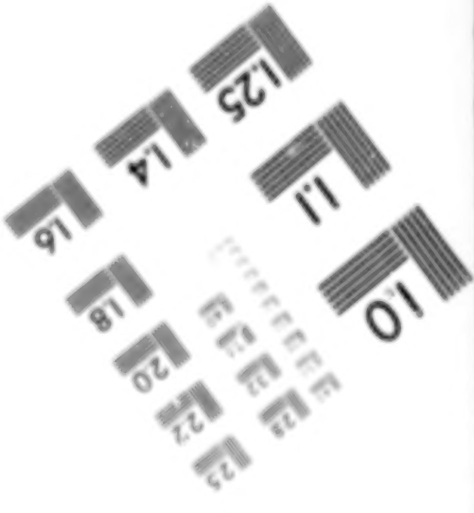
1.0
1.1
1.25
1.4
1.6
1.8
2.0
2.2
2.5
2.8

WHAT IS A WRAP-RIB REFLECTOR?

The Wrap-Rib Antenna is a deployable lightweight shaped reflector as shown in Fig. 1. It consists of a central hub, parabolic ribs, and an rf reflective mesh. The wrap-rib reflector approximates the desired surface by means of pie-shaped segments of parablic cylinders.

The wrap-rib concept has the advantage of a compact stowage container when the reflector is fully furled. The reflector will completely unfurl on command using the stored energy of the wrapped ribs when the peripheral cable securing the stowage doors is cut by a pyrotechnic operated cable cutter.

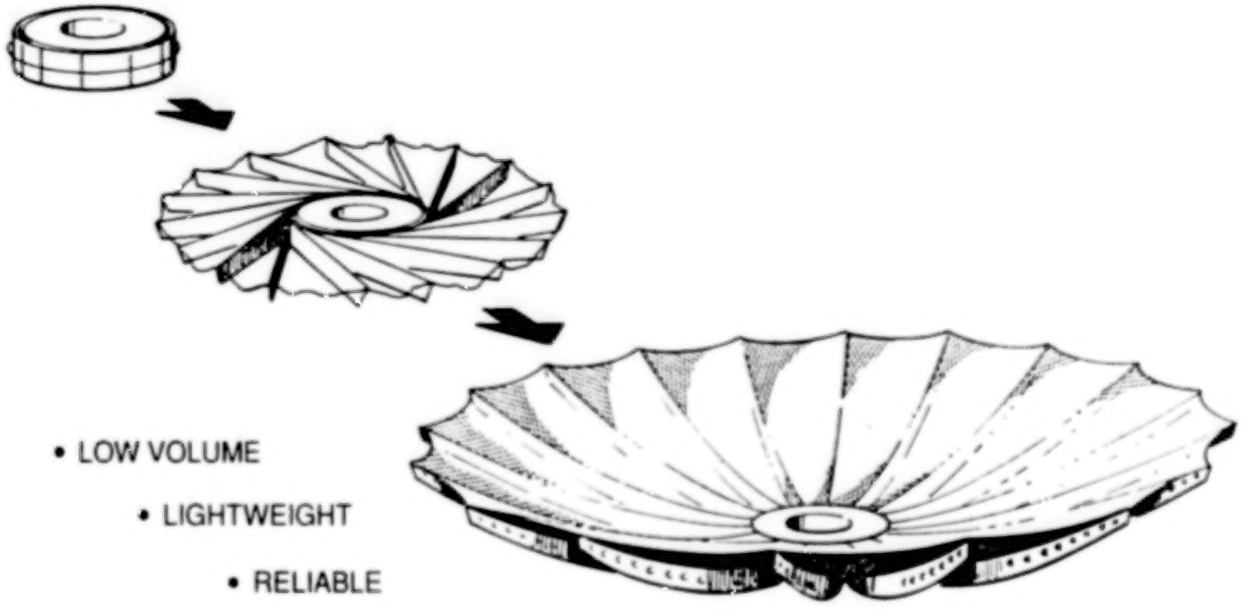

- LOW VOLUME
- LIGHTWEIGHT
- RELIABLE
- HIGH ACCURACY

Figure 1

WRAP-RIB DESIGN DRIVERS

Figure 2 shows a system-level overview of the reflector design parameters. The number of ribs employed is determined by the antenna operating frequency and the reflector size. The hub diameter is also dependent on the number of ribs needed for proper rf operation. The reflector container height can be held to approximately 3 percent of reflector diameter. The rib and mesh materials are selected to suit specific applications, e.g., at higher rf frequencies, ribs made of graphite/epoxy, and low CTE* mesh materials are needed to reduce the deleterious effects of thermal distortion.

---

*Coefficient of thermal expansion (CTE).

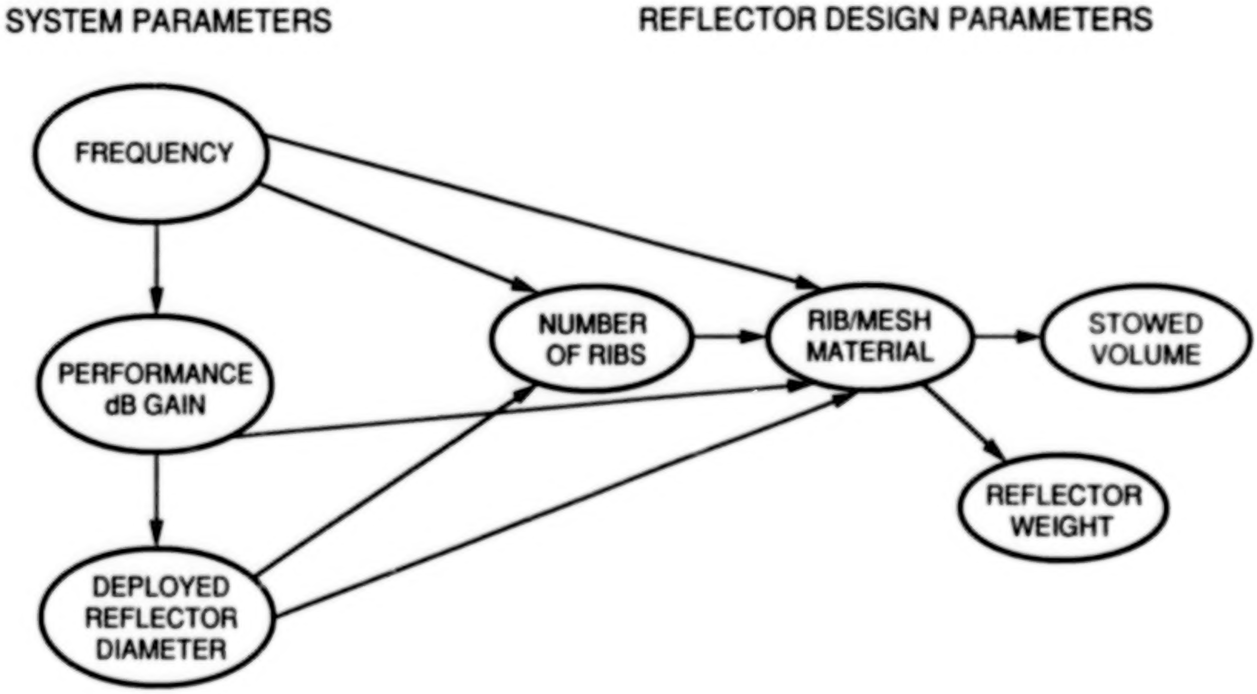
SYSTEM PARAMETERS
REFLECTOR DESIGN PARAMETERS
FREQUENCY
PERFORMANCE dB GAIN
DEPLOYED REFLECTOR DIAMETER
NUMBER OF RIBS
RIB/MESH MATERIAL
STOWED VOLUME
REFLECTOR WEIGHT

Figure 2

LMSC* REFLECTOR HISTORY

As shown in Fig. 3, LMSC Antenna Laboratory has been involved in the development of the wrap-rib reflector technology for the past 20 years. To date, the designs of 3-, 6-, 10-, 20-, and 30-ft-diameter reflectors have been manufactured and qualified for space application. The largest feasible diameter depends on the frequency of operation, but the designs for antennas as large as 150 ft in diameter have been studied. One of these studies led to a partial build of a 55-m-diameter antenna for a NASA contract during 1983-84.

*Lockheed Missiles and Space Company (LMSC).

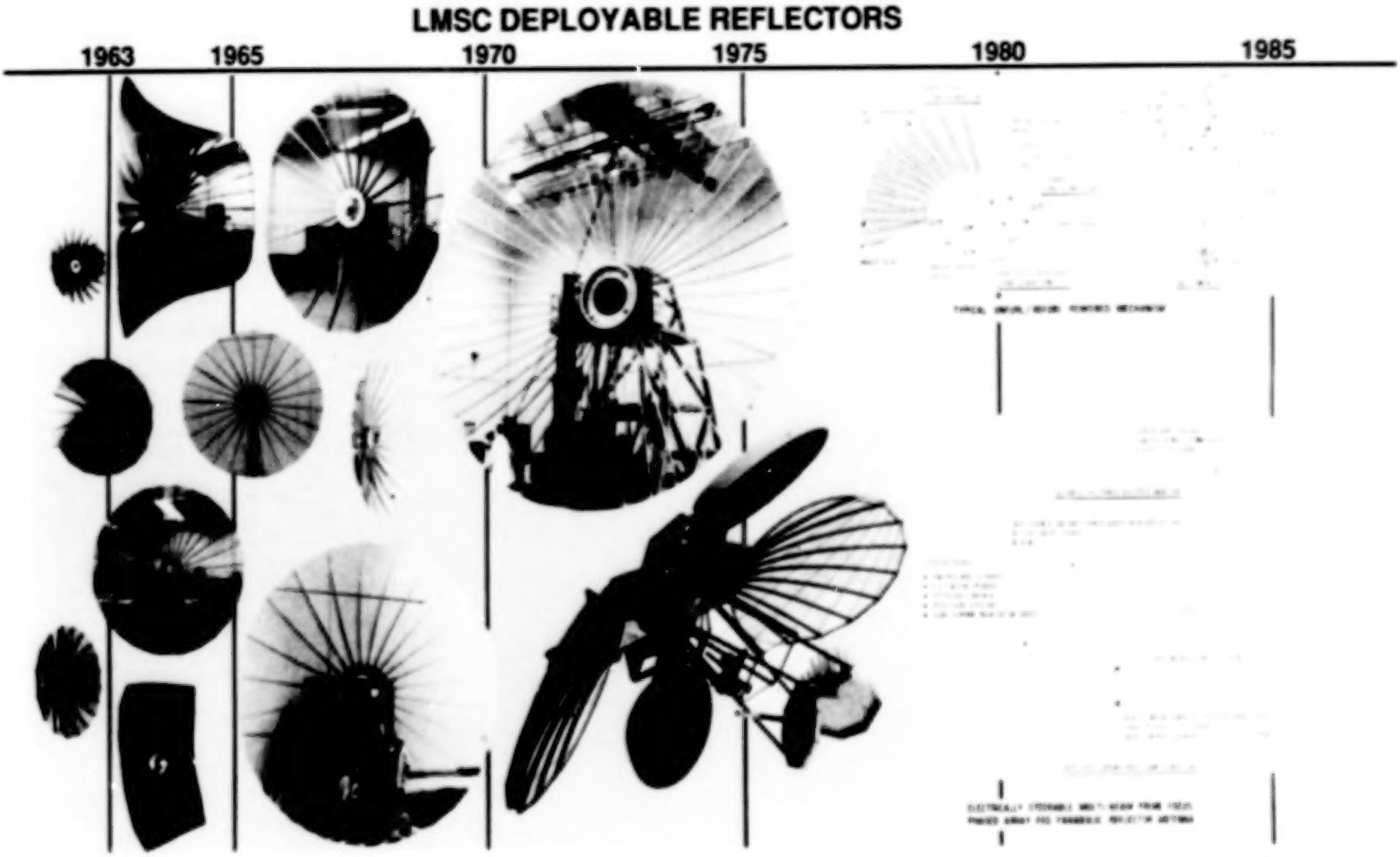

LMSC DEPLOYABLE REFLECTORS

Figure 3

MOTOR-DRIVEN, FLEX-RIB ANTENNA UNFURLING

Over the past several years, Lockheed has studied several controlled deployment concepts. The controlled deployment concept will reduce the impact of a sudden release of stored strain energy in the ribs. This will also reduce the effect of sudden reaction force on the spacecraft.

Two main concepts are shown in Figs. 4 and 5. The first is based on a gear and motor system where the hub is turned by the motor, and the ribs are guided through a set of candles. The second deployment is based on power-driven tape. The tape is attached to the central hub and wrapped circumferentially along every third rib. The tape travels over a set of idlers and then a slack take-up mechanics terminates at a spool that is part of the central hub.

The addition of these mechanism makes the design a lot more complicated and adds substantially to the system weight. The controlled deployment system is not recommended until the ground test or other system constraints prove that it is required.

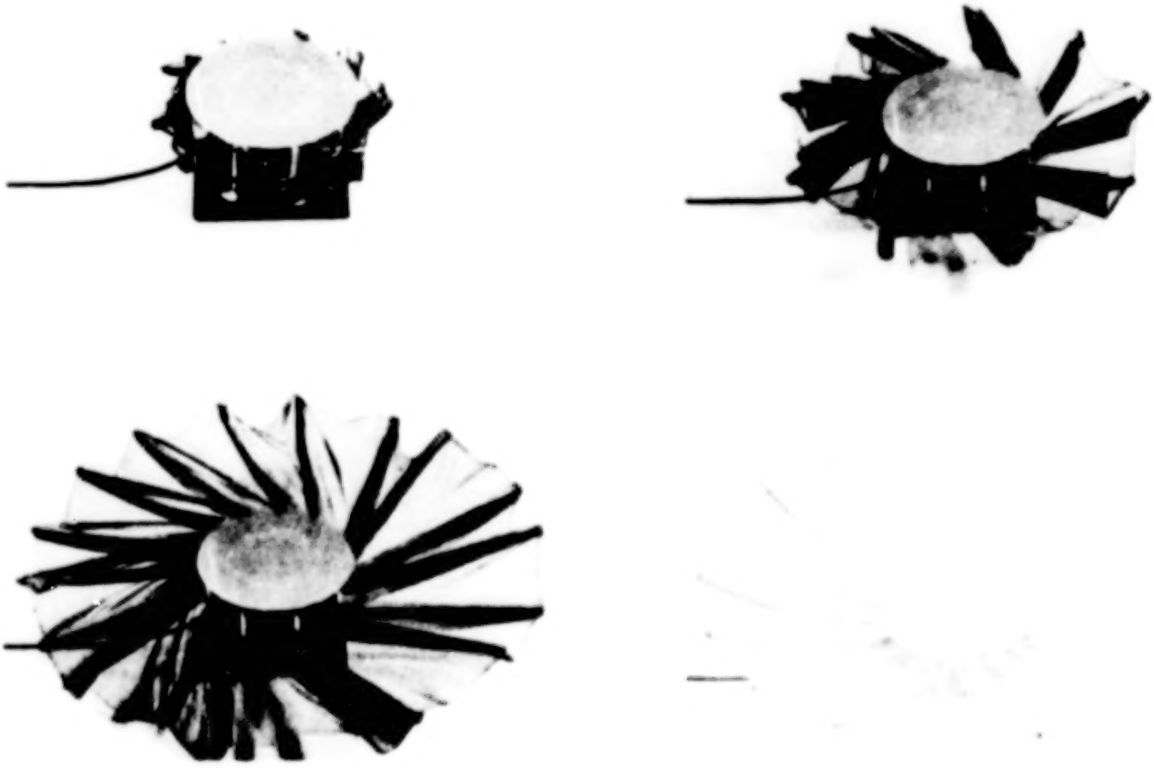

Figure 4

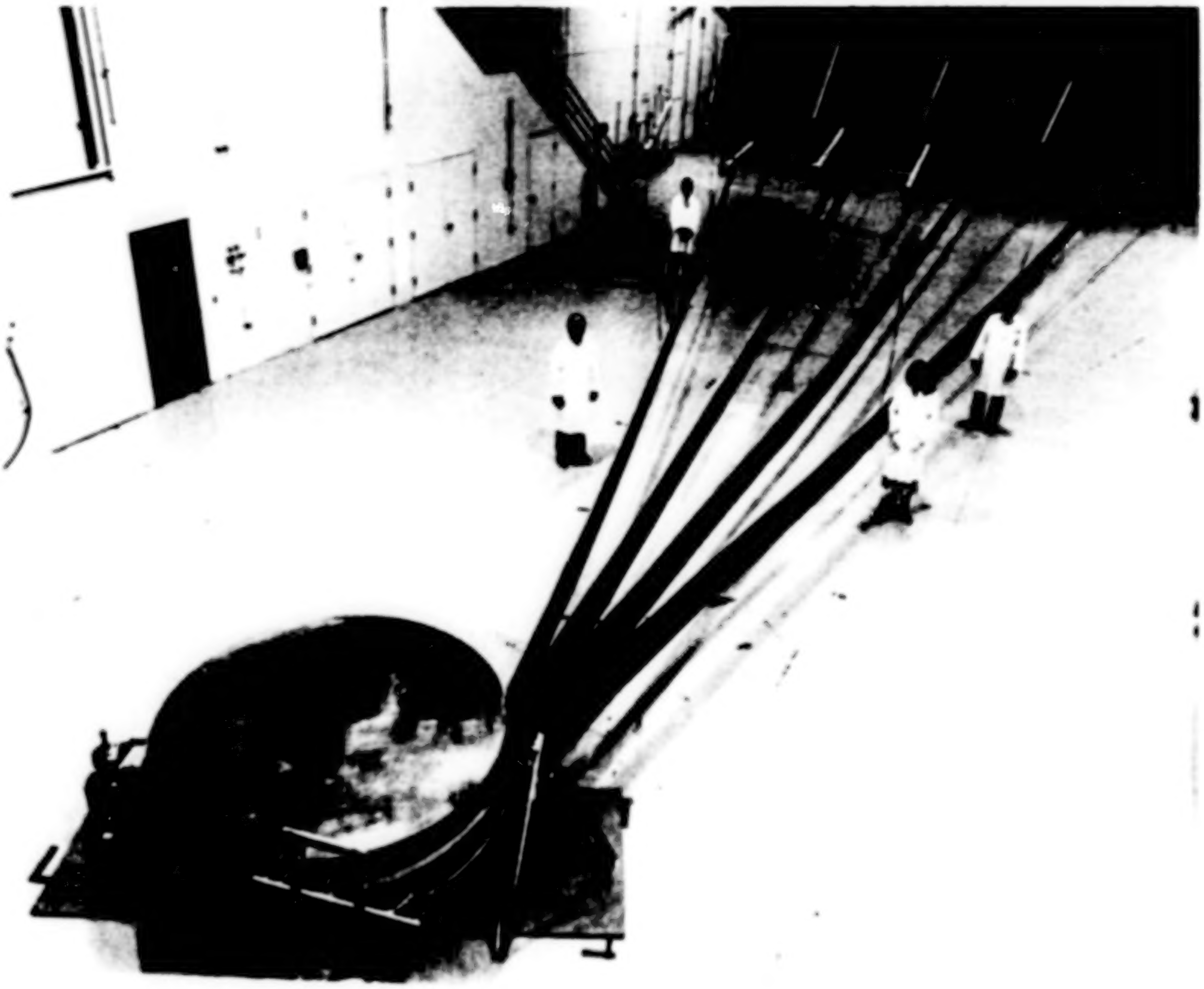

Figure 5

WRAP-RIB TECHNOLOGY STATUS

The ATS-6 spacecraft, shown in Fig. 6, carried a 30-ft-diameter wrap-rib antenna made of aluminum ribs and Dacron mesh. It was designed to operate up to an 8 GHz frequency. The deleterious effect of thermal distortion in space limits the use of such a system to relatively low frequencies. To overcome this limitation, LMSC has worked extensively on the development of thermally stable materials for ribs and mesh. These advances have made it possible to design an antenna system operable at 25 GHz with only a very low-gain degradation of 0.75 dB.

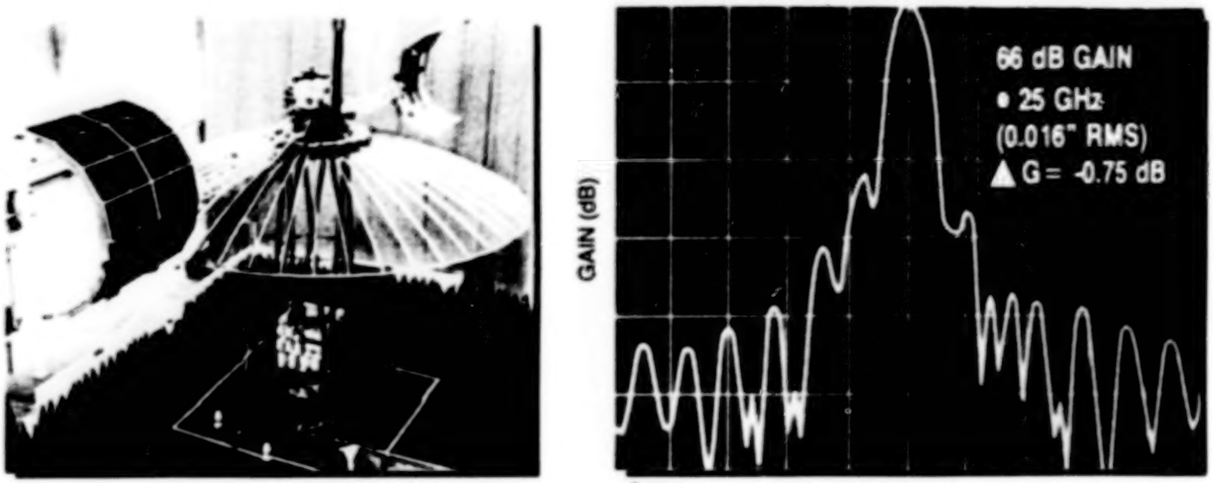

ATS-6 SPACECRAFT

30-ft DIA
WORST CASE PERFORMANCE

MODERN WRAP RIB KEY FEATURES

- ☐ GRAPHITE-EPOXY RIBS
- ☐ PROPRIETARY KEVLAR/BeCu MESH
- ☐ PASSIVE DEPLOYMENT
- ☐ PROVEN TECHNOLOGIES
- ☐ VERIFIED ANALYSIS
- ☐ PASSIVE INTERMOD PRODUCTS < -150 dB

Figure 6

WRAP-RIB TECHNOLOGY DEVELOPMENT

The wrap-rib technology development matrix, shown in Fig. 7, lists the various areas in which the technology development is taking place to meet the future application needs for higher frequencies and larger diameters. Advances in materials and design methodology have resulted in thermally and visco-elastically stable structure for the ribs. The same type of effort is focused in the area of developing thermally stable mesh designs. These activities in the rib and mesh materials are extensively supported by hardware tests. Some work has been done in the controlled deployment concept development, but it has not attracted concentrated attention. One of the major focuses has been to develop analytical methods to accurately predict the antenna far-field in an integrated way. The approach has been to integrate the various softwares in the rf and structural analysis areas.

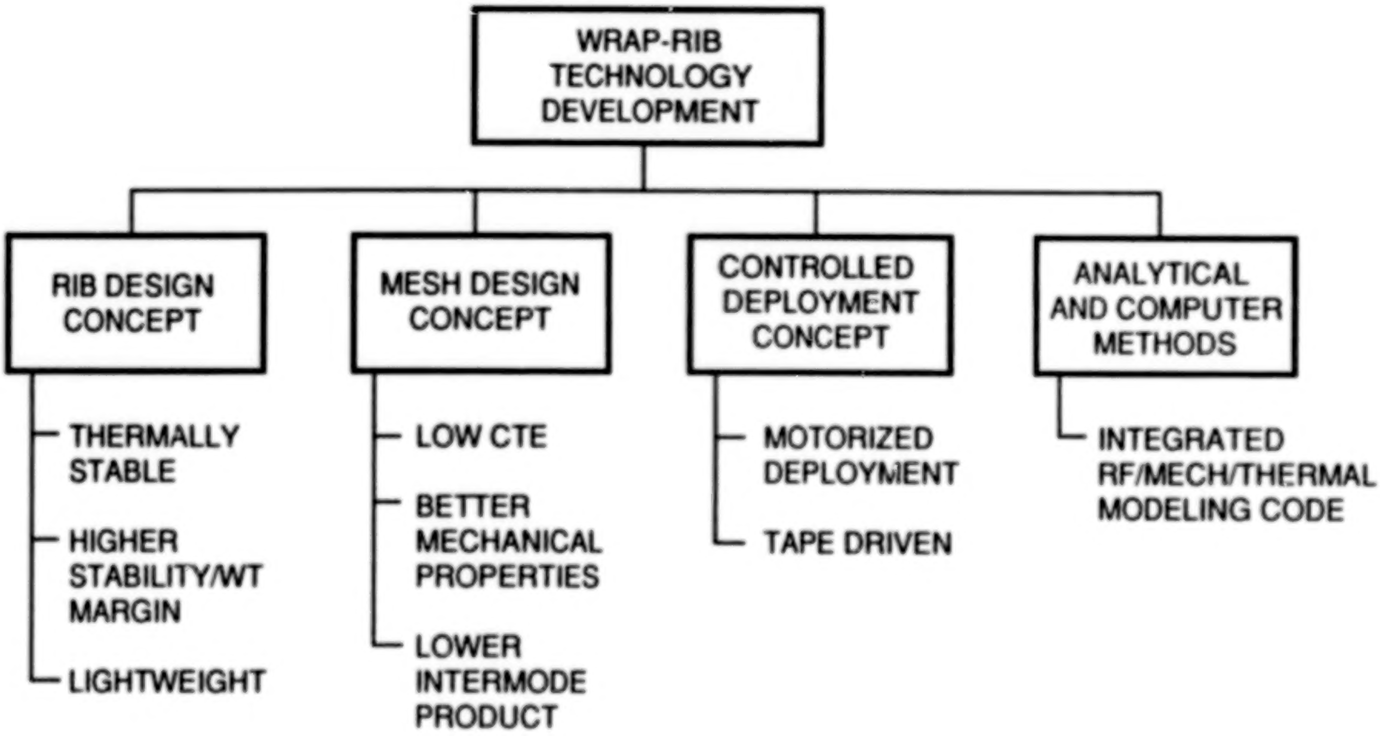
WRAP-RIB TECHNOLOGY DEVELOPMENT
RIB DESIGN CONCEPT
THERMALLY STABLE
HIGHER STABILITY/WT MARGIN
LIGHTWEIGHT
MESH DESIGN CONCEPT
LOW CTE
BETTER MECHANICAL PROPERTIES
LOWER INTERMODE PRODUCT
CONTROLLED DEPLOYMENT CONCEPT
MOTORIZED DEPLOYMENT
TAPE DRIVEN
ANALYTICAL AND COMPUTER METHODS
INTEGRATED RF/MECH/THERMAL MODELING CODE

Figure 7

Figure 8 shows the tested visco-elastic behavior of the newly designed C-section rib made of graphite-expoxy. In this test the long-term, visco-elastic behavior was simulated by submerging the specimen in hot water for 28 days and then recording its recovery over the next 14 days. As shown in the figure, the visco-elastic creep recovered to well within the 0.03 dB performance loss target that was set as our design requirement. This result is of great significance due to the fact that when a rib gets wrapped around the hub, it is subjected to stress levels very close to its yield limit and this had a tendency to produce appreciable creep deformation in the rib.

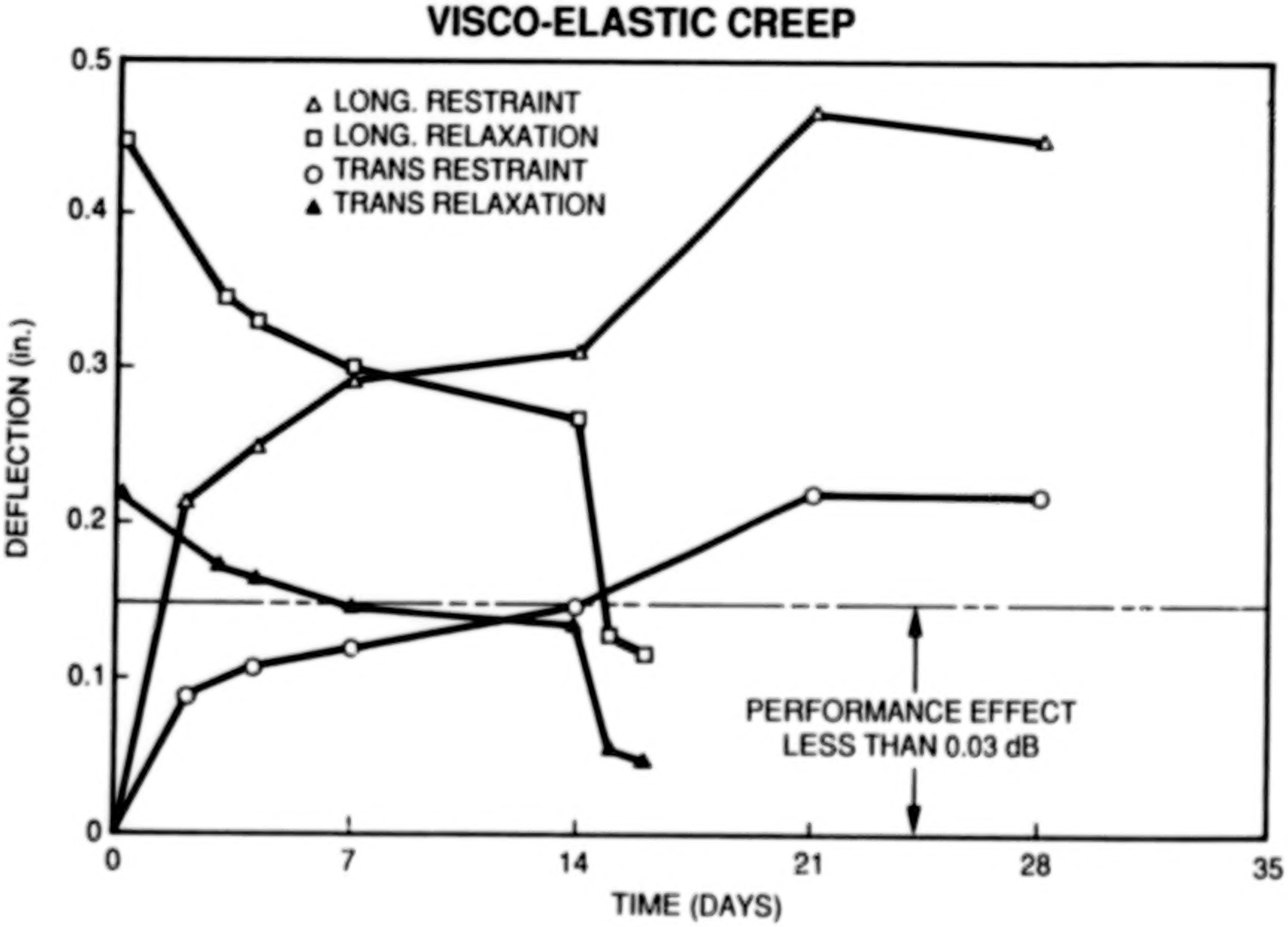

Figure 8

CTE STABILIZATION DATA

Figure 9 shows the results of CTE tests on the recently developed antenna mesh. As mentioned earlier, wrap-rib antenna design is a mesh-dominated design and any distortion of the mesh directly translates into the antenna performance degradation. Therefore, the goal was to design a zero CTE mesh, and from the test data one can determine that the new mesh CTE varies between -0.2×10^{-6} to 0.4×15^{-6} in./in/°F.

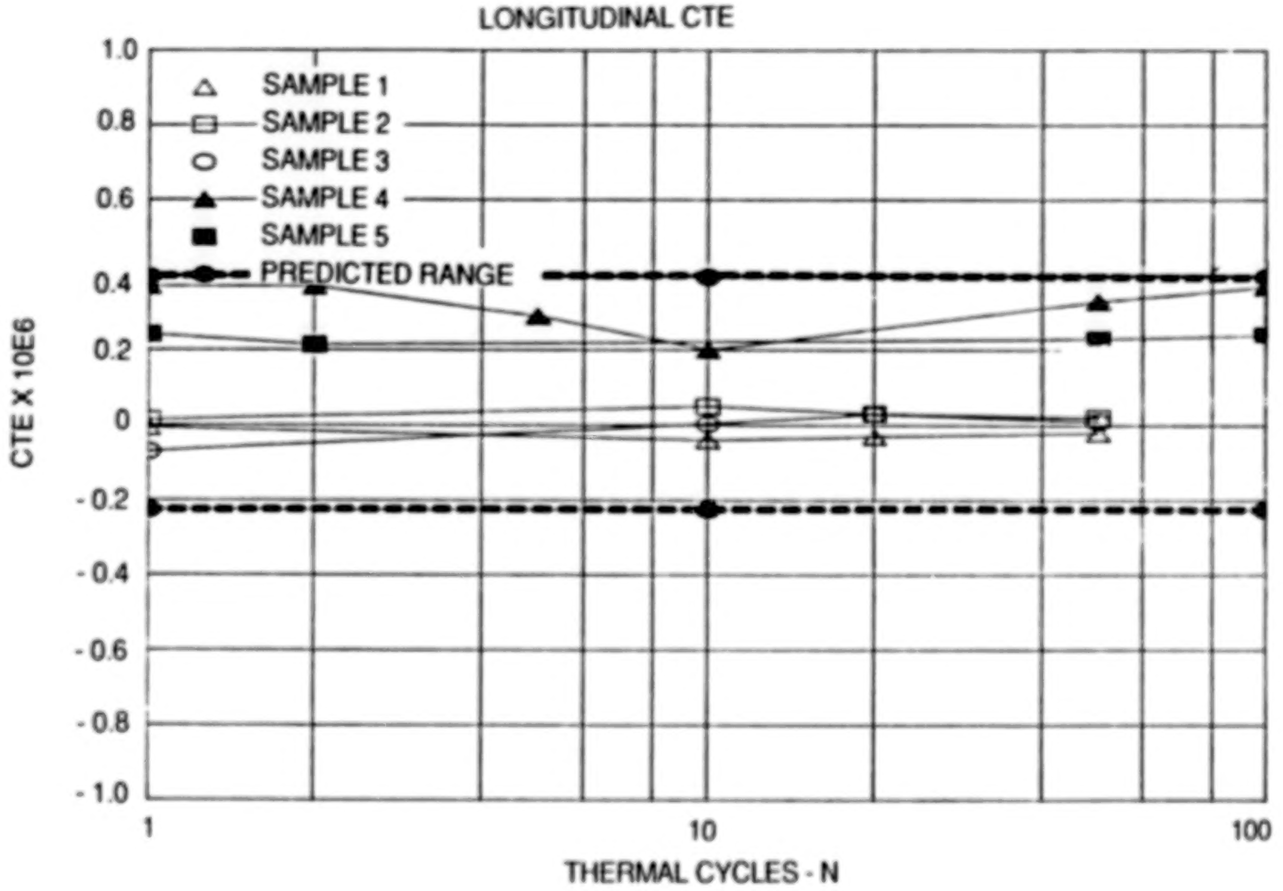

Figure 9

NEW MESH DATA

The material property table in Fig. 10 compares the data on the new mesh to the other types of mesh. It is obvious that the new mesh outperforms the moly/gold and Dacron in almost all the categories. For comparison, CTE improvement over the Dacron mesh which was used on the ATS-6 spacecraft is remarkable.

PROPERTY	BeCu - KEVLAR WEAVE	MoAu 2310/1012 KNIT	ATS DACRON WEAVE
ABSORPTIVITY/EMISSIVITY	0.289, 0.651 ①	0.480	0.167
CREEP RATE ② (in./in./day)			
WOOF/WALE	0	9.1×10^{-5}	- - -
WARP/COARSE	0	6.5×10^{-5}	- - -
COEFFICIENT OF THERMAL EXPANSION (10^{-6} /°F)	- 0.16	2.8	0.5 - 12.0 ③
RF REFLECTIVITY (%)	92.9 AT 25 GHz	99+ AT 25 GHz	99+ AT 8 GHz
SHEAR STIFFNESS (lb/in.)	(SEE NOTE 4)	1.9	- - -
SHEAR OVERSTRAIN	PASS	FAIL	PASS
TENSILE MODULUS (lb/in.)			
WOOF/WALE	45.9	5.3	(SEE NOTE 5)
WARP/COARSE	19.3	20.4	(SEE NOTE 5)

NOTES:

1. HIGHER α/ϵ VALUE IS FOR BeCu-KEVLAR WEAVE WITH A FLAT BLACK SILICONE OVERCOAT.
2. DUE TO THE SCOPE OF THE TESTING PROGRAM, CREEP RATES LISTED ARE GENERAL TENDENCIES DERIVED FROM THE DATA, NOT ABSOLUTE VALUES.
3. THE CTE FOR THE ATS DACRON MESH VARIES WITH TEMPERATURE FROM 12×10^{-6}/°F AT -280°F TO 0.5×10^{-6}/°F AT 80°F, WITH A TRANSITION DROP OF 8×10^{-6}/°F OCCURRING AT -80°F.
4. SHEAR STIFFNESS TESTING SUSPENDED DUE TO BUDGETARY CONSTRAINTS.
5. FOR ATS DACRON MESH, ONLY MODULUS OF A SINGLE STRAND IS AVAILABLE. ESTRAND = 3.6×10^{5} PSI.

Figure 10

Figure 11 shows the CTE stability of the new mesh over the temperature excursions to which antenna systems are subjected to while in an orbital environment. Again, the average values of CTE printed on the charge proves the thermal stability the new mesh.

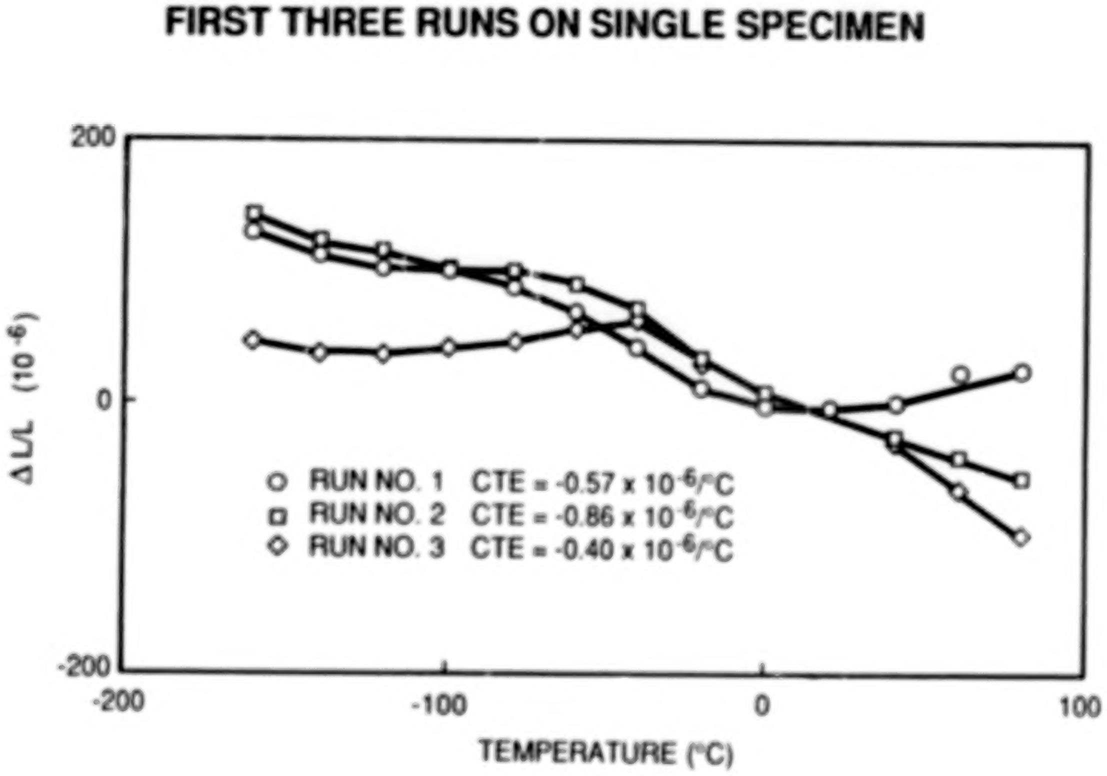

Figure 11

INTEGRATION RF PERFORMANCE EVALUATION

The flow chart in Fig. 12 shows the schematic of the integrated software analysis capability for antenna performance prediction. This spatial modeling of the antenna surface due to any perturbation mechanism includes the spacecraft dynamics and momentous transfer effect as a result of mechanical scanning. The analysis software can account for detailed thermal distortion as function of time and the orbital location. The rf prediction is based on physical optics formulation which is being updated to include the edge diffraction time using GTD technique.

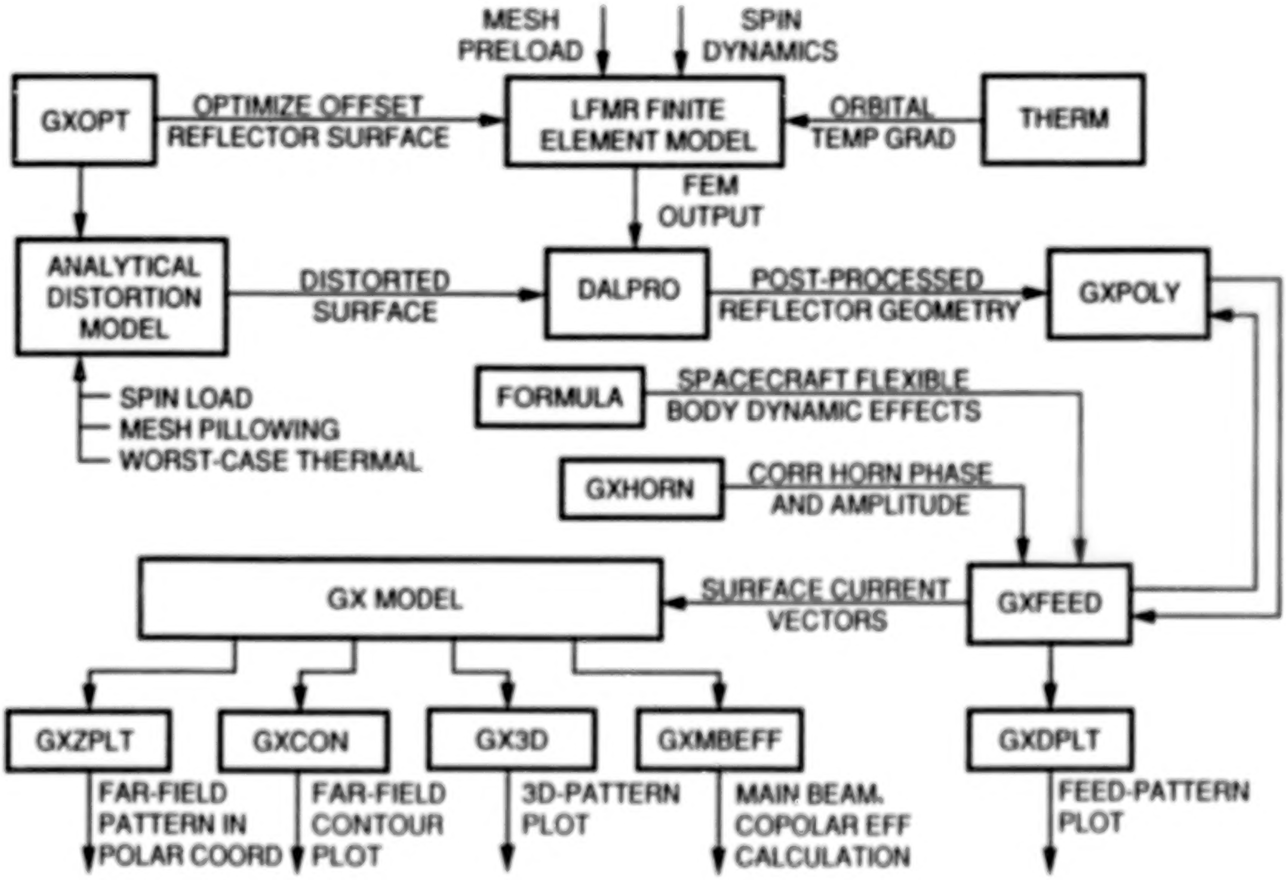
MESH PRELOAD
SPIN DYNAMICS
GXOPT
OPTIMIZE OFFSET REFLECTOR SURFACE
LFMR FINITE ELEMENT MODEL
ORBITAL TEMP GRAD
THERM
FEM OUTPUT
ANALYTICAL DISTORTION MODEL
DISTORTED SURFACE
DALPRO
POST-PROCESSED REFLECTOR GEOMETRY
GXPOLY
SPIN LOAD
MESH PILLOWING
WORST-CASE THERMAL
FORMULA
SPACECRAFT FLEXIBLE BODY DYNAMIC EFFECTS
GXHORN
CORR HORN PHASE AND AMPLITUDE
GX MODEL
SURFACE CURRENT VECTORS
GXFEED
GXZPLT
GXCON
GX3D
GXMBEFF
GXDPLT
FAR-FIELD PATTERN IN POLAR COORD
FAR-FIELD CONTOUR PLOT
3D-PATTERN PLOT
MAIN BEAM. COPOLAR EFF CALCULATION
FEED-PATTERN PLOT

Figure 12

RESULTS OF PERFORMANCE PREDICTION CODE

Figure 13 shows an example of the application of integrated software in solving the antenna far field. Segment (D) shows a finite-element model of 30-ft-diameter wrap-rib antenna. Segments (A) and (C) show the spatial temperature distribution on a typical rib and mesh respectively. And finally, segment (B) gives the antenna far field for the side-sun case. The asymmetrical distortion of the reflector surface for this side-sun case is graphically evident by the shift of the peak of the main beam.

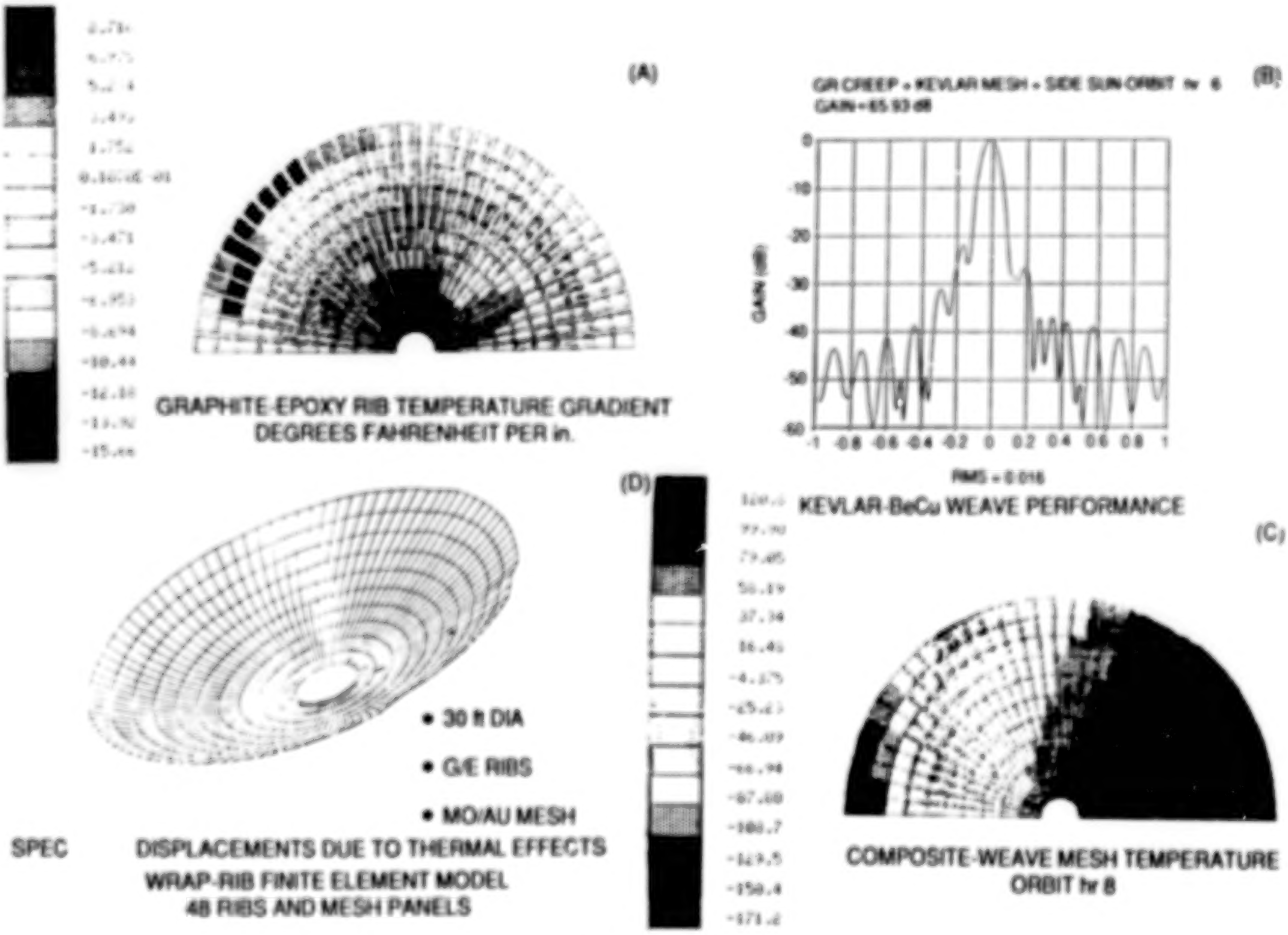

GRAPHITE-EPOXY RIB TEMPERATURE GRADIENT DEGREES FAHRENHEIT PER in.

KEVLAR-BeCu WEAVE PERFORMANCE

DISPLACEMENTS DUE TO THERMAL EFFECTS
WRAP-RIB FINITE ELEMENT MODEL
48 RIBS AND MESH PANELS

COMPOSITE-WEAVE MESH TEMPERATURE ORBIT hr 8

Figure 13

TECHNOLOGY RESULTS

Figures 14, 15, and 16 compare the results of new technology over the old technology vis-a-vis a baseline performance of 30-ft-diameter wrap rib with 68 ribs for a 25 GHz application. Under the old technology, an aluminum rib and Dacron mesh are used for the two worst orbital thermal conditions. As can be easily seen, the far-field pattern is badly degraded. There is approximately a 9 dB loss at 25 GHz. The same antenna made of composite mesh material and graphite-expoxy rib has only 0.3 dB loss for the worst thermal distortion case.

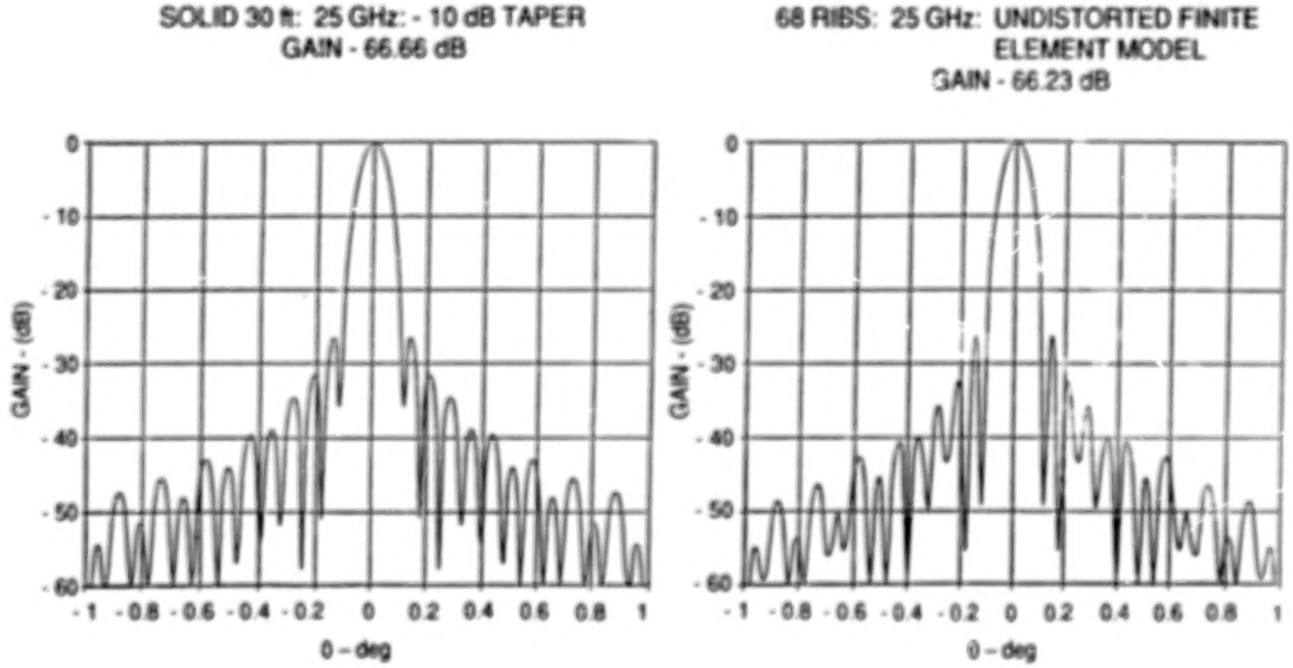
SOLID 30 ft: 25 GHz: - 10 dB TAPER
GAIN - 66.66 dB

68 RIBS: 25 GHz: UNDISTORTED FINITE ELEMENT MODEL
GAIN - 66.23 dB

ΔG = 0.43 dB (0.012 in. RMS)

Figure 14

OLD TECHNOLOGY WILL NOT MEET REQUIREMENTS

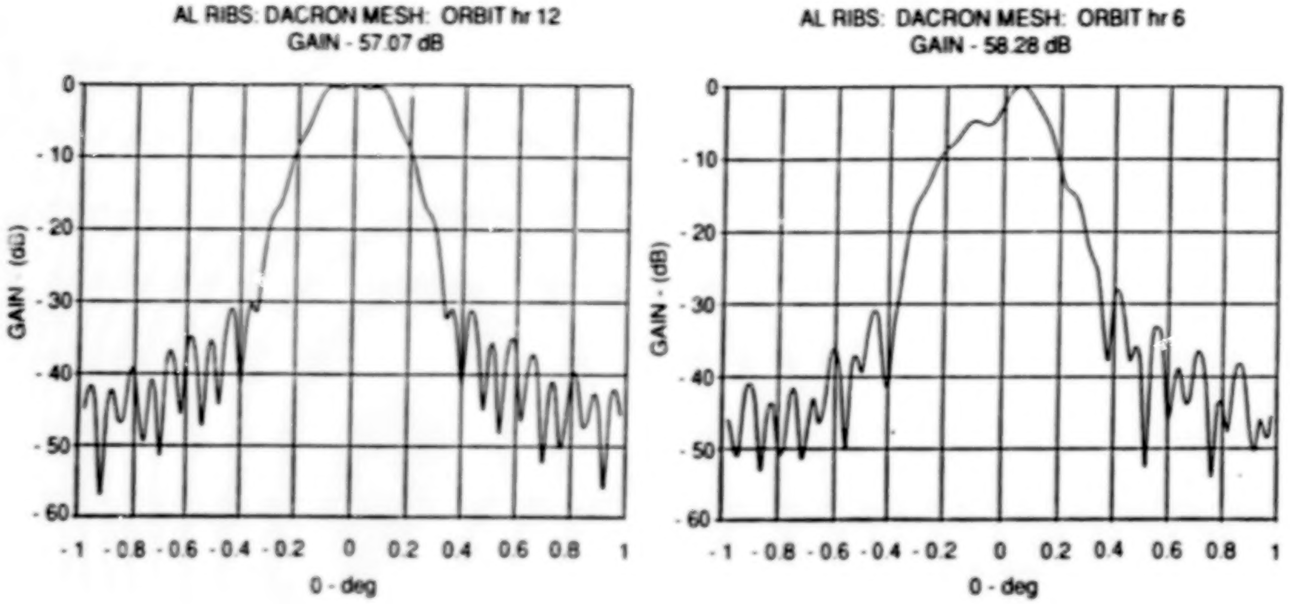

RMS = 0.056

RMS = 0.052

Figure 15

(U) KEVLAR-BeCu WEAVE PERFORMANCE

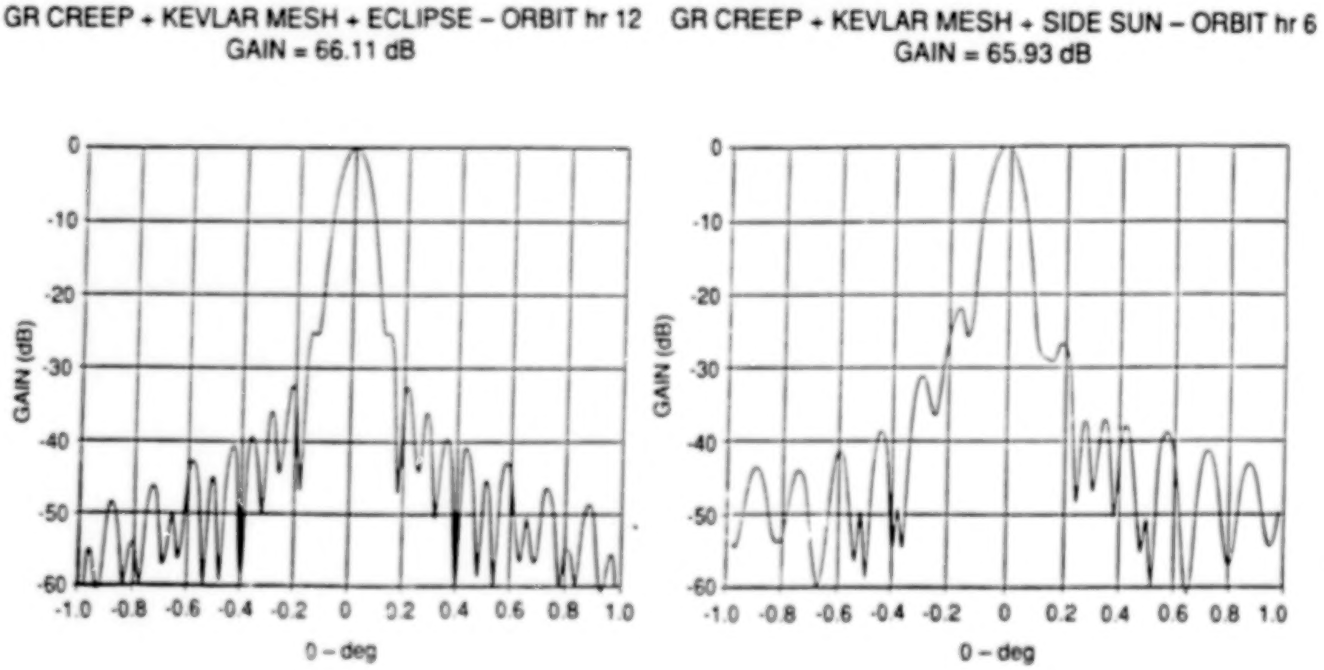

RMS = 0.013

RMS = 0.016

Figure 16

LMSC 50-FT WRAP-RIB REFLECTOR

The LMSC Antenna Laboratory (Fig. 17) has been involved in the development of 50-ft-diameter wrap-rib antennas for some time. Some of the early work in this area could not design and build thermally and disco-elastically stable ribs using a C-section for the rib. Then the effort was directed toward a closed-section design called lenticular-section rib. This presented problems with the free deployment characteristic of the wrap-rib antenna. The collapsed cross section of the lenticular rib could not recover fast enough to provide proper margin of stability. This meant that a controlled deployment device was needed.

Some of the most recent technology development effort has resulted in the design of a stable C-section rib which can be freely deployed.

GRAPHITE EPOXY RIB

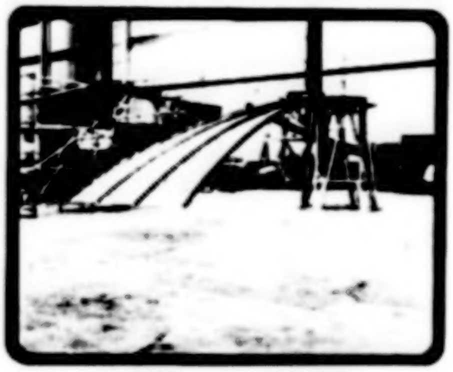

4-RIB – 3-GORE
REFLECTOR SEGMENT

KEY REFLECTOR REATURES

MAX RMS ERROR_____0.040

WEIGHT____________280 lb

STOWED DIAMETER____76 in.

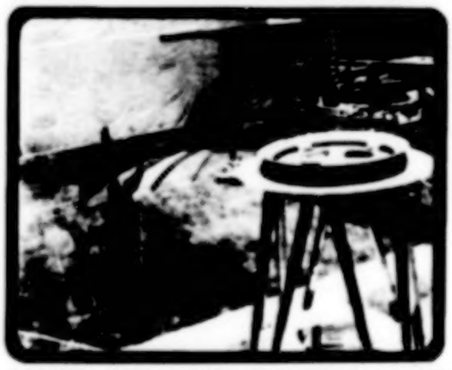

VIEW OF REFLECTOR HUB

Figure 17

PROPOSED C-SECTION RIB

The proposed 50-ft-diameter reflector rib is shown in Fig. 18. The unique feature of this rib is the continuously staggered layers of center and edge lands as a function of rib length. Various other section properties are also listed.

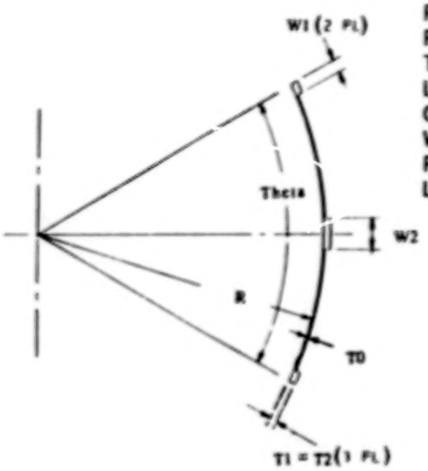

RIB RADIUS = 5.15 in.
ROOT HEIGHT = 7 in.
TIP HEIGHT = 1.75 in.
LENGTH = 270 in.
CENTER LAND WIDTH = 0.5 in.
WEIGHT = 3.45 lb
RIB THICKNESS = 0.030 in.
LAND THICKNESS/LAYER = 0.030 in.

EDGE LANDS		CENTER LANDS	
XN (in.)	FN NO. OF LAYERS	XN (in.)	FN
0	10	0	10
7	9	15	9
23	2	32	8
40	7	50	7
59	6	70	6
79	5	91	5
101	4	114	4
125	3	141	2
153	2	189	1
222	1		

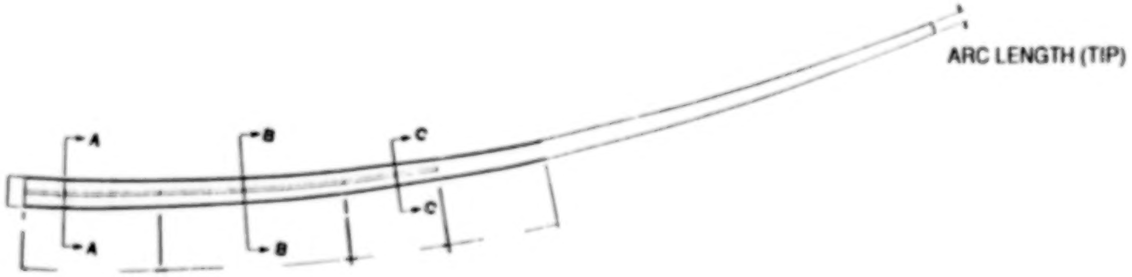

Figure 18

SAFETY DESIGN FACTORS

Figures 19 through 22 show the design factors of safety for parameters such as torsional stability, bending stability, yeild stress, and charcteristic radius. As illustrated in the figures, these factors of safety have met or exceeded the design margins for 1-g deployment and safe wrapping and unwrapping of the rib around the hub.

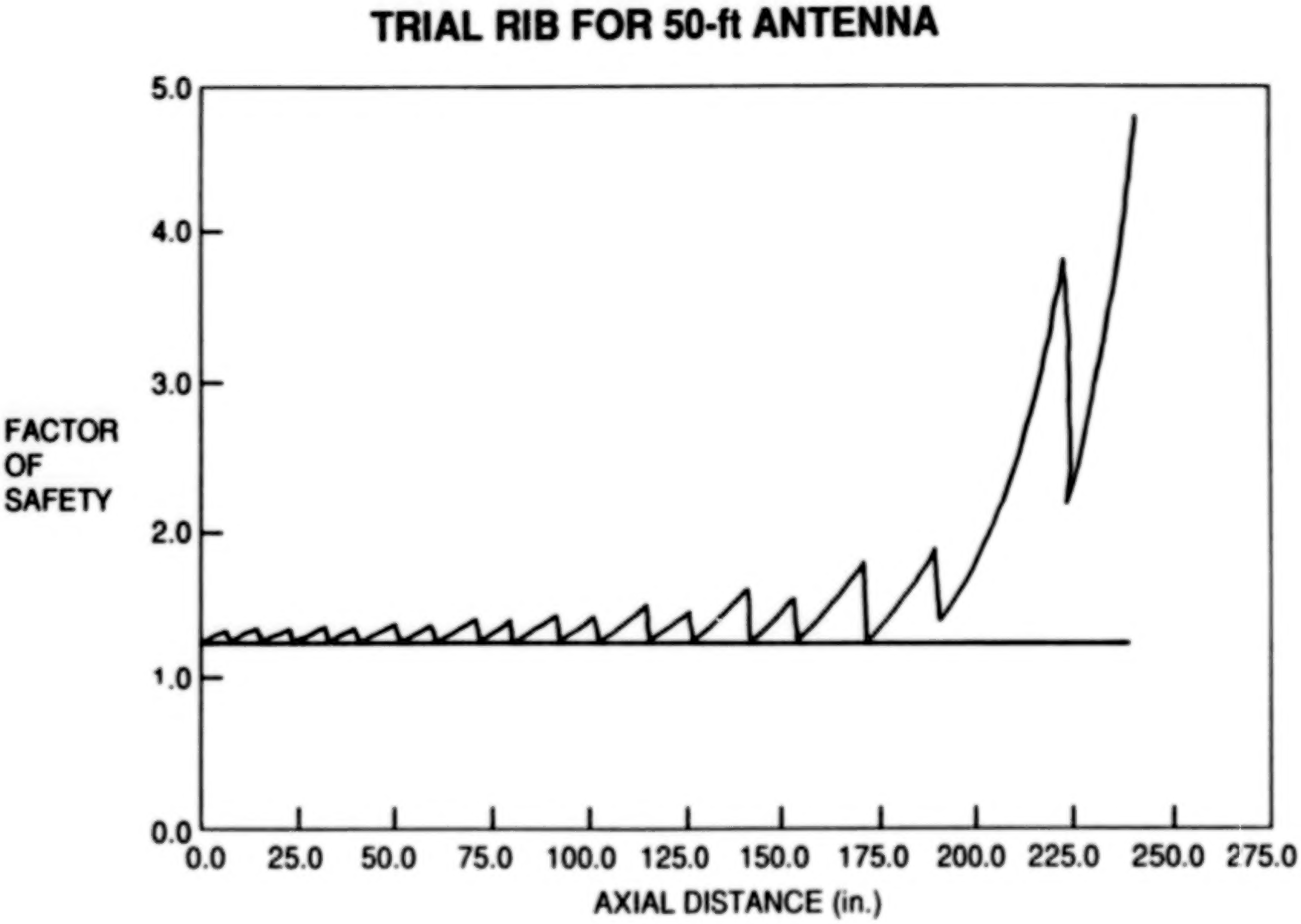

Figure 19

FACTOR OF SAFETY (TORSIONAL) vs. AXIAL DISTANCE

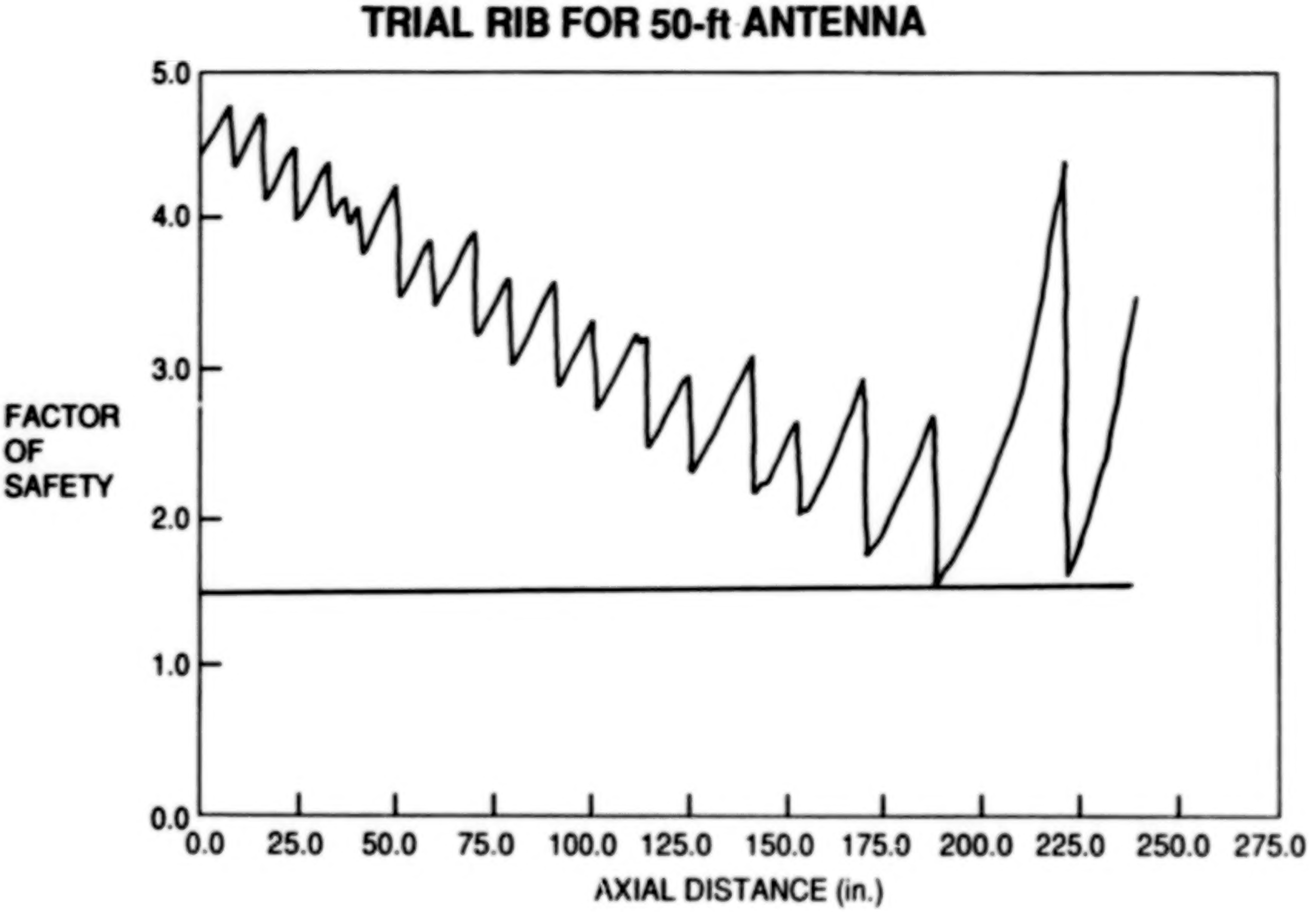

Figure 20

FACTOR OF SAFETY (STRESS) vs. AXIAL DISTANCE

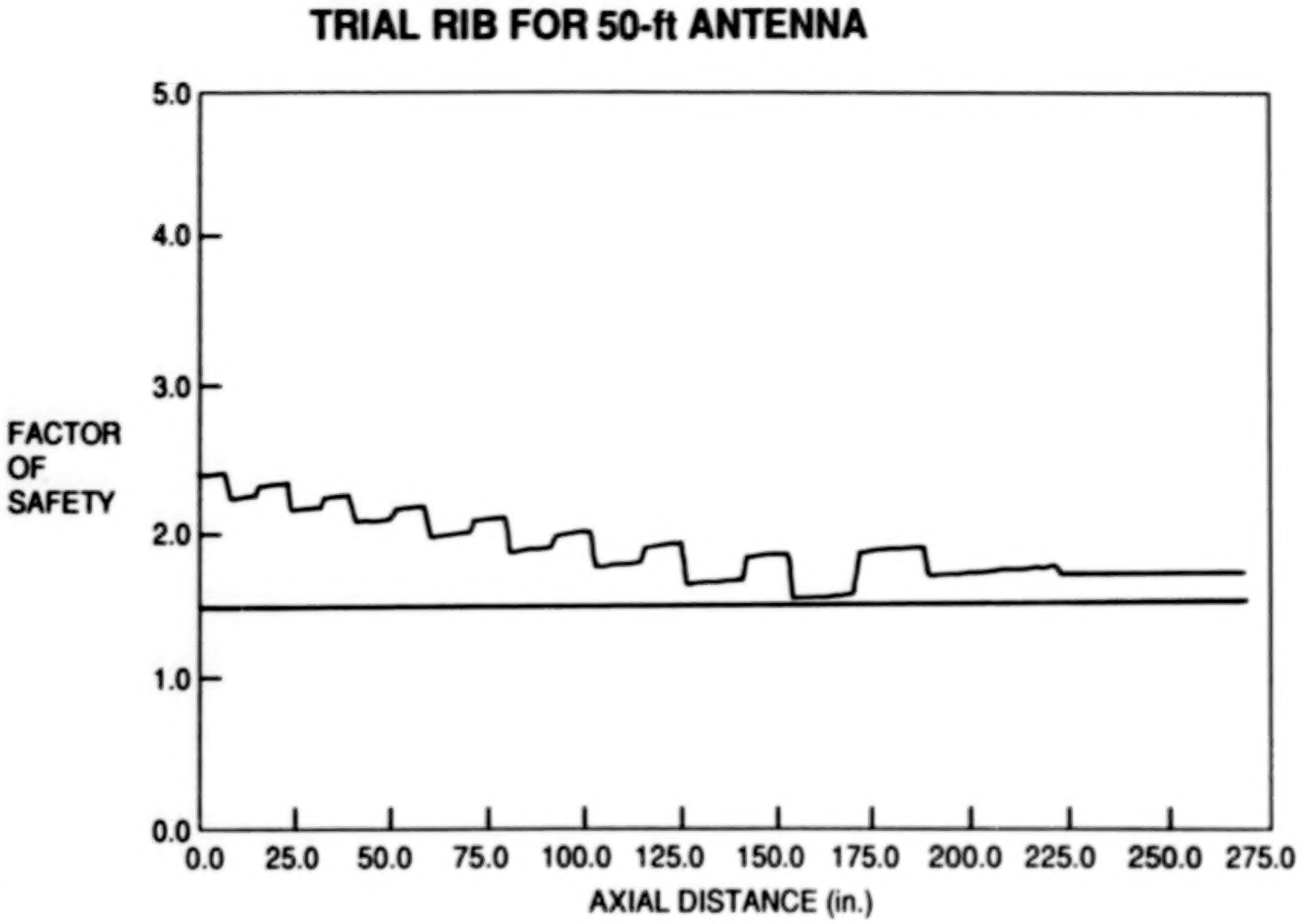

Figure 21

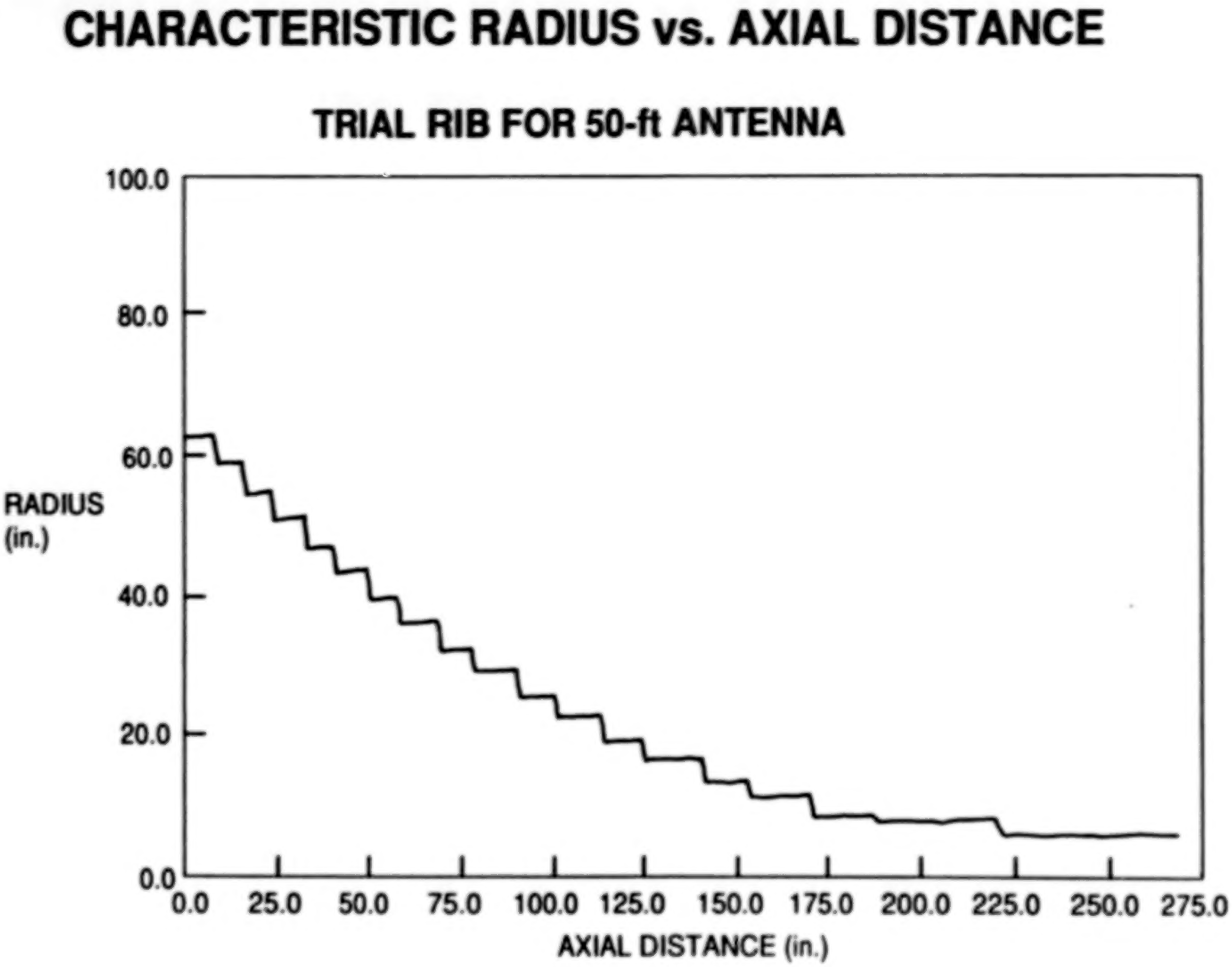
CHARACTERISTIC RADIUS vs. AXIAL DISTANCE
TRIAL RIB FOR 50-ft ANTENNA
100.0
80.0
60.0
40.0
20.0
0.0
RADIUS (in.)
0.0
25.0
50.0
75.0
100.0
125.0
150.0
175.0
200.0
225.0
250.0
275.0
AXIAL DISTANCE (in.)

Figure 22

STRUCTURAL CHARACTERISTICS

Figure 23 shows the structural characteristics of the 50-ft-diameter rib. Its lowest structural frequency is 0.62 Hz, which is the pin-wheel mode. Cup-up and cup-down stability numbers give the margins of the reflector's stability in a 1-G loading environment.

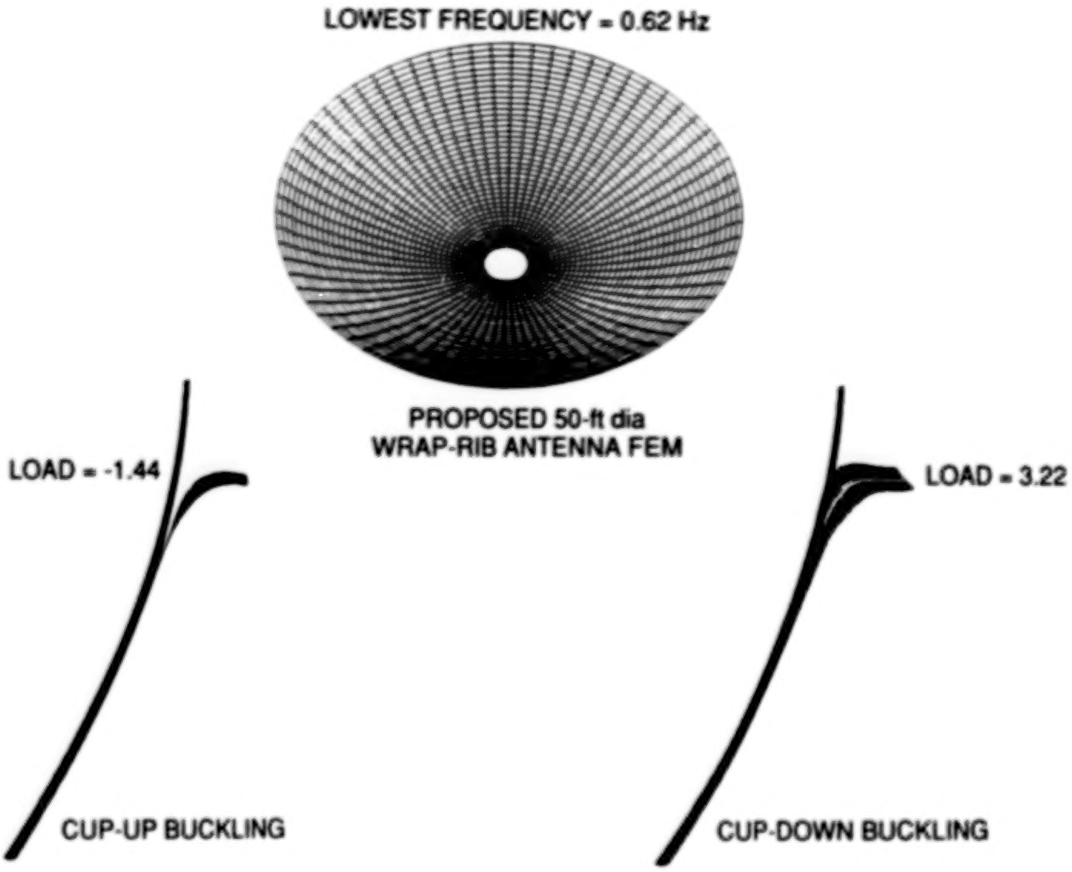
LOWEST FREQUENCY = 0.62 Hz
PROPOSED 50-ft dia
WRAP-RIB ANTENNA FEM
LOAD = -1.44
CUP-UP BUCKLING
LOAD = 3.22
CUP-DOWN BUCKLING

Figure 23

FAR-FIELD PERFORMANCE

Figure 24 showns the far-field performance of the 50-ft-diameter antenna for the worst distortion case. This was generated using the integrated rf/mechanical analysis code. This shows that far-field gain is quite respectable even for the worst case.

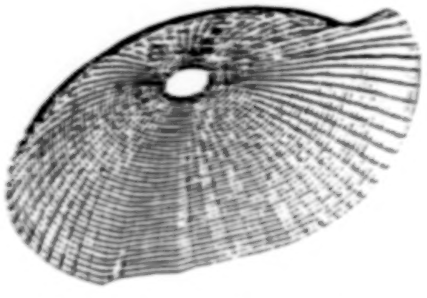

50 ft. DISH DISTORTED FOR SIDE SUN

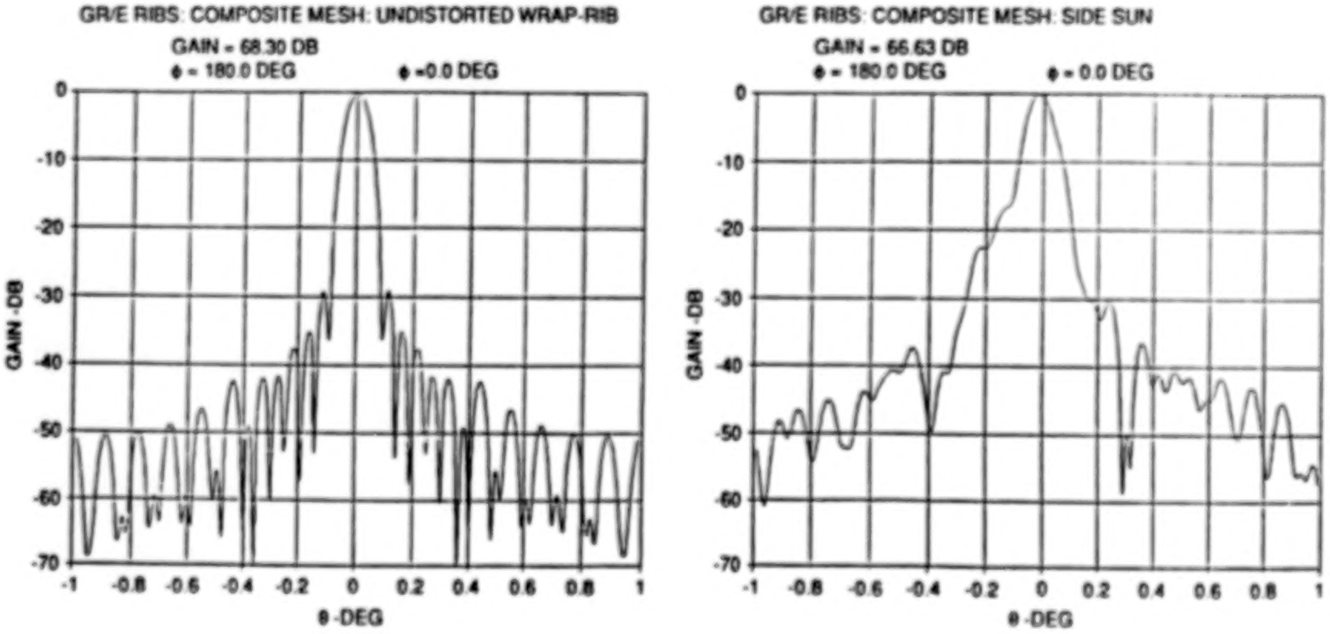

Figure 24

BASELINE 50-FT-DIAMETER WRAP-RIB DESIGN DATA

Figure 25 list an approximate system weight of a typical 50-ft-diameter wrap-rib antenna to be operable up to 20 GHz. The total weight of 522 lb assumes the hub structure is made of aluminum. This can be easily replaced by a graphite-epoxy material which will result in substantial weight saving.

HUB OUTER DIA	97 in.
HUB INNER DIA	72 in.
HUB WEIGHT	124 lb (ALUMINUM)
HUB HEIGHT	12 in.
TOTAL RIB WEIGHT	238 lb (FOR 68 RIBS)
TOTAL MESH WEIGHT	10 lb
APPROXIMATE FEED SUPPORT STRUCTURE WEIGHT	150 lb
TOTAL APPROXIMATE WEIGHT	522 lb

Figure 25

CONCLUSIONS

The technology for a 50-ft-diameter wrap-rib reflector for radiometric application for frequencies up to 20 GHz is near term. The elements of the total system can be designed to meet the specification. A full-up system build and contour verification must be accomplished before this size reflector can be declared space qualified.

STRUCTURES FOR REMOTELY DEPLOYABLE PRECISION ANTENNAS

J. M. Hedgepeth
Astro Aerospace Corporation
Carpinteria, California

INTRODUCTION

Future space missions such as the Earth Science Geostationary Platform (ESGP) will require highly accurate antennas with apertures that cannot be launched fully formed. The operational orbits are often inaccessible to manned flight and will involve expendable launch vehicles such as the Delta or Titan. There is therefore a need for completely deployable antenna reflectors of large size capable of efficiently handling millimeter wave electromagnetic radiation.

The parameters for the type of mission considered herein are illustrated by the heavy shaded horizontal bars in Figure 1. This logarithmic plot of frequency versus aperture diameter shows the regions of interest for a large variety of space antenna applications, ranging from a 1500-meter-diameter radio telescope for low frequencies (less than 10 MHz) to a 20-meter-diameter infrared telescope. For the ESGP, a major application is the microwave radiometry at high frequencies (up to 220 GHz) for atmospheric sounding. The heavy lines in Figure 1 occur at peaks and windows of the absorption spectra and are useful for the determination of atmospheric temperature, clouds, water vapor and precipitation; the width of the lines denotes the bandwidth of interest. The aperture diameters start at 4 meters, the size which can be launched without folding, and range up to the size yielding a resolution at the Earth's surface of about 6 km.

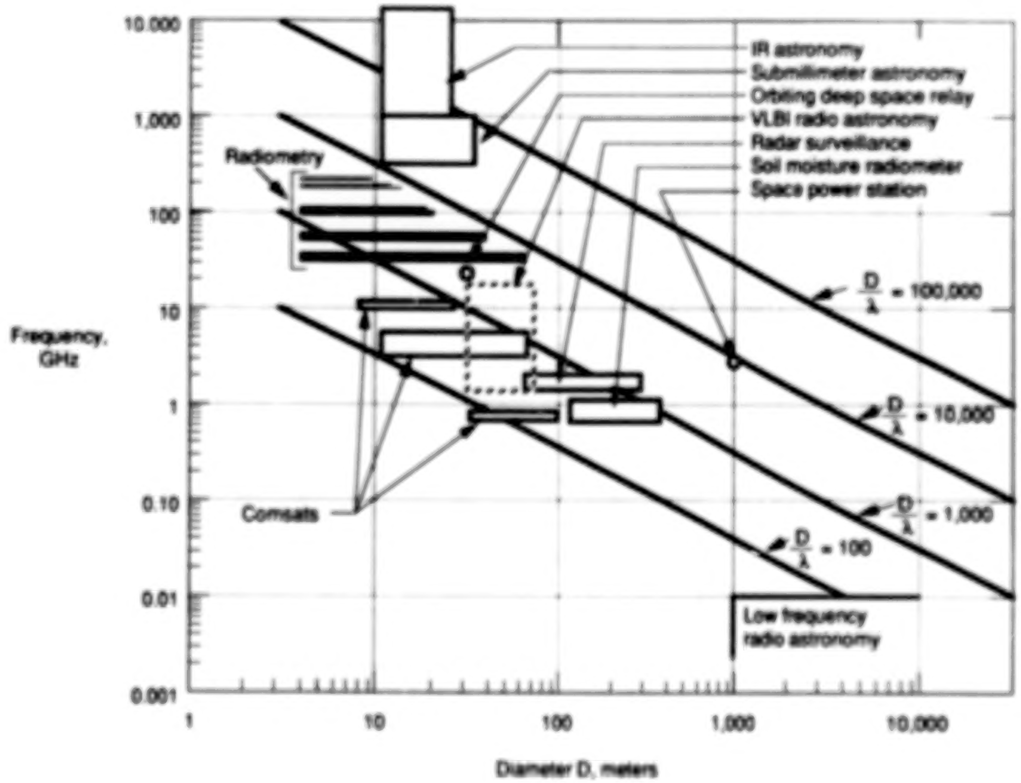

Figure 1. Large space antenna requirements

In figure 1, only those frequency bands above 30 GHz are shown. These higher frequencies require a solid reflector surface, perhaps segmented or inflated. On the other hand, the lower frequencies can be reflected efficiently by expandable mesh surfaces.

Almost all existing large antenna reflectors for space employ a mesh-type reflecting surface. Examples are shown and discussed in Reference 1, which deals with the various structural concepts for mesh antennas. Fortunately, those concepts are appropriate for creating the very large apertures required at the lower frequencies for good resolution.

The emphasis of this paper is on the structural concepts and technologies that are appropriate to fully automated deployment of dish-type antennas with solid reflector surfaces. First the structural requirements are discussed. Existing concepts for fully deployable antennas are then described and assessed relative to the requirements. Finally, several analyses are presented that evaluate the effects of beam steering and segmented reflector design on the accuracy of the antenna.

STRUCTURAL REQUIREMENTS

A probable configuration for the high-frequency radiometer antenna is shown in Figure 2. It consists of a primary reflector dish, a subreflector, and more than one feed system. For a structural point of view, each reflector consists of a reflecting surface and a structure to hold the reflecting surface in shape and position. In some cases, the two functions can be combined, but it is helpful to consider them separately.

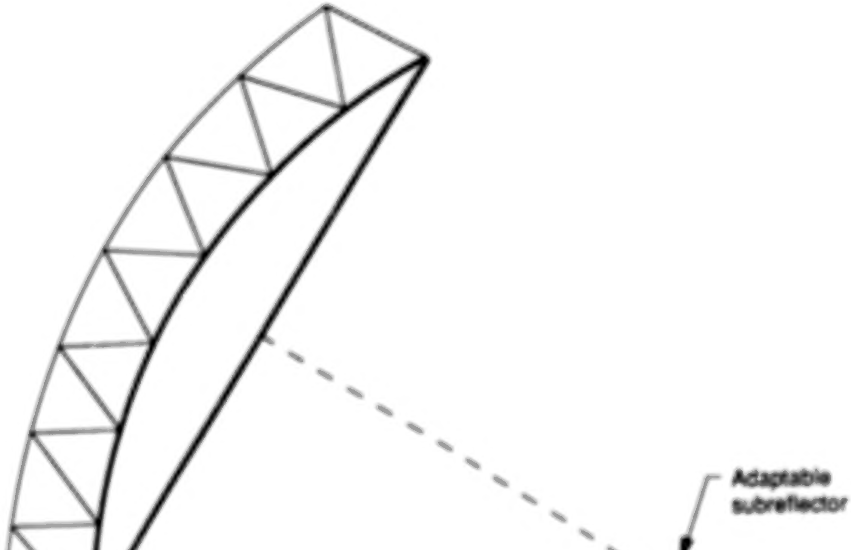

Figure 2. Example of multiband high-frequency radiometer antenna

Reflecting Surface

Passive microwave radiometers must have very high efficiency because of the feebleness of the received signal. Thus, the reflecting surface must cause minimum loss. This requires a surface of high conductivity. The surface can be very thin electrically because the skin depth of the surface currents is very small (much less than one micrometer). If the surface is a grid, low loss requires that the grid spacing be a small fraction of the wavelength λ, say $\lambda/50$. Similarly, the surface must be smooth, with roughness less than $\lambda/50$ for undulations having a spatial period of a half wavelength or more. Thus, the compliant knitted mesh that readily stows into a small package is not suitable for frequencies greater than about 30 GHz. Breaks or gaps in the reflecting surface are acceptable if they are many wavelengths apart and if the large ones do not form a regular pattern.

Supporting Structure

The supporting structure must be made sufficiently accurate, stiff, and dimensionally stable in order to meet the stringent requirements for diffraction-limited antenna performance. Not only must the antenna be efficient, but also it must exhibit small side lobes. Analysis (see Reference 2) shows that large-correlation-distance surface errors with an rms of $\lambda/50$ can raise the near-in side lobes by as much as 20 dB down from the main lobe. In addition, any distribution of surface normal errors with an rms of $\lambda/50$ will reduce the main-lobe efficiency by six percent. It appears, therefore, that a demanding mission such as microwave radiometry requires a smaller rms error, probably $\lambda/100$.

The ratio of rms error δ to aperture diameter D can be obtained as a function of the ground resolution as follows:

Let R be the range (36,000 km) and r be the resolution in kilometers. Then

$$\frac{r}{R} = 1.3\frac{\lambda}{D}$$

Setting $\lambda = 100\delta$ and solving for δ/D yields

$$\frac{\delta}{D} = 0.214 \times 10^{-6}\ r$$

For example, for a ground resolution of 20 km, the value of $\delta/D = 4.3 \times 10^{-6}$. For a 20 m aperture, $\delta = 85$ micrometers. On the other hand, for a resolution of 6 km and an aperture of 10 m, then $\delta = 12.8$ micrometers.

Clearly, very high accuracies will be demanded from the supporting structure for the high-frequency radiometry missions in Figure 1.

Shape Control

Some shape control is likely to be needed to obtain the required surface accuracies. Initial trimming in orbit will probably be desirable, if only to reduce the expense of testing before flight. Also, provision should be made to adjust the antenna figure to cope with long-term changes in the materials due to exposure.

A worthwhile objective will be to make the structure still enough and thermally stable enough that it can handle all the short-term excitations without deforming too much. Then the shape control system can be of the updating type and much less expensive than a full authority system would be.

Influence of Beam Steering and Band Switching on Structural Requirements

The radiometer must be able to direct its beam to any part of the Earth's disk; thus, it needs to scan about 8 degrees off axis. In addition, the scan must be rigid; in order to achieve the desired frequency of coverage, a scanning rate of hundreds of degrees per minute is needed. This will cause unacceptable shaking of the spacecraft if the scan is entirely mechanical. Therefore, the beam steering will need to be achieved mostly by electronic scanning. The simplest way to accomplish this is to move the effective feed point by varying the gain on individual feed elements (horns, perhaps) in a multi-element feed array. Unfortunately, steering the beam by feed movement results in large errors for angles more than ten to twenty beam diameters off axis. In order to cover the Earth, nearly 1,000 beam diameters need to be scanned.

Of course, the art of antenna engineering is able to achieve much smaller errors. One approach, for example, is to design subreflector and reflector geometries so as to minimize errors during scan. Another approach that shows promise is to use a phased array to illuminate the subreflector. Another possibility is to scan rapidly electrically in one direction while slowly moving the entire antenna mechanically in the perpendicular direction to cover the desired area.

In addition to steering, the several frequency bands also must be examined. The frequency range from 30 to 220 GHz is obviously too much to be handled with a single feed system. Multiple systems will be required, and their location will pose severe problems, especially since they will have to be large in order to produce the ±8 degree scan.

Beam and frequency agility is the responsiblity of the antenna engineer. From the structural point of view, the need for low spacecraft excitation also implies that the dynamic loads on the antenna reflectors will be low. It might be possible to ease the beam steering problem by actively shaping the subreflector and/or the primary reflector. The amounts of displacements required to eliminate the path length error are estimated later in the paper.

Finally, provision of the needed beam steering with multiple feed systems may result in new geometrical configurations for which new structural concepts will be required.

Packaging

The microwave radiometer operates in geosynchronous orbit. For the purposes of this paper, the assumption is made that the deployment will be in geosynchronous orbit and therefore remote. The launch system is assumed to be either the Titan IV or a Shuttle-OTV* combination, with cargo-bay diameter of 4.5 meters and an available length of over 10 meters. The Delta launch vehicle, with its smaller launch volume and lower payload, appears to be inapplicable for the ESGP mission.

*Orbiter Transfer Vehicle

DEPLOYABLE STRUCTURAL CONCEPTS

As in the preceding section, it is convenient to discuss concepts for the reflecting surface first.

Reflecting Surface

The requirement that the reflecting surface be solid limits consideration to reflective membranes and panels.

Membrane surfaces can be excellent radio-frequency reflectors. Some care must be taken to ensure that the surface conductivity of metalized plastic films is not degraded by cracks in the conductive layer caused by frequent creases. For dish-type surfaces, the membrane requires a transverse pressure loading to create a wrinkle-free surface of the correct shape. No suitable reflector membrane material has low enough in-surface stiffness to enable needed changes in Gaussian curvature without incurring high stresses. Membranes are pliable and can be stowed compactly.

The most prevalent approach for providing a reflector surface is to use an assemblage of stiff panels. A variety of shapes have been proposed, ranging from near-hexagonal segments, through ring sectors, to petals. In all cases, the panels butt together to produce the large dish-type reflector. For launch, the panels are folded or interleaved to fit in the launch vehicle. Each panel is considered to be stiff and precise enough to maintain its own shape. Panels can be built in several ways, the chief ones being as a honeycomb sandwich or a monocoque stiffened shell.

A novel approach that has been suggested by Composite Optics, Inc. of San Diego utilizes a reflector surface composed of a thin flexible shell of graphite-epoxy composite. Large areas of the shell can be rolled up for launch and allowed to unroll in orbit against a supporting truss structure. The shell could comprise the entire surface for smaller antennas. Rolled-up shell segments could be stowed with the folded truss for larger apertures.

Supporting Structure

Antenna reflector configurations using membrane reflector surfaces must provide some means for creating a pressure-type loading across the surface. If gas pressure is used, the reflecting surface is usually joined to a symmetrically shaped transparent film around the rim to create a closed pressure vessel. Examples are shown in Figure 3 taken from Reference 3. The rim must be capable of carrying the compression loading caused by the membranes' pulling inward at the rim. The rim may consist of an inflatable torus. The assembly is deployed by slow inflation and is intuitively very reliable.

Leakage caused by meteoroid penetration would necessitate a large supply of make-up pressurant for long time operation. This can be avoided by making the membrane stiff enough to provide its own structural integrity after deployment. The ECHO passive satellite, a 100-foot-diameter balloon, was launched early in the space age. Its shell was composed of a thin sandwich with Mylar-film face sheets and an aluminum-foil core. More recently, technology work in Europe has been under way since the early 1980s developing a Kevlar-epoxy composite surface which is cured and hardened on orbit after inflation. (See References 3 and 4.)

Inflatable antennas, while being vigorously promoted for the lower frequencies, are generally viewed as being inapplicable for the high frequencies being considered herein. Even when extreme care is exercised during fabrication, the available suitable materials lack the long-term dimensional stability and super-low coefficient of thermal expansion needed for very high precision. In addition, inflatable antennas, once fabricated, are difficult to "tune up," even during ground testing. Adjustments in orbit seem to be impossible.

Membrane antennas shaped and adjusted by electrostatic forces have been proposed and studied during the last decade. This technique shows good promise of being useful, particularly for shallow dishes. Deep dishes are less amenable to this approach because the high in-surface stiffness of the doubly curved membrane causes the shaping pressures to be large. Even for shallow dishes, the necessary electrostatic drivers and their support structure tend to be heavy and the charged devices must be shielded against arcing due to the in-space plasma. On the other hand, rapid adjustment of the lightweight film reflector can be accomplished with little disturbance of the spacecraft.

Supporting structures for panel-type reflector surfaces are often integrated with the reflecting surface itself. Indeed, this approach is used for the many solid dishes flying on communication satellites. Its simplicity is attractive and the resulting structure can be made dimensionally stable enough to be used at extremely high frequencies. Ingenious concepts have been devised for deploying large dishes by hinging between adjacent segments. One such technique, termed Sunflower, consists of petals which fold up around the symmetry axis and form a complete dish on

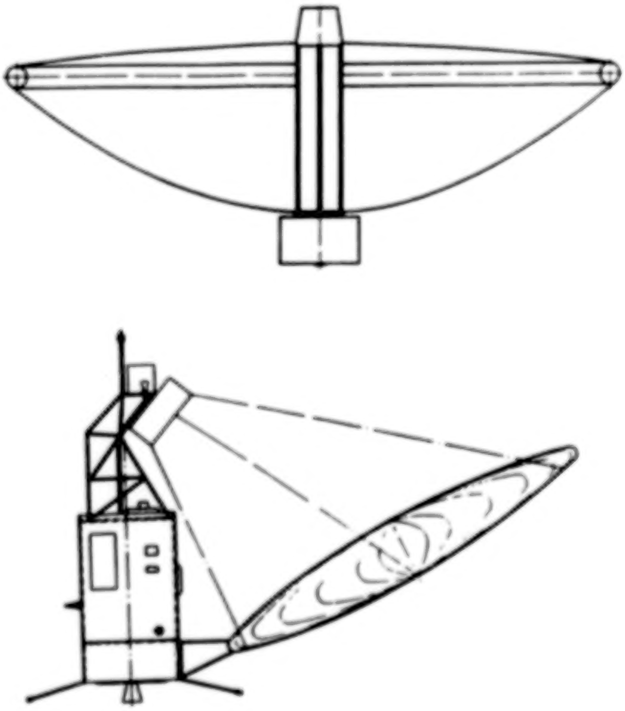

Figure 3. Symmetric and offset-fed antenna reflector configurations (from ref. 3; reprinted with copyright permission of Pergamon Press, Inc., New York)

deployment. The concept underwent significant development in the 1960s as a spaceborne solar-energy collector (see Reference 5). A recently designed descendant is shown in Figure 4. Note that this version deploys to a 15-meter diameter.

Another segmented-panel approach with integrated structure was designed for high-frequency antennas and is discussed in Reference 6. Figure 5, taken from Reference 6, shows the stack of stowed hexagonal panels, each one of which is rotated into position and fastened to its neighbor. Not shown are the mechanisms required to deploy and attach the segments together.

Integrated-structure, or panel-only, concepts are attractive because of their relative simplicity. They also use well established fabrication techniques and appear to be of low risk. They are, however, structurally "thin," so that small errors in individual parts grow into large distortions for large sizes. In addition, such structures are difficult to test in a one-g environment. Their flexibility combines with the gravity loading to produce deflections that are large in comparison to those acceptable for the present application. It is therefore difficult to achieve the desired accuracy, either by fabricating the component parts with enough precision or by "trimming" the structure by adjustments based on measurements obtained during ground testing.

The experience and information obtained by studies and tests over the past two decades have shown that structural configurations that are "deep" are much more suitable for large high-precision surfaces than are the "thin" ones. (See References 1, 7, 8, 9, and 10.) Not only is this notion intuitively obvious, but also detailed analyses have shown that very high precision is achieved with careful fabrication. For example, a recent simulation of a 20-meter-diameter tetrahedral-truss structure constructed from 2-meter struts which have random lengths with an rms variation of 20 micrometers showed an expected rms surface error of 43 micrometers. The worst of 100 cases had an rms surface error of 72 micrometers. Furthermore, analysis of the deflections caused by testing in a one-g field showed an rms error of about 100 micrometers; gravity compensation should be able to decrease that by an order of magnitude.

One antenna with a deep-truss support structure flew on the SEASAT spacecraft. As shown in Figure 6, the synthetic aperture radar antenna, which is 10.75 meters long, is supported by a deployable truss. The radiating panels are stowed and deployed with the truss as seen in Figure 7. This structure, which supported an L-band antenna ($\lambda = 20$ cm), was accurate to better than 2.5 mm maximum deflection. This was achieved, and demonstrated with care but without heroic efforts; the robustness of the configuration simplified analysis, integration and testing. Similar deployment truss concepts have been studied for possible use with dish-type reflector antennas; one of these is shown in Figure 8. This arrangement has the advantage that it allows the panel segment to nest, thereby saving package volume.

The structural performance of a petal-type deployable reflector can be greatly improved by mounting each petal on a stiffening truss. The approach has been suggested by Dornier and is shown in Figure 9. The application is an 8-meter reflector for infrared astronomy. Also being studied for this mission is a segmented three-section mirror in which the outer two segments fold inward over the central one to form an 8-meter-long package with a 4-meter cross section.

The foregoing truss-stiffened concepts are useful only for diameters smaller than the available package length, say up to 10 to 15 meters, depending on the launch vehicle configuration. For larger dishes, it will be necessary to divide the

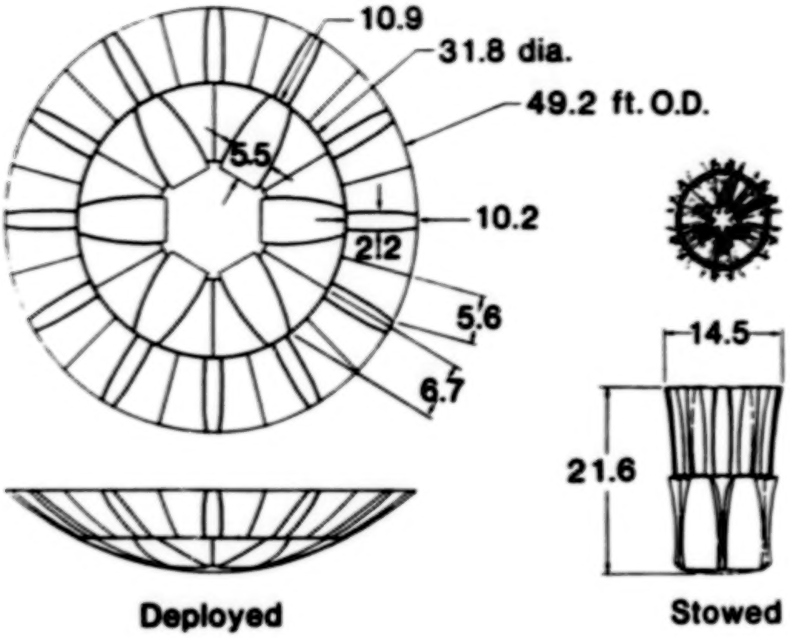
10.9
31.8 dia.
49.2 ft. O.D.
5.5
10.2
2.2
5.6
6.7
14.5
21.6

Deployed **Stowed**

Figure 4. Main panel double ring configuration

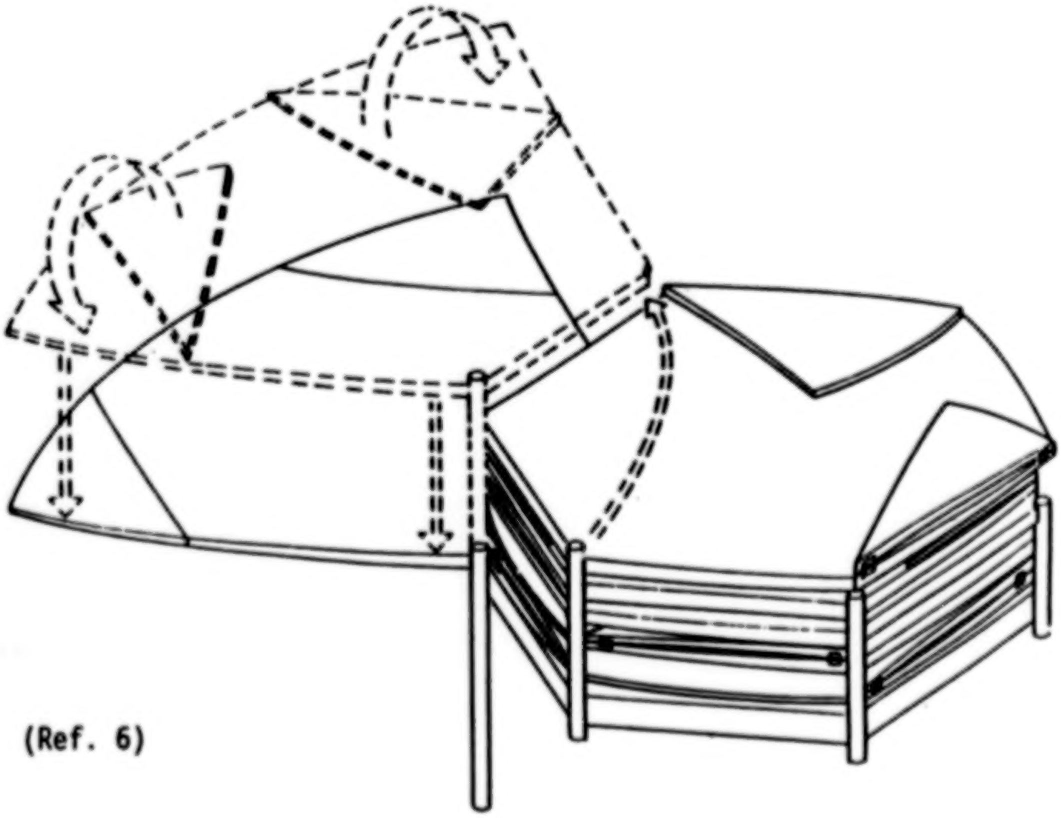

(Ref. 6)

Figure 5. View showing the first panel rotated out with its tips displayed and lowered for lockup on the center hexagonal hub

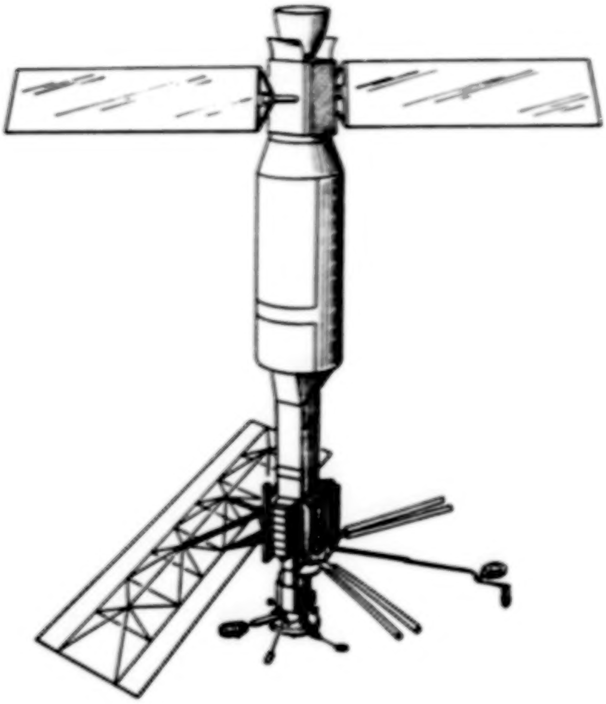

Figure 6. Extendible suport structure for SEASAT synthetic aperture radar antenna

Figure 7. ESS deployment sequence

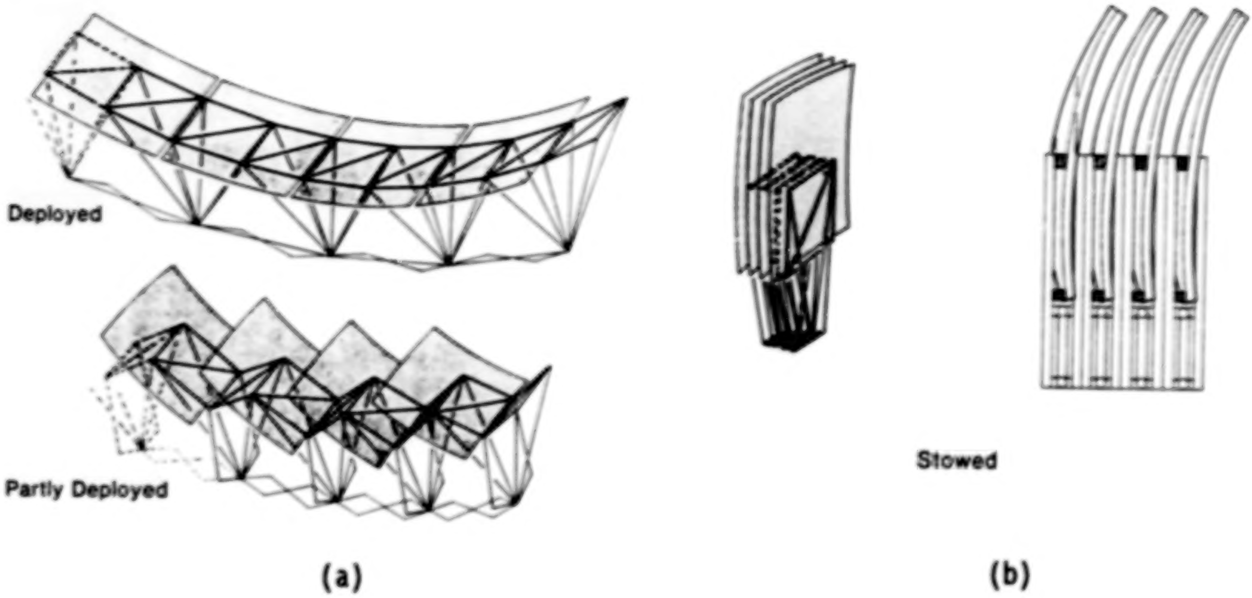
Deployed
Partly Deployed
Stowed

(a) (b)

Figure 8. Synchronously deployable Concept B (CREST) for stiff-panel reflectors

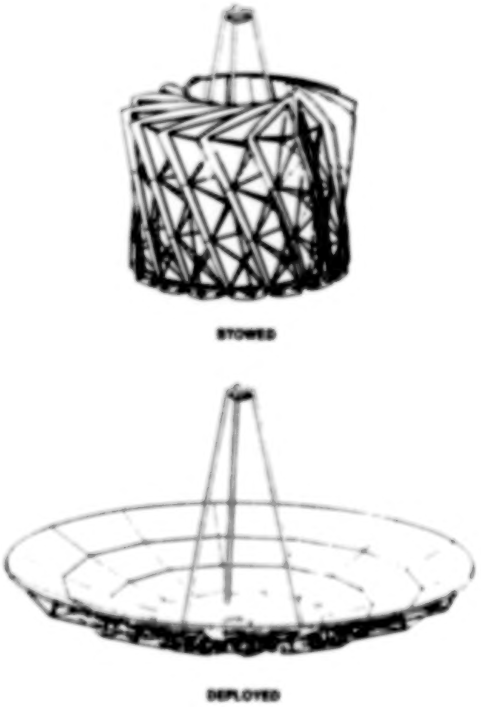
STOWED
DEPLOYED

Figure 9. Deployable reflector for FIRST (Dornier system)

reflector surface in both directions in the surface. This poses a severe problem because almost certainly the surface will have to be cut into segments and stowed separately. The supporting truss can be stowed separately also, and the panels can be assembled to the deployed truss by a robot as shown in Figure 10. Research is in progress at Langley Research Center on such robotic assembly. One concept for the deployable truss which is being extensively studied for various high-precision applications is the Pactruss shown in Figure 11. The deploying truss in this concept is very strongly synchronized and offers reliable deployment with a few actuators. See Reference 11 for the description of recent evaluations of precision application.

Another concept for constructing large segmented reflectors in remote locations is shown in Figure 12. Here, individual modules, each consisting of a panel and its associated support truss section (see Figure 13) are stowed in a deployment canister which walks around the dish, deploys modules and locks each to its neighbors. The development of this intelligent canister would require some effort but seems to be easier than using a robot. Use would be made of the fact that each module would be hinged, so far as possible, to its neighbors. The hinging would aid in control of the canister motions.

The furlable, thin-shell reflector panel described in a foregoing section might be stowable along with the deployable truss. The rolled-up segments could possibly be released after truss deployment and would then settle into frames created by the truss. In this case, the square form of Pactruss would probably be more attractive. The panels would then be nearly square. See Figure 14.

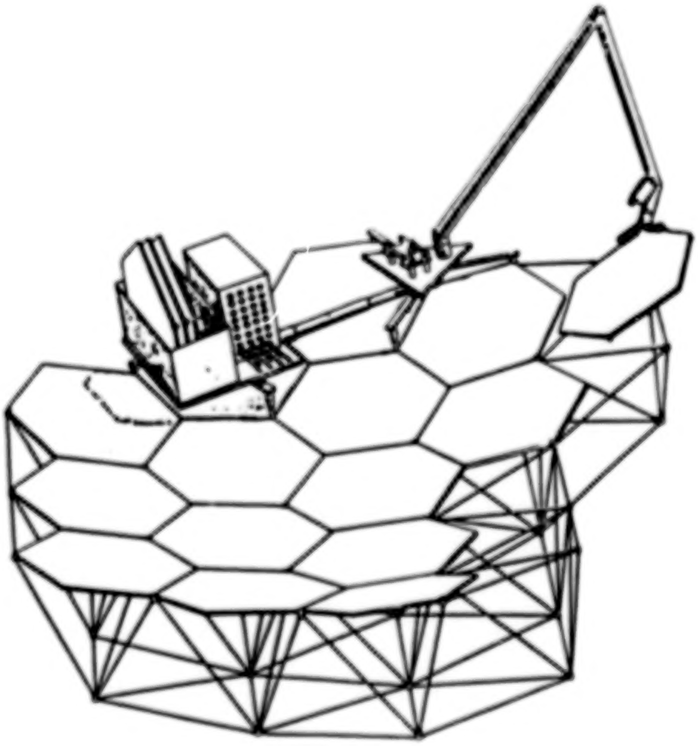

Figure 10. Automated curved surface construction concept

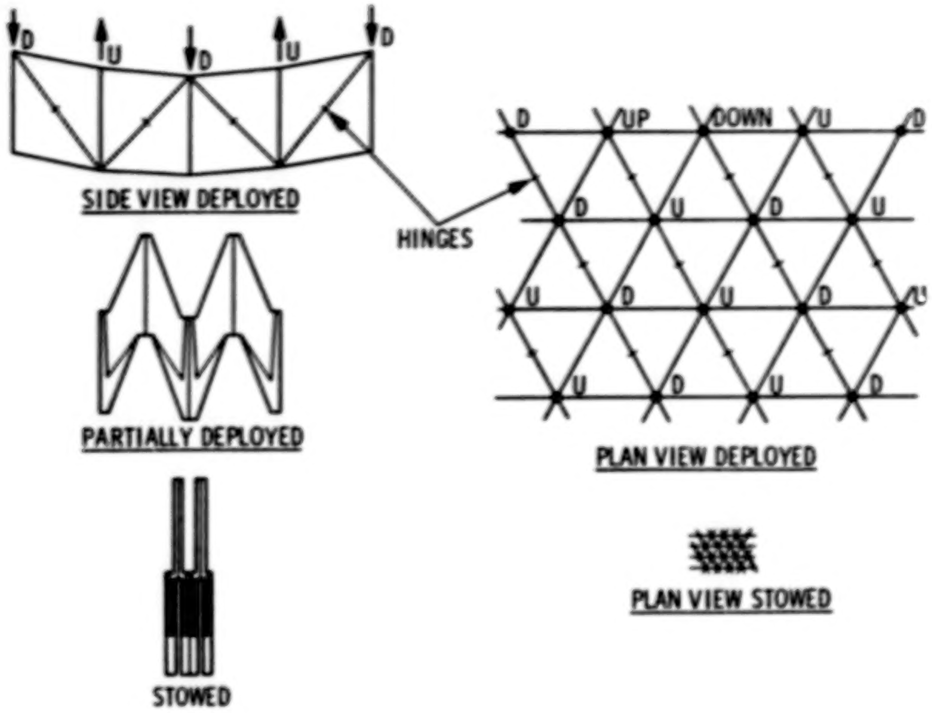
D
U
D
U
D
SIDE VIEW DEPLOYED
HINGES
D
UP
DOWN
U
D
D
U
D
U
U
D
U
D
U
U
D
U
D
PARTIALLY DEPLOYED
PLAN VIEW DEPLOYED
PLAN VIEW STOWED
STOWED

Figure 11. PACTRUSS concept

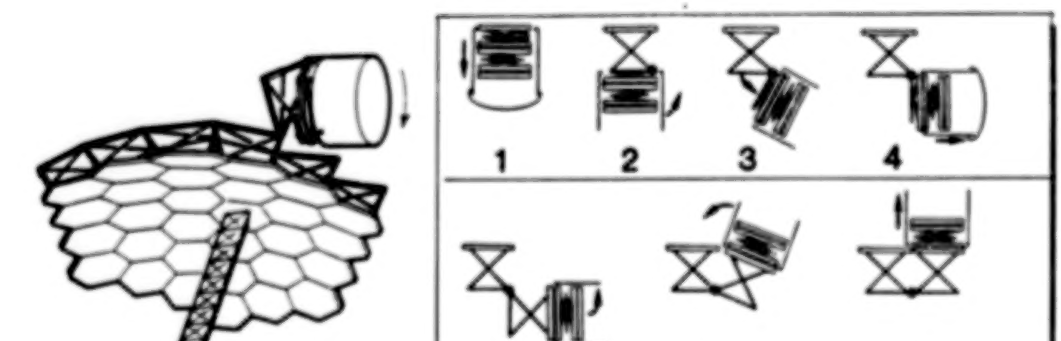
1
2
3
4
5
6
7
8
9
10
11
12
13

Figure 12. Sequentially deployable precision reflector

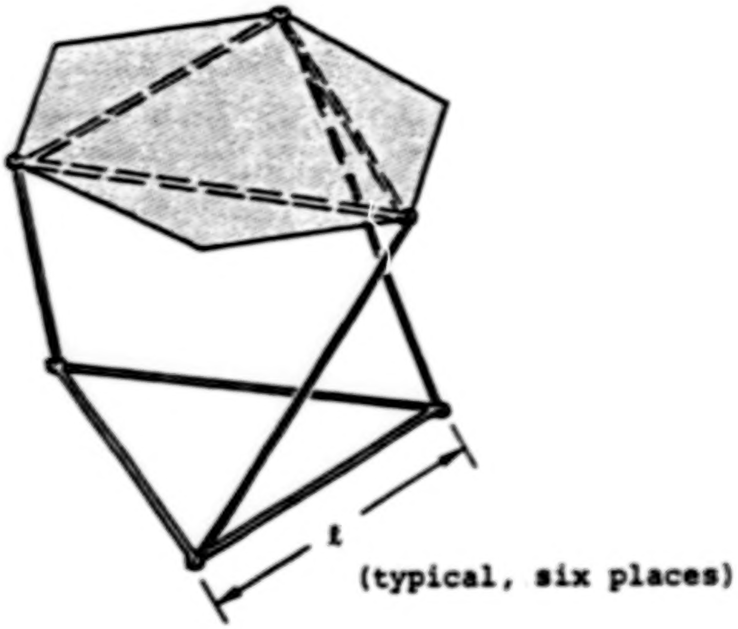
ℓ
(typical, six places)

Figure 13. Basic truss module

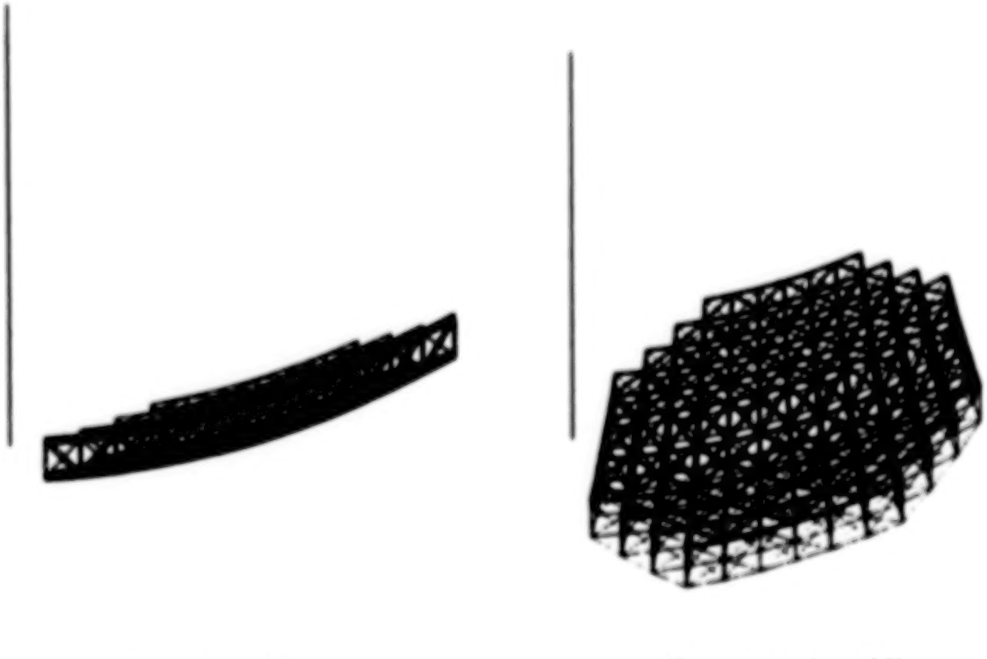
Elevation View

Perspective View

Figure 14. Views of PACTRUSS for offset paraboloid

PANEL DESIGN

In the fabrication of panels for large precise antenna reflectors, a mandrel is needed for laying up the panels. The mandrel would either be as large as the radius of the paraboloid or made in several pieces. In either case, the expense of the mandrel will be large.

One way to reduce cost is to make only a few mandrels (one, if possible) and replicate panels off of each, using them in the best way to minimize the shape error. The following analysis is aimed at finding the best single mandrel shape to produce identical panels which yield minimum rms error when mounted on the support truss at the optimum orientation and position relative to the exact paraboloidal surface.

Consider a paraboloid with focal length F, with its axis along the z axis and its vertex at the origin. Its equation is

$$z = \frac{r^2}{4F}$$

where

$$r = \sqrt{x^2 + y^2}$$

Let a be the offset of the center of the aperture from the axis of the paraboloid and D be the diameter of the aperture. Let ρ and ω be polar coordinates based on the center of the aperture. Inside the aperture, where $\rho < D/2$, and ω is measured from the direction of the offset, then

$$r = \sqrt{a^2 + \rho^2 + 2a\rho \cos \omega}$$

Consider a circular panel whose center is located at the location (r_0, z_0) on the paraboloid. Let ξ,η,ζ be a right-and coordinate system, with ξ and η tangent to the paraboloidal surface and ζ normal to it. Let ξ point in the meridional direction at the panel center.

Let the xz plane pass through the center of the panel. Then

$$x = r_0 + \xi \cos \phi_0 - \zeta \sin \phi_0$$

$$y = \eta$$

$$z = z_0 + \xi \sin \phi_0 + \cos \phi_0$$

where

$$\tan \phi_0 = \left.\frac{dz}{dr}\right|_{r=r_0}$$

$$= \frac{r_0}{2F}$$

Substituting x, y, and z into the equation of the paraboloid and solving for ζ gives

$$\zeta = \zeta^*$$

where

$$\zeta^* = \frac{\xi^2 \cos \phi_o + \eta^2}{\dfrac{2F}{\cos \phi_o} + \xi_\rho \sin \phi_o \cos \phi_o + \sqrt{\dfrac{4F^2}{\cos^2 \phi_o} + 4F\xi \sin \phi_o - \eta^2 \sin^2 \phi_o}}$$

Let the panel have curvatures in the meridional and circumferential directions of k_m and k_c, respectively. Also let the center displacement of the panel in the ζ direction be ζ_o and the tilt in the meridional plane be α. The equation of the panel surface is then

$$\zeta = \zeta_p + \zeta_o + \alpha\xi$$

where

$$\zeta_p = \tfrac{1}{2}(k_m\xi^2 + k_c\eta^2)$$

Then the local error in the normal direction between the panel and the paraboloidal surface is

$$\delta = \zeta_p - \zeta^* + \zeta_o + \alpha\xi$$

The mean-squared error is given by

$$\delta_{rms}^2 = \frac{\int_A \left[\zeta^* - \zeta_p - \zeta_o - \alpha\xi \right]^2 d\xi d\eta}{\int_A d\xi d\eta}$$

where the integrations are carried out over the area of the panel. The mean-squared error is minimized when

$$\zeta_o = \frac{\int_A \left[\zeta^* - \zeta_p \right] d\xi d\eta}{\int_A d\xi d\eta}$$

$$\alpha = \frac{\int_A \left[\zeta^* - \zeta_p \right] \xi d\xi d\eta}{\int_A d\xi d\eta}$$

This process yields the rms error for a particular value of r. The mean-square error for the entire antenna is obtained by averaging δ_{rms} over the aperture.

The computer code UNIPANL.C was written to perform the indicated integrations and averages, and determine the rms error for the antenna. The program is interactive, requesting inputs of D, F, and offset, then repeatedly asking for the panel size and ratio of circumferential to meridional curvature. The integrations are performed numerically with five intervals in the radius and 15 degree intervals around the circumference. The panel curvature that gives the least rms error over the entire aperture is found by a stepping type of search for the minimum.

Some results for panels which have the same curvature in both directions (spherical mandrel) are shown in Figure 15. Note that using an offset feed with an F/D of 1.5 yields almost the same results for inaccuracy as those for a centered-feed antenna with F/D = 1.0. To understand these results, consider a 20-meter diameter to be used at a frequency of 100 GHz and require $\lambda/100$ accuracy. Then $\delta_{rms}/D = 1.5 \times 10^{-6}$. With a centered-feed and F/D = 1.5, the panel size could be as large as 2 meters. For an offset feed and F/D of 1.5, the allowable panel size is only 1 meter. Note also that a resolution of 6 km for the ESGP radiometer would need a value of δ/D of about 1.3×10^{-6}. For the offset feed case, there would be about 20 panels needed across the aperture diameter.

Incidentally, some trials with the circumferential curvature slightly higher than the meridional indicates significant reduction in the error. Also, providing two mandrels would help a great deal.

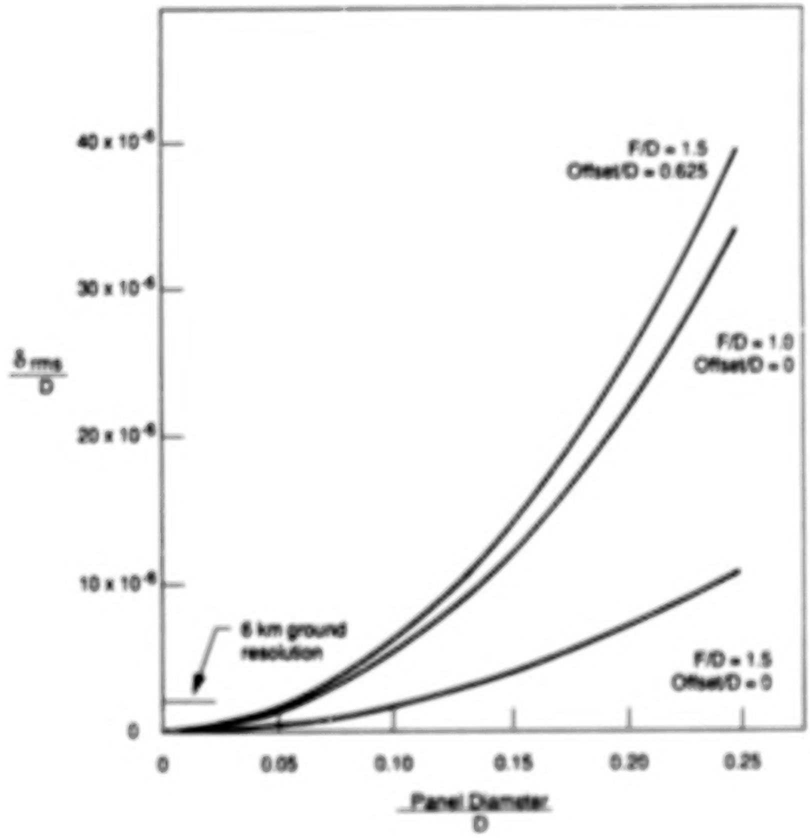

Figure 15. Antenna surface error caused by identical spherical panels

One approach to avoiding pattern deterioration when scanning would be to adjust the shape of the reflector as the scanning occurs. In order to determine the magnitude of the motions required of the surface, an analysis was made of the path-length error due to scanning. The approach used was to find the tilted paraboloid for which the mean-square normal distance from the original paraboloid was a minimum. This analysis is coded in the program ADJUST.C.

A sample of the output of ADJUST is included in Table 1. The case treated is a 20-meter-diameter offset-feed antenna with an F/D = 1.5 and an offset of 12.5 meters. The rms value of the correction is about 1.5 cm and the maximum value is about 5 cm. These are sizable motions, but not nearly as large as would occur if the beam were steered by rotating the entire antenna.

The indicated surface adjustment would be accomplished by actuators. If the surface were a continuous one, say an electrostatically controlled membrane, then the surface would tend to fair the shape between control points. If the surface is made up of segmented panels, then the control would be applied at the attachment points. Since the panels would each be shaped to conform to the untilted paraboloid, they would exhibit some unavoidable residual error when trying to fit the scanned paraboloid. The program ADJUST includes the ability to examine individual panels

Table 1. Reflector Corrections for Scan

```
F = 30.000000  D = 20.000000  r0 = 12.500000  delta = 8.000000  psi = 0.000000
Displacement of focal point = -3.916113, 0.000000, -1.946797
Rms path length error = 0.027682
New focal length = 27.796289   Rms correction = 0.015121

            0.2          0.4          0.6          0.8          1.0
  0    -1.481e-003  -6.442e-003  -1.562e-002  -2.967e-002  -4.924e-002
 15    -1.307e-003  -5.733e-003  -1.400e-002  -2.677e-002  -4.466e-002
 30    -8.270e-004  -3.783e-003  -9.546e-003  -1.875e-002  -3.198e-002
 45    -1.670e-004  -1.080e-003  -3.332e-003  -7.486e-003  -1.407e-002
 60     5.027e-004   1.701e-003   3.140e-003   4.380e-003   5.004e-003
 75     1.009e-003   3.867e-003   8.314e-003   1.409e-002   2.095e-002
 90     1.223e-003   4.888e-003   1.098e-002   1.946e-002   3.030e-002
105     1.093e-003   4.538e-003   1.057e-002   1.943e-002   3.131e-002
120     6.600e-004   2.957e-003   7.369e-003   1.437e-002   2.442e-002
135     4.544e-005   6.180e-004   2.386e-003   6.028e-003   1.223e-002
150    -5.790e-004  -1.801e-003  -2.867e-003  -2.950e-003  -1.202e-003
165    -1.040e-003  -3.602e-003  -6.814e-003  -9.766e-003  -1.151e-002
180    -1.209e-003  -4.266e-003  -8.276e-003  -1.230e-002  -1.536e-002
195    -1.040e-003  -3.602e-003  -6.814e-003  -9.766e-003  -1.151e-002
210    -5.790e-004  -1.801e-003  -2.867e-003  -2.950e-003  -1.202e-003
225     4.544e-005   6.180e-004   2.386e-003   6.028e-003   1.223e-002
240     6.600e-004   2.957e-003   7.369e-003   1.437e-002   2.442e-002
255     1.093e-003   4.538e-003   1.057e-002   1.943e-002   3.131e-002
270     1.223e-003   4.888e-003   1.098e-002   1.946e-002   3.030e-002
285     1.009e-003   3.867e-003   8.314e-003   1.409e-002   2.095e-002
300     5.027e-004   1.701e-003   3.140e-003   4.380e-003   5.004e-003
315    -1.670e-004  -1.080e-003  -3.332e-003  -7.486e-003  -1.407e-002
330    -8.270e-004  -3.783e-003  -9.546e-003  -1.875e-002  -3.198e-002
345    -1.307e-003  -5.733e-003  -1.400e-002  -2.677e-002  -4.466e-002
```

for their residual errors. Results for the worst-case panels are shown in Figure 16. Examination shows that the residual errors are similar to those due to using identical panels.

The foregoing results are calculated for scanning by simple feed motion. Much smaller errors will result from the more advanced scanning techniques that will be used. If variable geometry is used, the motions and residual errors would be accordingly smaller.

CONCLUDING REMARKS

The study reported herein is only a beginning. There remains a great deal of investigation before a good configuration can be selected for development. Among the questions are:

- What rms accuracy is needed by the radiometry mission? λ/30? λ/50? λ/100?
- How good can electronic scanning be? Feed-motion scanning becomes unacceptable at 10 beamwidths. The mission needs 1,000.
- Can robots or intelligent canisters be developed in time to be available for remote assembly of antennas needed in the year 2000?
- Can long-time microstrain stability for the available materials be assured?
- What are the magnitude and distribution of the forces required to adjust the shape of continuous reflecting surfaces?
- How accurately can large continuous shells be built?

The future is promising.

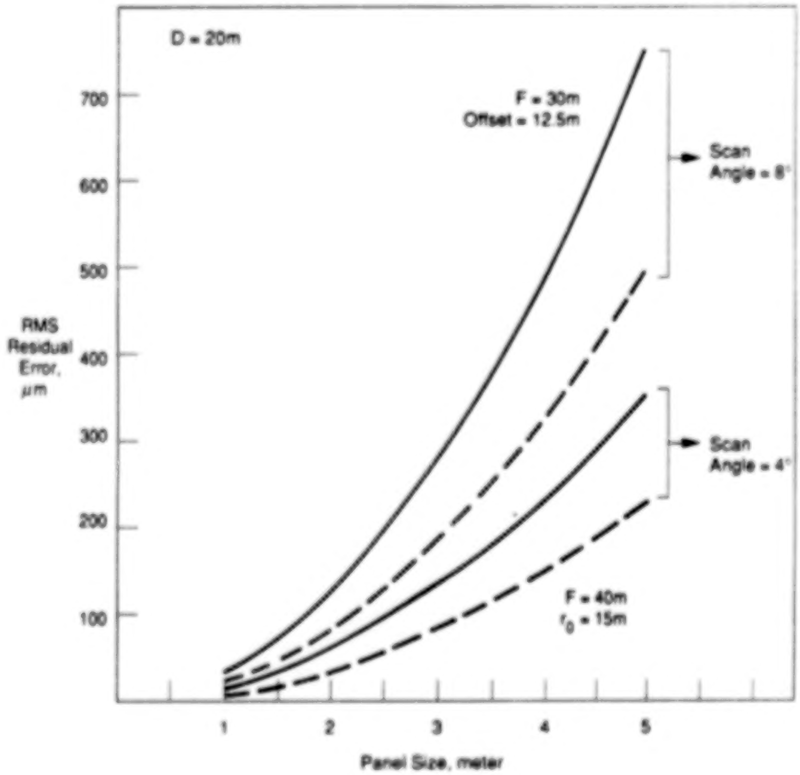

Figure 16. Worst-case residual errors after best adjustment of panel

REFERENCES

1. Hedgepeth, John M., and Louis R. Adams, "Design Concepts for Large Reflector Antenna Structures," NASA CR-3663, prepared under Contract No. NAS1-16134 for the National Aeronautics and Space Administration, Langley Research Center, Hampton, Virginia. Astro Research Corporation, Carpinteria, California, January 1983.

2. Hedgepeth, John M., and Karl Knapp, "Effects of Phase Errors on Antenna Performance," ARC-TN-1079, Astro Research Corporation, July 1980.

3. Bernasconi, M.C., and G.G. Reibaldi, "Inflatable, Space-Rigidized Structures: Overview of Applications and Their Technology Impact," preprint IAF 85-210, 36th Congress of the International Astronautical Federation, Stockholm, Sweden, October 1985.

4. Bernasconi, M.C., and G.G. Reibaldi, "Large Inflatable Space-Rigidized Antenna Reflectors," International Astronautical Federation, Paper IAF-87-315, 38th IAF Congress, Brighton, United Kingdom, October 1987.

5. Thompson Ramo Wooldridge, Inc., "Sunflower Solar Collector," NASA CR-46, prepared under Contract No. NAS5-462 for the National Aeronautics and Space Administration, Washington, D.C., May 1964.

6. Ard, K.E., "Design and Technology Study for Extreme Precision Antenna Structures," NASA CR-174861, prepared under Contract No. NAS3-23249 for the National Aeronautics and Space Administration, Lewis Research Center, Cleveland, Ohio. Harris Corporation, Government Aerospace Systems Division, Melbourne, Florida, August 1985.

7. Hedgepeth, John M., "Critical Requirements for the Design of Large Space Structures," NASA CR-3484, prepared under Contract No. NAS1-15347 for the National Aeronautics and Space Administration, Langley Research Center, Hampton, Virginia. Astro Research Corporation, Carpinteria, California, November 1981.

8. Hedgepeth, John M., "Influence of Fabrication Tolerances on the Surface Accuracy of Large Antenna Structures," AIAA Journal, vol. 20, No. 5, pp. 680-686, May 1982.

9. Hedgepeth, John M., "Accuracy Potentials for Large Space Antenna Reflectors with Passive Structure," J. Spacecraft and Rockets, Vol. 19, No. 3, pp. 211-217, May-June 1982.

10. Hedgepeth, John M., "Support Structures for Large Infrared Telescopes," NASA CR 3800, prepared under Contract No. NAS1-16923 for the National Aeronautics and Space Administration, Langley Research Center, Hampton, Virginia. Astro Research Corporation, Carpinteria, California, July 1984.

11. Hedgepeth, John M., Pactruss Support Structure for Precision Segmented Reflectors: Final Report," AAC-TN-1153, Astro Aerospace Corporation, Carpinteria, California, September 1988.

UNFURLABLE, CONTINUOUS-SURFACE REFLECTOR CONCEPT

J. E. Stumm and S. Kulick
Composite Optics, Incorporated
San Diego, California

INTRODUCTION

Various concepts for large, deloyable reflectors have been developed and some have flown. In each case the surface material was either a continuous mesh of some sort or an assembly of rigid, continuous-surface facets or petals. Performance issues arise in each case. For mesh, reflectance diminishes with increasing frequency. For rigid sections, one has to deal with seams and relative positioning of the segments. These two issues prompted the evolution of our concept of an Unfurlable, Continuous-Surface Reflector. This paper describes the concept and presents what we've learned, what we suspect will be learned, and also raises questions yet to be addressed.

THE CONCEPT

The apparent need for large (greater than 4.3 meters) high-frequency (K_a band and beyond) antenna reflectors has prompted the development of a concept centered around a thin membrane antenna reflector shell that can be rolled into a semi-cylindrical volume for stowage and then allowed to unroll and register against a deployable substructure to re-form the fabricated shape. The result is a smooth, continuous surface that promises to provide surface accuracies to date unachievable with any other well known deployable reflector concept. The basis is straightforward: If in-plane membrane stiffness is high compared to section stiffness and if the membrane is registered accurately, the membrane should assume the shape to which it was fabricated.

What we did to "reduce the concept to practice" was to fabricate a reflector shell (Figures 1 and 2) on an existing mold in a manner that we've employed several times in the past. In this case, we started with a one-meter, offset geometry male graphite/epoxy mold whose focal length is 24 inches. We laid up P75S graphite fiber, preimpregnated with the 930 resin system. Each 0.0025-inch layer was oriented to satisfy $(\pm 45^{\circ})_S$ laminate schedule to yield a total shell thickness of .010 inches. The axis about which there is a minimum bending stiffness of the lay-up coincides with the reflector symmetry axis. A flat, rectangular 4x16-inch piece was also fabricated with the same material and ply orientation. This flat piece was intended for release-of-stored-energy tests. We wanted to learn how close a rolled up sheet would return to its unrolled shape when it was allowed to do so. We rolled this piece on a 10-inch diameter cardboard cylinder and put it away.

In the meantime, we fashioned a support ring 2-inches-square cross-section of the same graphite/epoxy laminate whose diameter is slightly smaller than the one meter reflector shell. We also added a curved beam with the same cross section to the ring across the symmetry diameter so that when the deployed shell is resting on the ring it also rests on this curved beam as well (Figure 3). We employed two sets of restraints; one to hold the rolled up shell on the support ring and one to retain the shell on the ring once the shell is fully unfurled.

To describe the first set of restraints one must first understand that the rolled up shell does not form a cylinder. It forms a slender "football" shape with the "points" removed. Also, the two spots on the shell that rest on the ring are different when the shell is unfurled from when it is rolled up. And, of course, the shell surface at the support points rotates when going from the stowed to the deployed configuration. To accommodate all this, we designed a restraint at one end that allows for rotation only and at the other that allows for rotation and radial translation (Figure 4).

The second set of restraints is a bit simpler. We fastened one flexible magnetic strip on the inside upper edge of the ring (Figure 5) and oriented the surface to be parallel to the surface of the deployed shell. We also bonded a ferrous metallic strip on the back side of the shell to mate with the magnet (Figure 6). We did the same thing along the diameter support and mating shell surface as well (Figures 7 and 8). This scheme not only provides a means to retain the shell in the unfurled position against the support structure, but also aids in the deployment process by applying a magnetic force of attraction between the unfurling shell and support ring. The detailed design of this feature will, from the magnetic force sizing standpoint, be dictated by the deployment strain-residual test on the flat piece. It will also serve as a means of overcoming some gravitational forces that it must do to gain acceptance via a ground demonstration/ test program. This, too, will likely contribute to sizing the magnetic forces.

What happened when we assembled the rolled up shell on the ring and deployed it was, if not surprising, at least very satisfying. Everything worked! We constrained the shell by placing a strip of paper around the shell with masking tape overlapping the seam just an inch or so. We peeled it off with a lanyard string attached to the tape and when the rolled shell became unrestrained it unfurled and slapped against the ring support structure. Although we did not measure the surface, it appeared that the shell returned to its original, as-manufactured shape. There were no residual gaps between the back side of the shell and the ring magnet. In the event that happens, it is felt that these can be brought in by increasing the magnetic attraction forces somewhat since the shell does not appreciably resist forces normal to the surface. Following the "cup up" deployment, we re-oriented the ring to a vertical position at the edge of a table and repeated the test. We got the same results. We then leaned the ring past vertical about 5 degrees. It still worked. But when we repeated the test at approximately 10 degrees, it did not completely deploy. Overall it "looked" good. And we expect it will prove to be as precise as the original shape provided that the shell is supported properly, i.e., the points or arcs or rings of support must be correctly located on the support structure so that they lay on the imaginary surface of the correct shell shape and there must be sufficient magnetic forces to attract the shell snugly against the supports.

During this scale model development, we returned from time to time to our flat panel that we had rolled up on a cylinder. What we learned was that residual strains, if present at all, will likely be very small and forces necessary to "complete deployment" if there were residual strains would also be very small. We allowed the strip to unroll somewhat crudely on edge until we felt all deployment stresses had vanished. We then compared its relaxed shape to the line we drew on some paper coinciding to the original shape. The deployed panel matched the original line very well. We repeated this test after two years had gone by. We got the same results. We then brought a magnet near to a ferrous strip on the back side of the panel at the edge. The panel moved easily. This was hardly rigorous, but clearly was indicative that any restoring forces needed to take out residual strain should prove to be small.

There was some design work done on folding the support ring and concepts to retain the whole package as well as provide for sequential deployment, but no detailed design was performed, nor did we build a deployable ring as part of the concept demonstration, feeling that that technology in the form we designed it is not particularly new. And if a deployable truss proved advantageous we would be venturing into a field in which we are not expert. Suffice to say, the feasibility of an unfurlable continuous surface reflector concept has been demonstrated even though there are many questions remaining:

What materials are best suited to the laminate make-up?

Can the deployed shell be supported at discrete points, and if so, how many? Or must it be supported by continuous line or area contact?

How large a reflector can this concept support?

How accurate will the surface be?

What form does the support structure take?

Is there a relationship between shell size and shell thickness?

Should the structure have (remote) adjustment capability?

What kind of ground test program would demonstrate zero g capability without compromising the design?

How do you achieve very homogeneous mechanical properties throughout the shell surface?

What form should the magnetic latching mechanism take?

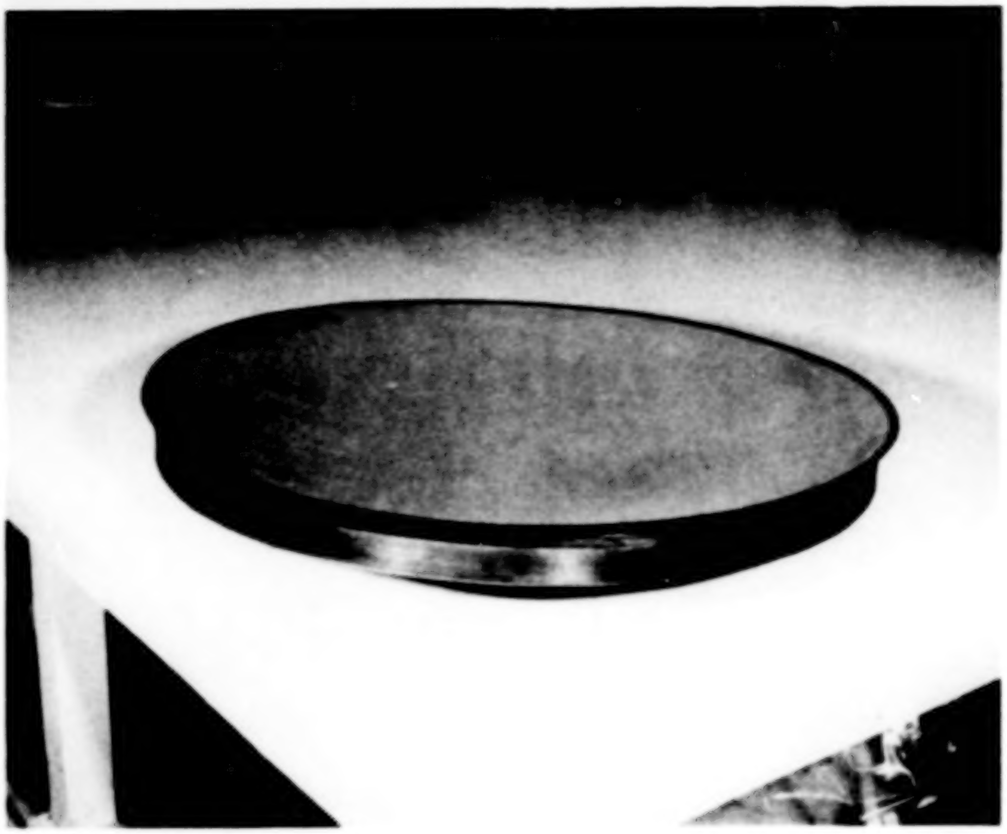

FIGURE 1

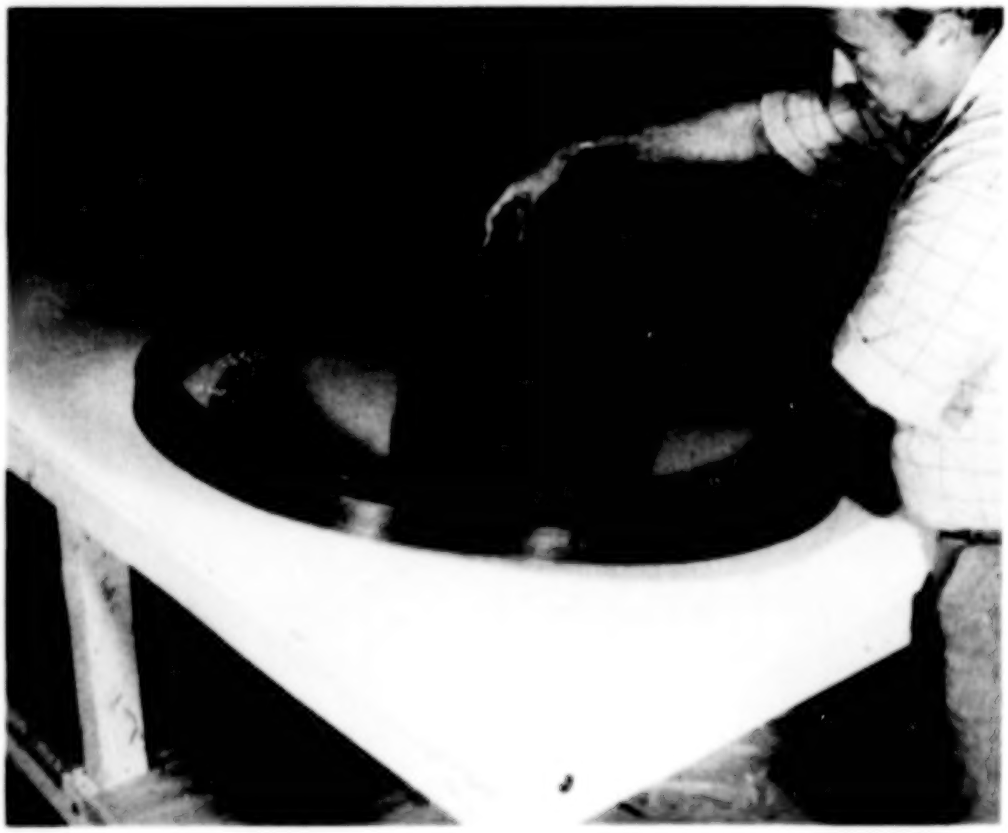

FIGURE 2

FIGURE 3

FIGURE 4

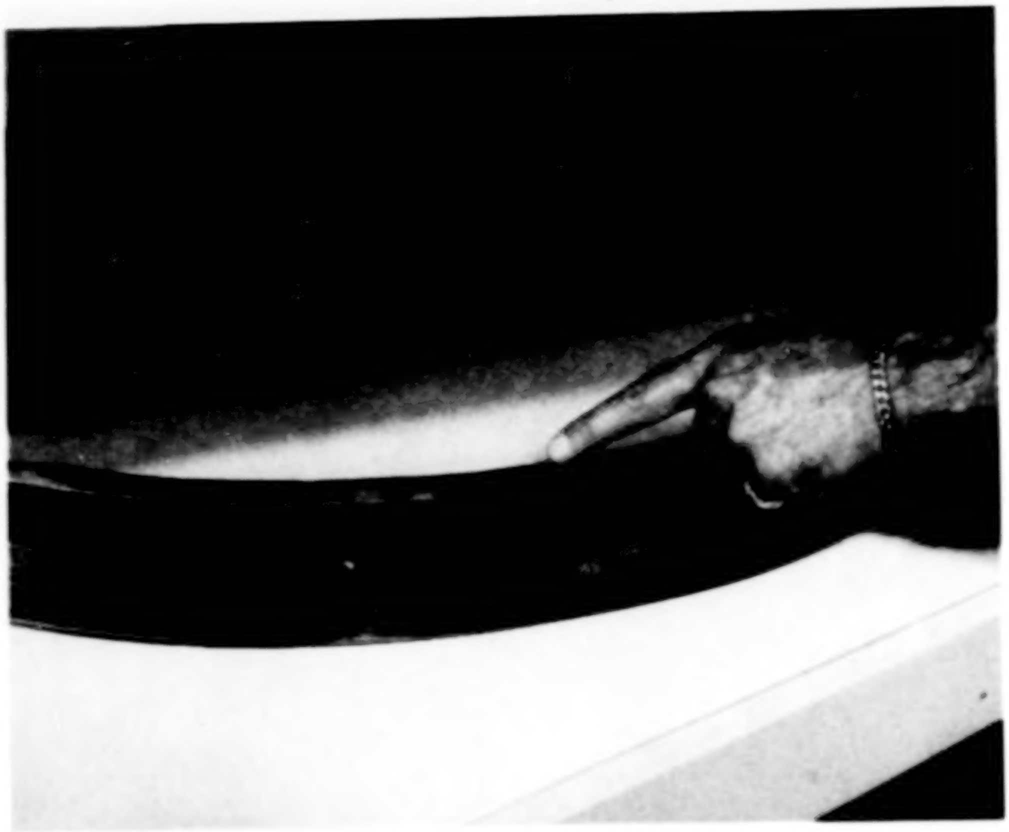

FIGURE 5

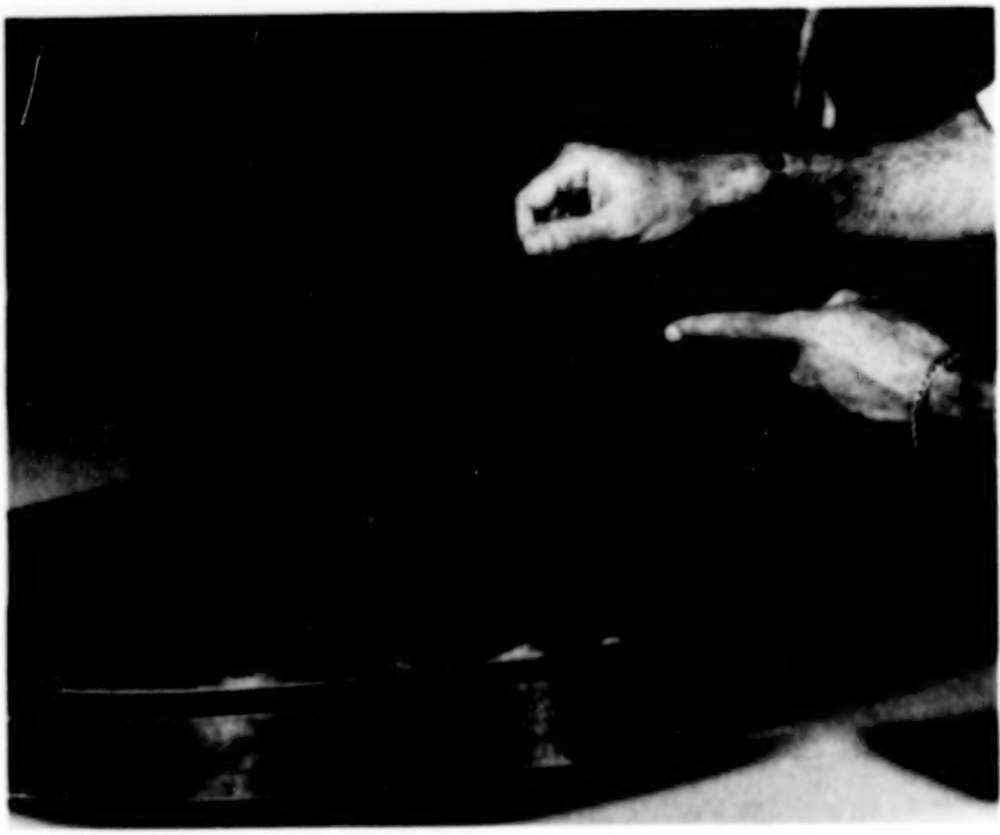

FIGURE 6

FIGURE 7

FIGURE 8

ADVANCES IN LARGE INFLATABLE REFLECTORS

M. Thomas and G. Williams
L'Garde, Inc.
Tustin, CA

Weight of Inflatable Antennas

For most applications in space for which they have been tried, inflatable structures show a significant weight reduction when compared to mechanical structures. The curves shown here for mechanical structures were compiled from a JPL report by Freeland (Reference 1) based on an industry survey of projections for weights of large antennas. The curves for inflatable antennas were produced by us during a 1983 NASA funded study (Reference 2). For this study only wavelengths longer than 1 cm were considered. The inflatables showed a large projected weight savings over even mesh deployables until very large diameters were desired (greater than 300 meters). These curves were based on using films routinely available off the shelf. Note that the curves begin to diverge upward from the straight line at lower diameters. The weight of such systems strongly depends upon the inflation pressure, since make-up gas is carried in the weight budget to allow for leakage over the projected ten-year life of these structures. The inflation pressure must be increased to provide sufficient stress in the film to remove packaging wrinkles if precision structures are needed (wavelengths shorter than 1 cm). This also increases the weight of the torus used to support the membrane due to the increased loads. For mm wavelengths, the weight of such structures at diameters in the ten meter range can be increased by a factor of ten if high precision is required.

1. Freeland, R. E., Industry Capability for Large Space Antenna Structures, Report 710-12, Jet Propulsion Laboratory, May 25, 1978.

2. Friese, G. J., G. D. Bilyeu and M. Thomas, Initial '80's Development of Inflated Antennas, NASA Contractor Report 166060, January, 1983.

0.006mm (1/4 mil) film

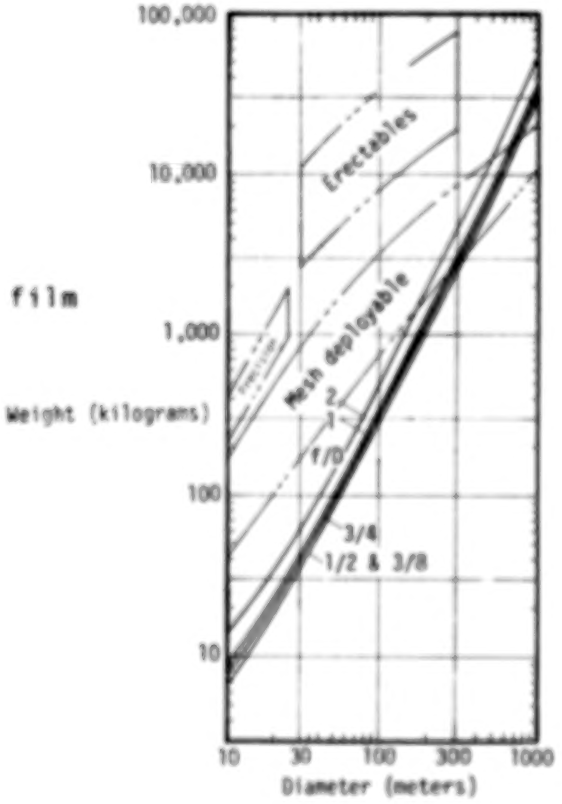

Packaged Volume of Inflatable Antennas

Inflatables are unmatched when compared to mechanical structures when packaged volume is considered. Furthermore, inflatables can be easily packaged in rather bizarre shapes to make use of available volumes. This flexibility is particularly important for space missions, since most shuttle payloads have been volume limited rather than weight limited. This figure shows the many orders-of-magnitude improvement in packaged volume available by using inflatables.

As for the previous weight chart, the data shown here was generated for relatively long wavelength electromagnetic radiation, and a factor of ten increase in required volume may be necessary at the lower diameters, if precision structures are needed. However, even for such an increase, the inflatable approach clearly provides a superior packaged density. Previous calculations have shown that a 700 m diameter microwave antenna could be carried into orbit by a single shuttle flight, if the antenna were an inflatable.

These calculations were performed for a 10 year life in orbit and wavelengths longer than 1 cm.

0.006mm (1/4 mil) film

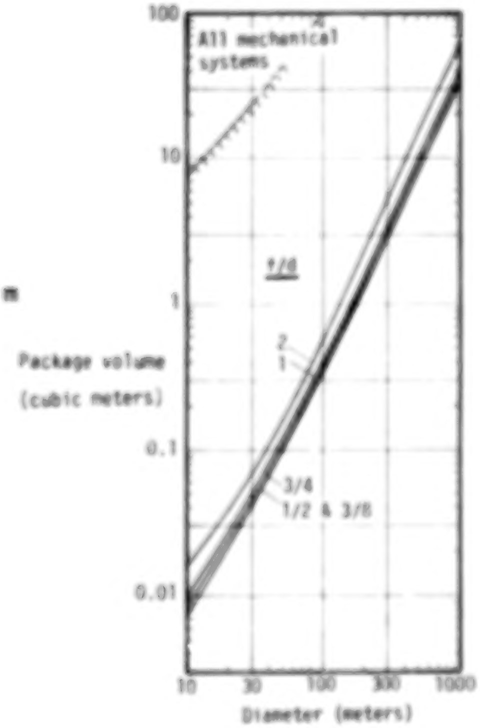

Other Advantages of Inflatable Antennas

The reliability of deployment of inflatable structures has been known for years. When properly designed, such a system is inherently more reliable than mechanically erected structures simply because it has very few points of failure. Furthermore, the deployment forces are distributed over large areas resulting in less local build-up of high forces. The structural strength of the ECHO satellites was evaluated by NASA in a zero-g environment created by inflating the satellites with a lighter-than-air mixture so that it floated in the laboratory. Similarly, an inflatable antenna is the only lightweight large space structure whose accuracy can be checked on the ground by using such a technique. The dynamics of inflatable structures are improved over mechanical systems because (1) the damping coefficients of typical thin films result in energy losses per cycle due to hysteresis hundreds of times greater than for typical high strength composites or metals, (2) the resonant frequencies of a large inflatable are dependent on inflation pressure, so another variable can be introduced into the structural design to adjust such frequencies, and (3) many of the distortions that motion induces into an inflatable fight a constant inflation pressure resulting in motion that is not simple harmonic and has no resonances at all. Another advantage of the inflatable that has been proved in many studies of USAF decoy systems is that the inflatable, being formed by a pressure over the surface, can naturally assume curved shapes, making precision easier to accomplish than with mechanical systems.

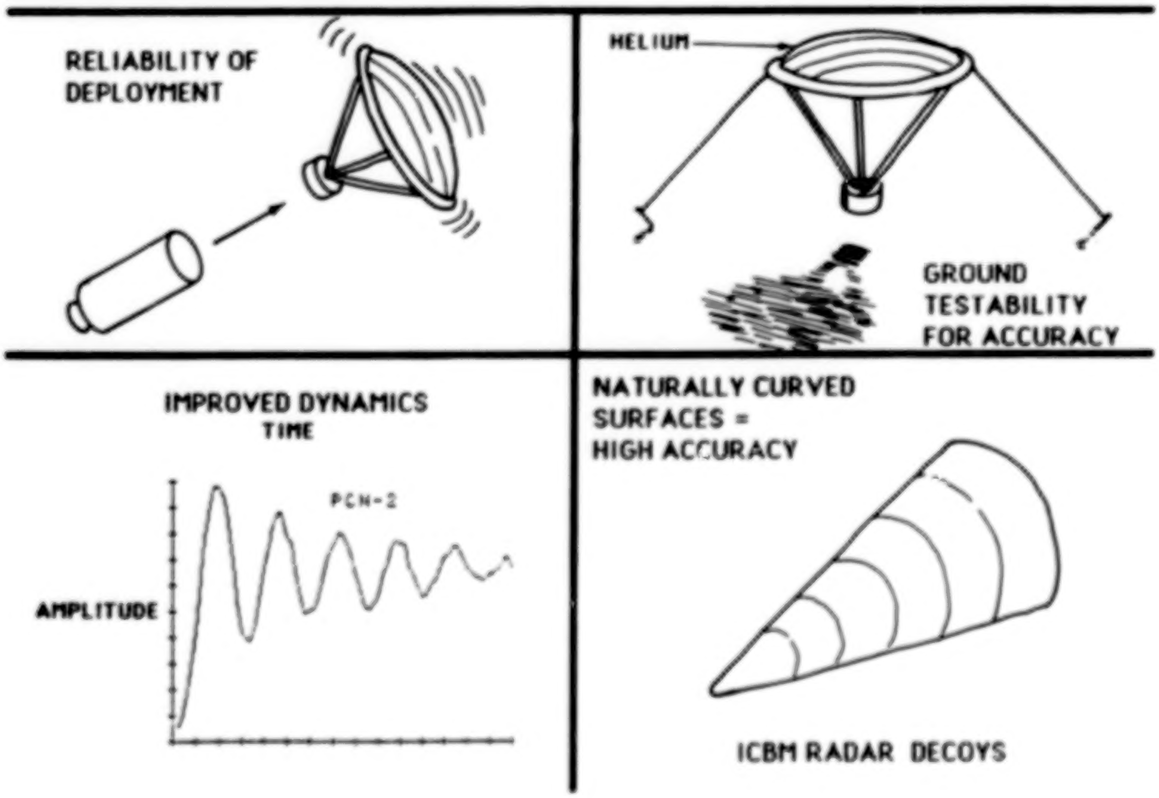

Fully Inflatable vs. Rigidized Inflatable

In the ECHO days, concern for meteoroid penetration led to a change in the emphasis of NASA inflatable research from pure inflatables to structures that deployed using inflation but were then rigidized. However, the meteoroid flux was overestimated by three orders of magnitude (1000) in those early days. Furthermore it was not generally understood that the larger the structure, the lower the required pressure, so that structures large enough can be kept fully inflated by carrying along make-up gas to compensate for loss through holes, and the weight of this gas would be insignificant. Thus, fully inflatable antennas again became a viable option.

Clearly if the weight of a fully inflatable including the make-up gas is less than the weight of an inflate-then-rigidize structure, the fully inflatable is preferred unless some other consideration enters. A rigidizing structure will be clearly less reliable since an additional mechanism is involved, and many of the advantages of the inflatable are lost--such as the ability to accurately measure performance on the ground, and improved dynamics. Furthermore, the act of rigidizing the inflatable requires new surface forces that are of the same order or higher than the inflation forces. As a result, the high-accuracy obtainable in the inflatable will be degraded.

The fully inflatables are generally the preferred structure for very large precision structures. The rigidized inflatables are preferred for small-volume structures where precision is not necessary. An inflatable antenna may be a hybrid, using rigidized components to provide structural support and mountings, and a fully inflatable to provide the reflecting membrane.

FULLY INFLATABLE

MAKEUP GAS MUST
BE SUPPLIED TO MAINTAIN P

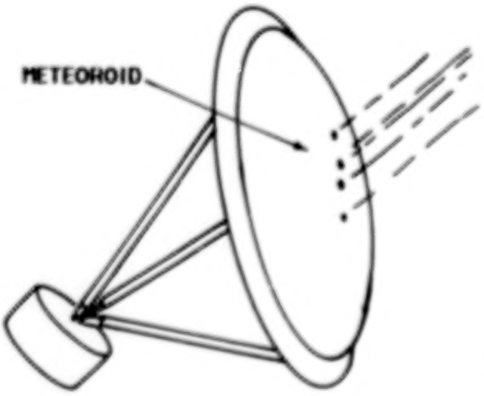

RIGIDIZED INFLATABLE

LOSS OF "OTHER" ADVANTAGES
OF INFLATABLE

SURFACE DEGENERATION

L'Garde Solar Concentrator Experience

Under the Highly Accurate Inflatable Reflector (HAIR) program for the Air Force Astronautics Laboratory, L'Garde has performed extensive experimental work leading to the development of these large inflatable reflectors for the solar rocket system.

In the first phase of this Small Business Innovation Research (SBIR) contract (F04611-83-C-0051) analytic and experimental studies showed that inflatable reflectors could be made with surface errors less than 0.1mm RMS. In the second phase of the contract (F04611-84-C-0054) a 3 meter diameter concentrator was built with less than 3 milliradians (mrad) RMS slope error. In addition, an inflated torus was built and attached to the two membranes (reflector and canopy) and testing of the rigidized aluminum truss cylinders was performed.

A follow-on AFAL contract to HAIR, the Deployable Solar Concentrator Experiment (DSCE) is now in progress (F04611-86-C-0112). In this program, subscale off-axis reflectors, such as those used on the solar rocket, are being developed. The first 2 x 3 meter membrane has been built and tested with good results--a 3 mrad RMS slope error. An upscaled 7 x 9 meter reflector will be built and tested next.

In parallel to the HAIR/DSCE ground test programs, L'Garde is performing a flight testing program, the Space Inflatable Reflector Experiment (SIREX). Phase I (F04611-86-C-0054) was a preliminary design/planning contract, while the current Phase II Program (F04611-87-C-0072) will take the flight test hardware all the way through development testing.

A new contract from NASA-Langley is the Inflatable Solar Concentrator Experiment (ISCE). This project will define space experiments to determine structural damping, materials survivability, and inflatant requirements.

HAIR I (AFAL)	1984	o One meter 0.1 mm accuracy	
HAIR II (AFAL)	1984 - 1986	o Three meter 3 mrad error	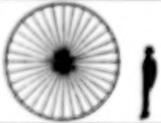
DSCE (AFAL)	1987 - 1991	o 2 x 3 meter 3 mrad error o 7 x 9 meter-1mrad goal	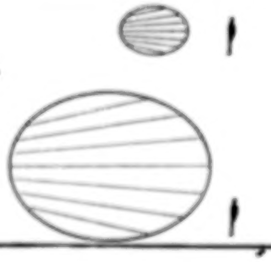
SIREX I (AFAL)	1986	o Space test plan	
SIREX II (AFAL)	1988 - 1991	o Space test hardware	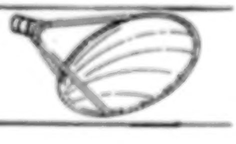
ISCE (NASA-LaRC)	1988	o Define space experiments	

Off-Axis Reflector Test Set-up

Shown in this figure is the test set-up for laser mapping the surface. The membrane is mounted to an elliptical aluminum ring on the wall. A vacuum is drawn on the rear side to pull the film into a parabolic dish. A laser is mounted to a steel structure (to the left of the photograph) and can traverse left-right and up-down to impinge on any portion of the reflector. The beam is then reflected to a target mounted on the adjacent wall for data collection. Shown is the first membrane built. The data have been recently reduced and yielded a 3 milliradian RMS slope error.

The goal under the current DSCE contract is to build an upscaled 7 x 9 meter off-axis reflector with an RMS slope error less than 1 milliradian.

Surface Mapping

The data for the 2 x 3 meter reflector is shown below. The contour map shows lines of equal slope error (in milliradians) about the axis shown. Slope errors are highest near the edges. The valley in the lower right-hand corner was due to a small tear in the membrane. A patch was placed over the tear, but still shows a slight stiffening effect.

The map is a result of running the laser from right to left at five different heights. The target (where the reflected beam hits) is shown at the left of the sketch below.

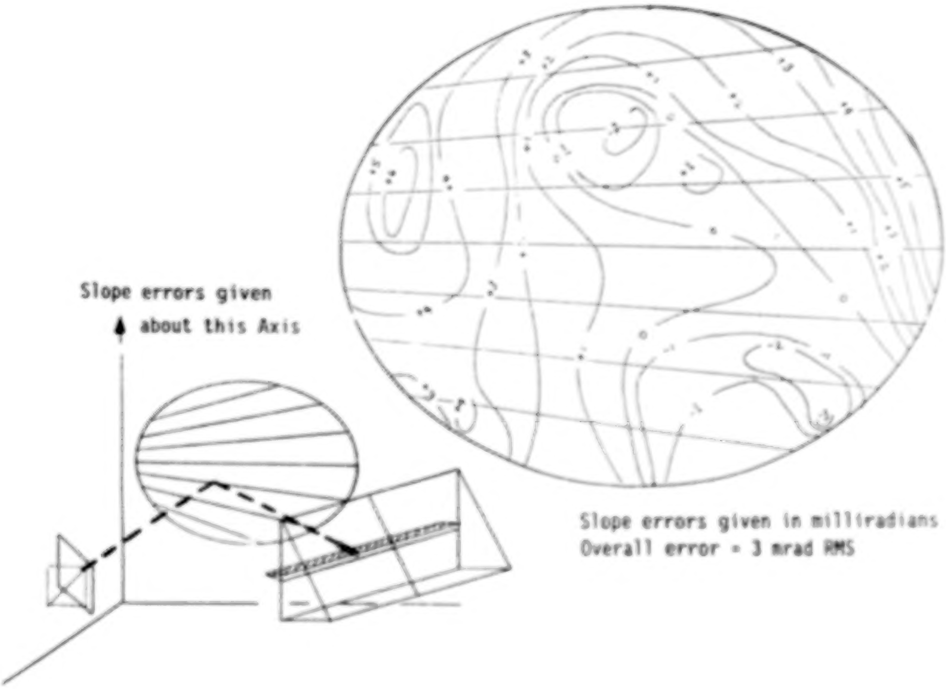

Slope errors given in milliradians
Overall error = 3 mrad RMS

Reflector Surface Rigidization

For some space applications, the fully inflated reflector is less than desirable, mainly due to an extreme make-up gas requirement. This can happen in several instances: The reflector is exposed to a severe debris environment, the inflation pressure is high in small reflectors, or there is not a severe requirement on surface accuracy.

L'Garde has attempted to rigidize the parabolic dish reflectors by applying Fiberglas cloth/resin to the back of an inflated dish. The problem here was in surface degradation; the fabric showed through the film. More recently, L'garde has done some subscale testing on a new method. Rather than using a fabric with a regular pattern that can show through the film, individual fibers are mixed with gelatin to form a thick resin layer between two layers of film. The top film is perforated to allow the water solvent to escape, while the bottom (reflector) layer is non-perforated. While the preliminary tests have yielded poor results due to excessive gelatin shrinkage, the development is continuing.

- NEED FLAT SURFACE FOR REFLECTIVE FILM
- FABRIC "SEE-THROUGH" PROBLEM
- RIGIDIZE WITH GELATIN/FIBER RESIN MIXTURE

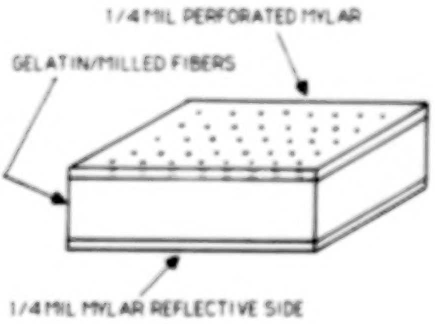

Cylinder Rigidization

This figure shows three possible methods of rigidization for torus/truss applications. In the first, an annulus is constructed of thin aluminum foil (3 mil) and is initially folded and packaged. Upon deployment, the cylinder unfolds and the aluminum skin is stressed to its yield point by pressurization. The inflatant is vented and the cylinder performs as a thin-walled tube. The second method is similar to the first except that liquid polyurethane foam is injected into the deployed cylinder to provide greater resistance to compressive loading and buckling. The liquid foam expands into the cylinder and hardens. Finally, the third method uses a Kevlar fabric soaked with a water soluble gelatin resin, made into an annulus. When exposed to the vacuum of space, the water solvent evaporates making the cylinder rigid. This last method has shown great success as shown in the next figure.

PRESSURIZED ALUMINUM CYLINDER

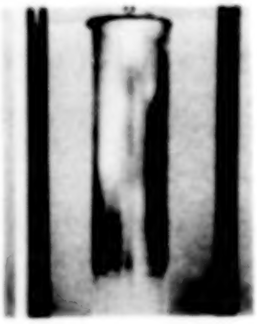

- **INITIALLY FOLDED**
- **INFLATE TO YIELD THIN ALUMINUM SKIN VENTED**
- **USE FOR TRUSS APPLICATIONS**

FOAM - FILLED CYLINDER

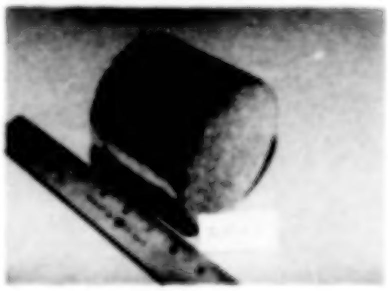

- **INITIALLY FOLDED**
- **INFLATE TO REMOVE WRINKLES**
- **FILL WITH POLYURETHANE FOAM**
- **USE FOR TORUS (HIGH BENDING) APPLICATIONS**

GELATIN/KEVLAR CYLINDER

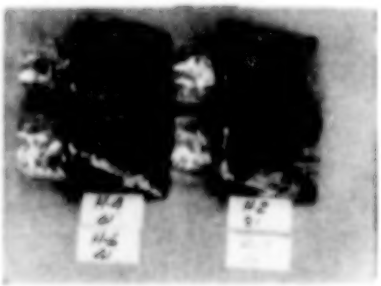

- **FABRIC INPREGNATED WITH WATER SOLUBLE GELATIN**
- **INITIALLY FOLDED**
- **INFLATE TO REMOVE WRINKLES**
- **ALLOW WATER SOLVENT TO EVAPORATE**
- **USE FOR TORUS OR TRUSS**

Strength Comparison of Rigidized Cylinders

L'Garde has performed a series of tests on a number of rigidization techniques. The strength comparison for the different methods is as shown below. The superiority of the newly developed Kevlar/Gelatin composite is obvious from strength comparisons. Planned tests include inflation/rigidization in a vacuum chamber, bending tests, and outgassing tests.

The Scot Foam/Gelatin Method was included in this chart for comparison. In this method, spongy Scot foam is soaked in liquid gelatin and then allowed to dry to allow the gelatin to perform as the matrix. This method was quickly disregarded due to its poor performance.

Description	Maximum Compressive Load (lbs.)	Weight of 12" Cylinder (lb.)	Strength/ Weight (lb/lb)
Scot Foam w/gelatin	125	.37	330
Stressed aluminum foil	33	.046	720
Polyurethane foam-filled cylinder	650	.44	1,480
Kevlar/Gelatin	2,002	.28	7,140

Meteoroids

For the Government, we recently investigated the impact of meteoroids on inflatable structures. Although much earlier data had been obtained for the high velocity impact of small particles on rigid structures, little was known about similar impacts with thin films. A series of tests were run at the Arnold Engineering Development Center (AEDC) on typical materials using 200 micron diameter particles at velocities above 27,000 fps.

In general it was found that the resulting holes from these polystyrene microspheres were larger than that expected from a "cookie cutter" model, by about a 1.5 times diameter. Furthermore, the use of the thin films as bumpers was explored, and the effect of spacing on second surface penetration was found to be significant. These data are still being analyzed.

AEDC Hypervelocity Range S-1

DATA-SHOT PARAMETERS

DATE	TARGET MATERIAL	TARGET OBLIQUITY	SABOT VELOCITY (FPS)	# OF PARTICLE IMPACTS ON LEADING TARGET	REAR TARGET PERFORATION
2-3-88	2 mil Tedlar	0°	27,560	3	No
2-4-88	1/4 mil Mylar	0°	27,870	5	Yes
2-11-88	1/2 mil Mylar	0°	27,100	**	**
2-12-88	1/2 mil Mylar	0°	27,600	2	Yes
2-15-88	1/2 mil Tedlar	0°	27,910	3	Yes
2-16-88	2 mil Tedlar	45°	27,980	3	No

** Excessive Gun Debris - No Data

Improvements in Gore Design Tools

L'Garde has been using its FLATE computer code to determine the gore shapes for the paraboloidal dishes. Although this has sufficed in the past, a certain amount of adjustment was required during each test (pulling the outer mounting tighter, etc.). To cut down on the trial and error test time, a finite element code is needed. Thus, the gore design output from FLATE can be input to the Finite Element Code to predict the paraboloid's shape upon inflation. Several standard computer models have been tried with no success. The deformations upon inflation are simply too large for these routines to handle. This has led to the development of the LDIPS (Large Deformation of Inflatable Parabolic Shells) code. At present the code has been written, but verification (comparisons) to actual test data is needed.

- Systematic Errors in Paraboloids
- Existing Finite Element Codes
  - ANSYS
  - ABACUS

  No Convergence
- Develop LDIPS Code
  - Given a specific gore shape, what will shell do upon inflation?
  - Due to symmetry, only one gore is analyzed.

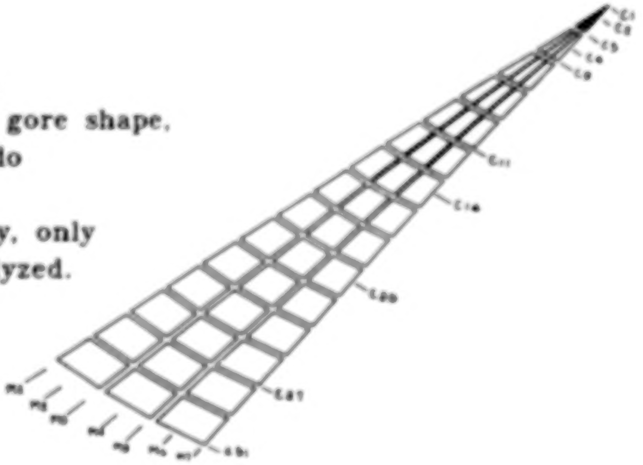

LDIPS Data

The LDIPS code is a general purpose deformation analysis tool. So far, the code has converged only for the circular membrane case, where the membrane is made of straight-edged triangular gores. This will create a deformed dish which is not paraboloidal, but nonetheless serves to verify the code. Shown below, the results from the finite element code coincide on the graph with the theoretical closed-form solution. The next step is to input the curved-edge gore of the parabolic membrane into the code for verification. This problem is much more complex; preliminary runs have shown that the convergence time on the computer is at least twice that for the straight-edged gore circular membrane.

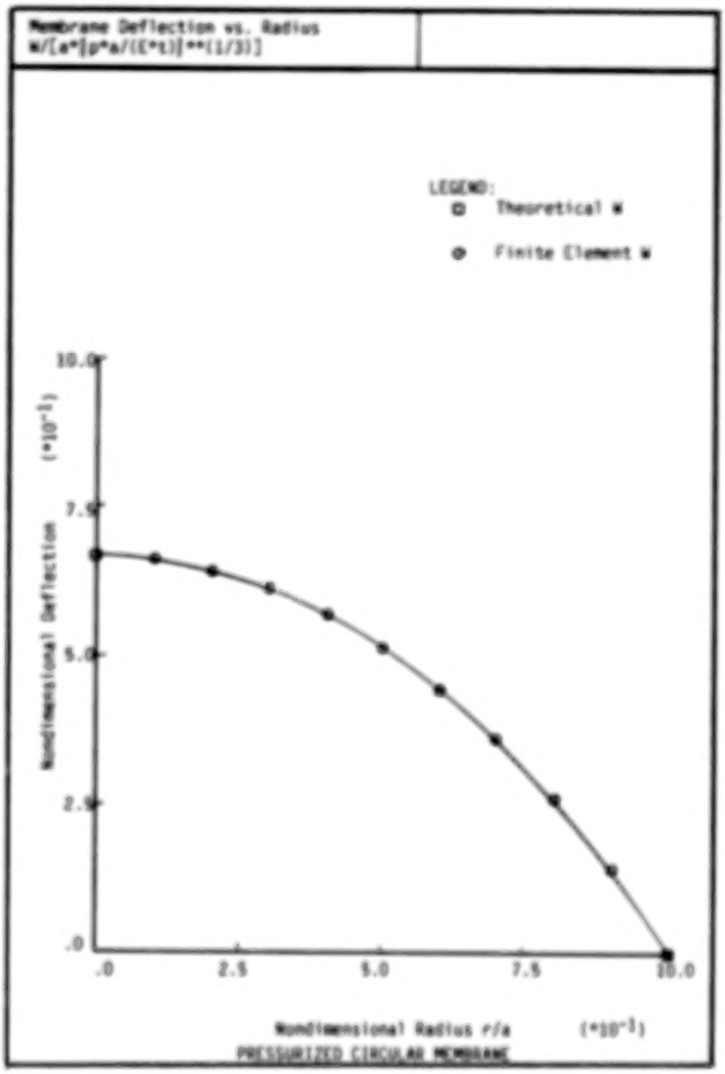

Expected Advances in Large Inflatable Antenna Technology in the Near Future

A variety of rigidization schemes have been used by investigators. Work currently going on at L'Garde will provide baseline data for all the concepts so that the most promising approach can be identified. Furthermore, for the precision reflector, we have identified the most promising approach for support structures and will be developing it. Attention is also turning at present to methods for protecting the various structures from the space environment (meteoroids, debris, oxygen-atom attack, space radiation, thermal effects) through coatings or multiple layers of film. The USAF plans to fly in space an inflatable concentrator soon to demonstrate the merging of these new technologies into a genuine system capability.

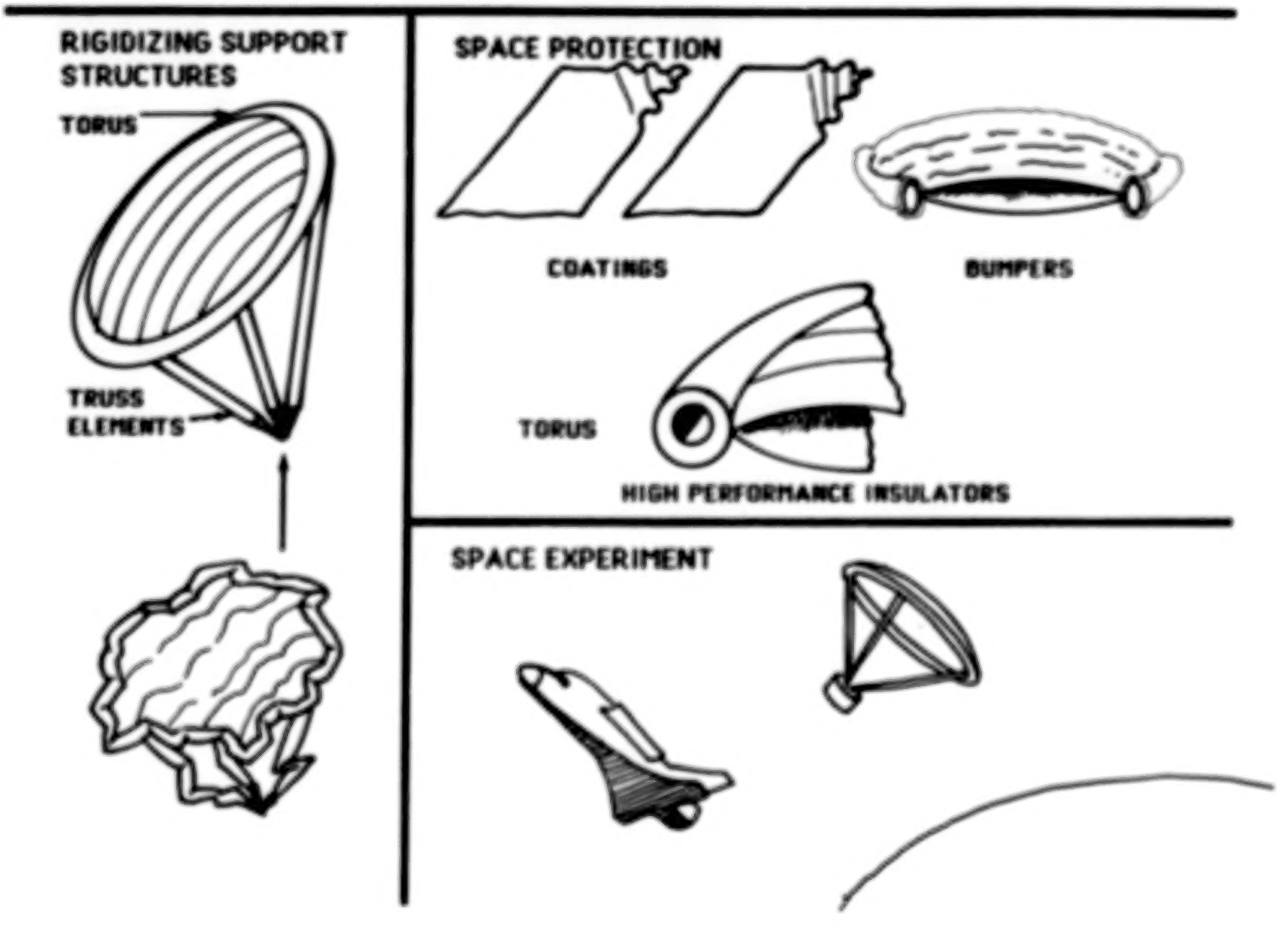
RIGIDIZING SUPPORT STRUCTURES
TORUS
TRUSS ELEMENTS
SPACE PROTECTION
COATINGS
BUMPERS
TORUS
HIGH PERFORMANCE INSULATORS
SPACE EXPERIMENT

Microwave Sensor Technology

Session Chairman: Calvin T. Swift
University of Massachusetts

BLANK PAGE

COHERENT RADAR MEASUREMENT OF OCEAN CURRENTS FROM GEOSTATIONARY ORBIT*

R. E. McIntosh
Department of Electrical and Computer Engineering
University of Massachusetts
Amherst, MA

*Original figures not available at time of publication

INTRODUCTION: Delta K Spectra for Ocean Waves

A coherent HF radar system developed by Barrick [1] has successfully measured ocean surface currents near shore. This innovative system, called CODAR, can map the current vector for coastal areas as large as $10^4 km^2$. CODAR's range is limited owing to the strong attenuation suffered by HF ground waves.

An alternate technique was proposed by Schuler [2], in which the cross-product power spectrum of two (different frequency) microwave signals is processed. The resulting power spectrum exhibits a resonant peak like that seen in Fig. 1. The frequency of the resonant peak corresponds close by to the Doppler shift of an ocean gravity wave traveling toward the radar at the phase velocity, v_p. The slight difference between the frequency of the measured resonant "ΔK" peak and the Doppler frequency shift caused by the motion of the gravity wave is attributed to be the current velocity in the pointing direction of the radar.

The Microwave Remote Sensing Laboratory (MIRSL) at the University of Massachusetts has considered the feasibility of using this technique to measure ocean surface currents from geostationary satellite platforms [3-5]. We discuss problems that must be overcome if a satellite current measurement system is to be realized. We describe MIRSL research activities that address some of these problem areas. We conclude the paper by presenting current measurements that were made using a specially-designed C-Band, step-frequency delta K radar. These measurements suggest that progress is being achieved in detecting ocean surface current motion for a wide variety of ocean surface conditions.

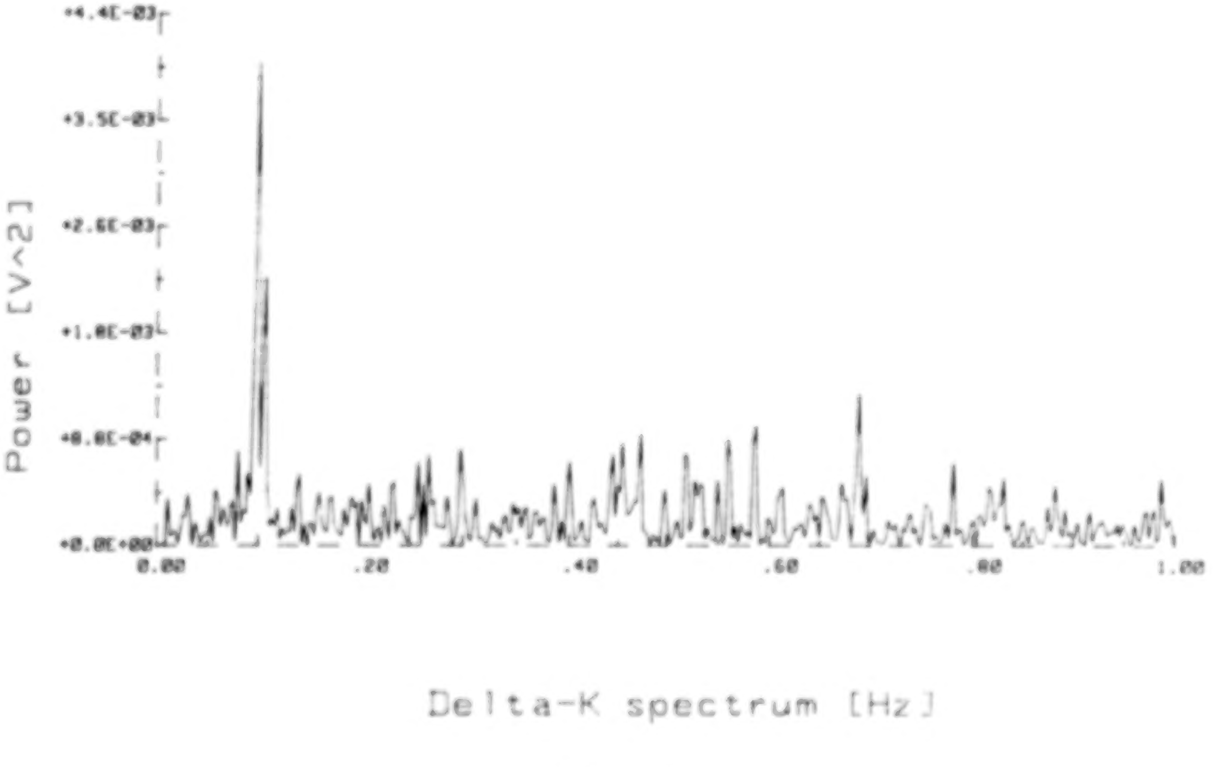

Figure 1

FEASIBILITY OF SPACE-BASED CURRENT MEASURING RADAR

The CODAR system cannot be installed on a satellite because (1) the HF radar signals cannot penetrate the ionosphere and (2) antennas must be too large if reasonable spatial resolution of the ocean surface currents is expected. Consequently, the use of dual-frequency, "ΔK" radars must be considered for this application. Such radars promise the advantages that they might operate from satellite platforms using realistic antennas. In addition, extremely large ocean areas might be mapped by radars mounted on geostationary platforms [3].

Figures 2a and b show the ocean surface area that might be viewed by two radars mounted on geostationary orbits separated in longitude by an angle β. In Fig. 2a, the minor circle, A, corresponds to the loci of points on the ocean surface for which the incident signals from radar #1 are close to grazing. The minor circle, B, corresponds to the locii of points for which the radar signals are almost normally incident on the surface. Only the ocean surface area lying between these circles can scatter ΔK radar signals that can be used to measure the surface current. Fig. 2b shows the area of the North Atlantic Ocean that can be simultaneously viewed by two radars mounted 15° apart in longitude. For this case, the maximum incidence angle is 70° and the minimum incidence angle is 20°.

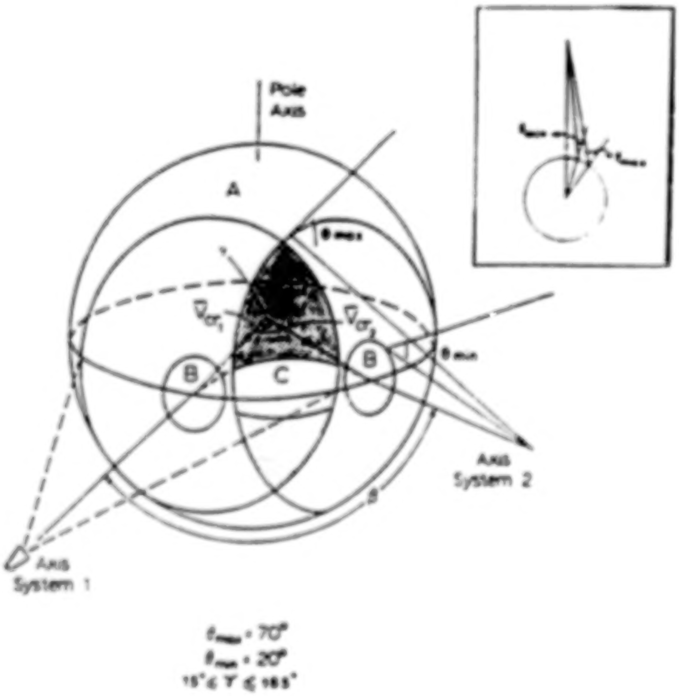
Pole Axis
A
θmax
$\nabla\sigma_1$
$\nabla\sigma_2$
B
C
B
θmin
Axis System 2
Axis System 1
β
$\theta_{max} = 70°$
$\theta_{min} = 20°$
$15° \leq \gamma \leq 165°$

Figure 2a

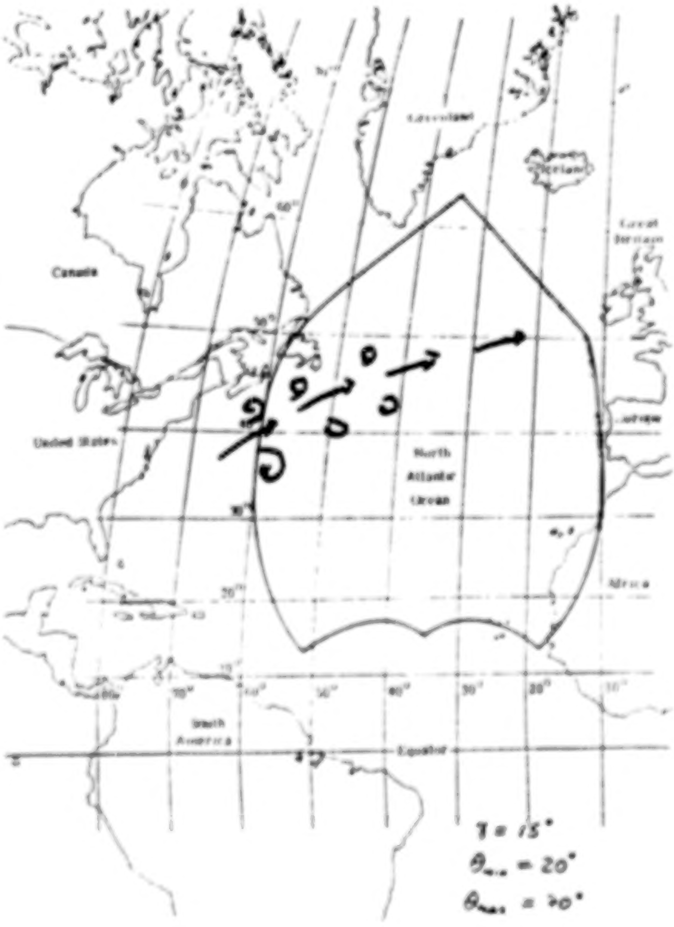
Canada
United States
North Atlantic Ocean
Africa
South America
Equator
Iceland
Great Britain
70°
60°
50°
40°
30°
20°
10°
$\gamma = 15°$
$\theta_{min} = 20°$
$\theta_{max} = 70°$

Figure 2b

SIGNAL-TO-NOISE RATIO OF MULTIFREQUENCY OCEAN CURRENT SENSING RADAR

We conducted a system feasibility study to determine the transmission power requirements of a ΔF radar operating from a geostationary platform. Fig. 3 shows how the signal-to-noise ratio of the received signal increases with transmitted power level when:

(1) The radar operates at X Band ($\lambda = 3cm$),
(2) The receiver temperature is 300°K,
(3) The Normalized Radar Cross Section σ° is -25 dB (near-grazing value)
(4) The transmitted pulse repetition rate is 400 Hz
(5) The transmitted pulse duration is 6 μs and,
(6) The antenna gain is 41.4 dB.

The feasibility study assumes two additional conditions that are not as straight-forward as those listed above.

The first condition assumes that the radar system can resolve pixels as small as 4km by 4km from geostationary altitudes. Resolving 4km dimensions in range is easily accomplished by transmitting pulses having 6μsec are shorter durations. Resolving 4km dimensions in azimuth would require the use of fairly sophisticated antenna systems that utilize direction finding techniques [5].

The second condition assumes that the ΔK peak of the cross-product spectra is always present and clearly distinguishable from spectal background noise peaks as shown in Fig. 1. The calculated S/N performance in Fig. 3 assumes that the peak power of the resonant ΔK peak is 10 dB greater than that of any other spurious peak in the cross-product spectrum. The validity of this last assumption has not yet been established because of the limited amount of experimental data that has been gathered with ΔK radars.

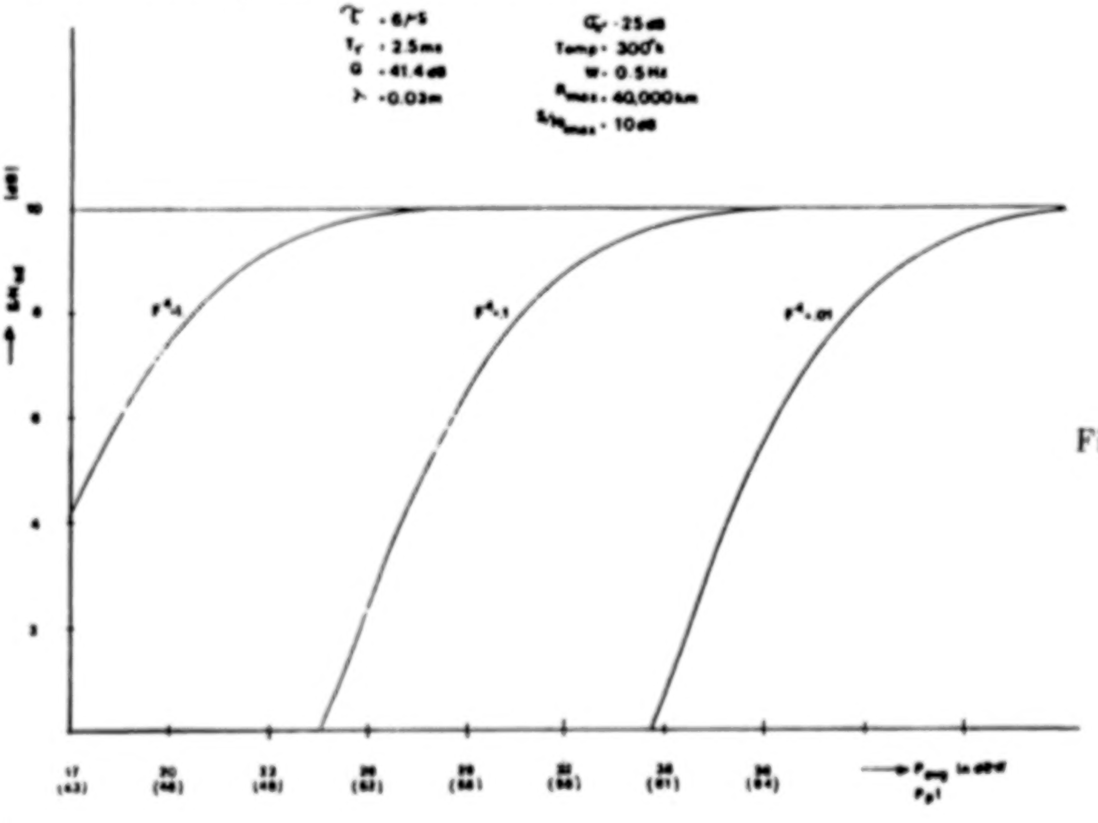

Figure 3

ENHANCEMENT OF CROSS-PRODUCT SPECTRUM MEASUREMENTS USING THE UMASS SFDK RADAR SYSTEM

During the past few years, MIRSL has considered techniques to enhance the resolution of the ΔK peak and minimize the background noise peaks seen in Fig. 1. To test these techniques we designed and built the SFDK radar system shown in Fig. 4a. This coherent C-Band radar system transmits microwave pulse pairs, where the frequencies of the two pulses are separated by a constant HF difference frequency. The radar can operate as a conventional dual-frequency, ΔK radar or the frequencies of the pulse pairs can be varied as shown in Fig. 4b. In the latter case, the HF frequency difference is maintained constant. Table 1 below specifies the characteristic of this system.

Table 1
System Specifications of UMass SFDK Radar

• transmitted power	30 dBm
• 16 carrier frequencies (16 simultaneous spectra)	5.95 to 6.28 GHz
• Δf frequency	2 to 40 MHz
• transmission pulse width	100 *ns* to 100 *μs*
• pulse repetition rate	1 *μs* to 100 *μs*
• antenna	1.5 m parabolic dish; 2.5° beamwidth
• three IF stages	160 MHz, 5.8 MHz, 200 Hz

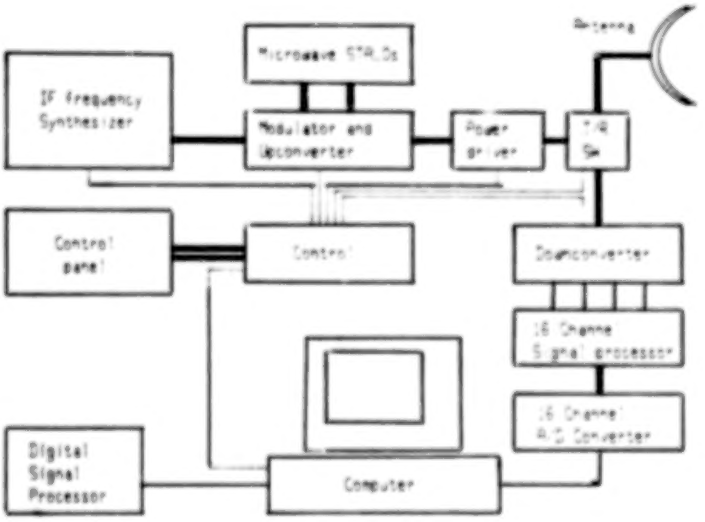
Antenna
Microwave STALOs
IF Frequency Synthesizer
Modulator and Upconverter
Power driver
T/R SW
Control panel
Control
Downconverter
16 Channel Signal processor
16 Channel A/D Converter
Digital Signal Processor
Computer

Figure 4a

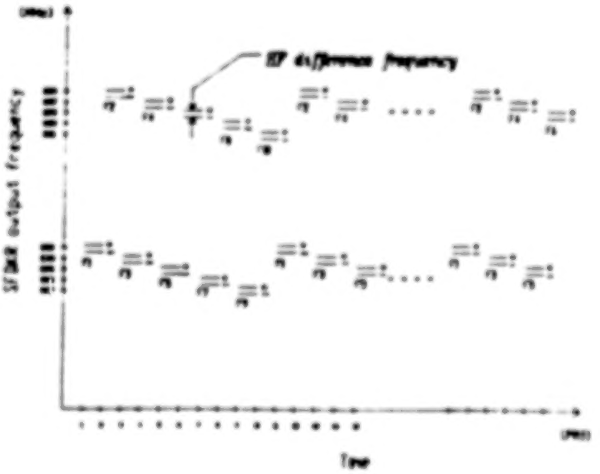

Figure 4b

ΔK SPECTRA OBTAINED USING SINGLE FREQUENCY PAIRS

In Fig. 5 we show ΔK spectra obtained by the UMass SFDK radar during a field experiment at North Truro, Massachusetts (Cape Cod). Each of the ten spectra shown were obtained during the same 80 second interval by using only pulse pairs having the same frequencies. For example, spectrum A was formed from returns indicated by frequencies, f_1^+ and f_1^- in Fig. 4a, spectrum B from frequencies f_2^+ and f_2^-, etc. Averaging the ten spectra result in the spectrum shown in Fig. 6. Note that reduction in the background spectrum results from this averaging.

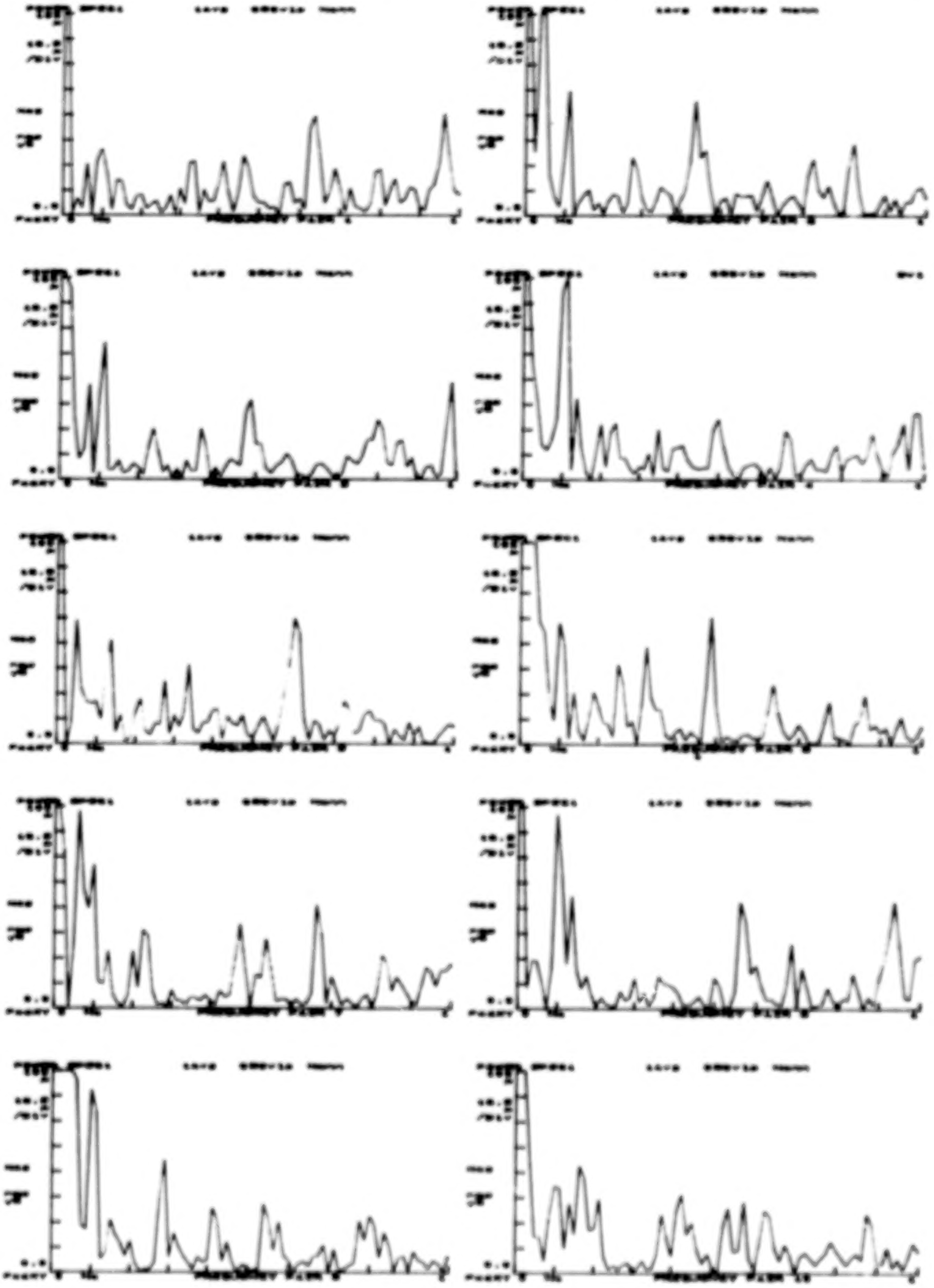

Figure 5

ΔK SPECTRUM OBTAINED BY AVERAGING SPECTRA OF FIG. 5

The UMass SFDK radar uses frequency agility to obtain a number of independent ΔK spectra during the same time interval when previous instruments obtained a single spectrum. We see enhancement of the ΔK peak relative to the background power of the ΔK spectrum in Fig. 6 because the resonant peak of each spectrum is caused by the same gravity waves that are responsible for the resonance in the other spectra. However, the backscatter that contributes to the background spectrum of the various spectra appear to be uncorrelated, indicating that independent samples are being achieved with each change in the carrier frequency.

To our knowledge, the ΔK spectra measured by the UMass SFDK radar are the first ones that demonstrate the ability to measure ocean currents with a C-Band system. This radar has been operating primarily at a test site at North Truro, Massachusetts during the past year. This shore site was chosen because it overlooks the open ocean from a height of approximately 150 feet above sea level.

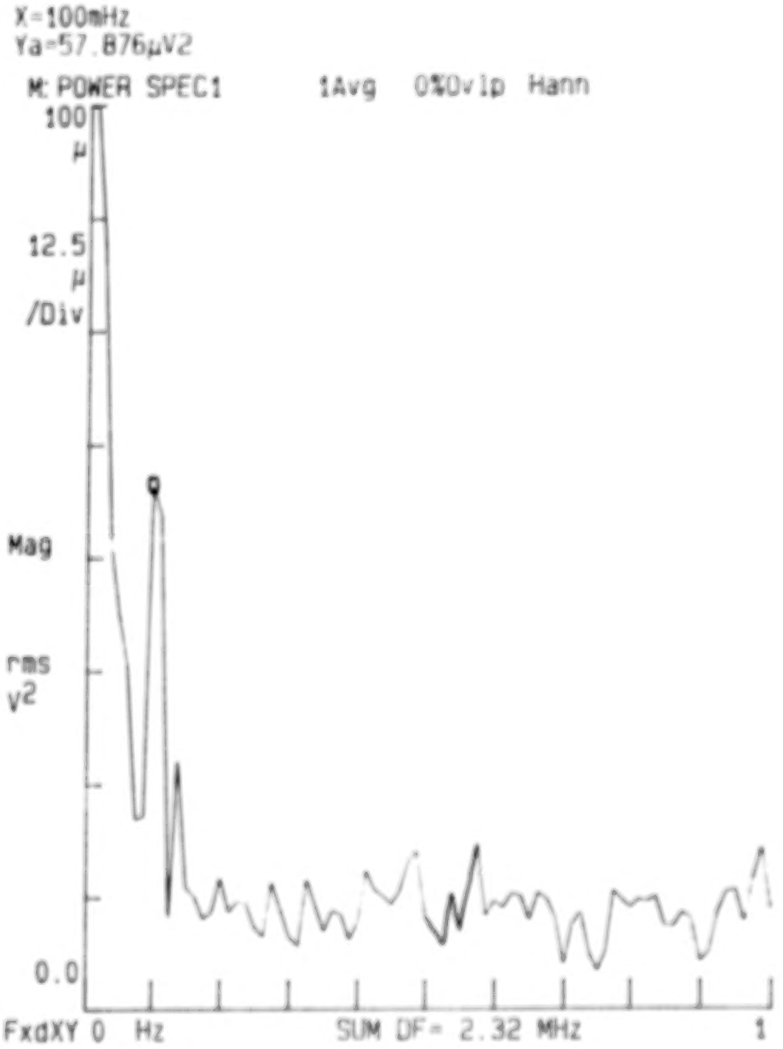

Figure 6

Δ*K* RESONANT PEAK AMPLITUDE AND DOPPLER FREQUENCY MEASURED BY UMASS SFDK RADAR AS FUNCTION OF TIME

We have automated the SFDK radar so that it can be operated for extended periods of time. We are able to monitor both the magnitude and the Doppler frequency shift of the resonance peak. Fig. 7 shows how the peak amplitude and frequency varied during an eleven hour period on December 23, 1986. Laboratory tests of the SFDK's frequency stability indicate that the frequency variations seen in Fig. 7 are caused by ocean surface effects and are not due to instrument frequency drifts. Thus the diurnal variation in the Doppler frequency shift of the Δ*K* line appears to be caused by tidal variations.

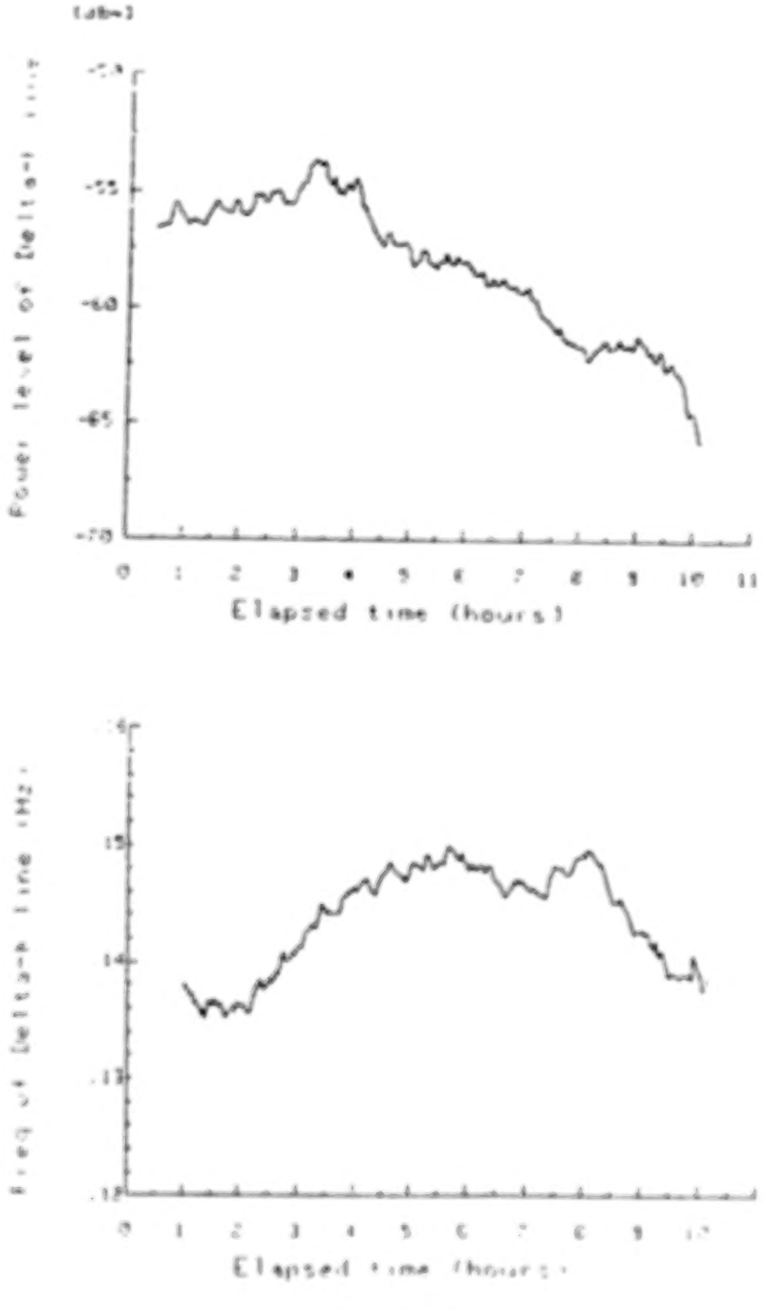

Figure 7

DOPPLER MEASUREMENTS OF OCEAN SURFACE CURRENT

MIRSL extended its field tests at the North Truro site to determine the reliability of measuring the Doppler frequency of the ΔK peak for a wide variety of ocean surface conditions. In addition, we wish to better understand the environmental conditions that affect the ocean surface current, which causes changes in the Doppler frequency of the ΔK peak.

MIRSL used the SFDK radar to monitor the ocean surface for approximately 720 hours during December 1986, March, August and October, 1987. During these field tests, the ocean surface varied between very calm (Beaufort index 1) to very rough (Beaufort index 5). The surface wind speed during these measurements varied between 0 and 30 mph. We observe that the variation of ΔK Doppler frequency shown in Fig. 8 has a diurnal component that may be ascribed to tidal currents. We have observed this periodicity in most of the SFDK data obtained from the North Truro tests.

The SFDK radar system has been able to clearly distinguish a resonant ΔK peak in more than 75% of the North Truro measurements. The ΔK peak tends to vanish whenever the surface winds fall below 4 mph and the capillary waves disappear from the ocean surface.

We believe that the reliability of the ΔK peak would increase beyond 75% if we could decrease the angle that the radar signal impinges on the ocean surface. Presently, this angle is more than 85° because the radar platform is only 150 ft. above the ocean surface. Thus, the incidence angle is substantially (15°) greater than the 70° worst-case incidence angle assumed in the system study of part II.

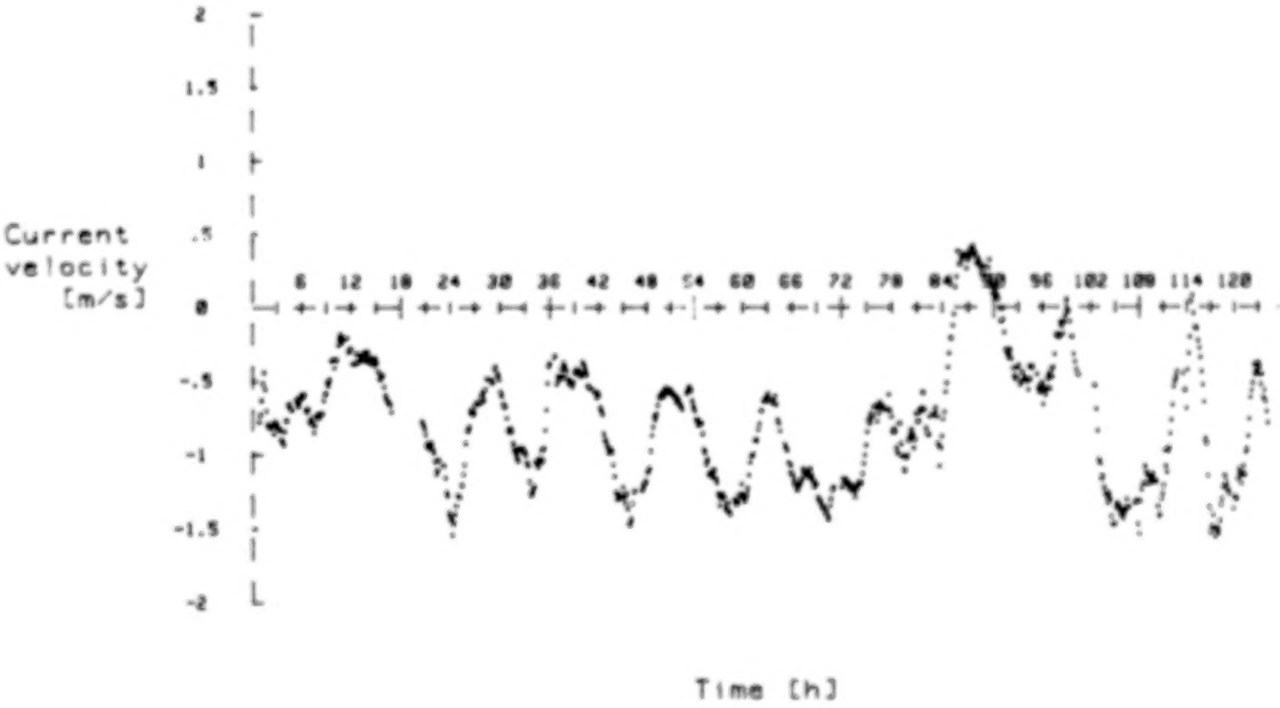

Figure 8

EFFECTS OF SURFACE WINDS ON MEASURED ΔK DOPPLER FREQUENCIES

The Doppler frequency in Figure 8 appears to vary with the tides during the first two days but we note that the ΔK frequency varies somewhat randomly on the third day. This random variation of the ΔK frequency occurred during a period when the wind speed and direction changed rapidly. Consequently, we conclude that the surface currents in the SFDK antenna footprint are strongly influenced by surface winds.

A clearer picture of the effect that surface winds have on the ΔK Doppler frequency measured by the SFDK radar is seen in Fig. 9. The surface wind was approximately 15 mph from the North East direction for the first seven hours, changed direction to come from the East for three hours, and changed back to its original orientation during the last two hours. In Fig. 9, we see that the ocean current measured by the SFDK radar varies somewhat diurnally during the twelve hour measurements, with the exception of the time following the change in wind direction (after the ninth hour). The observed dependence of the ocean surface current measured by the SFDK on the surface wind is not surprising, given that surface currents in the deep ocean are driven almost entirely by surface winds.

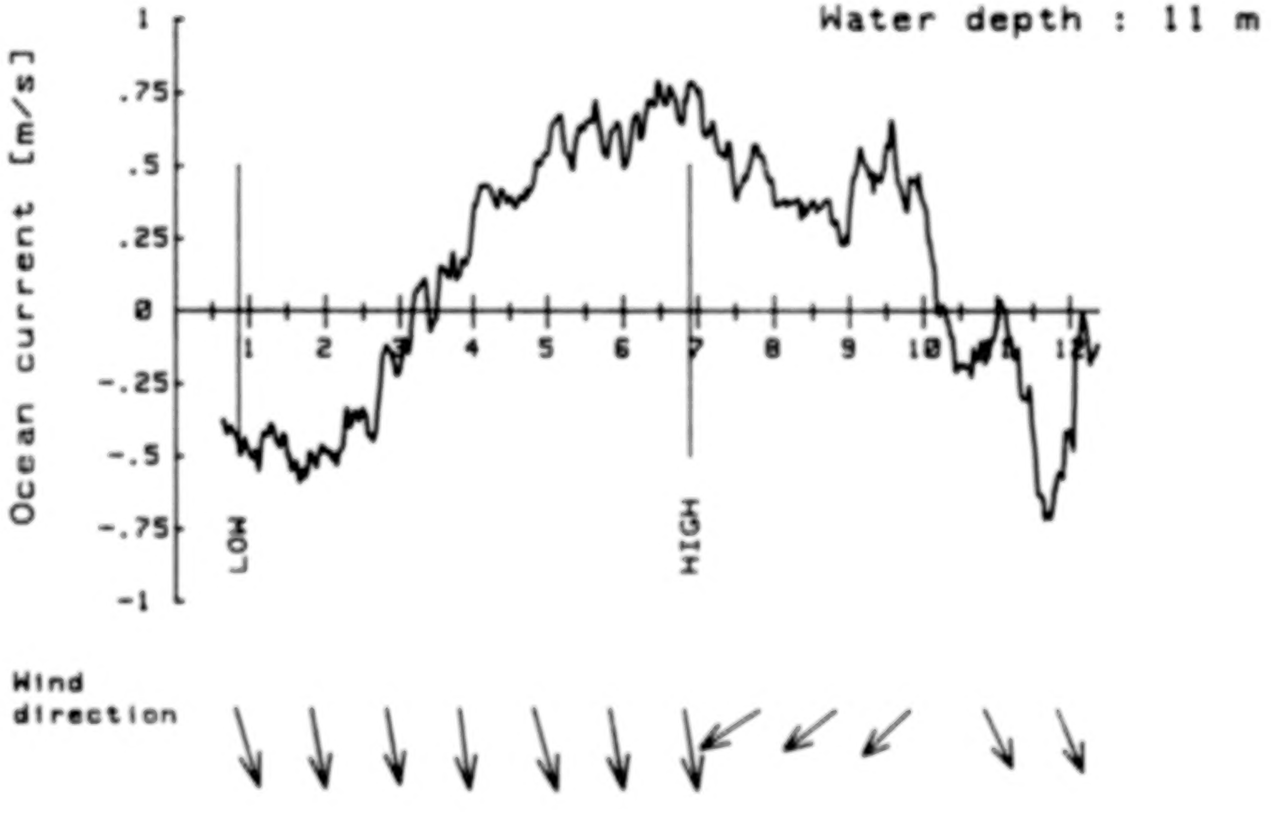

Figure 9

REFERENCES

[1] Barrick, D.E., M.W. Evans and B.L. Weber, "Ocean Surface Currents Mapped by Radar," Science, Vol. 198, No. 4313, pp. 138–144, Oct. 14, 1977.

[2] Schuler, D.L., "Remote Sensing of Directional Gravity Wave Spectra and Surface Currents Using a Microwave Dual-frequency Radar," Radio Science, Vol. 13, No. 2, pp. 321–331, March–April, 1978.

[3] McIntosh, R.E., C.T. Swift, R.S. Raghaven, A.W. Baldwin, "Measurement of Ocean Surface Currents with Multifrequency Microwave Radars - A Systems Analysis," IEEE Trans. on Geoscience and Remote Sensing, Vol. GE–23, No. 1, January 1985, pp. 1–12.

[4] Raghaven, R.S., R.E. McIntosh, and C.T. Swift, "Minimizing Errors of Ocean Currents Measured by Electromagnetic Backscatter," IEEE Trans. on Geoscience and Remote Sensing, Vol. GE–23, No. 1, January 1985, pp. 13–17.

[5] Raghaven, R.S., R.E. McIntosh, and C.T. Swift, "Increasing the Azimuthal Resolution of Ocean Surface Currents for Dual-Frequency Radars," IEEE Trans. on Geoscience and Remote Sensing, Vol. GE–23, No. 6, November 1985, pp. 906–909.

MILLIMETER RADIOMETER SYSTEM TECHNOLOGY

W. J. Wilson and P. N. Swanson
Jet Propulsion Laboratory
California Institute of Technology
Pasadena, CA

JPL has had a large amount of experience with spaceborne microwave/millimeter-wave radiometers for remote sensing. This has included the Microwave Sounder Units (MSU) at 50-60 GHz, for Nimbus temperature sounding, the Scanning Multichannel Microwave Radiometers (SMMR) (6-37 GHz) for Nimbus G, SeaSat and currently TOPEX, and the Upper Atmospheric Research Satellite (UARS) Microwave Limb Sounder (MLS) with frequencies between 63 and 205 GHz. Future plans include an EOS* MLS for atmospheric measurements from 63 to 650 GHz, the Sccut for interstellar oxygen and water vapor measurements from 60-550 GHz and the Submillimeter Explorer for astrophysical observation from 500-3000 GHz. In the long term we are planning the Large Deployable Reflector for astronomy in the 500-10,000 GHz frequency range. All of these instruments use filled aperture antenna systems from 5 cm diameter for the MSU, 1.6 m for the MLS to 20 m for LDR.

The advantages of filled aperture antenna systems are shown in Figure 1 below. For frequencies above 30 GHz, filled aperture antennas can provide the required footprints. A 10-m diameter deployable filled aperture millimeter-wave antenna could be made today with only limited development. The inner portion of this antenna could be made precise enough for operation to 183 GHz. In the future, a larger millimeter-wave antenna could be assembled at the Space Station and then sent up to geosynchronous orbit.

---

*Earth Observing System (EOS).

FILLED APERTURE ANTENNA SYSTEMS

- SIMPLE CONCEPT - PREVIOUS EXPERIENCE
    - DEPLOYABLE - 10m AT TRW
    - SPACE STATION ASSEMBLY - 30m BASED ON LDR TECHNOLOGY
- MULTIPLE FREQUENCIES
- FEED ARRAY WITH MULTIPLE RECEIVERS
- ACCURATE MEASUREMENTS
    - HIGH BEAM EFFICIENCY - 90-95%
    - LOW SIDE LOBES - <25 dB
- DATA PROCESSING STRAIGHTFORWARD

Figure 1

The footprint size (3 dB antenna beamwidth) at nadir vs antenna diameter and frequency are shown in Figure 2. To achieve a 20-km footprint at 183 GHz, a 4-m diameter antenna with a beamwidth of 1.7 arcmin will be required.

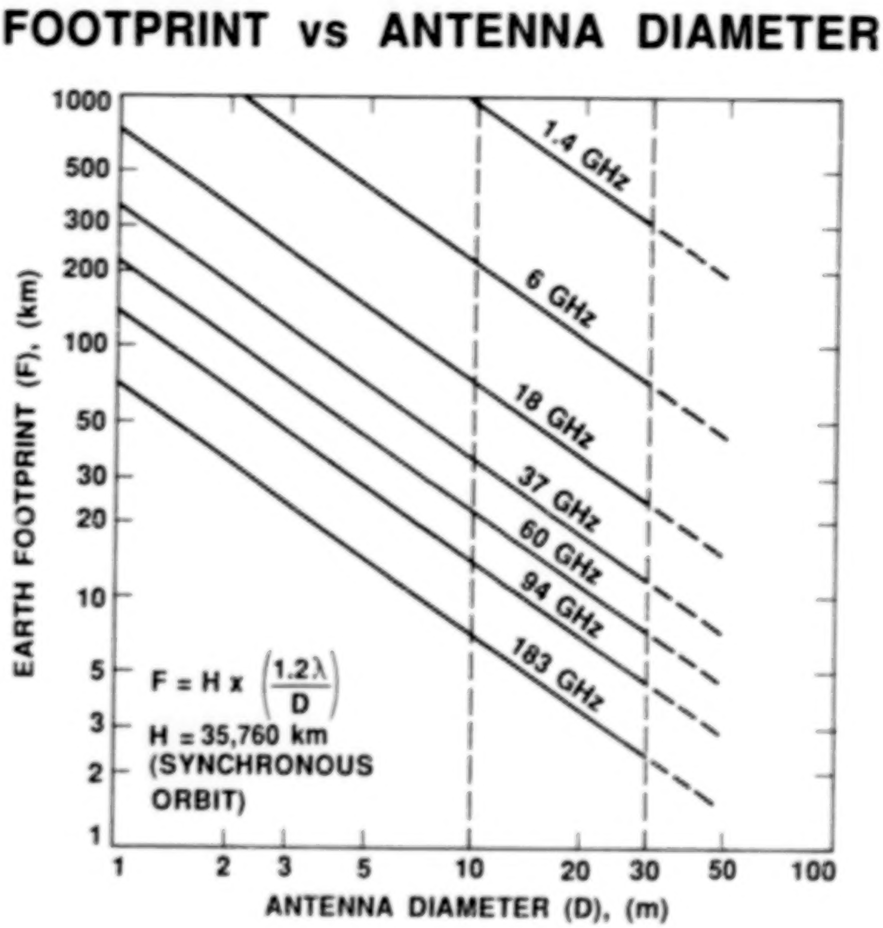

Figure 2

In Figure 3, the diameter requirements for a possible Geoplat antenna system are shown and are compared against existing ground based and proposed space telescopes. As seen, the technology required for a 10- to 30-m Geoplat antenna is well within the state of the art for a ground-based antenna. The challenge is to make this antenna in space.

DIAMETER vs OPERATING WAVELENGTH FOR VARIOUS CLASSES OF TELESCOPES

1	U. TEXAS
2	OVRO 10m
2A	CIT SUBMM OBSERVATORY
3	NRAO 11m
4	CRIMEA
5	NRAO VLA
6	OVRO 40m
7	BONN 100m
8	NASA DSN 64m
9	IRAM 15m SRC 15m
10	MPIFR/IRAM 30m
11	SIRTF
12	SPACE TELESCOPE
13	HALE 200"
14	U. OF TEXAS 300"
15	KECK TELESCOPE

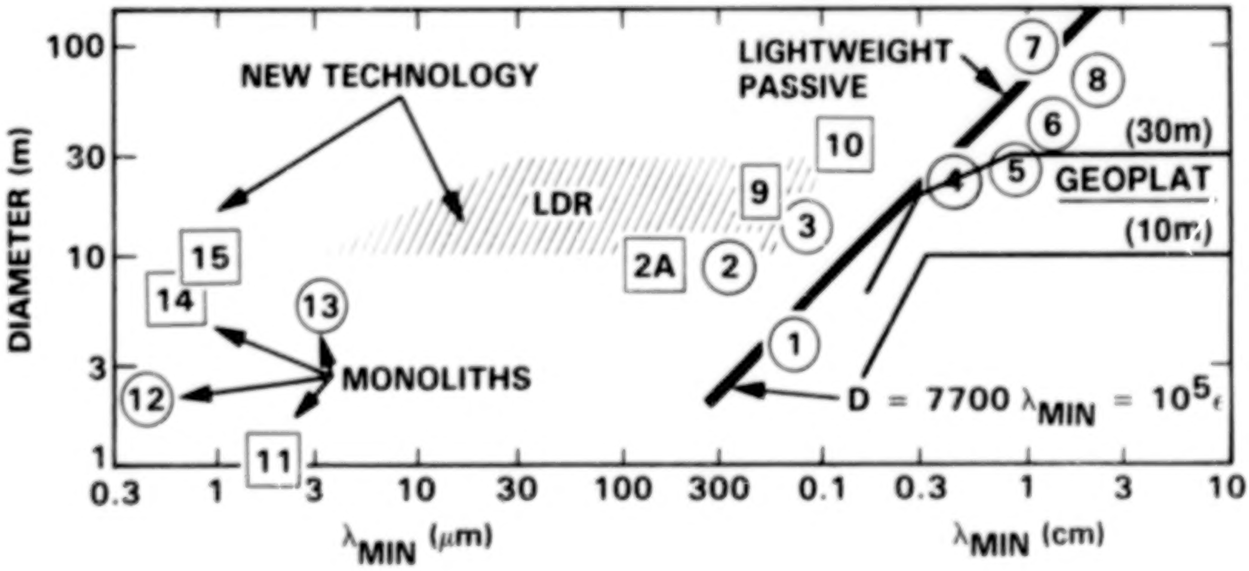

Figure 3

Figure 4 shows a number of proposed reflectors for space, with the type of construction indicated. For the 10-m Geoplat antenna, a passive precision deployable antenna could be built to satisfy the requirements.

REFLECTORS FOR SPACE

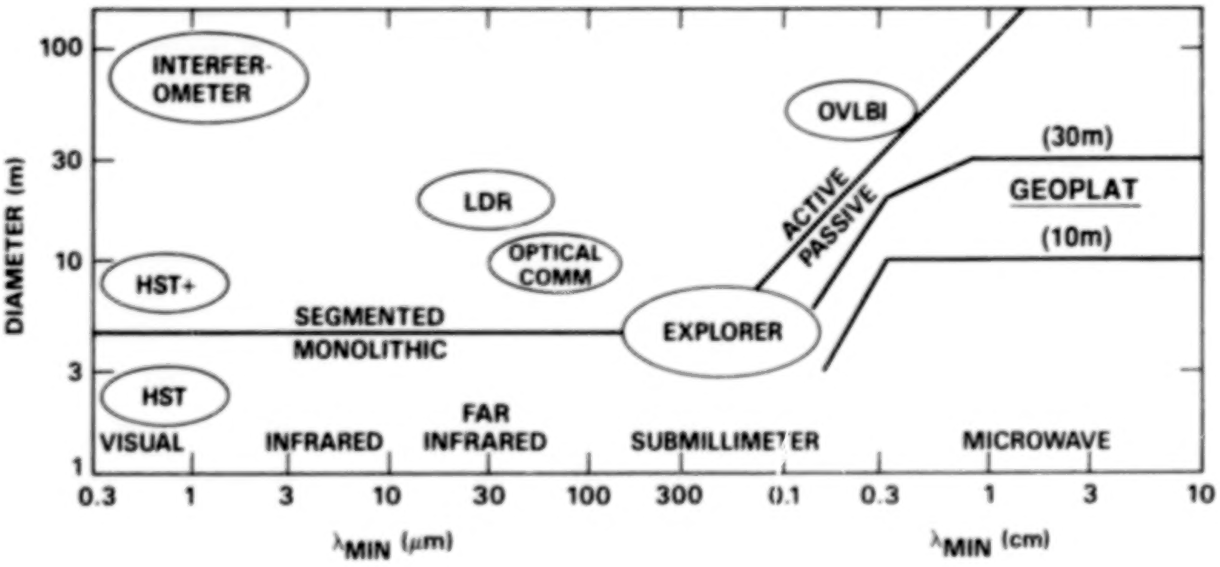

Figure 4

The current state of the art of receiver noise performance vs. frequency is shown in Figure 5. These data are from Weinreb, et. al., (ref. 1) with additional data on the new Hughes InGaAs HEMT* (ref. 2) added. For remote sensing of the Earth, a radiometer noise temperature <100 K would be adequate. Thus, for frequencies below 120 GHz, it is now possible to use HEMT amplifiers as the first radiometer stage. At 183 GHz it would be necessary to use a cooled Schottky mixer radiometer. For continuum receivers it is possible to have IF bandwidths of 10-25% of the center frequency. Each receiver channel will require 5-15 watts of DC power.

---

*High electron mobility transistor (HEMT).

STATE-OF-THE-ART OF NOISE PERFORMANCE FOR MICROWAVE/MM-WAVE DEVICES - 1988
(FROM WEINREB et al., 1988)

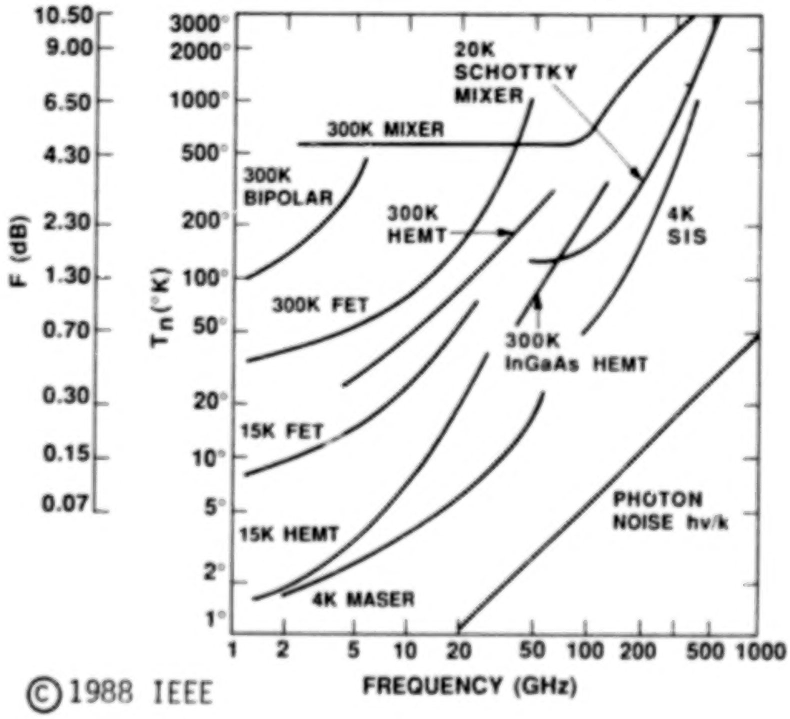

©1988 IEEE

Figure 5

A calculation of the performance for a possible radiometer system using a 10-m diameter antenna, scanning a 4,000-km diameter area within 0.5 hr. is shown in Figure 6. This system calculation assumed a multifeed system making a raster scan across the area of interest. The scan rate would be 11 degrees/minute. To reduce this scan rate, the number of receivers could be increased to increase the swath width or the revisit time increased. The technical parameters which can be traded off in this system design are the area scanned, time of the scan, scan width (number of receivers), and the rms noise ($\triangle$T). With the proper momentum compensation it should be possible to mechanically scan a 100-150 kg antenna system at these low scan rates.

Some technical areas that will require development for a Geostationary platform are:

(1) 10-m diameter deployable antenna operating to 100 GHz with the inner 4-m diameter operating to 183 GHz

(2) HEMT amplifiers operating to 118 GHz

(3) 4-6 element array feed systems for mm-wave antennas.

10- m MULTIFEED ANTENNA - SENSITIVITY AND SCANNING

FREQ (GHz)	F* (km)	Nrec	τ (ms)	Tsys** (K)	ΔT (K)
18	83	1	1588	344	0.01
37	40	2	376	355	0.01
60	25	4	143	451	0.12
95	16	6	57	586	0.04
118 #	20	5	92	698	0.23
183 #	20	5	92	887	0.29

* FOOTPRINT AT 30 deg LATITUDE

** T(BACKGROUND) = 270 K

# REDUCED ANTENNA SIZE USED

AREA DIAMETER = 4000 km

SCAN TIME = 0.5 hr

SCAN RATE = 11 deg/min

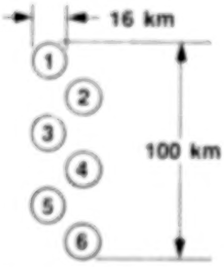

95 GHz BEAM PATTERN

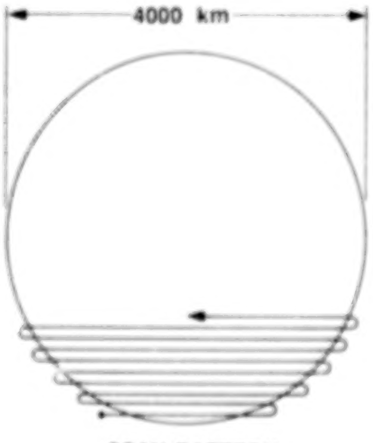

SCAN PATTERN

Figure 6

A description of the application of Microwave Limb Sounding is shown in Figure 7 along with the advantages of Geostationary observations.

MICROWAVE LIMB SOUNDING

- Performs measurements for monitoring depletion of stratospheric ozone
  - Measures key molecules in all known O_3 destruction cycles
  - Unique capability for measuring chemical radicals which control rate of O_3 destruction
  - Especially strong for monitoring depletion of O_3 by industrial chlorocarbons, and the Antarctic Ozone Hole
  - Measurements are of thermal emission and can be made any time of day or night
- Low Earth orbit experiments have been developed
  - MLS on the Upper Atmosphere Research Satellite
  - Enhanced MLS proposed for Eos
- Geostationary platform advantages
  - Optimization of latitude coverage between ±81 degrees
  - Detailed study of time variation at specific latitude bands
- Measurement capability and antenna size requirements

Figure 7

The key molecules for stratospheric ozone chemistry, can be measured with a Microwave Limb Sounder, and are shown in Figure 8.

MICROWAVE LIMB SOUNDING

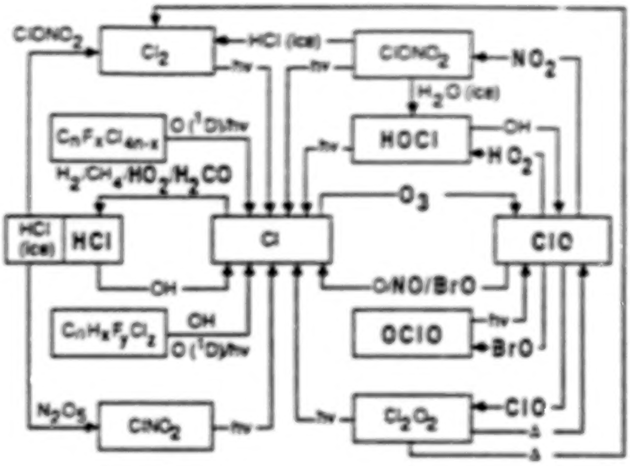
ClONO2
Cl2
HCl (ice)
hv
ClONO2
NO2
H2O (ice)
CnFxCl4n-x
O(1D)/hv
HOCl
OH
HO2
H2/CH4/HO2/H2CO
O3
HCl (ice)
HCl
Cl
ClO
OH
ClNO/BrO
CnHxFyClz
OH
O(1D)/hv
OClO
hv
BrO
N2O5
ClNO2
hv
Cl2O2
ClO
Δ

ODD-CHLORINE CHEMISTRY

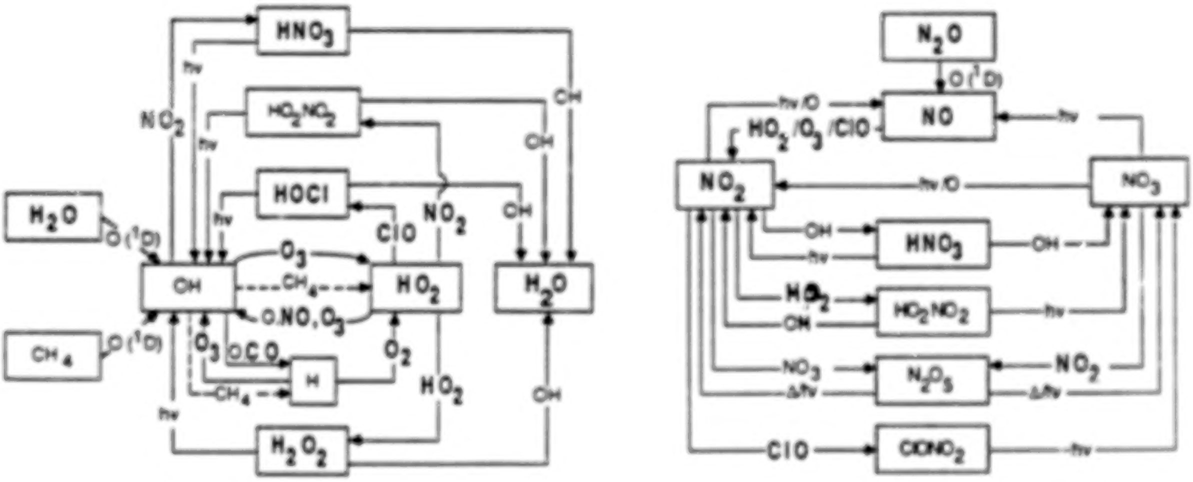
HNO3
hv
NO2
OH
HO2NO2
hv
OH
HOCl
hv
NO2
ClO
OH
H2O
O(1D)
OH
O3
CH4
O,NO,O3
HO2
H2O
CH4
O(1D)
O3
OCO
H
O2
CH4
HO2
OH
hv
H2O2
N2O
O(1D)
hv/O
HO2/O3/ClO
NO
hv
NO2
hv/O
NO3
OH
hv
HNO3
OH
HO2
OH
HO2NO2
hv
NO3
Δ/hv
N2O5
NO2
Δ/hv
ClO
ClONO2
hv

ODD-HYDROGEN CHEMISTRY

ODD-NITROGEN CHEMISTRY

Stratospheric Ozone Chemistry Schematics and Microwave Limb Sounding Measurements. Microwave limb sounding measurements which can be made by existing 600 GHz technology are shown in larger type. Technology advances to 2000 GHz will allow additional important measurements of OH and atomic O

Figure 8

The antenna requirements for a Submillimeter Limb Sounder are shown in Figure 9. For receivers in the 600-1200 GHz frequency range, antenna diameters of 3-8 m would be desirable.

MICROWAVE LIMB SOUNDING

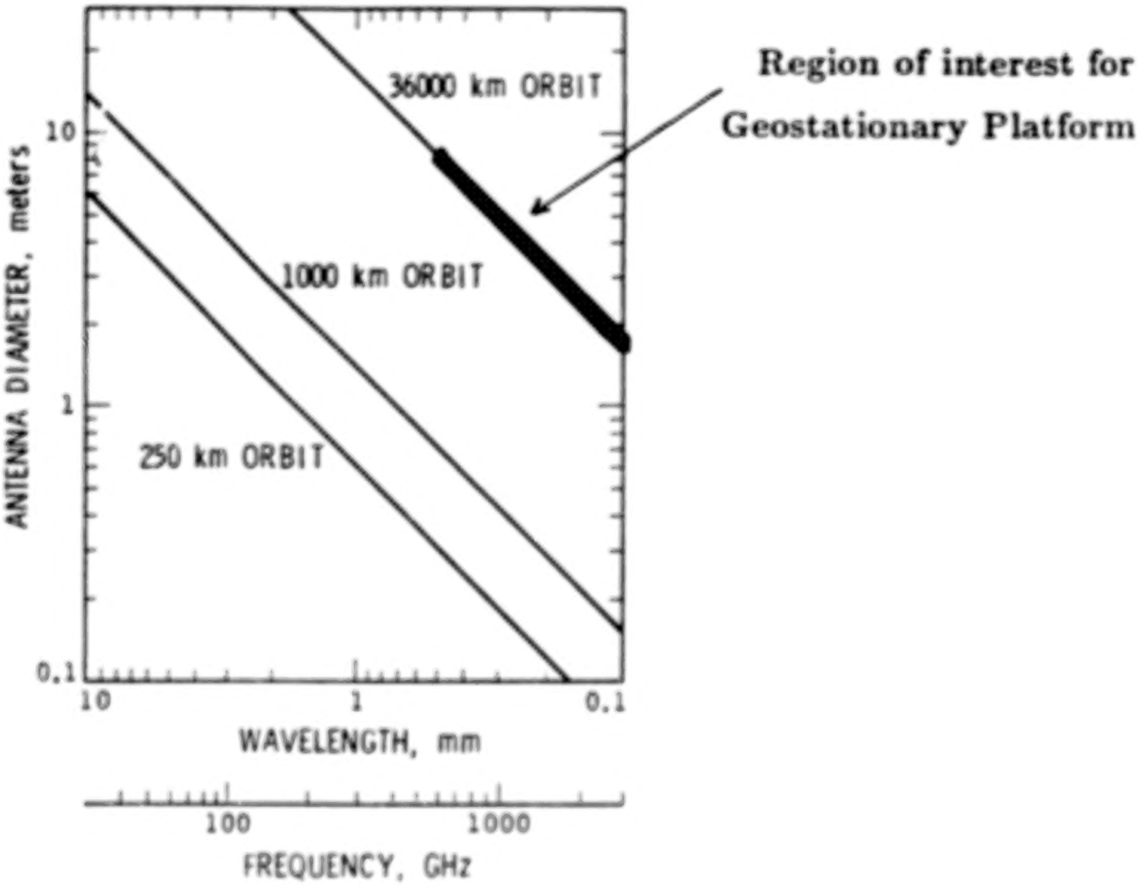

Region of interest for Geostationary Platform

ANTENNA DIAMETER FOR 3 km BEAMWIDTH AT TANGENT POINT FOR LIMB OBSERVATIONS

Figure 9

REFERENCES

1. Weinreb, S., Pospieszalski, M. W., and Norrod, R., "Cryogenic, HEMT, Low-Noise Receivers for 1.3 to 43 GHz Range," IEEE Microwave Theory & Techniques Symposium Digest, June 1988.

2. Greiling, P. T., "Low Noise HEMT Amplifier at 60 GHz," IEEE Device Research Conference, Boulder, Colorado, June 1988.

SYNTHETIC APERTURE
INTERFEROMETRIC RADIOMETER
(SAIR)

C. S. Ruf
Jet Propulsion Laboratory
California Institute of Technology
Pasadena, CA

The aperture size requirements of imaging microwave radiometers in geosynchronous orbit rule out filled aperture antenna systems below 10 GHz. In the region 10-30 GHz, filled apertures are only marginally practical. The size requirements in turn aggravate the problems with a mechanically steered antenna beam. Both the aperture size and steering problems are resolved with a Synthetic Aperture Interferometric Radiometer (SAIR).

SAIR imaging is based on a technically and analytically mature discipline, synthetic aperture radio astronomy (refs. 1 and 2). A two-dimensional array of antenna elements can be thinned by more than 99.9%. The remaining elements are cross-correlated and the output is recorded digitally. All antenna beams are then generated simultaneously in software.

THINNED APERTURE RADIOMETERS

- CORRELATION INTERFEROMETRIC IMAGING
- STRONG HISTORICAL PRECEDENT IN RADIO ASTRONOMY
- > 99.9% SAVINGS IN ANTENNA SIZE/WEIGHT
- NO MECHANICAL SCANNING

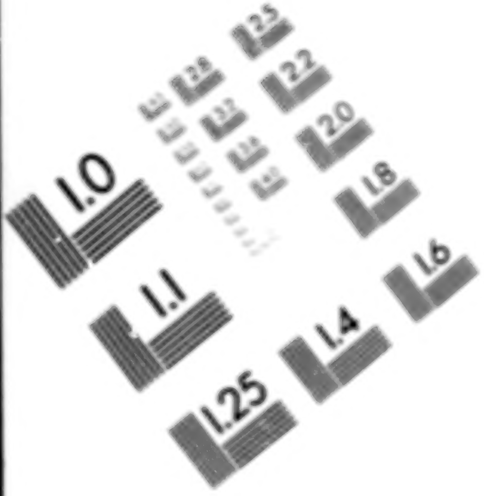
1.0
1.1
1.25
1.4
1.6
1.8
2.0
2.2
2.5
2.8
3.2
3.6
4.0

UNITED STATES OF AMERICA
GOVERNMENT PRINTING OFFICE

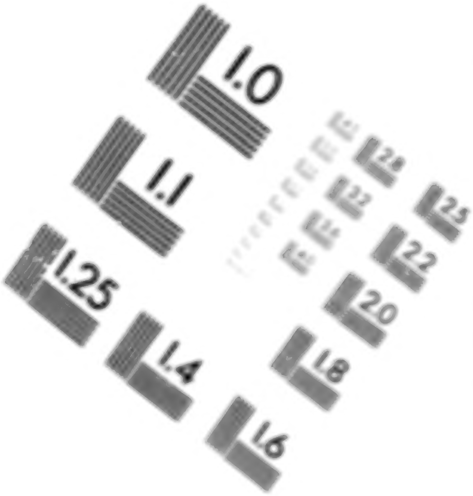
1.0
1.1
1.25
1.4
1.6
1.8
2.0
2.2
2.5
2.8
3.2
3.6
4.0

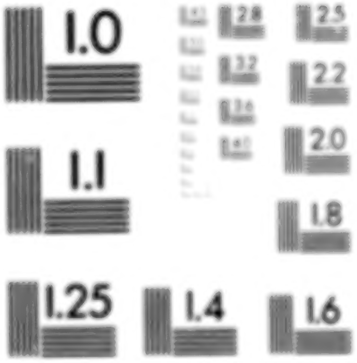
1.0
1.1
1.25
1.4
1.6
1.8
2.0
2.2
2.5
2.8
3.2
3.6
4.0

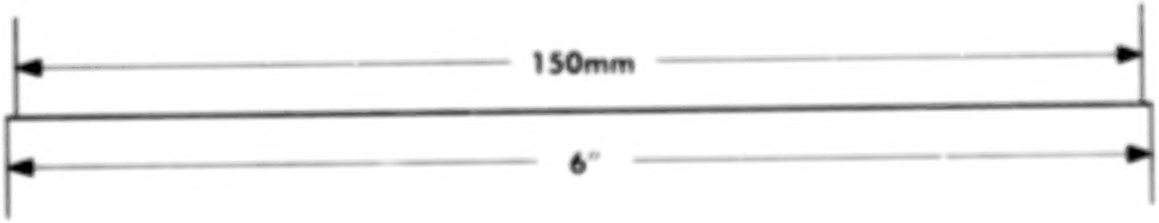

1.0
1.1
1.25
1.4
1.6
1.8
2.0
2.2
2.5
2.8
3.2
3.6
4.0

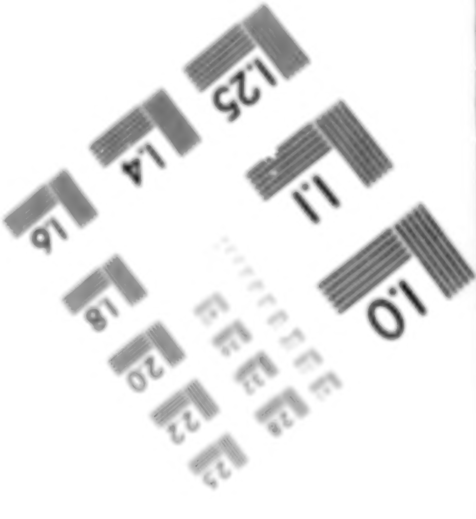
1.0
1.1
1.25
1.4
1.6
1.8
2.0
2.2
2.5
2.8
3.2
3.6
4.0

The cross-correlation of a pair of antenna elements in the SAIR thinned array produces a measurement referred to as the visibility function by radio astronomers. The visibility function is the two-dimensional Fourier transform of the brightness temperature distribution lying within the mainbeam of the individual antenna elements. The relative positions of the pair of elements determine which sample of the visibility function is measured. After enough different samples are made, the measurements are inverse Fourier transformed in software to reconstruct the brightness temperature distribution. The sinusoidal weightings on each sample in the software reconstruction are exactly analogous to the phase shifter settings on a conventional electronically steered phased array. One fundamental difference between a SAIR imager and a phased array, however, is the inability of the phased array to be thinned without raising its sidelobe levels.

CORRELATION INTERFEROMETER FUNDAMENTAL RELATIONSHIP

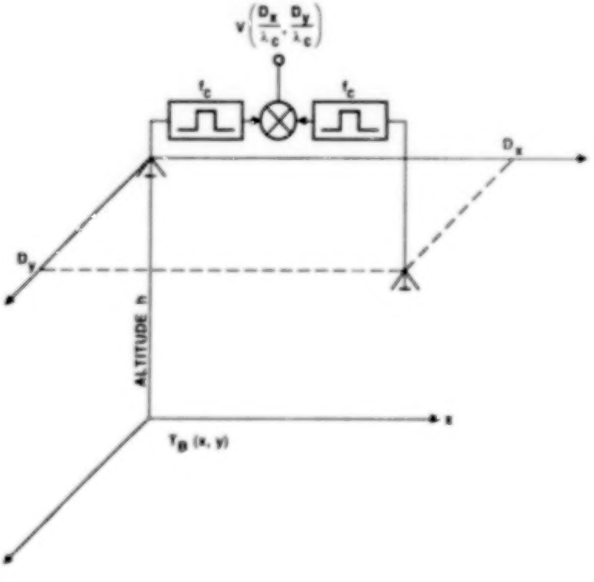

$$V\left(\frac{D_x}{\lambda}, \frac{D_y}{\lambda}\right) = \iint_{-\infty}^{\infty} T_B(x, y)\, e^{j2\pi\left(\frac{D_x}{\lambda}\frac{x}{h} + \frac{D_y}{\lambda}\frac{y}{h}\right)}\, dxdy$$

Samples are made of the visibility function at a wide variety of different relative antenna element spacings. There must be close and distant spacings, as well as a uniform distribution in-between. Also, the spacings must vary evenly in two perpendicular directions which lie in the plane of the thinned array. There are many configurations in which to construct the thinned array. A ring of elements - pseudo randomly thinned - provides an even distribution of spacings instantaneously (ref. 3). A "Y" configuration is presently used by the Very Large Array radio telescope in Socorro, NM. It relies on the Earth's rotation to produce much of the spacing. A rotating thinned line of elements would generate the proper distribution of spacings after 180° of rotation. Linear thinning algorithms have been studied for SAIR Earth remote sensing (ref. 4).

POSITION CORRELATION
(VARY $D_{x, y}$)

EXAMPLES OF SAMPLING LATTICE:

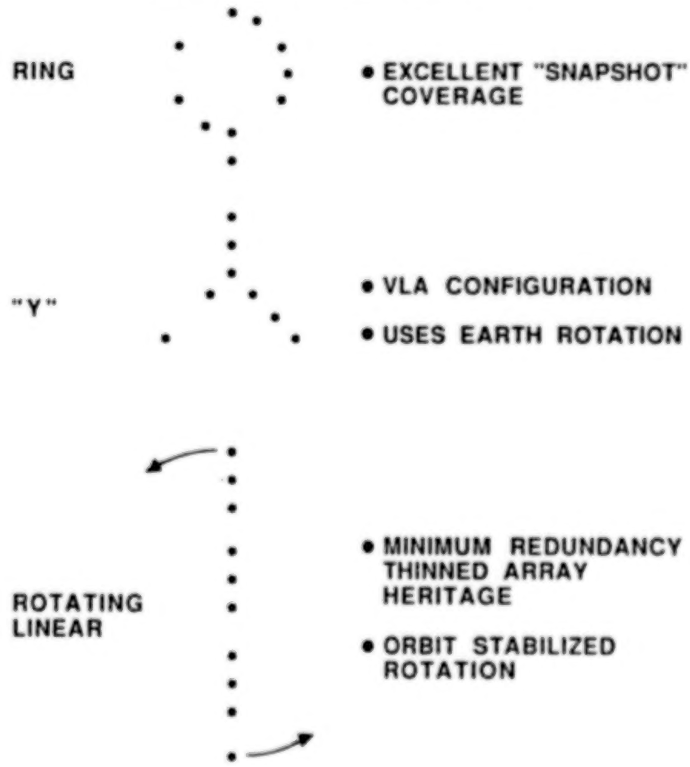

RING

- EXCELLENT "SNAPSHOT" COVERAGE

"Y"

- VLA CONFIGURATION
- USES EARTH ROTATION

ROTATING LINEAR

- MINIMUM REDUNDANCY THINNED ARRAY HERITAGE
- ORBIT STABILIZED ROTATION

The spatial resolution of a SAIR imager can be derived from standard Fourier transform theory. The visibility function is sampled over a region, the extent of which is determined by the maximum spacing between antenna elements in the thinned array. This effectively truncates the visibility function sample space. The truncation produces a smoothing, or "lowpass filtering" of the brightness temperature distribution reconstructed in software. The resulting resolution of the image is the same as would have been measured by a filled aperture, for example a very large reflector, with a diameter equal to the maximum spacing between antenna elements in the SAIR array.

CORRELATION INTERFEROMETRY SPATIAL RESOLUTION

- $T_B(x, y) = \mathcal{F}^{-2}\left\{V\left(\frac{D_x}{\lambda}, \frac{D_y}{\lambda}\right)\right\}$

- V SAMPLE-SPACE HAS FINITE EXTENT
  $\Rightarrow$ T_B IMAGE IS "LOWPASS FILTERED"

- IMAGE RESOLUTION = $\frac{1}{\text{V-SPACE MAXIMUM}}$

$$= \frac{\lambda_{\min}\, h}{D_{x,\, y\, \max}}$$

Examples of specific SAIR array configurations illustrate the large savings in size and weight possible relative to conventional filled array imagers. A SAIR imager capable of 100 km resolution from geosynchronous orbit at 10 GHz would require 20 array elements, each approximately 8 cm in diameter, deployed pseudo-randomly in a rotating line 10.7 m long. A phased array with the same image resolution would require 795 times as many elements. A 70 element SAIR imager, with 10 km resolution at 10 GHz, has the imaging performance of a filled array with 22,743 times as many elements. This extreme reduction in required aperture is, to a certain extent, offset by the increased complexity of the cross-correlation circuitry necessary in a SAIR system. Every possible pair of antennas is cross-correlated. For the 70 element array, this implies 2,415 cross-correlators. The streamlining, parallel processing, and, possibly, digitizing of this step is a key area for further development.

SPATIAL RESOLUTION EXAMPLES AT 10 GHz

RESOLUTION (km)	100	50	10
$D_{x,\,y\ max}$ (m)	10.7	21.5	107.5
# ELEMENTS IN FILLED ARRAY	15.9 K	63.7 K	1,592 K
# ELEMENTS IN ROTATING THINNED LINEAR ARRAY	20	30	70
% FILLED APERTURE	0.13%	0.05%	0.005%

Measurements of the visibility function are made over a region of its sample space. This corresponds to a range of spacings between different array elements. The required distribution of spacings over this range can be specified using Nyquist sampling theory. The field of view (FOV) imaged determines the incremental steps allowed between successive spacings. In the case of a filled phased array imaging the full 2 π steradian half space, this implies the standard half wavelength spacing between elements. From a geosynchronous platform, the FOV is significantly reduced and the increment between element-pair spacings increases to 2.84 wavelengths. The aliased responses generated by an image reconstruction from Nyquist samples are analogous to antenna grating lobes. These grating lobes are positioned off the limb of the Earth by the Nyquist condition and can be further suppressed, if necessary, by the individual array element patterns.

CORRELATION INTERFEROMETER SAMPLING THEOREM

- $V\left(\frac{D_x}{\lambda}, \frac{D_y}{\lambda}\right) = \mathcal{F}^2\,(T_B\,(x, y))$
- T_B SPATIAL EXTENT IS FINITE
  $\Rightarrow$ 2-d NYQUIST SAMPLING OF V

EXAMPLE: GEOSTATIONARY PLATFORM

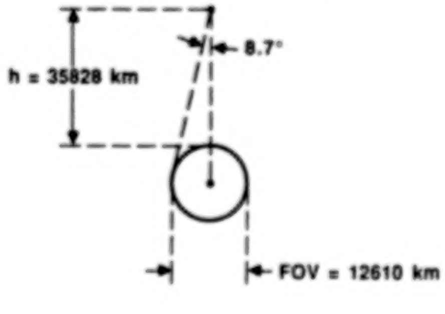

SAMPLING THEOREM:

$$\Delta\left(\frac{D_{x,y}}{\lambda}\right) = \frac{h}{FOV} = 2.84$$

Incomplete sampling of the visibility function by a SAIR array configuration results in a loss of beam efficiency in the synthetic antenna pattern. A particular example illustrates the sampling requirements of a SAIR array. Twelve antenna elements are arranged in a circular ring, either uniformly spaced or thinned according to an optimal thinning algorithm (ref. 3). The diameter of the ring is varied and, at each diameter, the beam efficiency of the corresponding synthetic antenna pattern is computed. The uniform distribution degrades as soon as the spacing between elements along the circumference of the ring significantly exceeds the Nyquist criteria. The performance of the thinned ring degrades when its diameter exceeds twelve times the Nyquist criteria. This degradation amounts to a rise in sidelobes near the mainbeam. The spatial resolution of the array is also plotted. A thinned SAIR ring with twelve elements can provide 500 km resolution with 90% beam efficiency. Increasing the resolution to 5 km should raise the number of elements needed to approximately 120 (ref. 5).

RING INTERFEROMETER BEAM EFFICIENCY

- ASSUMING 12 ANTENNA ELEMENT ARRAY
- OPTIMAL THINNING (T.J. CORNWELL, IEEE TRANSACTIONS ON ANTENNAS AND PROPAGATIONS, Vol. 36, No. 8, AUGUST 1988, pp. 1165-1167)
- BEAM EFFICIENCY ASSUMES UNIFORM APERTURE TAPER

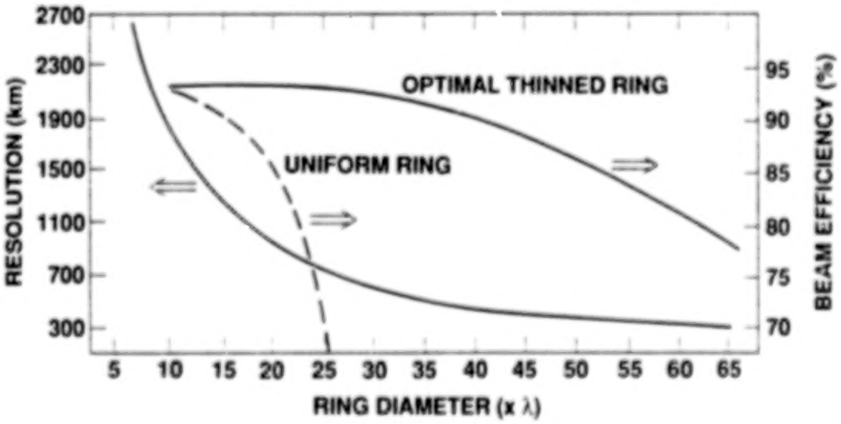

The radiometric noise floor of a SAIR image has been studied in detail (ref. 4). The noise floor of the individual measurements of the visibility function is simply that of a conventional correlation radiometer. The two-dimensional Fourier transform of these measurements can be viewed as a weighted summation of N^2 random variables, where N^2 is the number of measurements or the number of independent pixels in the brightness temperature image. The weights are the sinusoidal kernels of the transform and the resulting image has a noise floor which is approximately N times that of the individual measurements. This accumulation of noise is significantly offset by the fact that all pixels are imaged simultaneously, thus increasing the available integration time over that of a scanning imager. The SAIR system temperature can also be significantly reduced by using small array elements with antenna patterns much broader than the Earth disc. This technique must be traded off, however, against grating lobe suppression by the element patterns.

CORRELATION INTERFEROMETRY IMAGE SENSITIVITY

- **INDIVIDUAL MEASUREMENT NOISE FLOOR**

$$\Delta V = \frac{T_{sys}}{\sqrt{B\tau}}$$

WHERE $T_{sys} = T_{Rx} + \frac{\langle T_B \rangle \Omega_e}{2\pi}$

- **RECONSTRUCTED IMAGE NOISE FLOOR**

$$\Delta T = N \, \Delta V$$

WHERE N^2 = # OF PIXELS IN IMAGE

NOTE:

- $T_{sys} = T_{Rx} + \langle T_B \rangle = T_{Rx} + 200$ K FOR FILLED APERTURE (PENCIL BEAM) IMAGERS VERSUS $= T_{Rx} + 3$ K FOR CORRELATION INTERFEROMETER
- T_{Rx} IS MAJOR DESIGN DRIVER HERE

The noise floor of a brightness temperature image has been computed for three different radiometer systems: a mechanically scanning filled aperture, a SAIR ring array, and a SAIR rotating linear array. Radiometer operating parameters typical on a geostationary platform are assumed. The filled aperture system must sequentially sample the pixels in the image and its integration time per pixel is reduced accordingly. The linear SAIR system must rotate 180° to adequately sample the visibility function and its dwell time per sample is reduced. The SAIR ring array is assumed to have the double advantage of longest integration time and lower system temperature than the filled aperture imager. If this latter advantage is eliminated, then the filled aperture and ring array will have comparable noise floors. For 10 km image resolution, only the rotating linear SAIR array has an unacceptably high noise floor (8.1 K). The ring array, or perhaps some other two dimensional thinned configuration, becomes a performance necessity at this level of resolution.

CORRELATION INTERFEROMETRY SENSITIVITY EXAMPLE

- TOTAL INTEGRATION TIME $T = 1$ hr
- PRE-DETECTION BANDWIDTH $B = 100$ MHz
- RECEIVER NOISE $T_{Rx} = 150$ K
- # OF PIXELS IN IMAGE N^2

RESOLUTION (km)	100	50	10
N	126	252	1261

- INDIVIDUAL MEASUREMENT INTEGRATION TIME τ
- RECONSTRUCTED IMAGE NOISE FLOOR ΔT:

RESOLUTION (km)		100	50	10
IMAGER	τ			
MECHANICAL SCANNING PENCIL BEAM	$\frac{T}{N^2}$	0.08	0.17	0.83
RING	T	0.03	0.06	0.32
ROTATING LINEAR	$\frac{T}{N/2}$	0.26	0.72	8.11

REFERENCES

1. Pawsey, J. L. and Bracewell, R. N.: Radio Astronomy. London, Oxford, 1955.

2. Napier, P. J., et. al.: "The very large array: design and performance of a modern synthesis radio telescope." Proc. IEEE, Vol. 71, no. 11, Nov. 1983.

3. Cornwell, T. J.: "Crystalline antenna arrays." Millimeter Array Memo No. 38, NRAO, Socorro, NM.

4. Ruf, C. S., et. al.: "Interferometric synthetic aperture microwave radiometry for the remote sensing of the Earth." IEEE Trans. on Geo. and Rem. Sens., Vol. 26, No. 5, 597-611, Sept. 1988.

5. Ruzsa, I. Z.: "On difference-sequences." Acta Arithmetica, Vol. XXV, 151-157, 1974.

RAIN RADARS FOR EARTH SCIENCE GEOSTATIONARY PLATFORMS: SOME POSSIBILITIES

S. P. Gogineni and R. K. Moore
Radar Systems and Remote Sensing Laboratory
University of Kansas Center for Research, Inc.
Lawrence, KS

ABSTRACT

This paper presents results of a feasibility study for a geostationary rain radar. A 2-cm wavelength radar with a 15- or 20-mm antenna will be useful for general scale meteorology. The transmitter power of 500 W with a pulse compression ratio of 200 will provide adequate signal-to-noise ratio for a rain rate of 1 mm/hour. Various problems associated with a geostationary radar and solutions are also discussed.

INTRODUCTION

The availability of large antennas and relatively potent power supplies for geostationary satellites suggests their use for radars to map rainfall in the tropical and temperate zones. Calculations presented here show that such systems are feasible, although far from perfect.

Two major problems are:

(a) The footprint one can feasibly achieve from geostationary orbits is much too large to identify individual rain cells. Thus these radars can map area rainfall, but cannot identify individual squalls.

(b) The time required to map the entire area of interest can be quite large, although ways around this limitation can be developed.

The inability to profile rains vertically is undesirable, but a necessary consequence of the combination of minimum feasible vertical beamwidths and long ranges.

Here we have developed some of the necessary parameters for such a radar. With a 500 W peak power and pulse-compression ratio (PCR) of 200, high signal-to-noise ratios (SNRs) are possible for single cells 5 km in diameter up to 60° latitude for 1 mm/hour rains with a 15-m diameter antenna. Actually significantly less power is needed if enough samples can be averaged. A 0 dB SNR only requires about 25 W with a PCR of 200. To obtain more averaging, however, one would normally increase the peak power and reduce the PCR.

CONCEPT

The geostationary rain radar would use a large electronically scanned antenna at a wavelength of about 2 cm. The antenna could be either an array or a reflector with scanned feed. It might also be scanned mechanically at a slow rate if complete 360° coverage were desired, since the electronic scan cannot cover such a wide angular range.

It would use a pencil beam, but even the best pencil beam cannot reduce the resolution cell to a size comparable with rain-cell sizes (typically about 5 km in diameter). Thus the scans would show areas of rainfall, but not individual cells. Sensitivity calculations presented here, however, assume only one cell within the beam at a time. More cells would increase the signal, but it would be difficult to determine whether the increased signal was due to heavier rain or more area covered by rain.

The transmitter would send pulses with a pulse-repetition frequency (PRF) such that no two pulses would be present in the rain at one time. Thus the interval in space between pulses would be at least 55 km. With a high PCR, this would have to be increased to allow for the long duration of the expanded pulse. This would reduce the PRF and the number of independent samples of the fading signal from rain that could be averaged, but with high SNR this number can be minimized. Nevertheless, to obtain reasonable measurement precision of the fading signal, one would have to average at least 25 samples. This tradeoff requires more study.

Because of the long time needed to scan a large area, simultaneous multiple beams might be needed. Since each beam would require the same power as every other one, this would make the power requirement proportional to the number of beams.

PROBLEMS

The largest antenna one can expect to make successfully would be about 1000 wavelengths across, resulting in a 1-mR beamwidth. At 2-cm wavelength this requires a very precise antenna 20 meters in diameter. Even with such a large antenna, the footprints get quite large. Fig. 1 shows the footprint dimensions for such an antenna as a function of distance from the satellite. If the beamwidth is β in both directions, the footprint is an ellipse with

(1) Cell width = βR (minor axis)

and

(2) Cell length = $\beta R/\cos\theta_i$ (major axis),

where R is the slant range and θ_i is the angle of incidence. Because the angle of

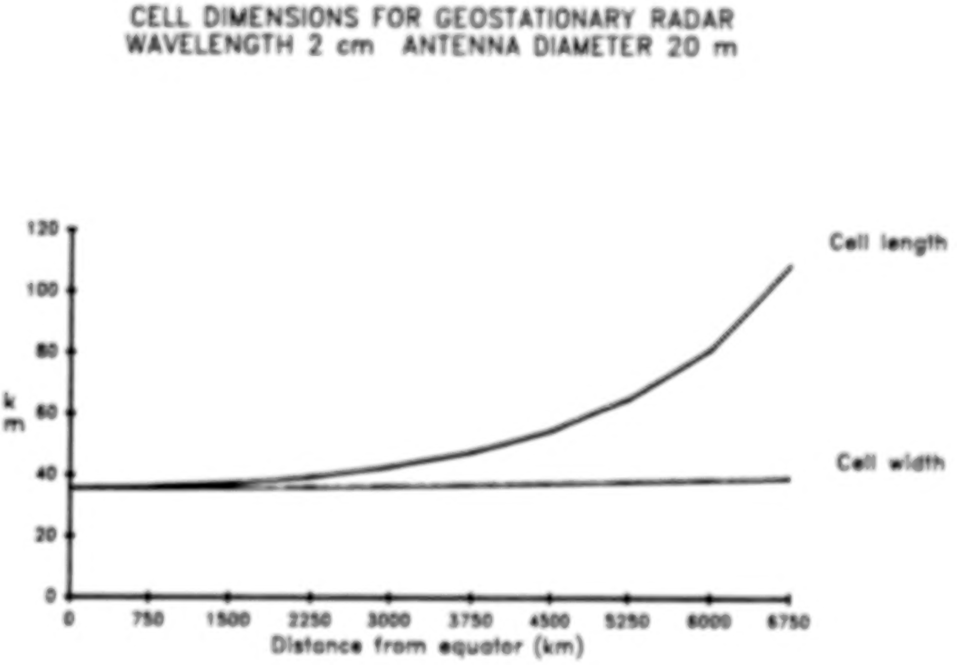
CELL DIMENSIONS FOR GEOSTATIONARY RADAR
WAVELENGTH 2 cm ANTENNA DIAMETER 20 m

Figure 1

incidence becomes 60° at 6750 km from the satellite, this larger dimension becomes 109 km. The cell width is almost constant because the range changes little. It is on the order of 40 km. The angle of incidence and the much smaller pointing angle at the satellite are shown in Fig. 2.

When the antenna diameter is reduced to 10 m, the cell sizes double. These cells are so large that they have little meteorological significance. Calculations were also performed for a 5-m diameter antenna, but the cells are so large that this is only of value to illustrate the effect. Fig. 3 shows the cell sizes versus antenna diameter.

A major problem is the time required to map the area. Calculations have been performed for a 360° arc about the spacecraft, and these can be readily reduced if the coverage is reduced. The problem arises because the 1-mR beamwidth of the 20-m antenna has so many cells around a circle. The antenna must dwell on each of these long enough to permit averaging enough samples.

Moreover, the time required for the signal to travel round-trip to the surface is about 0.25 sec, so time must be allowed for the received signal to return to the satellite. This time is considerably larger than that required for integration, so steps should be taken to avoid the problem it creates. The most logical step is to have two separate beams, one for transmitting and one for receiving. The scanning of the receiving beam would lag that of the transmitting beam by 0.25 sec. Although this introduces major complications in the system, it appears necessary for timely coverage.

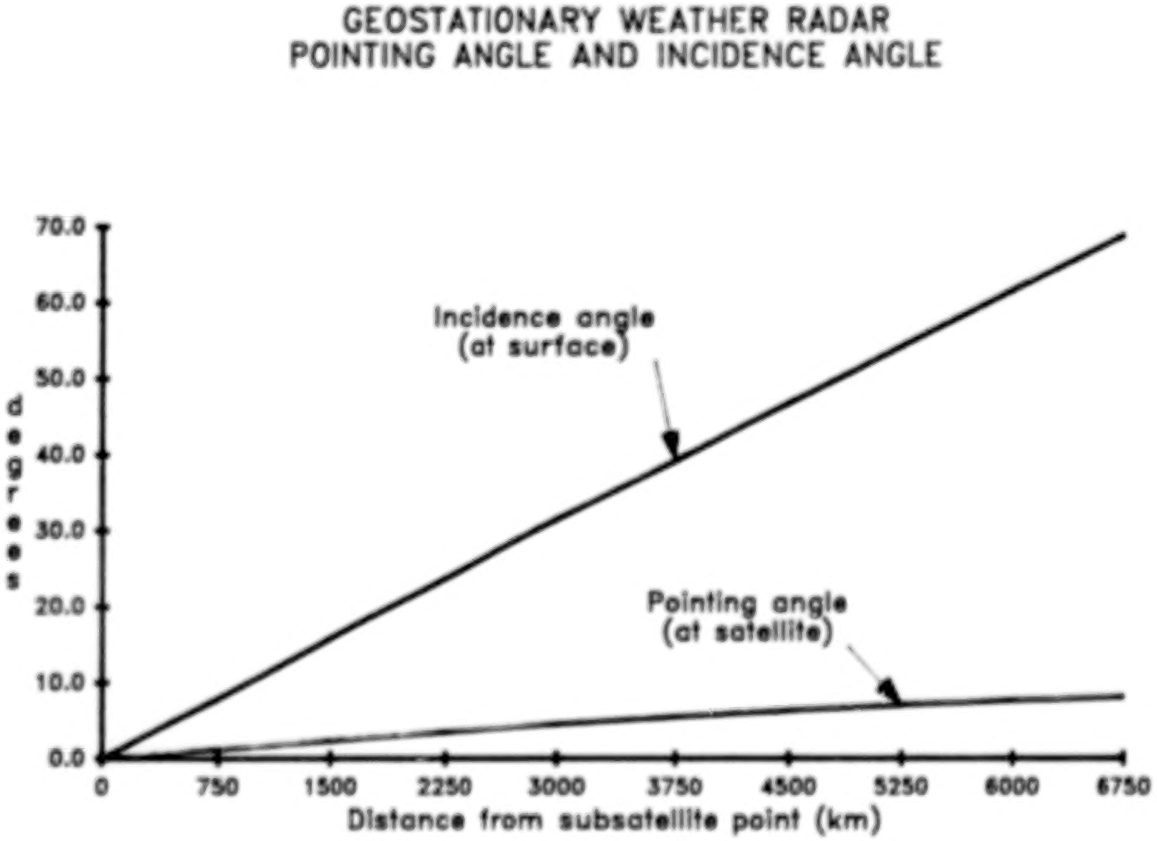

Figure 2

Table 1 illustrates the magnitude of this problem. For the table, we assume a PRF of 5000 (actually much too high for the PCR of 200 assumed later). This value assumes separate transmit and receive beams. In this case, we can integrate 100 samples (a reasonable number for reducing fading effects and allowing use of low values of SNR), while still observing 50 resolution cells per second.

TABLE 1
Calculations Regarding Coverage Time

Antenna diameter (m)	20	15	10	5
Beamwidth (mR)	1	1.33	2	4
Number of steps/circle	6283	4712	3142	1571
Number of circles (range)	142	107	71	36
Number of footprints (1000s)	892	502	223	56
Time for coverage at .26 s per cell (hours)	64	36	16	4
Time for coverage at 50 cells/sec (hours)	5.2	2.9	1.3	19 min

Clearly, the dual-beam system that allows 50 cells to be covered per second is preferable.

To achieve more adequate coverage in a short time, one should consider combining information from V-IR* scanners with the radar. There is no point in the

*Visible infrared (V-IR)

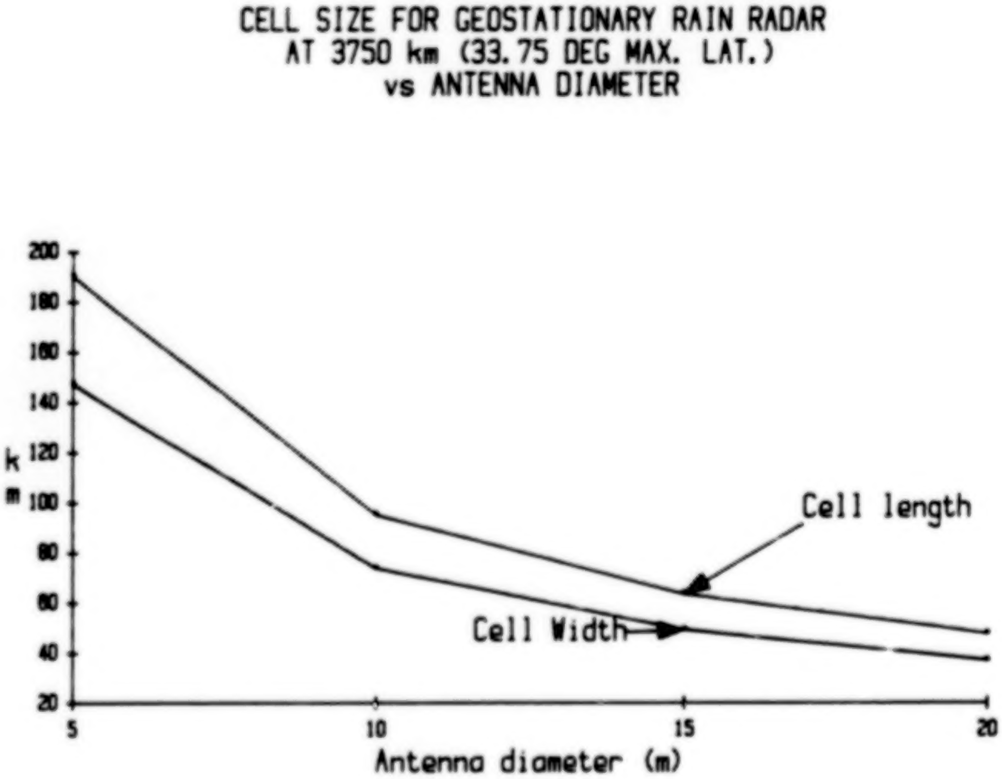

Figure 3

radar looking at areas where no clouds are present. The V-IR sensors can establish areas of clouds, and the radar can point only to these areas. Presumably this can make a major decrease in the required time for the radar to monitor the rain.

POWER CALCULATIONS

We calculated the power needed for a system such as this. The assumption is that one rain cell 5 km in diameter exists within a footprint and this cell extends from the ground to 5 km high. A further assumption (not justified for high rain rates) is that the scattering from the entire rain cell is received unattenuated at the satellite--except for spreading loss. The assumption of no attenuation was used for simplicity. We feel it was justified in this early-stage calculation, since the power limitation is set by the low rain rates where attenuation is small.

Figures 4, 5, and 6 show the SNR that can be achieved by a 500-W transmitter with a PCR of 200 for rain rates of 1 mm/hour to 20 mm/hour for antennas of different diameters. A standard Z-R relation for rain echoes was used. The SNR is 10 dB or better at all rain rates for a 15-m antenna. For a 10-m antenna the SNR at maximum range is only about 1 dB for 1 mm/hour, but this level is adequate if 100 samples are averaged. Moreover, the very large footprint of the 10-m antenna would almost certainly contain more than one rain cell, which would increase the SNR.

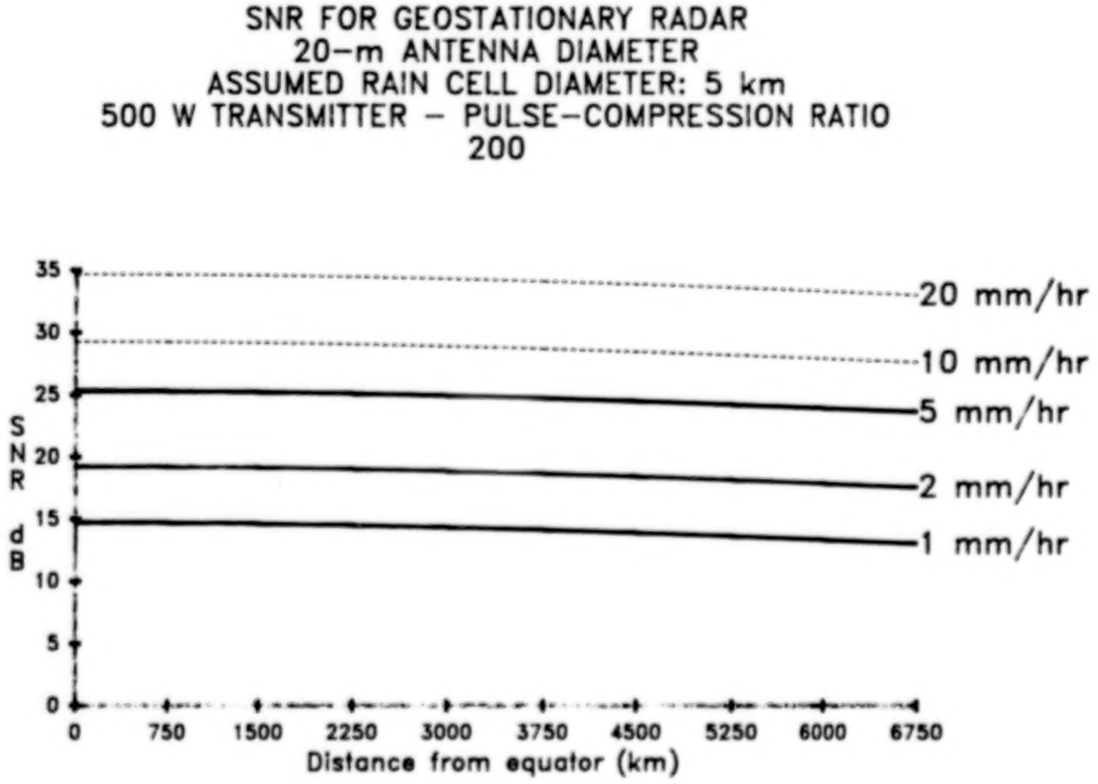

SNR FOR GEOSTATIONARY RADAR
20-m ANTENNA DIAMETER
ASSUMED RAIN CELL DIAMETER: 5 km
500 W TRANSMITTER - PULSE-COMPRESSION RATIO
200

Figure 4

SNR FOR GEOSTATIONARY RADAR
15–m ANTENNA DIAMETER
ASSUMED RAIN CELL DIAMETER: 5 km
500 W TRANSMITTER – PULSE–COMPRESSION RATIO
200

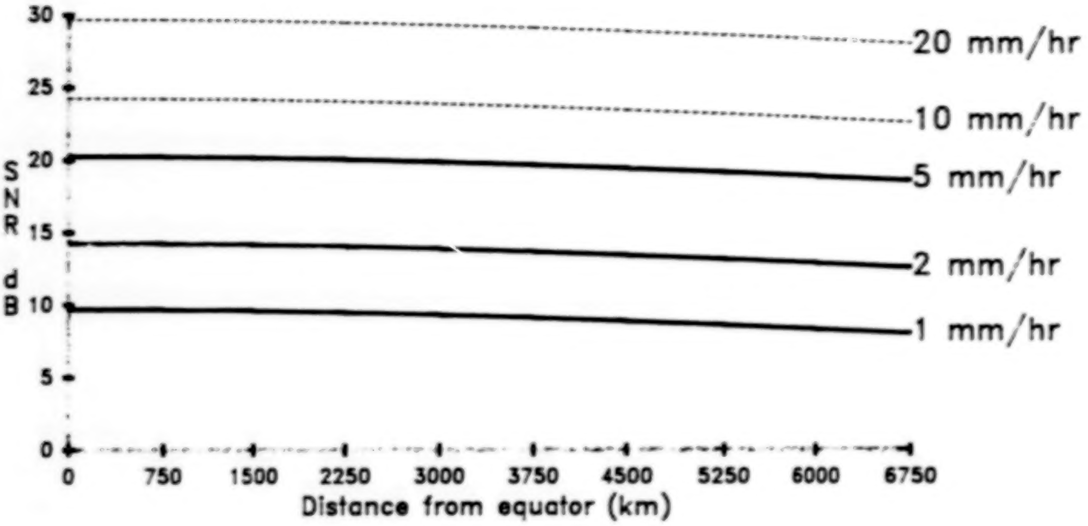

Figure 5

SNR FOR GEOSTATIONARY RADAR
10–m ANTENNA DIAMETER
ASSUMED RAIN CELL DIAMETER: 5 km
500 W TRANSMITTER – PULSE–COMPRESSION RATIO
200

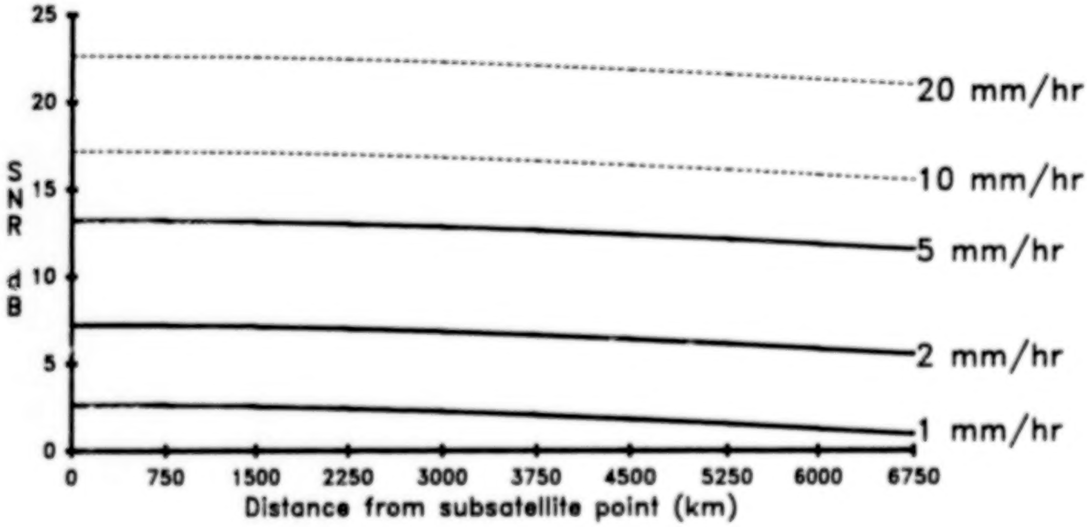

Figure 6

Fig. 7 plots the SNR at midrange (3750 km) versus antenna size for 1 mm/hour and 5 mm/hour. Clearly antenna size helps SNR, even though the resulting small footprints complicate the scanning.

In Fig. 8 we show the power required to achieve SNR=0 dB versus antenna diameter. The power levels are quite low for the larger antennas, but one must keep in mind that a PCR of 200 was assumed. Thus, without pulse compression, the powers would be higher by a factor of 200, making them totally unreasonable for the two smaller antenna sizes.

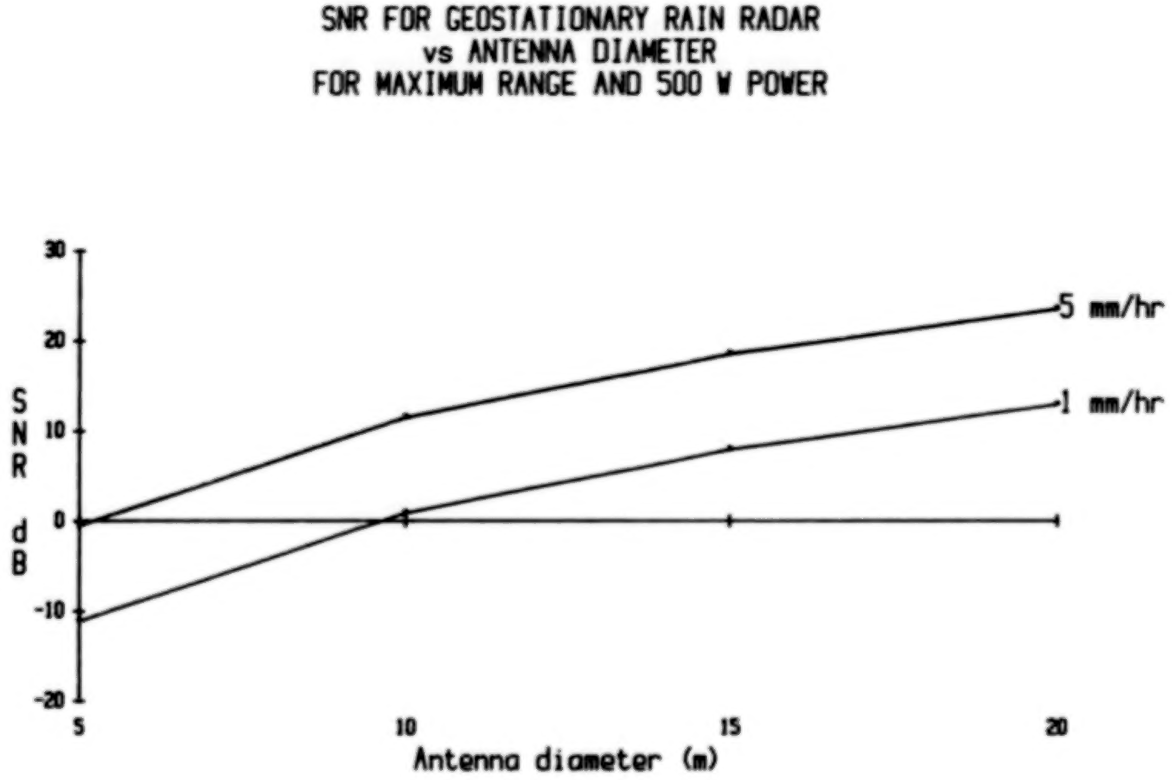

Figure 7

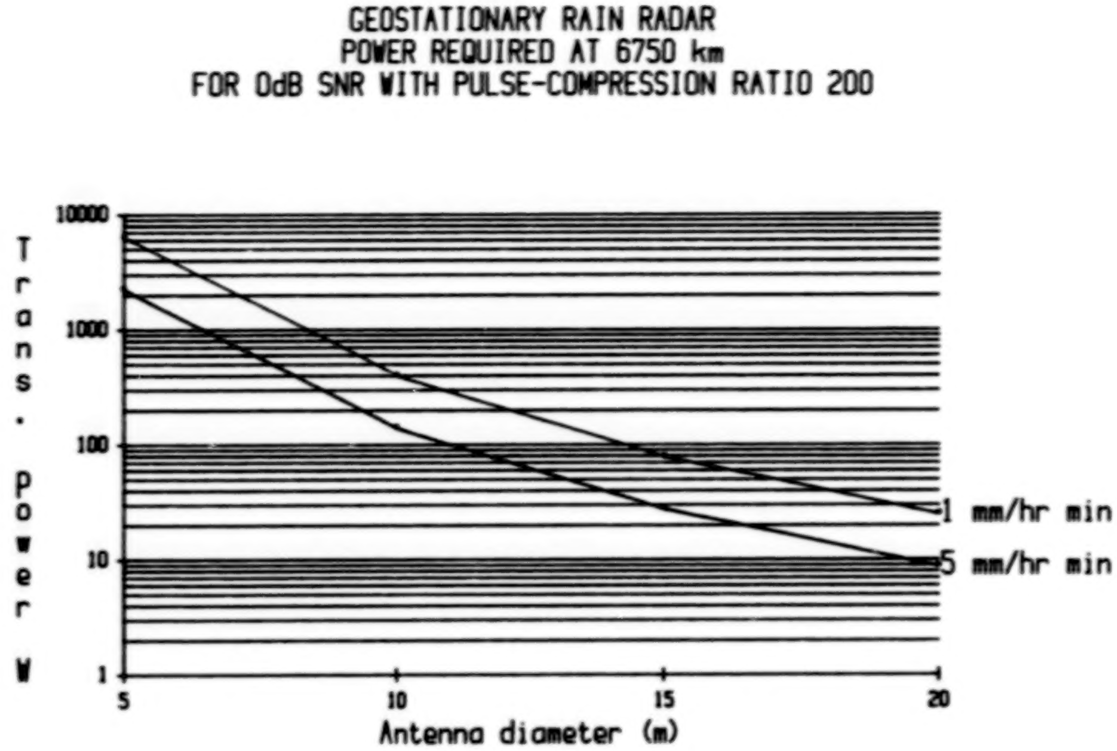

GEOSTATIONARY RAIN RADAR
POWER REQUIRED AT 6750 km
FOR 0dB SNR WITH PULSE-COMPRESSION RATIO 200

Figure 8

CONCLUSIONS

We have shown that a geostationary rain radar is feasible, though difficult. The biggest insoluble problem is the large footprint. However, the footprints for the 20-m and 15-m antennas considered should be useful for general-scale meteorology even if not for local scales. Scanning efficiency can be improved by using separately scanned beams for transmitting and receiving, so the long delay in receiving the echo does not slow down the scan. The situation can be further improved by using V-IR data to eliminate time wasted scanning clear areas.

This very preliminary study needs much refinement before we can be sure of the best design for a geostationary rain radar, as well as its cost and complexity. Nevertheless, this study is enough to show that the concept is a feasible one.

Electromagnetics - Phased Array Adaptive Systems Technology

ESGP

Session Chairman: Y. Rahmat-Samii
Jet Propulsion Laboratory

LARGE ANTENNA MEASUREMENT AND COMPENSATION TECHNIQUES *

Y. RAHMAT-SAMII
Jet Propulsion Laboratory
California Institute of Technology
Pasadena, CA

---

*Published in the Proceedings of the 11th ESTEC Antenna Workshop on Antenna Measurements held in Gothenburg, Sweden, June 20-22, 1988.

ABSTRACT

Antennas in the range of 20 meters or larger will be an integral part of future satellite communication and scientific payloads. In order to commercially use these large, low sidelobe and multiple-beam antennas, a high level of confidence must be established as to their performance in the 0-g and space environment. It is also desirable to compensate for slowly varying surface distortions which could result from thermal effects. An overview of recent advances in performing rf measurements on large antennas is presented with emphasis given to the application of a space-based far-field range utilizing the Space Shuttle. The concept of surface distortion compensation is discussed by providing numerical and measurement results.

1. INTRODUCTION

It is very likely that antennas in the range of 20 meters or larger will be an integral part of future satellite communication and scientific spacecraft payloads. For example, Fig. 1 depicts the conceptual evolution of the Land Mobile Satellite System which is anticipated to evolve from utilizing approximately 6-9 meter reflectors to 55 meter reflectors in the era spanning the late 1980's to early 2000's. In order to commercially use these large, low sidelobe and multiple-beam antennas, a high level of confidence must be established as to their performance in the 0-g and space environment. Certain ground (1-g) testing can be performed to validate the workability of different segments of such large structures; however, it will be a formidable task to characterize the performance of the entire structure on the ground.

For this reason, an overview of rf measurement techniques applicable to large antennas is provided. Attention will be focused on a conceptual study which has recently been initiated with the intent to describe an experiment aboard the Space Shuttle which would demonstrate the deployment reliability of the antenna structure, measure thermal and dynamic structural characteristics, and verify performance specification under all expected conditions.

The concept of surface distortion compensation is discussed by reviewing the applicability of different approaches. A technique based on the application of a compensating array feed is presented. Numerical results and measured data will be shown to demonstrate the utility of this compensation technique.

2. AN OVERVIEW OF MEASUREMENT TECHNIQUES

In the last twenty years significant developments have been reported on the subject of antenna measurements. Most importantly due to the improvement of

FIG. 1. Evolution of the proposed Land Mobile Satellite System (LMSS).

measurement systems in accurately measuring amplitude and phase, new methodologies have been advanced which have completely changed the nature of the classical far-field measurements. Among these new measurements concepts which are also applicable to large antenna measurements, one can refer to the following concepts [1-7]:

- Near-Field measurements
- Compact range measurements
- Modern far-field measurements
- Fly by measurements
- Microwave holographic measurements
- Integrated photogrammetric and rf measurements
- Integrated computer analysis and rf measurements
- In-space rf measurements
- Combination of the above techniques

Fig. 2 provides a block diagram for interrelating these measurement techniques. There is a considerable amount of published material on each of the above techniques to demonstrate their merits, advantages and disadvantages. It is the users responsibility to acquire an in-depth appreciation of the applicability of each of the above measurement concepts for the problem at hand. This means that the user should carefully identify what characteristics of the antenna need be measured for a given application and above all to identify the required accuracy in measuring the antenna parameters of interest. In the following, examples are given for selected measurement techniques applicable to large antennas based on the author's experience.

3. NEAR-FIELD MEASUREMENTS

Near-field measurement techniques have enjoyed much development and utilization among many rf measurement engineers. There are many organizations worldwide that use near-field measurement techniques on routine bases [1]. Here, two examples are given on the application of near-field measurement techniques to large deployable antennas.

The 4.8-meter mesh deployable antenna of the Galileo spacecraft has been measured in the near-field plane-polar facility at JPL. This facility has the unique characteristic which allows the skyward mounting of the antenna on the positioner. It is essential that large mesh deployable antennas be measured in this position if any meaningful rf measurements are to be performed on the ground. The reader is referred to [8] for a detailed description of this measurement. As shown in Fig. 3, the antenna rotates on its axis as the probe is advanced in the radial direction.

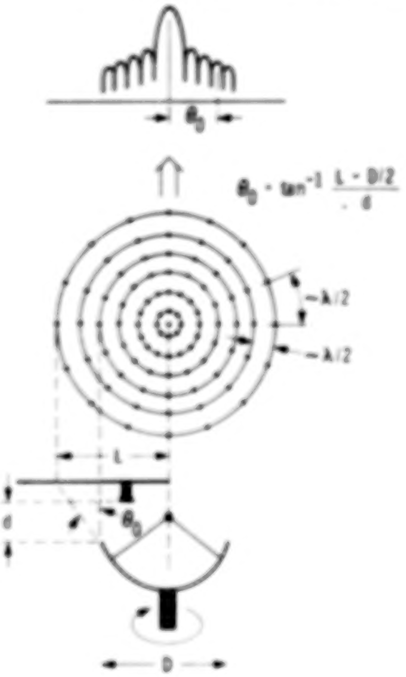
θ_0
$\theta_0 = \tan^{-1} \frac{L - D/2}{d}$
~λ/2
~λ/2
L
d
θ_0
D

FIG. 3 Plane-polar measurement technique.

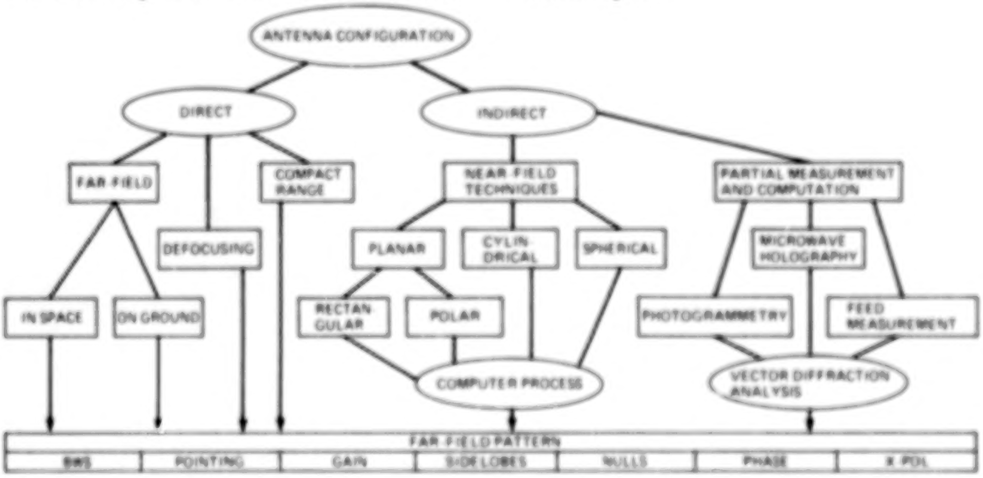
ANTENNA CONFIGURATION
DIRECT
INDIRECT
FAR FIELD
DEFOCUSING
COMPACT RANGE
NEAR FIELD TECHNIQUES
PARTIAL MEASUREMENT AND COMPUTATION
PLANAR
CYLINDRICAL
SPHERICAL
MICROWAVE HOLOGRAPHY
IN SPACE
ON GROUND
RECTANGULAR
POLAR
PHOTOGRAMMETRY
FEED MEASUREMENT
COMPUTER PROCESS
VECTOR DIFFRACTION ANALYSIS
FAR FIELD PATTERN
BWS
POINTING
GAIN
SIDE LOBES
NULLS
PHASE
X POL

FIG. 2. A block diagram for inter-relating various measurement techniques.

The near-field data are collected on concentric circles which are then transformed to the far field using either Jacobi-Bessel expansion or an FFT algorithm. A photo of the deployed antenna in the near-field chamber is shown in Fig. 4 and a representative far-field pattern is depicted in Fig. 5.

The largest deployable antenna commercially measured was the 15-meter hoop-column mesh antenna built by Harris corporation under a contract to NASA/LaRC [9]. This antenna was measured at the near-field facility of Martin-Marietta in a joint effort supported by LaRC/JPL/Martin-Marietta. The purpose of the measurement has been to demonstrate the utility of large mesh deployable antennas, to test the newly developed overlapping microstrip array feed cluster, and to test the accuracy of the computational techniques. A photo of this antenna deployed in the near-field chamber is shown in Fig. 6.

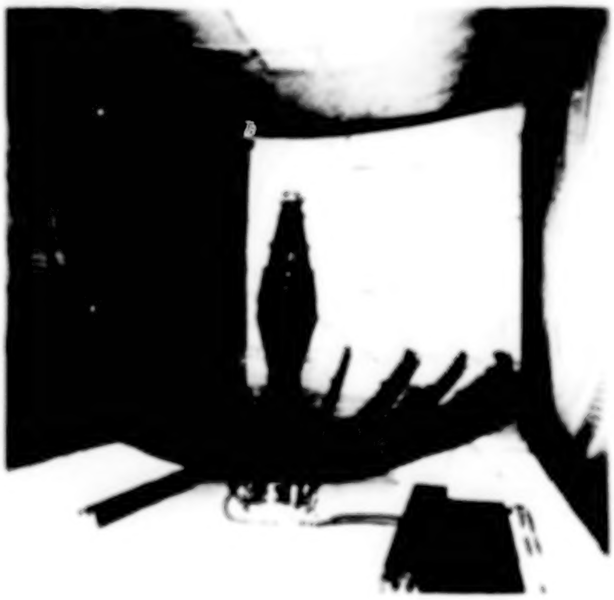

FIG. 4. Mesh deployable 4.8 meter Galileo antenna in the near-field facility.

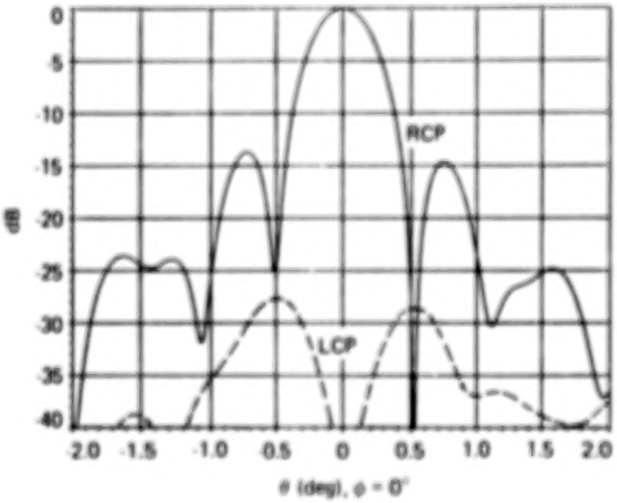

FIG. 5. Constructed far-field patterns for the circularly polarized Galileo antenna at 8.415 GHz.

It is important to realize that this hoop-column reflector antenna consists of four sub-apertures each of which is an offset parabolic surface. Again as seen from Fig. 6, the antenna is positioned skyward in the chamber which utilizes a rectangular near-field measurement setup. In order to correlate the results of the measurement with those based on computational techniques, a set of photogrammetry measurements was conducted to identify the location of the target points mounted on the reflector surface (Fig. 7). Fig. 8 shows the results of the comparison between the measurements and computations using the ideal parabolic surface. Also shown in Fig. 9 are the measured far-field patterns constructed from the near-field measurements using the overlapping feed cluster.

For large antennas, it appears that the near-field planar technique has the advantage over cylindrical and spherical techniques because of its simpler mechanical setup for the skyward positioning of the antenna. Recently attempts have been made to consider the utility of the combined plane-polar and

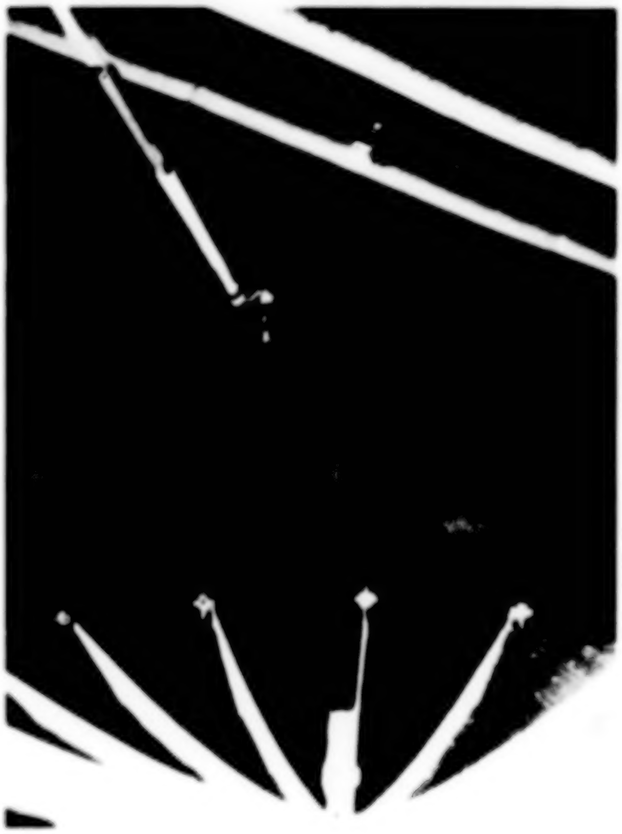

FIG. 6. 15-meter hoop-column antenna in Martin Marietta near-field facility.

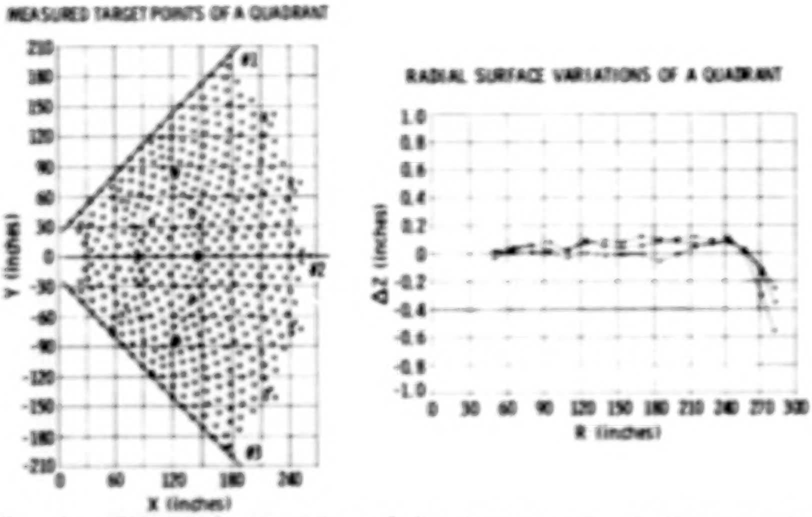

FIG. 7. Measured target points based on photogrammetry technique. ΔZ is the surface deviation from the best fit paraboloid.

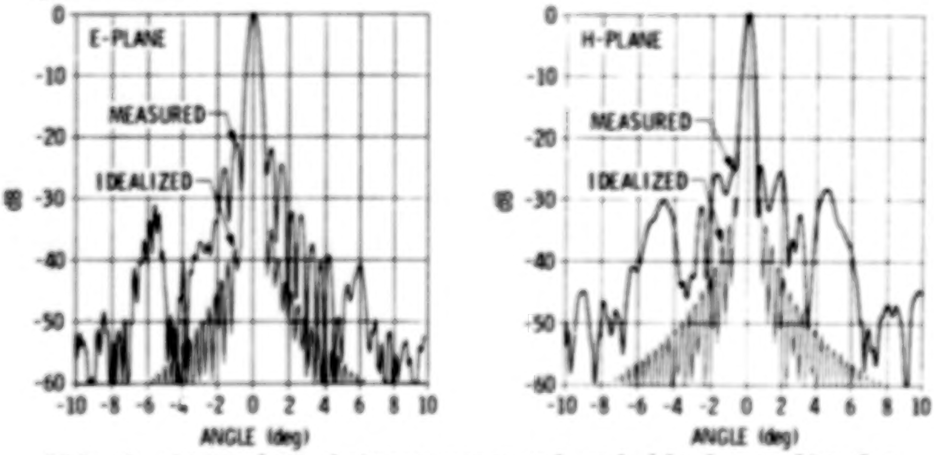

FIG. 8. Comparison between measured and ideal results for the 15-m antenna at 7.73 GHz.

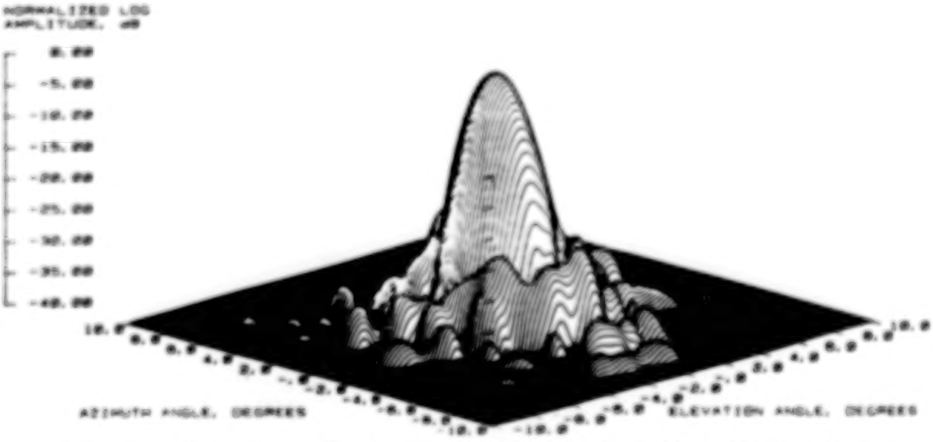

FIG. 9. Measured far-field pattern for the 15-m antenna using the overlapping feed cluster at 2.23 GHz.

cylindrical near-field technique as depicted in Fig. 10 [10]. Once operational this combined technique has the advantage of reducing the needed area of the near-field measurement of the plane-polar and the added feature of allowing the construction of the far-field pattern in wider angular range than is typically obtainable from the planar near field alone. The usefulness of this combined technique can be further improved by utilizing the modulated scattering approach for the reduction of the measurement time [11]. It is anticipated that such a measurement apparatus could be mounted aboard the Space Station for future in-space testing and verification of large antenna systems.

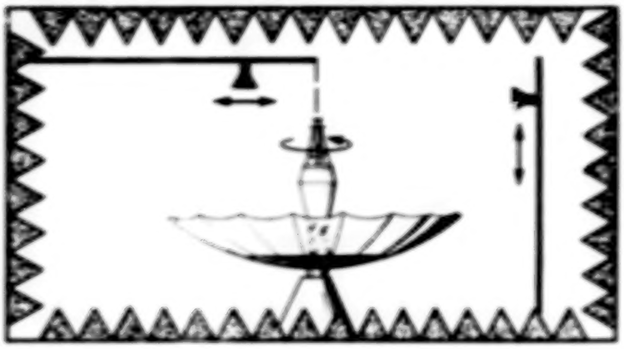

FIG. 10. A combined plane-polar and cylindrical near-field measurement technique.

4. MICROWAVE HOLOGRAPHIC METROLOGY

As mentioned before, photogrammetry has been used to determine the surface profile of large antennas. This technique utilizes optical cameras to take several photographs of the antenna covered by many target points. These photographs are then processed to finally identify the shape of the reflector surface [4].

Recently, attention is given to microwave holographic techniques which allow the determination of the reflector surface shape based on microwave measurements. This technique is unique in that it can be used in conjunction with far-field, near-field and compact range measurement techniques. Fig. 11 shows the steps involved in applying microwave holographic metrology for antenna diagnosis. The essence of the technique is based on the observation that the antenna far-field is proportional the Fourier transform of a function which is related to the induced current on the reflector surface. Therefore, once the amplitude and phase of the far-field pattern are measured in an appropriate angular interval, they can be used to determine the surface profile. This technique has been applied very successfully for measuring many large ground antennas worldwide [12,13,14]. It is expected that with some refinements the technique should also be applicable to the space antennas.

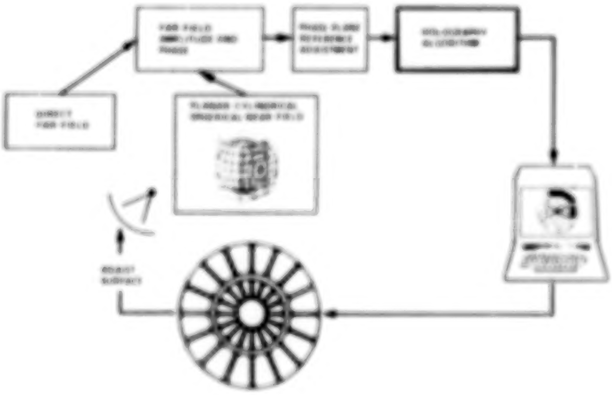

FIG. 11. Steps in applying microwave holographic diagnosis.

As an example, Fig. 12 shows the results of a recent measurement performed on one of the 64 meter antenna of NASA/JPL/Deep Space Network (DSN) reflector antennas. A photo of this antenna is shown in Fig. 13. It is anticipated that application of the microwave holographic metrology will

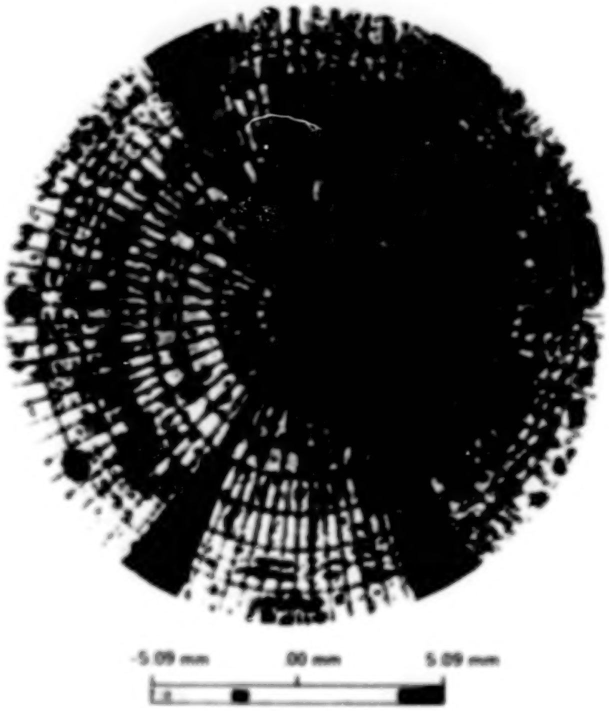

FIG. 12. Surface error map for the DSN reflector antenna.

FIG. 13. NASA/JPL 64-m Deep Space Network (DSN) antenna.

attract attention in diagnosis of large deployable antennas either measured in near-field facilities or far fields. As will be discussed later, the outcome of surface diagnostics can be used in applying surface distortion compensation.

As mentioned earlier, microwave holographic reconstruction may be used in conjunction with near-field measurements providing a useful diagnostic tool. This hybrid approach of combining near-field measurement and holographic reconstruction would allow an in-depth evaluation of the accuracy of the holographic technique because the spherical near-field measurement, in particular, provides accurate amplitude and phase far-field patterns for the entire angular range. The steps of this hybrid approach are depicted in Fig. 14.

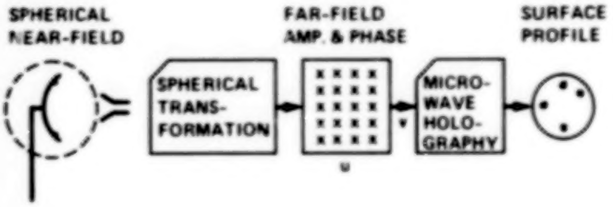

FIG. 14. Steps in performing Microwave Holographic Diagnosis using spherical near-field measurements.

Under controlled conditions, two sets of spherical near-field measurements were performed on a 156-cm reflector at 11.3 GHz. In the first measurement, the antenna was measured in its existing condition while in the second measurement, four bumps of different sizes and heights were attached at several locations to the reflector surface (see Fig. 15). These measured near-field data were used to generate the far-field amplitude and phase patterns of the reflectors using a spherical near-field to far-field algorithm. Then the steps of the block diagram shown in Fig. 14 were employed to generate the surface profiles.

Similar steps were followed for both the original and bumped reflectors. However, in order to demonstrate how successfully the bumps were recovered, the results of original and bumped reflectors were used to obtain the final result and to remove the contamination due to the reflector's original imperfection. To this end, the generated holographic surface profiles of the two measurements were subtracted to essentially remove the effects due to the original surface imperfection, struts diffraction, feed misalignments, nonspherical phase pattern of the feed, and other factors. Results are shown in Fig. 16 using the contour plot presentation, which clearly demonstrates how well the four attached bumps are recovered.

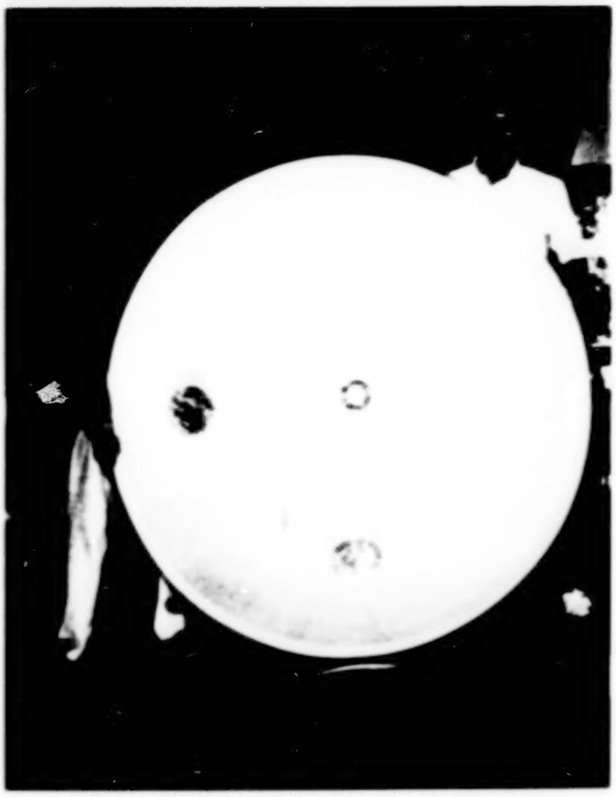

FIG. 15. Antenna with four attached bumps of different sizes and locations.

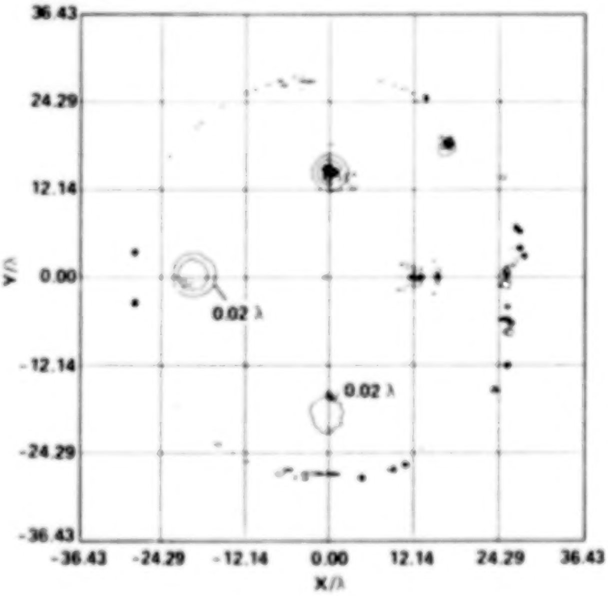

FIG. 16. Reconstructed surface profile after subtraction (11.3 GHz).

5. SHUTTLE BASED RF MEASUREMENTS

Since the actual space environment can only be achieved in space, special consideration is being given to the rf far-field pattern measurements of large antennas aboard the Space Shuttle. This measurement should provide the ultimate characterization for the antenna performance (Fig. 17).

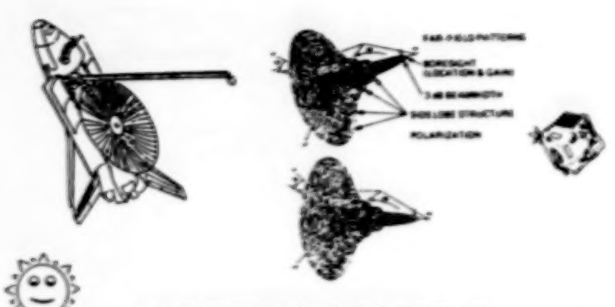

- MEASURE ON-AXIS AND OFF-AXIS BEAM PATTERNS AT L-BAND
  - MEASURE UNDER VARIOUS THERMAL CONDITIONS
  - MEASURE AFTER ON-ORBIT SURFACE RECONFIGURATION
- DEMONSTRATE IN-SPACE RF MEASUREMENT TECHNOLOGY
- CORRELATE MEASURED RF PERFORMANCE WITH MEASURED SURFACE AND FEED ALIGNMENT
- VERIFY AND UPDATE MATHEMATICAL AND COMPUTER MODELS OF RF PERFORMANCE ANALYSIS AND PREDICTION

FIG. 17. Spaced-based RF experiment objectives aboard the Space Shuttle.

Several potential scenarios have been considered and the relative merit of each of them are shown in qualitative manner in Fig. 18. Among all these possibilities the application of the scenario shown in the last row appeared most feasible. The rf experiment is anticipated to be performed on a 20-meter offset reflector at L-band using the Remote Mini-Flyer, a NASA-developed reusable and retrievable spacecraft (a modified Spartan), as the carrier for an rf beacon. This beacon is used to illuminate the antenna in a similar fashion as one does in the ground-based far-field ranges using transmit illuminators. An artist's rendition of this spaced-based experiment is depicted in Fig. 19.

Among the several rf measurement concepts studied, application of a far-field arrangement with an RF illuminator mounted aboard the free-flyer appeared to be the most feasible. Furthermore, in order to reduce the cost of the experiment, it has been anticipated that no gimbal mechanism will be used to accurately control the position of the antenna with respect to the illuminator. Instead, the relative motion of the Shuttle and free-flier in a controlled manner will be utilized to provide the angular range of interest. Depending on what the exact covered u-v space will be, several scenarios could be considered.

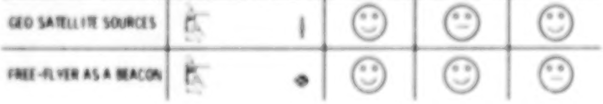

TECHNIQUES	CONFIGURATION	COMPLEXITY	USEFULNESS	COST
NEAR FIELD TECHNIQUES		☹	☺	☹
COMPACT RANGES		☹	😐	☹
BEACON ON THE GROUND		😐	☹	😐
RECEIVING CITIES ON THE GROUND		😐	☹	😐
RADIO STAR SOURCES		☺	😐	☺
GEO SATELLITE SOURCES		☺	😐	☺
FREE-FLYER AS A BEACON		☺	☺	😐

FIG. 18. A qualitative comparison of different measurement techniques aboard the Space Shuttle.

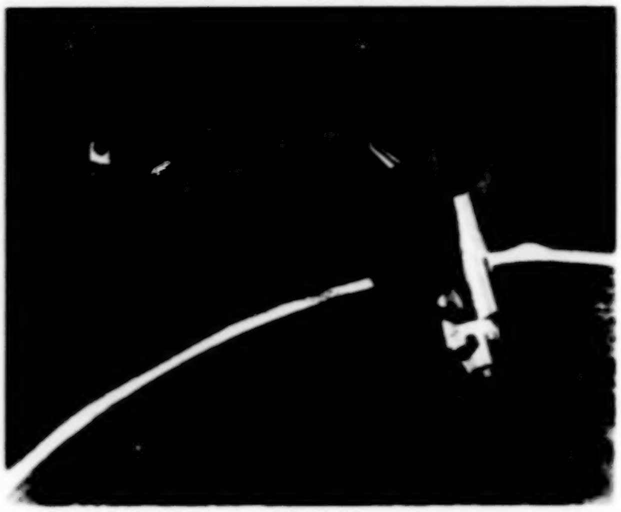

FIG. 19. An artist's rendition of the proposed large antenna Shuttle experiment.

Since without any gimbal system it will be impractical to measure antenna patterns in specified ϕ cuts, one may have to perform the measurement in a specified u-v angular range in a time period in which the antenna structure is not changed appreciably from an rf viewpoint. Fig. 20 shows the possibility of measuring very dense but nonuniformly measured data points from which the needed ϕ-cuts or contour patterns can be constructed. If it is proved that the possibility of measuring a very dense set of data may not be realistic, an alternate scheme should be available. This alternate scheme is depicted in Fig. 21, which assumes that

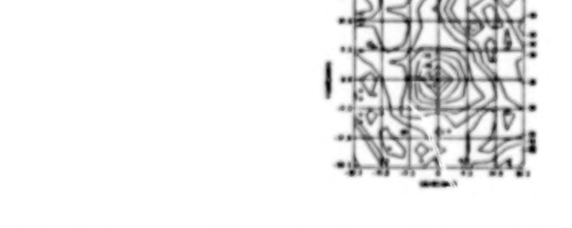

FIG. 20. Schematic of nonuniform and very densely measured sampled points.

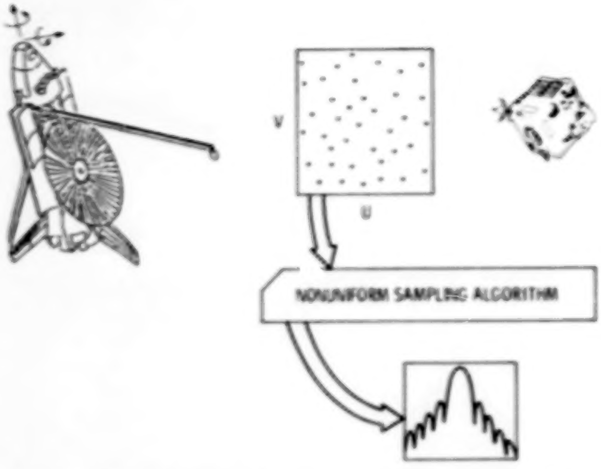

FIG. 21. Schematic of a nonuniform and relatively sparsely measured sampled points.

the measured (amplitude and phase) are obtained at relatively sparse and nonuniformly distributed u-v points. The question is, then, whether or not one can construct the ϕ-cuts from a set of nonuniformly distributed measured data points?

Recently, Rahmat-Samii and Cheung [7] have demonstrated that a two-dimensional nonuniform sampling technique which utilizes irregularly spaced samples (amplitude and phase) can be used to generate the far-field patterns. The mathematical developments of this two-dimensional nonuniform sampling technique have been detailed in [7]. Additionally, a powerful simulation algorithm has then been developed to test the applicability of this sampling technique for a variety of reflector measurement configurations. For example, Figs. 22 and 23 show the simulated nonuniform sample points and the reconstructed far-field patterns in specified ϕ-cuts for a 20 meter offset reflector antenna with a defocused feed operating at L-band [7]. In these figures the solid curves are reconstructed co-polar and cross-polar patterns using the nonuniform sampling technique. It is noted that even though no sample points are captured in these cuts, the reconstructed patterns agree well with the ideal patterns in the angular range where the nonuniform sample points have been generated. Many tolerance studies have also been performed to demonstrate the required measurement accuracies in applying the nonuniform sampling technique [7].

To validate the accuracy of nonuniform sampling technique for antenna pattern construction, several measurements have been performed as reported in [15]. In one of the measurements JPL's 1200-ft far-field range was used, where a 1.47-m circularly polarized Viking reflector antenna (Fig. 24) was measured at X-band (8.415 GHz) using a corrugated horn as the illuminating antenna. The far-field amplitude and phase were measured in the directions shown in Fig. 25 which consisted of 585 nonuniformly distributed sampled points in (u,v) coordinates.

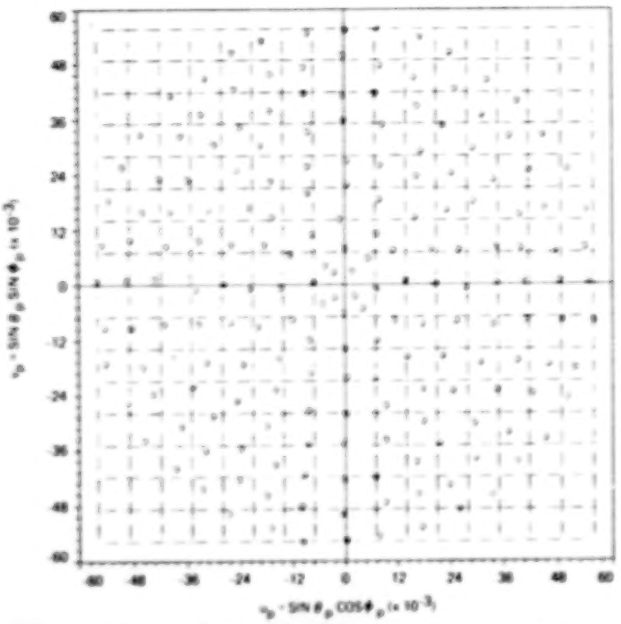

FIG. 22. One hundred ninety two nonuniform sampled point distribution in (u,v) coordinates which covers an angular region of θ = ±3.2 degrees.

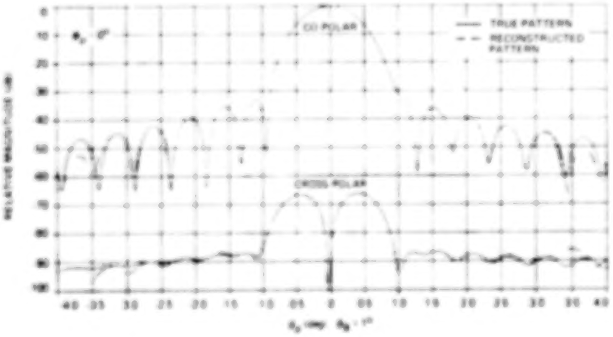

FIG. 23. Far-field patterns reconstructed using nonuniform sampling technique.

The co-polar far-field pattern for ϕ = 90 degrees is depicted in Fig. 26. The solid curves are the standard azimuth cuts and the dashed curves are the reconstructed patterns using the nonuniform sampling technique. These patterns are constructed by utilizing the window concept as discussed in [7,15]. Note that asymmetric patterns have resulted even though a symmetric reflector was used. this is due to the feed and strut blockage effects. In the angular range of 16.8 degrees where the measured data are available, the comparison between the solid and dashed curves demonstrates close agreement. Note that even though no sampled point has been used at the boresight, the peak of the beam has been reconstructed very well.

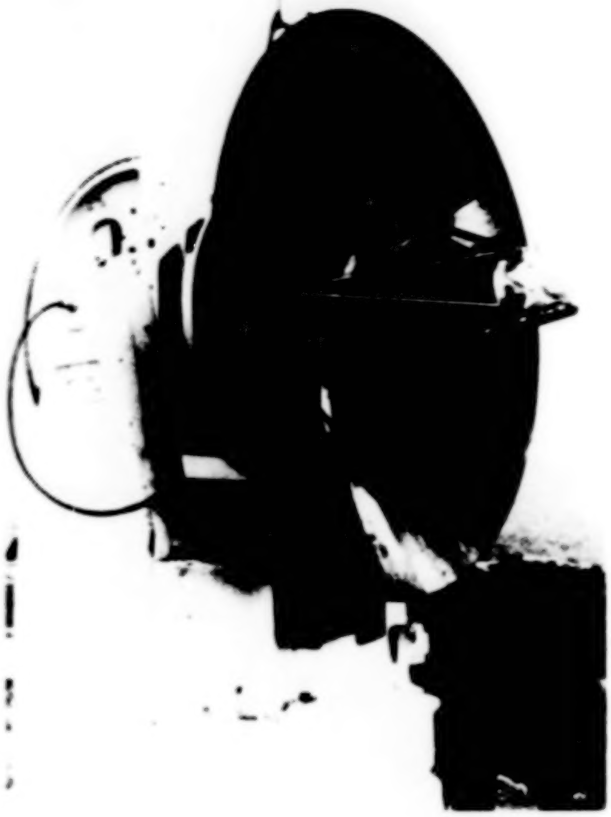

FIG. 24. The 1.47-m circularly polarized Viking reflector antenna operating at X-band (8.415 GHz).

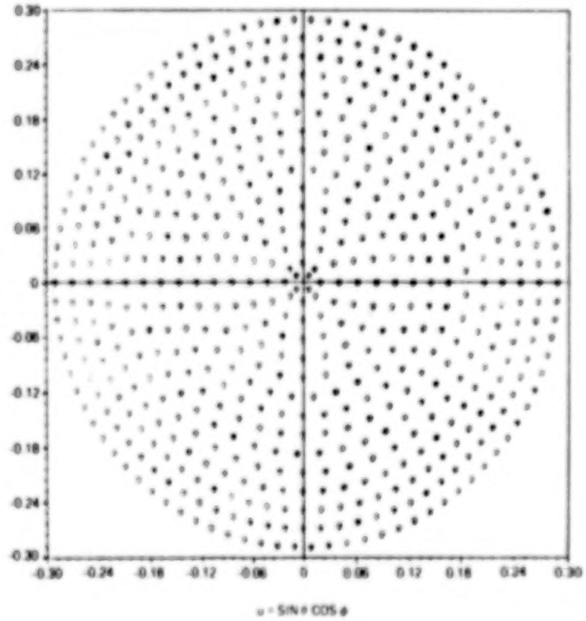

FIG. 25. Five hundred eighty five measured data point distribution in (u,v) coordinates which covers an angular region of $\theta = \pm 16.8$ degrees.

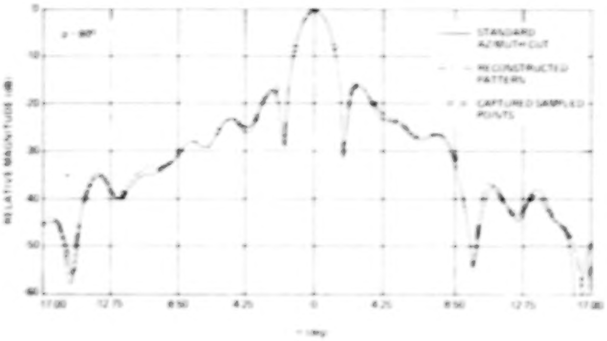

FIG. 26. Reconstructed co-polar far-field patterns of the Viking reflector at X-band using nonuniformly distributed measured data.

6. ANTENNA DISTORTION COMPENSATION

Recent communication system demands require application of very large antennas. Furthermore, it is anticipated that these antennas produce high gain and low sidelobes for future multiple beam satellites. Among different antenna concepts, reflectors still enjoy more acceptance among the designers of large antenna configurations. However, in the space environment the surface of these large reflectors will be distorted resulting in degraded antenna performance [5].

It is very likely that large antennas will suffer from distortions regardless of how rigid the antenna construction is. For this reason, application of an apparatus which would be able to compensate for the distortion will be highly desirable provided that this apparatus can be implemented in a cost effective manner. Fig. 27 shows the mechanism which results in the antenna performance degradation due to reflector surface distortion. The main cause is the introduction of effective aperture phase errors due to the distortion. Fig. 28 summarizes how a corrective apparatus may be used to compensate for the radiated distorted phase front.

Among different possibilities suggested in Fig. 28, recent investigations have revealed the effectiveness of compensating for reflector surface distortions using array feeds [16,17]. This approach is particularly useful in situations for which the reflector distortion is slowly varying, as is typically the case, for example, with large reflectors subject to thermal or gravitational distortions. Additionally, array feeds can be used to improve wide angle radiation characteristics of antennas or to provide low sidelobes.

As presented in [17], a generalized diffraction analysis computer program has been developed which generates complex excitation coefficients for each feed element and then produces the compensated

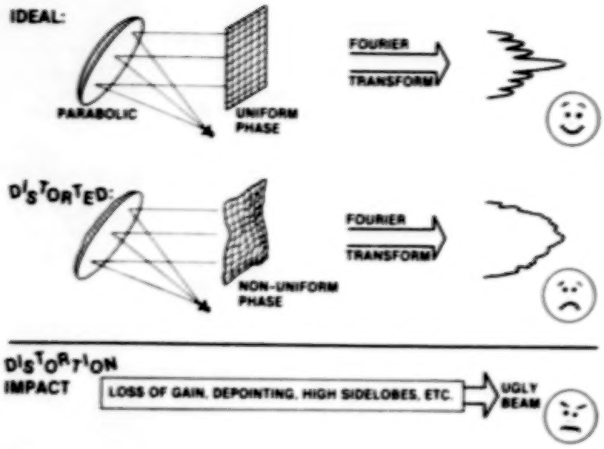
IDEAL:
FOURIER
TRANSFORM
PARABOLIC
UNIFORM PHASE
DISTORTED:
FOURIER
TRANSFORM
NON-UNIFORM PHASE
DISTORTION IMPACT
LOSS OF GAIN, DEPOINTING, HIGH SIDELOBES, ETC.
UGLY BEAM

Fig. 27. Schematic presentation of how surface distortions result in degraded antenna performance.

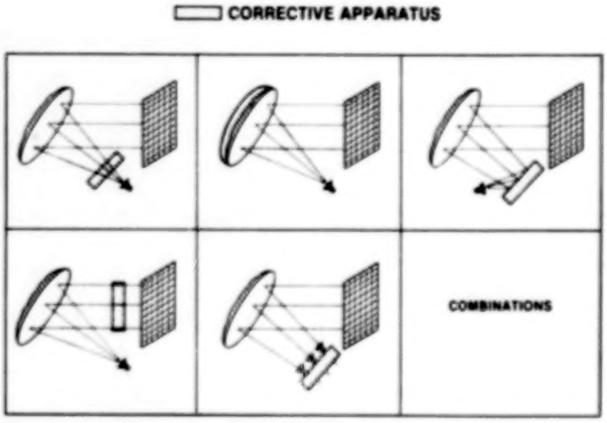
CORRECTIVE APPARATUS
COMBINATIONS

Fig. 28. A conceptual consideration for the utilization of a corrective apparatus.

far-field pattern, either for gain or sidelobe control. Fig. 29 depicts the steps necessary to implement this compensating diffraction algorithm.

The concept of conjugate field matching is used to determine the complex excitation coefficients of the array feed. This approach can provide the array excitation coefficients which either maximize the reflector gain in the desired direction or control the sidelobe levels [17]. For the experimental study, it is assumed that the reflector surface is distorted in the fashion shown in Fig. 30, which describes a dominant term in a typical thermal distortion. A pictorial presentation of the reflector surface and its residual deviation from the best fit parabolic surface are shown in Fig. 30. The functional expression in Fig. 30 has been used to fabricate a test reflector in order to demonstrate the utility of the compensation technique via measured data.

A 16-element array feed utilizing cigar elements has been used to perform the experiment (in practice, other array elements such as microstrip elements can be also utilized). Based on this configuration numerical studies were conducted with the results shown in Fig. 31, where significant improvement is achieved using the array feed. Additional numerical studies were performed to identify the accuracies required to position array elements and to set their excitation coefficients; these results were employed in the design of the experiment.

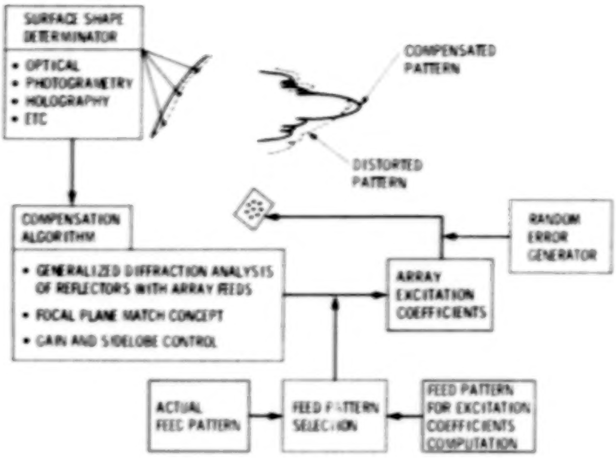
SURFACE SHAPE DETERMINATOR
• OPTICAL
• PHOTOGRAMETRY
• HOLOGRAPHY
• ETC
COMPENSATED PATTERN
DISTORTED PATTERN
COMPENSATION ALGORITHM
• GENERALIZED DIFFRACTION ANALYSIS OF REFLECTORS WITH ARRAY FEEDS
• FOCAL PLANE MATCH CONCEPT
• GAIN AND SIDELOBE CONTROL
RANDOM ERROR GENERATOR
ARRAY EXCITATION COEFFICIENTS
ACTUAL FEED PATTERN
FEED PATTERN SELECTION
FEED PATTERN FOR EXCITATION COEFFICIENTS COMPUTATION

Fig. 29. A generalized block diagram for the incorporation of the array feed compensating algorithm using reflector diffraction analysis.

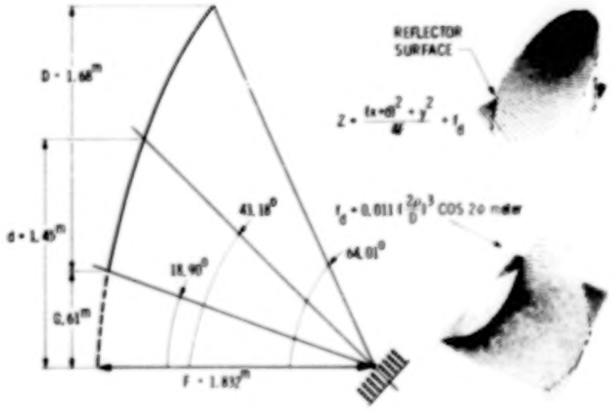
D = 1.68m
d = 1.45m
0.61m
F = 1.832m
18.90°
43.18°
64.01°
REFLECTOR SURFACE
Z = ((x+d)² + y²)/4F + f_d
f_d = 0.011 (2ρ/D)³ COS 2φ

Fig. 30. Reflector surface configuration and its functional representation incorporating slowly varying distortion.

The geometry of the 16-element array feed is shown in Fig. 32. This array consists of 16 cigar elements spaced at 1.06λ (at 8.45 GHz), with an analog phase shifter and variable attenuator behind each element. Since the excitation of each element is set using the corresponding variable attenuator and phase shifter, considerable effort went into proper calibration of this network.

To demonstrate the practical utility of array feeds for the compensation of the

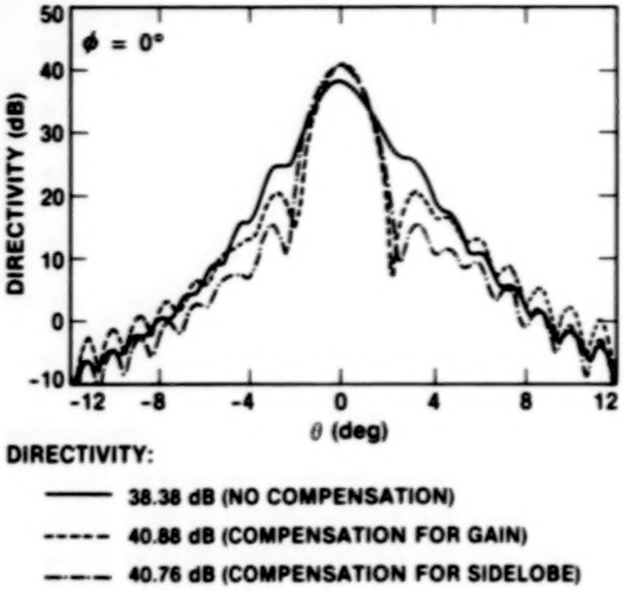

Fig. 31. Compensated and non-compensated far-field patterns generated by diffraction analysis computer program in two different cuts.

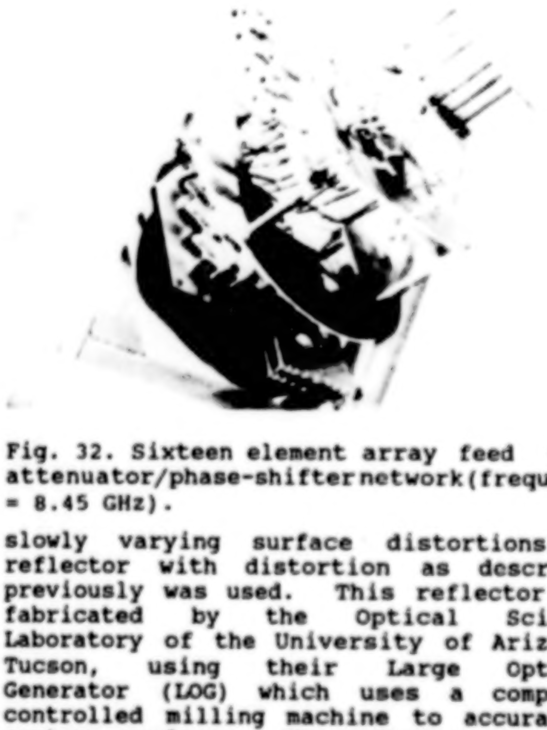

Fig. 32. Sixteen element array feed with attenuator/phase-shifter network (frequency = 8.45 GHz).

slowly varying surface distortions, a reflector with distortion as described previously was used. This reflector was fabricated by the Optical Science Laboratory of the University of Arizona, Tucson, using their Large Optical Generator (LOG) which uses a computer controlled milling machine to accurately contour surfaces. The reflector consists of aluminum honeycomb backing structure surfaced with a machinable foam. After the foam was shaped to the specified profile, a conductive glass fiber material was applied to the surface to make it reflective at microwave frequencies. The steps of this contouring process are shown in Fig. 33.

The photo of this reflector and the 16-element array feed is shown in Fig. 34.

Fig. 33. Surface shaping using the Large Optical Generator (U. of Arizona) to result in a reflector surface as per Fig. 30.

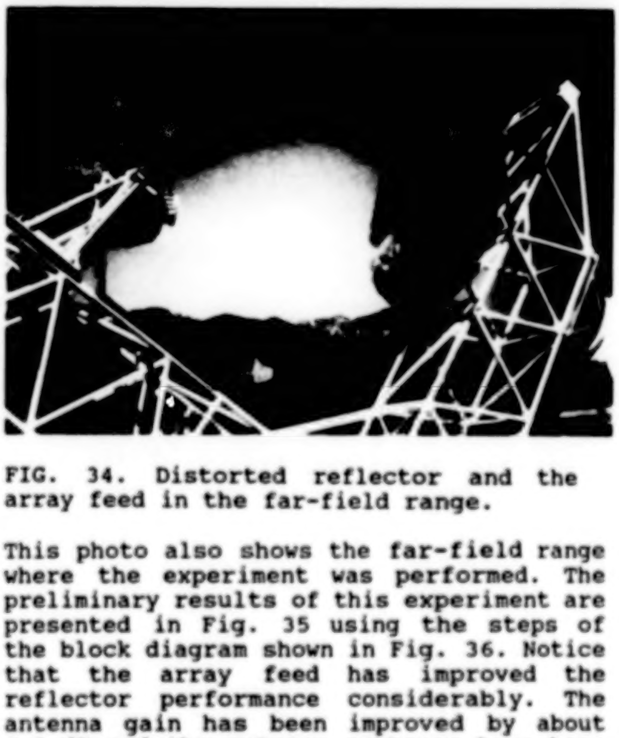

FIG. 34. Distorted reflector and the array feed in the far-field range.

This photo also shows the far-field range where the experiment was performed. The preliminary results of this experiment are presented in Fig. 35 using the steps of the block diagram shown in Fig. 36. Notice that the array feed has improved the reflector performance considerably. The antenna gain has been improved by about 2.5 dB and the antenna patterns have been considerably improved. Additional experiments are being conducted to further improve the sidelobe levels of the compensated patterns.

These results clearly demonstrate the applicability of an adaptive scheme to directly identify the required excitation coefficients of the compensating feed array without actually measuring the reflector surface. This, we believe, is an essential step if such a compensating algorithm is going to be utilized with future large space antennas. It is also anticipated that this compensation technique will be applied to large ground antennas such as Deep Space Network (DSN) antennas.

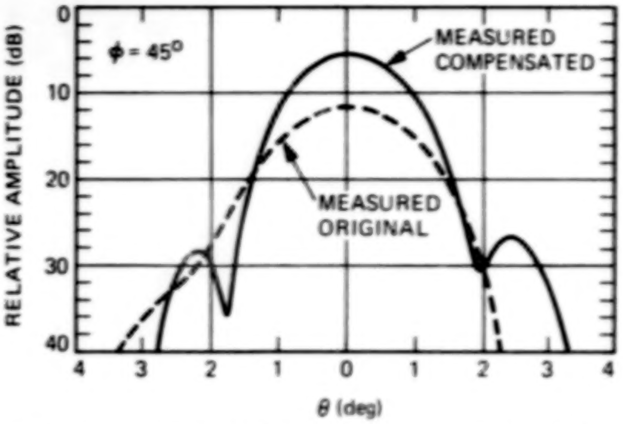

FIG. 35. Comparison between measured patterns for the original and the compensated cases.

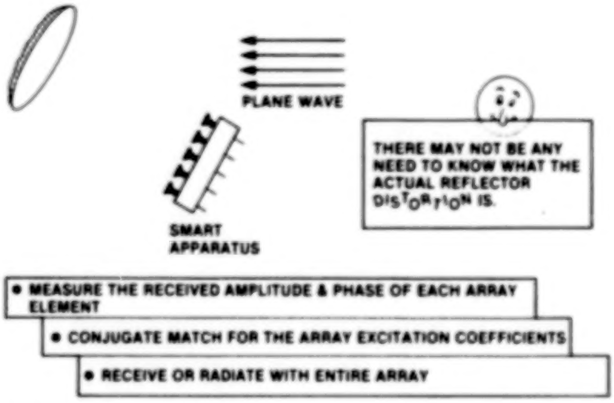
PLANE WAVE
SMART
APPARATUS
THERE MAY NOT BE ANY NEED TO KNOW WHAT THE ACTUAL REFLECTOR DISTORTION IS.
• MEASURE THE RECEIVED AMPLITUDE & PHASE OF EACH ARRAY ELEMENT
• CONJUGATE MATCH FOR THE ARRAY EXCITATION COEFFICIENTS
• RECEIVE OR RADIATE WITH ENTIRE ARRAY

FIG. 36. Steps in implementing an adaptive surface compensation algorithm.

7. ACKNOWLEDGEMENTS

The research described in this paper was carried out at the Jet Propulsion Laboratory, California Institute of Technology, under contract with the National Aeronautics and Space Adminstration. The author would like to thank his colleagues at JPL for their helpful discussions during the preparation of this manuscript.

8. REFERENCES

1. Bennet J. C., "Recent developments in near-field antenna measurements," IEE Fifth International Conference on Antennas and Propagation, ICAP 87, pp. 476-472, York, U.K., April 1987.

2. Johnson R. C., et al, "Compact range techniques and measurements," IEEE Trans. Antennas Propagat., vol. 17, pp. 568-576, Sept. 1969.

3. Rahmat-Samii Y., "Microwave Holographic Metrology for Antenna Diagnosis," IEEE Antenna & Propagat. Newsletter, vol. 29, pp. 5-16, June 1987.

4. Fraser C. F., "Photogrammetric measurement of antenna reflectors," Antenna Measurement Techniques Association Meeting, pp. 374-379, Seattle Washington, Sept. 1987.

5. Rahmat-Samii Y., "Effects of deterministic surface distortions on reflector antenna performance," Annales Des Telecommunications, vol.40, no. 7-8, pp. 350-360, August, 1985.

6. Rahmat-Samii Y., "Vector diffraction analysis of reflector antennas with mesh surfaces," IEEE Trans. Antennas Propagat., vol. 33, pp. 76-90, Jan. 1985.

7. Rahmat-Samii Y. and R. Cheung, "Nonuniform sampling techniques for antenna applications," IEEE Trans. Antennas Propagat., vol. 35, pp. 268-279, 1987.

8. Rahmat-Samii Y. and M. Gatti, "Far-field patterns of spaceborne antennas from plane-polar near-field measurements," IEEE Trans. Antennas Propagat., vol. 33, pp. 638-648, 1985.

9. Baily M. C., et al, "Near-field test results and plans for the 15-meter hoop-column antenna," Antenna Measurement Techniques Association Meeting, pp. 230-234, Seattle Washington, Sept. 1987.

10. Rahmat-Samii Y., "A combined scanning configuration for near-field antenna measurements," NASA Tech Brief, vol. 10, no.5, pp. 44-45, Sept./Oct. 1986.

11. Bolcmey J. Ch., et al, "Reduction of near-field techniques duration," Antenna Measurement Techniques Association Meeting, Sept., 1986.

12. Godwin M. P., et al, "Improvement of the Effelsberg 100 meter telescope based on holographic reflector surface measurement," Astron. Astrophys., vol 167, pp. 390-394, 1986.

13. Mayer C. E., et al, "A holographic surface measurement of the Texas 4.9-meter antenna at 86 GHz," IEEE Trans. Instru. Meas., vol. IM-32, pp. 102-109, 1983.

14. Rahmat-Samii Y., "Microwave holography of large reflector antennas -- simulation algorithms," IEEE Trans. Antennas Propagat., vol. AP-33, pp. 1194-1203, 1985 (see minor corrections in vol. AP-34, pp. 853, 1986).

15. Cheung R. and Y. Rahmat-Samii, "Experimental verification of nonuniform sampling technique for antenna far-field construction," Electromagnetics, vol. 6, no. 4, pp.277-300, 1986.

16. Rudge A. W. and D. E. N. Davies, "Electronically controllable primary feed for profile-error compensation of large parabolic reflectors," Proc. IEE, no. 117, pp. 351-358, 1970.

17. Rahmat-Samii Y., "A generalized reflector/array surface compensation algorithm for gain and sidelobe control," 1987 IEEE AP-S Symposium, Blacksburg, VA, June 15-19, 1987.

A COMPARISON OF REFLECTOR ANTENNA DESIGNS FOR WIDE-ANGLE SCANNING

M. Zimmerman, S. W. Lee, B. Houshmand

University of Illinois, Urbana-Champaign, Urbana, IL.

Y. Rahmat-Samii

Jet Propulsion Laboratory, Pasadena, CA

R. J. Acosta

NASA-Lewis Research Center, Cleveland, OH

Abstract

Conventional reflector antennas are typically designed for up to ±20 beamwidths scan. In this paper, we try to stretch this scan range to some ±300 beamwidths. We compare six single and dual reflector antennas. It is found that a symmetrical parabolic reflector with focal length f to diameter D ratio of f/D=2 and a single circular waveguide feed has the minimum scan loss (only 0.6 dB at θ_0=8°, or a 114 beamwidth scan). The scan is achieved by tilting the parabolic reflector by an angle equal to the half-scan angle. The f/D may be shortened if a cluster 7 to 19 elements instead of one element is used for the feed. The cluster excitation is adjusted for each new beam scan direction to compensate for the imperfect field distribution over the reflector aperture. The antenna can be folded into a Cassegrain configuration except that, due to spillover and blockage considerations, the amount of folding achievable is small.

I. Introduction

Traditionally, reflector antennas are designed for limited scan. A symmetrical parabolic reflector with f/D=0.4 can only scan ±5 beamwidths (BW) with less than 2 dB loss [1]. If the reflector diameter is 1,000 λ, the ±5 BW scan corresponds to only ±0.5°, which is a very narrow field of view.

In some future applications, the antenna requirements will be quite different from what they presently are. One example is the NASA Earth Science Geostationary Platform Project. The preliminary antenna specifications are as follows:

Frequency range	20 GHz - 200 GHz
Antenna diameter	15 m (1,000 λ - 10,000 λ)
Scan range 1	±2° (±33 BW - ±330 BW)
Scan range 2	±8° (±133 BW - ±1,333 BW)

Note that the scan requirement has been significantly increased from the traditional value of ±5 BW. Usually a phased array design is used to satisfy specifications such as these.

A phased array antenna design is an order of magnitude more complicated than a reflector design. This is due to the large number of array elements and the beam-forming network contained in the design. Reflector antennas have the additional advantage of being less expensive and lighter in weight than phased arrays. Therefore, it is desirable to use a reflector antenna design if at all possible. The question then is can a reflector antenna be designed that is capable of meeting these specifications?

This paper examines and compares six different reflector designs. We intend to show how far the reflector performance can be stretched. The object is to achieve a wide-angle scan that will satisfy requirements such as those listed. The first three designs, P1, P2, and P3, are parabolic single reflector designs. These three designs are considered in Section II. The first design is a center-fed, single-element feed design with f/D=2 (Fig. 1a). Scanning is accomplished by mechanically tilting the reflector. The second design has f/D=1 and uses a 19 element cluster feed but otherwise is similar to the first design (Fig. 1b). The third design is an off-set reflector with f/D=2 and an electronically scanned cluster feed (Fig. 1c).

The last three designs, C1, C2, and C3, are dual reflector Cassegrain designs. They are considered in Section III. The three designs all use the same reflector geometry. The first design scans by mechanically tilting the main reflector (Fig. 2a). The second design scans by mechanically tilting the subreflector (Fig. 2b). The last design scans by tilting both the main reflector and the subreflector (Fig. 2c).

Data on extremely wide-angle scans of reflector antennas are scarce in the literature. Hung and Mittra [2] in 1986 did analyze a center-fed symmetrical parabolic reflector with a cluster feed, and calculate patterns up to a hundred beamwidth scan. We have verified our single reflector computer code by comparing with their results.

II. Single Reflector Antennas

P1: Symmetric Parabolic Reflector with f/D=2

Two contributing factors to poor scanning ability are (i) short focal length and (ii) high off-set. For these reasons, the first design considered is a symmetrical parabolic reflector with an unusually long focal length. Design P1 has a diameter D=1,000 λ and a focal length f=2,000 λ, thus giving f/D=2. The feed is a long circular open-ended waveguide with radius a=3 λ. A study was done of the directivities and beam efficiencies corresponding to various feed radii. The results are shown in Figure 3, with directivities converted to antenna efficiency. Antenna efficiency is defined as the fraction of the nominal directivity that the given directivity is, namely,

$$\eta_{ant} = (\text{Directivity})/(\pi D/\lambda)^2 \quad (1)$$

In this case, the nominal directivity $(\pi D/\lambda)^2$ is 69.9 dB. The radius value chosen was that which maximized beam efficiency. The antenna has a half-power beamwidth

HPBW=0.07°. Beam efficiency is calculated as the fraction of power hitting the reflector that is contained in the beam defined as being 2.5 times as large as the HPBW [3]. In this case, the beam has a half angle of approximately 0.09°. Note that this definition of beam efficiency does not take into account spillover loss. The chosen radius value of 3λ produces the highest beam efficiency, $\eta=0.91$. Scanning is accomplished by tilting the main reflector. Tilting the main reflector by α degrees results in a scan angle $\theta \approx 2\alpha$. The main advantage of tilting the reflector instead of moving the feed element is that the scan angle is twice the angle of the tilt. If the feed were moved then the angle of scan would be equal to the angle that the feed was moved through. This is referred to as the mirror effect. Since for any reflector design, the scan loss increases as the feed moves away from the reflector's focal point, a significant reduction in scan loss is gained by tilting the reflector instead of shifting the feed.

Features of reflector P1 are:

1. Virtually no feed blockage due to the small size of the single element feed.
2. Depending on the exact arrangement, there is a lossy transmission distance between the feed and the receiver/transmitter. To avoid excessive transmission loss at high frequency applications (60 GHz or more), it may be necessary to connect the feed and the receiver/transmitter via a beam waveguide.
3. Because of the mirror effect, the scan range is twice as far as the conventional shifted feed design.

The radiation pattern for the on-axis beam is shown in Figure 4. The radiation pattern is calculated by a standard physical optics reflector code [4]. The directivity is 66.7 dB which includes the following losses:

Nominal directivity $(\pi D/\lambda)^2$	69.9 dB

Feed spillover loss	- 0.6 dB
Amplitude taper over reflector surface	- 2.6 dB
Directivity	66.7 dB

The above directivity, as usual, does not include the loss due to the feed transmission line. The 3 λ radius feed produces a pattern that has a null before the edge of the reflector (Fig. 5). This pattern results in a side lobe level of -31 dB. It is a commonly used rule of thumb that to maximize beam efficiency, the first feed pattern null should lie on the reflector edge, which is at $\theta_{max}=14.25°$. The first null lay on the reflector edge for feed radius a=2.3 λ. This value produces close to a maximum in beam efficiency (see Fig. 3).

This reflector has extremely good scan characteristics because of the long f/D and the mirror effect. The scan loss in only 0.6 dB at $\theta_0=8°$ (Fig. 6), corresponding to a 114 beamwidth scan. The sidelobe level does increase from -31 dB to -13 dB as expected. At a larger scan angle $\theta_0=20°$ (286 beamwidth scan), the scan loss is 5.1 dB and the pattern is badly distorted with a high shoulder (Fig. 7).

P2: Symmetric Parabolic Reflector with f/D=1

A drawback of P1 is its excessively long focal length (2,000 λ). Now let us reduce it by one half, giving a f/D=1. Then wide-angle scan is possible only if a cluster feed is used. A brief explanation of the cluster feed concept is in order at this point. The feed cluster consists of N identical elements with complex excitations

$$\mathbf{I}=[I_1, I_2,\ldots,I_N] \qquad (2)$$

We wish to determine **I** so that, when the beam position is at θ_0, a prescribed antenna parameter such as directivity, beam efficiency, or sidelobe level is optimized. To this end, let us introduce an element secondary pattern vector **E** such that

$$E(\theta_0)=[E_1(\theta_0), E_2(\theta_0),\ldots,E_N(\theta_0)] \qquad (3)$$

where $E_2(\theta_0)$, for example, is the co-polarization secondary pattern in direction θ_0 when element 2 is excited with

$$\begin{cases} I_2 = 1 \\ I_m = 0 \ , \quad \text{for all } m \neq 2 \end{cases} \tag{4}$$

There exist three methods for determining **I** in literature.

(i) Conjugate Field Matching [5-12]. The cluster excitation is simply set equal to the complex conjugate of $E(\theta_0)$, i.e.,

$$\mathbf{I}=[\mathbf{E}(\theta_0)]^* \tag{5}$$

Strictly speaking, such a choice of cluster excitation does not optimize any particular antenna parameter. For practical purposes, however, it does lead to nearly optimum directivity in most cases.

(ii) Optimum Directivity [13]. For a feed cluster with prescribed primary patterns and element locations, the directivity in direction θ_0 is optimized by choosing

$$\mathbf{I} = \bar{\bar{A}}^{-1} [\vec{E}(\theta_0)]^* \tag{6}$$

where $\bar{\bar{A}}$ is a N x N square matrix with elements

$$A_{mn} = \frac{1}{C}\int_0^{4\pi} (E_m E_n) \, d\,\Omega \tag{7}$$

where C is a normalization constant, and the integration is over 4π - radiation sphere. When the element spacing of the cluster is large (a few wavelengths), matrix $\bar{\bar{A}}$ is nearly an identity matrix. Then the solution in (6) reduces to that in (5).

(iii) Sidelobe Control [14,15]. The element secondary pattern vector **E** in (3) is normally calculated in a transmitting approach. By reciprocity, it can be equally calculated in a receiving approach when the reflector is illuminated by an incident plane wave from direction θ_0. In the receiving approach, there is an additional advantage that the amplitude of the plane wave can be tapered. It is found that the amount of taper controls the side lobe level of the final secondary pattern when the whole cluster is turned on.

Return now to P2 in Figure 1. A 19-element cluster feed is used. The individual elements are circular feeds with radius a=1.2 λ. This value is chosen to maximize directivity for a single feed scanned on-axis. This radius feed also produces a relatively good beam efficiency with η=0.88. The maximum beam efficiency was η=0.89, which is recorded for a feed with radius a=1.3λ. Sidelobes for the a=1.2 λ feed were -23 dB. This was not nearly the best possible sidelobes value, as a feed with radius a=1.5 λ had sidelobes that were -32 dB, along with η=0.87. The primary pattern of the a=1.2 λ circular waveguide feed was approximated by a $\cos^q\theta$ pattern with q=9.5. This value of q gave good sidelobe matching but the main lobe was 0.6 dB higher, with a maximum directivity of 68.9 dB. Spillover loss for the $\cos^q\theta$ feed pattern was 0.4 dB for a=1.2 λ. The cluster feed is used to help compensate for the higher scan losses that result from the lower f/D. At small scan angles only the center feed element has a relatively strong excitation (Fig. 8a). For an 8° scan (i.e. the reflector is tilted 4°) only two of the outer ring elements have significant excitations (Fig. 8b). This indicates that for scans under 8°, a 7-element cluster feed would probably work almost as well as a 19-element feed. When the reflector is tilted 10° for a scan angle of 20°, nearly all of the elements are excited (Fib. 8c). At θ_0=8°, the scan loss is 3.7 dB (Figs. 9, 10) and at θ_0=20°, the scan loss is 7.4 dB (Fig. 11). Very similar scan loss results were obtained with a=1.5 λ feed. This is not as good as the results for P1, but it is only a few dB worse. The advantage of P2 over P1 is that the focal length has been cut in half. The disadvantage is that a 19-element feed is much more complicated than a single element feed. For both of these center-fed designs the feed blockage is negligible.

Though design P2 has a higher scan loss at θ_0=20°than P1, the beam is less distorted (see Fig. 7 and Fig. 11). This is because at scan angles of this size, the cluster feed is able to form a much better beam pattern than a single element feed. For angles below θ_0=8°, there is no benefit to design P1 from using a cluster feed. However, scan loss could be reduced for large scan angles by using a cluster feed.

P3: Off-set Parabolic Reflector

Design P3 is an off-set parabolic reflector. Off-set height must be kept as small as possible to avoid intolerably high scan loss. Unfortunately, small offset leads to serious feed blockage. A possible way out of this dilemma is to use two identical reflector antennas: one for scanning up and one for scanning down as sketched in Fig. 1. The focal length is 2,000 λ and the reflector diameter is 1,000 λ, for a f/d=2. The off-set height is zero. In contrast to P1 and P2, this design utilizes electronic scanning. This means that a large feed array is used. Up to 19 elements are excited at any time. In order to cover a scan range from θ_0=0° to θ_0=8°, a semicircular array with a radius of 283 λ must be used. The individual feed element has a radius a=1.065 λ, meaning that roughly 65,000 feed elements are needed for the entire device. This feed size is chosen so that if the excited element is turned off and an adjacent element is turned on, then the beam is scanned 1 BW. This antenna has an on-axis directivity of 66.2 dB when a single element is turned on. The spillover loss is 3.5 dB. This is quite high since the feed element is so small. Note that this antenna has roughly the same as P1, which uses a feed that is three times larger in radius.

The advantage of electronic scan is well-known: it is fast and inertialess. However, electronic scanning forces the use of a feed array that has half the diameter of one of the reflectors used. Therefore, this design uses about a fourth as many elements as a phased array with the same aperture size. The savings in complexity are almost lost. In addition, the overall volume occupied by this antenna is much larger than that needed by the previous designs. For the on-axis beam, only the center element of the 19-element cluster is significantly excited (Figs. 12, 13), with a directivity of 67.3 dB. This is slightly higher than that excited by a single element feed (66.2 dB). Although excited with small excitations, the surrounding elements do help to reduce the spillover (Fig. 14).

Another problem is that the design puts a physical limitation on the maximum scanning angle. This is because the feed elements do not move. The previous designs could have been scanned farther than 20° if it had been desired. This design has a directivity of 67.3 dB, with BW=0.06° and sidelobes at -18 dB. Patterns were computed at scan angles $\theta_0=0°$and $\theta_0=8°$. The feed excitations used to get these results are shown in Figure 12. At ,$\theta_0=8°$ scan loss is already 6.3 dB (Fig. 13, 15). The advantages of electronic scanning are that it is quicker than mechanical scanning and that it will not upset the equilibrium of the spacecraft since there is no physical motion. Some of the drawbacks listed could be avoided by mechanically moving a 19-element feed cluster instead of electronically scanning. However, this design has much more scan loss at $\theta_0=8°$ than designs P1 and P2.

III. Dual Reflector Antennas

C1: Cassegrain Reflector with Tilted Main Reflector

Design C1 is a dual-reflector Cassegrain antenna. The main reflector is parabolic with a focal length of 2,000 λ and a diameter of 1,000 λ for a f/D=2. A Cassegrain antenna may be considered as a folded version of a parabolic reflector. In many applications, it is desirable to reduce the length of the antenna and to place the feed directly behind the vertex of the main reflector. These are the reasons for folding the antenna. With f/D=2 for the present case, it is not possible to fold the feed close to the vertex without either excessive spillover loss or an excessively large subreflector or even both. In the present design (Fig. 2), the hyperbolic subreflector has a diameter of 115 λ and is located 1,650 λ from the main reflector vertex. The circular feed has a radius a=1.5 λ and is located 1,300 λ from the main reflector vertex. This feed size is chosen to produce 10 dB edge taper on the subreflector. Directivity for this design is 67.1 dB, with BW=0.06° and a -18 dB sidelobe level. Scanning is accomplished by tilting the main reflector. The scan angle $\theta_0 \approx 2\alpha_1$, where α_1 is the angle that the main reflector is tilted. The performance of C1, shown in Figures 14, 16 and 17, is similar to that of P1, the unfolded version of C1. The use of the subreflector does change the aperture taper. Consequently, the sidelobes of C1 and P1 are different.

C2: Cassegrain Reflector with Tilted Subreflector

Design C2 has the same geometry as C1. Scanning is accomplished by tilting the subreflector instead of the main reflector. Due to the substantial difference in size, tilting the subreflector is much easier mechanically than tilting the main reflector. Electrically, however, tilting the subreflector for wide-angle scan is not feasible because

(i) the subreflector must be tilted by a much larger angle α_2 in order for the beam to scan. The approximate relation between the two angles is

$$\theta_0 \approx \alpha_2/M$$

where $M=D_{main}/D_{sub}$=magnification factor.

(ii) When the subreflector is tilted by a large angle, there is an excessive spillover loss.

In this case M=8.7. The scan loss is quite high. At θ_0=1.75°, the scan loss is 6.6 dB (Fig. 18). At θ_0=3.32°, the scan loss is 36.3 dB. This would seem to indicate that tilting the subreflector is not a viable option for wide-angle scan.

C3: Cassegrain Reflector with Both Reflectors Tilted

Design C3 has the same geometry as C1 and C2. Scanning is accomplished by tilting both the subreflector and the main reflector. The idea is to use the main reflector for coarse scanning, and to use subreflector tilting for local scanning within a small angular region. The scan angle $\theta_0=2(\alpha_1+\alpha_2/M)$. Given α_1 and α_2, the scan loss can be obtained by looking at the results for C1 and C2.

IV. Conclusions

We have studied the wide-angle scan ability of the six reflector antennas shown in Figures 1 and 2. All reflectors have a circular diameter of 1,000 λ and f/D=2, except that P2 has a shorter focal length f/D=1. The scan loss is summarized in Figure 19. Conclusions are listed below.

(i) For mechanical scan by tilting reflectors, the best system is P1. The scan loss at $\theta_0=8°$ (114 beamwidth) is only 0.6 dB (Figs. 5, 6). The sidelobe level for the $\theta_0=8°$ position is increased considerably (from -31 dB to -13 dB). This problem may be alleviated by using the cluster compensation method [10, 12, 14], and needs to be studied.

(ii) The folded version of P1 is the Cassegrain antenna C1. In the present study, the feed is taken to be a single open-ended circular waveguide with a=3λ. As a consequence, the amount of folding achieved is small (the length reduction is from 2,000 λ to 1,650 λ). If more folding is desired, a much larger feed should be used.

(iii) To shorten the f/D from 2 to 1, reflector P2 must rely on a cluster feed to reduce its scan loss. The excitation of the cluster varies as the beam scans. The scan performance of P2 is still not as good as that of P1, indicating that a 19-element cluster cannot totally compensate the reduction in f/D.

(iv) Tilting the subreflector of a Cassegrain antenna can only achieve a small scan (about ±15 BW). It can be used in conjunction with the electrically more effective but mechanically more costly main reflector tilting to achieve a small local scan.

(v) Among the six antennas, only the off-set parabolic reflector P3 scans the beam electronically. The price is steep since (a) there are two identical antennas, one to scan up and one to scan down, (b) the feed has 65,000 elements, and (c) with a 19-element feed cluster, the scan loss at $\theta_0=8°$ is 6.3 dB. Without the cluster, the loss is 15.4 dB. This is much worse than the 0.6 dB loss for P1.

REFERENCES

[1] Y. Rahmat-Samii, "Reflector Antennas" *Antenna Handbook*, Eds. Y. T. Lo and S. W. Lee, Van Nostrand Reinhold Company, Inc., pp. 15-61, 1988.

[2] C. C. Hung and R. Mittra, "Wide-angle scanning for reflector antennas," *URSI Sym. Digest*, pp. 75, 1983.

[3] J. C. Shiue and L. R. Dod, Chapter 22 of *Antenna Handbook* (see [1]).

[4] P. T. Lam, S. W. Lee, C. C. Hung, and R. Acosta, "Strategy for reflector pattern calculation: Let the computer do the work," *IEEE Trans. Antennas & Propagation*, Vol. 34, pp. 592-594, 1986.

[5] H. C. Minnett and B. MacA. Thomas, "Fields in the image space of symmetrical focusing reflectors," *Proc. IEEE*, Vol. 115, pp. 1419-1430, 1968.

[6] A. W. Rudge and M. J. Withers, "Design of flared-horn primary feeds for parabolic reflector antennas," *Proc. IEEE*, Vol. 117, pp. 1741-1749, 1970.

[7] H. H. S. Luh, "On the radiation pattern of a multibeam antenna," *IEEE Trans. Antennas & Propagation*, Vol. AP-24, pp. 101-102, 1976.

[8] Y. Rahmat-Samii and S. W. Lee, "Applications of the conjugate field matching technique to reflector antennas - a critical review," *URSI Digest*, pp. 85, 1981.

[9] A. V. Mrstik and P. G. Smith, "Scanning capabilities of large parabolic cylinder reflector antennas with phased-array feeds," *IEEE Trans. Antennas & Propagation*, Vol. AP-31, pp. 756-763, 1983.

[10] C. C. Hung and R. Mittra, "Secondary pattern and focal region distribution of reflector antennas under wide-angle scanning," *AP Digest*, Vol. AP-31, pp. 463-470, 1983.

[11] H. Y. Jong, B. Popovich, W. R. Adams, and A. W. Love, "Analysis of paraboloidal reflector fields under oblique incidence," *AP Digest*, Vol. 1, pp. 305-308, 1984.

[12] R. J. Acosta, "Compensation of reflector surface distortion using conjugate field matching," *AP-S International Symp. Digest*, Vol. 1, pp. 259-262, 1986.

[13] P. T. Lam, S. W. Lee, D. C. D. Chang, and K. C. Lang, "Directivity optimization of a reflector antenna with cluster feeds: A closed form solution," *IEEE Trans. Antennas & Propagation*, Vol. AP-33, pp. 1163-1174, 1985.

[14] R. Acosta, A. Zaman, E. Bobinsky, A. R. Cherrette, and S. W. Lee, "Case study of active array feed compensation with sidelobe control for reflector surface distortion," *AP-S International Symp. Digest*, Vol. 2, pp. 863-867, 1988.

[15] R. Acosta, "Active feed array compensation for reflector antenna surface distortion," NASA TM100826, NASA Lewis Research Center, Cleveland, OH, June 1988.

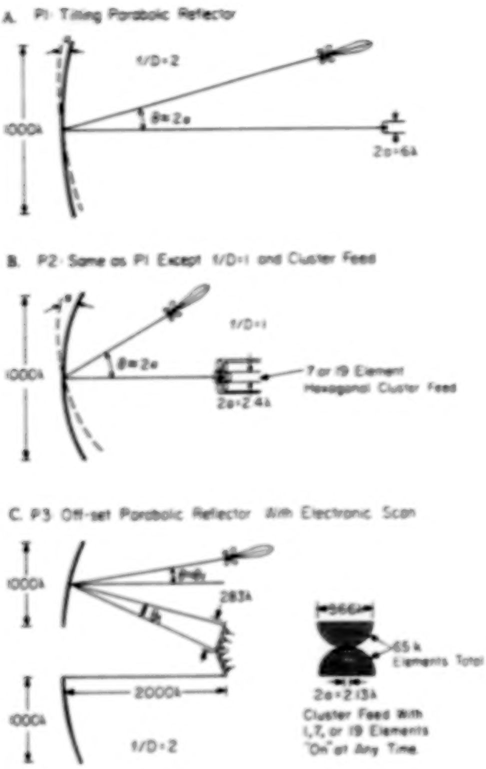
A. P1 Tilting Parabolic Reflector

B. P2 Same as P1 Except f/D=1 and Cluster Feed

C. P3 Off-set Parabolic Reflector With Electronic Scan

f/D=2
1000λ
θ=2α
2a=6λ
f/D=1
1000λ
θ=2α
2a=2.4λ
7 or 19 Element Hexagonal Cluster Feed
1000λ
283λ
366λ
65 λ Elements Total
2000λ
1000λ
f/D=2
2a=2.13λ
Cluster Feed With 1,7, or 19 Elements "On" at Any Time

Figure 1. Single Reflector Antenna System

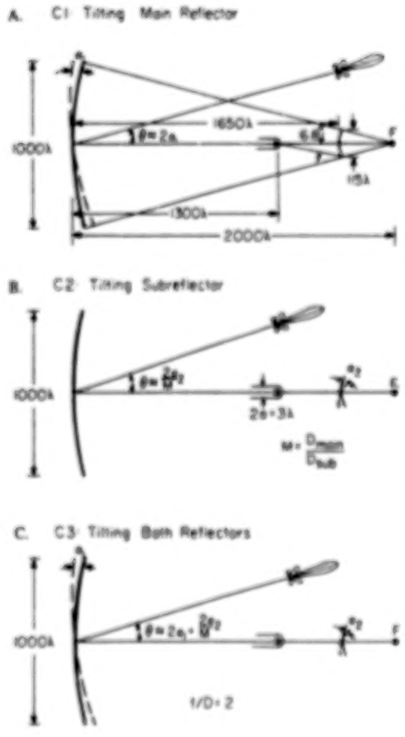
A. C1 Tilting Main Reflector

B. C2 Tilting Subreflector

C. C3 Tilting Both Reflectors

1000λ
1650λ
θ=2α
6.6°
F
15λ
1300λ
2000λ
1000λ
θ=$\frac{2}{M}\alpha_2$
2a=3λ
α_2
F
M=$\frac{D_{main}}{D_{sub}}$
1000λ
θ=2α$_1$+$\frac{2}{M}\alpha_2$
α_2
F
f/D=2

Figure 2. Cassegrain Dual Reflector Antenna Systems

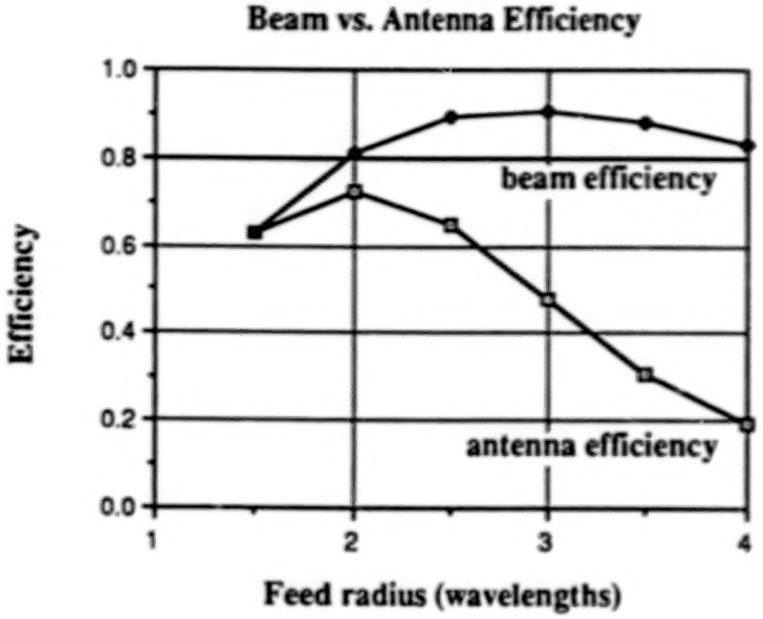

Figure 3. Beam efficiency and antenna efficiency for P1 symmetrical parabolic reflector as a function of feed radius. The feed is an open-ended circular waveguide.

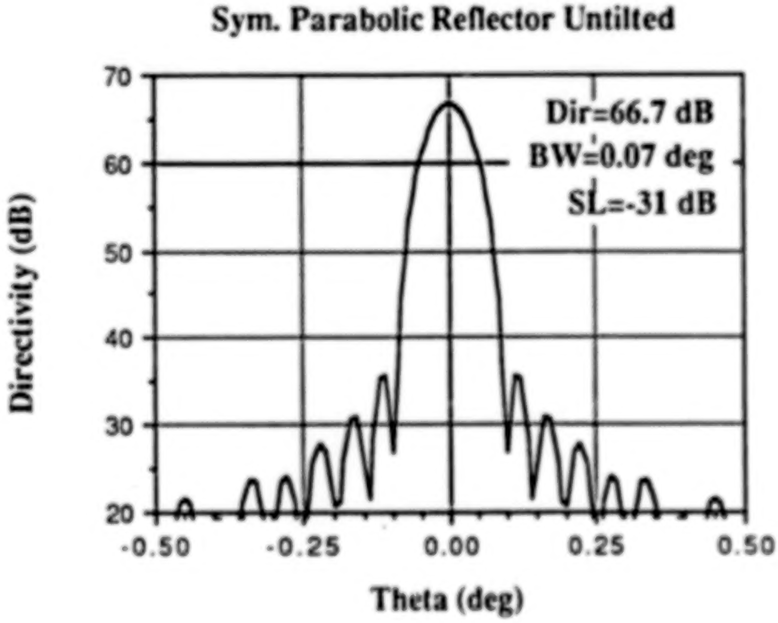

Figure 4. P1 symmetric parabolic reflector far-field pattern for 0° scan.

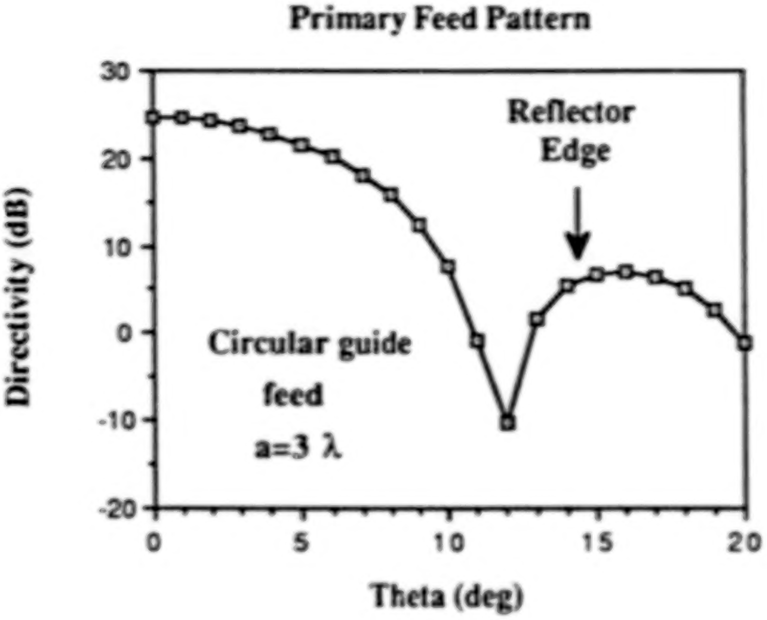

Figure 5. Primary feed pattern for P1 symmetrical parabolic reflector. The feed is an open-ended circular waveguide.

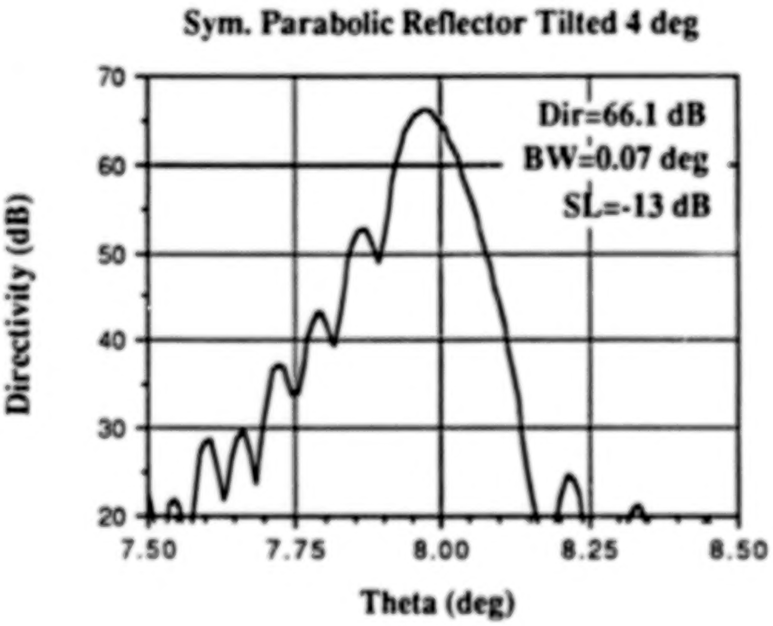

Figure 6. P1 symmetrical parabolic reflector far-field pattern for 8° scan (114 beamwidth scan).

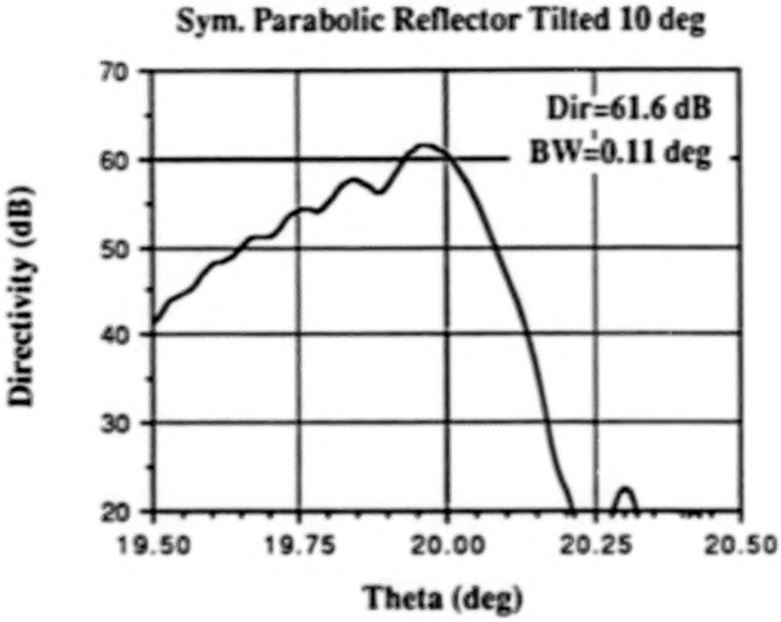

Figure 7. P1 symmetrical parabolic reflector far-field pattern for 20° scan (286 beamwidth scan).

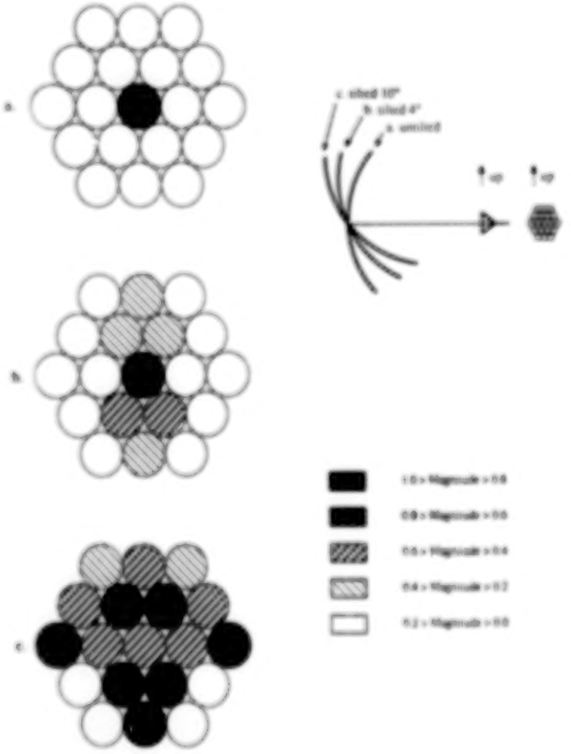
a.
b.
c.
c. tilted 10°
b. tilted 4°
a. untilted
up
up
1.0 > Magnitude > 0.8
0.8 > Magnitude > 0.6
0.6 > Magnitude > 0.4
0.4 > Magnitude > 0.2
0.2 > Magnitude > 0.0

Figure 8. Relative excitations for the 19-element feed cluster in P2 symmetrical parabolic reflector: (a) beam scanned 0°, (b) beam scanned 8°, and (c) beam scanned 20°.

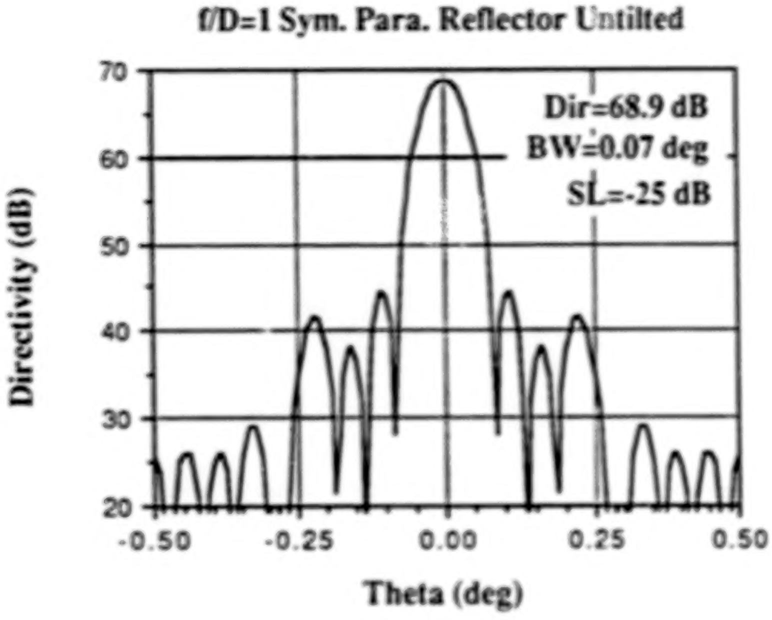

Figure 9. P2 symmetric parabolic reflector far-field pattern for 0° scan.

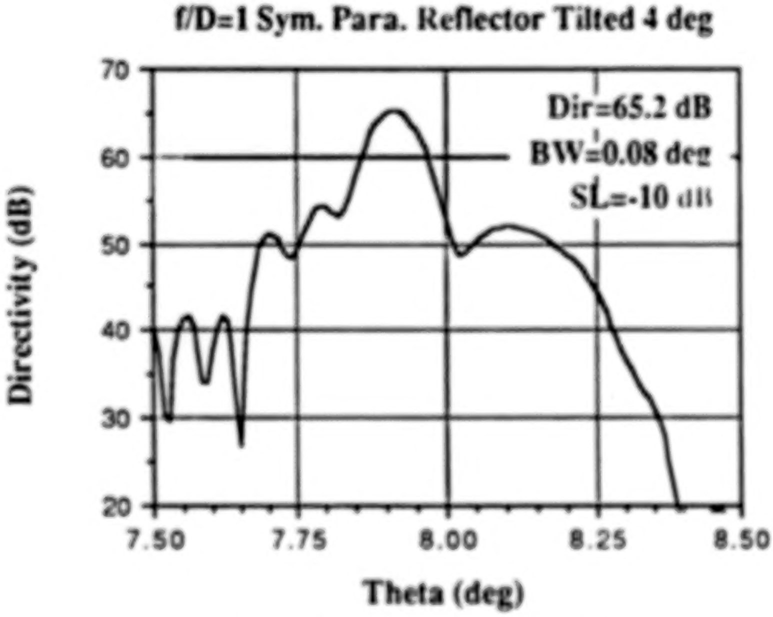

Figure 10. P2 symmetric parabolic reflector far-field pattern for 8° scan.

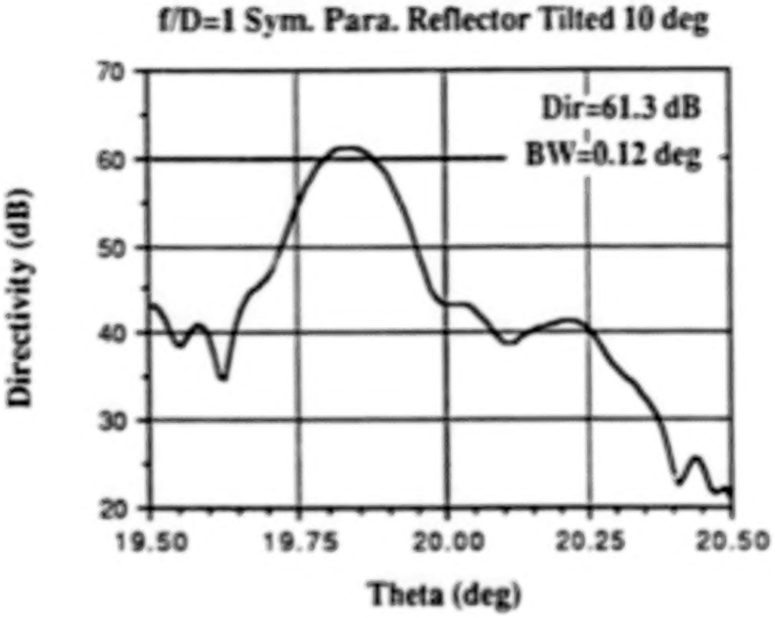

Figure 11. P2 symmetric parabolic reflector far-field pattern for 20° scan.

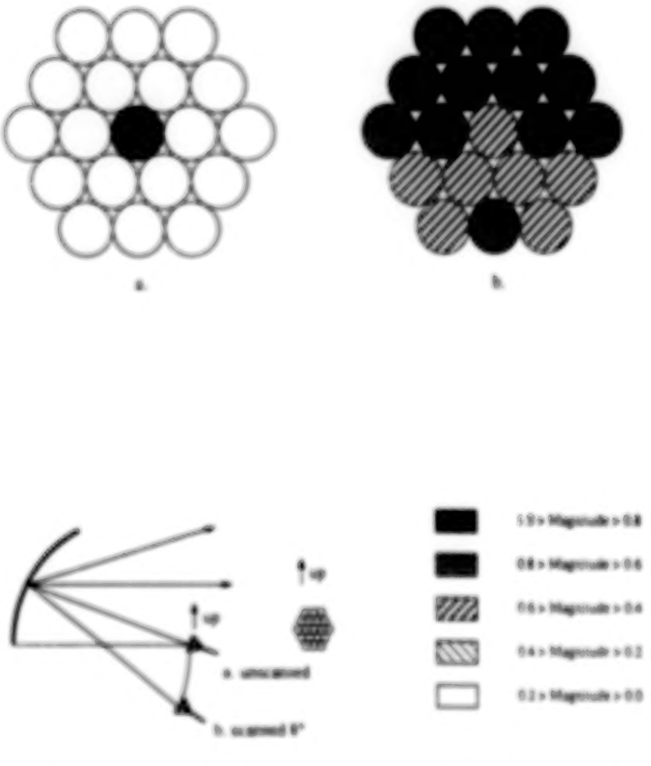
a.
b.
up
up
a. unscanned
b. scanned 8°
1.0 > Magnitude > 0.8
0.8 > Magnitude > 0.6
0.6 > Magnitude > 0.4
0.4 > Magnitude > 0.2
0.2 > Magnitude > 0.0

Figure 12. Relative feed excitations for the P3 off-set parabolic reflector.
a. Beam unscanned. b. Beam scanned 8°.

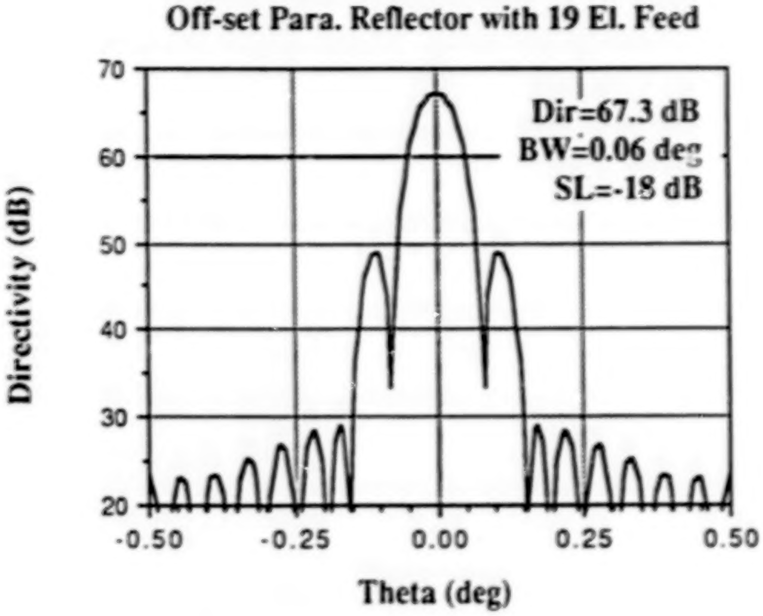

Figure 13. P3 off-set parabolic reflector far-field pattern for 0° scan.

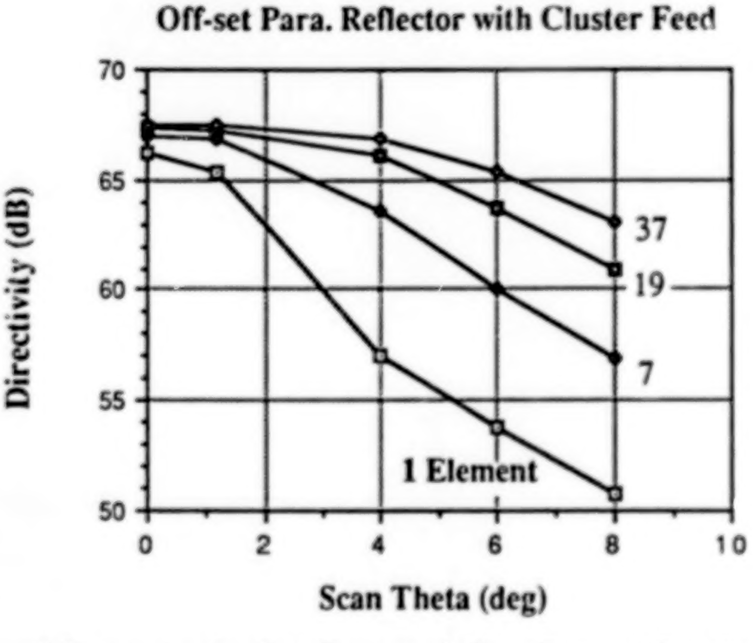

Figure 14. Directivity vs. scan for the off-set parabolic reflector. Note that as the number of cluster elements increases, so does the directivity.

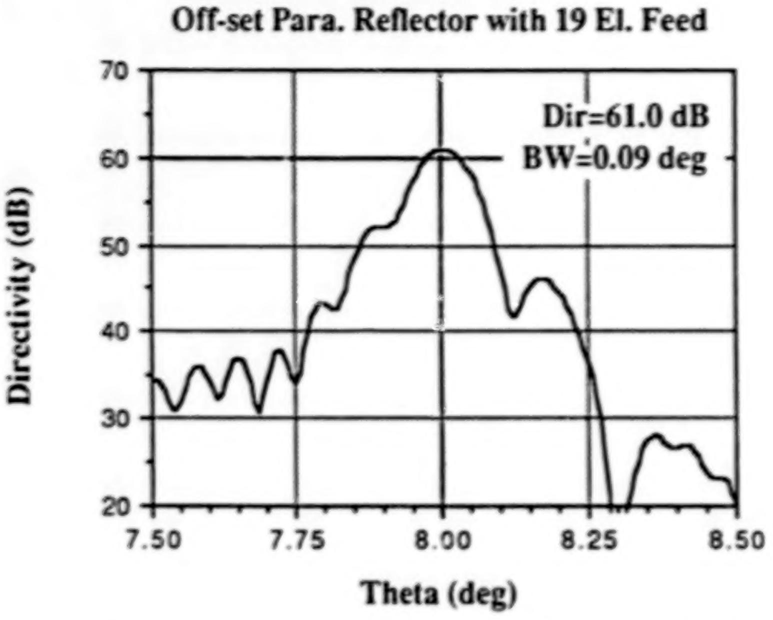

Figure 15. P3 off-set parabolic reflector far-field pattern for 8° scan.

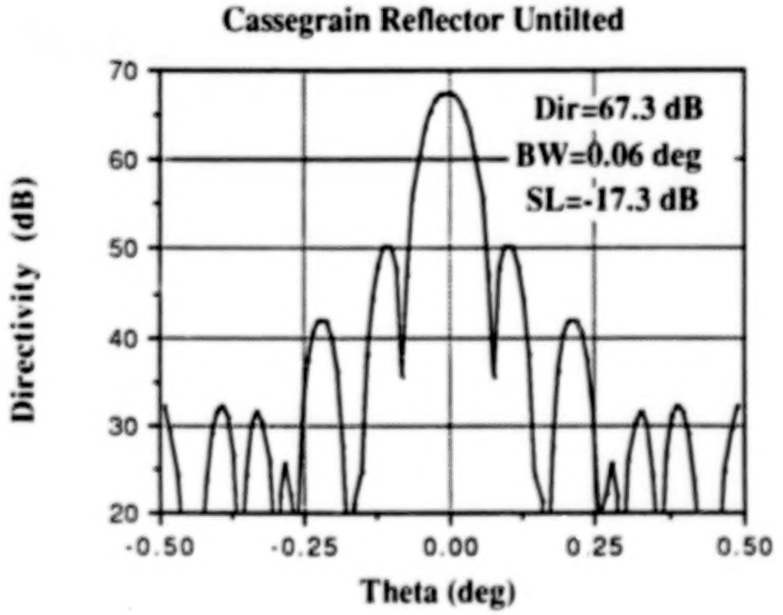

Figure 16. Symmetrical cassegrain reflector far-field pattern for unscanned beam. C1, C2, and C3 have identical patterns for this case.

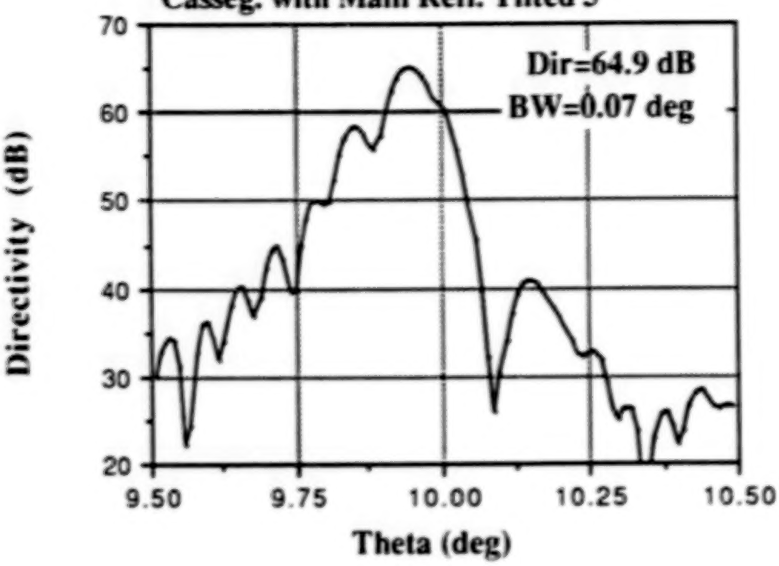

Figure 17. C1 symmetrical cassegrain reflector far-field pattern with main reflector tilted to produce 9.96° scan.

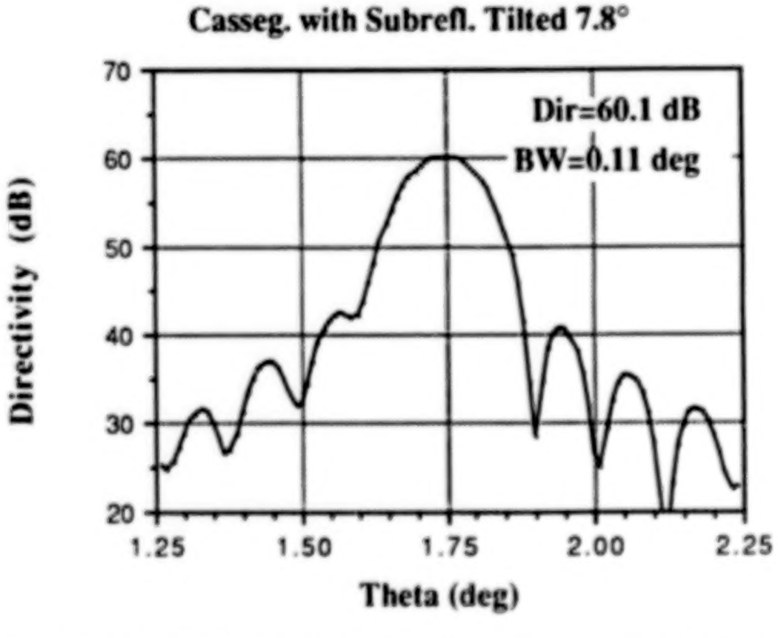

Figure 18. C2 symmetric cassegrain reflector far-field pattern with subreflector tilted to produce 1.75° scan.

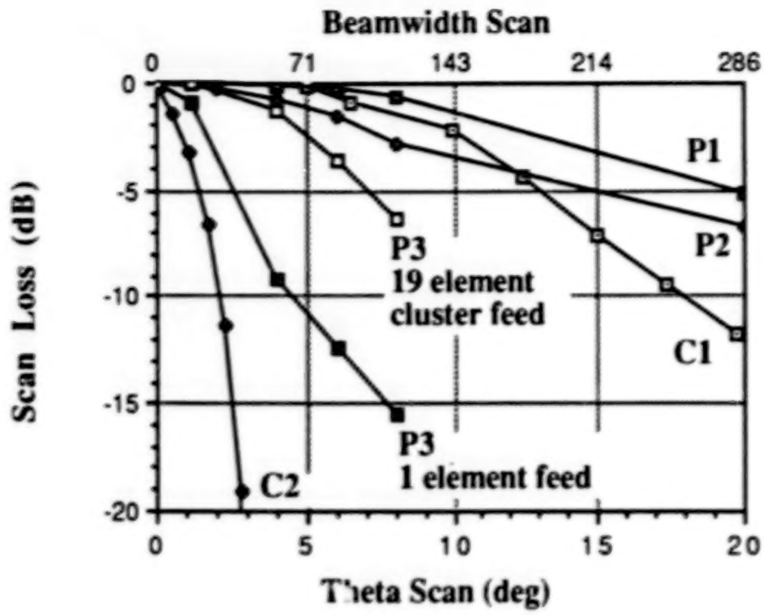

Figure 19. Scan loss of the six reflector antennas shown in Figures 1 and 2.

ARRAYS FOR SPACE APPLICATIONS[*]

Harvey K. Schuman,
Paul Antonik, and
Carmen Malagisi
Atlantic Research Services Corporation
Rome, New York

---

[*] Original figures not available at time of publication.

EXISTING ARRAY CONCEPTS FOR LARGE FOV

The following pictures are of concepts that were studied for application in Space Based Radar (SBR) systems. These antenna systems were for low Earth orbit and required large fields of view (FOV). They included both space-fed and corporate-fed arrays.

ARRAY FOR SPACE APPLICATION

- WHY ARRAY?
  - ELECTRONIC SCANNING - BEAM AGILITY
  - ADAPTIVE BEAM CONTROL
    - LOW SIDELOBES
    - SURFACE CORRECTIONS
  - MORE TOLERANT TO SURFACE ERRORS THAN REFLECTORS

EXISTING ARRAY CONCEPTS
LARGE FOV

- SPACE-FED ARRAYS
  - WIRE WHEEL
  - ROLL OUT
- CORPORATE-FED ARRAYS
  - FOLD-OUT

WIRE-WHEEL CONCEPT

This figure is of a wire-wheel configuration with a diameter of 70 meters and a focal length/diameter (F/D) of 1.5. The cutaway view of the lens shows the dipoles on either side of a T/R* module. This concept was proposed by Grumman Aerospace Corporation.

*T/R, transmit and receive

SPACE-FED PHASED ARRAY-SBR ANTENNA

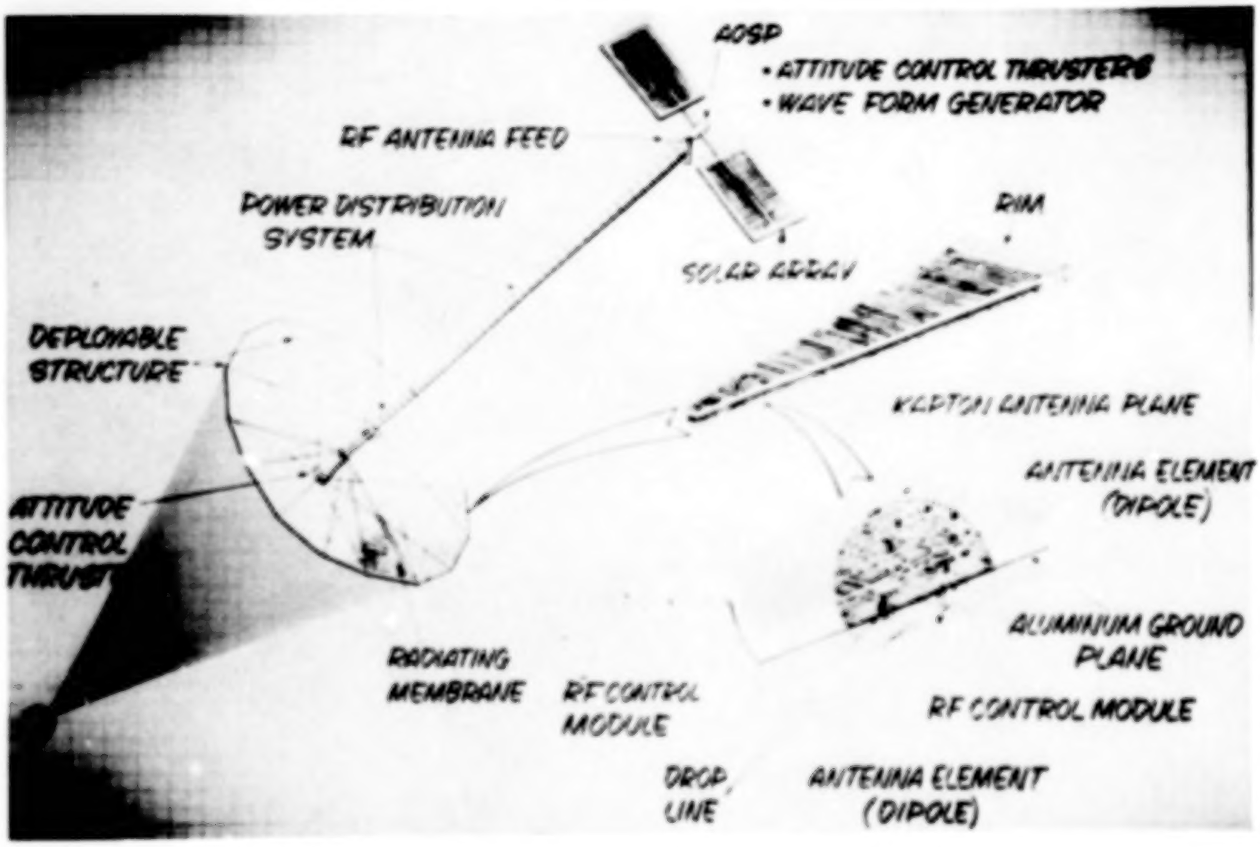
AOSP
• ATTITUDE CONTROL THRUSTERS
• WAVE FORM GENERATOR
RF ANTENNA FEED
POWER DISTRIBUTION SYSTEM
RIM
SOLAR ARRAY
DEPLOYABLE STRUCTURE
KAPTON ANTENNA PLANE
ANTENNA ELEMENT (DIPOLE)
ATTITUDE CONTROL THRUST
RADIATING MEMBRANE
RF CONTROL MODULE
ALUMINUM GROUND PLANE
RF CONTROL MODULE
DROP LINE
ANTENNA ELEMENT (DIPOLE)

WINDOW SHADE CONCEPT

This figure shows a window shade concept of a space-fed array that is 60 meters by 40 meters and has a focal distance of 40 meters. This configuration has no center mast aperture blocking. This concept was proposed by Grumman Aerospace Corporation.

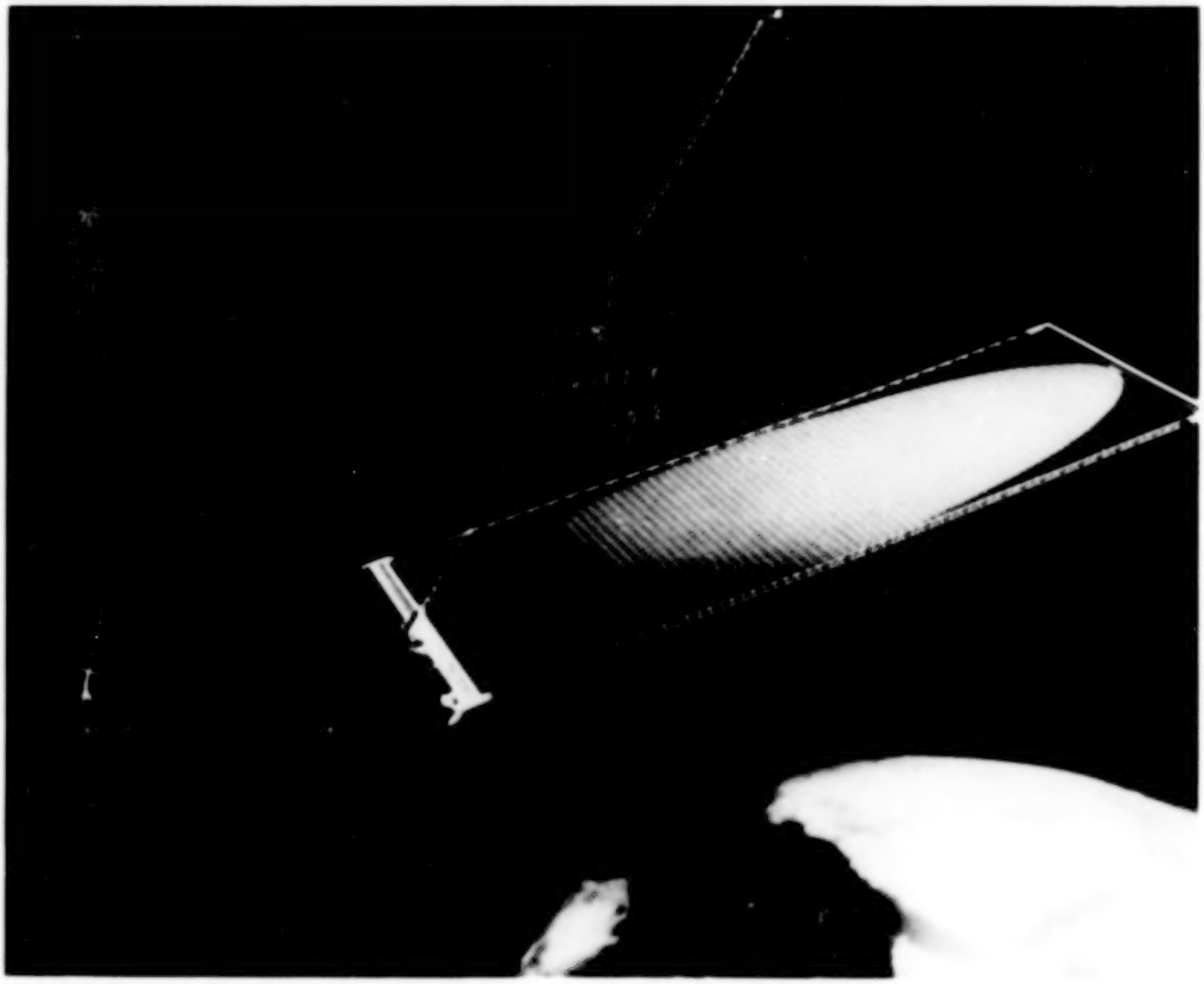

WINDOW SHADE CUTAWAY VIEW

This figure shows a cutaway view of the lens with dipoles, ground screen, and T/R modules. This concept was also proposed by Grumman Aerospace Corporation.

SPACE-FED PHASED ARRAY-SBR ANTENNA

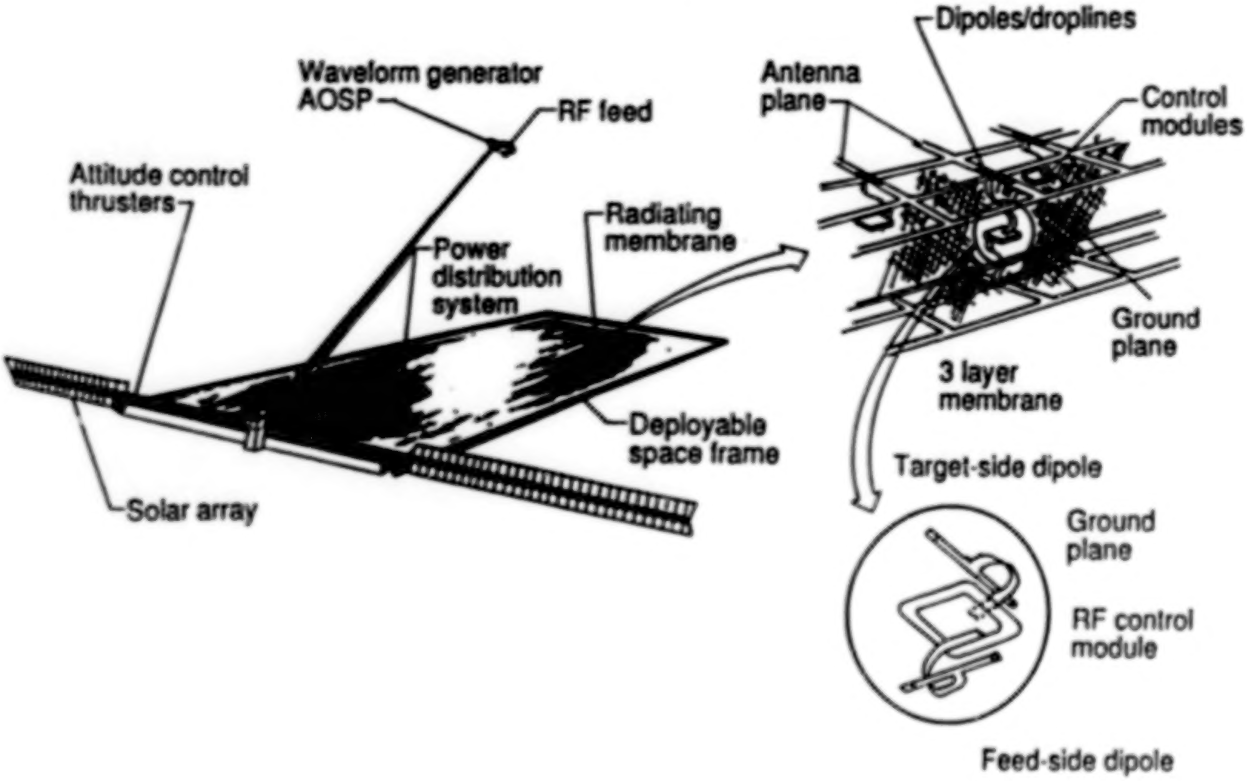
Waveform generator
AOSP
RF feed
Attitude control thrusters
Power distribution system
Radiating membrane
Solar array
Deployable space frame
Dipoles/droplines
Antenna plane
Control modules
Ground plane
3 layer membrane
Target-side dipole
Ground plane
RF control module
Feed-side dipole

SEASAT CONCEPT

This picture is a concept of SEASAT with a fixed beam corporate-fed array of microstrip antenna elements, similar to the one for the SIR-A antenna shown on the next page. This antenna is a foldout panel deployment configuration whose concept originated at Ball Aerospace Corporation.

SEASAT-A

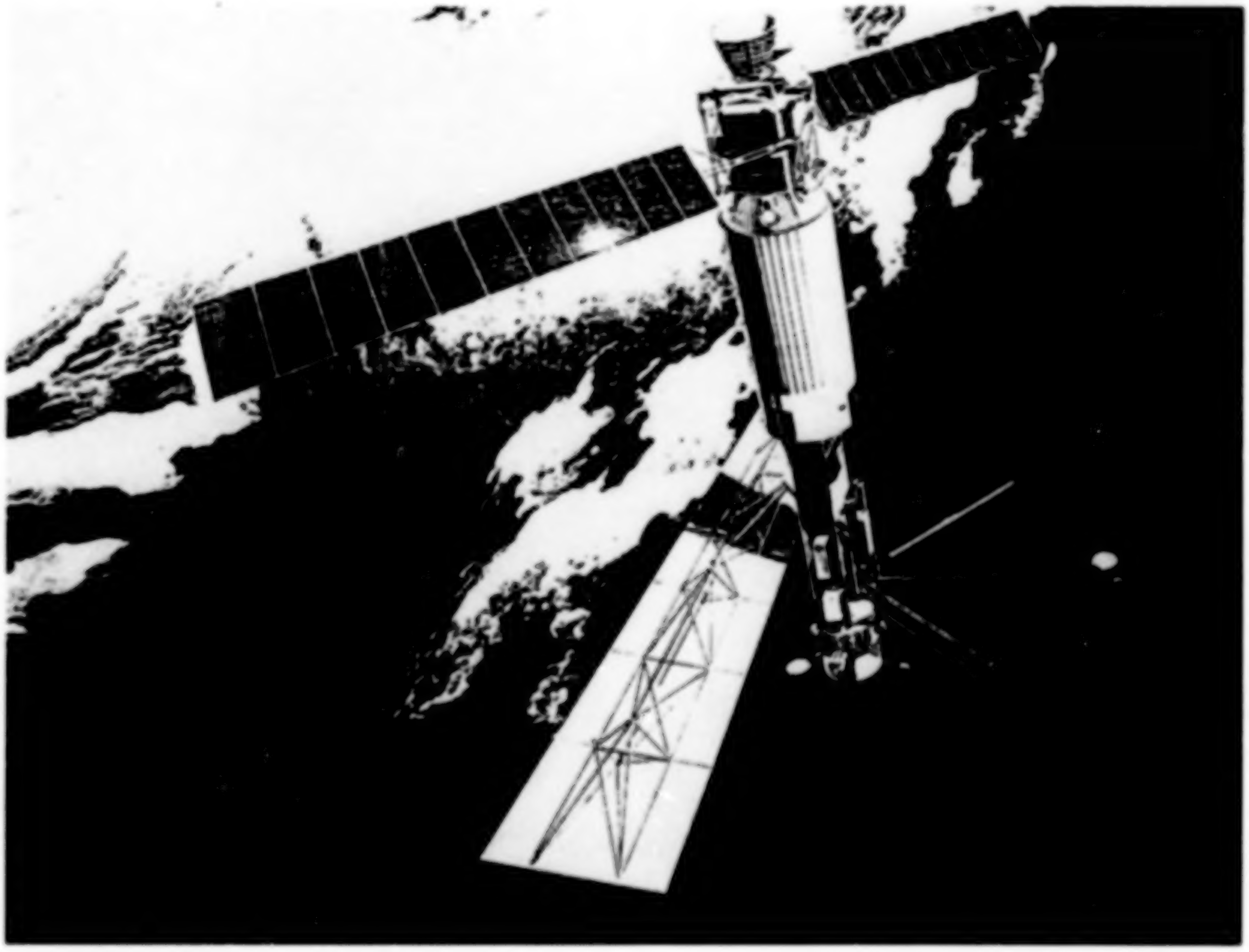

SIR-A ANTENNA

Shown below is the SIR-A antenna flown on the shuttle. This antenna is a foldup microstrip fixed-beam array.

SHUTTLE BAY SAR ANTENNA (SIR-A)

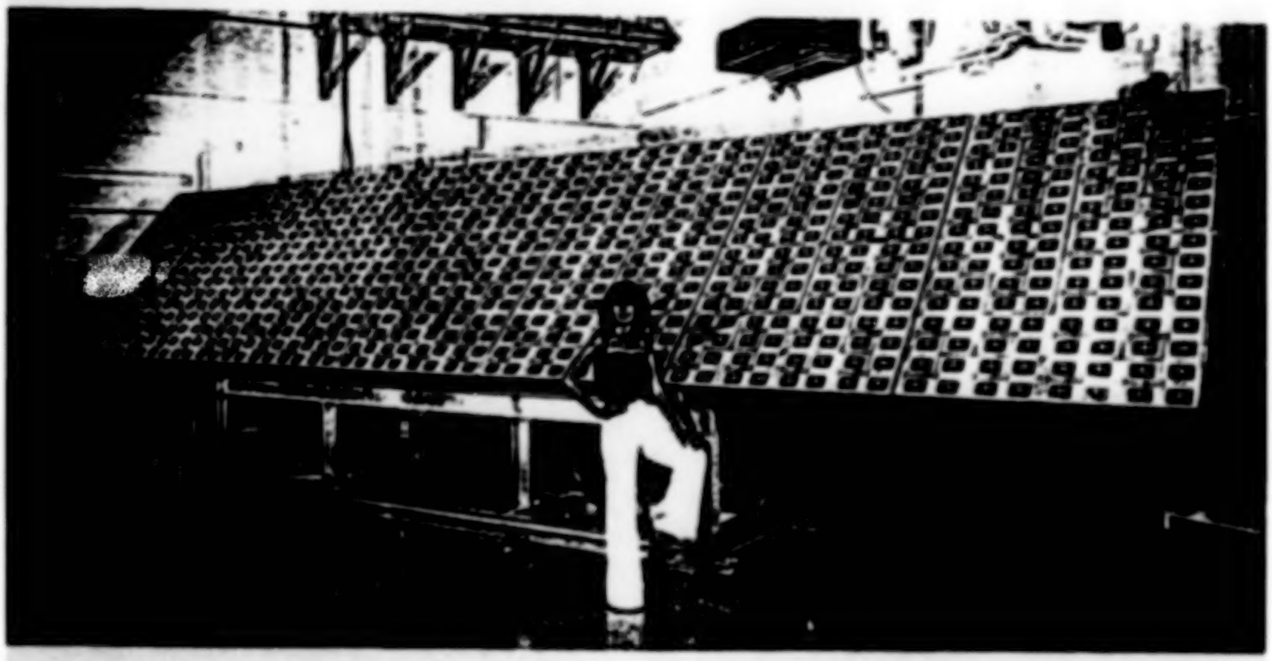

- L-BAND, SAR
- EARTH RESOURCES
- FIRST SHUTTLE EXPERIMENT
- 33 DB GAIN

CORPORATE FED PHASED ARRAY CONCEPT

This figure shows a foldout concept of a microstrip phased array for Space Based Radar (SBR). Both the deployed and stowed configurations are shown. The array is approximately 13 meters wide by 64 meters long. This concept is proposed for SBR by Ball Aerospace Corporation.

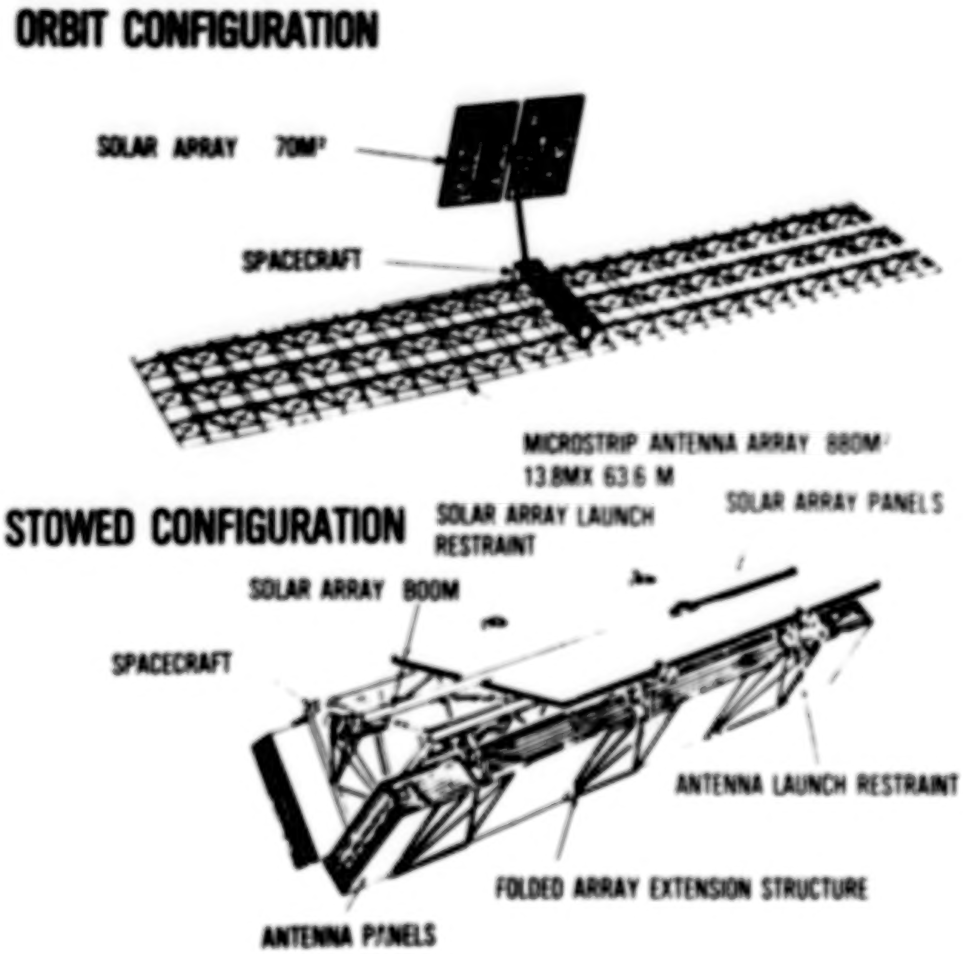
ORBIT CONFIGURATION
SOLAR ARRAY 70M²
SPACECRAFT
MICROSTRIP ANTENNA ARRAY 880M²
13.8MX 63.6 M
STOWED CONFIGURATION
SOLAR ARRAY LAUNCH RESTRAINT
SOLAR ARRAY PANELS
SOLAR ARRAY BOOM
SPACECRAFT
ANTENNA LAUNCH RESTRAINT
FOLDED ARRAY EXTENSION STRUCTURE
ANTENNA PANELS

FOLDOUT DEPLOYMENT

Constrained Feed:

A corporate fed array uses elements of an array with each output phase adjusted for collimating the received energy from a particular direction. The output of each element is then combined through a series of power combiners as shown to a single output.

Space Feed:

A space fed array uses elements of an array with each output phase adjusted for collimating the received energy from a particular direction. The output of each element is then used to feed a corresponding element on the back side of the array (bootlaced lens array). The phase shifters in the bootlaced lens array are also used to produce a converging circular wavefront to converge at a feed for single output.

Each of these antenna system concepts requires prime power distribution to each phase shifter module. All modules require control signals from some central beam steering command center. These modules produce heat and, therefore, temperature control will be required, especially for space application. These modules could also have transmitters and or receivers in them.

CONSTRAINED FEED

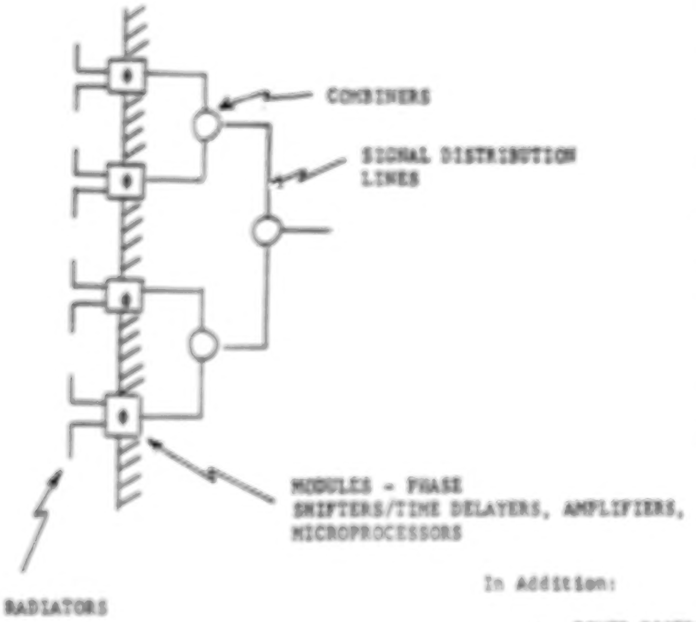
COMBINERS
SIGNAL DISTRIBUTION LINES
MODULES - PHASE SHIFTERS/TIME DELAYERS, AMPLIFIERS, MICROPROCESSORS
RADIATORS

SPACE FED

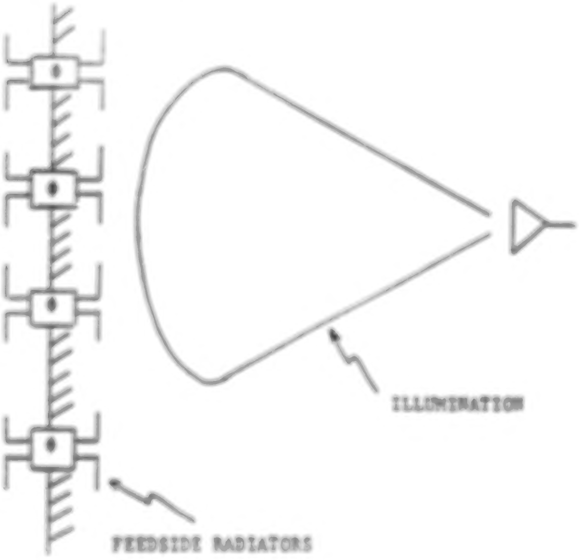
ILLUMINATION
FEEDSIDE RADIATORS

In Addition:

- POWER DISTRIBUTION
- TEMPERATURE CONTROL
- MODULE CONTROL

LOSS VERSUS PHYSICAL DEFORMATION

The three curves on this graph, (1) Reflector, (2) Corp-Fed Array, and (3) Space-Fed Array show the loss in gain as a function of edge deflection in wavelengths and in centimeters for each respective frequency from 5 to 200 GHz as shown. The curves clearly show that the surface of a corporate fed array is twice as tolerant as a reflector antenna system and the space-fed array is 10 times more tolerant than the corporate fed array. The reason for this is that in the space-fed array, any deformation of the array in the plane normal to the array causes a delay or advance of phase with respect to a plane wave and on the opposite side a corresponding advance or delay is naturally created. Hence, the deformation is automatically compensated for with deformations up to about one wavelength for 0.5 dB loss in gain. Also, the flat surface of a lens would be much easier to maintain flat than to maintain a reflector surface parabolic.

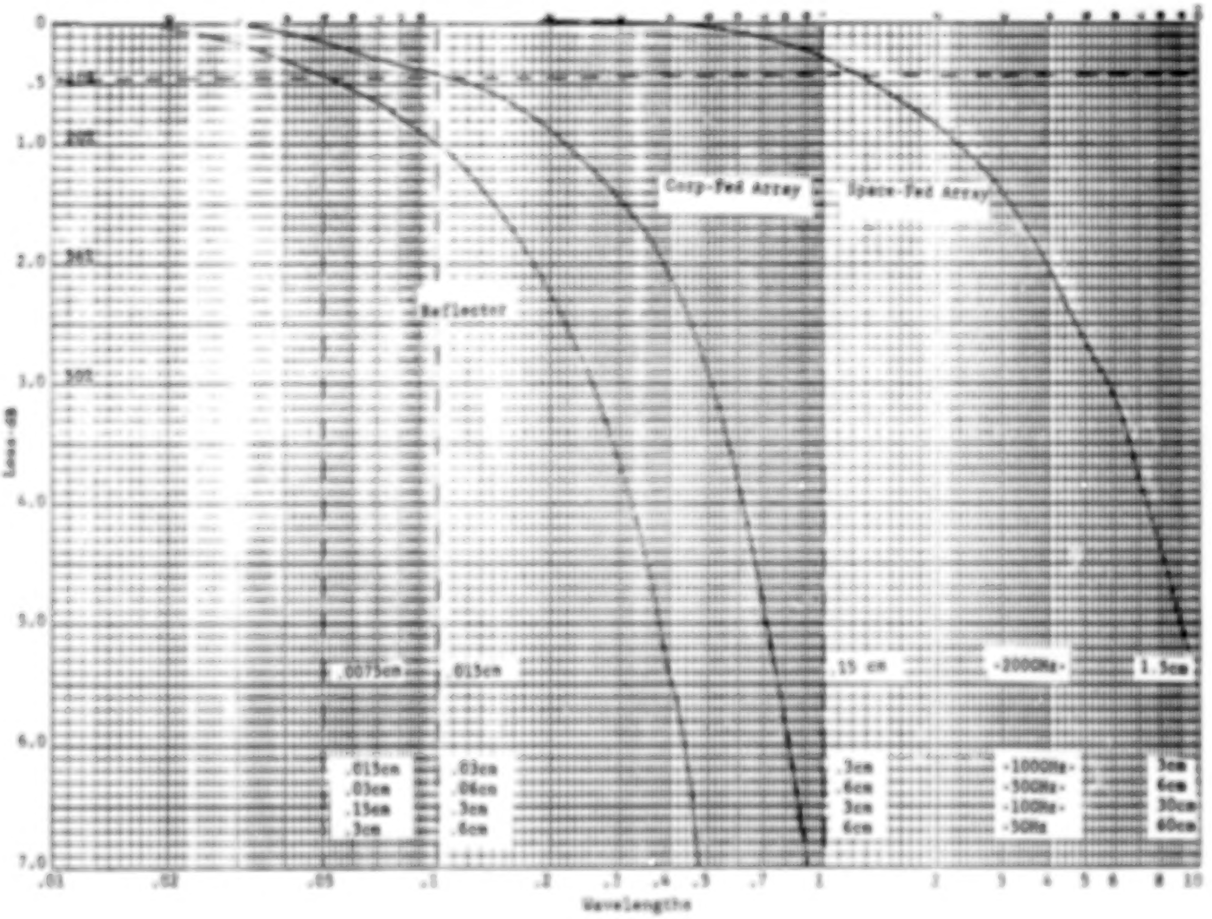

EARTH SCIENCES GEOSTATIONARY PLATFORM ANTENNA REQUIREMENTS

The requirements specified on this chart are the general specifications the authors have gleaned from previous presentations by other organizations. They are not necessarily the requirements for ESGP. These were requirements used to size a sample antenna system and to present possible concepts that could be used to meet these performance requirements.

- GEOSYNCHRONOUS ORBITS
    - SCAN ± 9 DEGREES
- FREQUENCY 5-200GHz
- PASSIVE RECEIVE ONLY (RADIOMETRIC)
- BEAMWIDTH <0.1 DEGREE
- GAIN >60DBI
- SIDELOBES <0DBI

GRATING LOBE LIMITATION ON FOV

This graph shows the required element spacing of a phased array as a function of scan angle such that no grating lobe enters the scan cone (FOV). As an example, for geosynchronous orbit (23,500 mm altitude) a scan volume or FOV of plus and minus nine (9) degrees would require approximately a three (3) wavelength element spacing.

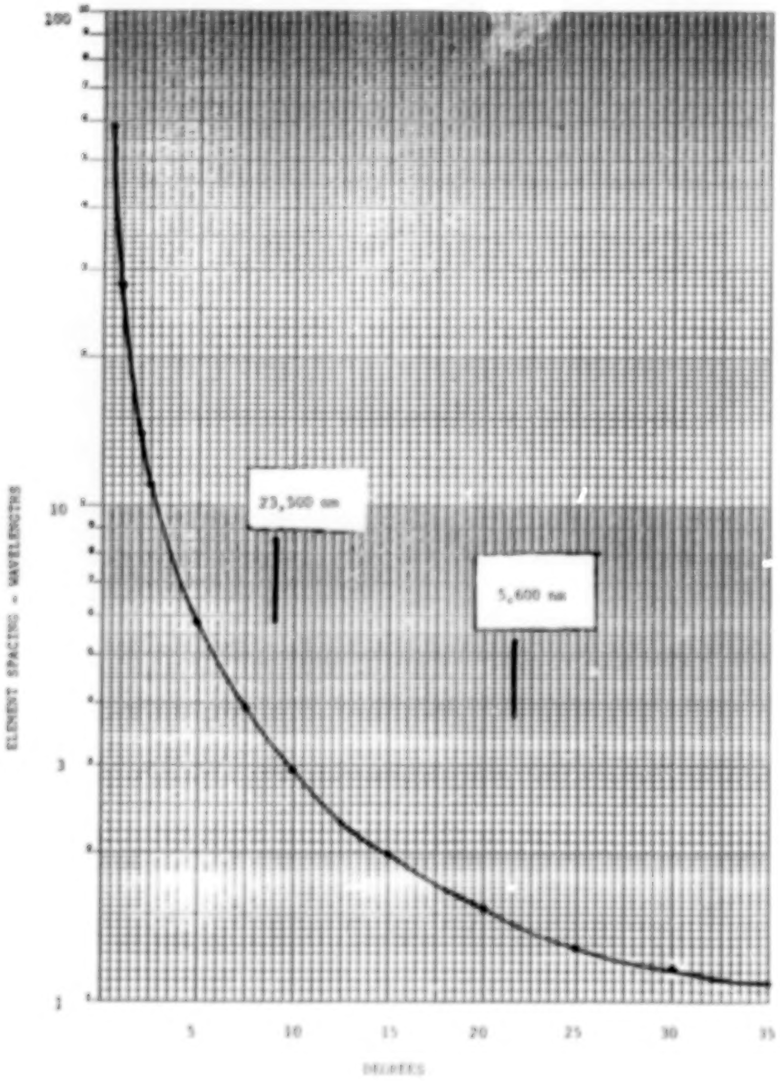

PHASE SHIFTER SAVINGS DUE TO SUBARRAYING

The area of a subarray is given by the product of the number of elements in the subarray (subarray element size) and the interelement area. An optimum interelement area was defined as the maximum for which no part of a subarray pattern grating lobe enters the visible range. With this choice of interelement area and the criteria that the interelement area be uniform throughout the array, the percent reduction in required number of phase shifters resulting from nonoverlapping subarrays is given by the curves shown in the figures. The percent reduction is a function of maximum scan angle as well as subarray element size because the nonsubarrayed interelement spacing decreases with maximum scan angle and the subarrayed "optimum" interelement spacing is independent of maximum scan angle.

With nonoverlapping subarrays the gain gradually deteriorates with increasing scan. The maximum acceptable gain loss and maximum scan angle essentially define the field of view. Gain loss curves of .5 dB, 1 dB and 3 dB are shown in the figure. For example, a field of view = ±8° with maximum acceptable gain loss of 1 dB would result in a greater than 80 percent savings in number of phase shifters. Nine radiators would be combined with a single phase shifter. Also, a FOV = ±9° with maximum acceptable gain loss of 3 dB would result in a greater than 90 percent savings in number of phase shifters. Sixteen radiators then would be combined with a single phase shifter.

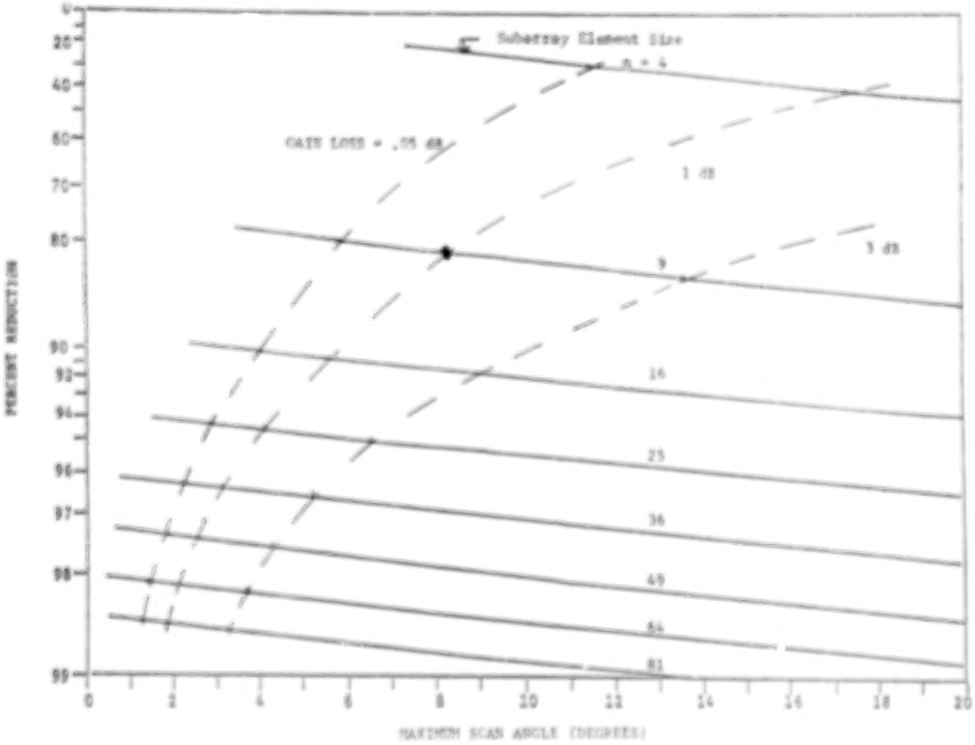

ANTENNA ARRAY DESIGN PARAMETERS

This graph shows parametric curves of antenna aperture diameter in meters, as a function of frequency, diameter in wavelengths, number of elements or subarrays of three (3) wavelengths on a side or $(9\lambda^2)$, beamwidth in degrees and Earth surface resolution at the antenna 3 dB beamwidth. As an example, an 0.1 degree beamwidth at 10 GHz with a 20 meter diameter antenna would require 48,000 subarrays and produces a resolution cell of 40 nautical miles. Other antenna diameters and frequencies with corresponding parameters can be extracted from the graph.

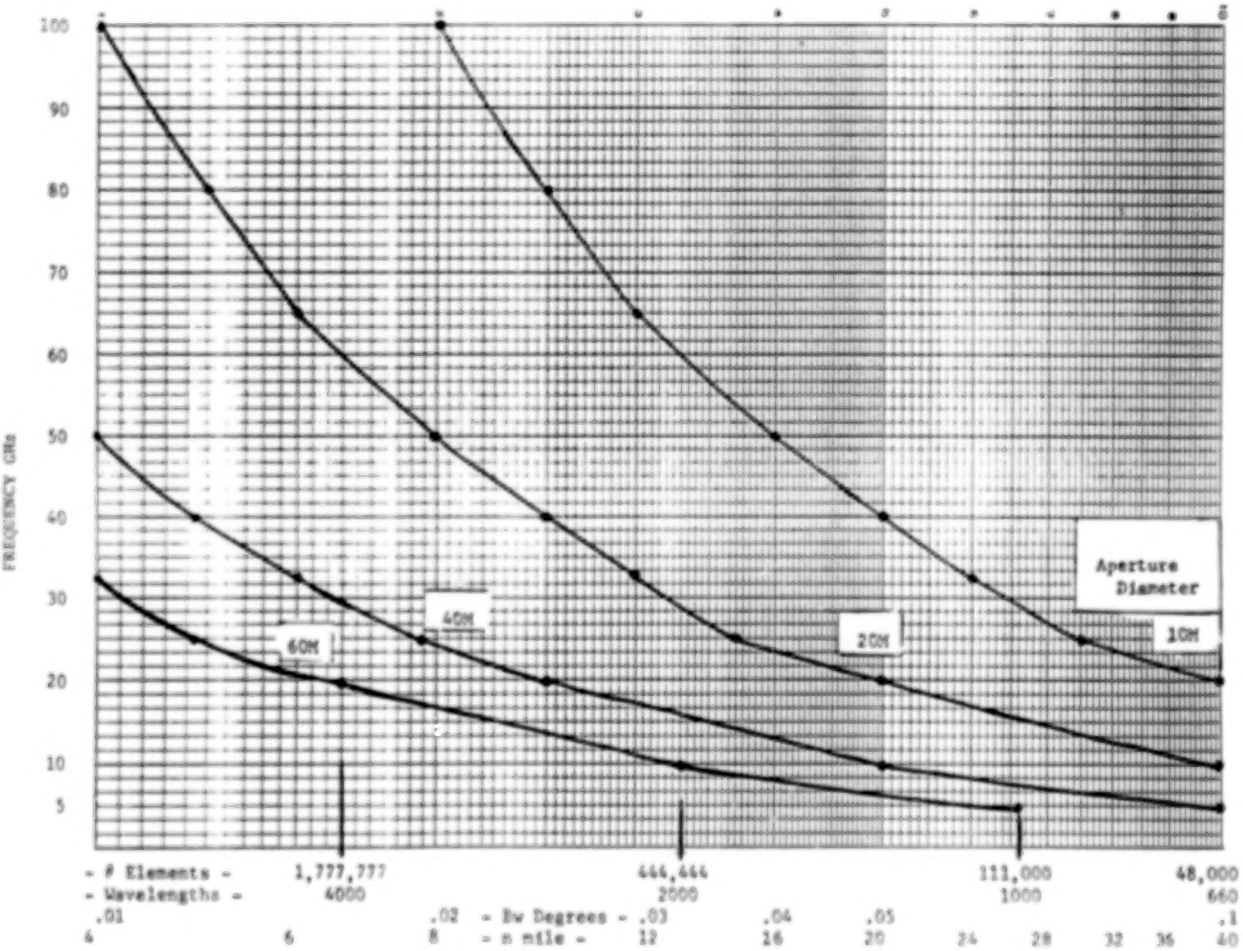

NEW IDEAS
FOR
NARROW FOV

- ARRAYS
- SUBARRAYS
- SPACE-FED ARRAYS

NARROW BEAM, WIDE FOV

Narrow beam implies large aperture and wide field of view implies small interelement spacing (as dictated by the onset of grating lobes at the edge of the scan volume). Consequently, narrow beam, wide FOV electronically scanned antennas typically contain large numbers of phase shifter/radiators. If the number of phase shifter/radiators is reduced and their placement randomized (to suppress grating lobes), the sidelobes will rise and the gain will diminish (but the beam will remain narrow).

NARROW BEAM, WIDE FIELD OF VIEW PHASED ARRAYS ARE EITHER

- **FULLY POPULATED**
  - **REQUIRE LARGE NUMBER OF PHASE SHIFTERS**
- **RANDOM SPARSE**
  - **HIGH SIDELOBES**
  - **DIMINISHED GAIN**

IMPACT OF LIMITED FOV

A limited field-of-view system requires fewer phase shifters. The phase shifter reduction can be accomplished by subarraying whereby each of the remaining phase shifters is tied to a group (subarray) of radiators. The subarrays can be disjoint or overlapping. Disjoint subarrays are less effective but simpler to implement especially for constrained feed arrays. Overlapped subarrays are especially suited for fixed focus array lenses and reflectors whereby the subarray signal distribution is via the space feed.

EARTH VIEWING, GEOSYNCHRONOUS SENSOR HAS LIMITED FIELD OF VIEW (~ $\pm 8^{o}$). NUMBER OF PHASE SHIFTERS CAN BE REDUCED BY EITHER

- **NONOVERLAPPING (CONVENTIONAL) SUBARRAYS**
  - **GAIN LOSS WITH SCAN**
  - **CLOSE IN SIDELOBES INCREASE WITH SCAN**
- **OVERLAPPING SUBARRAYS**
  - **NOT PRACTICAL FOR CONSTRAINED FEED**
  - **ATTRACTIVE FOR**
    - **FIXED FOCUS ARRAY LENS**
    - **REFLECTOR**

NONOVERLAPPING SUBARRAYS

Consider, first, nonoverlapping subarrays. A rectangular lattice 2 x 2 (4:1) subarray is identified by the dashed contour.

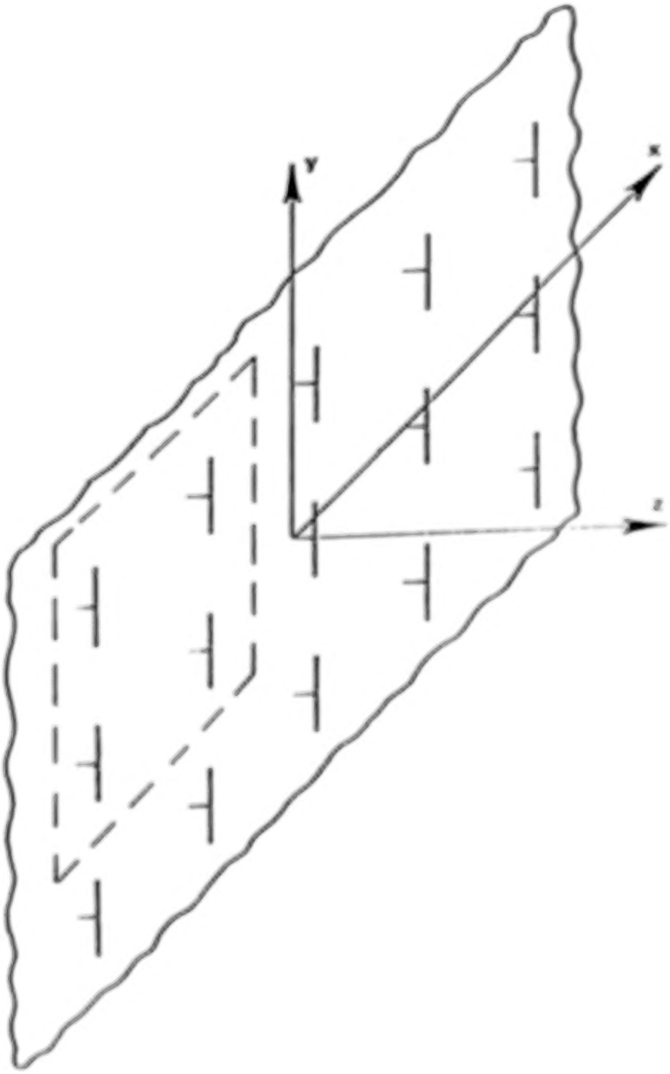

NONOVERLAPPING SUBARRAY PATTERN COMPONENTS

Typical subarray pattern and subarray array factor main lobe and first grating lobe are shown in the figure. Radiator interelement spacing is assumed to be uniform throughout the array and the "optimum" interelement spacing is chosen to be the maximum spacing for which no part of a subarray pattern grating lobe falls within the visible range. Neglecting impedance mismatch loss and beam broadening, scan loss is given by the subarray pattern gain rolloff. This roll off is gradual and corresponds to the positioning of subarray array factor grading lobes in the main lobe of the subarray pattern.

The subarray weights can be adjusted to reduce subarray pattern sidelobes and, hence, full array far sidelobes. However, close in high sidelobes are inevitable as a consequence of grating lobes in the subarray pattern main lobe.

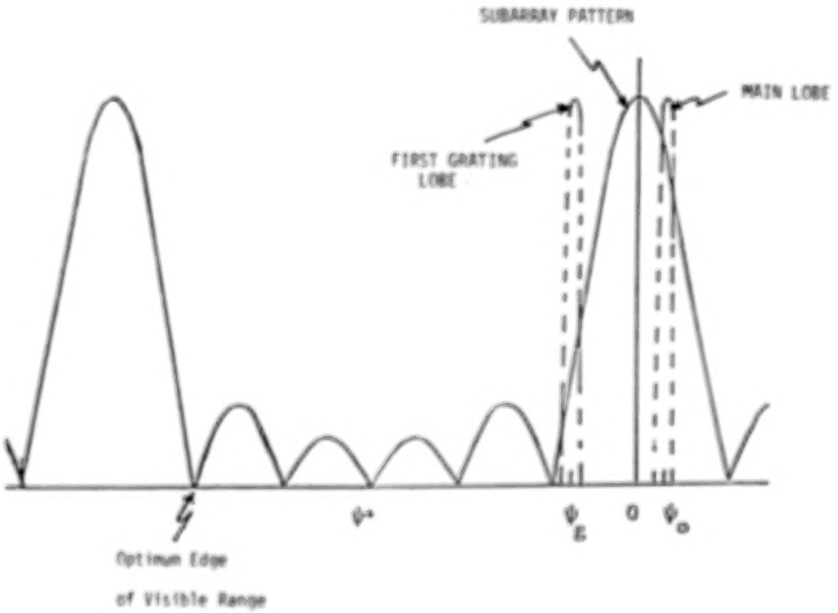

OVERLAPPING SUBARRAYS

Now consider overlapping subarrays. A fully overlapped, "orthogonal beam", subarray pattern is shown in the figure. There is minimal gain loss throughout the field of view. The subarray centers must be spaced such that a subarray array factor grating lobe, at maximum scan, would just be excluded from the field of view. Low level close in sidelobes, as well as ultralow far out sidelobes, are feasible design specifications.

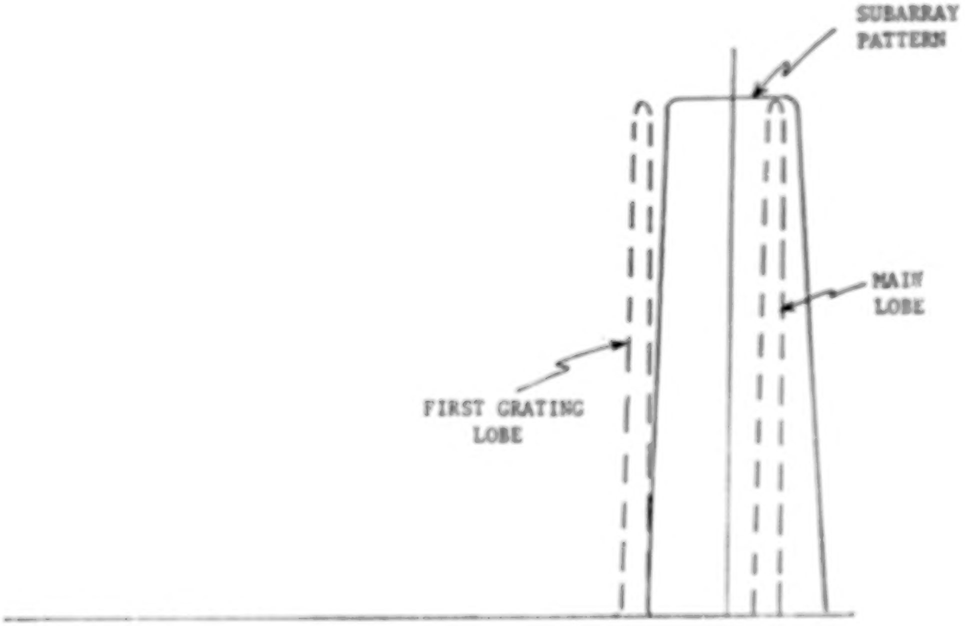

SPACE FED LENS OVERLAPPING SUBARRAY CONCEPT

A practical overlapping subarray concept is shown in the figure. This concept was analyzed by G. Borgiotti as reported in IEEE T-AP, Vol. AP-25, No. 2, March 1977. The focal plane array can be implemented as a conventional Butler matrix. In addition to being a lightweight, practical implementation of overlapping subarrays, the concept has inherent wide bandwidth, in excess of 20 percent, as a consequence of the frequency independence of the pattern beamwidth and of the array factor main beam direction. Performance is limited in part by the finite lens length, beamforming hardware (transmission lines, combiners, etc.) bandwidth and loss, and radiating element impedance match (mutual coupling).

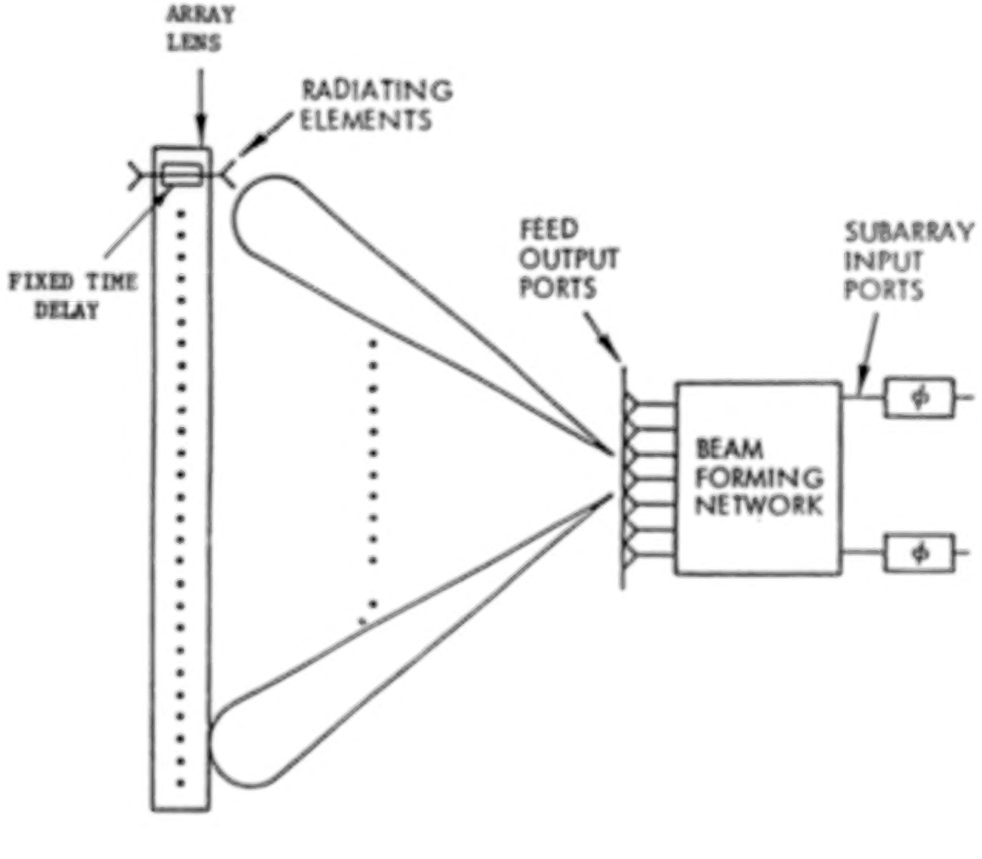
ARRAY LENS
RADIATING ELEMENTS
FIXED TIME DELAY
FEED OUTPUT PORTS
SUBARRAY INPUT PORTS
BEAM FORMING NETWORK
ϕ
ϕ

CRITICAL TECHNOLOGY AREAS

- RECEIVE MODULES (ACTIVE LENS)
- DEPLOYMENT
- PRIME POWER DISTRIBUTION (ACTIVE LENS)
- FEED SYSTEM (TRANSFORM FEED)
- LOW LOSS LENS (PASSIVE)
- BANDWIDTH (ELEMENTS-FEED-LENS)

VALIDATION

ANOTHER MAJOR "TECHNOLOGY" CONCERN IS VALIDATION

- SPACE TESTING TOO EXPENSIVE
- GROUND TESTING NOT FEASIBLE WITH FULL-SCALE SYSTEM

DETAILED COMPUTER SIMULATIONS PRESENT A SOLUTION

- SOFTWARE CAN BE VALIDATED WITH MANAGEABLE GROUND-BASED EXPERIMENTS
- APPLIED TO VALIDATING FULL-UP SYSTEM
- NOW AVAILABLE (E.G. RADC'S[*] "PAAS" PROGRAM - CONTACT J. CLEARY)

[*] Rome Air Development Center, Rome, NY

CONJUGATE FIELD APPROACHES FOR ACTIVE ARRAY COMPENSATION

R. J. ACOSTA
NASA LEWIS RESEARCH CENTER
CLEVELAND, OHIO

CONJUGATE FIELD APPROACHES FOR ACTIVE ARRAY COMPENSATION

Two approaches for calculating the compensating feed array complex excitations are namely, the indirect conjugate field matching (ICFM) and the direct conjugate field matching (DCFM) approach (Ref 1.). In the ICFM approach the compensating feed array excitations are determined by considering the transmitting mode and the reciprocity principle. The DCFM "in contrast" calculates the array excitations by integrating directly the induced surface currents on the reflector under a receiving mode. DCFM allows the reflector to be illuminated by an incident plane wave with a tapered amplitude. The level of taper can effectively control the sidelobe level of the compensated antenna pattern.

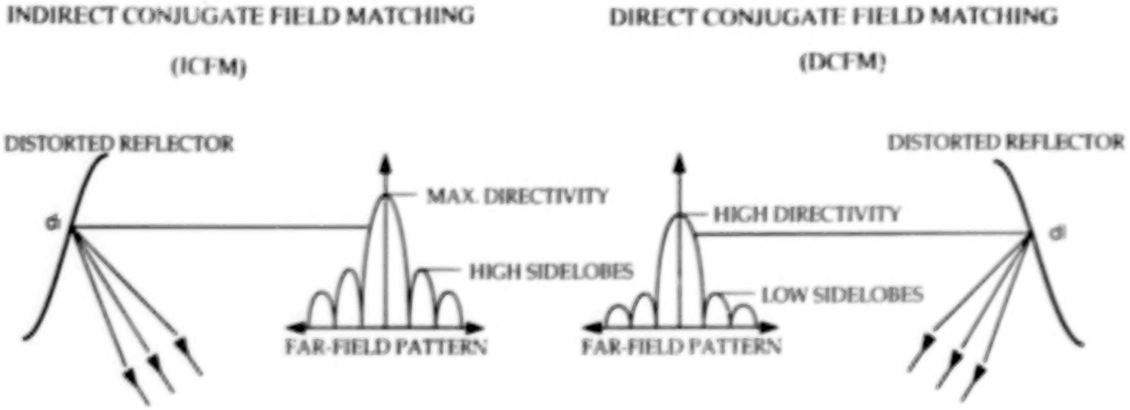
INDIRECT CONJUGATE FIELD MATCHING

(ICFM)

DIRECT CONJUGATE FIELD MATCHING

(DCFM)

DISTORTED REFLECTOR
di
MAX. DIRECTIVITY
HIGH SIDELOBES
FAR-FIELD PATTERN
HIGH DIRECTIVITY
LOW SIDELOBES
FAR-FIELD PATTERN
DISTORTED REFLECTOR
di

ICFM FEATURES

- RECIPROCITY APPLIES (TRANSMITTING CODES)
- MAXIMUM DIRECTIVITY IS ACHIEVABLE

DCFM FEATURES

- DIRECT CONTROL OF SIDELOBES
- DIRECTIVITY WITHIN 2DB OF MAXIMUM
- EASY TO IMPLEMENT

CONJUGATE FIELD MATCHING PRINCIPLE

The DCFM approach is based on the receiving antenna mode, as outlined below. Let the distorted antenna be illuminated by an incident plane wave from a prescribed direction and with a prescribed polarization. That direction and polarization are those of the main beam when the antenna is in the transmitting mode. The plane wave has a planar phase front as in an ordinary plane wave case, but with the option of having a uniform amplitude (ICFM) or a tapered amplitude (DCFM). Using this concept, the resulting fields in the focal plane of the reflector antenna can be calculated by integrating the induced current distribution on the distorted reflector surface. The set of excitation coefficients of the compensating feed array is obtained as complex conjugate of the received focal plane electric field distribution.

SOLUTION

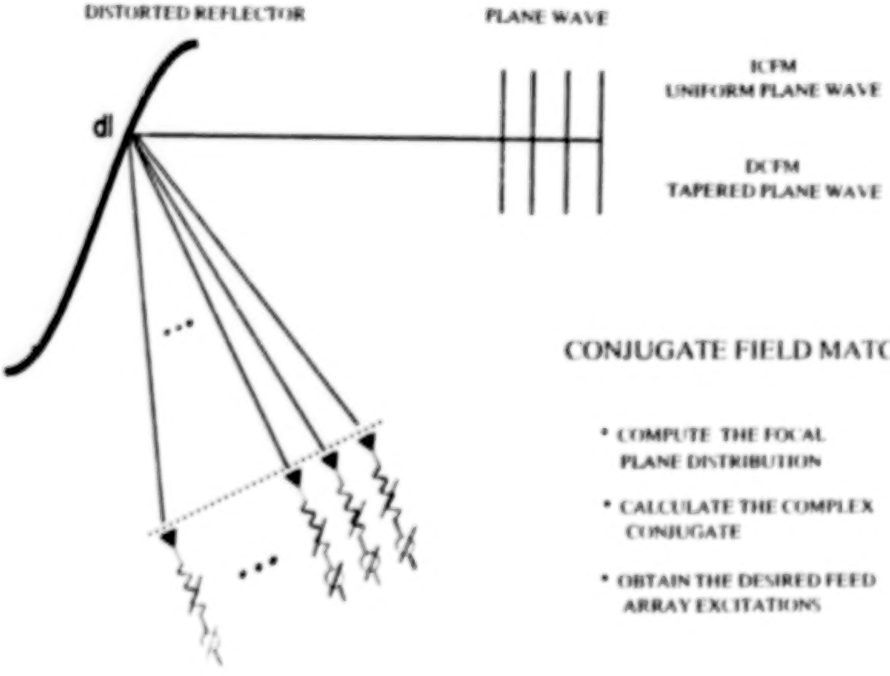

CONJUGATE FIELD MATCHING

- COMPUTE THE FOCAL PLANE DISTRIBUTION
- CALCULATE THE COMPLEX CONJUGATE
- OBTAIN THE DESIRED FEED ARRAY EXCITATIONS

ASSUMPTION REFLECTOR DISTORTION KNOWN

DIRECT CONJUGATE FIELD MATCHING
COMPUTER IMPLEMENTATION

A block diagram of a numerical implementation for the DCFM approach is illustrated below. It determines the focal plane electric field distribution due to a tapered plane wave incident on the distorted reflector from a known observation direction. The algorithm uses physical optics technique for obtaining the focal region fields. The compensating feed array are obtained by assigning the complex conjugate values of the focal region fields at the corresponding feed element location. Basically, two inputs are to be defined, the feed array geometry and the distorted reflector surface points.

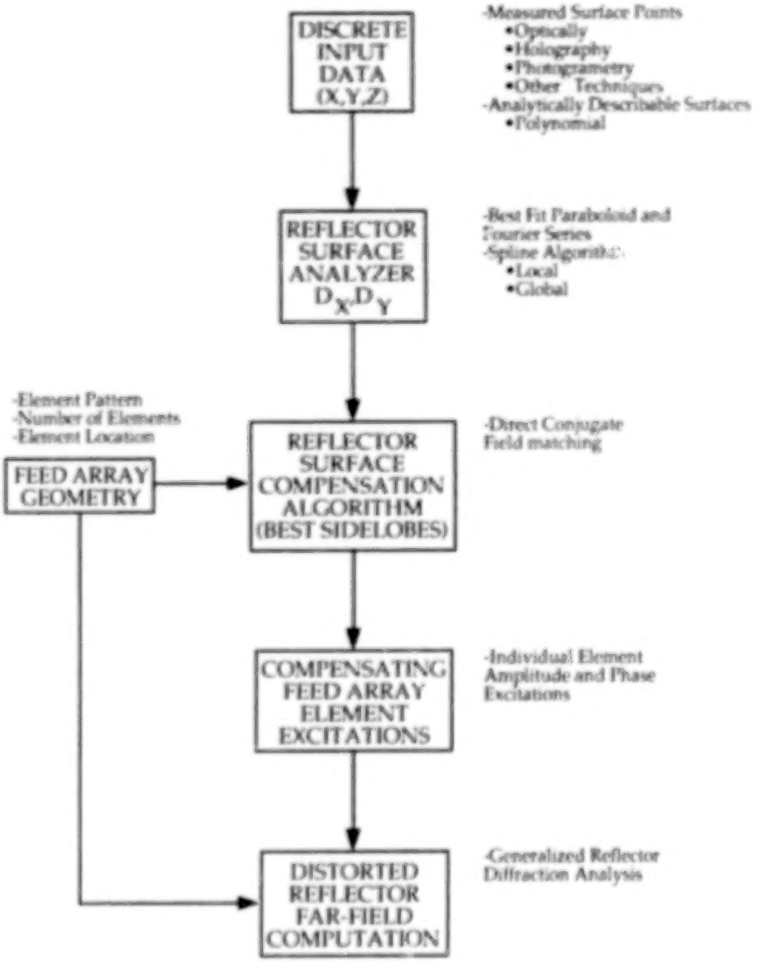
DISCRETE INPUT DATA (X,Y,Z)
-Measured Surface Points
•Optically
•Holography
•Photogrammetry
•Other Techniques
-Analytically Describable Surfaces
•Polynomial
REFLECTOR SURFACE ANALYZER D_X, D_Y
-Best Fit Paraboloid and Fourier Series
-Spline Algorithms
•Local
•Global
-Element Pattern
-Number of Elements
-Element Location
FEED ARRAY GEOMETRY
REFLECTOR SURFACE COMPENSATION ALGORITHM (BEST SIDELOBES)
-Direct Conjugate Field matching
COMPENSATING FEED ARRAY ELEMENT EXCITATIONS
-Individual Element Amplitude and Phase Excitations
DISTORTED REFLECTOR FAR-FIELD COMPUTATION
-Generalized Reflector Diffraction Analysis

EXAMPLE OF CALCULATION

Let us consider the undistorted offset parabolic geometry and surface error profile illustrated in the figure below. Also presented in the figure are the feed parameters and the undistorted E-plane radiation pattern obtained by placing a single feed at the focal point.

PROBLEM DESCRIPTION

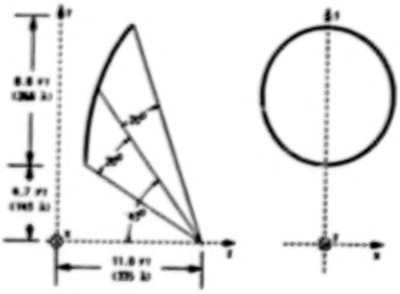

UNDISTORTED ANTENNA GEOMETRY

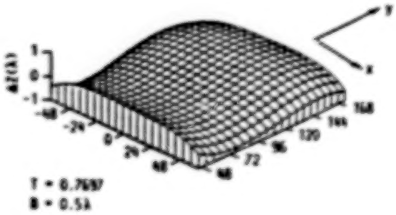

SURFACE DISTORTION PROFILE

OPERATING FREQUENCY, GHz	30
FEED POLARIZATION	LINEAR
E-PLANE PATTERN $\cos^{qE}(\theta)$	qE = 20
H-PLANE PATTERN $\cos^{qH}(\theta)$	qH = 20
FEED LOCATION (FOCUS), METERS	(0,0,3.35)
EDGE TAPER, dB	-11

SUMMARY OF FEED PARAMETERS

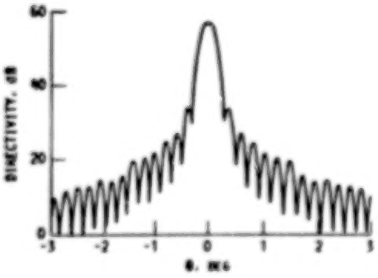

UNDISTORTED FAR FIELD PATTERN

RESULTS

The figure below presents the distorted far-field, compensated far-field of DCFM solution, compensated far-field of ICFM solution and the compensating feed array geometry. The ICFM approach assumes a uniform plane wave incident on the distorted reflector. The compensated directivity for both approaches was within 2 DB of the undistorted value. The major differences occurred in the compensated sidelobe level envelope. Note that the sidelobe level for the DCFM approach was 3 to 5 DB lower than those produced by the ICFM approach. This result indicates that the amplitude tapering of the incident plane wave has a direct control over the compensated sidelobe envelope.

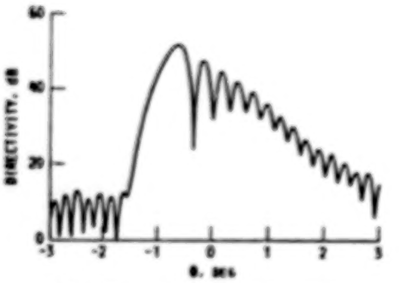

DISTORTED FAR-FIELD PATTERN
(FEED AT FOCUS)

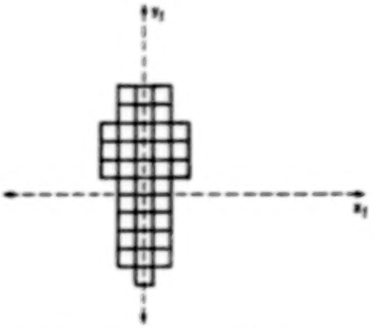

COMPENSATING FEED ARRAY
GEOMETRY (37 ELEMENTS)

RESULTS

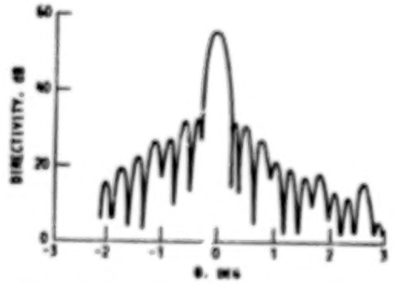

DCFM COMPENSATED FAR-FIELD PATTERN

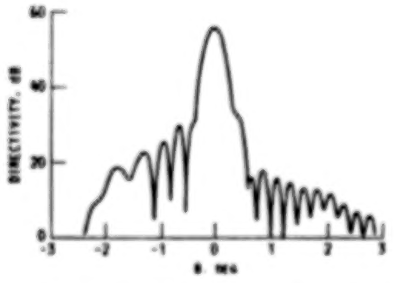

ICFM COMPENSATED FAR-FIELD PATTERN

REFERENCE

1. Acosta, R. : Active Feed Array Compensation for Reflector Antenna Surface Distortion. NASA TM 100826, June 1986.

Reflector Surface Distortion Analysis Techniques (Thermal Distortion Analysis of Antennas in Space)

R. Sharp, M. Liao, J. Giriunas, J. Heighway,
A. Lagin, and R. Steinbach
NASA Lewis Research Center
Cleveland, Ohio

DISTORTED ANTENNA PERFORMANCE ANALYSIS

A group of large computer programs are used to predict the far-field antenna pattern of reflector antennas in the thermal environment of space (Ref 1). TRASYS* is a thermal radiation analyzer that interfaces with SINDA**, a finite difference thermal analysis program. The resulting temperatures must be corrolated by SNIP (Ref 2), a new interfacing program. The SNIP+ results become an input file to NASTRAN, a well-known finite-element structural analysis program that results in displacements of the elements of the model. A continuous function is needed for the new physical optics RF analysis. This is provided by a new spline program that creates continuous surface functions from the ungridded data. The RF program results in plots of the far-field RF energy distribution of the antenna.

The entire thermal distortion analysis process is very labor intensive. For large thermal and structural models, individual analysts are usually needed for the TRASYS, SINDA and NASTRAN programs. Interim and final results are interpreted by the full group of analysts.

*Thermal Radiation Analysis System (TRASYS)
**Systems Improved Numerical Differencing Analyzer (SINDA)
+SINDA-NASTRAN Interfacing Program (SNIP)

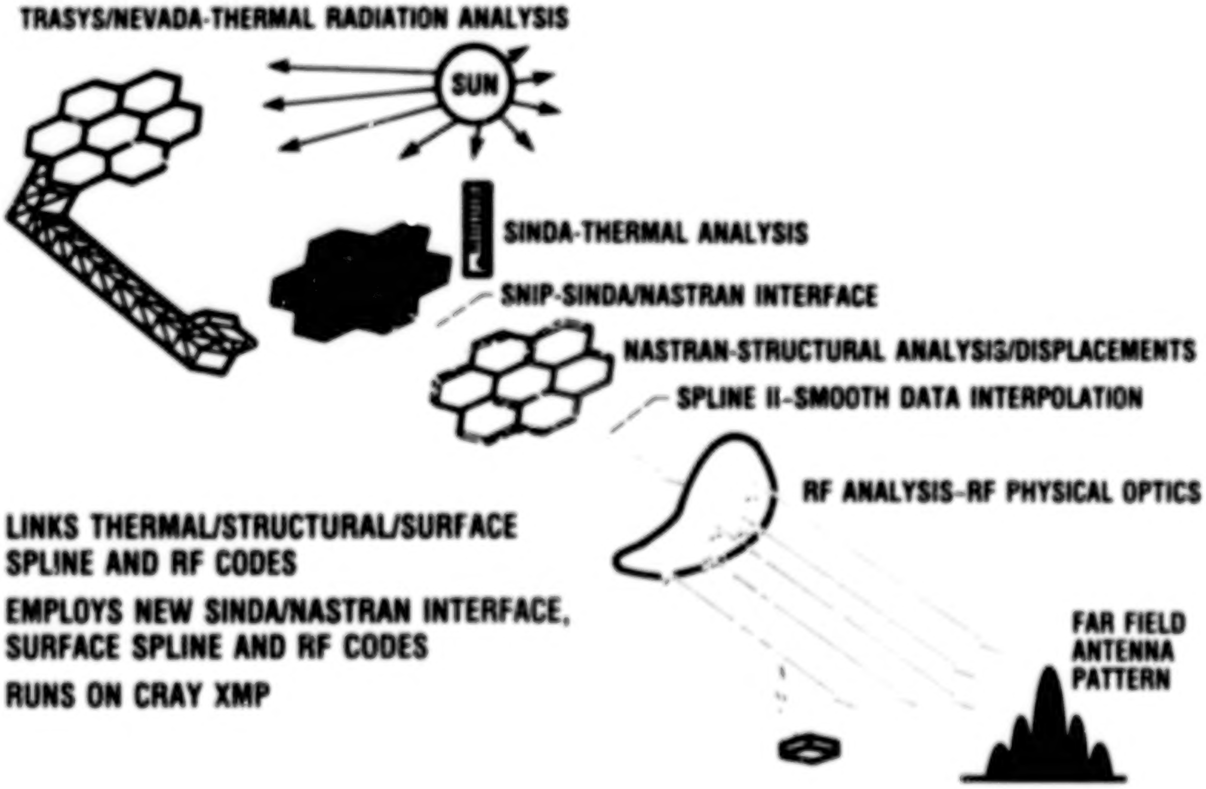
TRASYS/NEVADA-THERMAL RADIATION ANALYSIS
SUN
SINDA-THERMAL ANALYSIS
SNIP-SINDA/NASTRAN INTERFACE
NASTRAN-STRUCTURAL ANALYSIS/DISPLACEMENTS
SPLINE II-SMOOTH DATA INTERPOLATION
RF ANALYSIS-RF PHYSICAL OPTICS
FAR FIELD ANTENNA PATTERN

- **LINKS THERMAL/STRUCTURAL/SURFACE SPLINE AND RF CODES**
- **EMPLOYS NEW SINDA/NASTRAN INTERFACE, SURFACE SPLINE AND RF CODES**
- **RUNS ON CRAY XMP**

ADVANCED COMMUNICATION TECHNOLOGY SATELLITE

The Advanced Communications Technology Satellite (ACTS) is an experimental NASA satellite scheduled to be flown in geosynchronous orbit in the early 1990s. It employs data communication links at the Ka band using 30 GHz uplinks and 20 GHz downlinks. It was used as the spacecraft thermal model for the antenna reflector thermal distortion analysis because it is a representative geosynchronous spacecraft with all of the shadowing and eclipse solar radiation geometries that typify that class of spacecraft.

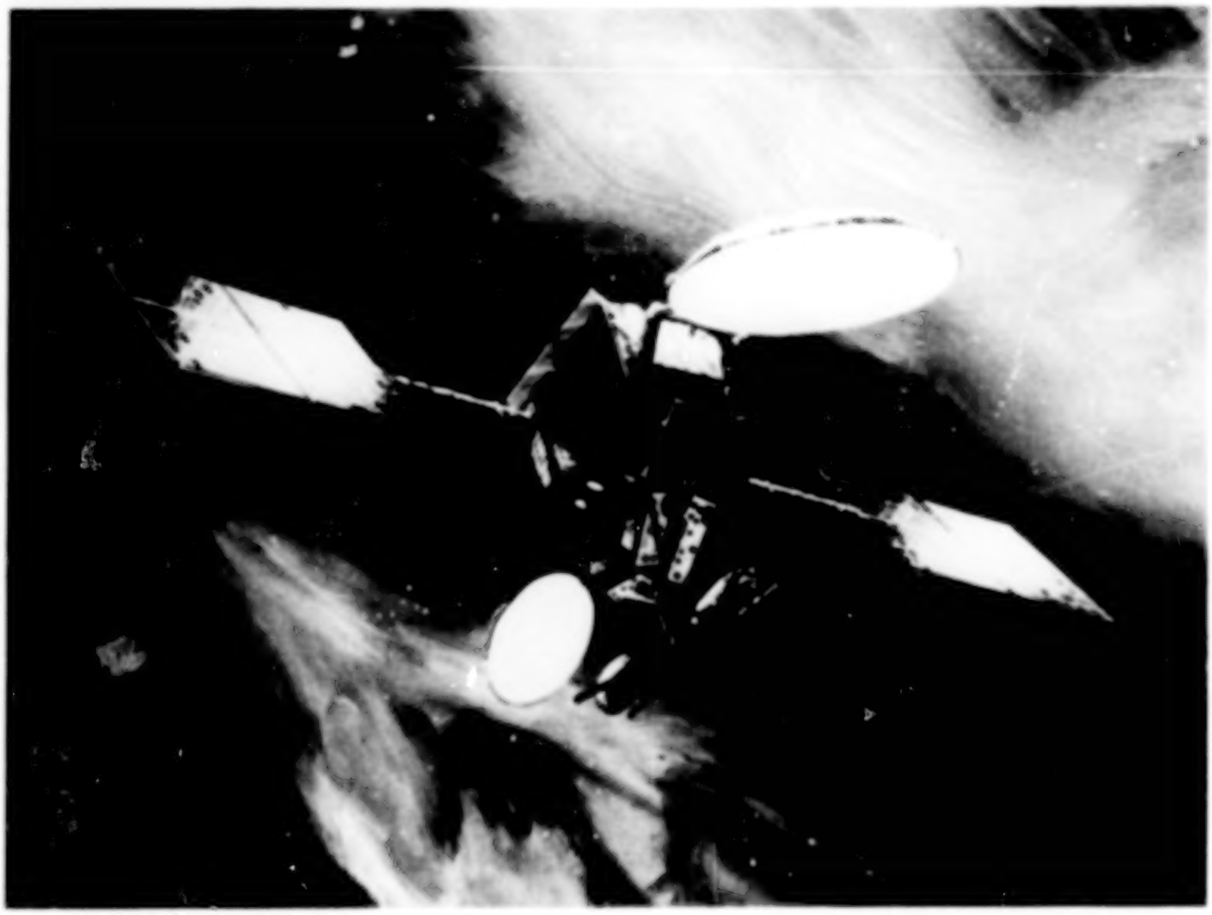

PRECISION FLIGHT REFLECTOR (REINFORCING RIB AND MLI SIDE)

A precision flight reflector of NASA design was substituted for the actual ACTS transmit antenna for this analysis. This was done so that the effects of various geometries and materials on antenna performance could be explored. The design chosen was a space flight version of a high precision ground based experimental antenna reflector. The 3.3 M antenna reflector is a lightweight composite structure comprising reflector face, strongback ribs and multi-layer insulation (MLI). This view is of the reinforcing rib side of the reflector.

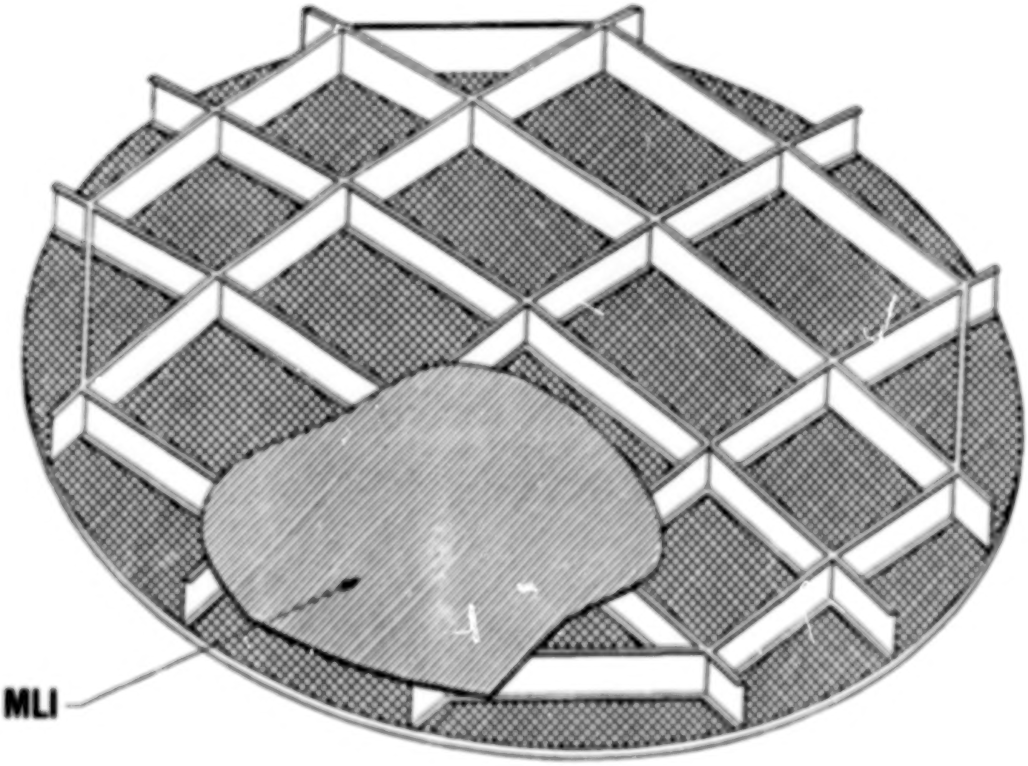

PRECISION FLIGHT REFLECTOR-REFLECTOR SIDE

The reflector side of the Precision Flight Reflector would first be machined and then covered with a surface that would be aluminized by vapor deposition for RF reflectance.

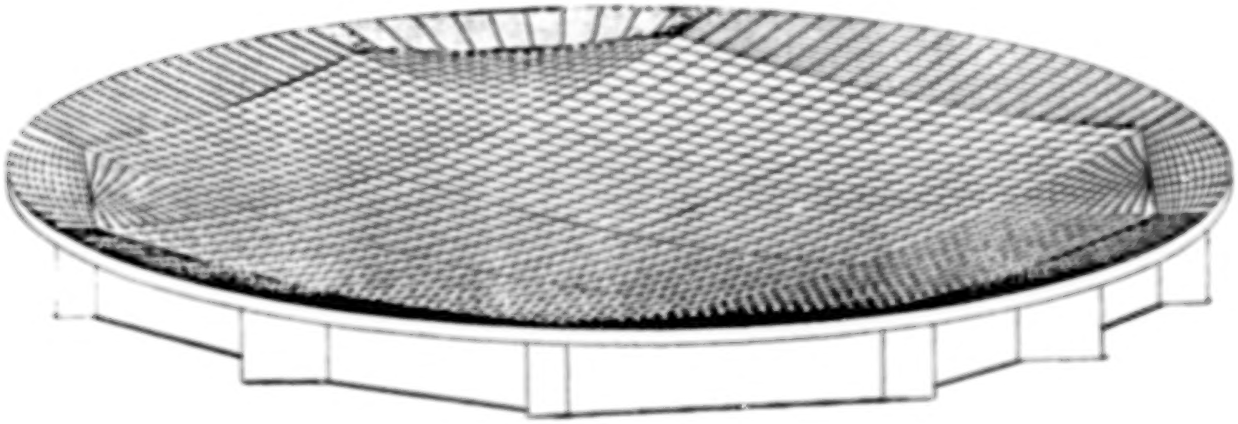

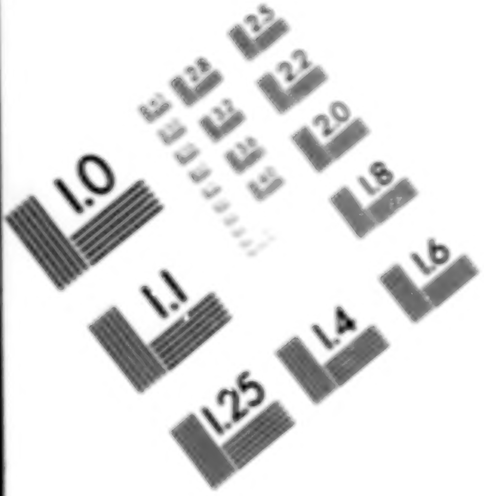
1.0
1.1
1.25
1.4
1.6
1.8
2.0
2.2
2.5
2.8

UNITED STATES OF AMERICA GOVERNMENT PRINTING OFFICE

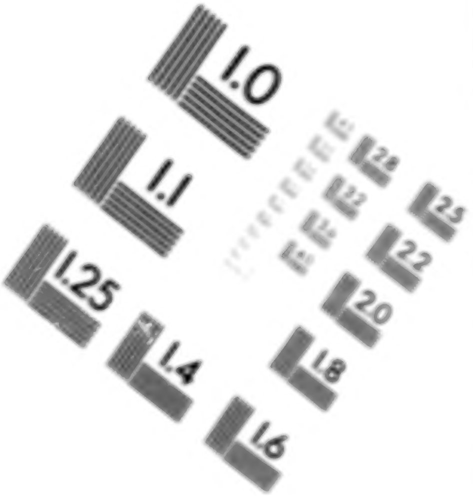
1.0
1.1
1.25
1.4
1.6
1.8
2.0
2.2
2.5
2.8

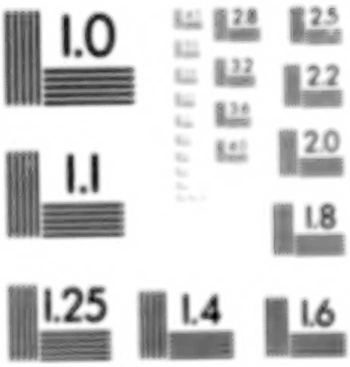
1.0
1.1
1.25
1.4
1.6
1.8
2.0
2.2
2.5
2.8
3.2
3.6
4.0

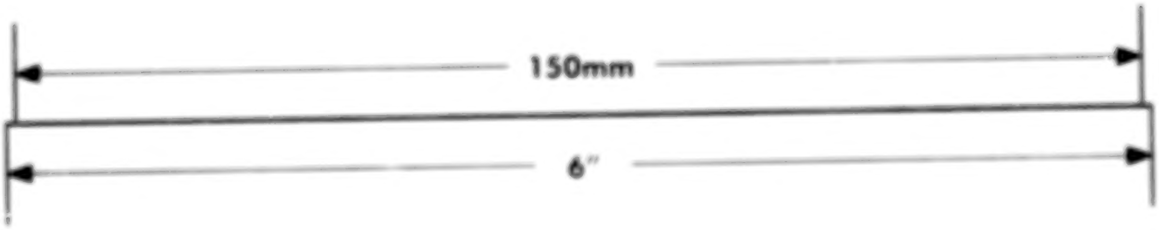

1.0
1.1
1.25
1.4
1.6
1.8
2.0
2.2
2.5
2.8

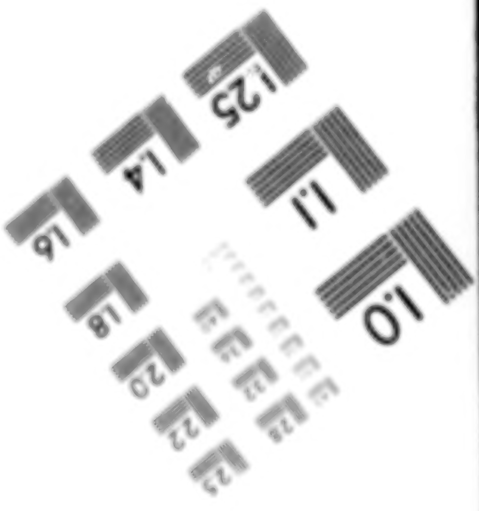
1.0
1.1
1.25
1.4
1.6
1.8
2.0
2.2
2.5
2.8

PRECISION FLIGHT REFLECTOR-SECTIONAL VIEW

The cross-sectional view depicts the construction of the 3.3 M antenna reflector. The back of the reflector is covered with a multilayer insulation blanket. The back-up channel is constructed using graphite/epoxy material. The lower channel flange uses unidirection plies while the channel is constructed using cross plied fabric. Flat aluminum core honeycomb sandwich panels with six ply graphite face sheets are used for mounting the Nomex honeycomb core (Hexcel Corp.) that is then machined to the required contour. This machined core material is then covered with a very thin fiberglass-epoxy adhesively bonded face sheet that is finally aluminized by vapor deposition for the reflective surface finish. White paint would then be applied to this surface for thermal control.

The purpose of this type of construction was to fabricate a reflector that was less expensive than others because no molds would be needed and little accuracy would be needed for the back-up structure. It would be resistant to thermal distortion by nature of the construction and basic materials used and yet accurate because the final reflective surface could be applied to a precisely machined surface.

3.3 METER DIAMETER
PREDICT SURFACE DEFORMATION DUE TO THERMAL LOADING

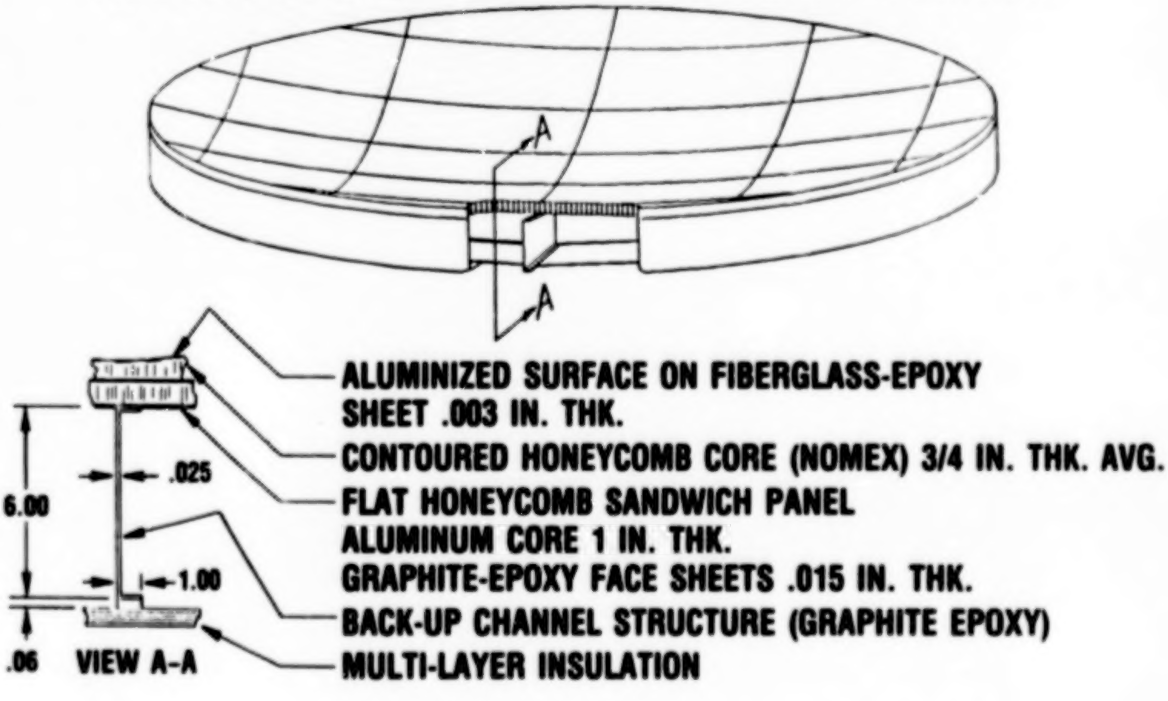
A
A
ALUMINIZED SURFACE ON FIBERGLASS-EPOXY SHEET .003 IN. THK.
CONTOURED HONEYCOMB CORE (NOMEX) 3/4 IN. THK. AVG.
FLAT HONEYCOMB SANDWICH PANEL ALUMINUM CORE 1 IN. THK. GRAPHITE-EPOXY FACE SHEETS .015 IN. THK.
BACK-UP CHANNEL STRUCTURE (GRAPHITE EPOXY)
MULTI-LAYER INSULATION
.025
6.00
1.00
.06
VIEW A-A

THERMAL RADIATION ANALYSIS SYSTEM

The computer code TRASYS (Thermal Radiation Analysis System) was used to characterize the thermal environment of the spacecraft in a geosynchronous orbit. The model geometry, surface properties, orbit and spacecraft orientation must be defined. Then TRASYS takes into account radiation from direct solar, planet albedo, planet infrared, specular and diffuse reflections of both solar and IR wavebands, transmissivity of surfaces and spacecraft self-shadowing. TRASYS then generates the radiant heat interchange factors and the radiant heat inputs to each element of the model and these become the input to the SINDA thermal analyzer.

Our TRASYS model consists of approximately 350 elements. The 20 GHz 3.3 M diameter antenna main reflector was modeled with relatively small triangular elements. The remainder of the spacecraft structure was modeled with much less detail since it is only of interest in how it shadows the antenna main reflector.

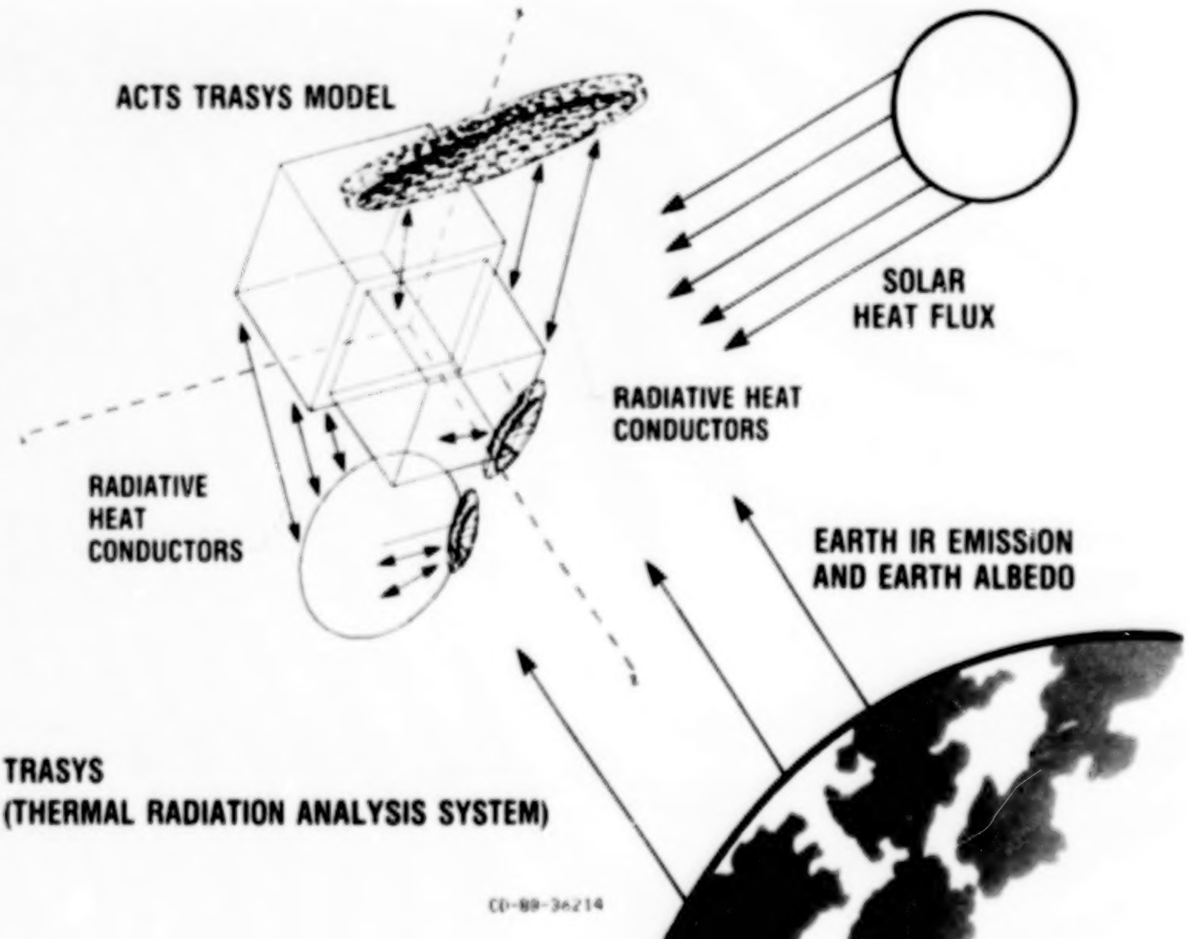
ACTS TRASYS MODEL
SOLAR HEAT FLUX
RADIATIVE HEAT CONDUCTORS
RADIATIVE HEAT CONDUCTORS
EARTH IR EMISSION AND EARTH ALBEDO

TRASYS
(THERMAL RADIATION ANALYSIS SYSTEM)

CD-88-36214

SYSTEMS IMPROVED NUMERICAL DIFFERENCING ANALYZER

SINDA (Systems Improved Numerical Differencing Analyzer) is a lumped capacitance, finite difference thermal analyzer. Each node in the SINDA model may be thought of as a point having thermal capacitance. All nodes are connected to other nodes by linear (i.e. thermal conductance) and non-linear (i.e., radiation heat transfer) conductances.

The figures illustrate the 3.3 M diameter reflector SINDA model and its resistance-capacitance (R-C) network. The antenna reflector consists of two honeycomb sandwich layers, a stiff strongback rib structure and multi-layer insulation (MLI) covering the back of the reflector. A total of eight layers of SINDA nodes were used through the depth to model the three face sheets, two honeycomb core layers, rib, rib tip and MLI respectively. This large SINDA model comprises 849 thermal nodes and 6561 conductors. Among these, 2028 are linear conductors and 4533 are radiative conductors.

SINDA REFLECTOR MODEL

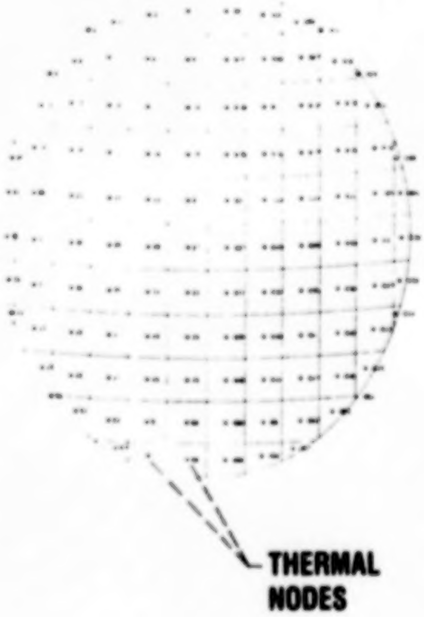
THERMAL NODES

SINDA R-C (RESISTANCE-CAPACITANCE) NETWORK

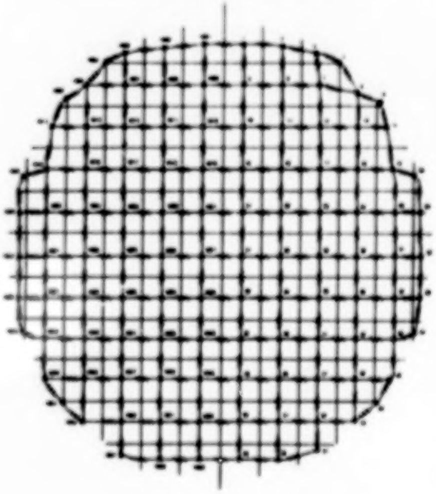

R-C NETWORK THROUGH REFLECTOR DEPTH

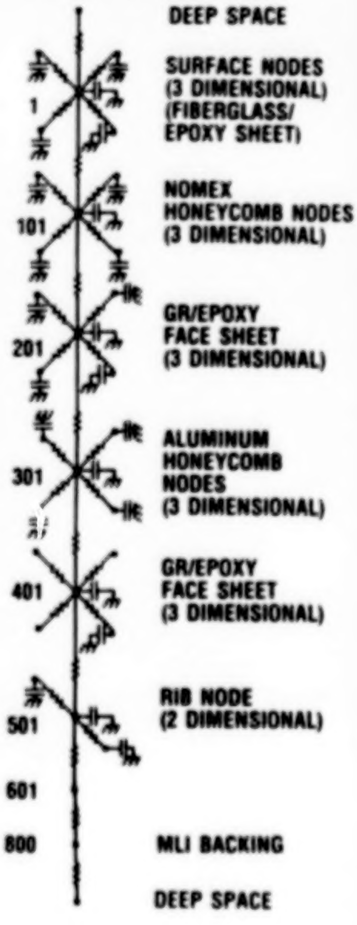
DEEP SPACE
SURFACE NODES (3 DIMENSIONAL) (FIBERGLASS/ EPOXY SHEET)
1
NOMEX HONEYCOMB NODES (3 DIMENSIONAL)
101
GR/EPOXY FACE SHEET (3 DIMENSIONAL)
201
ALUMINUM HONEYCOMB NODES (3 DIMENSIONAL)
301
GR/EPOXY FACE SHEET (3 DIMENSIONAL)
401
RIB NODE (2 DIMENSIONAL)
501
601
800
MLI BACKING
DEEP SPACE

SINDA-NASTRAN INTERFACING PROGRAM

Predicting thermal distortions and thermal stresses in structures requires the generation of both thermal and structural models of the structure under consideration. Standard practice often entails generation of finite difference thermal models, using a program such as SINDA, to predict temperatures in the structure, and generation of finite element structural models, using programs such as MSC/NASTRAN to predict thermal deformations and stresses in the structure. Correlation of information generated by the SINDA program into the NASTRAN format without the use of an interfacing computer program would be a very long and labor intensive process.

The SINDA-NASTRAN Interfacing Program (SNIP) is a FORTRAN computer code that generates NASTRAN structural model thermal load cards when given SINDA (or similar thermal model) temperature results and thermal model geometric data. SNIP generates thermal load cards for NASTRAN plate, shell, bar, and beam elements.

SNIP uses a geometric search routine and a numerical coding scheme to relate the less dense thermal model nodes to the more numerous structural model elements. SNIP then calculates element temperatures based on the weighted average of temperatures of the thermal nodes related to each element. User controlled input parameters provide control over node-to-element correlation.

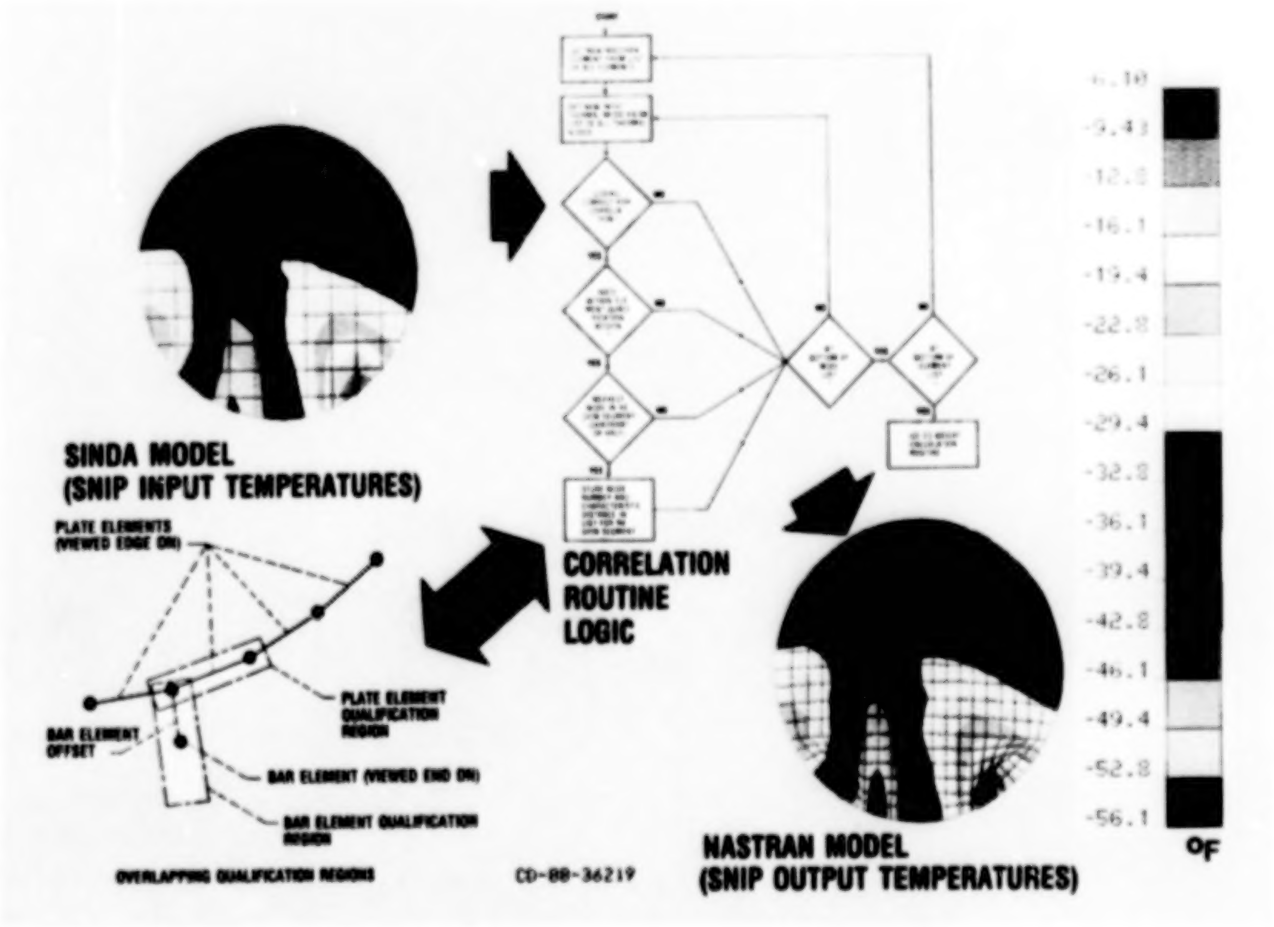
SINDA MODEL
(SNIP INPUT TEMPERATURES)
CORRELATION
ROUTINE
LOGIC
NASTRAN MODEL
(SNIP OUTPUT TEMPERATURES)
-6.10
-9.43
-12.8
-16.1
-19.4
-22.8
-26.1
-29.4
-32.8
-36.1
-39.4
-42.8
-46.1
-49.4
-52.8
-56.1
°F
PLATE ELEMENTS (VIEWED EDGE ON)
PLATE ELEMENT QUALIFICATION REGION
BAR ELEMENT OFFSET
BAR ELEMENT (VIEWED END ON)
BAR ELEMENT QUALIFICATION REGION
OVERLAPPING QUALIFICATION REGIONS
CD-88-36219

MSC/NASTRAN
(MACNEAL-SCHWENDLER CORP/NASA STRUCTURAL ANALYSIS)

MSC/NASTRAN (NAsa STRuctural ANalysis) was used to analyze the 3.3 M diameter antenna reflector to predict its thermal deformation in the space environment. MSC/NASTRAN is a proprietary finite element structural analysis program of the MacNeal-Schwendler Corporation which is used widely in the aerospace industry, providing both static and dynamic analysis capabilities.

The antenna reflector model was constructed using NASTRAN plate and beam type elements which display bending behavior caused by temperature gradients through the element thickness. CADAM (Computer Aided Design and Manufacturing, CADAM Inc.) was used to actually construct the model while PATRAN (PDA Engineering Inc.) was used to display the temperature and displacement data.

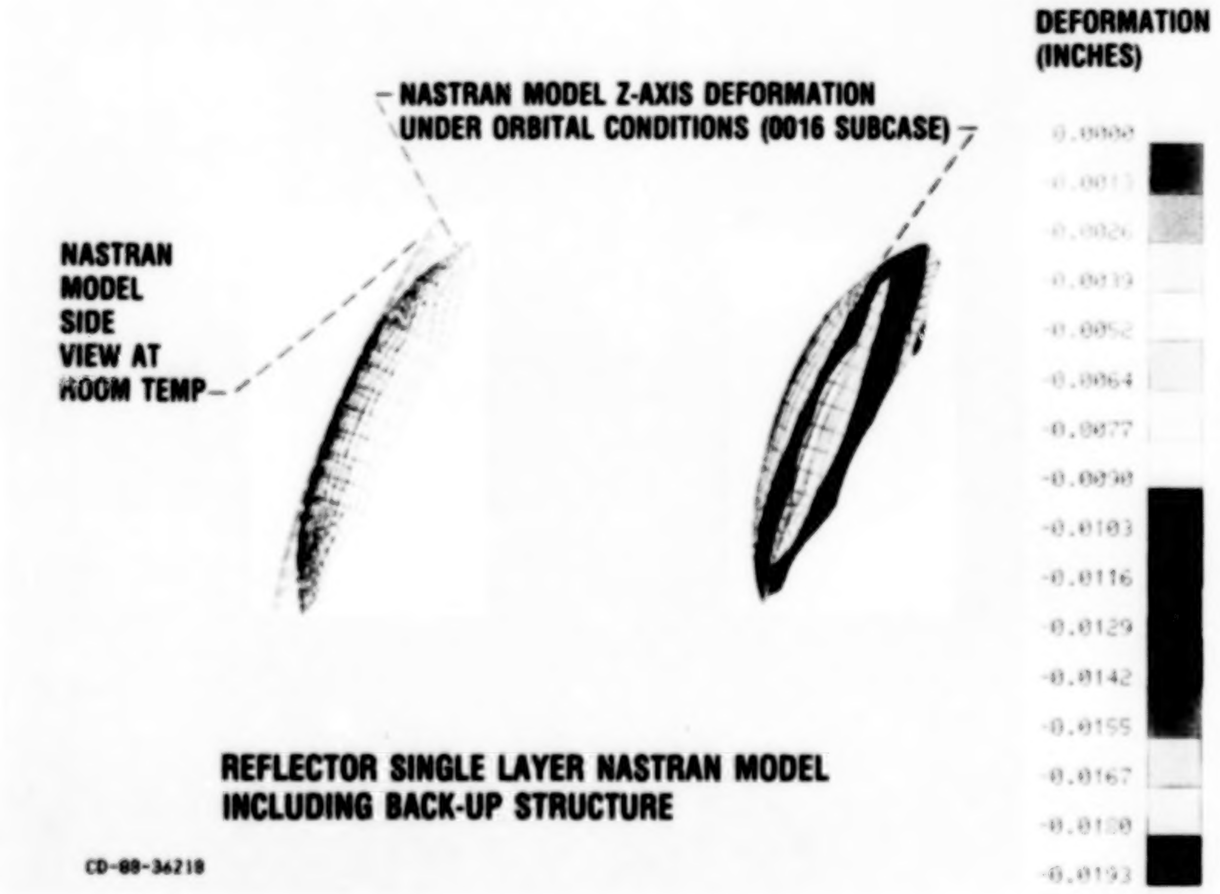
DEFORMATION (INCHES)
NASTRAN MODEL Z-AXIS DEFORMATION UNDER ORBITAL CONDITIONS (0016 SUBCASE)
NASTRAN MODEL SIDE VIEW AT ROOM TEMP
0.0000
-0.0013
-0.0026
-0.0039
-0.0052
-0.0064
-0.0077
-0.0090
-0.0103
-0.0116
-0.0129
-0.0142
-0.0155
-0.0167
-0.0180
-0.0193

REFLECTOR SINGLE LAYER NASTRAN MODEL INCLUDING BACK-UP STRUCTURE

CD-88-36218

A COMPUTER PROGRAM FOR THE INTERPOLATION OF UNGRIDDED DATA

This is a method of bi-variate interpolation for fitting a continuous function with continuous first partial derivatives (a C^1 function), $Z(X,Y)$, through given points (X_i,Y_i,Z_i) whose projections onto the base plane do not conform to any regular grid.

A new interpolation method was needed because other spline programs used higher order polynomials for interpolation and this resulted in high order ripples in the resulting surface of a distorted antenna reflector. These ripples in turn resulted in errors principally in the far sidelobes of the far-field antenna pattern. The purpose of this new interpolation method was to represent the surface with a lower order polynomial that was free of these high order ripples.

Operationally, the program first triangulates the grid points. Next, these triangles are each divided into three sub-triangles. Each sub-triangle is represented by a double cubic function. Slope is then matched along all boundaries of the sub-triangles including the tangent flats. This results in the deformed surface being represented by local double cubic functions that match value and surface normal across all edges.

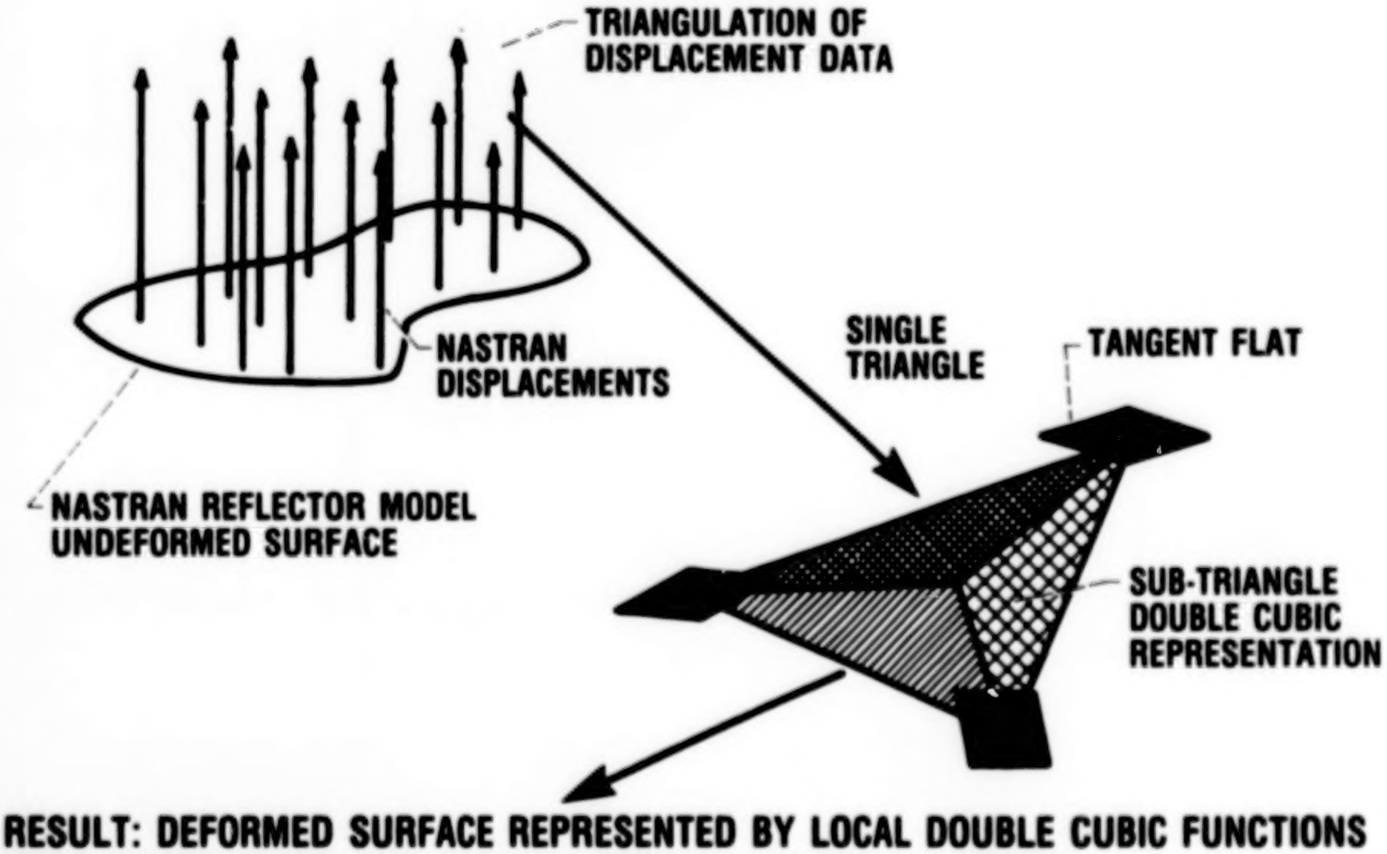
TRIANGULATION OF DISPLACEMENT DATA
NASTRAN DISPLACEMENTS
SINGLE TRIANGLE
TANGENT FLAT
NASTRAN REFLECTOR MODEL UNDEFORMED SURFACE
SUB-TRIANGLE DOUBLE CUBIC REPRESENTATION

RESULT: DEFORMED SURFACE REPRESENTED BY LOCAL DOUBLE CUBIC FUNCTIONS THAT MATCH VALUE AND SURFACE NORMAL ACROSS ALL EDGES

PHYSICAL OPTICS - DUAL REFLECTOR ANALYSIS RF PROGRAM

The RF program calculates the far-field antenna pattern resulting from a given Cassagrainian reflector configuration profile. It generates two-dimensional graphs of dB directivity versus polar angle for azimuthal angles and produces a table of parameters characterizing beam shape.

This is accomplished by first calculating the current density on the sub-reflector induced by the feed. Next, the current density on the main reflector induced by the sub-reflector is calculated. Finally, the far-field directivity distribution across the polar and azimuthal angles is calculated.

The advantages of this program are that it addresses the more sophisticated Cassagrainian configuration; the modular implementation allows for future configuration flexibility and it utilizes the current distribution method of analysis. This method makes possible the straightforward analysis of the secondary effects of the reflector back on to the sources. Intermediate calculations are also available for auxillary causal analysis.

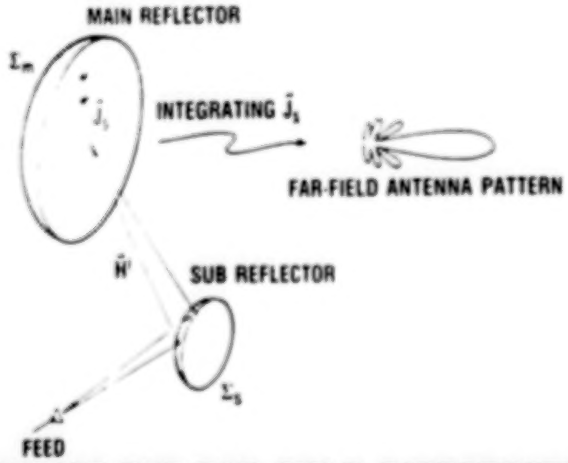

- **OBJECTIVE—TO CALCULATE THE FAR FIELD DIRECTIVITY PATTERN RESULTING FROM A GIVEN CASSEGRAIN REFLECTOR CONFIGURATION PROFILE.**
- **APPROACH—PHYSICAL OPTICS.**
- **FEATURES**
  - **ADDRESSES THE MORE SOPHISTICATED CASSEGRAIN CONFIGURATION.**
  - **MODULAR IMPLEMENTATION ALLOWS FOR FUTURE CONFIGURATION FLEXIBILITY.**
  - **UTILIZES THE CURRENT DISTRIBUTION METHOD OF ANALYSIS WHICH:**
    - **MAKES POSSIBLE THE STRAIGHT-FORWARD ANALYSIS OF SECONDARY EFFECTS OF THE REFLECTOR BACK ONTO THE SOURCES.**
    - **INTERMEDIATE CALCULATIONS ARE AVAILABLE FOR AUXILIARY CAUSAL ANALYSIS.**

DAILY TEMPERATURE CONTOUR PLOTS (TWO-HOUR PERIOD)

The temperature contour plots for the geosynchronous orbit on April 15 with sun declination at +9° are shown below: The sub-reflector and spacecraft body cast the maximum shadow on the reflector at this sun declination. The numbers on the upper left corner of each plot indicate the time of day for the satellite. The time of day for the satellite is arbitrary. In our case, 0 hour was defined when the satellite lay on a direct line between the sun and the earth.

At the 0th hour, the reflector is facing the earth and deep space with the sun illuminating the MLI. By the ninth hour, the main antenna reflector is starting to catch the sun. At the 13th hour, the entire main antenna reflector is facing the sun and this is the hottest case of the day with temperatures of up to +16°F. The spacecraft shadows the main antenna reflector between the 13 and 18 hours. After the 19th hour, the antenna reflector is pointing away from the sun and facing deep space again. The coldest case of the day occurs at the 24th hour when the reflector is fully facing deep space with temperatures down to -140°F.

April 15 (Sun Declination +9)

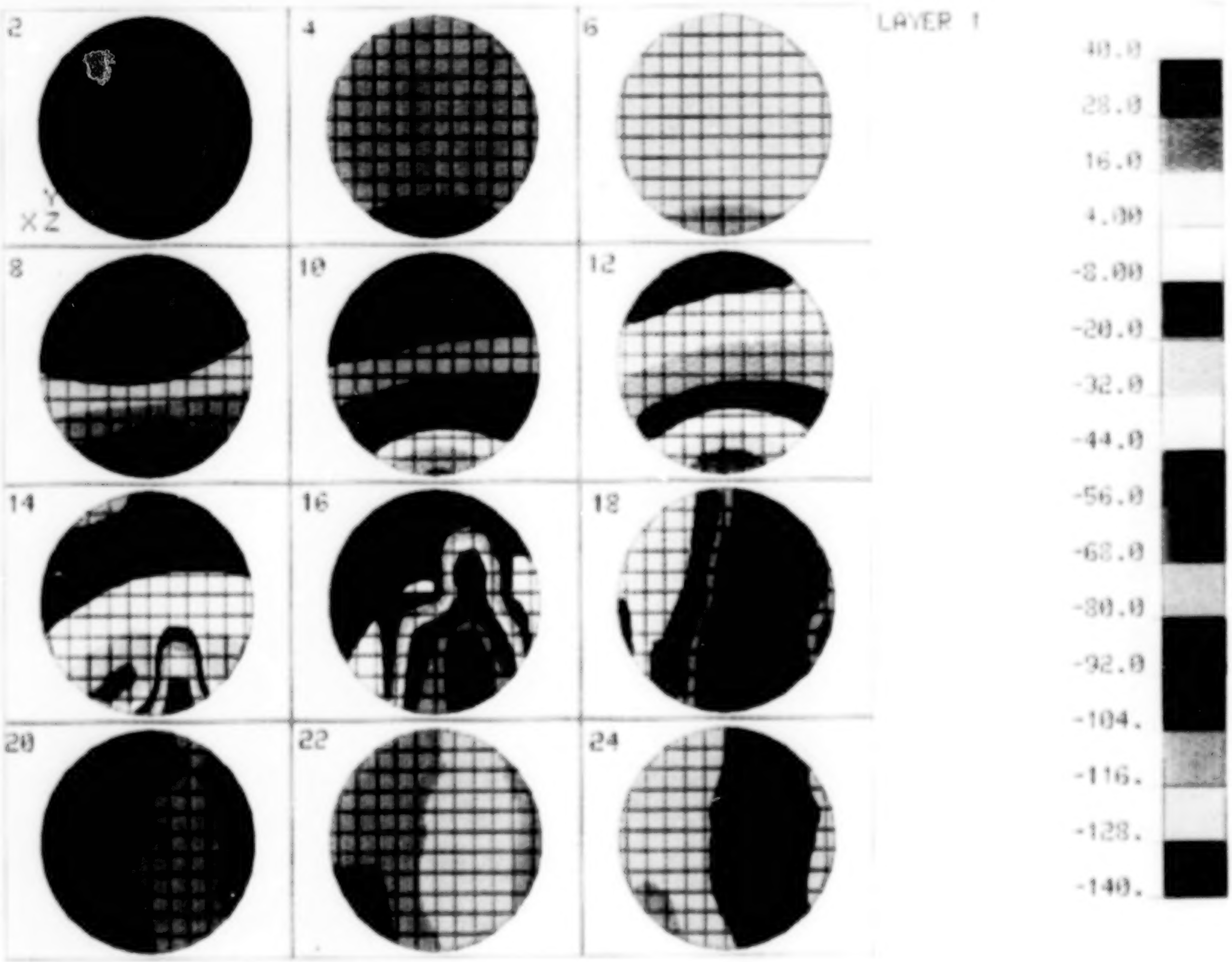

DAILY TEMPERATURE CONTOUR PLOTS (ONE-HALF HOUR PERIOD)

In order to visualize the effects of spacecraft shadowing on the 3.3 meter main antenna relector in more detail and determine the time of the day for maximum reflector temperature gradient, reflector temperature contours were plotted at ½ hour increments.

Maximum Temperature Gradient Reflector Temperatures at One-Half Hour Increments for April 15 (Sun Declination +9)

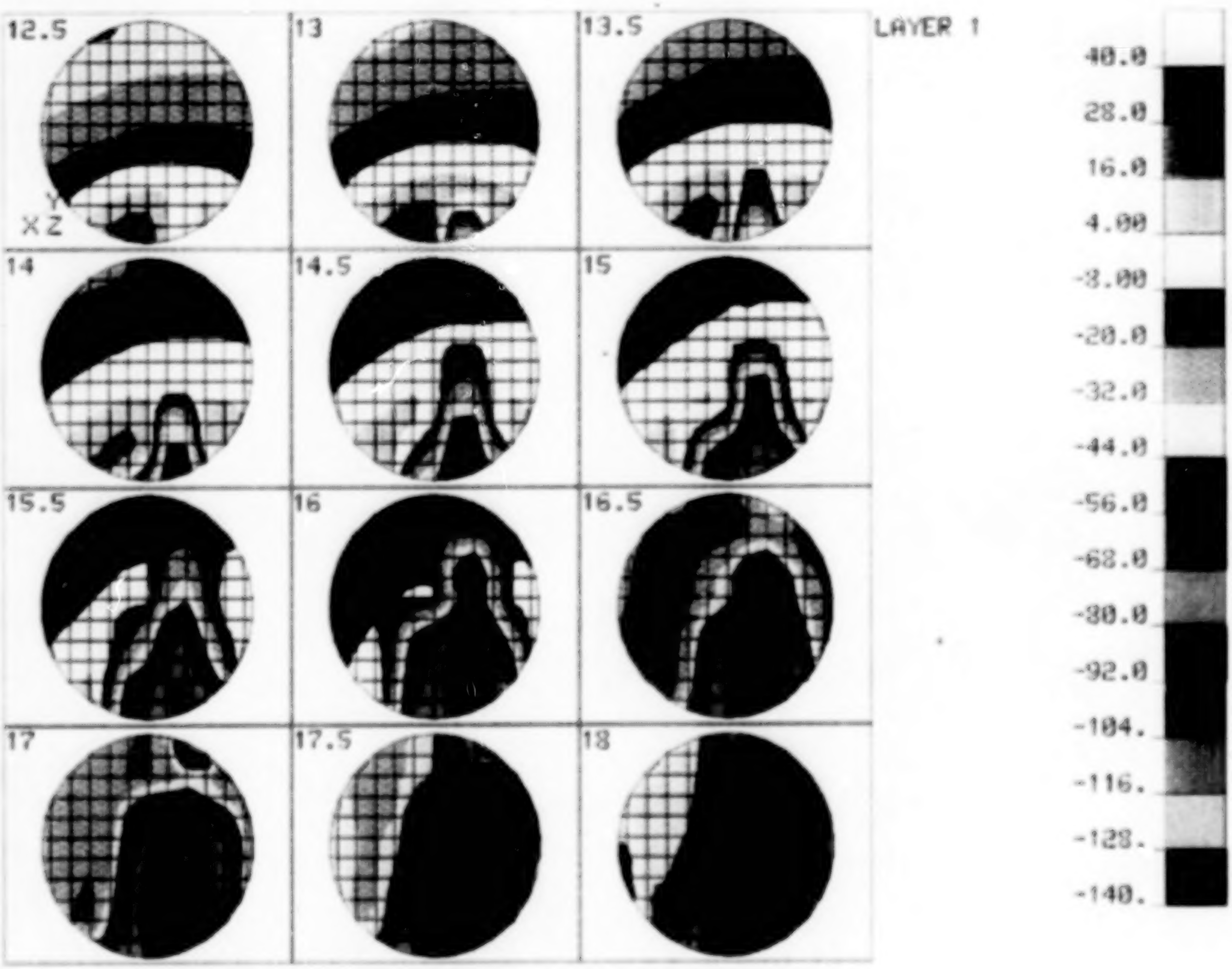

ACTS SPACECRAFT ATTITUDE FOR MAXIMUM REFLECTOR TEMPERATURE GRADIENT

The ACTS Spacecraft is shown here at a solar declination of +9 degrees. At the sixteenth hour of orbit time, the large main antenna reflector shown on the viewer's right is rotating away from the viewer, who is in the position of the sun. At this sixteenth hour, one can see that the large main reflector is rapidly becoming shadowed by the sub-reflector and the spacecraft body, thus producing the maximum temperature gradient across the reflector surface.

View From Sun

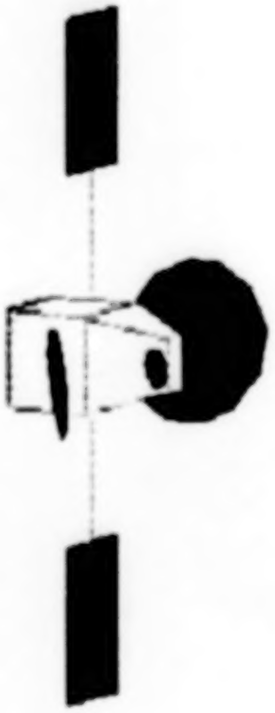

Orbit Time (Hours) = 16
Solar Declination (Deg) = 9
Anomaly (Deg) = 60
Eclipse Duration (Min) = 0.0

HOT, COLD AND MAXIMUM TEMPERATURE GRADIENT REFLECTOR TEMPERATURES

The two previous reflector temperature contour plots are for two-hour increments and one-half hour increments respectively for the specific date of April 15 which corresponds to a solar declination of +9 degrees. From these plots for this specific day, the hottest temperatures of -44°F to +28°F occur at the orbit time of 13 hours; the coldest case is at 24 hours when the temperature varies from -140°F to -116°F and the maximum temperature gradient of 72°F across the center of the reflector occurs at approximately 16 hours. All these times are approximate since the temperatures must be examined in continuously finer time increments to obtain the exact times. It should also be understood that hotter and colder cases than shown here occur at other times of the orbit year. The April 15 date was picked because near maximum shadowing occurs at this time.

April 15 (Sun Declination +9)

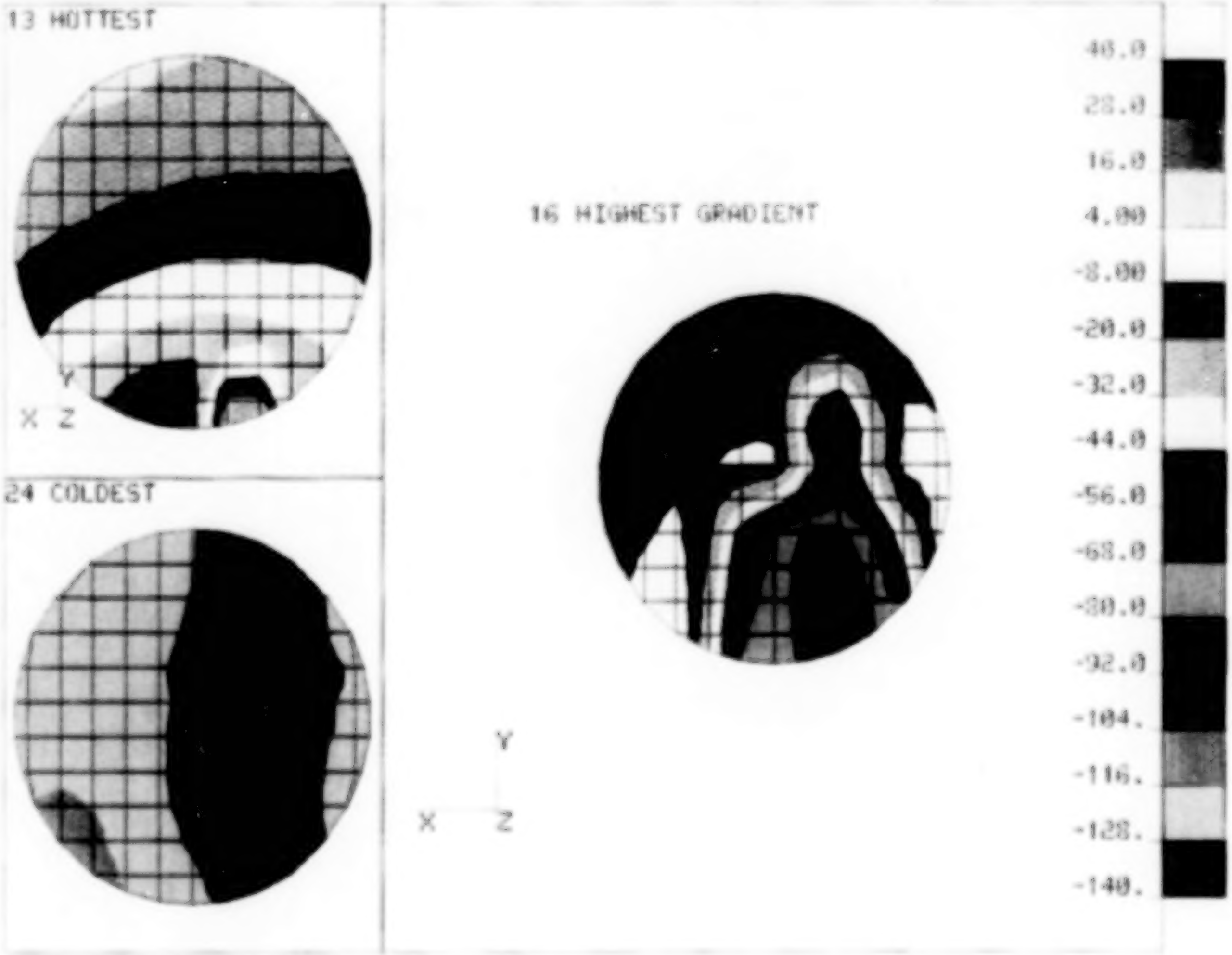

HOT, COLD AND MAXIMUM TEMPERATURE GRADIENT REFLECTOR DEFLECTIONS

The reflector deflections in the Z axis are shown for the hottest, coldest and maximum reflector temperature gradient cases of the previous figure. The displacements are plotted on the NASTRAN finite-element grid. The plots were created using PATRAN. Note that the finite-element grid is much finer than the grid used for the SINDA model shown on the previous chart. This occurs because SINDA does not allow models as large as NASTRAN and also much of the SINDA input must be hand calculated.

All deflections shown are in the minus Z direction. Thus, the reflector has a concave deflection superimposed on the parabola of revolution for all cases. For the hottest case, and concave deflections are fairly uniform varying from -.030 inches to -.021 inches at the reflector outside perimeter with the reflector center at 0.0 inches deflection. For the coldest case, the concavity becomes more exaggerated varying from -.030 inches to -.045 inches. For the maximum temperature gradient case, a saddle shape is superimposed on the basic concave shape with edge deflections varying from -.012 inches to -.021 inches.

April 15 (Sun Declination +9)

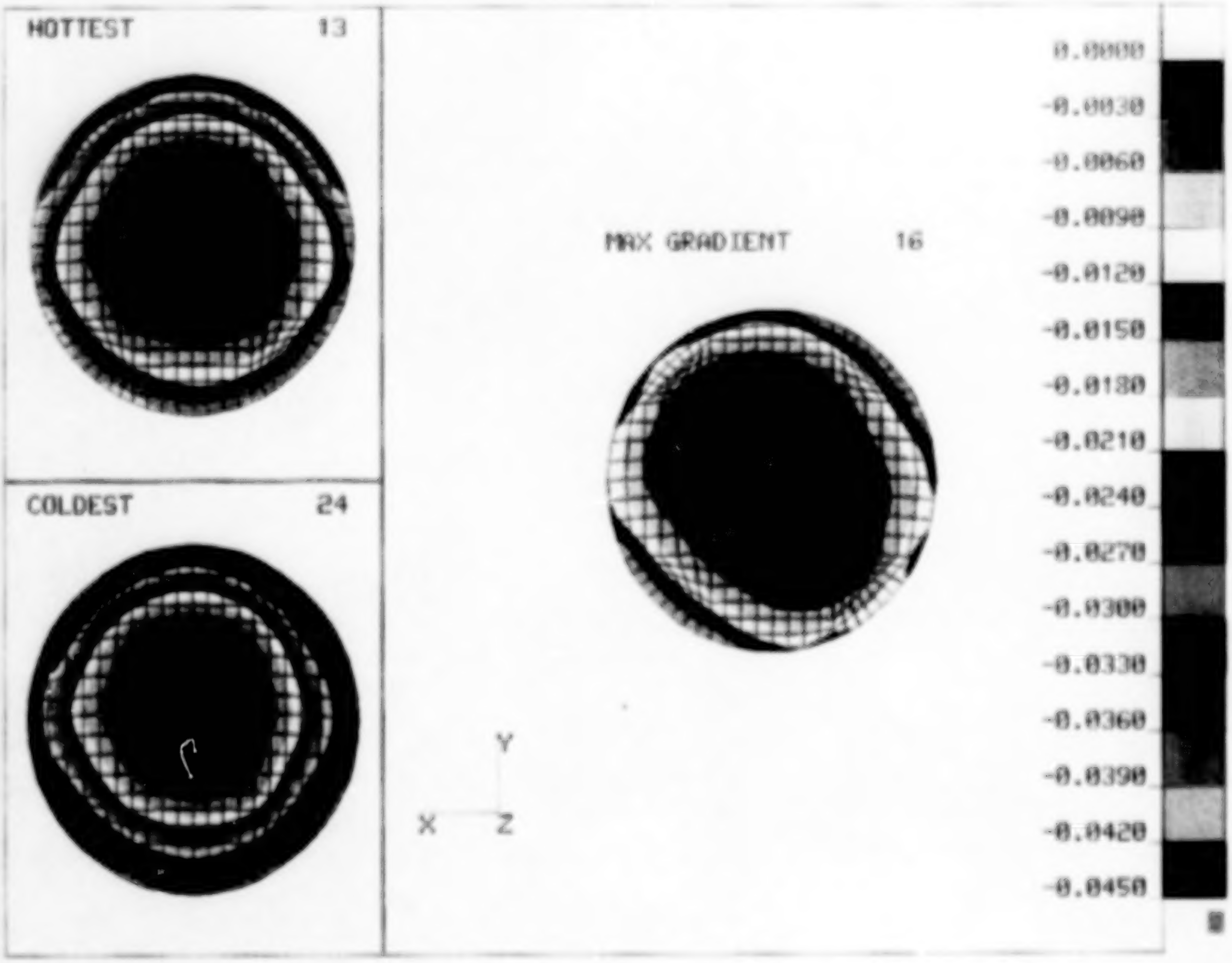

RF PATTERNS RESULTING FROM THE HOT, COLD AND MAXIMUM TEMPERATURE GRADIENT CASES

The RF patterns shown are for the reflector deflections for the hot, cold and maximum temperature gradient cases shown on the previous page. For this RF analysis, a feed horn with a 17 dB taper was assumed. The dotted line plots are for perfect optics for comparison purposes.

At the time of publication, the new spline and RF programs were not fully operational. These plots were produced using presently available spline and RF programs. The results are correct for the perfect optics cases. However, for the distorted antenna reflector cases, small errors occur in the far sidelobes that are caused by high spacial frequency ripples in the surface calculated by the earlier spline program. These should be corrected when the new spline program becomes operational.

The results calculated using the earlier Geometric Optics single reflector RF program should be the same as for the new multiple reflection RF Physical Optics program. The reason is that the ACTS dual-reflector antenna was modeled as a direct fed single reflective surface for purposes of this simplified analysis.

RF PATTERNS RESULTING FROM THE HOT, COLD AND MAXIMUM TEMPERATURE GRADIENT CASES

APRIL 15 (SUN DECLINATION +9)

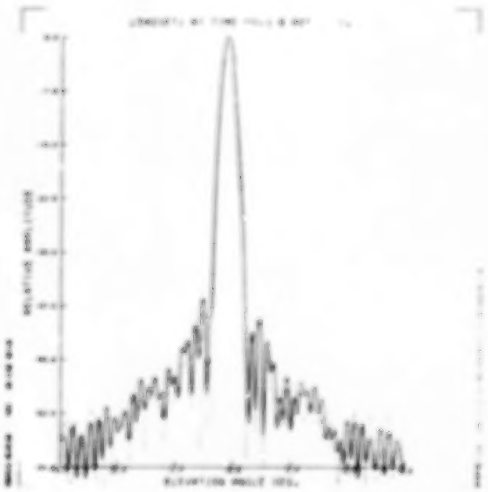

HOTTEST

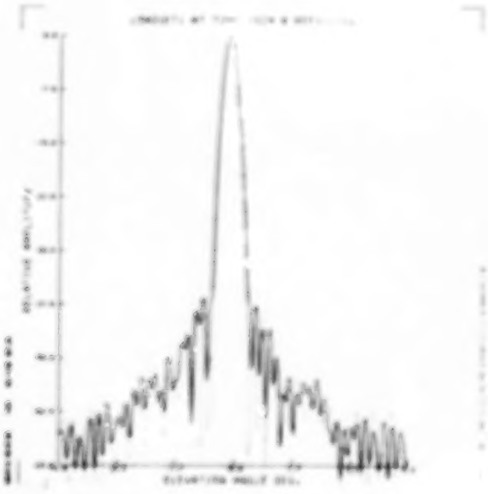

COLDEST

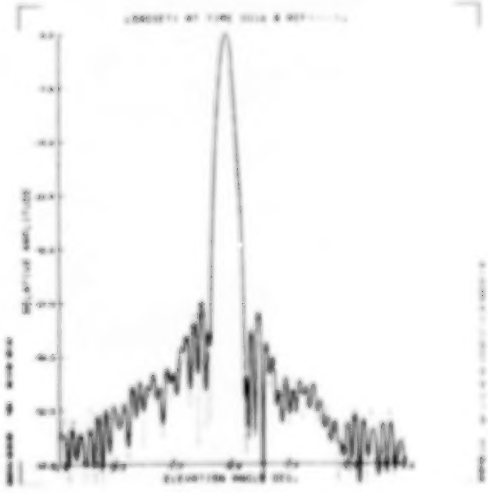

MAXIMUM GRADIENT

CONCLUSIONS

The programs linked together for this analysis can now be used to predict antenna performance in the constantly changing space environment. They can be used for very complex spacecraft and antenna geometries. Performance degradation caused by methods of antenna reflector construction and materials selection are also taken into consideration. However, the principal advantage of using this program linkage is to account for distortions caused by the thermal environment of space and the hygroscopic effects of the dry-out of graphite/epoxy materials after the antenna is placed into orbit.

The results of this type of analysis could ultimately be used to predict antenna reflector shape versus orbital position. A phased array antenna distortion compensation system could then use this data to make RF phase front corrections (Ref 3). That is, the phase front could be adjusted to account for the distortions in the antenna feed and reflector geometry for a particular orbital postion.

However, before this can be done, the analysis system would need to be experimentally verified. Also, an amplitude measurement system would probably be needed to measure displacements of key antenna dimensions in space in order to calibrate the whole analytical model. This could be accomplished by a new combined analytical and experimental program

- **PROGRAMS CAN BE USED TO PREDICT ANTENNA SYSTEM RF PERFORMANCE IN SPACE**
  - **ACCOUNT FOR PERFORMANCE DEGRADATION CAUSED BY:**
    - **METHODS OF CONSTRUCTION AND MATERIAL SELECTION**
    - **THERMAL AND HYGROSCOPIC DISTORTIONS**
- **SHOULD BE POSSIBLE TO USE PROGRAM TO PREDICT ANTENNA REFLECTOR SHAPE vs ORBITAL POSITION FOR USE WITH COMPENSATION SYSTEMS. HOWEVER, NEED:**
  - **PROGRAM ACCURACY VERIFICATION TEST TO VERIFY DISTORTION ANTENNA SHAPES (THERMAL MODES)**
  - **AMPLITUDE MEASUREMENT SYSTEM TO MEASURE DISPLACEMENTS OF KEY ANTENNA DIMENSIONS IN SPACE**

REFERENCES

1. Steinback, R. E.; and Winegar, S. R.: Interdisciplinary Design Analysis of a Precision Spacecraft Antenna. 26th Structures, Structural Dynamics, and Materials Conference, Part 1, 1985, pp. 704-712.

2. Winegar, S. R.: SINDA-NASTRAN Interfacing Program Theoretical Description and User's Manual. NASA TM 100158.

3. Sharp, G. R.; Acosta, R. J.; Bobinsky, E. A.; and Shaker, F. J.: A Conceptual System Design for Antenna Thermal and Dynamic Distortion Compensation Using a Phased Array Feed. NASA/DOD Control/Structures Interaction Technology 1987 pp. 145-162.

MESH SURFACES FOR REFLECTOR APPLICATIONS

Frank Kauffman
Department of Electrical and Computer Engineering
North Carolina State University
Raleigh, North Carolina

OUTLINE

The topics listed in Figure 1 are those which I believe should be addressed in assessing the current state of metallic mesh technology for spaceborne reflector antennas. The work I shall discuss involves only the study of the properties of the conducting mesh material. To calculate the radiation patterns of antennas with conducting mesh reflectors, the electromagnetic properties of the mesh material must be integrated into an appropriate reflector antenna computer code. Such a code would take into account such factors as the curvature of the reflector surface, the radiation pattern(s) of the feed(s), etc. Many organizations have developed their own codes for these calculations. An excellent example of such a code is the one developed by Rahmat-Samii and Lee (ref. 1).

I. Why Mesh Reflectors?

II. Methods of Analysis

III. Measurements

IV. Problems of Current Interest

V. Future Research

Figure 1

MESH REFLECTORS BECAUSE

Listed in Figure 2 are three major reasons why metallic mesh materials are attractive for use as the reflector surface in large aperture reflector antennas in space.

1. **Weight**
2. **Relative ease of deployment for required aperture size**
3. **Provides a reflector surface which can be adjusted in orbit**

Figure 2

METHODS OF ANALYSIS

Figure 3 lists the methods which have been developed by various workers to calculate the electromagnetic properties - transmission and reflection coefficients as a function of angle and polarization - of infinite, periodic, rectangular wire grids.

The "average boundary condition" method (refs. 2 and 3) gives results which agree well with other methods as long as the grid opening is electrically small - less than 0.1 wavelength.

Rahmat-Samii and Lee (ref. 1) have studied the mesh material using two different methods of analysis. They used the average boundary condition method to model the mesh as a rectangular wire grid. They also modeled the mesh as "strip-apertures" - an infinite periodic array of apertures cut in a thin perfectly conducting plate. The analysis of the strip-apertures was carried out using a moment method technique similar to that reported by Chen (ref. 4). The wire-grid mesh formulation and the strip-aperture mesh formulation are not in agreement for all values of the mesh parameters. In particular, they found that the wire-grid mesh model did not obey reciprocity and, hence, the strip-aperture formulation was the more accurate of the two.

The Fourier series method of Hill and Wait (ref. 5) is very slowly converging for some values of mesh parameters.

The Spectral Domain Conjugate Gradient (SDCG) technique developed by Christodoulou and Kauffman (ref. 6) is an iterative technique for which convergence is guaranteed. The iterates are chosen so as to minimize the number of iterations required. This formulation can also accommodate grids with arbitrary surface impedance.

1. Average Boundary Conditions
   Kontorovich, 1963
   Astrakhan, 1968

2. Moment Methods - Strip Apertures
   Chen, 1970
   Rahmat-Samii & Lee, 1985

3. Fourier Series Expansion
   Hill & Wait, 1974

4. Spectral Domain Conjugate Gradient
   (SDCG)
   Christodoulou & Kauffman, 1986

All treat rectangular mesh openings

Figure 3

ACTUAL MESH SURFACE

Figure 4 is a line drawing of the actual woven mesh material magnified many times. Note the many small openings and loop contact points in addition to the large openings which correspond to the rectangular apertures in the mathematical models.

The meshes which have been fabricated have been woven using gold-plated molybdenum wire about 1 mil in diameter. The plating is typically around .25 μm thick. Meshes have been woven with anywhere from 10 to 32 openings per inch.

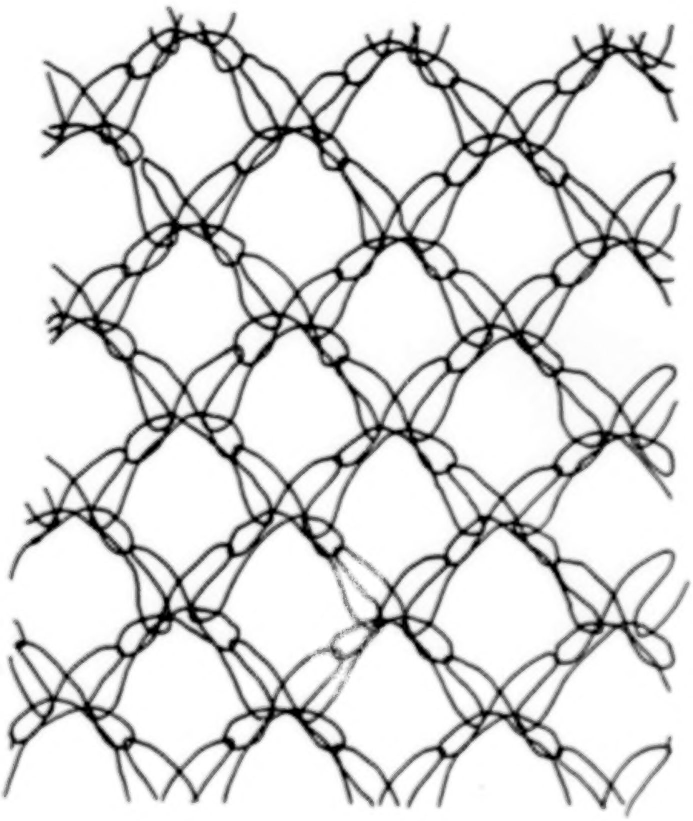

Figure 4

WIRE-GRID MESH AND STRIP-APERTURE MESH MODELS

The sketches shown in Figure 5 define the geometries used in the mathematical analysis of the conducting mesh material.

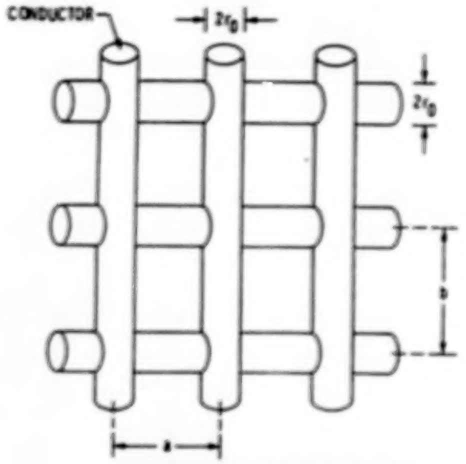
CONDUCTOR
$2r_0$
$2r_0$
b
a

Wire-grid mesh with rectangular lattice.

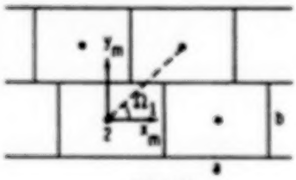
y_m
Ω_1
x_m
z
b
a

LATTICE
(a)

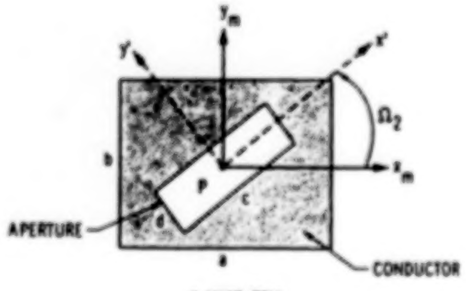
y_m
y'
x'
Ω_2
x_m
b
p
c
d
APERTURE
a
CONDUCTOR

A UNIT CELL
(b)

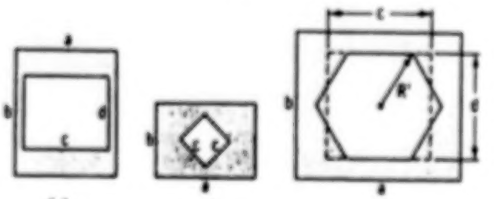
a
b
d
c
b
c
c
a
c
b
R'
d
a

(c) (d) (e)

Strip-aperture mesh model with different lattice configurations.

Figure 5

TRANSMISSION COEFFICIENTS USING WIRE-GRID AND STRIP-APERTURE MODELS

The mesh transmission coefficients versus angle of incidence, calculated using both the wire-grid and the strip-aperture formulations,are shown in Figure 6. Notice that $T_{\theta\phi} \neq T_{\phi\theta}$ for the wire-grid model indicating that the formulation does not obey reciprocity.

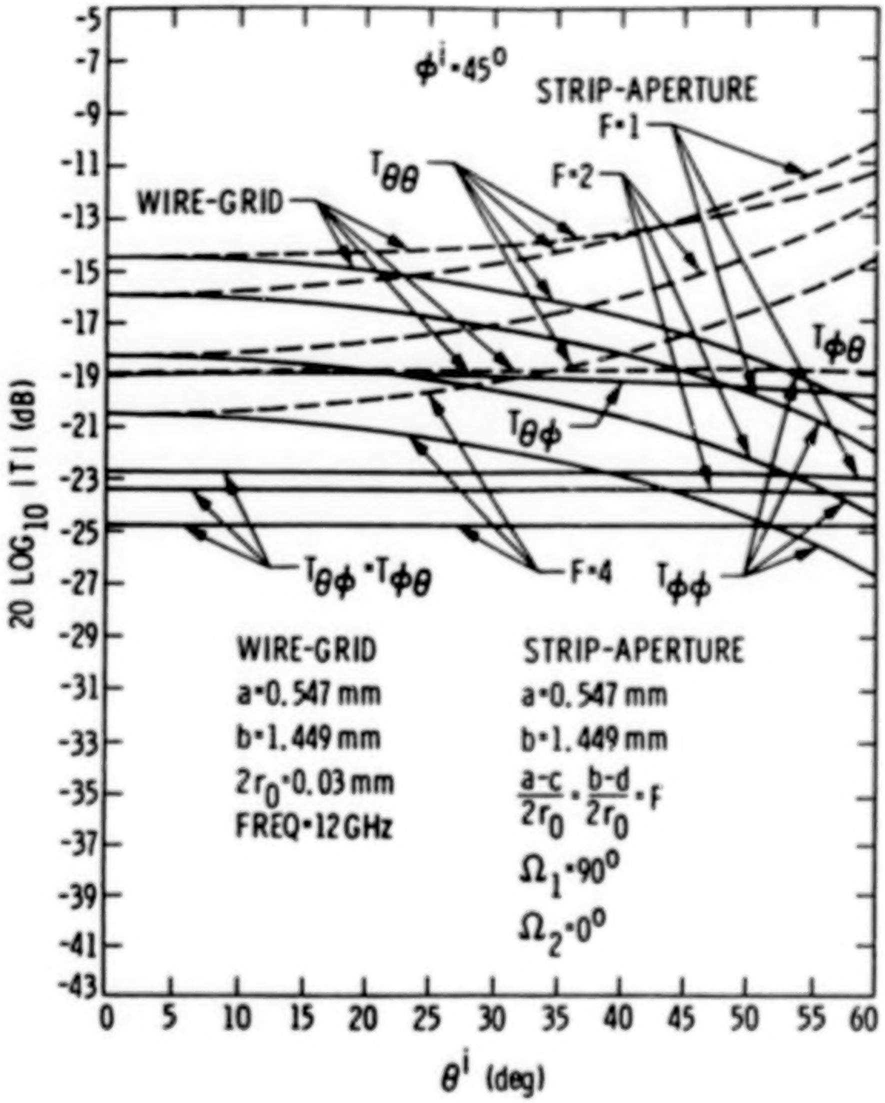

Figure 6

REFLECTION COEFFICIENT VS. MESH OPENING - TM POLARIZATION

Figure 7 shows a comparison of the reflection coefficient vs. mesh opening in wavelengths calculated by the method of Hill and Wait (ref. 5) and by the SDCG method of Christodoulou and Kauffman (ref. 6). As can be seen in the figure, the agreement between the two methods is quite good. This can be said of all of the analytical methods discussed earlier with the exception of the average boundary condition, which gives poor results for large mesh openings.

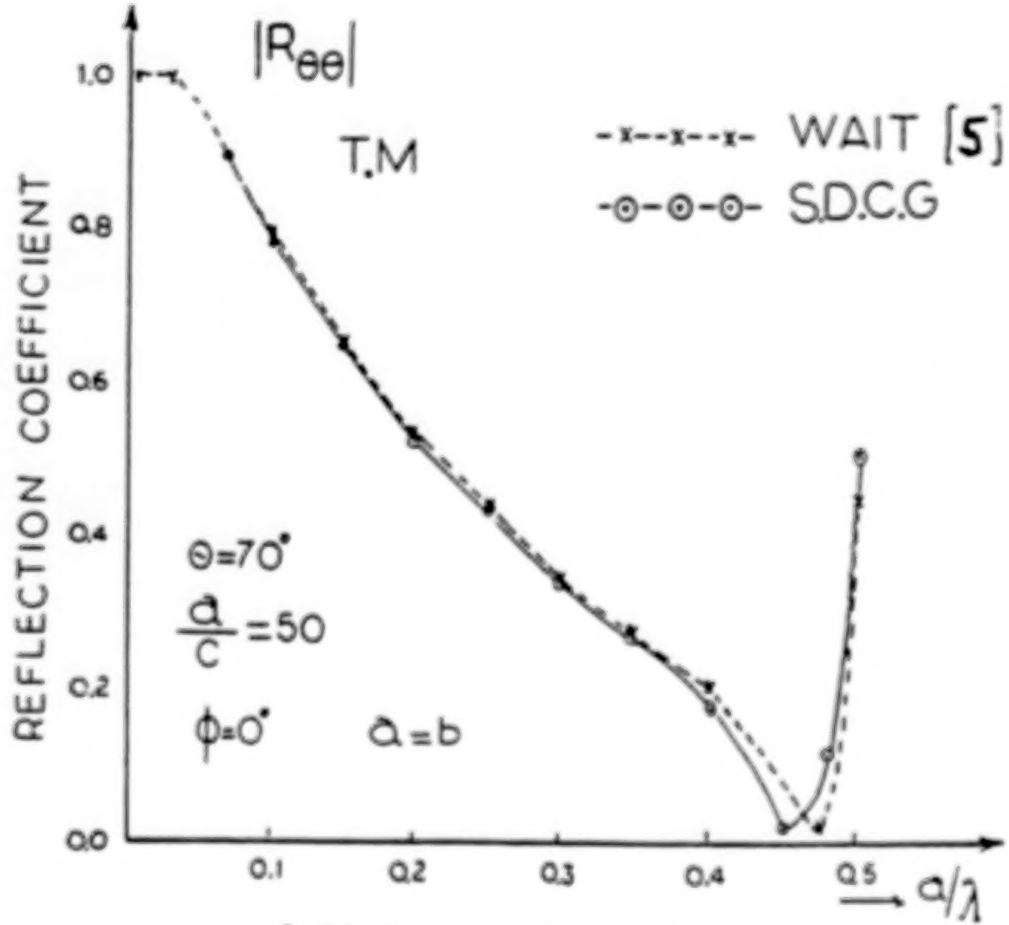

θ=70 deg., and ϕ=0 deg.

Figure 7

REFLECTION COEFFICIENT VS. MESH OPENING - TE POLARIZATION

Figure 8 shows the reflection coefficient vs. mesh opening for the orthogonal polarization. The same remarks made in discussing Figure 7 apply to Figure 8. Also, seeing comparisons with other calculations but not with measurements points toward one of the areas very much in need of further work: careful measurements of reflection and transmission coefficients as a function of angle of incidence, frequency, polarization and mesh opening. Our calculations agree well with one another but do they do a good job of modeling the actual mesh material?

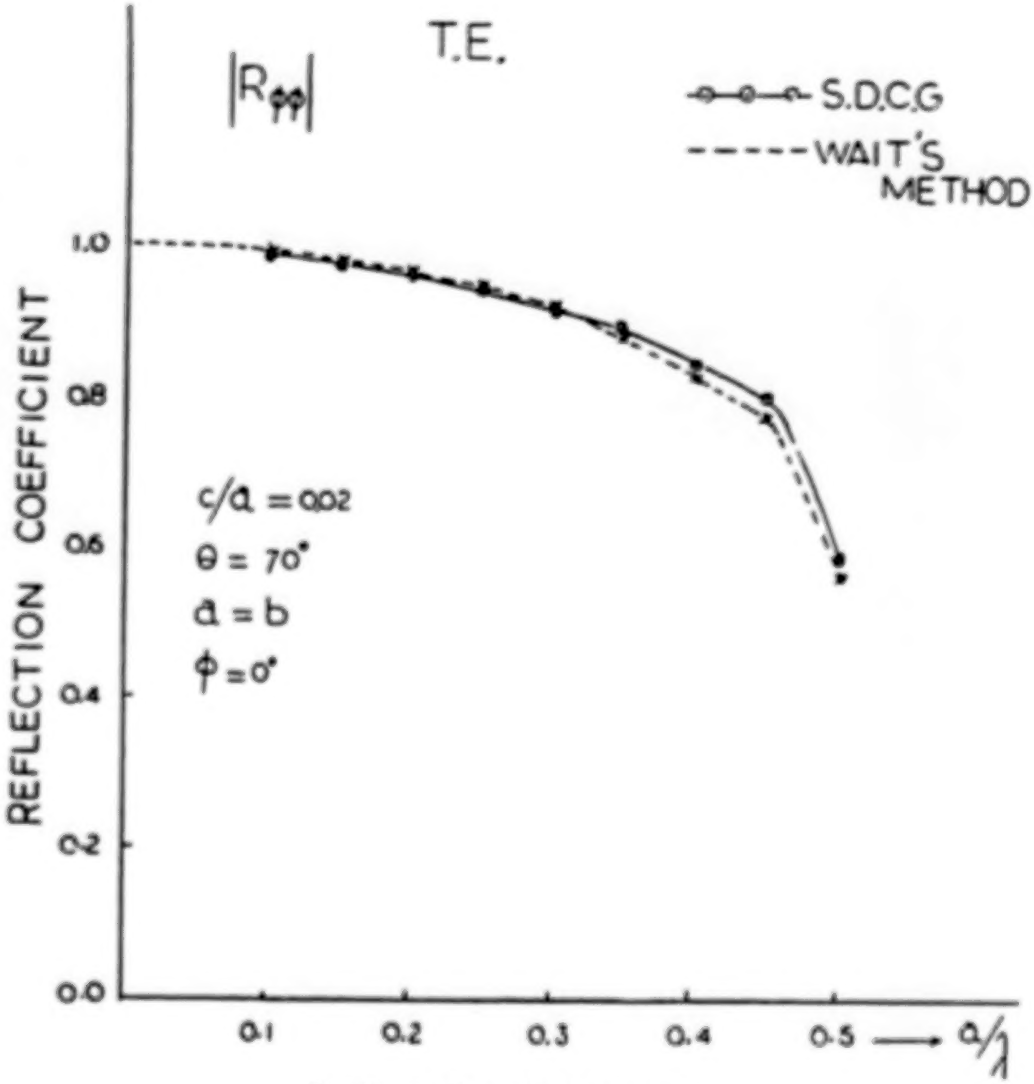

θ=70 and φ=0 degrees

Figure 8

SKETCH OF THE 5.2 GHZ BUCKET RADIOMETER SET-UP

We leave now the discussion of the analytical methods which have been developed and turn our attention to the measurements which have been made.

Radiometer techniques offer a means of determining the ohmic losses of the mesh material. These measurements are power measurements: power reflected - reflectivity, power transmitted through the mesh - transmissivity, power absorbed - emissivity. The power emitted, or radiated, by the material is equal to the power absorbed if one neglects scattering. Measurements have shown this to be a good assumption. Conservation of energy requires that the sum of these three quantities, expressed as fractions of the incident power, be equal to one.

Knowledge of ohmic losses is very important if the material is to be used in a reflector antenna in a radiometer system. Such losses cause the brightness temperature measured by the system to be in error if they are not calibrated out or accounted for by some other means.

Figure 9 is a sketch of a system used by Harrington and Blume (ref. 7) to measure the emissivity, transmissivity and reflectivity of the gold-plated molybdenum mesh at 5.2 GHz. Four measurements with four different test configurations are required.

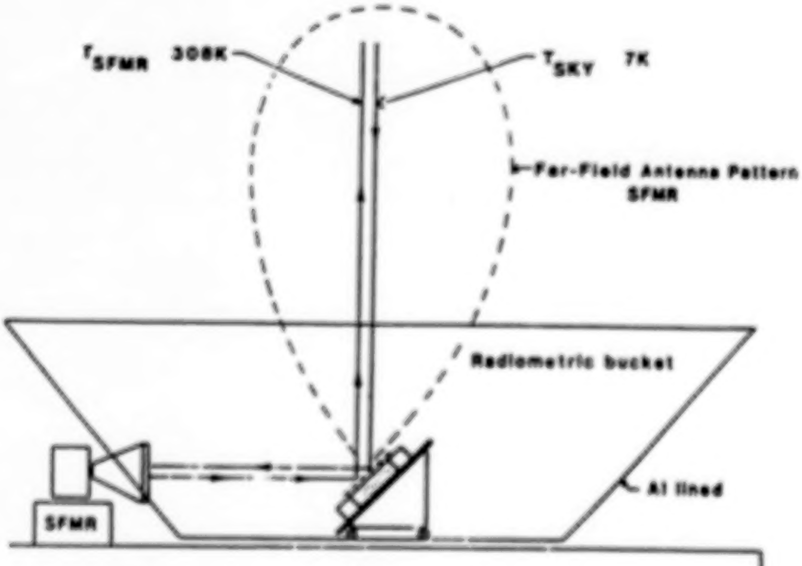

Figure 9

2.65 - GHZ CLOSED RADIOMETER

Figure 10 is a sketch of the radiometer used by Harrington and Blume (ref. 7) to measure the emissivity of the gold-plated molybdenum mesh at 2.65 GHz. Both of these systems and the measurements required are discussed in detail in the reference cited.

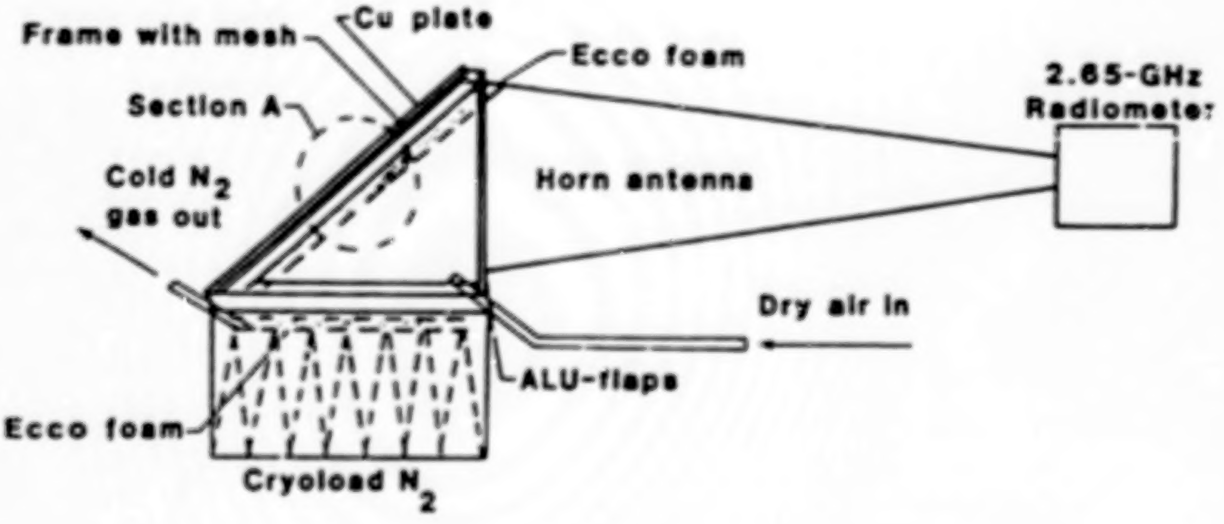
Frame with mesh
Cu plate
Ecco foam
2.65-GHz Radiometer
Section A
Cold N2 gas out
Horn antenna
Dry air in
ALU-flaps
Ecco foam
Cryoload N2

Figure 10

RADIOMETERIC TEST RESULTS

Figure 11 shows the test results at both 5.2 GHz and 2.65 GHz (ref 7).

TEST RESULTS-RADIOMETRIC BUCKET
(5.2 GHz)

SAMPLE NO.	GD001	GD002
EMISSIVITY	.0048 ± .0002	.0050 ± .0003
	.0041 ± .0003	.0054 ± .0012
	.0049 ± .0003	.0050 ± .0003
	.0051 ± .0003	.0050 ± .0003
	.0046 ± .0004	.0059 ± .0004
MEAN:	.0047 ± .0004	.0053 ± .0004
REFLECTIVITY	.9724 ± .0005	.9743 ± .0005
	.9716 ± .0008	.9693 ± .0006
TRANSMISSIVITY	.0266 ± .0006	.0190 ± .0006
	.0213 ± .0008	.0233 ± .0003

(a)

TEST RESULTS-CLOSED SYSTEM (2.65 GHz)

SAMPLE NO.	GD001	GD002
EMISSIVITY	0.0185	0.0156
	0.0287	0.0167
	0.0134	0.0255
	0.0129	0.0183
	0.0137	0.0168
	0.0130	
MEAN:	0.0167 0.0062	0.0186 0.004

(b)

Figure 11

ADVANTAGES/DISADVANTAGES OF THE 5.2 GHZ AND 2.65 GHZ RADIOMETERIC MEASUREMENTS

Figure 12 lists the quantities measured and the problems encountered using the two systems.

A COOPERATIVE LaRC/NRL PROGRAM HAS DEVELOPED TWO DIFFERENT METHODS FOR MEASUREMENT OF THE ELECTROMAGNETIC PROPERTIES OF MESH MATERIAL.

(1) Radiometric bucket method

Measures reflectivity, emissivity and transmission
Problems: RFI, solar interference, weather, multiple measurements

(2) Closed system

Measures emissivity directly
Problems: Limited intergration time, heating/cooling rate limitations

Figure 12

PROBLEMS OF CURRENT INTEREST

Listed in Figure 13 are problems which have come to the attention of workers in this area which must be solved if mesh utilization for spaceborne antennas is to reach its full potential.

The first problem listed comes from observations on shuttle missions in which gold-plated materials, when exposed to the plasma discharge around the vehicle in low earth orbit, would oxidize in such a way as to form a Schottky barrier junction. These observations are discussed by Blume (ref. 8). If the contact points of the woven wire mesh form junctions of the type, its reflection and transmission properties and its ohmic losses would be altered dramatically. I will discuss this problem in more detail using the next two figures. However, before I do, let me mention briefly the second and third problems on the list.

The second problem comes from a desire for a mesh which performs well at higher frequencies - above 60 GHz. Such a mesh must be much smoother, with smaller cell size, than the current technology can provide. Some cooperative work between LaRC and a textile mill in North Carolina is being done to address this problem.

The third problem is listed simply to provide the information that Chase Hearn at LaRC has developed a resonant cavity technique for measuring the ohmic losses of these mesh materials.

1. Modeling Wire Mesh Contact Points
2. Woven Mesh Technology
3. Cavity-type Mesh Measurements (Power)

Figure 13

GOLD - MOLYBDENUM OXIDE - GOLD JUNCTION

Figure 14 provides a sketch of the Schottky barrier junction which may be formed by the oxidation of the material due to the action of the plasma discharge around the spacecraft in low earth orbit. Dr. Blume is currently planning an experiment to determine whether or not the gold/molybdenum mesh oxidizes as have similar materials during earlier space flights.

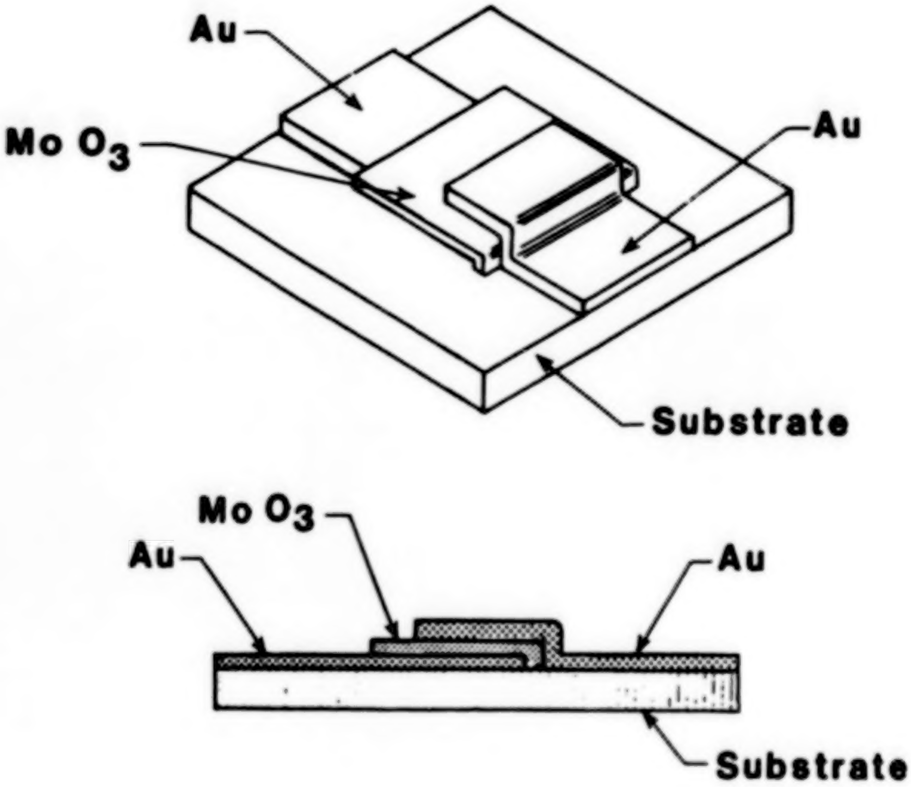

Figure 14

CAPACITANCE VS. TEMPERATURE FOR A SCHOTTKY BARRIER JUNCTION

Figure 15 is a graph of capacitance of the diode versus temperature. Such variation is a cause for concern because spaceborne antennas are subjected to extreme temperature changes and thermal gradients. If the mesh contact points behave in this fashion, the reflection, transmission and loss properties of the mesh will undergo wide fluctuations with temperature.

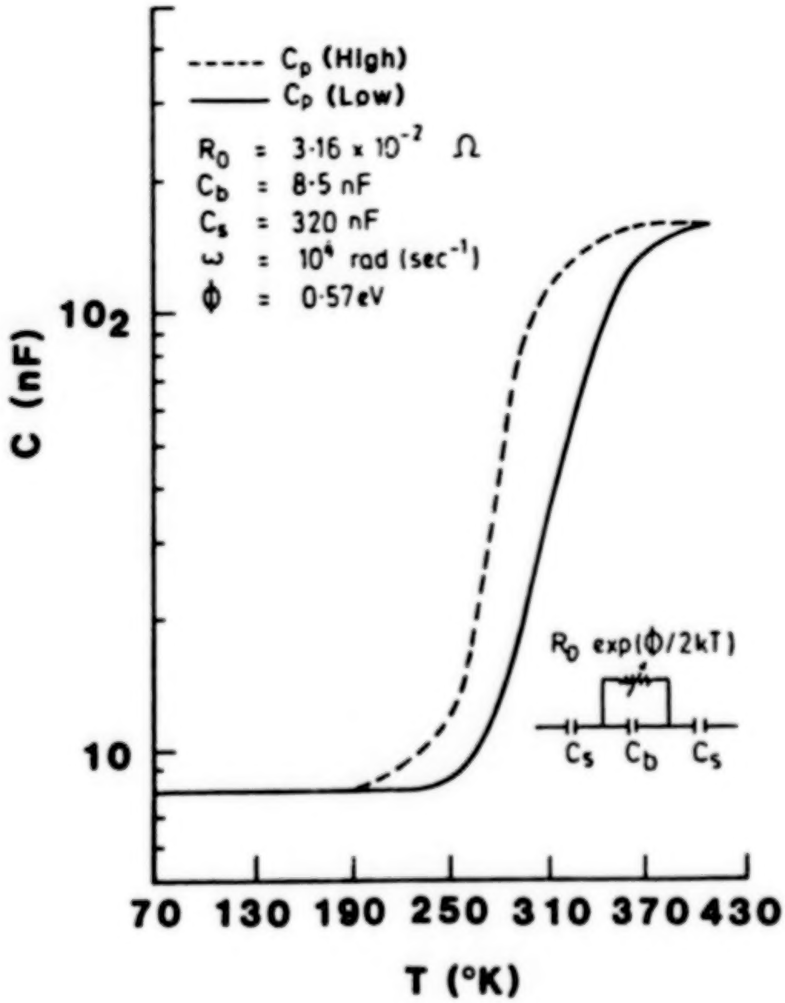

Figure 15

FUTURE RESEARCH

Figure 16 offers a list of those problems which, in my opinion, require further research.

A comprehensive set of measurements is needed not only to expand our knowledge of the mesh material but also to judge the adequacy of our analytical techniques.

The first gold - mobybdenum oxidation experiments are now being planned by Dr. Blume at LaRC with assistance from faculty and students at Old Dominion University.

Very limited tests are now under way on weaving tighter conducting mesh materials. Much more must be done if these materials are to be used at millimeter wavelengths.

1. **Measurement of Wave Properties - Reflection, Transmission, Polarization**
2. **Gold - Molybdenum Oxidation Experiments**
3. **Smoother, Tighter Woven Meshes for Higher Frequencies**

Figure 16

ANTENNAS FOR 20/30 GHz AND BEYOND

C. Harry Chen, William C. Wong and S. Jim Hamada
TRW Electronic Systems Group, Antenna Systems Laboratory
Redondo Beach, CA

SPACEBORNE ANTENNAS FOR 20/30 GHz AND BEYOND

In the past three decades, NASA has been the prime mover in a series of experimental satellites, which then expanded into the space industry. NASA sponsored the basic research and development and the industry developed and optimized the performance of the systems. This is shown by the development of the space communications technology, in which several NASA programs played significant milestones as shown in Figure 1. Figure 1 also shows that the spaceborne antenna technology trend is moving up into 20/30 GHz and even higher frequency bands.

The advantages of high frequency have long been recognized, i.e. smaller hardware size, lighter weight, higher antenna gain (for the same aperture size), narrower beamwidth (thus better resolution), and broader baseband bandwidth (for the same percentage bandwidth). The challenges to successfully design and develop a spaceborne antenna are also numerous: the design and analysis capability to achieve and assure the high performance; the component/device availability to put a system together; the manufacturing capability to meet the tight tolerances; and the integration and test capability to precisely assemble and align the antenna system and accurately verify the performance. This paper describes how the industry faces these challenges using primarily the Multibeam Antenna (MBA) system of the Advanced Communication Technology Satellite (ACTS) [1] as an example. Even though the technology and the hardware developed in this program are for space communications application, they are applicable to other space applications requiring 20/30 GHz and higher frequency.

ACTS — A Showboat of Ka-Band Technology

Satellite	Launch	Comments
NASA SYNCOM	1963	First communication satellite at geosynchronous altitude
Intelsat I	1965	C-band
Intelsat II	1967	C-band
Intelsat III	1968	C-band
Intelsat IV	1971	C-band
NASA ATS-6	1974	Demonstrated the full technology and capability of communications satellite
Intelsat IV-A	1975	C-band
NASA CTS	1976	Demonstrated Ku-band technology
Intelsat V	1980	C- & Ku-bands
Intelsat VI	Under construction	C- & Ku-bands
NASA ACTS	1990	To demonstrate Ka-band technology

Figure 1

ACTS MULTIBEAM ANTENNA SYSTEM DESIGN

The ACTS MBA system was designed to demonstrate a spaceborne antenna's capability of producing multiple fixed, scanning and overlapping beams with a single aperture while maintaining good isolation between beams and precise pointing of each beam. The beamwidth is approximately 0.3 degrees with 0.01 degree pointing accuracy. This extremely narrow beamwidth along with the weight and stowage constraints of the Space Shuttle cargo bay dictates that a reasonably large antenna aperture operating at 20/30 GHz must be used. To allow frequency reuse on as many fixed beams (which serve high data rate) as possible, sidelobe roll-off (below -30 dB) and high cross-polarization (also below -30 dB) are of utmost importance as these determine the minimum allowable beam spacing to meet the beam-to-beam isolation requirement. For the overlapping beams (which serve low data rate to scan sectors), the beam-to-beam isolation is attained through cross-polarization and/or time division multiplexing (TDM). The TDM coverage of each scan sector is accomplished by the beam forming network (BFN). The scan spot beams, usable as high data rate fixed beams or low data rate TDM beams, are also connected to the BFN. The ACTS MBA beam coverage and polarization, including 3 fixed beams, 13 scan spot beams and 2 scan sectors, are illustrated in Figure 2. The 3 fixed beams are Cleveland, Atlanta and Tampa. The Cleveland beam also serves as the tracking beam.

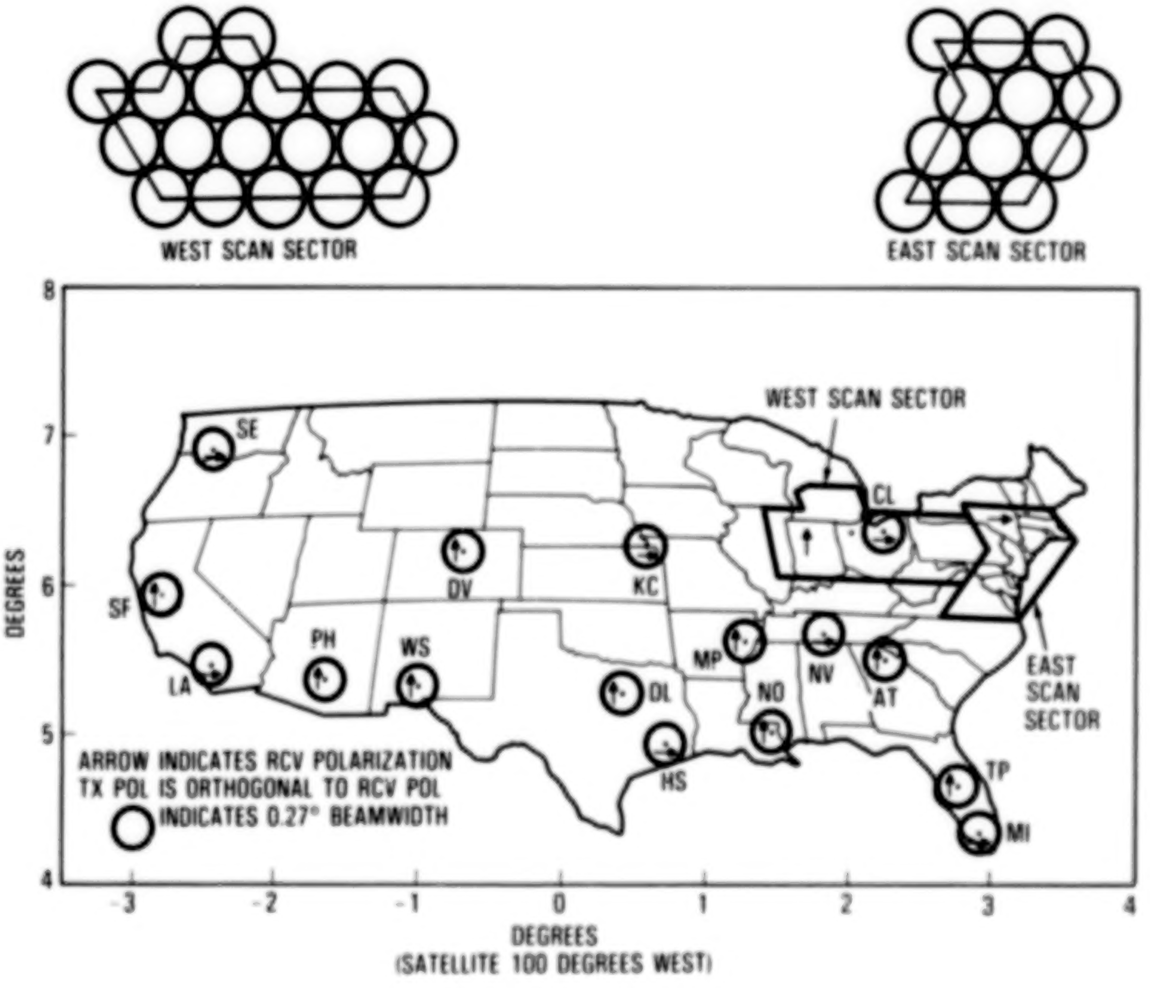
WEST SCAN SECTOR
EAST SCAN SECTOR
WEST SCAN SECTOR
EAST SCAN SECTOR
SE
SF
LA
PH
WS
DV
KC
DL
HS
MP
NO
NV
AT
CL
TP
MI
ARROW INDICATES RCV POLARIZATION
TX POL IS ORTHOGONAL TO RCV POL
INDICATES 0.27° BEAMWIDTH
DEGREES
8
7
6
5
4
-3
-2
-1
0
1
2
3
4
DEGREES
(SATELLITE 100 DEGREES WEST)

Figure 2

ACTS MULTIBEAM ANTENNA CONFIGURATION

The capabilities that ACTS MBA's are required to demonstrate were never before demanded of a communications satellite antenna, leading to antenna configurations with unprecedented complexity. Both receive and transmit MBA's are offset Cassegrain systems with dual subreflectors in a piggyback arrangement (Figure 1). The Cassegrain system is used to obtain large equivalent F/D, thus minimizing the scan loss. (Some spot beams, e.g. San Francisco, scan as far as 15 half-power beamwidth.) The offset configuration eliminates the gain and sidelobe degradation due to blockage. The front subreflector is gridded, transparent to one sense of polarization and reflective to the orthogonal sense of polarization. The polarization passing through the front subreflector is reflected by the solid back subreflector and passes through the front subreflector again. The polarizer characteristic of the front subreflector enhances the cross-polarization isolation by at least 10 dB between orthogonally polarized beams. To avoid mechanical interference, the focal axes of the two subreflectors are symmetrically displaced from the main reflector axis by an angle of 10 degrees, creating two focal regions for the two feed assemblies and BFN's. The important design parameters of the MBA's are listed in Figure 3.

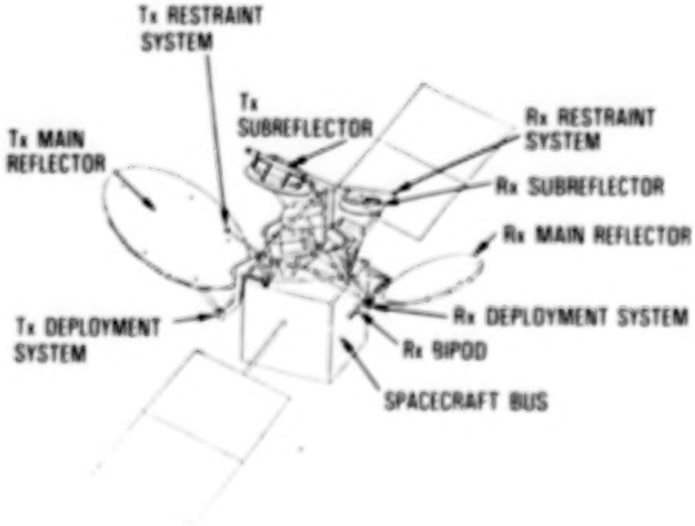
Tx RESTRAINT SYSTEM
Tx MAIN REFLECTOR
Tx SUBREFLECTOR
Rx RESTRAINT SYSTEM
Rx SUBREFLECTOR
Rx MAIN REFLECTOR
Tx DEPLOYMENT SYSTEM
Rx DEPLOYMENT SYSTEM
Rx BIPOD
SPACECRAFT BUS

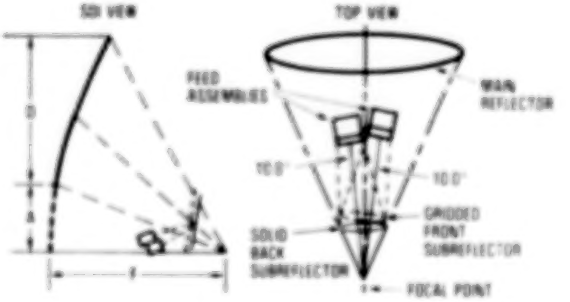
SIDE VIEW
TOP VIEW
D
A
F
FEED ASSEMBLIES
MAIN REFLECTOR
10.0°
10.0°
SOLID BACK SUBREFLECTOR
GRIDDED FRONT SUBREFLECTOR
FOCAL POINT

Parameter	ACTS		Breadboard (30 GHz)
	20 GHz	30 GHz	
D (Main reflector diameter) (meters)	3.3	2.2	2.7
A (Offset distance) (inches)	50.0	44.0	56.12
F (Main reflector focal length inches)	132.0	88.0	132.0
Gridded front subreflector			
Focal length (inches)	69.0	44.5	84.0
Magnification factor	2.0	2.0	2.0
Solid back subreflector			
Focal length (inches)	52.4	32.4	66.0
Magnification factor	2.0	2.0	2.0

Figure 3

REFLECTOR SURFACE CONTROL FOR LOW SIDELOBE PERFORMANCE

The deviation of the reflector from the prescribed surface affects both the amplitude and phase distribution in the aperture plane, causing both wide angle sidelobe and near-in sidelobe degradations. This effect is illustrated in Figure 4. With surface distortion, the well-behaved sidelobe structure of concentric rings as observed on the pattern without distortion is disturbed. These patterns were computed for the ACTS breadboard MBA. The pattern with distortion was obtained by incorporating the measured distortion profile of the breadboard reflector (0.0057 inch rms error) into the computation model. The distortion causes the first sidelobe level to degrade from -29 dB to -26 dB, which was later verified by the near-field testing. Traditionally, the surface distortion is characterized by root-mean-square error under the assumption that the distortion is of the random type. In reality, the distortion, closely relating to the manufacturing procedure and the reflector's supporting structure, is deterministic and the distortion profile determines how the sidelobe is degraded. Therefore, in addition to the stringent manufacturing tolerance (4 mils for receive and 6 mils for transmit), the ACTS reflectors are also subject to post-fabrication adjustment to correct the surface anomaly. If the surface distortion analysis based on the measured distortion profile predicts that the particular profile will cause excessive sidelobe degradation, the surface is adjusted.

Sidelobe Degradation Due to Reflector Surface Distortion

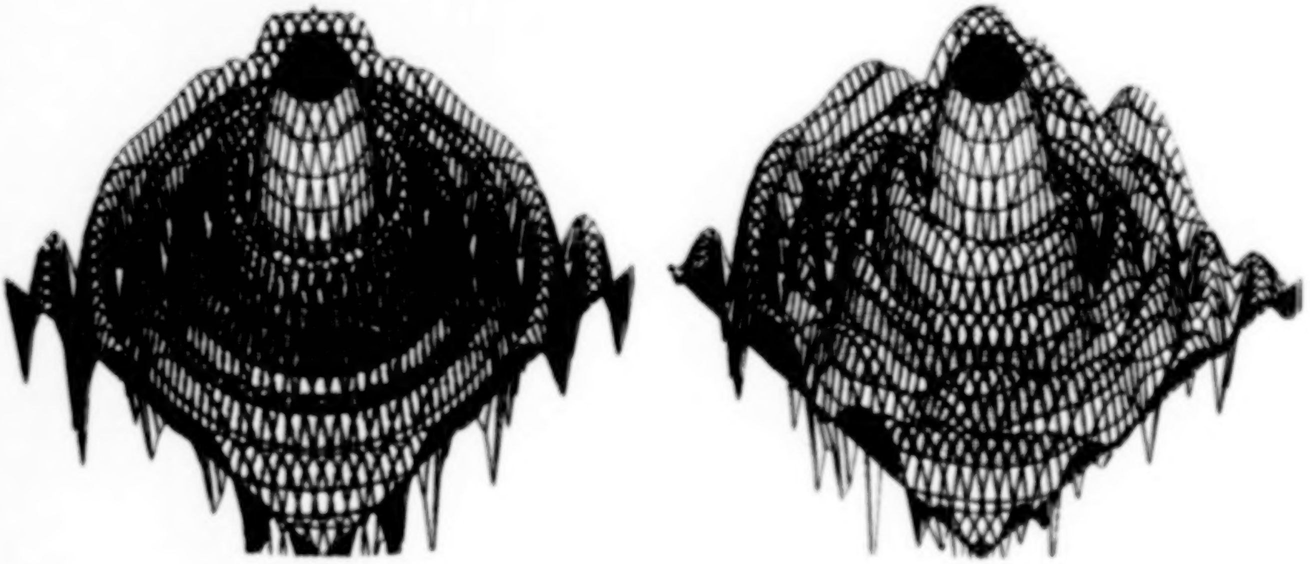

THEORETICAL RADIATION PATTERN WITHOUT REFLECTOR SURFACE DISTORTION

THEORETICAL RADIATION PATTERN WITH REFLECTOR SURFACE DISTORTION

Figure 4

ON-ORBIT THERMAL DISTORTION

On-orbit thermal conditions introduce additional distortion to the reflector surface. The thermal conditions vary from time to time, from day to day and from season to season and thus the thermal distortion effects are time-variant. An example is illustrated in Figure 5 where the sun illuminates the ACTS MBA's at 20:00 hours Eastern Standard Time during winter solstice. The receive antenna is half-shadowed by the subreflectors, resulting in maximum temperature gradient and thus the maximum surface distortion. The transmit antenna, illuminated on the backside in this case, is not very much affected due to the thermal blanket protection. The three-step thermal distortion analysis procedure is summarized in Figure 5. Results obtained from several study cases on the ACTS MBA's [2] show that, without the assistance of an autotracking system, the thermal distortion may cause as high as 0.02 degree pointing error. (Notice that the half-power beamwidth is 0.3 degrees.) The gain degradation may be as high as 0.6 dB.

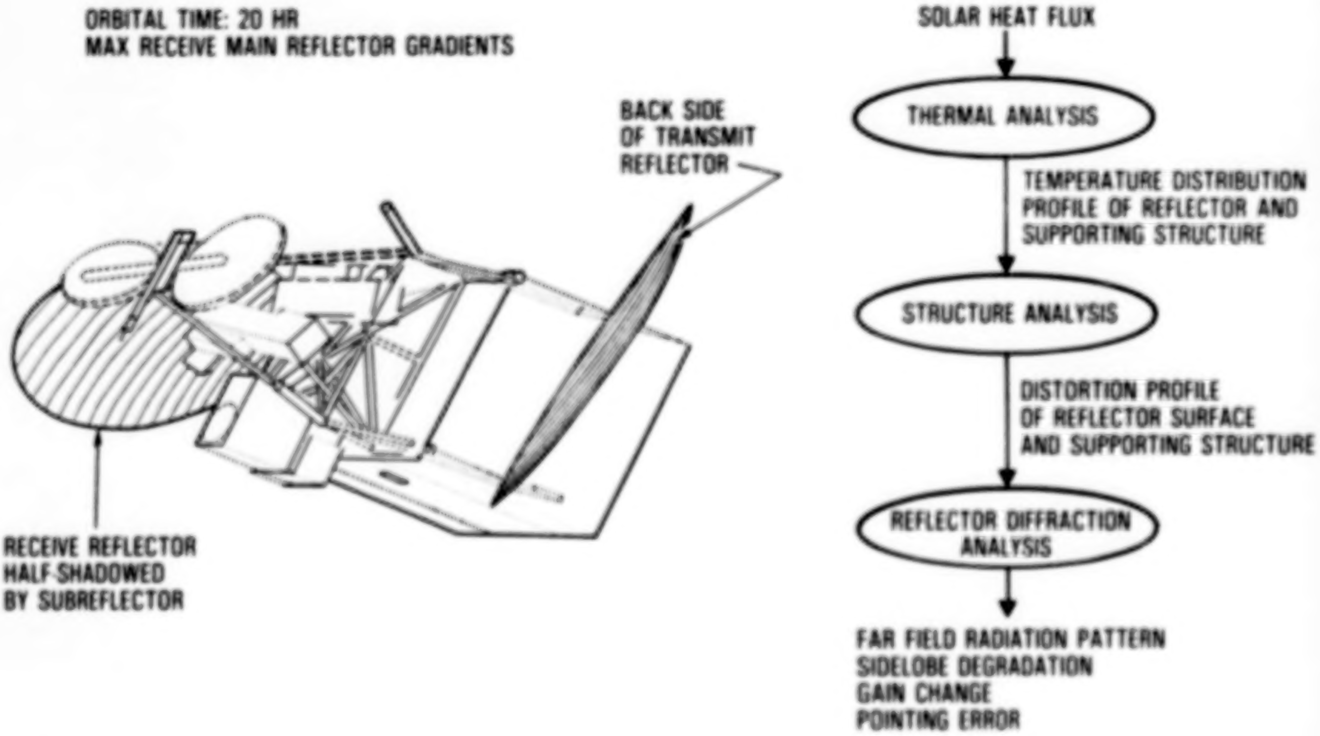
ORBITAL TIME: 20 HR
MAX RECEIVE MAIN REFLECTOR GRADIENTS
BACK SIDE OF TRANSMIT REFLECTOR
RECEIVE REFLECTOR HALF-SHADOWED BY SUBREFLECTOR
SOLAR HEAT FLUX
THERMAL ANALYSIS
TEMPERATURE DISTRIBUTION PROFILE OF REFLECTOR AND SUPPORTING STRUCTURE
STRUCTURE ANALYSIS
DISTORTION PROFILE OF REFLECTOR SURFACE AND SUPPORTING STRUCTURE
REFLECTOR DIFFRACTION ANALYSIS
FAR FIELD RADIATION PATTERN
SIDELOBE DEGRADATION
GAIN CHANGE
POINTING ERROR

Figure 5

MULTI-FLARE FEEDHORN

ACTS MBA's use multiflare horns as the primary illuminators [3]. Efficient reflector illumination requires the primary field to be rotationally symmetrical with low sidelobe levels. For maximum gain, the primary field illuminates the reflector with approximately -10 dB edge taper while, for low sidelobe, -17 dB or even higher. Among the three types of feedhorns often used as the primary feeds: dual mode horn (Potter horn), corrugated horn, and multiflare horn, the corrugated horn is most often used due to its broadband performance and good edge taper control. The following table compares the three types of horns. In many applications, the bandwidth requirement excludes using the narrow-band dual mode horns. The major advantage of a multi-flare horn is that it generates radiation patterns similar to that of a corrugated horn (Figure 6) with reasonable bandwidth performance and much simpler mechanical design. The fabrication of the horn throat matching and the grooved walls of a corrugated horn becomes difficult in the millimeter frequency range.

Horn Type	Bandwidth	Impedance Matching	Structure Complexity	Fabrication Cost
Dual-mode horn	Narrow (~4%)	VSWR 1.2:1	Moderate	Moderate
Corrugated horn	Very wide (>30%)	Require throat matching to obtain low return loss	Complicated	High
Multi-flare horn	Wide (~15%)	VSWR 1.07:1 over 20% BW without matching device	Simple	Low

Comparison Between Multiflare Horn and Corrugated Horn

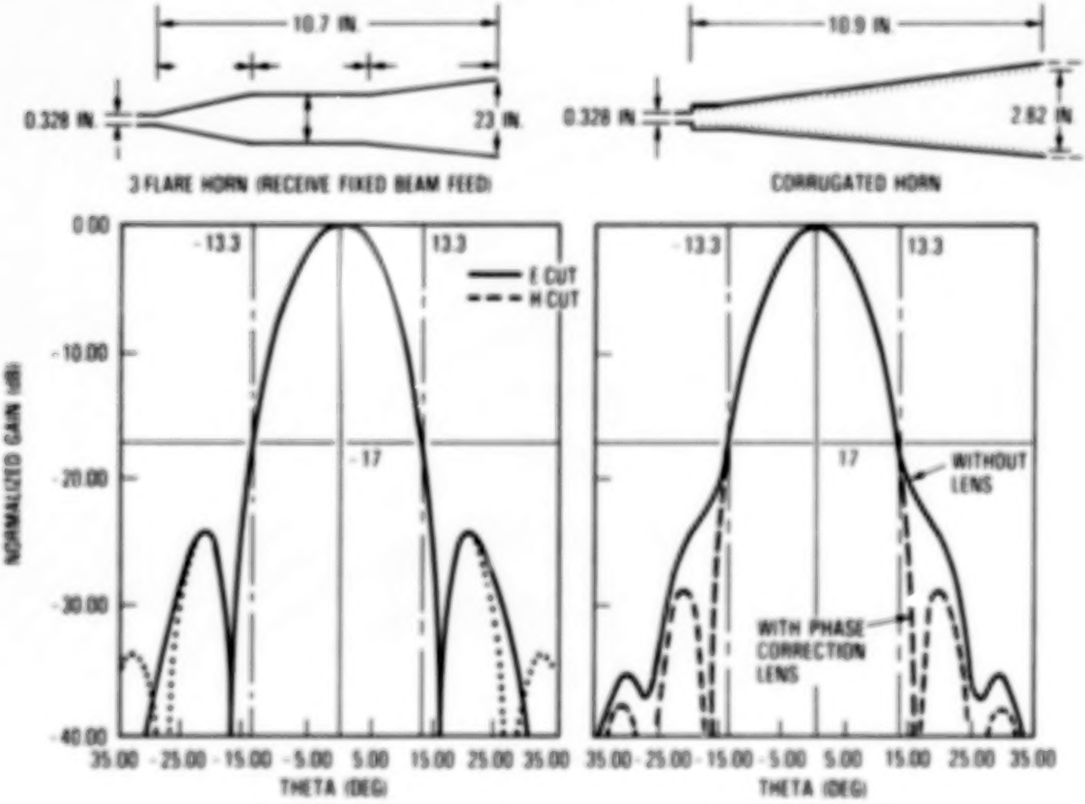

A. 3 FLARE HORN

Figure 6

B. CORRUGATED HORN

MULTI-FLARE HORN: SUM AND DIFFERENCE MODES

With the use of a tracking mode coupler [4], higher waveguide modes can be excited in a multiflare horn, providing difference patterns for tracking, a more efficient tracking system than the traditional five-horn system. The ACTS MBA autotracking system uses three waveguide modes, TE_{11}, TE_{21} and TM_{01}. The fundamental mode, TE_{11}, serves as a reference signal, the TE_{21} generates an error signal in the azimuth direction, and the TM_{01} generates an error signal in the elevation direction. The two error signals are then biphase-modulated and combined with the reference signal to produce an amplitude modulated signal to be fed into a tracking receiver for autotracking. Theoretical analysis based on mode matching at the flare break to compensate for phase front curvature change [5] and taking into account the differential phase shift of each waveguide mode between flare breaks predicts a multi-flare horn's radiation pattern well, both sum and difference, as shown in Figure 7.

Multiflare Horn Sum (TE_{11}) and Difference (TM_{01}, TE_{21}) Pattern

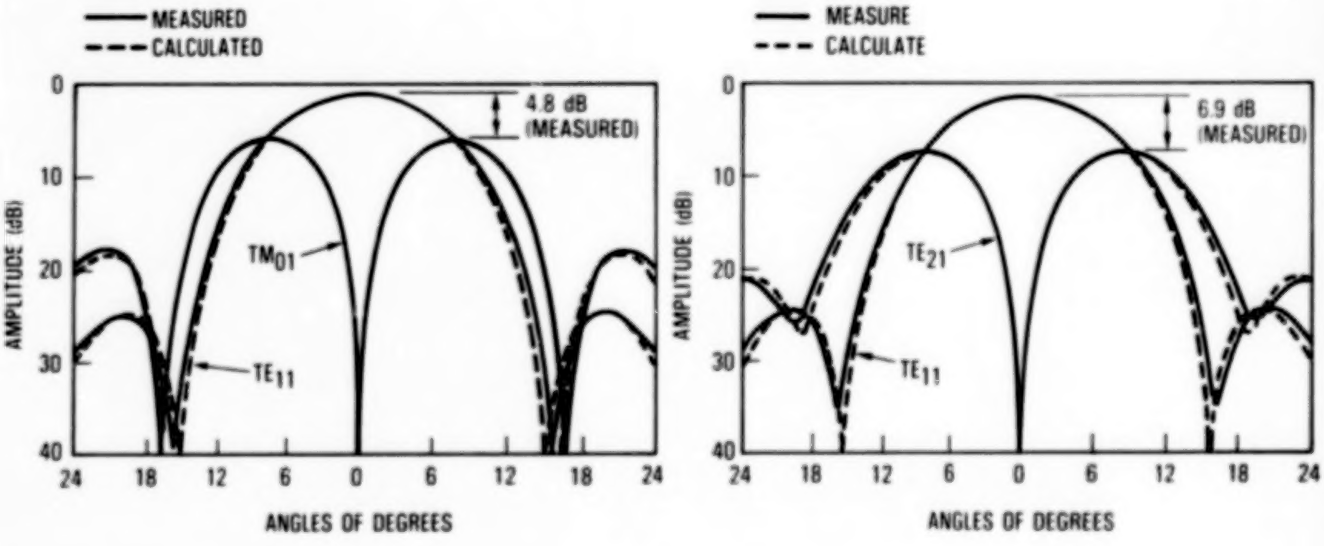

TE_{11} AND TM_{01}

TE_{11} AND TE_{21}

Figure 7

SIDELOBE CANCELLATION

Besides the accurate reflector surface control and the use of an efficient primary radiator with high edge taper, the low sidelobe performance can further be improved using a feed cluster. This is achieved by carefully spacing the feed so that the first sidelobe (of the secondary pattern) of the center feed coincides with half of the main lobe of the adjacent feed and the second sidelobe of the center feed coincides with the first sidelobe of the adjacent feed. Under this condition, the sidlobes of the adjacent feeds are approximately out of phase and will cancel each other with proper amplitude adjustment. Figure 8 demonstrates the improvement on sidelobe level using this technique. The technique was not used on ACTS MBA since the sidelobe level achieved by surface tolerance control and high edge taper is sufficient to meet the system requirement.

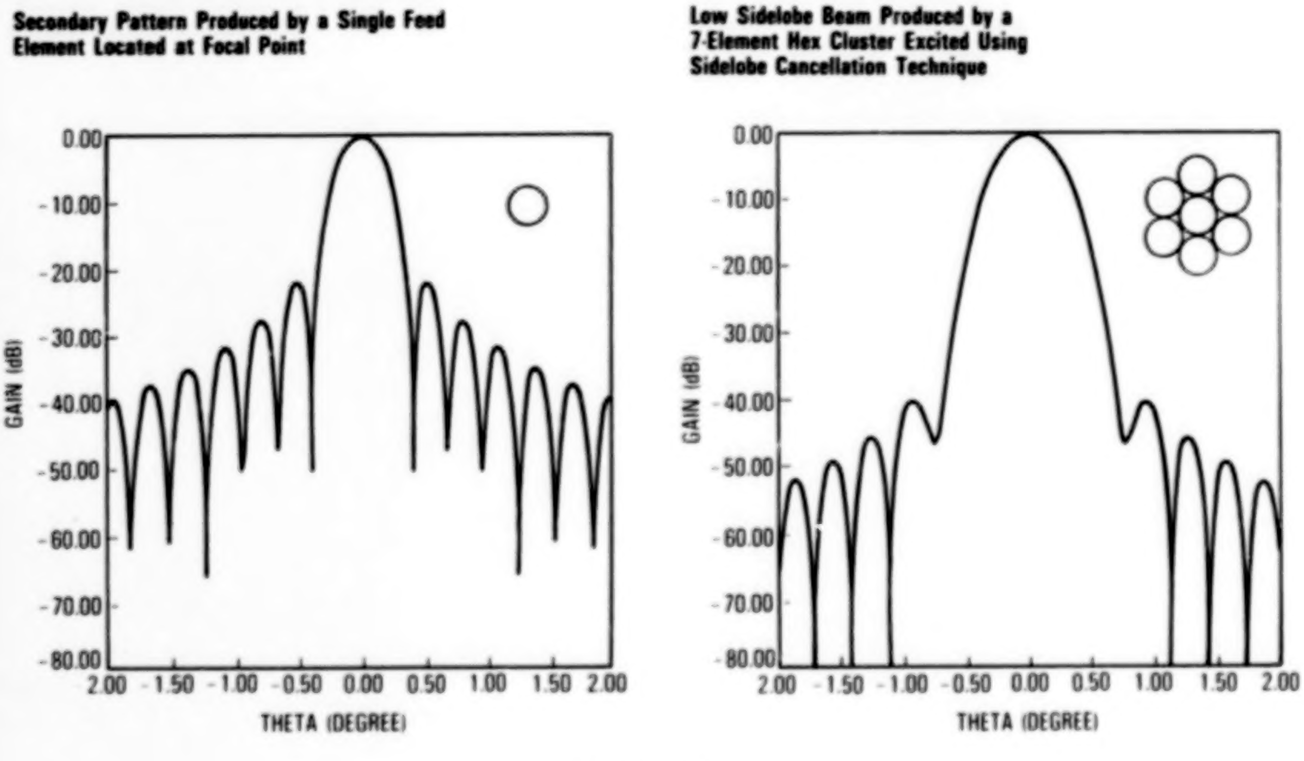

Secondary Pattern Produced by a Single Feed Element Located at Focal Point

Low Sidelobe Beam Produced by a 7-Element Hex Cluster Excited Using Sidelobe Cancellation Technique

Figure 8

BEAM FORMING NETWORK

The beam scanning capability of a MBA is provided by the Beam Forming Network (BFN). The ACTS MBA has four BFN's, each provides one of two polarizations for either the receive or the transmit antenna. Figure 9 shows the schematic diagram of the horizontally polarized receive BFN. The BFN consists of an RF switch network and redundant control electronics. The RF switch network is formed by a number of latching ferrite switches, a fixed power combiner and interconnecting waveguides. The control electronics include switch drivers and a controller to accept and interpret switching commands. Depending on the switching status of the network, a feed is selected. The scanning is achieved by sequentially selecting different feeds. When scanning within a scan sector, three adjacent feeds (one from each of the groups A, B and C) are selected to form a triplet. By hopping from triplet to triplet, the entire sector is covered. Typical BFN performances are:

Switching Time : less than 0.8 microsecond
Insertion Loss : less than 0.1 dB per switch
Isolation : better than 25 dB per switch

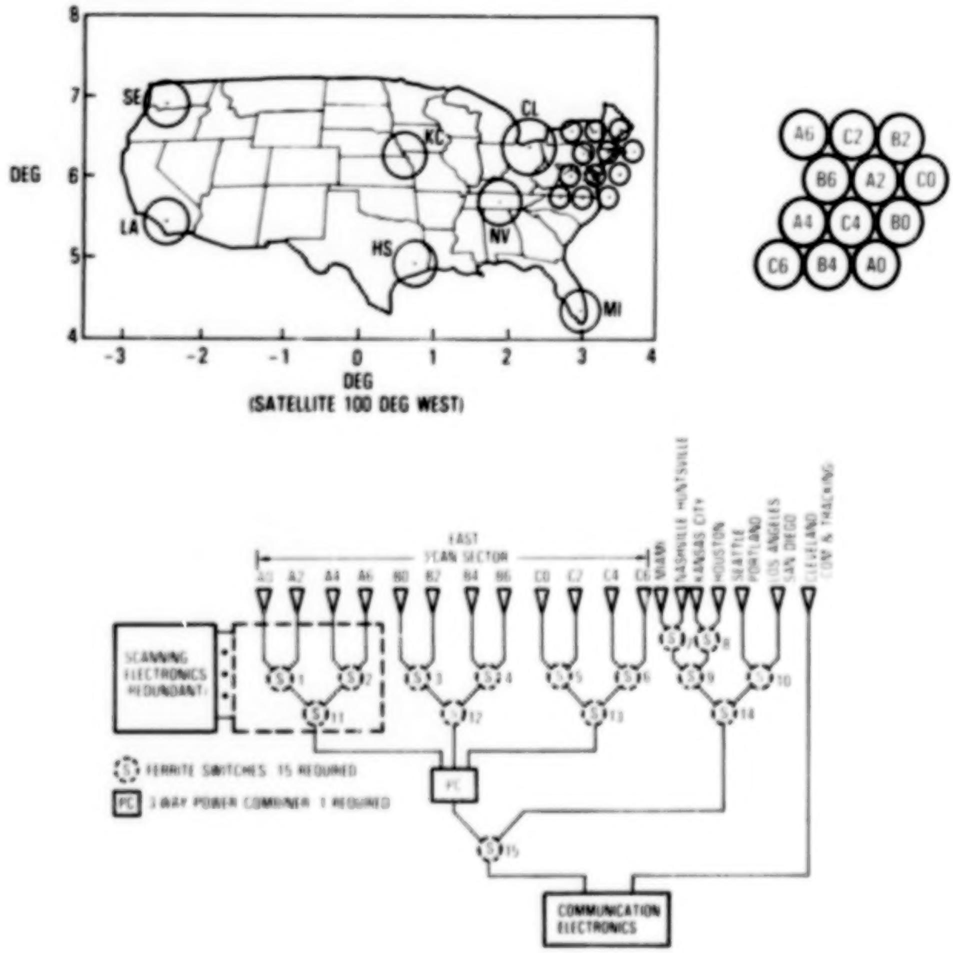
8
7
6
5
4
DEG
SE
LA
KC
HS
CL
NV
MI
-3
-2
-1
0
1
2
3
4
DEG
(SATELLITE 100 DEG WEST)
A6
C2
B2
B6
A2
C0
A4
C4
B0
C6
B4
A0
EAST SCAN SECTOR
A0
A2
A4
A6
B0
B2
B4
B6
C0
C2
C4
C6
MIAMI
NASHVILLE HUNTSVILLE
KANSAS CITY
HOUSTON
SEATTLE
PORTLAND
LOS ANGELES
SAN DIEGO
CLEVELAND
CDV & TRACKING
SCANNING ELECTRONICS (REDUNDANT)
S 1
S 2
S 3
S 4
S 5
S 6
S 7
S 8
S 9
S 10
S 11
S 12
S 13
S 14
S 15
PC
S FERRITE SWITCHES 15 REQUIRED
PC 3 WAY POWER COMBINER 1 REQUIRED
COMMUNICATION ELECTRONICS

Figure 9

FEED ASSEMBLY

Figure 10 illustrates the physical implementation of the BFN of Figure 9 and the feed assembly. Notice that the Nashville and Miami horns are not shown to expose the trimode tracking system described in Figure 7. The interconnecting waveguides of BFN were electroformed to achieve the required bending and twisting, as well as low loss. The BFN and the feed horns are enclosed in a graphite fiber reinforced plastic (GFRP) housing to achieve high structural rigidity. The near-zero thermal expansion of the GFRP housing provides feedhorns with positional stability throughout the operational and non-operational environments to meet the pointing accuracy requirement. The feed assemblies, the main reflector, and the subreflectors will have to be aligned precisely with respect to each other during the final assembling of the entire MBA so that all beams will simultaneously point to the designed directions. This is discussed in the figure for near-field testing on ACTS breadboard MBA.

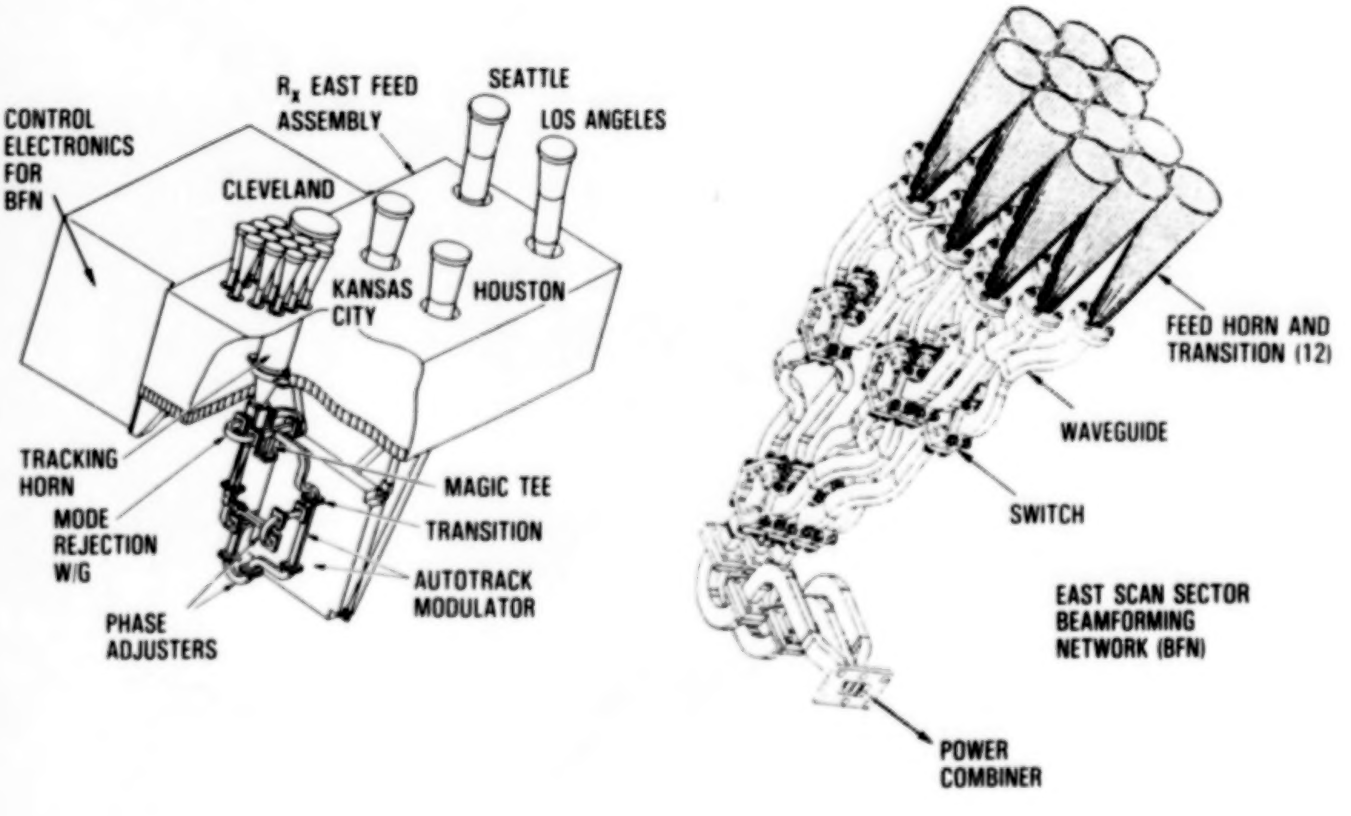
R_x EAST FEED ASSEMBLY
SEATTLE
CONTROL ELECTRONICS FOR BFN
LOS ANGELES
CLEVELAND
KANSAS CITY
HOUSTON
TRACKING HORN
MODE REJECTION W/G
MAGIC TEE
TRANSITION
AUTOTRACK MODULATOR
PHASE ADJUSTERS
FEED HORN AND TRANSITION (12)
WAVEGUIDE
SWITCH
EAST SCAN SECTOR BEAMFORMING NETWORK (BFN)
POWER COMBINER

Figure 10

ANTENNA NEAR-FIELD TESTING

The ability of testing performance and verifying design of mechanically complicated, high-performance antennas such as ACTS MBA's requires the most advanced antenna testing system. The traditional far-field antenna test ranges are outdoor and subject to weather, environmental and security problems. Controlled environmental antenna testing can be performed in an anechoic chamber, but is limited to physically small antennas. Large aperture antenna testing (especially at high frequency) needs a fairly long distance between the source antenna and the AUT (Antenna under Test), and certainly cannot be carried out in an anechoic chamber. For example, testing ACTS 2.2 meter antenna at 30 GHz will require a distance of almost 1000 meters. With the near-field measurement technique, testing large aperture antennas in a controlled environment is possible. In addition, the near-field measurement provides the complete azimuth and elevation radiation patterns, not just a few cuts. Figure 11 shows the ACTS breadboard MBA under near-field testing. As will be described in Figure 12, the near-field range is an integration and test facility, unlike the far-field range - a testing only facility, implying cost and time saving in developing a complicated spaceborne antenna.

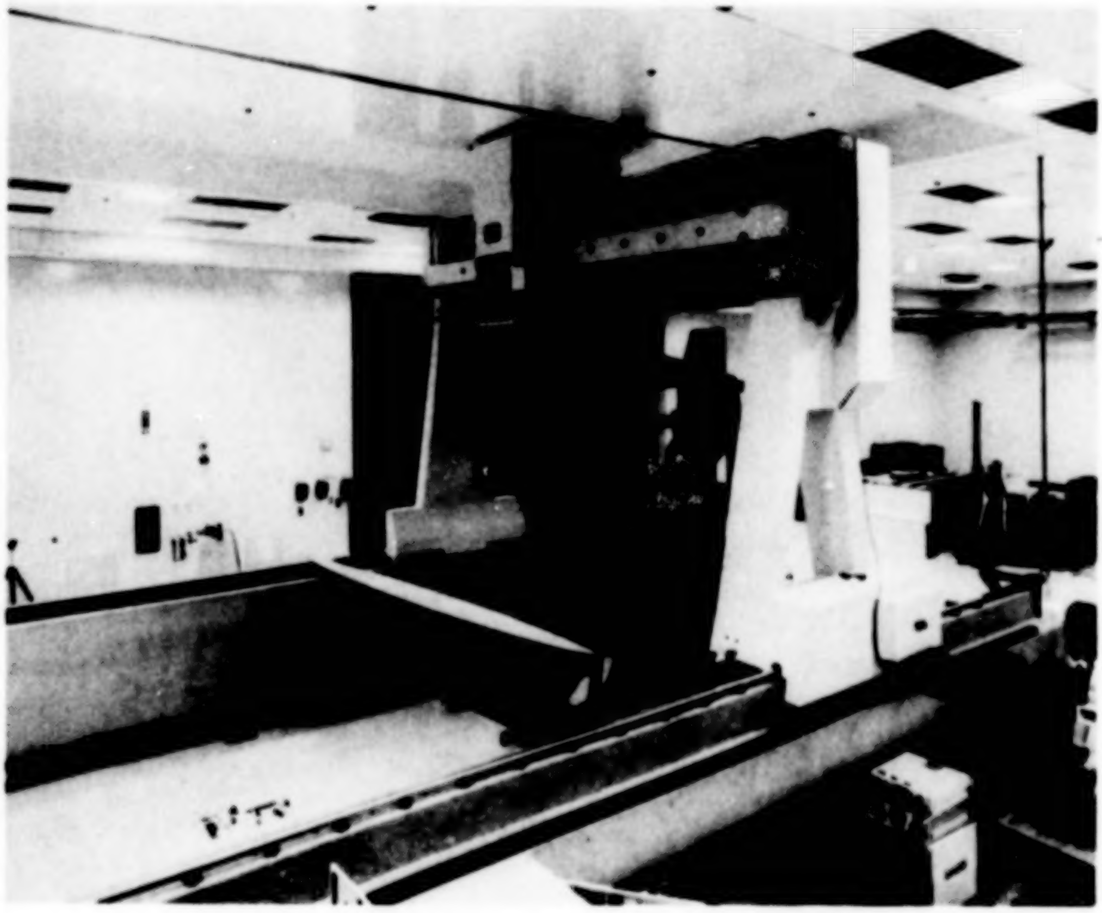

Figure 11

NEAR-FIELD TESTING ON ACTS BREADBOARD MBA

Before the RF test started, the ACTS breadboard MBA was assembled and aligned in the near-field range using the scanner as a precision position measuring system [6]. The RF probe was replaced by a mechanical touching probe. The antenna was aligned with the aid of several tooling balls installed on the MBA at various locations. The ball position as measured by the touching probe was compared to the designed position such that necessary adjustments to the antenna could be made to minimize the difference. The procedure iterated on all tooling balls until the position differences between the measured and the designed were all within tolerance. Assembling and testing the antenna at the same location result in substantial time and cost saving (especially when adjustment is necessary after initial testing), considering the efforts involved in mounting, dismounting and transportation of a complicated antenna.

Figure 12 shows the typical correlation between the calculated and the measured radiation patterns. Other performance parameters assessed include gain, sidelobe level and pointing error [6]. With the above antenna assembly and alignment procedure, a pointing error of less than 0.016 degrees was achieved in one iteration. The breadboard MBA near-field testing verified the ACTS MBA design, developed the flight MBA alignment procedure and provided engineering data to substantiate the flight MBA performance. Most important is that it demonstrates the powerfulness and effectiveness of a near-field test range in developing and testing a complicated antenna system.

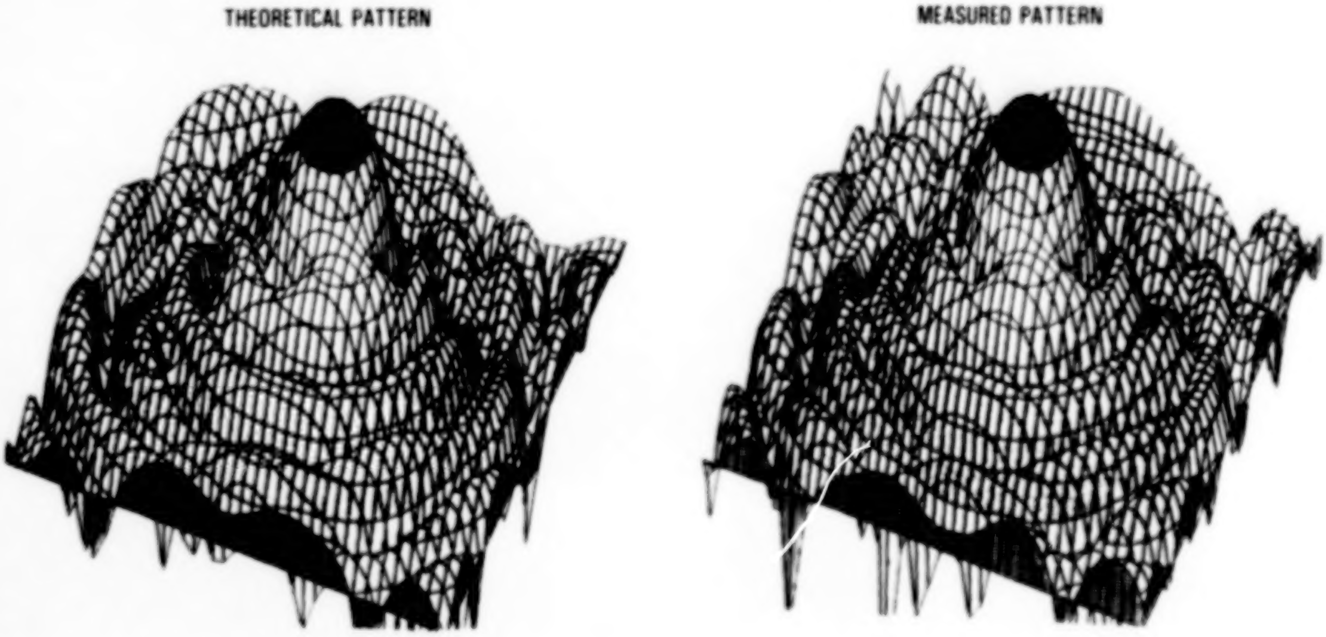

Figure 12

ADAPTIVE MULTIBEAM ANTENNA (AMBA)

An adaptive antenna optimizes the radar or communication system performance (signal-to-noise ratio) via its capability of automatic null steering and notching out interferences in the spatial domain, the frequency and polarization. The interferences may be clutter scatterer returns, natural noise source, unintentional RF interference, or adverse jammers. An adaptive antenna, in the form of a sidelobe canceller, offers an alternate solution to low sidelobe performance requirement.

Even though adaptive antennas are mostly of the phased array type, they can be of the MBA type. An adaptive MBA (Figure 13) [7] is similar to an adaptive phased array pre-weighted with a Butler matrix or a Rotman lens [8] in terms of adapting principle, but less lossy in terms of hardware implementation. Other AMBA advantages include wide bandwidth, large aperture and no grating nulls.

A key component in a adaptive antenna is the weight module which controls amplitude and phase of each feed. The ACTS MBA is not adaptive, nor does the system use any weight module. Nevertheless, the device, developed for other space programs, is available in SHF/EHF* ranges. The AMBA shown in Figure 13 with approximately 150 wavelength reflector is capable of effectively suppressing interference very close to the desired signal.

*Super-high-frequency/extremely high-frequency (SHF/EHF)

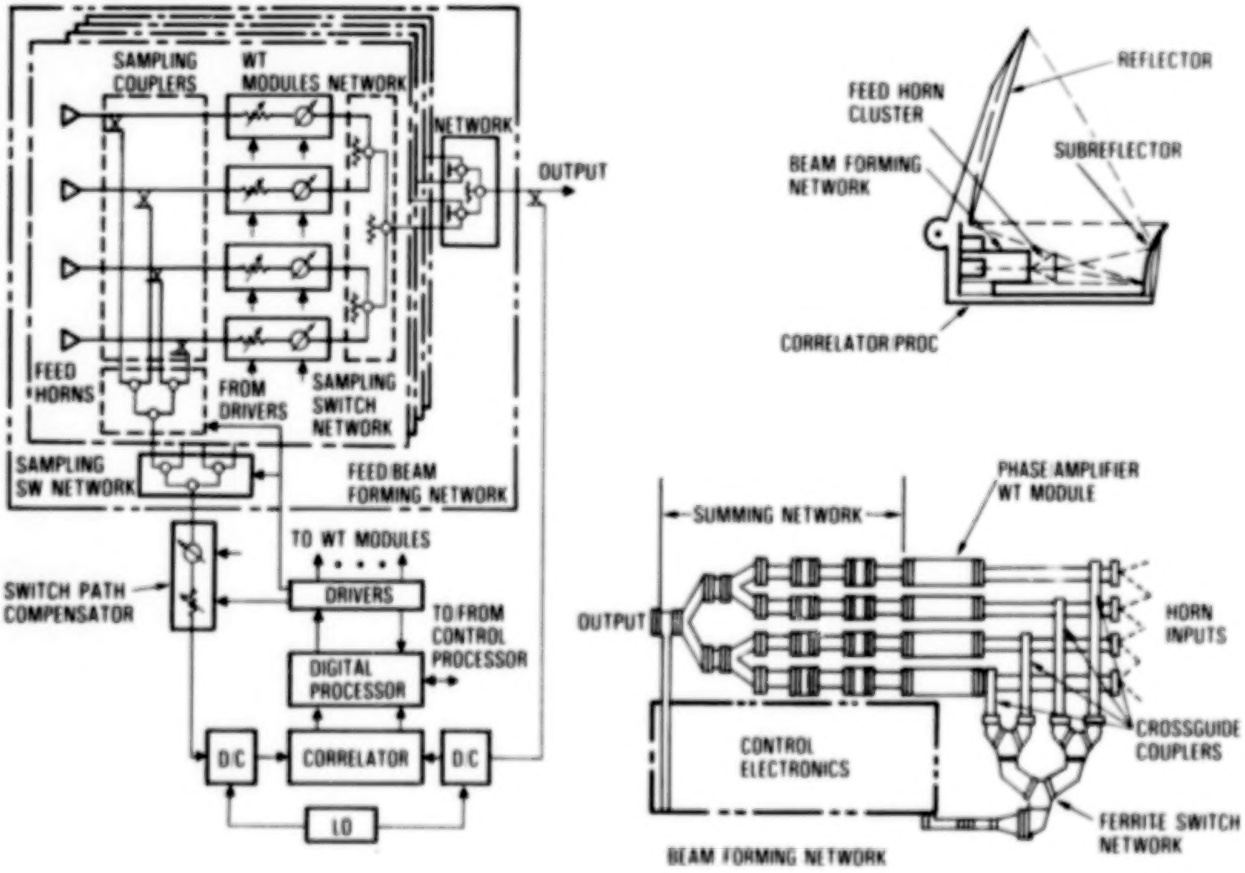
SAMPLING COUPLERS
WT MODULES
NETWORK
NETWORK
OUTPUT
FEED HORNS
FROM DRIVERS
SAMPLING SWITCH NETWORK
SAMPLING SW NETWORK
FEED/BEAM FORMING NETWORK
TO WT MODULES
SWITCH PATH COMPENSATOR
DRIVERS
TO/FROM CONTROL PROCESSOR
DIGITAL PROCESSOR
D/C
CORRELATOR
D/C
LO
REFLECTOR
FEED HORN CLUSTER
SUBREFLECTOR
BEAM FORMING NETWORK
CORRELATOR/PROC
PHASE/AMPLIFIER WT MODULE
SUMMING NETWORK
OUTPUT
HORN INPUTS
CROSSGUIDE COUPLERS
CONTROL ELECTRONICS
FERRITE SWITCH NETWORK
BEAM FORMING NETWORK

Figure 13

CONCLUSIONS

Antennas of 20/30 GHz and higher frequency, due to the small wavelength, offer unique capabilities for many space applications. With the government-sponsored space programs (such as ACTS) in recent years, the industry has gone through the learning curve of designing and developing high-performance, multi-function antennas in this frequency range. Design and analysis tools (such as the computer modelling used in feedhorn design and reflector surface and thermal distortion analysis) are available. The components/devices (such as BFN's, weight modules, feedhorns and etc.) are space-qualified. The manufacturing procedures (such as reflector surface control) are refined to meet the stringent tolerance accompanying high frequencies. The integration and testing facilities (such as Near-Field range) also advance to facilitate precision assembling and performance verification. These capabilities, essential to the successful design and development of high-frequency spaceborne antennas, shall find more space applications (such as ESGP) than just communications.

REFERENCES

1. Y. Choung, W. Stiles, J. Wu, W.C. Wong, C.H. Chen and K. Oye, "NASA ACTS Multibeam Antenna System," 1986 IEEE Eascon, Washington, D.C., pp 191 - 196.

2. D.Y. Kim, C.H. Chen, K. Oye, W.C. Wong and S.J. Hamada, "Thermal Distortion Analysis on ACTS Multibeam Antenna," 1988 IEEE Antenna and Propagation Symposium Digest, Vol.3, pp. 1310-1313, Syracuse, New York, June 1988.

3. C.H. Chen, Y. Choung and D. Palma, "A Compact Multiflare Horn Design for Spacecraft Reflector Antenna," 1986 IEEE Antenna and Propagation Symposium Digest, Vol.2, pp. 907-910, Philadelphia, Pennsylvania, June 1986.

4. M. Shiau, Y. Choung, C.H. Chen and M. Chen, "NASA ACTS Autotrack Antenna Feed System," 1986 IEEE Antenna and Propagation Symposium Digest, Vol.1, pp. 83-86, Philadelphia, Pennsylvania, June 1986.

5. S.B. Cohn, "Flare Angle Changes in a Horn as Means of Pattern Control," Microwave Journal, Vol. 13, pp 41-46. October 1970.

6. C.H. Chen, W.C. Wong and S.J. Hamada, " Near Field Testing on ACTS Breadboard Multibeam Antenna (MBA)," 1988 IEEE Antenna and Propagation Symposium Digest, Vol.3, pp. 1107-1109, Syracuse, New York, June 1988.

7. P.G. Ingerson, "An Adaptive Nulling MBA Antenna," 1983 IEEE Military Communications Conference, October 31-November 2, 1983, Washington, D.C.

8. J.P Shelton and K.S. Kelleher, "Multiple Beams from Linear Arrays," IRE Transactions on Antennas and Propagation, AP-9, No. 1, P 154, March 1961.

Optical Metrology Technology

E
S
G
P

Session Chairwoman: Sharon LaFleur
NASA Langley Research Center

APPLICATIONS OF FM-CW LASER RADAR TO ANTENNA CONTOUR MAPPING

A. R. Slotwinski
Digital Signal Corporation
Springfield, Virginia

FM-CW COHERENT LASER RADAR CONCEPT

The FM-CW coherent laser radar concept is based on the FM radar principle which makes use of the coherence and tunability of injection laser diodes. The optical frequency of the laser is swept linearly as a function of time. This signal is divided and used both as a local oscillator and as the signal to be transmitted. In addition, it is injected into a reference path of known length to provide a calibration mechanism, as shown in Figure 1. After being time delayed by the round trip time delay to the target, the received signal is mixed with the optical local oscillator onto an optical detector. The resultant beat frequency is equal to the sweep rate of the optical signal multiplied by the time delay between the received signal and the local oscillator. Since the time delay is proportional to target distance, the RF beat frequency will also be proportional to target distance. In a similar manner, since the reference distance is known, the reference beat frequency is proportional to the optical sweep rate of the laser

Thus, it is not necessary to directly measure the optical sweep rate, ΔF, if the reference arm length, X_{ref}, is known precisely. In this system the range is given by the ratio of the number of range counts to the number of reference counts multiplied by X_{ref}.

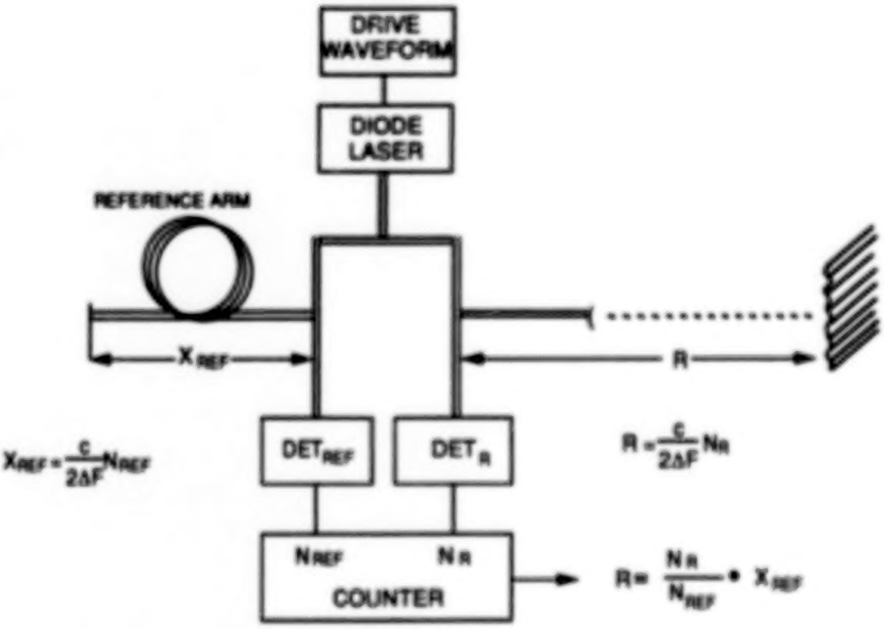
DRIVE WAVEFORM
DIODE LASER
REFERENCE ARM
X_{REF}
R
$X_{REF} = \frac{c}{2\Delta F} N_{REF}$
DET_{REF}
DET_R
$R = \frac{c}{2\Delta F} N_R$
N_{REF}
N_R
COUNTER
$R = \frac{N_R}{N_{REF}} \bullet X_{REF}$

Figure 1

LASER RADAR PRECISION/TIME TRADEOFFS

The laser radar system precision/time tradeoff is given by:

$$dR(\tau)^{\frac{3}{2}} = \frac{\left((NEP)_h P_s\right)^{\frac{1}{2}}}{dF/dt}$$

where dR is the measurement error, τ is the measurement time, $(NEP)_h$ is the heterodyne noise equivalent power, P_s is the optical power collected from the target and dF/dt is the time rate of change of the laser frequency sweep. Figure 2 shows the expected measurement error as a function of the time based upon currently available laser diode source parameters. Due to the inability of current laser sources to sweep more than ~30 GHz before becoming spectrally unstable, long sweep rates are not possible. Thus, precision measurements (i.e., 1 mil in 1 sec) are achieved by averaging many laser sweeps. This incoherent averaging increases the measurement time needed to achieve precise measurements and is indicated in the figure by a change in the slope of the tradeoff line. Electronically tunable lasers that can be swept both faster and further have been produced. Once available, the precision/time tradeoffs will improve as indicated on the graph.

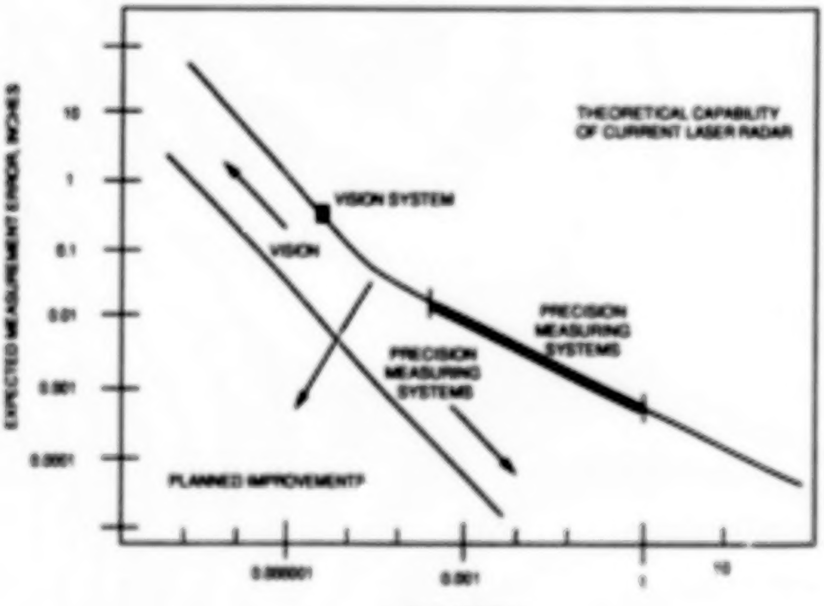

Figure 2

LASER RADAR SYSTEM BLOCK DIAGRAM

As shown in the system block diagram given in Figure 3, the laser source is frequency modulated via a waveform provided by the laser driver. The optical output of the laser is divided between the radar optics and the calibration optics. The calibration optics consist of a temperature controlled fiber optic Mach Zehnder interferometer with an optical path length of 4 meters. The ranging beam is directed to the target area of interest via an X-Y galvanometer scanner and the beam is focused on the target by means of an autofocus unit consisting of a lens arrangement mounted in a linear translator. Both the reference and ranging signals are detected and processed by the RF section. Prior to being counted, each signal is sent to a tunable standing acoustic wave (SAW) filter controlled by a frequency synthesizer to minimize the measurement bandwidth. A microprocessor controls the autofocus unit, galvanometer scanner, and frequency synthesizer and converts the counter output to range information. Coordinate transformation functions and a graphics package are also included with the microprocessor. Output data are available on both an RS-232 line and an IEEE-488 line. User control is implemented via the IEEE-488 line.

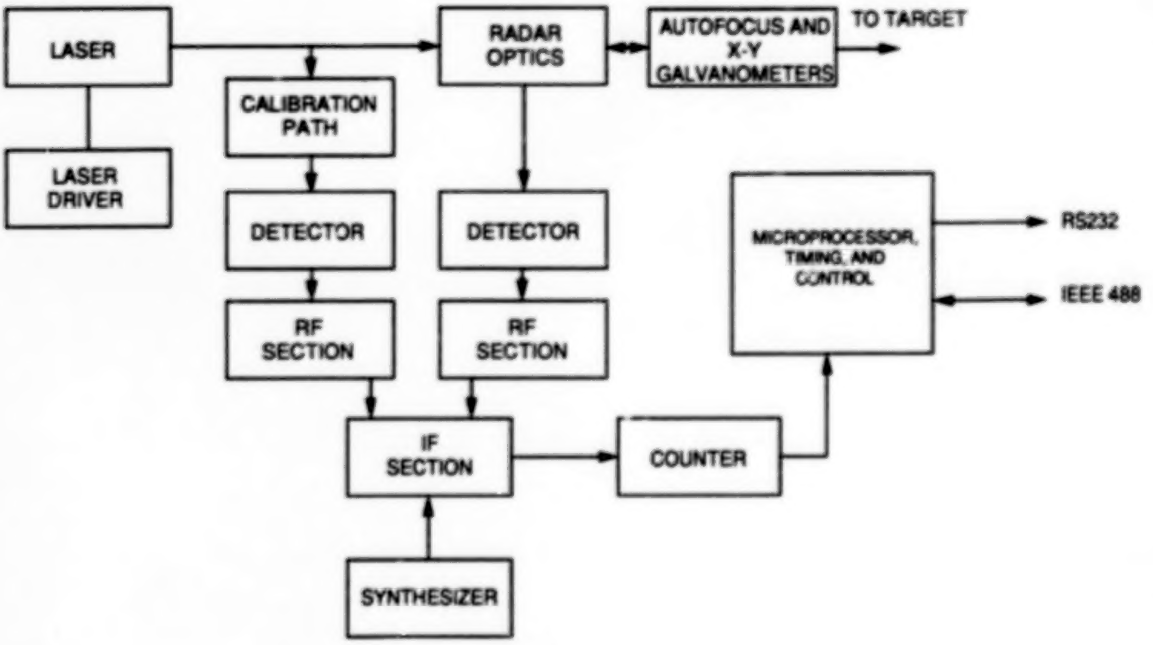
LASER
LASER DRIVER
CALIBRATION PATH
RADAR OPTICS
AUTOFOCUS AND X-Y GALVANOMETERS
TO TARGET
DETECTOR
DETECTOR
RF SECTION
RF SECTION
IF SECTION
COUNTER
SYNTHESIZER
MICROPROCESSOR, TIMING, AND CONTROL
RS232
IEEE 488

Figure 3

LASER RADAR SYSTEM PERFORMANCE

A number of laser radar measurement systems have been constructed. The maximum operating range of these units is 5 meters, which corresponds to the coherence length limit of the 30 mW laser diode sources. A new type of diode laser has recently become available with a maximum output power of 100 mW and a coherence length an order of magnitude greater than the currently employed sources. It is anticipated that these lasers will extend the operating range limit to 60 meters.

The galvanometer scanner range is ±20° horizontal and vertical with 50 μradians short-term scan repeatability. The autofocus unit allows instantaneous range coverage over the entire operating range. However, the time needed to implement the autofocusing routine does effect the time/precision product as illustrated in Figure 4. With the autofocus disabled (AD), the system achieves a range accuracy or measurement error of 2.5 mils in 0.1 sec and 0.63 mils in 1.0 sec. With the autofocus enabled (AE), the measurement error increases to 1.2 mils in 1.0 sec. Finally, the system design permits operations with target reflectivities as low as 10 dB below that of an isotropic reflector.

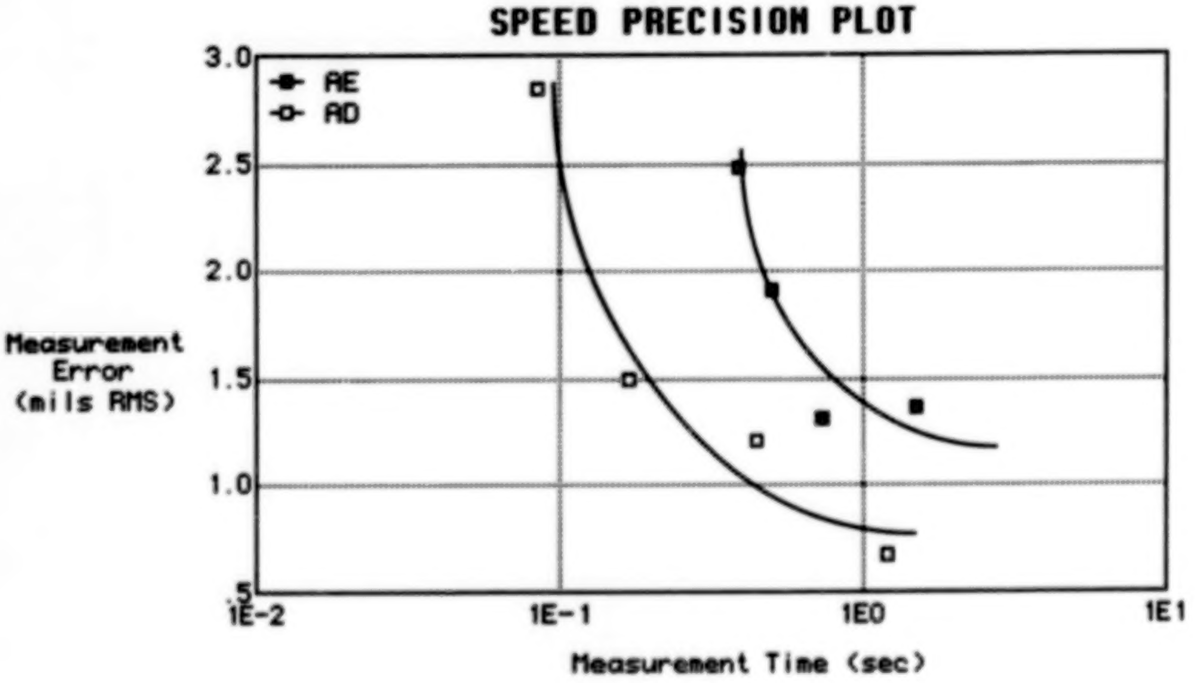

Figure 4

FIBER OPTIC SYSTEM IMPLEMENTATION FOR 15-METER HOOP/COLUMN ANTENNA

To reduce the size and weight of the optical sensor head for space applications, the entire optical subassembly can be implemented entirely in optical fibers. Figure 5 shows a configuration suitable for the 15-meter hoop/column antenna geometry. In this configuration, the laser light is injected into the input fiber after passing through an optical isolator. Using fiber optic power dividers, part of the optical energy is diverted to the reference interferometer and the rest of the energy is divided up between the four quadrants of the antenna. While a scanner can be used to point the beam to the antenna sections of interest, the measurement speeds needed for closed-loop control of the antenna surface are such that a more preferable geometry would be to incorporate a fiber optic switch with a fiber/lens combination for each measurement point. This allows rapid and programmable monitoring of the desired points.

The use of a fiber optic implementation provides a great deal of geometric flexibility in the sensor head design. To overcome laser coherence length limitation to the measurement range, a delay loop is added to the local oscillator path as illustrated in Figure 5. This configuration extends the working range of the system by a factor of one-half of the delay added.

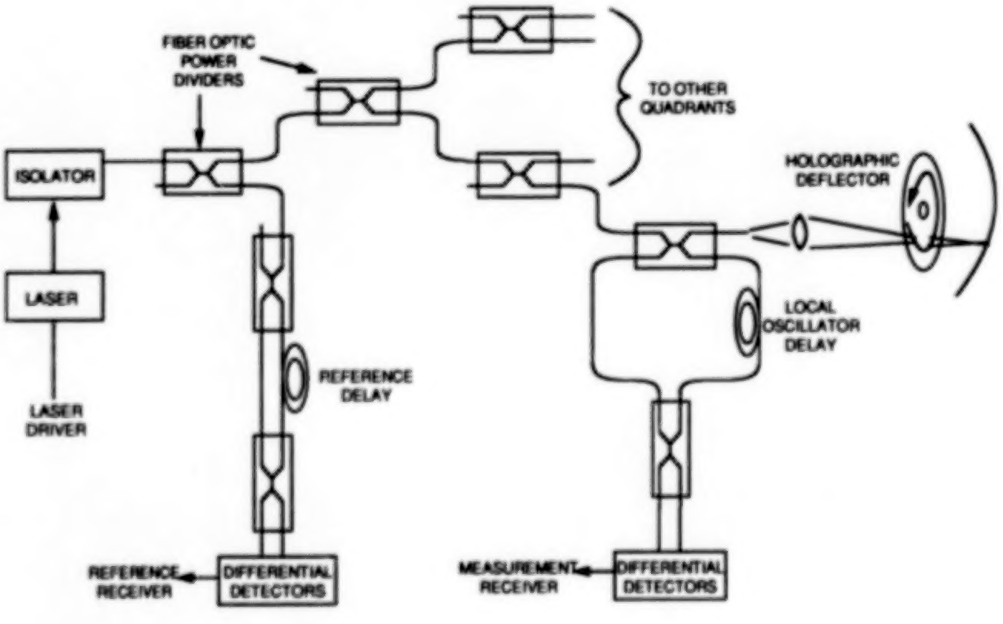
FIBER OPTIC POWER DIVIDERS
TO OTHER QUADRANTS
HOLOGRAPHIC DEFLECTOR
ISOLATOR
LASER
LASER DRIVER
REFERENCE DELAY
LOCAL OSCILLATOR DELAY
REFERENCE RECEIVER
DIFFERENTIAL DETECTORS
MEASUREMENT RECEIVER
DIFFERENTIAL DETECTORS

Figure 5

RECEIVER IMPROVEMENTS

With the use of extended coherence length laser diode sources and various system geometries, such as the delayed local oscillator concept, the effective measurement range can be extended beyond 60 meters. By optimizing the receiver electronics system performance can further be improved. The current counter-based receiver suffers from unnecessary breakdown at a 12 dB SNR while the non-linear drive waveform causes excessive receiver noise bandwidth and gate bias noise. Also, the use of a single counter for both the measurement and reference arms doubles the needed measurement time.

By linearizing the drive waveform and developing a receiver based upon spectrum estimation, a faster system can be developed. A digital processor based receiver allows for parallel processing of the reference and measurement arms, extended source FM sweep, and implementation of future improvements with no hardware changes.

Figure 6 shows a graph of the current receiver performance versus the advanced receiver under similar conditions for a 10 msec integrated measurement time. Not only does the accuracy increase by an order of magnitude but the range performance also increases since a 12 dB SNR is no longer a limiting factor.

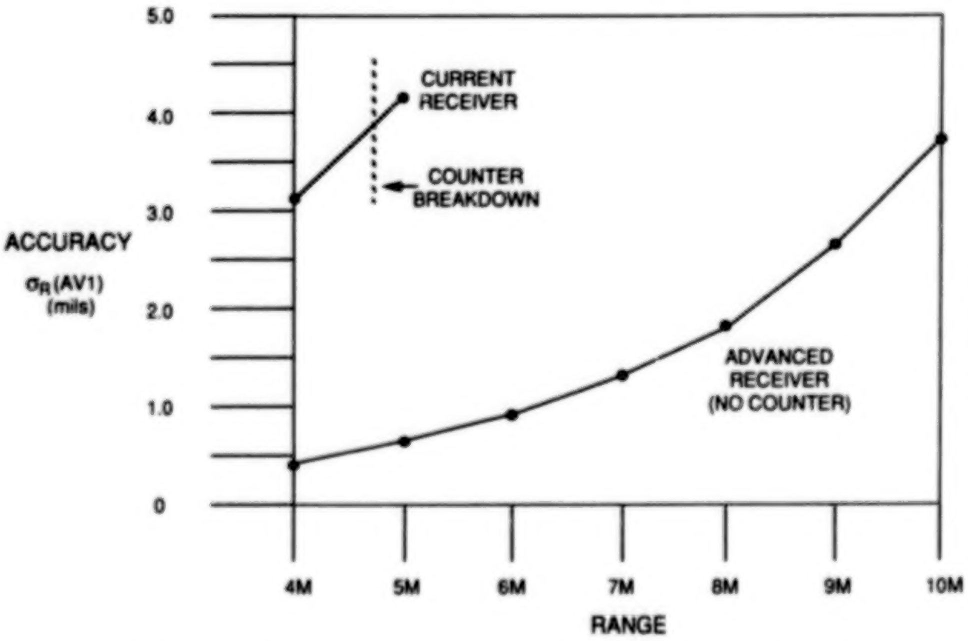

ACCURACY VS. RANGE FOR 10 msec INTEGRATED MEASUREMENT TIME

Figure 6

REMOTE ATTITUDE MEASUREMENT SENSOR
(RAMS)

H. W. Davis
Ball Aerospace Systems Group
Boulder, Colorado

LARGE SPACE STRUCTURE (LSS) ISSUES

The use of large space platforms for Earth observations is advantageous because it results in improved capabilities such as coincident observations, shared resources, serviceability and growth potential. However, large platform structures produce lower mechanical resonance frequencies and dynamic structural interactions which create severe problems for precision-pointed instruments.

Growth in spacecraft size drives us to flexible structures because rigid structures would exceed launch weight constraints. Flexible structures further complicate control system modeling and analysis, so on-orbit system identification is needed. Thermal effects are exaggerated by increased structural dimensions, resulting in larger distortions to surface figure and structural alignment. If distortions become untolerable, active structural control may be required. In any event, some form of active vibration damping may be necessary to reduce payload instrument disturbances caused by structural vibrations and spacecraft subsystem disturbance sources.

When payload instruments were mounted on smaller, rigid platforms, pointing knowledge could be derived from the spacecraft attitude control system (ACS). With flexible platforms, this is no longer feasible. Payload pointing accuracy is degraded by onboard disturbances that excite resonance modes above ACS cutoff (approximately 0.1 Hz) and below the region where intrinsic structural damping becomes effective (approximately 100 Hz). Isolation of payloads from these base motion disturbances requires precise, high bandwidth position data such as that provided by Ball's Remote Attitude Measurement Sensor (RAMS). Other equally important uses of RAMS include alignment calibration and coalignment of payload instruments and transfer of alignment/attitude information between inertial reference units and payload mounting surfaces.

- **Flexible structure**
  - **Launch weight limitations preclude rigid structure**
  - **On-orbit system identification needed**
  - **Attitude control is more difficult**
  - **Thermal distortions exaggerated by size**
  - **Active structural control may be required**
  - **Active vibration isolation may be required**

- **Payload pointing**
  - **Determination of pointing knowledge**
  - **Compliance with accuracy requirements (stability, jitter)**
  - **Isolation from base motion disturbances**
  - **Calibration and coalignment of payloads**
  - **Alignment transfer may be required**

SYSTEMS INTEGRATION AND VALIDATION

Recent conference publications (refs. 1 and 2) have recognized the importance of an integrated system-level approach to the design of active structural control systems. Control/structures interaction was the theme of two recent NASA/DOD technology conferences that promoted interdisciplinary cooperation as the essential element for optimal design of LSS. Extensive efforts have been devoted to each of the technology elements shown below, and much progress has been made. Advances have been made in the development of piezoelectric actuators, viscoelastic damping materials, low-expansion composite materials, and advanced processors for distributed control systems. Up until now, however, the sensor technology area seemed to be trailing the other technologies in meeting the needs of structural characterization and control. RAMS is the only optical sensor today that satisfies the LSS requirements for accuracy, update rate, number of targets, simplicity, reliability, and technological maturity.

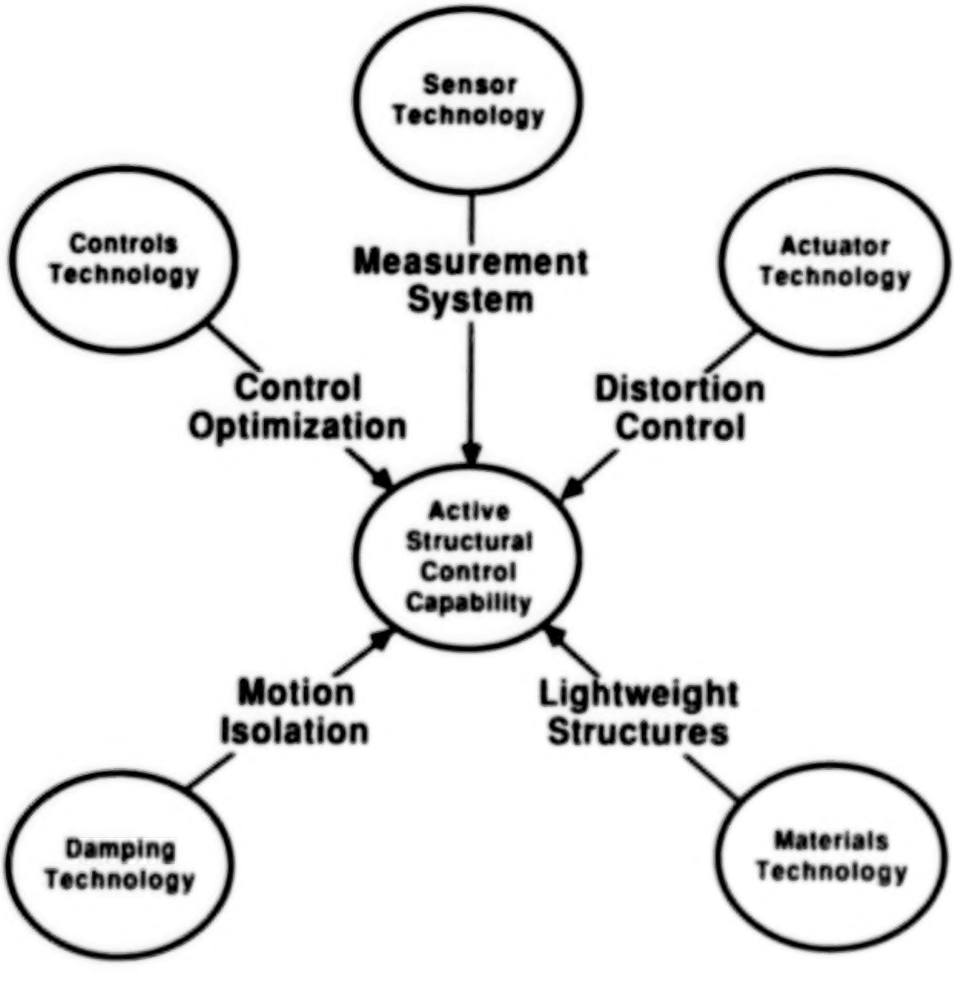
Sensor Technology
Controls Technology
Measurement System
Actuator Technology
Control Optimization
Distortion Control
Active Structural Control Capability
Motion Isolation
Lightweight Structures
Damping Technology
Materials Technology

SPACE SYSTEMS REQUIRING HIGH-ACCURACY, HIGH-BANDWIDTH SENSORS

There are many space applications which require or benefit from the use of high-accuracy, high-bandwidth sensors such as RAMS. Space structures, especially large, flexible structures, require a means of measuring both translation and rotation of numerous points on the structure for systems identification and for active control of the surface figure or alignment of the structure. Deployable structures also benefit from sensors that monitor the deployment, control deployment sequences and rates, and verify proper alignment and latching when deployment is completed. Attached payloads need alignment information for calibration purposes and for proximity operations during docking, installation, or servicing. If the payload requires precise pointing, transfer of attitude data from the platform's inertial reference unit may also be needed. Finally, a variety of space vehicles planned for support of space station operations (OTV, OMV,* polar and co-orbiting platforms) will require proximity knowledge for docking, interfacing, and avoidance.

---

*Orbital Transfer Vehicle (OTV); Orbital Maneuvering Vehicle (OMV).

- **Space structures:**
  - **Active control**
  - **Deployment**
  - **Surface figure**
  - **Systems identification (Structural dynamics)**
- **Payloads:**
  - **Alignment calibration**
  - **Alignment transfer**
  - **Coalignment of multiple payloads**
  - **Docking (Installation, servicing)**
- **Vehicles (OTV, OMV, platforms):**
  - **Docking**
  - **Proximity operations**
  - **Attitude transfer**

DESIRED ATTRIBUTES OF LSS SENSORS

The primary attributes sought in any LSS sensor are listed below. Although performance characteristics vary with each specific application, accuracy in the sub-millimeter range and update rates of at least 250 Hz are generally required to support systems identification and active control of LSS with disturbances up to 25 - 50 Hz. The greater the number of targets (structural locations) monitored, the better the characterization of its dynamic behavior. Low complexity leads to higher reliability and maintainability. Sensors having a non-obtrusive (non-contacting) nature can be used to study photovoltaic solar arrays and other film-like structures without the sensor's mass influencing the dynamics of the structure. Lastly, it is desirable that the LSS sensor have broad application (multiple uses) and be versatile (to accommodate configuration changes easily).

- **High accuracy**
- **High update rate**
- **Multiple targets**
- **Low complexity**
- **Low cost**
- **Reliable**
- **Non-obtrusive**
- **Broad application**

LSS SENSOR TRADEOFFS

Ball's selection and pursuit of the RAMS concept as the preferred LSS sensor resulted from comparisons and tradeoffs of many competing technologies. After 30 years of electro-optical sensor experience, including star sensors, Sun sensors, laser rangefinders, lidars, and interferometers, we clearly understand the capabilities and limitations of each. We have actually built and tested sensors from each of these technologies. RAMS was developed using space-proven technology directly applicable to LSS. Proprietary algorithms developed as part of our star tracker work permit subpixel interpolation and focus compensation. Ball also built the Retroreflector Field Tracker (RFT), the first solid-state sensor flown in space. The RFT measured dynamic structural behavior as part of the Solar Array Flight Experiment (SAFE). Finally, we conducted an extensive literature search and evaluated many sensor concepts before recommending the RAMS concept to Goddard Space Flight Center for coalignment of Shuttle payloads.

- **Based on 30 years of electro-optical sensor experience**
  - **Star trackers**
  - **Star scanners**
  - **Sun sensors**
  - **Laser rangefinders**
  - **Interferometers**

- **Derived from space-proven LSS technology**
  - **Star tracker algorithms**
  - **Retroreflector field tracker (RFT)**

- **Supported by the NASA/GSFC payload coalignment study literature search and evaluation**

RETROREFLECTOR FIELD TRACKER (RFT) WAS TESTED ON STS 41-D

The RFT was designed to monitor the structural shape of a large, flexible solar array panel deployed from the cargo bay of the Shuttle. The RFT used five laser diodes to illuminate 23 retroreflective tape targets distributed throughout the surface area of the panel. The sensor head was mounted at the base of the array, set back 75 in., and tilted 14.8 deg from vertical in order to have a clear view of all targets. Reflected images were focused onto a 256 x 256 pixel charge injection device (CID) detector and tracked with the aid of three Z-80 microprocessors (ref. 3).

The solar array panel was 12 ft wide and 105 ft long when fully deployed. At maximum range (i.e., top of the array), the RFT was capable of measuring displacements of ±3 mm with an update rate of 2 Hz. Due to concerns about the dynamic uncertainties of this structure, the panel was never deployed beyond 70 percent of its length. All RFT on-orbit testing took place in orbital darkness; a companion sensor using photogrammetric techniques was employed during the sunlit half of the orbit.

The demonstrated technology derived from RFT has been improved greatly and incorporated in RAMS. Accuracy has been increased by a factor of 200 and update rate has been improved by a factor of 100. The number of targets tracked simultaneously has also increased four-fold. These dramatic improvements combined with proven sensor technology offer low-risk, low-cost solutions to a variety of space sensor needs.

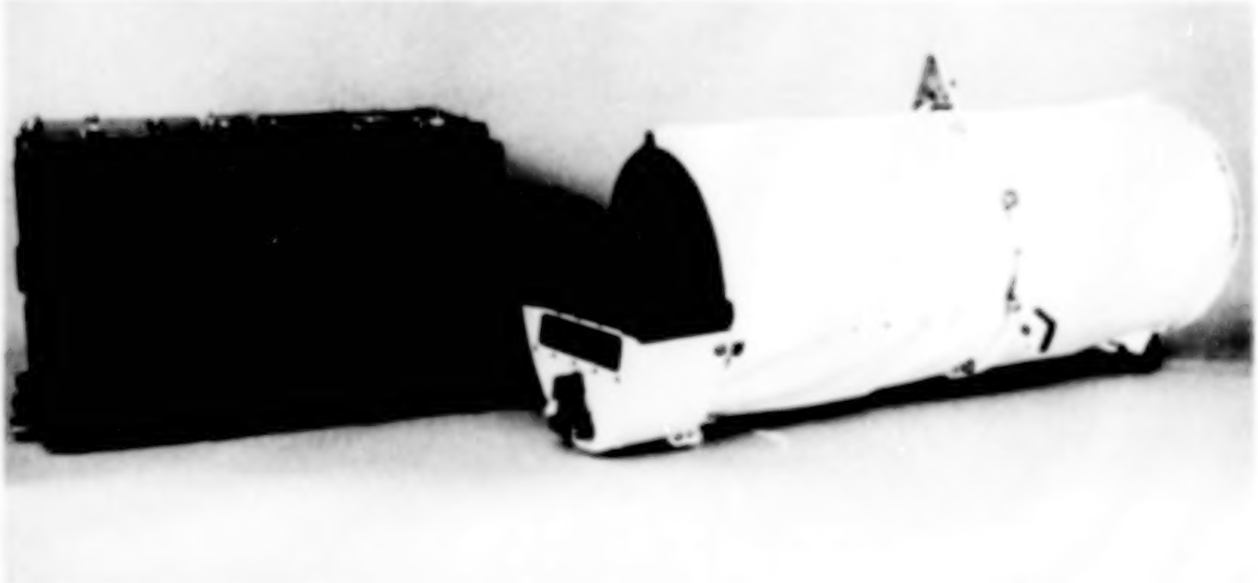

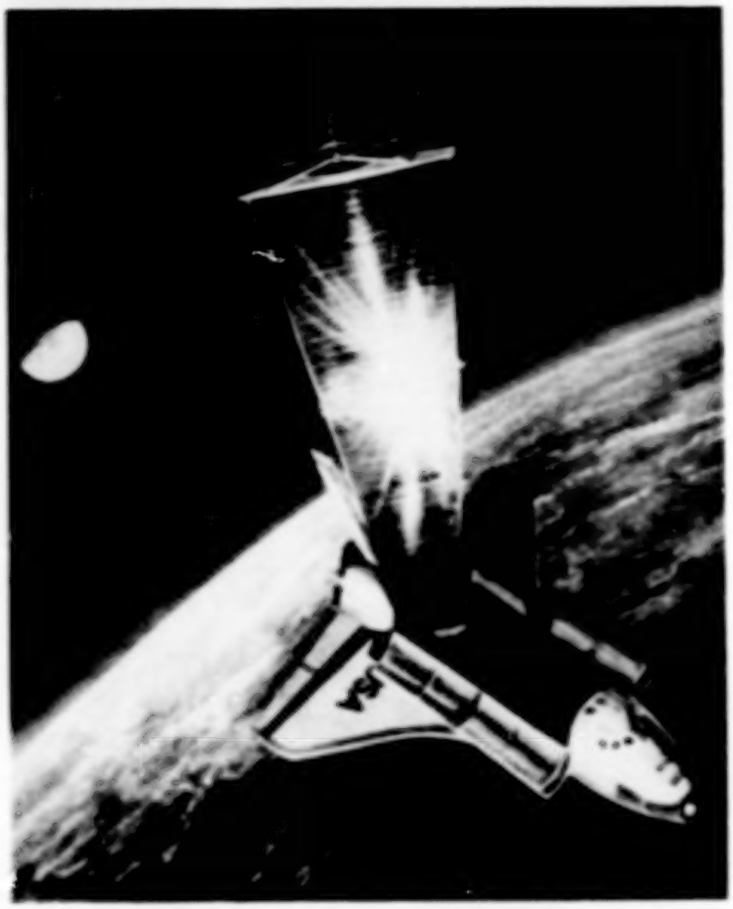

- RFT monitored structural shape of a large, flexible solar panel
  - 12 ft x 105 ft array
  - Acquired and tracked 23 retroreflective targets
  - Accuracy: +3 mm at 32m range
  - Update rate: 2 Hz

- RFT's space-proven technology is directly applicable to:
  - Large space structure alignment control
  - Star tracking
  - Rendezvous and docking sensor
  - Mirror shape control

SAFE/RFT FLIGHT EXPERIMENT "LESSONS LEARNED"[1]

The SAFE solar array panel and supporting mast behaved characteristically like a generic class of future large space structures. The structure exhibited very low natural frequencies (0.035 Hz, first mode) and densely spaced modes (> 33 modes per Hz). Other similarities included type of construction, strength-to-weight ratios, and the inability to adequately perform dynamic tests on the ground (ref. 4).

An unexpected curvature of the solar array occurred on the dark side of the orbit, resulting in higher stiffness than predicted by analyses. Flight configuration differed from pretest analysis to such an extent that update of the analytical models was necessary for correlation and verification. It is significant that this anomaly occurred despite the normal care taken in design to envision and prepare for on-orbit use. Thus, this anomaly may well be representative of "surprises" to be expected of future LSS.

One favorable observation from the experiment was that structural damping was significantly higher than previous launch or space vehicle experience, and higher than the 0.5 percent predicted during pretest analyses.

- **Behaved characteristically like large space structures:**
  - **Very low natural frequencies (0.035 Hz, first mode)**
  - **Densely spaced modes (>33 modes per Hz)**

- **Unexpected curvature of solar array occurred on the dark side of the orbit**
  - **Flight configuration differed from analysis model**
  - **Anomaly occurred despite care taken in design**

- **Damping of the SAFE was significantly higher than previous launch or space vehicle experience**

---

[1] Schock, Richard W., "Solar Array Flight Dynamics Experiment," AAS Guidance and Control Conference, Keystone, Colorado, February 1-5, 1986

SOLAR ARRAY CURVATURE EXPERIENCED DURING DEPLOYMENT FROM STS CARGO BAY

This picture shows the solar array curvature experienced during orbital darkness while deployed to 70 percent of its length. The maximum measured curvature was 40 cm in depth and occurred near orbital midnight. The RFT was designed to track all targets and to label them with respect to predefined windows or "boxes." The unexpected curvature caused some targets to be displaced outside of the "boxes" and to be mislabelled. However, all targets were tracked and correct labelling was reconstructed after the mission using angular data. Thus, no target information was lost and the RFT's performance was declared 100 percent successful.

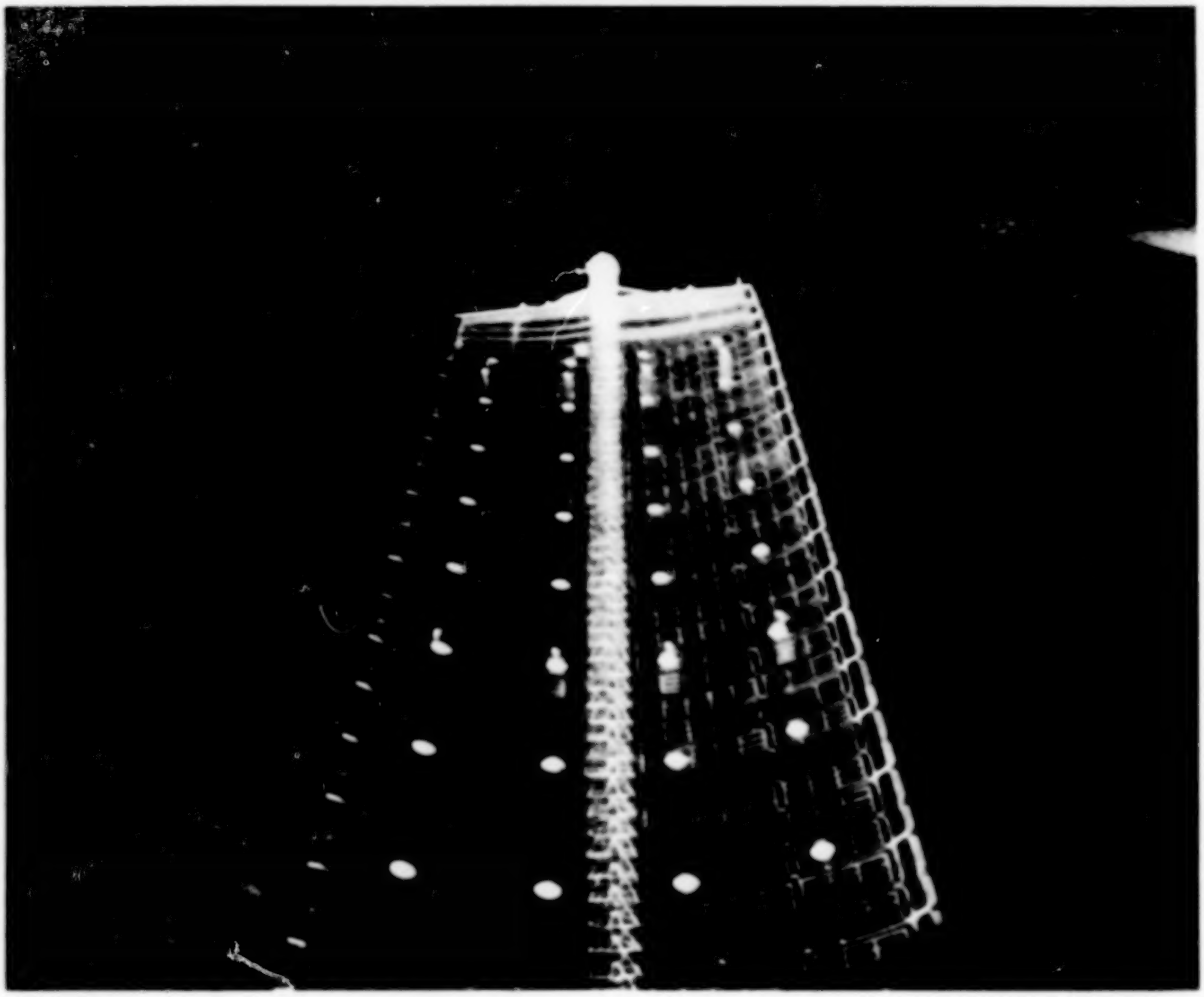

- **Control of flexible structures**
- **Calibration/alignment of payloads**
- **Coalignment of multiple payloads**
- **Attitude transfer**
- **Surface figure measurement**

RECOMMENDED APPROACH

Ball has evaluated many of the foreseeable applications for high-accuracy sensors with large space structures (systems identification, active structural control, vibration isolation, surface figure measurement, alignment transfer, alignment/coalignment of payloads, and others), based on our experience and our knowledge of state-of-the-art sensor technologies. As a result, we have concluded that RAMS offers the optimal solution for most of these applications. RAMS consists of a simple electro-optical design, much less complex than lidar or interferometric devices. It can be applied to a wide variety of applications as suggested earlier, and its design is founded on well-established space sensor heritage. No other sensor offers equivalent high levels of resolution, target capacity, and update rate in a single device while accommodating the need for unobtrusive and versatile usage. RAMS provides direct position readout, eliminating the need to integrate a signal that represents an acceleration value. RAMS can also measure static displacements, another shortcoming of accelerometer-based sensor systems. Finally, the maturity and space heritage of RAMS technology makes it available at reasonably low cost and with low technological risk.

Review of applications and sensor concepts resulted in selection of the RAMS for monitoring of large space structures

- **Simple electro-optical design**
- **Broad application**
- **Well established heritage**
- **High precision (1:100,000)**
- **Accommodates many targets (>100)**
- **High data rates (up to 10 KHz-all targets)**
- **Non-contacting (unobtrusive)**
- **Versatile and easily installed**
- **Direct position readout**
- **Low cost**
- **Low risk**

REMOTE ATTITUDE MEASUREMENT SENSOR (RAMS)

This drawing represents an early prototype concept for RAMS and illustrates the principal elements of the sensor system. A light source (typically a laser diode) is used to illuminate a reflective target attached to the structure of interest. The target might be a flat mirror, a retroreflective mirror, or retroreflective tape, depending on the type of displacements to be measured (translation or rotation). In some cases, active targets (e.g., laser diodes) might be used. The reflected image is focused by a cylindrical lens in the sensor head onto a linear (i.e., single row of pixels) charge coupled device (CCD) detector. Displacement of the mirror will cause the focused image to move along the CCD, giving an indication of the angular change. As illustrated here, a 2,048-pixel CCD with the characteristics shown can provide angular resolution of 0.1 arcsecond and translation resolution of 1.3 micrometer at 2.5-meter range. Position readings for three targets are displayed with light-emitting diodes mounted in a separate display box.

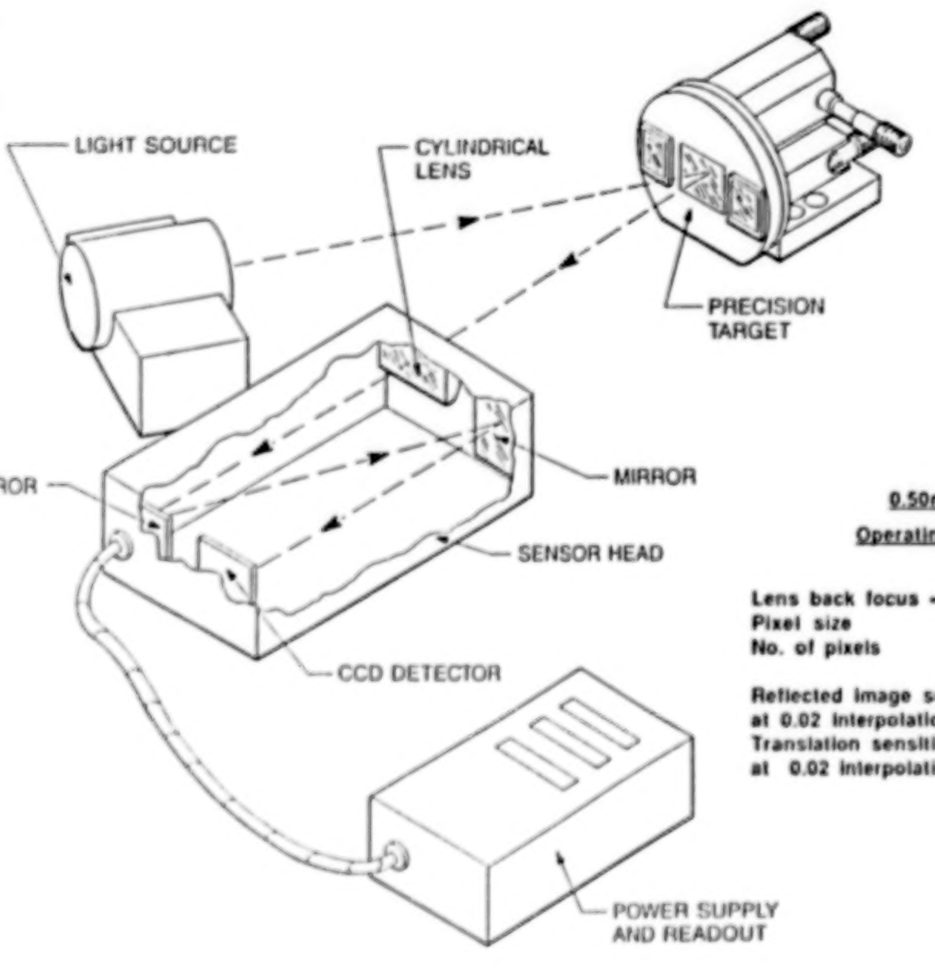

0.50m BFL Sensor

Operating Characteristics

Lens back focus =	0.50m
Pixel size	13 μm
No. of pixels	2,048

Reflected image sensitivity - 5.36 arc sec/pixel
at 0.02 interpolation = 0.1 arc sec
Translation sensitivity (2.5m range)
at 0.02 interpolation = 1.3 μm

SENSOR CONCEPT

The cylindrical lens creates a line image and ensures that the target image is focused on the narrow, linear CCD detector. This configuration provides a sensitive plane (as shown) parallel to the length of the CCD and a nonsensitive plane perpendicular to it. Thus, one CCD and lens assembly provides a single-axis displacement sensor. If two-axis measurements are needed, two linear CCDs can be mounted orthogonally with individual lens assemblies inside a single sensor head, giving the capability to measure two-axis displacements. This same configuration can also provide data about a third axis (rotations about the line of sight), provided that two retroreflective mirrors are used with adequate spacing to ensure proper resolution.

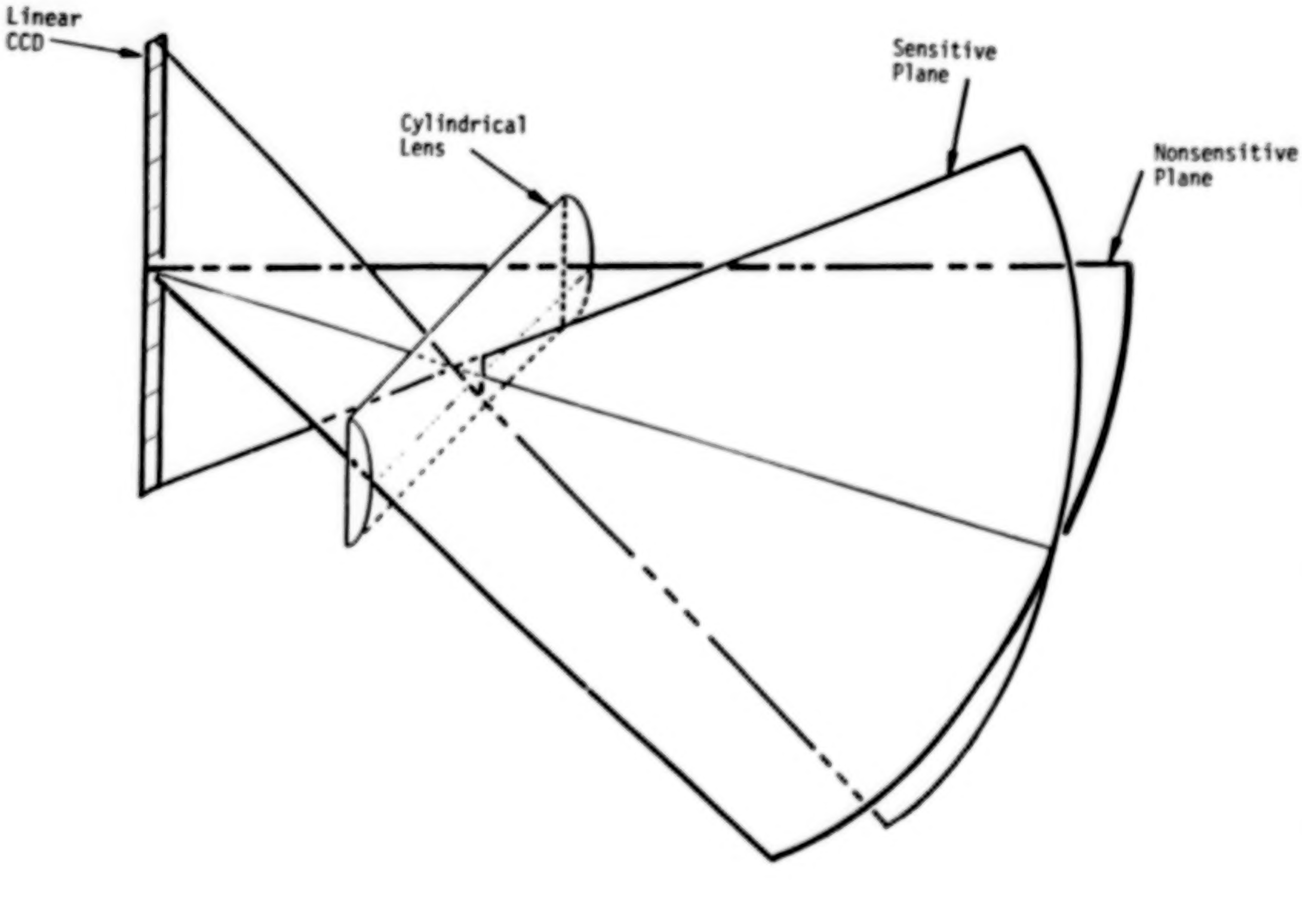

SUBPIXEL SENSING

This figure illustrates the concept used to achieve high resolution with RAMS. When the target image is focused on the CCD, its energy is spread over several pixels as shown. Unique Ball algorithms are employed to identify the radiometric center of the distributed image and to interpolate its position to 1.5-percent of a pixel. These proprietary algorithms were developed by Ball as part of our star tracker development efforts and have been conclusively demonstrated.

BASG interpolation algorithms achieve 0.015-pixel resolution

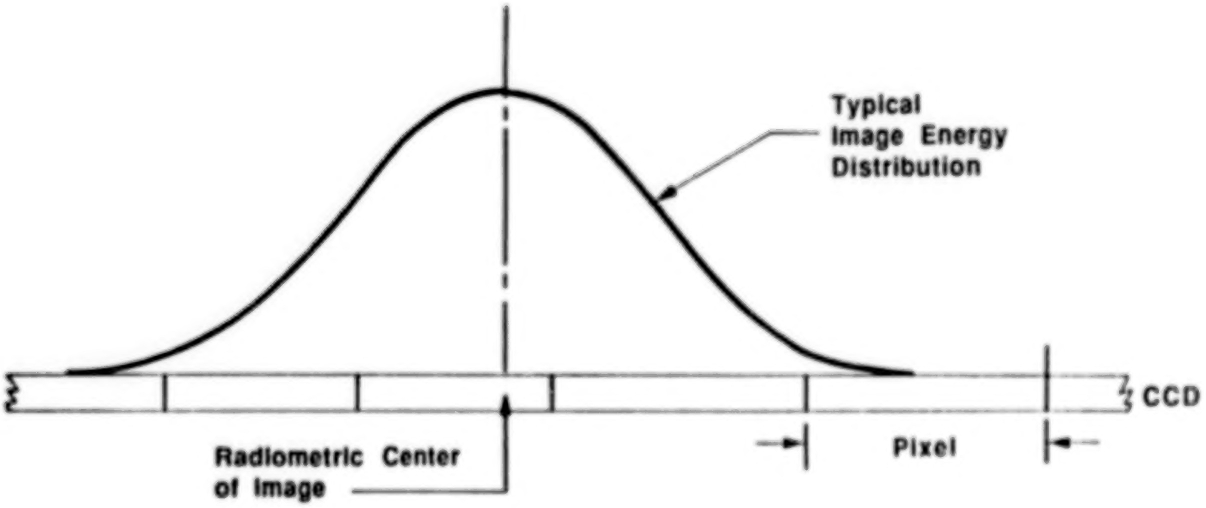
Typical
Image Energy
Distribution
CCD
Pixel
Radiometric Center
of Image

IN-PLANE SENSING

This figure further illustrates the relationship between angular target rotation and displacement measurements by the linear CCD. As depicted, an angular rotation about the X-axis that produces a line-of-sight displacement of the reflected image, delta-theta-X, results in an image displacement along the CCD that is directly proportional to the angular displacement of the mirror. This linear displacement along the CCD is measured by the change in pixel position (both integer and fractional values).

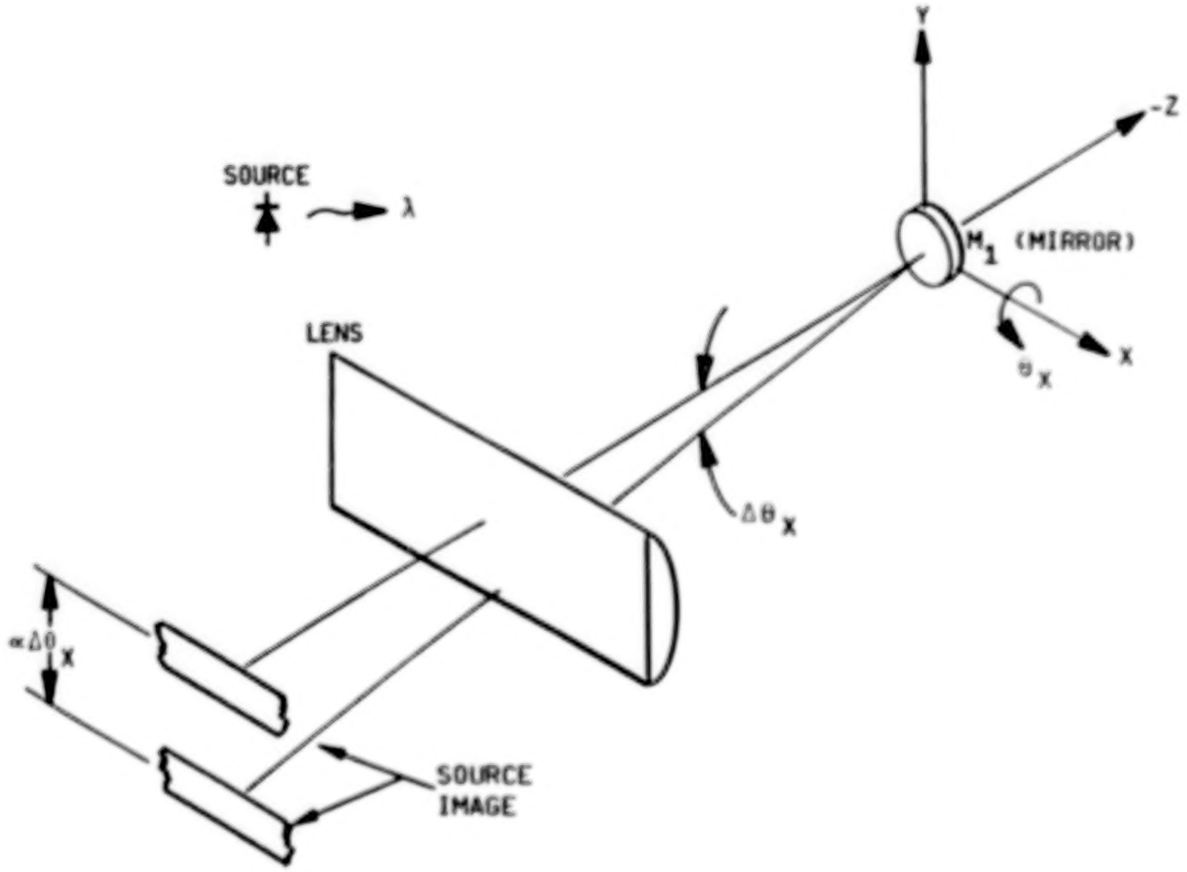

RAMS SENSOR HEAD

The prototype RAMS sensor head (shown here) incorporates a single linear CCD detector and a cylindrical lens. The enclosure on the rear houses the preamplifier circuit boards. The post above the sensor head supports a laser diode used for illumination of mirrors or retroreflective targets. To illustrate the compact nature of this sensor head, the length of the front edge of the base plate is only 6-5/8 in.

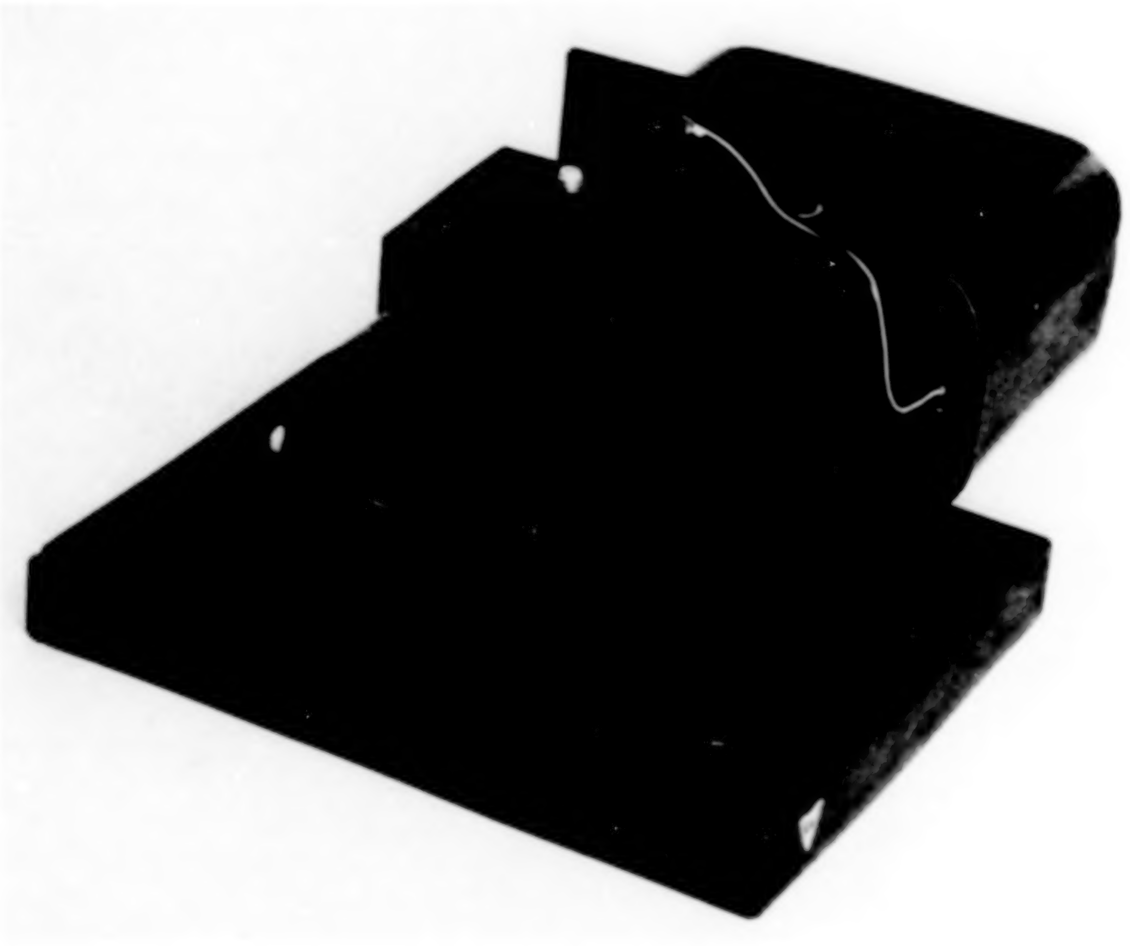

RAMS DISPLAY BOX

The display box for the prototype RAMS incorporates the analog and digital processing circuitry, a power supply, and three light-emitting-diode (LED) displays. These displays depict position data for three targets in terms of pixel position (integer and fractional values). For example, the top LED shows "1063.458," indicating the image centroid is located approximately at the midpoint of the 1,064th pixel. For the optical configuration and target geometry used in this demonstration, a change in position reading of one pixel represented an angular displacement of the reflected image of approximately 25 arcseconds (121 microradians). In most laboratory demonstrations of this prototype, stable readings have been achieved on the order of one arcsecond.

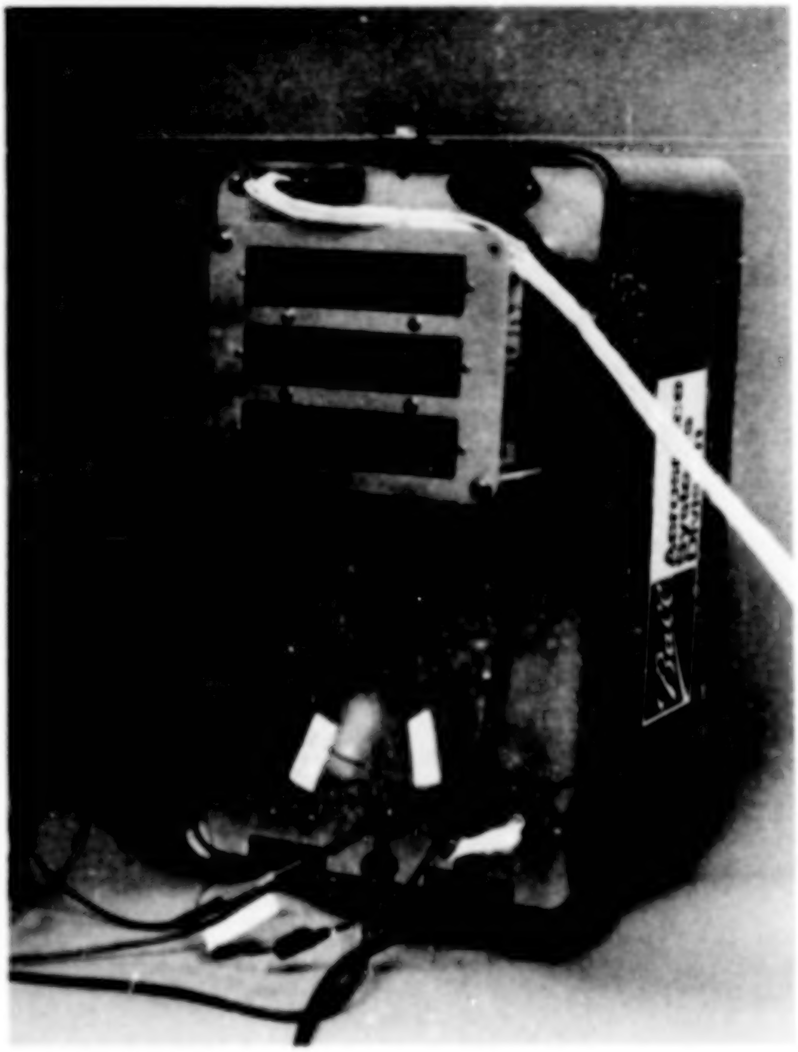

SENSOR SIGNAL DISPLAY SHOWING TWO TARGETS AND INDIVIDUAL PIXELS

This photograph of an oscilloscope display shows the CCD detector response to two reflected images, one from a flat mirror and one from a retroreflector. Both images are distributed over multiple pixels, and the individual pixel responses can clearly be seen. The distinction to be made between the two types of targets is that the flat mirror is sensitive to angular displacements and the retroreflector is sensitive to translation displacements. With the proper mix of both types of targets, simultaneous translation and rotation measurements can be decoupled from each other.

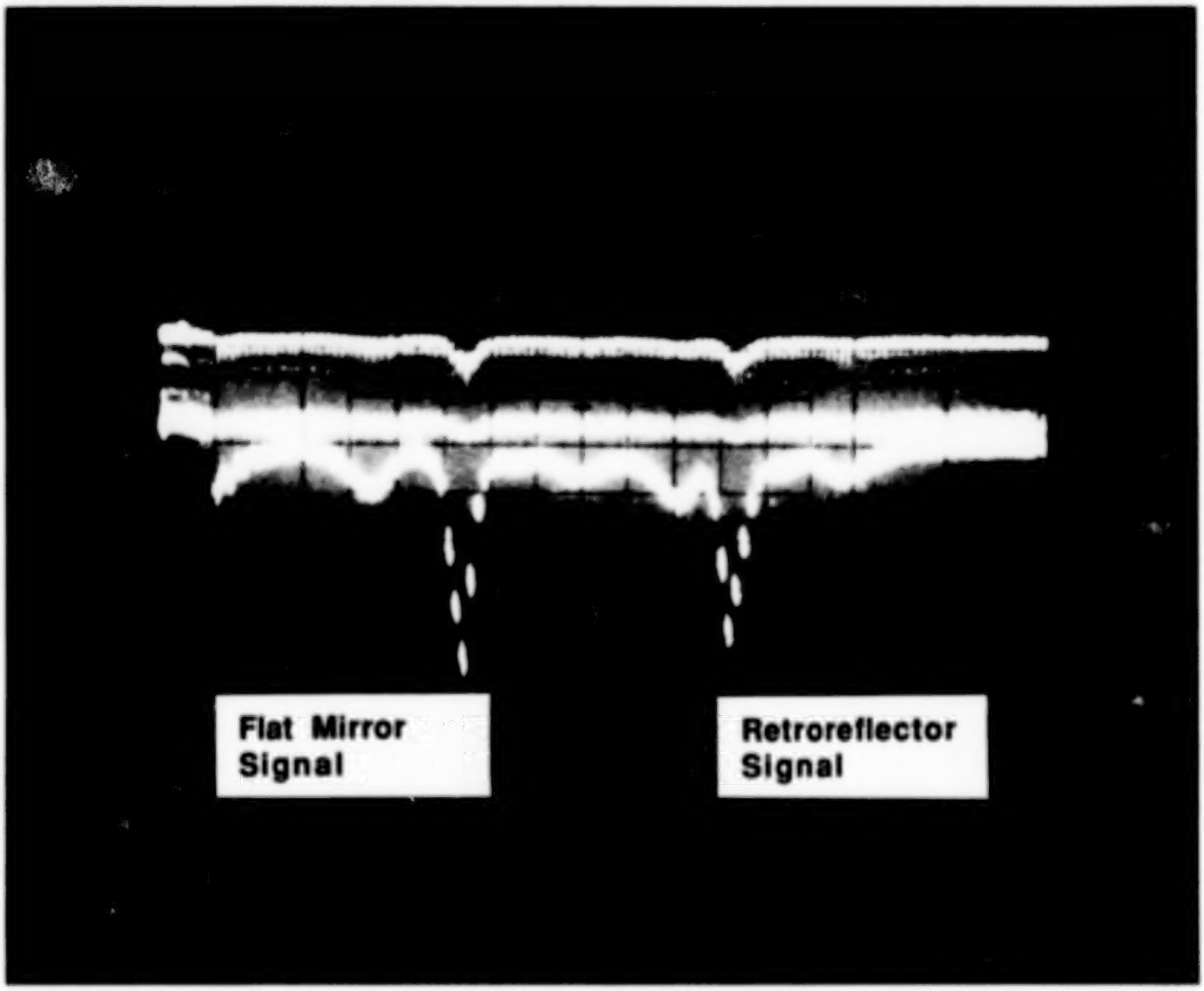

RAMS PROTOTYPE

This table describes the characteristics of Ball's current RAMS prototype hardware. It incorporates a 2,048-pixel linear CCD array and a 106-mm cylinder lens. A field flattener is used for specific optical configurations. Three laser diodes serve as active targets, but the option remains to use a single laser diode to illuminate passive targets (either retroreflectors or flat mirrors). In the present configuration, each pixel subtends an angle equivalent to 25 arcseconds. Applying a conservative 2-percent interpolation factor, the sensor's resolution is 0.5 arcsecond of rotation and 0.0003 in. translation (at 11.1 ft range). Although the prototype can display target position for only three targets at once, it is capable of measuring 100 targets simultaneously and updating each target 250 times per second. This update rate is achieved with off-the-shelf electronics parts. Proper screening of parts would permit a 1000 Hz update rate with no change in design.

- **Sensor: CCD linear array (2048 pixels, each 13 μm wide)**
- **Optics: Cylinder lens (106 mm); field flattener**
- **Sources: Laser diodes (3 mW maximum power)**
- **Reflectors: Retroreflectors; flat mirrors**
- **Sensitivity: 25 arc sec per pixel**
- **Accuracy (at 0.02 interpolation):**
  - **Rotation: 0.5 arc sec**
  - **Translation: 0.3 mils (at 11.1 ft range)**
- **Update rate: 250 Hz (capable of 1000 Hz)**
- **Capacity: Measures up to 100 targets simultaneously (prototype limited to 3 displays)**

RAMS APPLICATIONS

Many of the potential applications for RAMS have already been mentioned or alluded to, but a summary is appropriate here. Control of flexible structures includes displacement sensor feedback for a variety of large flexible structures (platforms, trusses, booms) to monitor and control quasi-static distortions and dynamic disturbances. Calibration/alignment of payloads includes measurements to confirm that the payload instrument is properly mated with its support structure and that the instrument's axes (or boresight) are properly oriented for its mission. Coalignment of multiple payloads includes concurrent alignment measurements for two or more instruments to verify that all are pointed at the same target. Attitude transfer implies measuring the relative attitude differences between an instrument payload and an inertially referenced fixture, and calculating the inertial attitude of the instrument based on these differences. Finally, surface figure measurement includes measuring the position of numerous points on the surface of an antenna or other structure to verify the maintenance of proper shape or figure.

SPACE STATION STRUCTURAL CHARACTERIZATION EXPERIMENT (SSSCE)

This figure illustrates the Phase 1 configuration for the Space Station Freedom, scheduled to be constructed in space starting in 1995. The Space Station Structural Characterization Experiment (SSSCE) is a proposed space flight experiment to examine structural dynamic behavior of the station as part of an OAST Space Technology Program. SSSCE objectives include identifying mode shape, frequency, and damping of targeted structural modes for each stage of assembly through Phase 1. Structural behavior of the truss assembly will be measured in response to intentional excitations. The experiment will provide data with which to evaluate math modeling and ground test technology for large space structures. The RAMS concept has been evaluated and determined to be the leading displacement measurement candidate for the SSSCE.

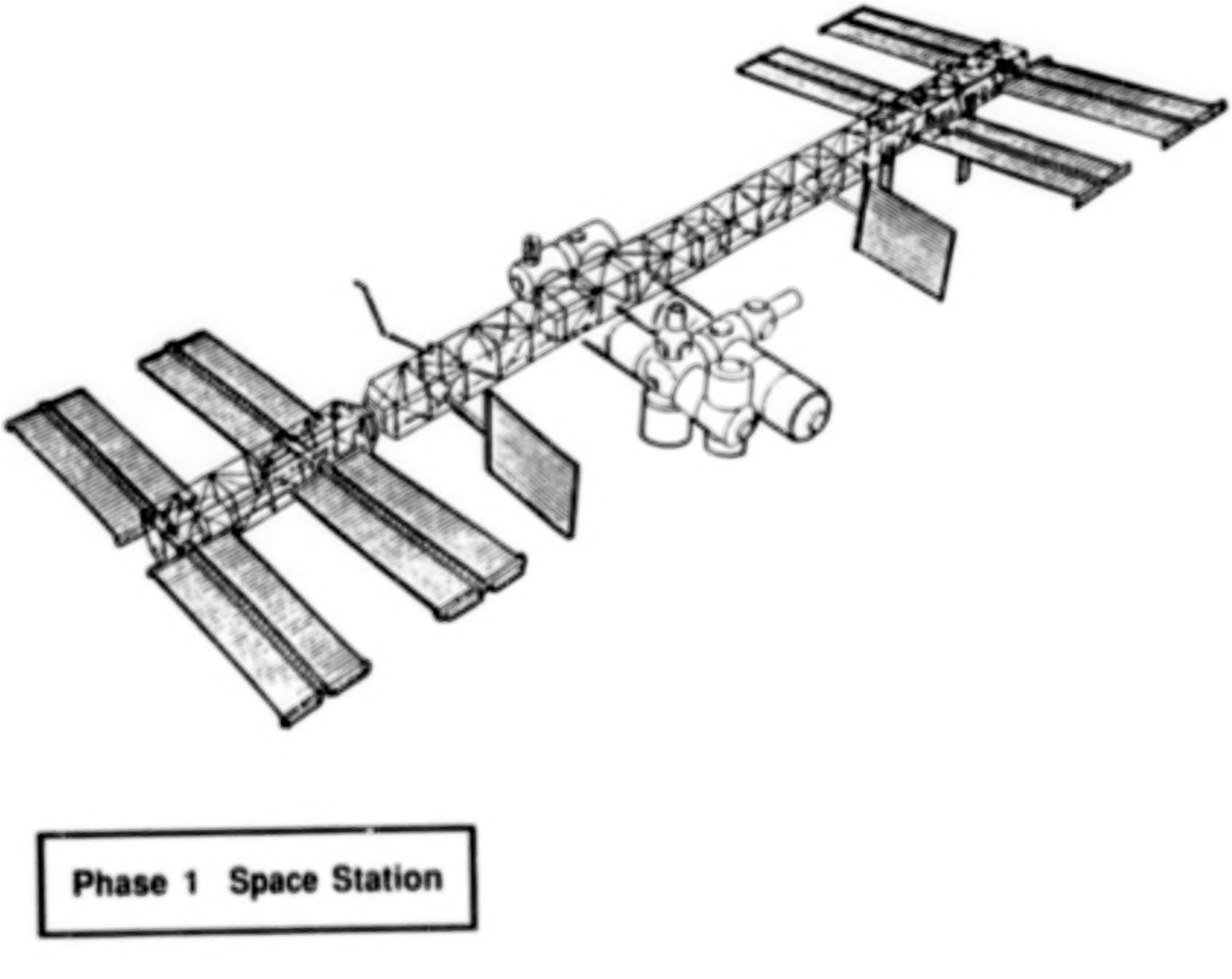

Phase 1 Space Station

SSSCE BASELINE CONFIGURATION WITH RAMS

This figure illustrates the baseline configuration for using RAMS to monitor truss distortions and disturbances on the station. RAMS is shown mounted on the Mobile Transporter (MT), a translating platform equipped with a remote manipulator arm and used for servicing of payloads and other hardware on the station. The MT is positioned in the center of the transverse boom during RAMS measurements and rigidly attached to the truss structure. Using a spherical lens with a 14.9 deg field of view, RAMS can monitor retroreflective tape targets attached to each structural node (at 5m spacings) between the 5m and 70m range. A total of six sensors are required to view both halves of the transverse boom and measure displacements normal to the longitudinal axis of the boom (X and Z) as well as rotation about the longitudinal axis (Y). With this configuration, RAMS can sense displacements as small as 137 μm at the maximum range of 70m.

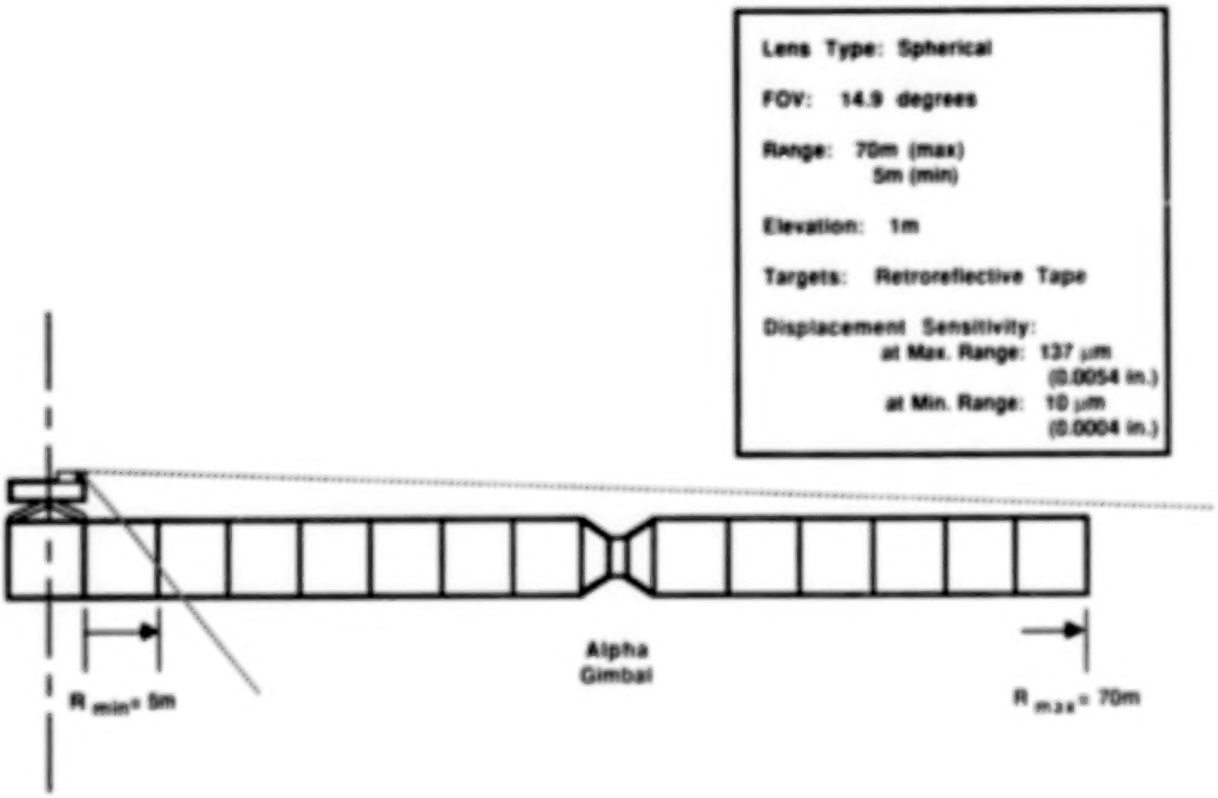
Lens Type: Spherical

FOV: 14.9 degrees

Range: 70m (max)
5m (min)

Elevation: 1m

Targets: Retroreflective Tape

Displacement Sensitivity:
at Max. Range: 137 μm (0.0054 in.)
at Min. Range: 10 μm (0.0004 in.)

CONTROL AND STRUCTURES EXPERIMENT IN SPACE (CASES)

CASES is another on-orbit structural dynamics experiment with applications for RAMS. This shuttle-based experiment includes a boom tip assembly or mask mounted on top of a 32m-long flexible boom. The experiment incorporates both science (x-ray imaging) and technology (structural system identification and control) objectives and is similar in design to a future space station payload, the Pinhole Occulter Facility. RAMS would provide displacement data for both the boom and the mask to support on-orbit modal tests, disturbance isolation, closed loop tests of the controller, and active structural control of the structure during astrophysics activities.

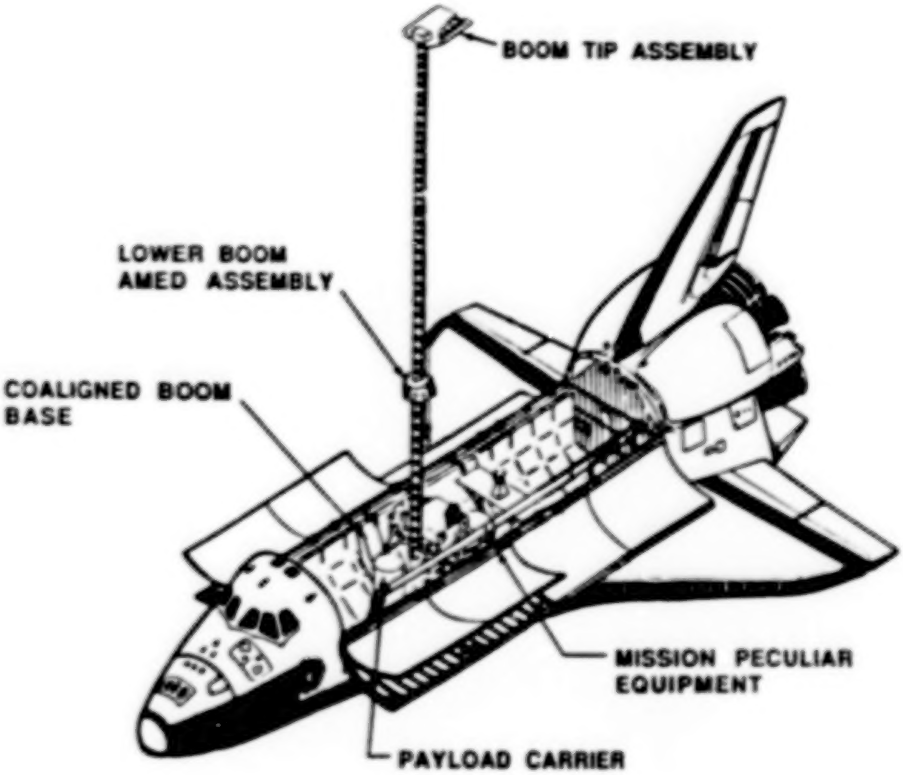
BOOM TIP ASSEMBLY
LOWER BOOM
AMED ASSEMBLY
COALIGNED BOOM
BASE
MISSION PECULIAR
EQUIPMENT
PAYLOAD CARRIER

DISPLACEMENT SENSING WITH RAMS

This figure illustrates how RAMS could be used to measure the structural shape of the CASES boom and the orientation of the mask. Two single-axis sensors mounted orthogonally on the base (as shown) can provide X and Y displacement data within an accuracy of 0.0025 in. for targeted locations along the boom. If we assume that the last two targets on the upper end of the boom are linear, normal to the mask, and adequately spaced (e.g., 3 ft), then we can determine the inclination of the mask within 15 arcseconds. Although not illustrated here, the twist of the mask about the Z axis can also be measured within 15 arcseconds by using the two targets mounted on the lower side of the mask, provided they are located at least 3 ft from the center of the boom. The displacement data can be processed with shape algorithms followed by control algorithms to produce command signals for actuators that ultimately control the structural shape and orientation of the CASES experiment.

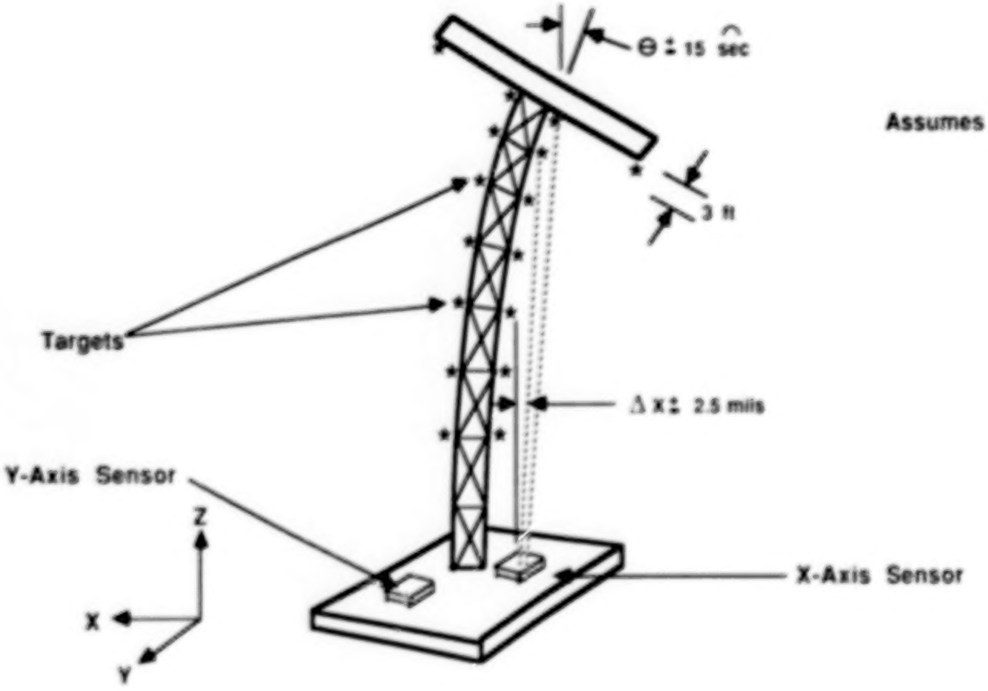

Assumes EFL = 0.1 m

MEASURING SURFACE FIGURE OF REFLECTORS

The surface figure or shape of a reflector can be defined by the elevation angle ϕ for each point along any given cross-section, provided that the reflector materials are dimensionally stable (i.e., they do not stretch). Under these conditions, the performance of the reflector (expressed as 3dB beamwidth half-angle, β) is a function of the wavelength (or frequency) and the diameter of the reflector.

$$\text{3dB beamwidth half-angle } \beta = \frac{7\times10^4}{fD} \quad \text{(deg)}$$

where f = frequency (MHz)
d = diameter (ft)

For a 20 GHz parabolic reflector with 49.2 ft diameter and 24.6 ft focal length, β is 0.071 deg. If the angle ϕ for the most extreme target is 20 deg, and if surface displacement at the extreme target $(\Delta r)_{MAX}$ is $\frac{\lambda}{10}$ alignment sensor like RAMS mounted at the center of the reflector would require only a 1:2,000 resolution to sense such a displacement. This is well within the 1:100,000 resolution capability of RAMS.

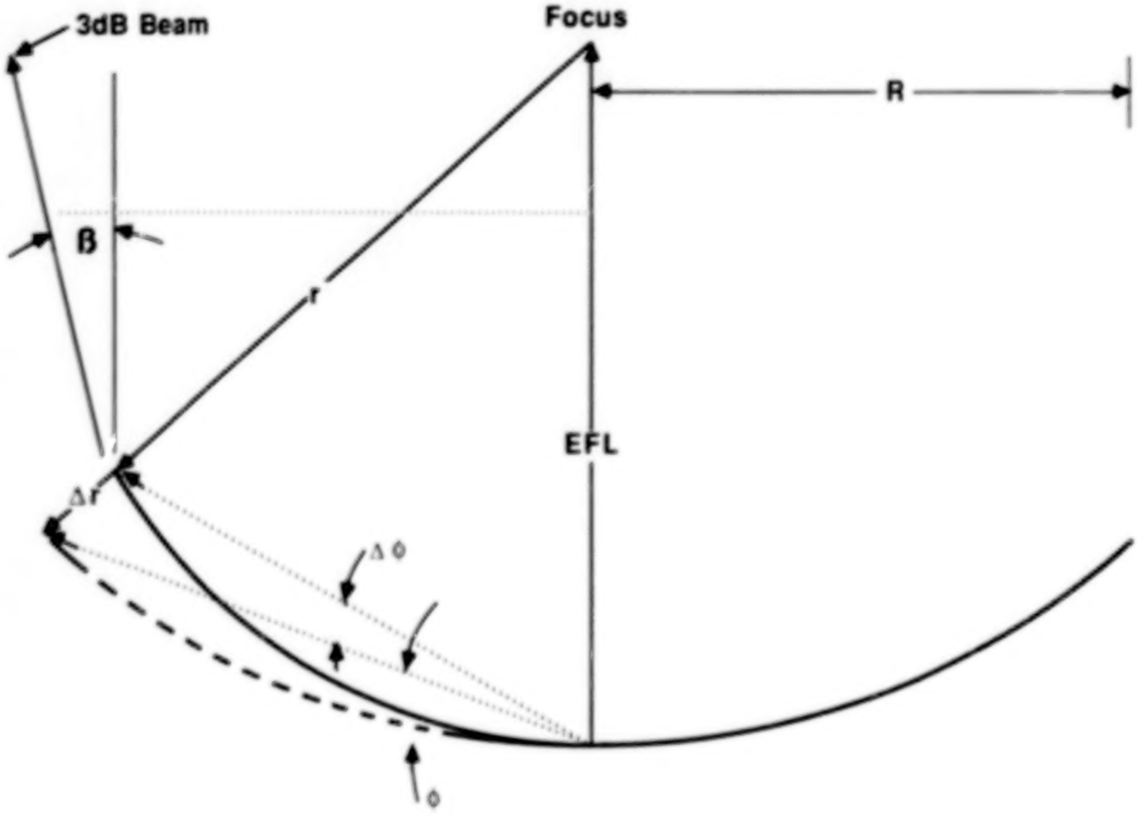

SCANNING CONCEPT FOR RAMS

This figure illustrates one scanning concept that might be used with large reflectors. One linear CCD can provide the radial field-of-view shown at the bottom of the figure and scan surface targets attached at selected points along each rib or segment of the reflector. A second linear CCD, mounted orthogonally to the first, can provide axial sensing of targets along the line of sight of the reflector. This second sensor could provide both feedhorn position relative to the reflector and verification of axial alignment of the scanning mechanism. Several options have been considered for the method of scanning. One is to physically rotate the sensor head with an axial gimbal and transfer power and data across the rotating interface with slip rings. A preferred option is one that uses a rotating prism mounted above the stationary sensor head to achieve scanning. This second option adds complexity to the optical and mechanical design but results in a less expensive and more reliable design.

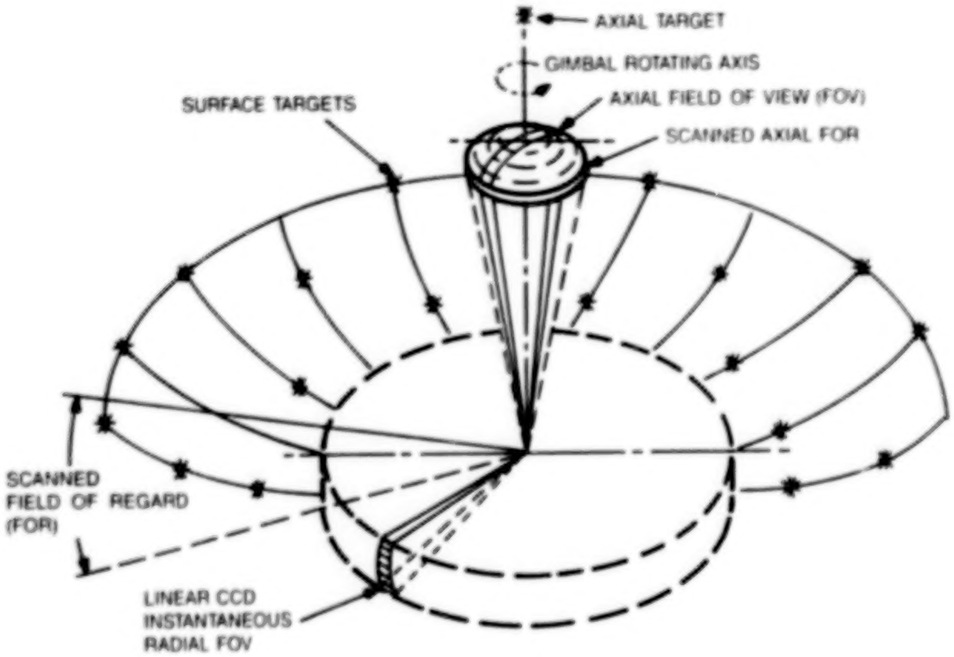
AXIAL TARGET
GIMBAL ROTATING AXIS
SURFACE TARGETS
AXIAL FIELD OF VIEW (FOV)
SCANNED AXIAL FOR
SCANNED FIELD OF REGARD (FOR)
LINEAR CCD INSTANTANEOUS RADIAL FOV

RAMS DESIGN DRIVERS

Each RAMS application is unique, and generally requires a unique optical configuration for optimal performance. However, the electronics circuitry is standard for all applications, provided the current performance limits for accuracy, update rate, and number of targets are sufficient. At the present time, the requirements of most applications can be satisfied with a 1-arcsecond accuracy, 250 Hz update rate, and up to 100 targets. Other design drivers are listed in the table below. Geometry requirements can usually be accommodated. Target selection, radiometry considerations, and background illumination may require innovative approaches, such as pulsed laser diode targets, diffuse target backgrounds, etc. The dynamic behavior of the structure will define displacement characteristics and influence target design. Physical and resource requirements should not be a significant constraint. Based on the RAMS prototype hardware, we expect a single-axis sensor to weigh less than 10 lb and to use less than 20W power.

- **Structure/sensor geometry**
  - **Clear line of sight to targets**
  - **Field of view**
  - **Depth of field**
  - **Separation between targets**

- **Number of targets**
  - **Target separation**
  - **Target displacements**

- **Active vs passive targets**
  - **Unobtrusive sensing**
  - **Weight constraints**
  - **Lead-wire interference**
  - **Radiometry considerations**
  - **Background illumination**
  - **Stray light or reflections**

- **Dynamic behavior of structure**
  - **Modal characteristics (frequency, amplitude)**
  - **Target displacements**
  - **Target rates**
  - **Required update rate**

- **Physical requirements**
  - **Size limitations**
  - **Weight constraints**

- **Resource requirements**
  - **Power requirements**
  - **Data I/F requirements**
  - **Thermal requirements**

SUMMARY

RAMS offers a low-cost, low-risk, proven design concept that is based on mature, demonstrated space sensor technology. The electronic design concepts and interpolation algorithms have been tested and proven in space hardware like the Retroreflector Field Tracker and various star trackers. The RAMS concept is versatile and has broad applicability to both ground testing and spacecraft needs. It is ideal for use as a precision laboratory sensor for structural dynamics testing. It requires very little set-up or preparation time and the output data is immediately usable without integration or extensive analysis efforts. For on-orbit use, RAMS rivals any other type of dynamic structural sensor (accelerometer, lidar, photogrammetric techniques, etc.) for overall performance, reliability, suitability, and cost. Widespread acceptance and extensive usage of RAMS will occur only after some interested agency, such as OAST, adopts the RAMS concept and provides the funding support necessary for further development and implementation of RAMS for a specific program.

- **RAMS offers a proven design concept based on mature, demonstrated technology**
- **RAMS has broad applicability to both ground testing and spacecraft needs:**
  - **Precision lab sensor**
  - **On-orbit system identification**
  - **Structural characterization**
  - **Active control feedback**
  - **Alignment/attitude transfer**
- **Further development efforts and funding support are needed to satisfy specific applications and objectives**

REFERENCES

1. Studer, P.A.; Davis, H.W.: Quiet Structures For Precision Pointing. NASA/DOD Control/Structures Interaction Technology Conference (Colorado Springs, Colorado), November 1987.

2. Garibotti, J.F.: Industry Overview/Issues. NASA/DOD Control/Structures Interaction Technology Conference (Norfolk, Virginia), November 1986.

3. Wargocki, F.E.; Ray, A.J.; Hall, G.E.: Retroreflector Field Tracker, State-of-the-Art Imaging Arrays and Their Application. Keith N. Prettyjohns, Editor, Proc. SPIE 501, p. 283.

4. Schock, R.W.: Solar Array Flight Dynamic Experiment. AAS Guidance and Control Conference (Keystone, Colorado), February 1-5, 1986.

PRECISION SEGMENTED REFLECTOR , FIGURE VERIFICATION SENSOR

Paul K. Manhart
Steve A. Macenka

Optical Sciences and Applications Section 385
Jet Propulsion Laboratory
California Institute of Technology
Pasadena, California

ABSTRACT

The Precision Segmented Reflector (PSR) program currently under way at the Jet Propulsion Laboratory is a test bed and technology demonstration program designed to develop and study the structural and material technologies required for lightweight, precision segmented reflectors. This paper describes a Figure Verification Sensor (FVS) which is designed to 1) monitor the active control system of the segments, 2) to define a 'best fit' surface and to 3) assess image or wavefront quality of the assembled array of reflecting panels.

INTRODUCTION

The need for large diameter optical instruments for astronomical research has been recognized since the invention of the telescope. Large diameter optical systems are attractive for their increased light gathering capability and angular resolution in object space. Large diameter optics allow one to see fainter objects, and to see them in more detail. Many future missions in astrophysics and spacecraft optical communications will utilize very large diameter, precision reflectors. However, there is a practical limit for ground-and space-based optical instruments with monolithic mirrors. With ground-based systems you have exponentially increasing cost for the telescope mounts and support structures as the weight of the mirror goes up and weight and mass scal as the diameter is cubed. Atmospheric cell size and thermal equilibrium problems also tend to limit the usefulness of very large diameter ground-based telescopes. For space-based telescopes, the limiting factors are launch weight, serviceability, fabrication cost and risk. In short, weight, fabrication difficulties, and high costs for high quality, large aperture mirrors are driving factors which put an upper limit on aperture size for ground-based telescopes and space systems. A new technology therefore is needed to make these missions feasible.

A variety of new technologies, such as lightweight graphite/epoxy reflective panels, and studies, such as LDR, have opened new avenues toward being able to build affordable, large aperture reflectors. However, additional technologies are required to make these segmented reflector systems feasible. Many of these challenges are currently being addressed by the Precision Segmented Reflector (PSR) program at the Jet Propulsion Laboratory.

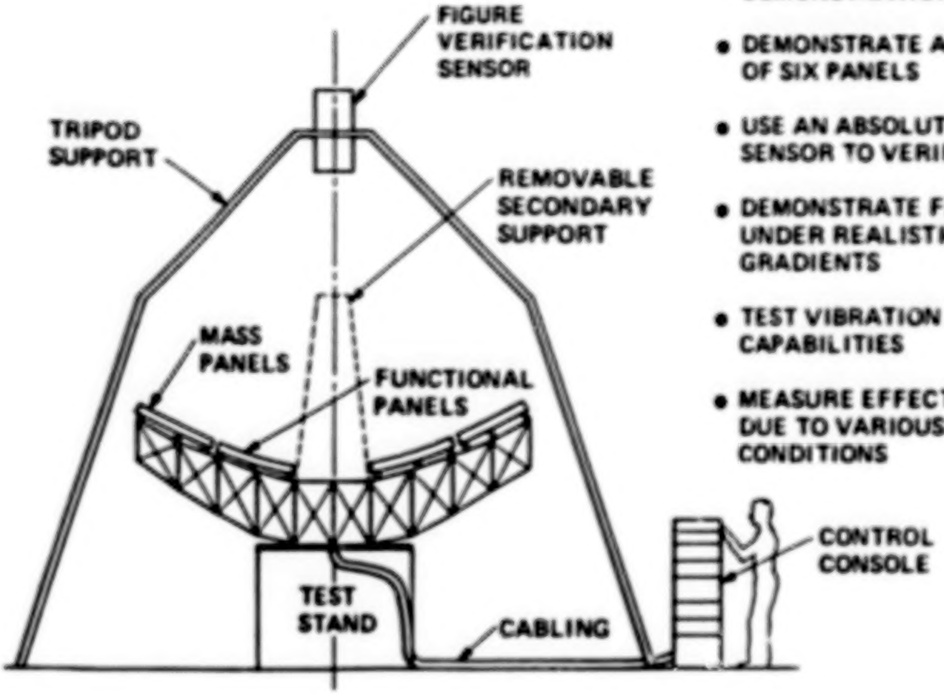

- DESIGN AND FABRICATE TECHNOLOGY VALIDATION DEMONSTRATION HARDWARE
- DEMONSTRATE ACTIVE CONTROL OF SIX PANELS
- USE AN ABSOLUTE FIGURE SENSOR TO VERIFY FIGURE
- DEMONSTRATE FIGURE CONTROL UNDER REALISTIC THERMAL GRADIENTS
- TEST VIBRATION SUPPRESSION CAPABILITIES
- MEASURE EFFECTS ON FIGURE DUE TO VARIOUS VIBRATION CONDITIONS

FIGURE 1. PSR TEST BED

PSR is a Civilian Space Technology Initiative (CSTI) program at JPL serving as a test bed and technology demonstration of a large diameter (5 meter), parabolic, actively controlled, segmented mirror telescope. The 1-meter segments are hexagonal in shape and composed of epoxy/graphite. The major objectives of the PSR effort are 1) to develop the enabling technologies for advanced, large, lightweight segmented reflector systems for space and 2) to validate design concepts for actively controlled, multi-segmented, precision reflectors by means of a system demonstration.

The critical new technology areas required to make space-based, segmented reflector systems feasible include the lightweight reflector panels, the interface structure for connecting the panels, the control and measurement system needed to maintain extremely precise alignment and dynamic stability of the optical components, and advanced optics (such as two-stage optics and internal wavefront sensing). Each of these technology areas must be addressed and advanced in order to evaluate and develop lightweight segmented optics. The PSR test bed, (see Figure 1) concentrates on the lightweight segmented reflector along with the interface structure and control system. To evaluate and develop these new technologies; however, a method must be devised which can quantify the behavior and performance of the system.

FIGURE VERIFICATION SENSOR (FVS)

The first set of requirements for PSR optics is to design a Figure Verification Sensor (FVS) to monitor the optical quality of the wavefront and the behavior of the control system used to position the lightweight reflectors. Since PSR is primarily a materials and structures development program, the FVS should be responsive to structural changes due to thermal gradients and vibrations.

The requirements of the FVS are to 1) quantify the behavior of the control system, and 2) quantify the optical quality of the assembly of panels. The initial positioning of each panel is assumed to be ± 1 mm and the smallest increment in positional change that must be detected is 0.1 µm. The requirements for the FVS are difficult to achieve with a single instrument for the following reasons.

1) The dynamic range out to 1 mm precludes most conventional optical techniques that measure wavefront quality.

2) The expected surface error of the epoxy/graphite panels is 3-5 µm RMS. Figure errors of this magnitude limit the degree to which 'best focus' can be determined; thus, the figure errors tend to mask the minute changes in panel position and put a limit on resolution.

Assuming perfectly made parabolic segments, it would be a simple task to bring all the panels into the range of a visible interferometer with a star, or focus test, which would phase each panel segment with respect to some common focal point. Conventional interferometric techniques in the visible would then be used to finely tune the system and accurately monitor any change in panel position due to structural or control changes. A 3-5 µm RMS surface error on each panel, however, gives 12-20 waves RMS optical path difference in the visible. This magnitude of error gives about a ±0.5 mm focus uncertainty when using a star test. It also means that there could easily be 2π ambiguities at the edges of the panels. These ambiguities preclude full aperture, single wavelength interferometry. The precision of fitting the focus and tilt terms of Zernike polynomials on individual, off-axis, parabolic segments gives at best a ±50 µm repeatability, provided the fringes can be analyzed.

BASELINE FIGURE VERIFICATION SENSOR DESIGN

The baseline FVS design consists of a Shack-Hartmann setup with a battery of integrated optical tests all contained in a compact, versatile package which gives precise information on panel tilt, piston and wavefront quality. In conjunction with the Shack-Hartmann test, the FVS utilizes a dual wavelength laser distance measurement system to accurately monitor panel motion as described by piston. Figure 2 shows a conceptual layout of the FVS testing the PSR primary mirror in a paraxial center of curvature,(null lens') configuration. The laser distance measurement system is not shown in the figure but is assumed to have one laser beam per panel which is returned to the interferometer via a small retro-reflector on the panel surface. The sensor consists of a Shack-Hartmann slope error test with a multiple wavelength, Shack cube, moire interferometer capable of performing star tests, knife edge tests, wire tests and multiple wavelength interferometry.

The Shack-Hartmann test provides accurate tilt information by monitoring centroid positions of the test path with respect to those of the reference path. The centroids from the reference path define the perfect system. Minimizing the RMS difference in centroid position between the reference path and the test path for each panel also gives an indication of the 'best fit' parabolic surface. Note that this test is very sensitive to changes in panel tilt but insensitive to panel focus. The multiple wavelength interferometer is used to assess wavefront quality. The star test is used for rough alignment and visual assessment of the image, and a wire, knife edge and Focault test are used for slope measurements. A tunable laser operating in the visible is used with the interferometer. The first interferogram at λ_1 is recorded on a thermoplastic camera and developed in place. The second interferogram at λ_2 is imaged on top of the first. The resulting moire pattern is that of an interferogram at

$$\lambda_{\text{effective}} = (\lambda_1 \cdot \lambda_2)/(\lambda_1 - \lambda_2).$$

The advantages of this sensor over others that were studied are its sensitivity, versatility, dynamic range and proven technology.

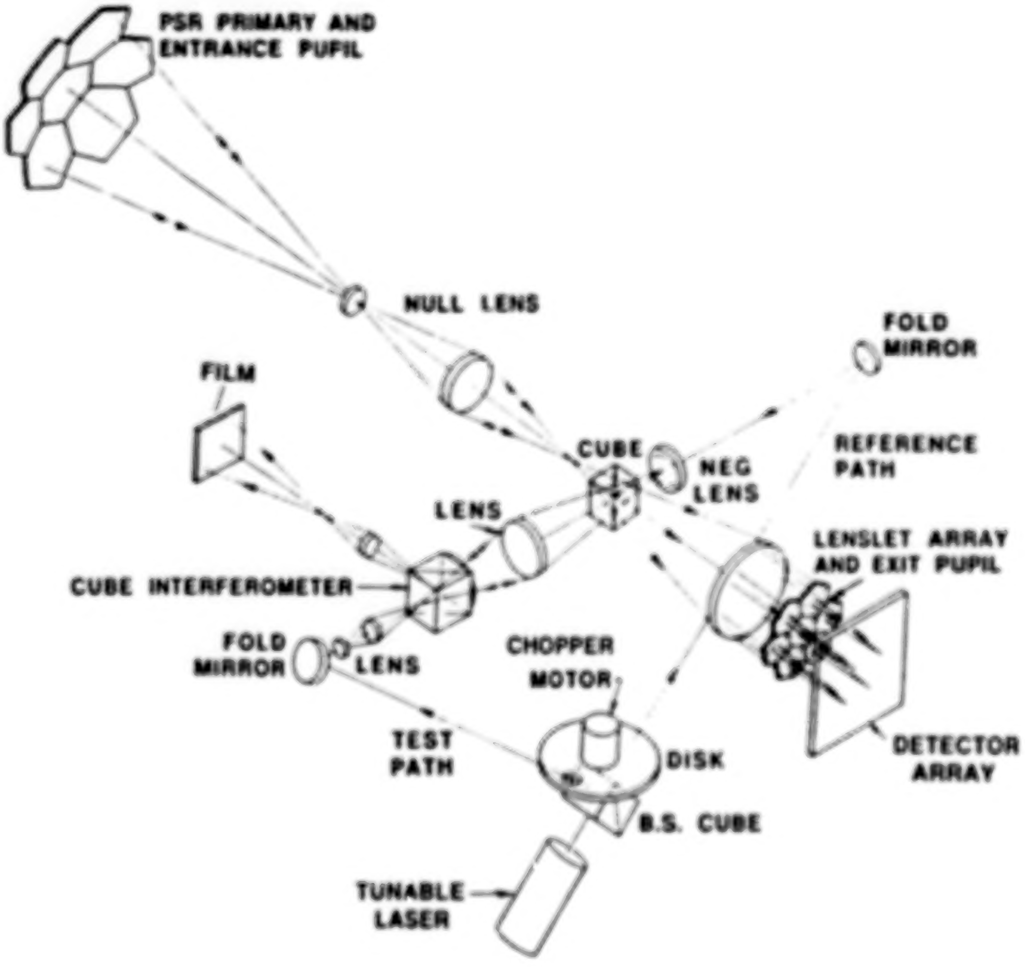
PSR PRIMARY AND ENTRANCE PUPIL
NULL LENS
FOLD MIRROR
FILM
CUBE
NEG LENS
REFERENCE PATH
LENS
LENSLET ARRAY AND EXIT PUPIL
CUBE INTERFEROMETER
FOLD MIRROR
LENS
CHOPPER MOTOR
TEST PATH
DISK
DETECTOR ARRAY
B.S. CUBE
TUNABLE LASER

FIGURE 2. FIGURE VERIFICATION SENSOR

Figure 2 shows a tunable laser being split into two separate paths by a cube beamsplitter. The reference path goes through the beamsplitter to a fold mirror and a beam diverger to define the paraxial center of curvature focal point. The reference beam is collimated and directed into the Shack-Hartmann lenslet array. The Shack-Hartmann array is represented by three or more lenslets per panel (shown here as seven lenslets per panel). The light passing through the lenslets focuses onto a detector array and the centroids for the reference path are noted. The energy in the test path is focused on the paraxial center of curvature focal point, but the light is diverted to the PSR primary mirror. Upon returning from the primary mirror, the energy passes through the collimating lens and lenslet array, and focuses onto the detector array. The chopper blade located near the first beamsplitter can be used to blink between the two paths. The Shack cube interferometer, inserted in the test path, is used for initial alignment and assessment of wavefront quality.

SUMMARY

The combined dynamic range and sensitivity requirements for the PSR Figure Verification Sensor precluded any single conventional optical technique that measures wavefront quality. The initially expected 3-5 µm RMS surface error of the panel figure masks the minute changes in panel position (focus) and puts a limit on resolution. The proposed FVS design satisfies the initial requirements and does not require any technology development to implement. A Shack-Hartmann setup with a battery of integrated optical tests all contained in a compact, versatile package gives precise information on panel tilt, wavefront quality and panel alignment. The two wavelength, moire interferometry extends the dynamic range of the instrument in its ability to quantify optical performance. The star tests and shadowgrams give visual assessment and the laser distance measurment system gives precise information on panel piston motion.

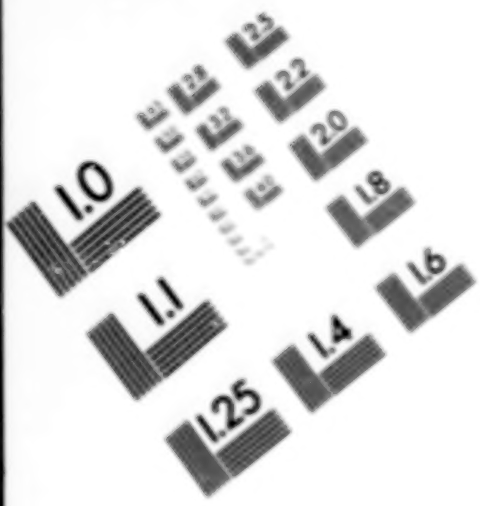
1.0
1.1
1.25
1.4
1.6
1.8
2.0
2.2
2.5
2.8
3.2
3.6

UNITED STATES OF AMERICA
GOVERNMENT PRINTING OFFICE

1.0
1.1
1.25
1.4
1.6
1.8
2.0
2.2
2.5
2.8

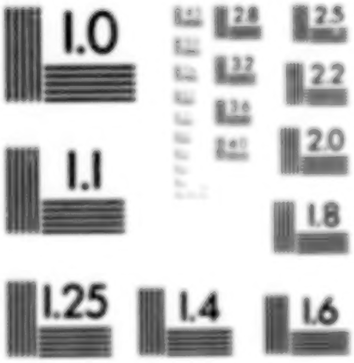
1.0
1.1
1.25
1.4
1.6
1.8
2.0
2.2
2.5
2.8
3.2
3.6
4.0

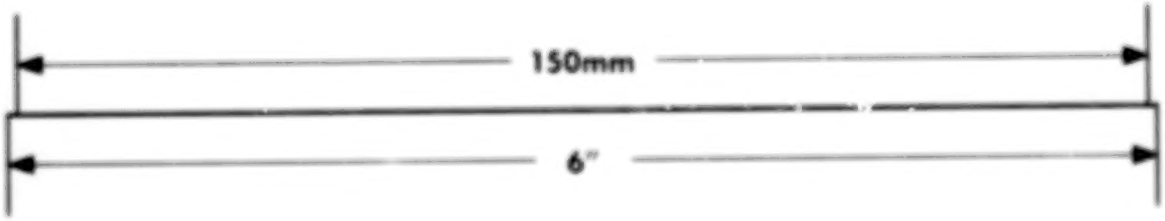

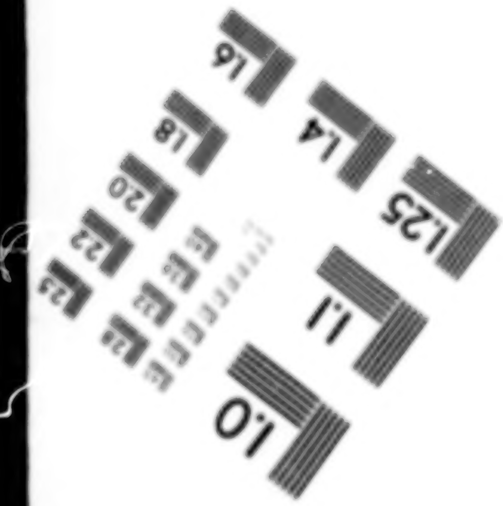
1.0
1.1
1.25
1.4
1.6
1.8
2.0
2.2
2.5

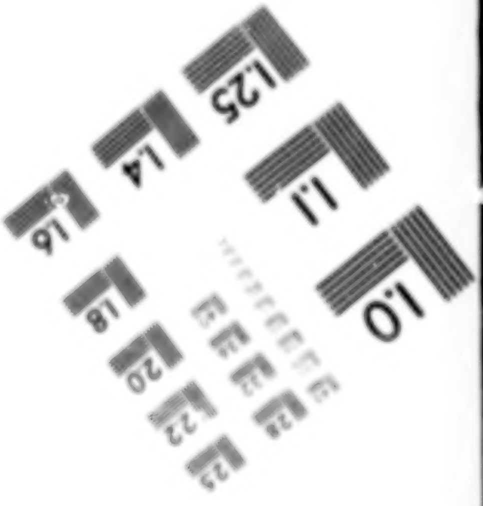
1.0
1.1
1.25
1.4
1.6
1.8
2.0
2.2
2.5
2.8

EARTH SCIENCE GEOSTATIONARY PLATFORM
TECHNOLOGY... NASA CONFERENCE PUBLICATION 3040
NAS 1.55:3040 ... NASA... SEPTEMBER 21-22,1988

5 OF 5
24X
SUPTDOCS/GPO
P.0375-0399

Technology Panel Reports

E
S
G
P

Report of the Science Panel

A. J. Gasiewski
Massachusetts Institute of Technology

The conclusions of the Science Panel relative to our near- and far-term goals are shown in figure 1. The near-term goal involves the use of 90, 118, 160, 183, and 220 GHz frequencies with a full aperture of 4.4 m (suitable for Space Shuttle delivery). A system with higher frequencies is desirable, but it is important that we have the 4.4-m system ready for launch in the mid 1990's. Reduction of the frequency to 60 GHz is also desirable for the 4.4-m system, but it is ancillary.

For the far-term goals, the panel split the frequency channels into low- and high-frequency goals. Two routes are recommended for the low-frequency regime. A mesh deployable system seems to be limited in diameter to about 20 m. If the frequencies are limited by the available mesh size, then 20 m will be the maximum diameter. The usefulness of a 20-m-diameter system to the scientific community is questionable, but more input is needed before that decision can be made. If the mesh deployable system cannot be used or is deemed not worthwhile, synthetic apertures or phased arrays with diameters less than or equal to 200 m and frequencies of 6, 10, 18, 22, and 37 GHz are appropriate. For the high-frequency regime, frequencies of 90, 118, 160, 183, and 220 GHz (with 37 and 60 GHz frequencies optional) and antenna diameters of 20 m to 30 m are desirable.

Based on the current scientific requirements, this report summarizes the consensus of the Science Panel.

Microwave Apertures For ESGP Near and Far Term Science Report

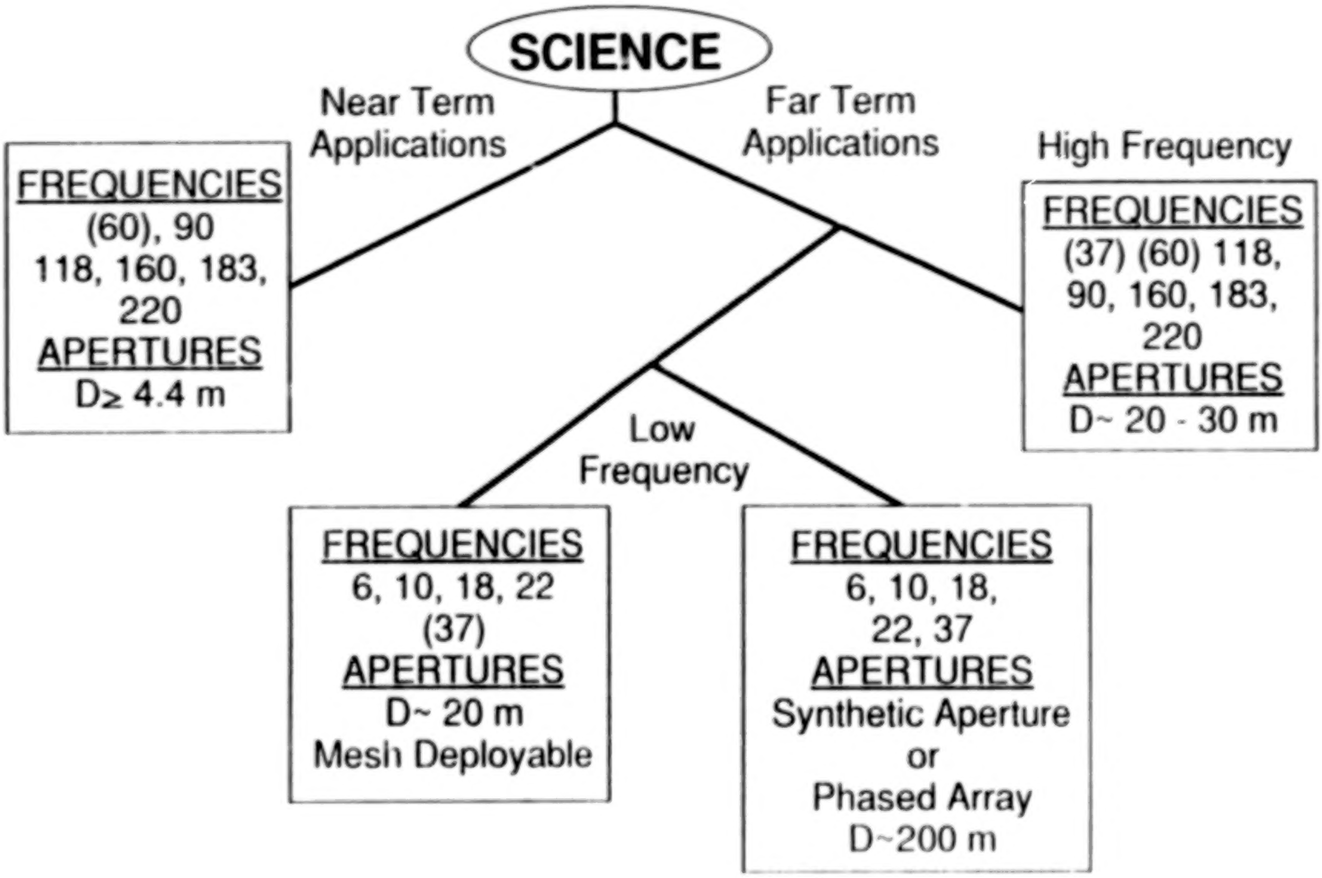
SCIENCE
Near Term Applications
Far Term Applications
High Frequency
FREQUENCIES
(60), 90
118, 160, 183,
220
APERTURES
D≥ 4.4 m
FREQUENCIES
(37) (60) 118,
90, 160, 183,
220
APERTURES
D~ 20 - 30 m
Low Frequency
FREQUENCIES
6, 10, 18, 22
(37)
APERTURES
D~ 20 m
Mesh Deployable
FREQUENCIES
6, 10, 18,
22, 37
APERTURES
Synthetic Aperture
or
Phased Array
D~200 m

Figure 1

Report of the Large Space Antenna Technology and Electromagnetics - Phased Array Adaptive Systems Technology Panels

Allan W. Love
Rockwell International

and

Y. Rahmat-Samii
Jet Propulsion Laboratory

The combined Large Space Antenna Technology and Electromagnetics - Phased Array Adaptive Systems Technology Panels derived the set of requirements shown in figure 1. In the low-frequency region (6, 10, 18, and 22 GHz) and for the near to not-too-far term, mesh certainly looks feasible for antennas up to diameters of 15 m to 20 m. Inflatable antennas also would have a place in this frequency regime. In addition, concepts that do not appear in the figure are the electrostatic control membrane and the preformed (unfurlable) membrane. The space-feed array system is questionable. Inherent losses in a phased array always tend to be high. The scanning capabilities of the phased array for large space antenna application is limited to approximately plus or minus 8 degrees. An 8-degree half-cone angle would seem well within the capabilities of the phased array and makes it an attractive alternative. The loss problem can be eliminated by placing low-noise preamplifiers at each of the elements. The problem of operating over different frequency bands within the low-frequency range (6, 10, 18, and 22 GHz) remains difficult for the space-feed arrays. The synthetic space aperture combines some of the attractive features of the aperture synthesis technique. The synthetic space aperture has definite promise for apertures greater than 20 m (up to 100 m), but would not be used for apertures less than 20 m.

In the medium-frequency range, channels at 37, 60, and 80 GHz are needed and 10-m-diameter reflectors with solid panels are feasible. The unfurlable or preformed membrane-type antenna is a candidate; the electrostatically controlled membrane also could be applicable, although it may be more applicable in the far term than the near term.

In the high-frequency range, frequencies of 100 GHz to 200 GHz must be accommodated. As indicated by the Science Panel, the 4.4-m-diameter reflector is feasible in the near term with an increase in size up to 10 m in diameter possible. More understanding of beam efficiency in this range is needed. Can high beam efficiencies be reached and maintained for off-axis scan angles when scanning to the edge of, or near, the limb of the Earth? Beam degradation obviously becomes a problem as soon as the scan goes off-axis. As soon as the beam begins to degrade, beam efficiency drops, quite rapidly in some cases. More study is needed here. In the area of scan and scan performance, subcategories include electronic, mechanical, and a combination of electronic and mechanical scan. Electronic scan obviously requires an array type of feed with electronic switching between feeds, feed elements, or a combination of overlapped feed elements. Mechanical scanning can be performed in two ways. By tilting the reflector only, an amplification factor of two (due to the reflection of the rays from the feed) is obtained. For example, a four-degree reflector tilt produces an eight-degree scan. With the 4.4-m-diameter antenna, the concern was that the stiffness and surface accuracy could not be maintained while performing mechanical scanning without introducing tremendously difficult momentum-compensation problems. With the combined electronic-mechanical system, a number of feeds (perhaps up to 10) could be placed in a line and, with a suitable f/D ratio of perhaps unity (and maybe less than unity for a 4.4-m reflector), the off-axis performance in the Coma lobe would not be too serious. With these 10 feeds, a swath of 10 times the antenna-beam width of the single feed could be created. Combining the two approaches provides a less mechanical scan.

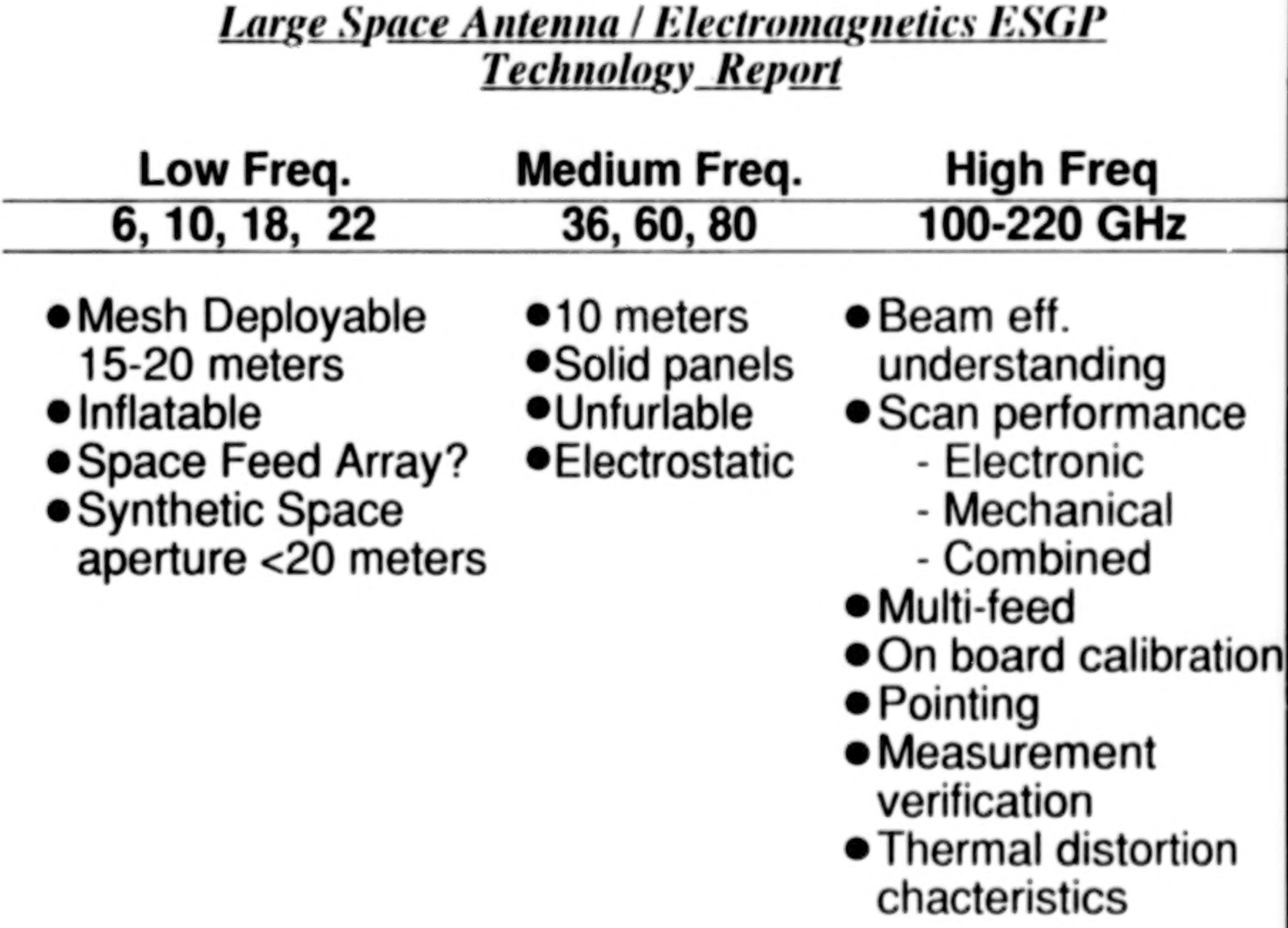

Large Space Antenna / Electromagnetics ESGP Technology Report

Low Freq.	Medium Freq.	High Freq
6, 10, 18, 22	36, 60, 80	100-220 GHz
● Mesh Deployable 15-20 meters ● Inflatable ● Space Feed Array? ● Synthetic Space aperture <20 meters	● 10 meters ● Solid panels ● Unfurlable ● Electrostatic	● Beam eff. understanding ● Scan performance - Electronic - Mechanical - Combined ● Multi-feed ● On board calibration ● Pointing ● Measurement verification ● Thermal distortion chacteristics

Figure 1

Report of the Microwave Sensor Technology Panel

Calvin T. Swift
University of Massachusetts

One of the first concerns (fig. 1) of the Microwave Sensor Technology Panel involved the OAST/OSSA partnership: is this a myth or a reality? Typically, OSSA needs its information yesterday and OAST looks into the far future (i.e., the year 2025). Both organizations could benefit researchers by establishing a common ground. One recent move that will help make this common ground a reality is the establishment of centers of technology, such as the one at the University of Michigan. This center focuses primarily on space science and seems to be a real move toward cooperation. Certainly much technology needs to be developed before it can be placed on the scientific stage. With the establishment of the space science center of technology as a precedent, perhaps a university center should be established in microwave and millimeter-wave Earth remote sensing. In surface observations at microwave and millimeter waves, very little advancement in sensor technology has been made since 1972. The SEASAT scatterometer was built then; the N-ROSS scatterometer looks exactly like it, except for the addition of a third stick in the digital processor. Part of the problem is that no advancement in the microwave sensor technology (which is OAST's turf) has been made. A microwave and millimeter-wave technology center might work with the NASA centers as shown in figure 1. OSSA would be in the driver's seat where the science is defined. Their blessing would be given to OAST who would define the technology and supply the funds to develop the technology through the technology centers. From past and present experience, NASA and the universities can work quite well together, especially when they work in a complementary situation. Here, a university center working in technology with Langley Research Center, Lewis Research Center, and the Jet Propulsion Laboratory (JPL) would also have the scientific know-how to work with Goddard Space Flight Center and JPL, with ties back to OSSA to further define the science.

The panel questioned the use of radar in geostationary orbit. No substantial technology concern exists, even though GEO is a long distance from Earth, but radar use should be looked into. The panel felt that a Phase A study was appropriate at this time. The study should look at the satellite in general, the requirements not only for ocean sensing but also for precipitation sensing, and combining options to satisfy more than one user. Antenna size and peak power are definite design drivers, and a Phase A study could better quantify these parameters. Radar and radiometers are generally complementary (more information can be obtained from using both than using either separately).

In addressing advances in millimeter component technology, the panel strongly advocates development of 100-GHz-plus amplifiers. Presently, with no front-end amplifiers, mixers inherently lose 3 dB off the top and typically a 6 dB conversion loss is observed. Better front-end components are needed. Another need is the development of aperture-synthesis techniques and systems (the University of Massachusetts has developed a flyable system) and the improvement of correlation techniques. As was discussed in the previous panel report, improved calibration techniques are a concern. Lastly, the development of a 10-mm deployable antenna that operates at 100 GHz has been rumored. If it does exist, it should be investigated and possibly even the technology should be advanced.

The bottom line is funding: how much is it going to cost to fly the spacecraft? A hypothetical plot of cost versus antenna diameter (fig. 2) is presented for the filled aperture and thinned array antennas. Obviously, zero diameter costs nothing. For the filled aperture, cost will increase in some nonlinear fashion until a critical diameter is reached. From this point the cost will escalate and the antenna will not be affordable. With the thinned array, the cost for the smaller diameters will be greater because so much money goes into receivers. However, a crossover point will occur where both will cost the same amount. Beyond this point, real savings will be obtained for the larger diameter antennas. Some funds should be expended to generate real cost/diameter curves (or a family of curves as a function of different frequencies) for the thinned array antenna to determine its best application.

Microwave Sensor ESGP Technology Report

- OAST/OSSA partnership required for mission success (establishment of University Research Center for THz technology)
- University Center must work with NASA Centers on microwave and millimeter wave Earth Remote Sensing

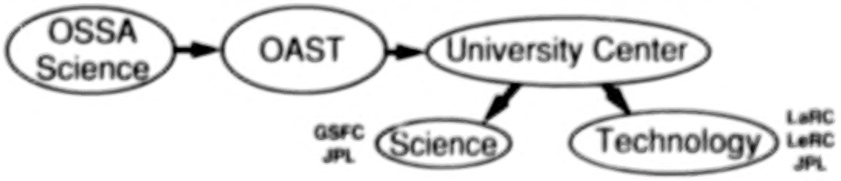

- No major technology problem in developing radar for GEO applications
  - Phase-A study needed
  - Antenna size / power is driver
  - Radars and radiometers are complementary
- Millimeter wave technology required
  - Develop 100+ GHz amplifiers
  - Integrated front end design

- Development of aperture synthesis (systems) required

- General:
  - Improved calibration techniques required
  - Deployable antenna technology at 10 m, 100 GHz
  - Trade-off of aperture development , filled aperture vs. thinned array

Figure 1

TRADE-OFF OF APERTURE DEVELOPMENT

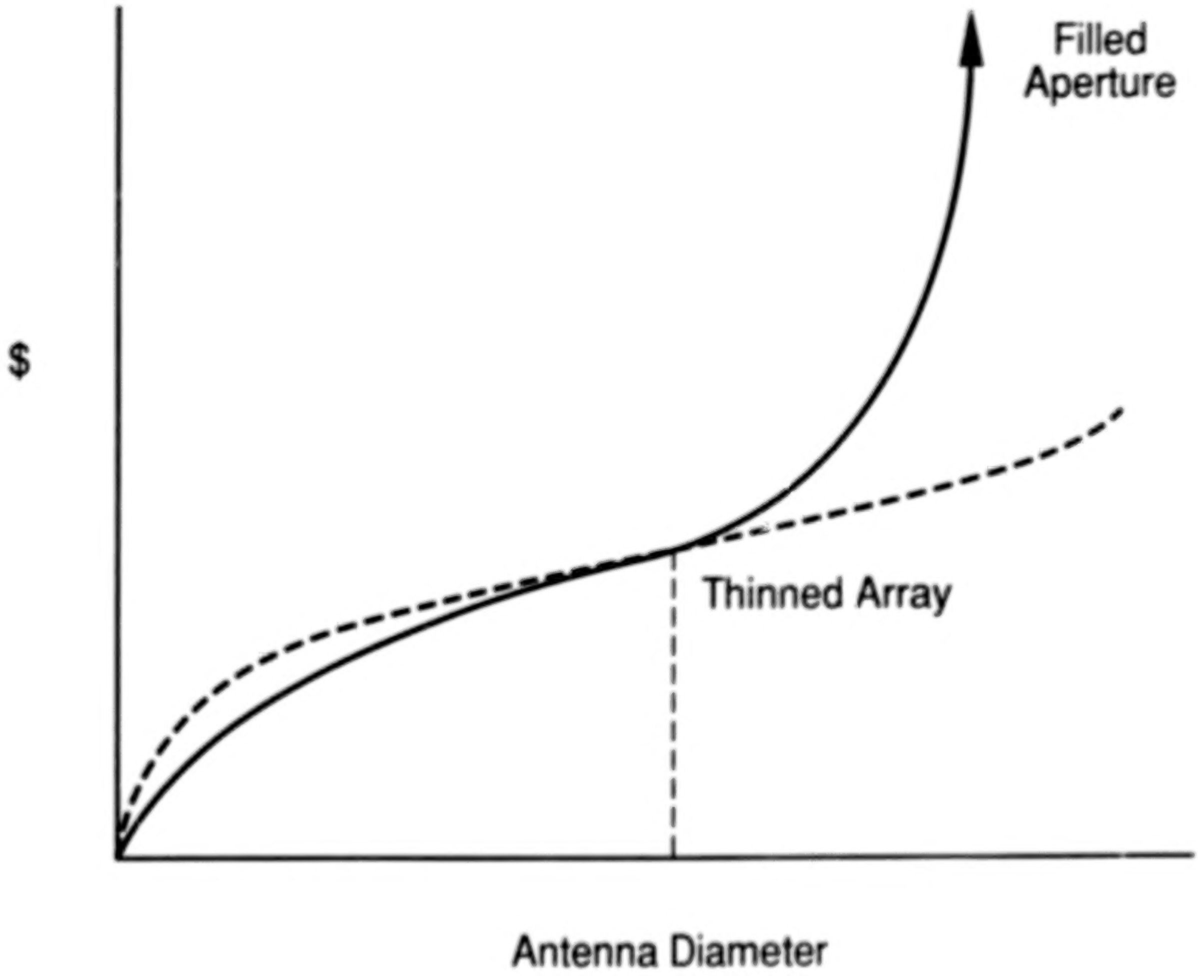

Figure 2

Report of the Optical Metrology Technology Panel

Sharon LaFleur
NASA Langley Research Center

The consensus of the Metrology Panel was that the requirements for metrology or sensors for reflectors and large space structures are either not defined or ill-defined. The first task that should be accomplished is to better define the mission requirements and then to more specifically define the RF system requirements. Langley Research Center learned a valuable lesson in developing an optical sensing system for the hoop-column antenna. First, a control for the hoop-column system was developed under the premise that the surface and other portions of the structure could be actively controlled. Then the antenna was developed, with the assumption that a sensor would be available at the time of flight, and it was expected to be flown. Unfortunately, no sensor was available. Last year, an optical metrology group met at Langley to assess the needs of many different programs in terms of optical metrology, including the hoop/column antenna. The good news is that sensors capable of making the measurements are available, but the systems integration and calibration problems are horrendous.

As for the capability of existing technology (fig. 1), it is fairly safe to say that the skill exists to measure $\lambda/50$ at 1 mm or 1 arc second in angular resolution. There are different types of optical sensing systems which are capable of these measurement accuracies.

The technology exists for building the measurement system for the ESGP, and it should be built to demonstrate its capability using ESGP requirements. Specific numbers (measurements parameters) have been quoted as essential. Initially, we need to study what optical sensing systems are available, then we need to build the sensors. The systems integration/calibration problem will be difficult. The sensing system ultimately will be a combination of many different sensing systems.

The panel felt that two major issues remained. The first issue is antenna pointing accuracy and stability. Although a separate issue, sensor measurement needs exist in connection with pointing accuracy and stability. The second issue is, of course, the structure deformation and vibrations which were focused on in this meeting.

Optical Metrology ESGP Technology Report

- Capability of existing technology is:

  λ / 50 for λ = 1mm
  or
  angular resolution of 1 arc second

- Technology exists for ESGP but measurement system needs to be built to demonstrate capability using ESGP requirements

- Remaining issues for ESGP
  - Pointing accuracy and stability
  - Structure deformations and vibrations

Figure 1

Summary of Questionnaire Responses

1. What is the state of technology readiness in Large Space Antenna Systems, Microwave/ Millimeter Wavelength Sensors, Adaptive Phased Array Systems, and Optical Metrology to meet the science objectives for the proposed ESGP mission? (Comment on areas of interest)

- Large Space Antenna Systems
  - Technology demonstrated for diameters up to 15 meters at frequencies up to 12 GHz. (Possibly 20 to 30 GHz with improved mesh technologies)
  - Operational systems technology diameters at 5 meters, 20 GHz
  - More technology required in self-rigidized, inflatable reflectors
  - Multiple Beam Antenna technology demonstrated for 20/30 GHz solid reflectors
  - Solid Aperture Antenna technology 4 to 5 meters (without wide scanning capability)
- Microwave Sensors
  - Receiver technology demonstrated at 183/118/60 GHz
  - Signal correlators: 100 MHz analog / 100 MHz digital with 30dB dynamic range
  - Further development needed in low noise amplifiers, microwave integrated circuits for radiometers (60 to 183 GHz) mixers, all front-end components
- Electromagnetics / Adaptive Phased Arrays
  - Phased Array technology for remote sensing is lagging
  - Development required for unfilled array configurations
  - Synthetic Aperture Radiometer system performance analysis needed
  - More analysis needed on beam efficiency considerations / requirements for large-aperture, millimeter wave radiometers
- Optical Metrology
  - No responses to questionnaires

. What high-risk technology areas are not likely to be ready for the ESGP mission even if additional funding is made available?

- Lower frequency antenna arrays will not be ready for near term ESGP platform
- Assembly of large aperture antenna system in space and installation of active alignment system
- Synthetic Aperture concept technique for mm wave applications and near mm wave frequencies, especially for sounding applications where absolute accuracy and calibration requirements are important
- Very high (<10 km pixel) filled apertures (~30 GHz) imaging radiometer
- Filled apertures > 15 meters

3. What high-risk technology areas are likely to be available for ESGP if additional funding is made available?

- Multi-channel, cluster feed technology for limited scanning for reflector with F/D>1
- Improved low-noise amplifiers integrated with beam forming networks (60 - 183 Ghz)
- Variable / controllable amplitude and phase modules for phased arrays
- Manufacturing capability of mm wave antenna surfaces, etc..
- 10-meter diameter mm wave antenna structures
- Thinned-array concepts with data processing techniques
- Solid aperture with contour error control (fab stage) and mechanical scanning and momentum compensation to address near term
- Low-noise mixers and HEMTs at mm wavelength
- Quasi-optical multiplexing techniques to reduce front-end losses
- Digital correlation processor for synthetic aperture Interferometric Imaging radiometer

4. What programmatic and engineering steps would you suggest for demonstrating the technology readiness to impact the ESGP System Architecture?

- Prioritization of technology needs for ESGP
- Establish a 5-year technology development plan with resource estimates
- ESGP Science Steering Committee assign project directives to selected individuals
- Form a project team for advocating technology development and enlist support from National Science Foundation
- Fund following tasks:
  - LNA development at 118 GHz
  - System study for an unfilled aperture for performance projections with a filled aperture
  - Microwave integrated circuit (MIC) radiometers to reduce size and power requirements
  - Development of a 10-meter mm wave deployable antenna
  - Development of a 4~5 meter diameter solid aperture antenna for testing, i.e. thermal distortion model and beam chacteristics
- Conduct system study of space implementation of Synthetic Aperture Interferometric Imaging radiometer
  - Correlations
  - Antenna configurations
  - Antenna position knowledge
  - Distributed phase-locked oscillators
  - Sensitivity analysis
  - Image reconstruction algorithm (selective nulling of of Sun)
- Development of ground-based / aircraft prototype to demonstrate Synthetic Aperture concept with 2-D imaging and with many (50-100) pixels
- A basic study needs to be done to bring together the actual limitations of large aperture system at geostationary altitudes
- Need to determine cost vs. frequency and the results of study need to be compared against benefits of optical and infrared systems
- Establish a university center to consider advanced systems concepts; this center could work with industry to generate new concepts and assess candidate concepts

Concluding Remarks

CONCLUDING REMARKS

Martin Sokoloski
Information Sciences and Human Factors Division
NASA Office of Aeronautics and Space Technology

With reference to the relationship between OAST and OSSA, there was a non-interaction in the past but that has changed in the last couple of years.

OAST has a large program in submillimeter wave technology, heterodyne technology, and mixers, and I was hoping that some of this technology could be used in the heterodyne sensor area. For instance, one speaker is using mixing and heterodyning at a number of these frequencies, and very cleverly is using diplexers and doubling and tripling in order to cover a large percentage of these frequency regimes. This leads me to believe that we now have a reason for high school students to learn about lowest-common-denominator multipliers. We have a definite need for it here.

I hoped that a prioritized list of the various technologies would have been developed. For instance, we heard that spin stabilization is out in future NOAA missions; they are going to use three-axis stabilization. The end result is that mechanical scanning is very questionable. We also have to realize that the platform has instruments other than the radiometer aboard. I would be very shaky if I had to scan either the 4.4-m- or the 15-m-diameter antenna (for the lower frequencies) with mechanical scanning only. I would be even more apprehensive if I had a mesh antenna with only mechanical scan of the possible deformations, with no way to affix and correct the large-fiber mesh, and I opted not to go to phased arrays to fix the far field. So, indeed, we need to develop a funding strategy.

In addition, we have to pursue some short-term technological fixes for OSSA. It appears that the 4.4-m antenna is going to be the radiometer of choice for the first flight mission, and the lower frequencies will be addressed later. We need to determine which of the suite of antennas, phased arrays, partially filled apertures, and measuring metrology that have been described over the last two days will give the most science return for the least amount of money. Also, we must determine which one looks the most promising for the lower frequencies, and which one gets around the use of large filled antennas (if we want to obtain precipitation measurements at 10-20 GHz or ocean winds measurements at 10 GHz-37 GHz). These are vital scientific parameters that have been included by the science working group and which OSSA will eventually measure. We have our backs against the wall because the only radiometer that can measure these parameters with the required resolution is a large-aperture antenna. There were some key questions about the unfilled antenna; namely, how can we push that technology to a higher frequency? Is it possible to push it to higher frequencies and, if so, is it technically feasible? We need to put money into this area.

To sum up, I feel that we've had an interesting and productive two days here. I think that my colleague from OSSA was surprised at the amount of work that is really going on in OAST, especially some of the work in communications that obviously has application in this area. There are certain things that can possibly be used now, such as the massive computer code that is run on the Cray XMP at NASA Lewis Research Center to perform the entire simulation of a large structure in space and that ultimately gets down to deformations in the far-field pattern. This is a tool that can be used as soon as the antenna is funded.

CONCLUDING REMARKS

James Dodge
Mesoscale Atmospheric Research
NASA Office of Space Sciences and Applications

It is always difficult to sum up something like this workshop, with all of the technology presented over the last several days. I would like to express my appreciation for all of the time spent to educate me and to arrive at a consensus of what you have to offer for the geostationary platform opportunity. We have never met like this before and have never considered each other in the same time frame. OAST was always looking out into the future and OSSA was in the immediate present. Yet, we actually are considering what we have that we can use on the near-term and far-term geostationary platforms.

This workshop has presented a bewildering array of technology for someone who is more attuned, perhaps, to parameterization, the algorithms, and the interpretation of the data. So, some of these things are very hard for someone in my position to chose between, and you will have to help me as time goes by. When I came here, I knew we had the problem with large-filled-aperture solid antennas, and I had heard of mesh, panel antennas, and aperture synthesis. I have radio astronomy in my background and had hoped that aperture synthesis was the solution to the problem, especially for the lower frequencies. Some of the things I heard today, such as measuring every single beam and calibrating them independently, are a little frightening. It is much more comfortable to have a solid antenna, calibrate it once, and just move it. You may have underestimated the problem of momentum compensation with even the 4.4-m antenna. The crudest optical instrument planned for this platform is the GEOMODIS (geostationary moderate-resolution imaging spectrometer). It is undefined at this time, but the scientists want as many bands as they can get. They want to image the Earth simultaneously in 10, 15, 20 bands to investigate vegetation color, ocean color, water vapor, and clouds, and they want to measure it down to a half-kilometer resolution. That means when the big 4.4-m antenna or its feeds swing and stop, the remainder of the platform cannot deviate by one pixil (or a half-kilometer on the Earth). This is, of course, the worse case. With the GEOHYRIS (geostationary high-resolution imaging spectrometer), they are talking about resolution in meters, which is ridiculous. The GEOHYRIS may therefore be possible only from an airplane and impossible from a geostationary orbit. I'm looking forward to more work on the aperture systhesis technique.

The workshop presented much of the early antenna work related to synthetic apertures, but very little related to the calibration problem. I presume that the solution to the calibration problem can be obtained after considerable work, but if it can't be calibrated, from a radiometric point of view, it won't be of much use. Many different types of antennas, structures, and surfaces have been discussed; most were developed for communication or military purposes. To meet our requirements, more emphasis must be placed on the radiometer, careful calibration, stability, unchanging beam patterns, beam widths, and resistance to thermal distortion. I am pleased that so much work has already been done, but I think that, even for the near-term platform, phase A studies will be required.

I'd like to make a comment on the establishment of university centers for science and technology. We are in the midst of reviewing 450 Earth Observing System (EOS) proposals. We are literally inundated with proposals at this point, from single investigators to entire university departments (with as many as 30 co-investigators) that want to work on multidisciplinary Earth science. So, university centers of science and technology may come about naturally and the proposals may already be in relative to this issue.

OSSA is working with OAST and attending the various advisory committee meetings, trying to iterate the requirements from the science steering committee so that we can better define the ESGP system over the next few years.

NASA
National Aeronautics and Space Administration

Report Documentation Page

1. Report No.
NASA CP-3040

2. Government Accession No.

3. Recipient's Catalog No.

4. Title and Subtitle
Earth Science Geostationary Platform Technology

5. Report Date
July 1989

6. Performing Organization Code

7. Author(s)
Robert L. Wright and Thomas G. Campbell, Editors

8. Performing Organization Report No.
L-16612

9. Performing Organization Name and Address
NASA Langley Research Center
Hampton, VA 23665-5225

10. Work Unit No.
506-44-21-03

11. Contract or Grant No.

12. Sponsoring Agency Name and Address
National Aeronautics and Space Administration
Washington, DC 20546-0001

13. Type of Report and Period Covered
Conference Publication

14. Sponsoring Agency Code

15. Supplementary Notes

16. Abstract

This publication summarizes the needs and technology readiness presented at the Earth Science Geostationary Platform Workshop held at the NASA Langley Research Center, Hampton, Virginia, on September 21-22, 1988. The objective of the workshop was to address problems in science and in four technology areas (Large Space Antenna Technology, Microwave Sensor Technology, Electromagnetics-Phased Array Adaptive Systems Technology, and Optical Metrology Technology) related to Earth Science Geostationary Platform missions.

17. Key Words (Suggested by Author(s))
Earth science missions
Geostationary platforms

18. Distribution Statement
Unclassified - Unlimited

Subject Category 15

19. Security Classif. (of this report)
Unclassified

20. Security Classif. (of this page)
Unclassified

21. No. of pages
410

22. Price
A18

NASA FORM 1626 OCT 86

For sale by the National Technical Information Service, Springfield, Virginia 22161-2171

NASA-Langley, 198

399

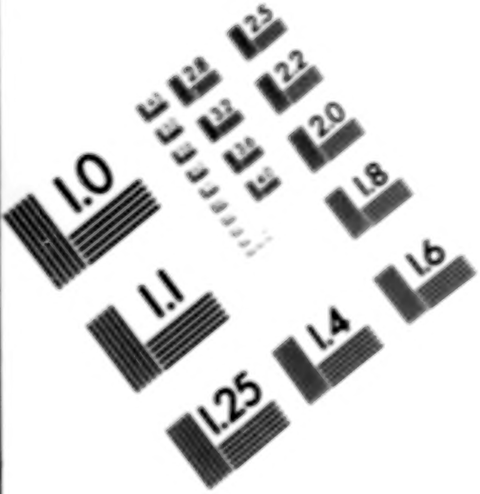
1.0
1.1
1.25
1.4
1.6
1.8
2.0
2.2
2.5
2.8
3.2
3.6
4.0

UNITED STATES OF AMERICA
GOVERNMENT PRINTING OFFICE

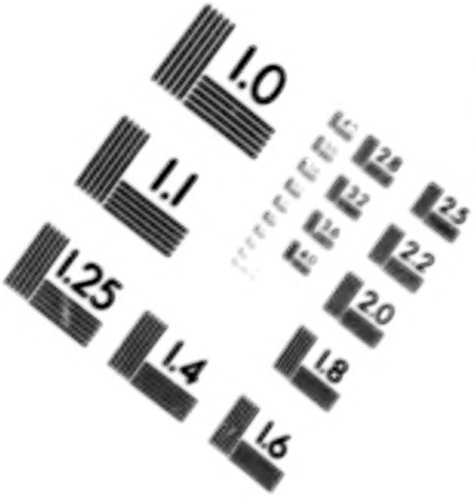
1.0
1.1
1.25
1.4
1.6
1.8
2.0
2.2
2.5
2.8
3.2
3.6
4.0

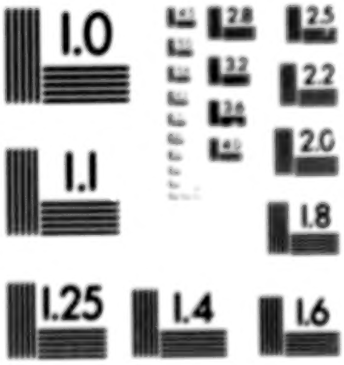
1.0
1.1
1.25
1.4
1.6
1.8
2.0
2.2
2.5
2.8
3.2
3.6
4.0

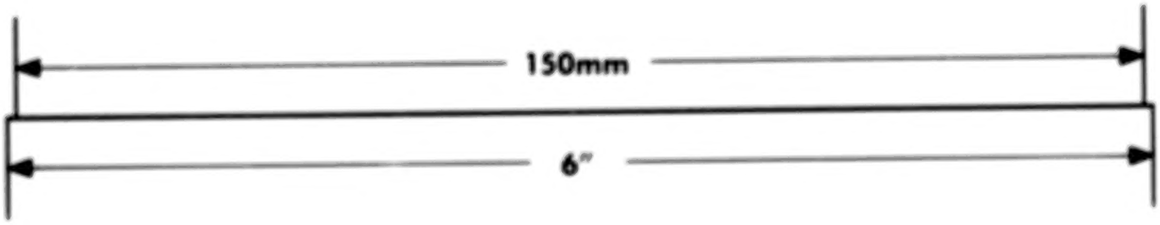

1.0
1.1
1.25
1.4
1.6
1.8
2.0
2.2
2.5
2.8
3.2
3.6
4.0

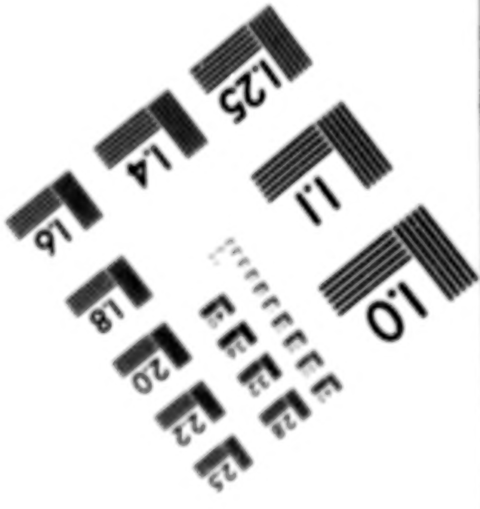
1.0
1.1
1.25
1.4
1.6
1.8
2.0
2.2
2.5
2.8
3.2
3.6
4.0